SANDIA REPORT
SAND2022-0199
Printed January 10, 2022

Sandia National Laboratories

Sierra/SD – Verification Test Manual – 5.4

Sierra Structural Dynamics Development Team

Latest Software Release:
5.2-Release 2021-09-15

Prepared by
Sandia National Laboratories
Albuquerque, New Mexico 87185
Livermore, California 94550

Issued by Sandia National Laboratories, operated for the United States Department of Energy by National Technology & Engineering Solutions of Sandia, LLC.

Available to DOE and DOE contractors from

U.S. Department of Energy
Office of Scientific and Technical Information
P.O. Box 62
Oak Ridge, TN 37831

Telephone: (865) 576-8401
Facsimile: (865) 576-5728
E-Mail: reports@osti.gov
Online ordering: http://www.osti.gov/scitech

Available to the public from

U.S. Department of Commerce
National Technical Information Service
5301 Shawnee Road
Alexandria, VA 22312

Telephone: (800) 553-6847
Facsimile: (703) 605-6900
E-Mail: orders@ntis.gov
Online order: https://classic.ntis.gov/help/order-methods

ABSTRACT

This document presents tests from the Sierra Structural Mechanics verification test suite. Each of these tests is run nightly with the **Sierra/SD** code suite and the results of the test checked versus the correct analytic result. For each of the tests presented in this document the test setup, derivation of the analytic solution, and comparison of the **Sierra/SD** code results to the analytic solution is provided. This document can be used to confirm that a given code capability is verified or referenced as a compilation of example problems.

CONTENTS

LIST OF FIGURES

LIST OF TABLES

Acknowledgments

The **Sierra/SD** software package is the collective effort of many individuals and teams. A core Sandia National Laboratories based **Sierra/SD** development team is responsible for maintenance of documentation and support of code capabilities. This team includes Dagny Beale, Gregory Bunting, Mark Chen, Nathan Crane, David Day, Clark Dohrmann, Sidharth Joshi, Payton Lindsay, Julia Plews, Brian Stevens, and Johnathan Vo

The **Sierra/SD** team also works closely with the Sierra Inverse and Plato teams to jointly enhance and maintain several capabilities. This includes contributions from Wilkins Aquino, Brett Clark, Murthy Guddati, Sean Hardesty, Chandler Smith, Benjamin Treweek, and Timothy Walsh.

The **Sierra/SD** team works closely with other Sierra teams on core libraries and shared tools. This includes the DevOps, Sierra Toolkit, Solid Mechanics, Fluid Thermal Teams. Additionally, analysts regular provide code capabilities as well as help review and verify code capabilities and documentation. Individuals directly contributing to the **Sierra/SD** documentation or code base during the last year include Samuel Browne, Victor Brunini, Pete Coffin, Jonathan Clausen, Gabriel de Frias, Mike Glass, Jacob Koester, Mark Merewether, Scott Miller, Kendall Pierson, Vincent Pericoli, Timothy Smith, and Alan Williams.

Historically dozens of other Sandia staff, students, and external collaborators have also contributed to the **Sierra/SD** product its documentation.

Many other individuals groups have contributed either directly or indirectly to the success of the **Sierra/SD** product. These include but are not limited to;

- Garth Reese implemented the original **Sierra/SD** code base. He served as principal investigator and product owner for **Sierra/SD** for over twenty years. His efforts and contributions led to much of the current success of **Sierra/SD**.
- The ASC program at the DOE which funded the initial **Sierra/SD** (Salinas) development as well as the ASC program which still provides the bulk of ongoing development support.
- Line managers at Sandia Labs who supported this effort. Special recognition is extended to David Martinez who helped establish the effort.
- Charbel Farhat and the University of Colorado at Boulder. They have provided incredible support in the area of finite elements, and especially in development of linear solvers.
- Carlos Felippa of U. Colorado at Boulder. His consultation has been invaluable, and includes the summer of 2001 where he visited at Sandia and developed the HexShell element for us.
- Danny Sorensen, Rich Lehoucq and other developers of ARPACK, which is used for eigenvalue problems.

- Esmond Ng who wrote *sparspak* for us. This sparse solver package is responsible for much of the performance in **Sierra/SD** linear solvers.
- The *metis* team at the university of Minnesota. *Metis* is an important part of the graph partitioning schemes used by several of our linear solvers. These are copyright 1997 from the University of Minnesota.
- Padma Raghaven for development of a parallel direct solver that is a part of the linear solvers.
- The developers of the SuperLU Dist parallel sparse direct linear solver. It is used through GDSW for a variety of problems.
- Leszek Demkowicz at the University of Texas at Austin who provided the HP3D[24] library and has worked with the **Sierra/SD** team on several initiatives. The HP3D library is used to calculate shape functions for higher order elements.

This work was supported by the Laboratory Directed Research and Development (LDRD) program.

EXECUTIVE SUMMARY

Verification and validation (V&V) of scientific computing programs are important at *Sandia National Labs* due to the expanding role of computational simulation in managing the United States nuclear stockpile. The complexities of structural response calculations used to analyze physical problems, the varieties of codes applied to the calculations, and the importance of accurate predictions when assessing field conditions demand confidence in the consistency and accuracy of computer codes. Confidence in the accuracy of the predictions arising from computer simulations must ultimately be gained through verification and validation.

The Sierra structural dynamics analysis code (**Sierra/SD**) plays a central role in the qualification of weapon systems and components for normal and hostile environments throughout the Stockpile-to-Target Sequence. **Sierra/SD** is used:

- To redesign weapon components.
- To certify weapon components and systems for target environments such as hypersonic vehicles.
- To certify that components will survive the thermal mechanical shock loads associated with hostile environments.
- To evaluate current stockpile issues, including issues associated with uncertainty quantification.
- To address many other problems that are encountered in stockpile management.

Furthermore, **Sierra/SD** is an engineering code that is used at Los Alamos National Laboratories (LANL), and elsewhere.

This document describes the verification plan for the **Sierra/SD** code. Additionally detailed description is provided for several key verification tests. The verification tests assure that the mathematics and numerical algorithms associated with functionality describing engineering phenomena in **Sierra/SD** are implemented correctly. The suite of verification tests will evolve as the functionality of **Sierra/SD** evolves.

Sierra/SD is developed in accordance with a set of Software Quality Engineering (SQE) practices.[11] These procedures conform to those outlined in,[58] but are tailored to **Sierra/SD** development. It is important to understand the role that these SQE practices play in the overall verification and validation effort.

1. PROCEDURES

1.1. Overview

This document contains a verification overview for the software package **Sierra/SD**. In contrast to the *User's Manual*,[46] which demonstrates how to use the code, and the Theory Manual,[47] which details the underlying mathematics of the code, the verification manual is a list of well documented verified examples demonstrating how the code performs on a subset of verification problems. In additional to the verification tests detailed in this document high confidence in the correctness of **Sierra/SD** is maintained by an extensive test suite, several code quality tools, and rigorous team processes. The intent is to verify each capability in **Sierra/SD**. This manual should be used to gain a level of confidence in the rigor for which **Sierra/SD** is verified for high consequence analysis. However, quality verification is a journey of continuous improvement. There may be gaps in the verification coverage. If there is a clear gap in the verification coverage that is essential to analysis, the **Sierra/SD** team should be contacted at sierra-help@sandia.gov.

1.2. Code Development Practices

The first step to a well verified code is code development practices that ensure all new code features are properly tested. The **Sierra/SD** team follows the laws of test driven development (TDD) coding practice as outlined in Clean Code.[35] The three laws of TDD are

1. You may not write production code until a failing unit test is written.
2. You may not write more of a unit test than is sufficient to fail.
3. You may not write more production code than is sufficient to fix the currently failing test.

Following these laws ensures that all new capability is covered by tests, and that all capability modified through user stories or corrected by user support is also covered by tests. However, these practices fail to ensure that *all* legacy capability is adequately covered, or that all permutations of capability are well verified. The **Sierra/SD** process for covering permutations of capability is outlined in 1.8. In addition to the enumerated TDD practices the **Sierra/SD** development team also uses code reviews, pair programming, and external beta testing as additional safeguards to prevent coding errors.

1.3. Overview of testing Pyramid

To efficiently maintain code quality, a test pyramid is needed. Most tests are fast and test individual capabilities. The pyramid is capped by a few large and complex tests. There are many types of tests for **Sierra/SD**: Unit, Fast (Continuous), Performance, Verification, Regression, and Acceptance. For tests to have value they most be run regularly and in an automated fashion. With the exception of a few large acceptance tests the entire **Sierra/SD** test suite is run nightly.

- *Unit Tests:* a test of an individual source code function. Unit tests are generally run through the Google GTEST framework. A unit test can be used to verify a given function has the correct behavior for every possible input. Unit tests are fast. **Sierra/SD** currently uses many thousand unit tests.
- *Fast Tests:* a test that must run in under ten seconds. Fast tests are run every hour on the release branch of the Sierra code base. This high run frequency allows quickly pinpointing any issues introduced into the code base. The fast test suite is designed to give a broad coverage of all core **Sierra/SD** features. **Sierra/SD** uses about a thousand fast tests.
- *Verification Tests:* a test that compares test outputs to an analytic result or confirms the test has some expected property (such as a convergence rate.) Verification tests are one of the most valuable test types and the verification test suite will continue to be expanded over time. **Sierra/SD** maintains about a thousand verification tests.
- *Regression Tests:* a test confirming that the code produces an expected output, but without rigorous mathematical demonstration that the output is indeed correct. Generally a test case is produced and then engineering judgment used to confirm the test case is behaving as expected. The test then confirms this approved behavior is maintained. An example would be the modal decomposition of a complex shape part. Currently **Sierra/SD** uses several thousand regression test. Regression tests are a necessity, but the **Sierra/SD** development team is moving over time to a larger balance of tests in the more valuable unit and verification categories.
- *Performance Tests:* a test used to confirm **Sierra/SD** maintains acceptable runtime and memory use bounds. These tests are expensive and **Sierra/SD** maintains about a hundred.
- *Acceptance Tests:* a test of an analysis use case provided by an analyst. Acceptance tests are the largest and most complex tests in the system. An acceptance test ensures the work flow for an entire complex analysis chain maintains functionality. As acceptance tests are expensive **Sierra/SD** maintains about a dozen to cover the most important and commonly used work flows.

1.4. User Support Process

The key to credible capability is a user support process that identifies, patches, and tests against any bugs found by **Sierra/SD** analysts. When a bug report is submitted a minimal representative example of the bug is produced by the developers and added as a test to the nightly test suite. After necessary development is done to resolve the issue the new nightly test ensures that the bug will not reappear in future releases.

1.5. Verification Policy for New Features

When new capability is added to **Sierra/SD**, the code development processes outlined in Clean Code[35] and Test Driven Development are followed. The new development *always* begins with a unit testing of new functionality. After completing the unit test, a self-documenting verification test is added that demonstrates the capability reproduces an analytical result. Additionally, regression tests may added that exercise the range of inputs of the capability. Once these tests are in place, an acceptance model, received from key analyst stakeholders, is run to ensure the capability behaves as expected and gives an acceptable result.

The **Sierra/SD** team migrated to a structure of individual test documentation maintained in the test repositories in 2013. The legacy formats are also included in this document, and eventually will be migrated to the new format. Thus though all verification tests are verified to a high level of rigor, not all verification tests are included in this verification test manual.

1.6. Nightly Testing Process

Every night the entire code base is compiled on multiple platforms with multiple compilers. Some subset of the nightly tests are run on each platform. Every fast and nightly test is run on the development platform, compiled with both debug/release and gcc/intel compilers. Additionally, all nightly tests are run on the Trinity surrogate (both Haswell and Knights Landing chips). The entire test suite (including performance tests) are run on intel-release on the primary HPC production platform dedicated to Nuclear Deterrence. Some subsection of the tests are run on experimental platforms, such as Darwin (MAC-OS), Broadwell, and Ride (GPU). These tests are useful because they may identify software quality issues that don't cause problems in the production platforms, but could in the future as new platforms move into production.

1.7. Other SQA Tools

In addition to the nightly testing process, other software quality tools are run nightly to check for possible code errors or gaps in testing coverage. These tools include the memory

checker Valgrind, the Feature Coverage Tool (FCT), and the Line Coverage Tool (LCOV).

1.7.1. Valgrind

Valgrind is a tool used to check for memory leaks and memory errors. A memory leak is when memory is allocated, but never freed while the program is still running. The existence of memory leaks within loops can lead to a simulation taking an increasing amount of memory as simulation time increases, eventually leading to code failure. A memory error represents the executable accessing memory that has not been allocated, or is otherwise out of bounds. A memory error generally results in unpredictable behavior, and can lead to fatal segmentation faults. Valgrind is run nightly on both the "nightly" and "fast" tests. All memory leaks and errors are eliminated for every sprint snapshot and release version of **Sierra/SD**.

1.7.2. LCOV

The coverage tool For **Sierra/SD**, LCOV, measures the code source line coverage of unit, fast, and nightly testing. The LCOV tool reports how many times each line of code is called for the respective test suite. For each file, folder, and executable in Sierra LCOV reports the percentage of lines in the code that are covered by at least one test. For example, as of the 4.56 release, unit tests cover 49.5% and all tests cover 87.9% of the code base. It is up to the development team to ensure that all new features are well covered. The **Sierra/SD** development team strives to improve test code coverage over time. However, 100.0% coverage is not always practical. Some uncovered code is either non-released research capability or deprecated legacy capability. Additionally, many error messages do not have a test that hits the error message, therefore the line of code with the error message may be uncovered.

1.8. FCT

For **Sierra/SD** the Feature Coverage Tool (FCT) creates three documents from an input file; the annotated input file, the two-way coverage graph and the list of best matching tests. The FCT can be used by analysts to assess the **Sierra/SD** verification rigor for a specific analysis. Additionally the **Sierra/SD** development team can use output of the FCT prioritize needs for verification test suite improvement.

The annotated input file shows the features (corresponding to input deck lines) that are used in verification tests (in green), regression tested (yellow) or untested (red). Developers and analysts can use this tool to see if for an analysis in question untested features are used and take action to mitigate or explain them. One mitigation strategy is to create a new verification test for the feature. An explanation is needed if the FCT has indicated a false positive (the FCT tool is helpful, but still in development).

The second document produced by FCT is the two-way coverage chart. The two-way coverage chart indicates for any two features if a verification or regression test exists that uses both of those features simultaneously. It can be impractical to add a verification test every possible feature combination. However, the two-way coverage report can be used to see if certain key feature combinations are tested together, such as damping in a transient analysis or strain output on shell elements. Lack of a two-way coverage test may indicate additional verification testing is needed, though engineering judgment must be applied to identify the most critical feature combinations.

The third FCT output is a of list the top 5 verification tests nearest to (in the sense of using the same capabilities) as used in the input file. If an analysis has a closely matching rigorous verification test is gives high confidence that the entire use case of the analysis and all feature combinations used are well verified in conjunction.

2. TESTS

2.1. Craig Bampton Reduction

The goal of the test is to verify both generation of a Craig-Bampton (CB) reduction and associated matrix sensitivities as well as the Taylor series expansion of the resulting matrices to generate a point evaluation of a parameter.

2.1.1. One Hex Models

The model is shown in Figure 1-1. There are two hex elements in the structure. The element on the right of the figure will be reduced to a superelement. The element on the left is the "residual structure," which uses the previously generated superelement. It is clamped on the left surface. Analysis is performed in two stages. First, the CB reduction is performed and sensitivity matrices dKr/dp and dMr/dp are generated. The reduction is performed in two ways: by constant vector, and by finite difference approaches. Following sensitivity analysis and model reduction, a system analysis is performed where those matrices are used in a Taylor series expansion.

For this analysis, we use the material density as the sensitivity parameter. The model is selected so there are no repeated frequencies.

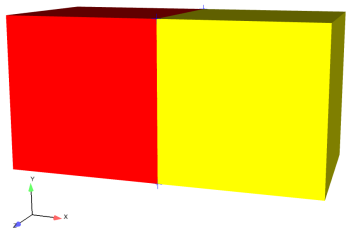

Figure 1-1. – One Hex superelement model

2.1.2. Analysis

2.1.2.1. Analytic Analysis

For a constant vector sensitivity analysis, the reduced order matrices are given by,

$$\tilde{k}_o = T_o^T K(p_o) T_o \tag{2.1.1}$$
$$\tilde{k}_1 = T_o^T K(p_o + \Delta p) T_o \tag{2.1.2}$$
$$\frac{d\tilde{k}}{dp} \approx \frac{\tilde{k}_1 - \tilde{k}_o}{\Delta p} \tag{2.1.3}$$

Here,

T_o	is the transformation matrix evaluated at p_o,
p_o	is the nominal value of the sensitivity parameter,
Δp	is the change of the sensitivity parameter,
$\tilde{k}$	is the reduced stiffness matrix, and
$K()$	is the unreduced stiffness matrix.

Identical relations exist for the mass matrix.

In our example, the density of a single element is the only sensitivity parameter. The density has no impact on the stiffness matrix, so $\tilde{k}_1 = \tilde{k}_o$, and $d\tilde{k}/dp = 0$. There is a change in the mass matrix, which will affect the system eigen frequencies.

For a **finite difference** sensitivity analysis, the relations are somewhat different.

$$\tilde{k}_o = T_o^T K(p_o) T_o \tag{2.1.4}$$
$$\hat{k}_1 = T_1^T K(p_o + \Delta p) T_1 \tag{2.1.5}$$
$$\frac{d\tilde{k}}{dp} \approx \frac{\hat{k}_1 - \tilde{k}_o}{\Delta p} \tag{2.1.6}$$

Here,

T_1	is the transformation matrix evaluated at $p_o + \Delta p$,

Because T_1 depends on the density, the reduced stiffness matrix is affected by the transformation. Interestingly enough, the reduced mass matrix is impacted less because of normalization of the fixed interface nodes, which counter the effect of increased mass. The 1,2 and 2,2 sections of the matrix do change.

2.1.2.2. Numerical Results

Figure 1-2 shows a comparison of the system level solutions as a function of density. Three curves are shown. The exact solution shows results obtained by rebuilding the superelement using the parameter, and without sensitivities. The other two curves evaluate dk/dp at the nominal value, and estimate the superelement contribution using a Taylor series expansion. Results are shown for mode 3. A comparison of the error is shown in Figure 1-3

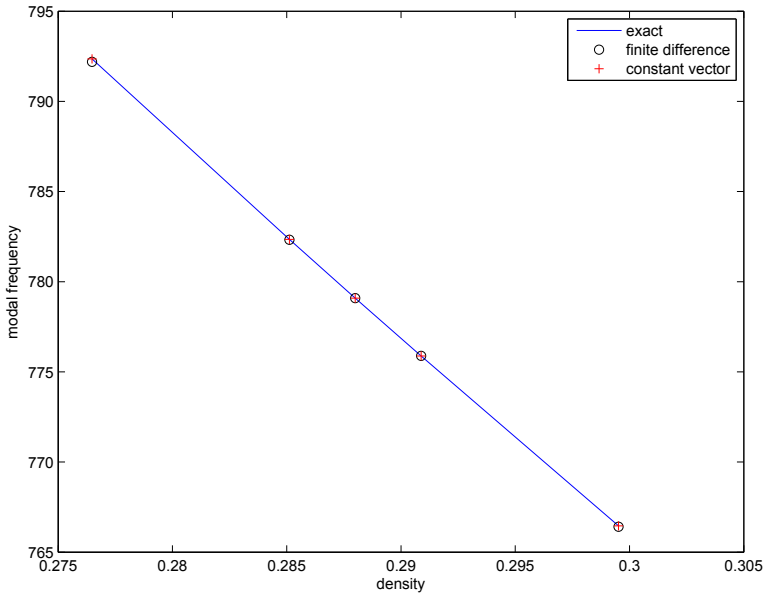

Figure 1-2. – Modal Frequency Variation with Density

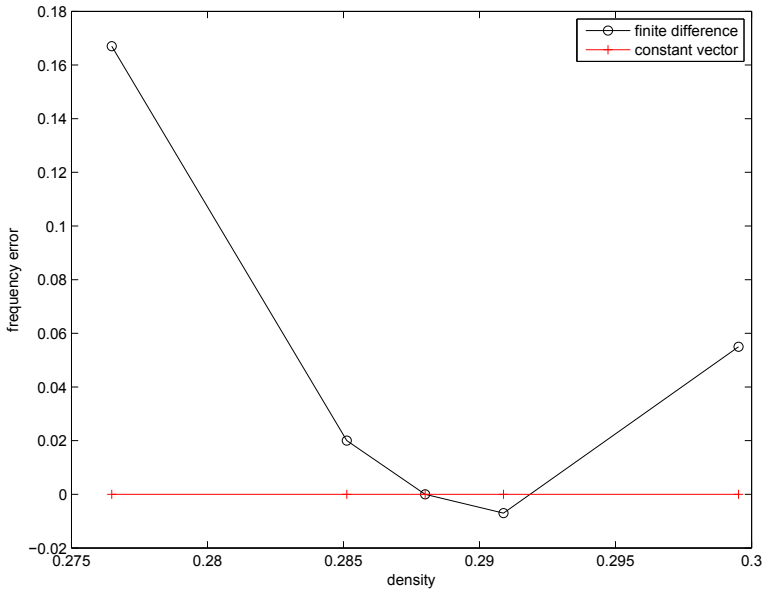

Figure 1-3. – Modal Frequency Error with Density

2.1.3. Summary

These analyses compare results for application of sensitivity matrices to superelement analysis. In this extremely simple example, the constant vector method is exact, while finite difference methods introduce a slight error. That is not a general case. For input deck see Appendix 11.4.

2.2. Superelement Damping

A superelement can have block proportional damping in Sierra SD.[1] A model was created consisting of two steel blocks acting as a cantilever beam. To incorporate block proportional damping into a system two parameters may be used, `blkalpha` and `blkbeta`. Blkalpha is mass proportional damping and blkbeta is stiffness proportional damping. For this model stiffness damping has the largest impact on the system. The damping parameters are set low enough for energy to enter block two, but high enough to absorb energy. A pressure load is applied on the top surface of block 1. A transient analysis is run with and without superelements and compared. Block 2 is reduced to a superelement and contains block proportional damping. The damping parameters for the superelement run are entered in the block section of the input deck during the CBR solution. Figure 2-5

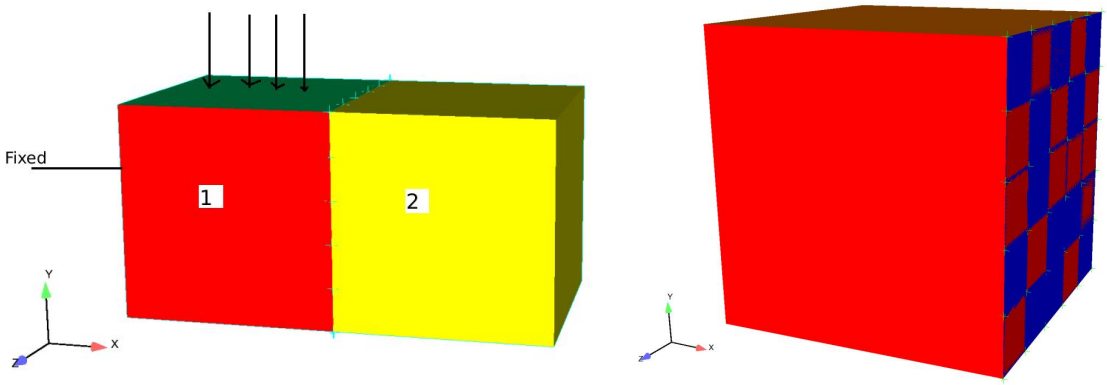

Figure 2-4. – Initial model and model with superelement

consists of three curves including the undamped full system solution, the damped solution with no superelements, and the damped solution with superelements. The damped model with superelements traces the damped model without superelements well. A full convergence study was not preformed as the two damped models will not match perfectly due to model truncation. For input deck see Appendix 11.5.

[1] System proportional damping does not create a damping matrix and cannot be used to generate a reduced order damping matrix.

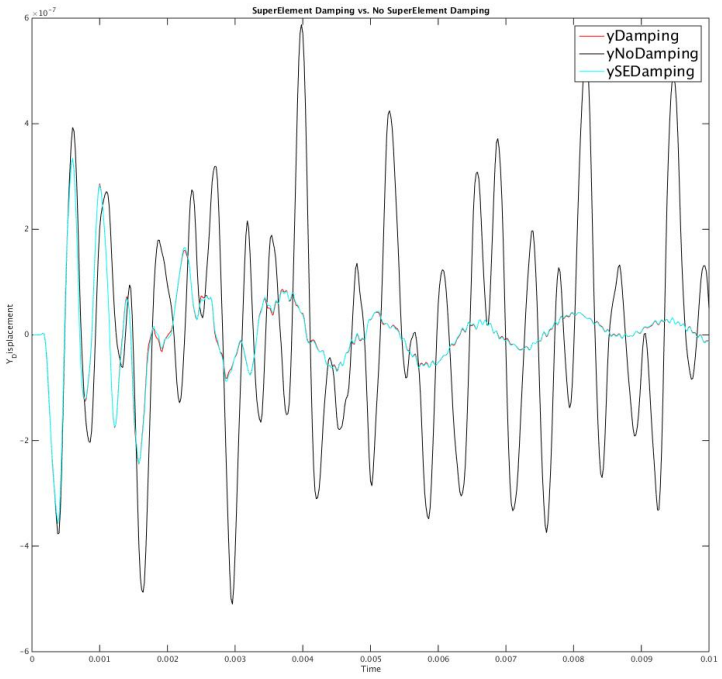

Figure 2-5. – Superelement Damping Results. Damped and undamped response of full system models compared with damped model of the reduced order model.

2.3. SierraSM to Sierra/SD Coupling

2.3.1. Deflection of Axially Loaded Beam

This verification test computes deflections of beams with axial preload. Comparisons are made between analytic solutions, nonlinear static **Sierra/SM** analysis, and linear static **Sierra/SD** analysis with geometric stiffness from preload.

The idealized beam model is shown in Figure 3-6. The finite element model geometry is shown in Figure 3-7. The red block is a uniform elastic material. The green dots represent nodes at which boundary conditions are applied. The left node is fixed in x and y to represent a pin. The right node is fixed in y and has the applied axial force P. The whole model is fixed in z. The gray blocks on each end of the beam are a very stiff material used to prevent large local deformations around the pinned nodes. The small yellow sideset at the center of the beam is used for applying a traction to generated the applied lateral force F.

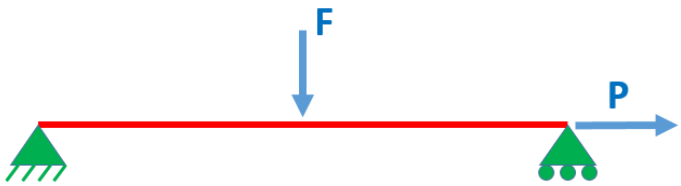

Figure 3-6. – Idealized Model Setup

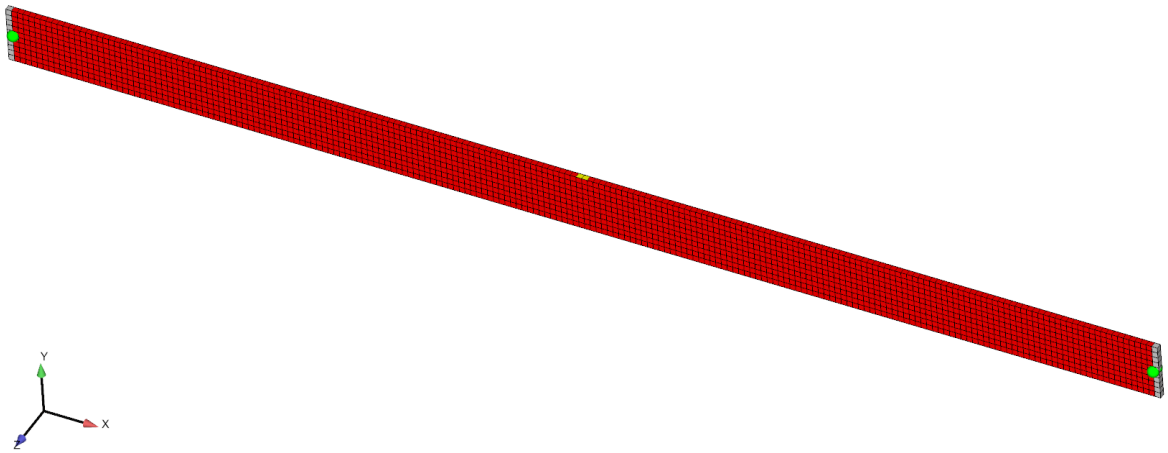

Figure 3-7. – Meshed Beam

Verification checks of the model vs. analytic solutions are made looking at the maximum lateral deformation δ under various conditions. This maximum lateral deformation always occurs at the beam mid-span. Deflections are kept small in order to approximate the linearized simple beam equations. The specific geometry and loads considered are given in Table 3-1. The test directory contains a Mathematica notebook file that gives the beam analytic solutions and detailed numeric results for the specific geometry and loads considered.

Table 3-1. – Model Parameters

Parameter	Value	Description
L	20	Beam Length in X direction
H	1	Beam Height in Y direction
W	0.1	Beam Width in Z direction
E	7.8e+7	Material Young's Modulus
F	2000	Lateral Force
P	-5000, 0, or 5000	Axial Force

2.3.1.1. Basic Beam Deflection

The beam moment of inertial I is given by Equation 2.3.1.

$$I = \frac{WH^3}{12} \tag{2.3.1}$$

In absence of an axial load, the expected beam deflection δ_{bend} is given by Equation 2.3.2.

$$\delta_{bend} = \frac{FL^3}{48EI} \tag{2.3.2}$$

The expected numeric result for the geometry is $\delta_{bend} = 0.512$. **Sierra/SM** computes a value of 0.521 and **Sierra/SD** a value of 0.516. The discrepancy is due to limited mesh resolution and small deviations between idealized Euler-Bernoulli beam theory and the 3d model. Generally, the comparison is good, indicating that the finite element model closely aligns with the beam theory assumptions.

2.3.1.2. Beam Deflection with Axial Preload

With the addition of an axial preload P, an additional $P-\delta$ effect becomes relevant. A lateral deformation at the end of the beam causes the axial force P to generate an extra moment on the beam. When P is compressive, this extra moment magnifies the lateral

displacement. When P is tensile, the this extra moment reduces the lateral displacement. The analytic solution can be found by considering half the beam as a cantilever as shown in Figure 3-8. The equation for the displacement of a cantilever beam with an end load is given in Equation 2.3.3.

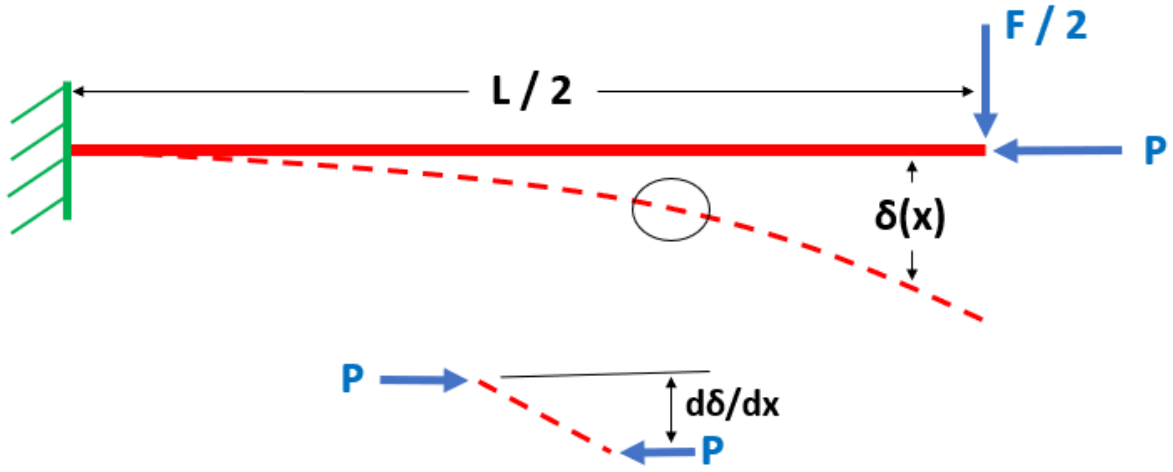

Figure 3-8. – Cantilever Beam With Axial Load

$$\delta_{bend}(x) = \frac{3FLx^2 - Fx^3}{6EI} \tag{2.3.3}$$

The axial preload applied to the deformed shape generates a distributed moment given in Equation 2.3.4.

$$M_1(x) = P\frac{d\delta_{bend}(x)}{dx} = \frac{PF(2L-x)x}{2EI} \tag{2.3.4}$$

The additional increment of deformation δ_1 of a cantilever subjected to the extra moment from Equation 2.3.4 is given in Equation 2.3.5.

$$\delta_1(x) = \int\int \frac{M_1(x)}{EI} d^2x = -\frac{FP(20L^3x^2 - 5Lx^4 + x^5)}{120E^2I^2} \tag{2.3.5}$$

This additional deformation causes additional cycles of moment and deflection given in Equations 2.3.6 and 2.3.7.

$$M_{n+1}(x) = P\frac{d\delta_n(x)}{dx} \tag{2.3.6}$$

$$\delta_{n+1}(x) = \int\int \frac{M_{n+1}(x)}{EI} d^2x \tag{2.3.7}$$

The exact result for expected deformation can be found by summing the series shown in Equation 2.3.8.

$$\delta(x) = \delta_{bend}(x) + \delta_1(x) + \delta_2(x) + ... + \delta_n(x) \tag{2.3.8}$$

This series converges to a high-precision value after a few terms (unless P is above the buckling load, in which case the series diverges). The Mathematica notebook included in the test directory sums many terms of the series to produce an exact analytic solution. The analytic and computed solution for tensile and compressive preload are given in Table 3-2.

The **Sierra/SM** nonlinear static solution can directly solve for the preloaded beam deflection. To solve in **Sierra/SD**, first **Sierra/SM** is used to apply the axial preload. The preload stress state is imported into **Sierra/SD** with the `receive_sierra_data` solution case. A lateral load is then applied as a linear static load in **Sierra/SD**. The preloaded stress state alters the element geometric stiffness allowing the correct ultimate deflection to be extracted in **Sierra/SD**.

Table 3-2. – Max Displacement Preloaded Beam

	Analytic Result	**Sierra/SM**	**Sierra/SD** after **Sierra/SM** Preload
Compressive Preload	0.741	0.757	0.748
Tensile Preload	0.392	0.399	0.394

A close match is obtained using both the direct **Sierra/SM** solution method and the **Sierra/SM** axial preload followed by **Sierra/SD** lateral load on the preloaded structure.

2.3.1.3. Preload Equilibrium and Preload Options

By default, the **Sierra/SD** `receive_sierra_data` solution case imports the preload stress state and computes the initial internal force produced by that stress state. The internal force computed from a stress state should be in equilibrium with the external force that caused that stress state. If **Sierra/SD** imports a stress state and applies the same external loads as were applied in **Sierra/SM**, the model should be in equilibrium and compute zero displacement in the **Sierra/SD** solution. The result for this case is given in the first row of Table 3-3. Some small deformation happens in **Sierra/SD**, but it is small compared to the nominal displacement of the system (0.512). The small discrepancy is related to incompatibilities in element formulation between **Sierra/SM** and **Sierra/SD** as well as

minor geometric nonlinearities in the **Sierra/SM** solution that cause the **Sierra/SM** equilibrium state to not exactly match the **Sierra/SD** equilibrium state.

As a corollary to maintaining equilibrium, if the preloaded stress state is read into **Sierra/SD** using default options, but no loads are applied in **Sierra/SD**, then the initial forces computed from the stress preload should snap the deformation back to the unloaded state. This result is given in the second row of Table 3-3. The comparison is good, with small discrepancies related to the formulation differences between **Sierra/SD** and **Sierra/SM**.

The option `include_internal_force` for the `receive_sierra_data` solution case controls whether the internal force associated with the stress state is added to the solution right hand side. By default, this option is true and this force is included, which accounts for the expected results in the first two columns of Table 3-3. This option can be turned off, in which case the resultant internal force from integrating the stress state is not included. If a model is preloaded in **Sierra/SM** and the preload-causing external forces are not included in the **Sierra/SD** model definition, then the `include_internal_force` option should be set to off. Effectively, this asserts that the preloaded state should be treated as an exact equilibrium state. The check on this result is given in the third row of Table 3-3. When the initial model state is treated as an exact equilibrium, exactly no displacement is produced in the unloaded **Sierra/SD** model.

A second check of the `include_internal_force` option is given in the fourth row of Table 3-3. In this example, a tensile preload is applied in **Sierra/SM**, and **Sierra/SD** imports this stress state. The **Sierra/SD** model turns off the initial internal force calculation, and consistent with that, does not apply the tensile external force. When this **Sierra/SD** model is subjected to lateral force, it produces the expected deformation of a cantilever with axial tension.

Table 3-3. – Equilibrium Test Cases

Loads	Options	Analytic Expected Max Displacement **Sierra/SD** Result	Computed **Sierra/SD** Result
Lateral load in **Sierra/SM** same **Sierra/SD**	Defaults	0.0	0.0023
Lateral load in **Sierra/SM**, no load in **Sierra/SD**	Defaults	-0.512	-0.513
Lateral load in **Sierra/SM**, no load in **Sierra/SD**	`include_internal_force=off`	0.0	0.0
Tensile load in **Sierra/SM**, lateral load in**Sierra/SD**	`include_internal_force=off`	0.392	0.395

2.3.1.4. Geometric Stiffness Options

Usually, the primary reason to include preload is to take into account the geometric stiffing or softening effects of that preload stress. **Sierra/SD** has an option `no_geom_stiff` to ignore this effect. This option can be used to debug models and to see whether the geometric stiffness is causing issues for solvers. Sufficiently large compressive stress can cause stiffness to go negative (physically buckling). Such states will often not solve or could cause stability problems. With the geometric stiffness turned off, **Sierra/SD** will still import the deformed shape and parameters that relate to the the material tangent stiffness. A check of the `no_geom_stiff` option is given in Table 3-4. Here, the deformation of the beam ignoring geometric stiffness is nearly the deformation of a beam without any axial preload. The slight deviation between the tensile and compressive preload state relates to reading the initial model geometry from the **Sierra/SM**-deformed shape, which is slightly different for the compressive and tensile preloads. This result demonstrates that for this example, correct calculation of geometric stiffness is very important to obtain analytic results, while use of the deformed state has very little effect.

Table 3-4. – Geometric Stiffness Test Cases

Loads	Options	Analytic Expected Max Displacement **Sierra/SD** Result	Computed **Sierra/SD** Result
No preload, lateral **Sierra/SD** load		0.512	0.516
Compressive **Sierra/SM** preload, lateral **Sierra/SD** load	no_geom_stiff	0.741	0.515
Tensile **Sierra/SM** preload, lateral **Sierra/SD** load	no_geom_stiff	0.392	0.517

For input deck see Appendix 11.20.1.

2.3.2. *Preloaded Beam Eigen Mode, Abaqus Comparison*

This is a verification test comparing Abaqus to Salinas using selective deviatoric hex8 elements. The geometry of this model can be seen in Figure 3-9. The model is a bar that is fixed on one end and constrained in the y and z direction on the other. A prescribed displacement is applied in the x direction in Adagio, and then a modal analysis is performed in Salinas. For verification, the first 4 modes are compared to the Abaqus finite element code. The Eigenvalue results are shown in Table 3-5.

Figure 3-9. – Geometry of Bar

Table 3-5. – Beam Preload Verification

Mode Number	Salinas	Abaqus
1	1834.47	1834.50
2	10175.2	10176.0
3	12469.1	12472.0
4	12469.1	12472.0

2.3.3. *Preloaded Plate Eigen Mode, Abaqus Comparison*

This example is a similar to the previous model, except that it has the geometry of a plate, as shown in Figure 3-10. The plate consists of selective deviatoric hex8 elements and is fixed on one side and constrained in the y and z directions on the other. A prescribed displacement is applied in the x direction in Adagio, and then a modal analysis is performed in Salinas. For verification, the first 5 modes are compared to the Abaqus finite element code. The Eigenvalue results are shown in Table 3-6.
The path to these verification tests is
`Salinas_rtest/verification/adagio_coupling/barModelPreload`.

For input deck see Appendix 11.20.2.

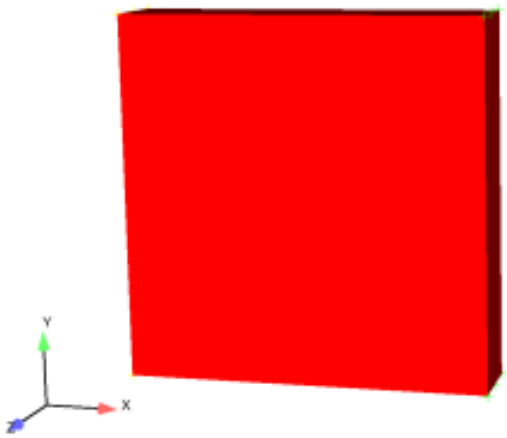

Figure 3-10. – Geometry of plate

Table 3-6. – Plate Preload Verification

Mode Number	Salinas	Abaqus
1	1380.37	1406.60
2	1834.47	1834.50
3	5208.10	5212.80
4	7234.86	7236.60
5	8911.89	8914.00

2.4. Eigenvalue Restart with Virtual Nodes and Elements

A transient restart model was created and tested including virtual nodes and elements, tied joints and superelements. The model is shown in Figure 4-12. For restart analysis two solution cases and input decks are needed. First, a restart=write solution where the desired amount of steps are analyzed and a output file is created with results. Second, a restart=read solution where the output file that was created is now read in and analyzed to the new desired amount of steps. For this test the write file had 10 steps and the read in file had 20 steps. This test includes superelements, infinite elements, and tied joints. A truth model was constructed with no restart and used for verification. Figure 4-11 shows the comparison of the truth model with no restart and the model with restart.

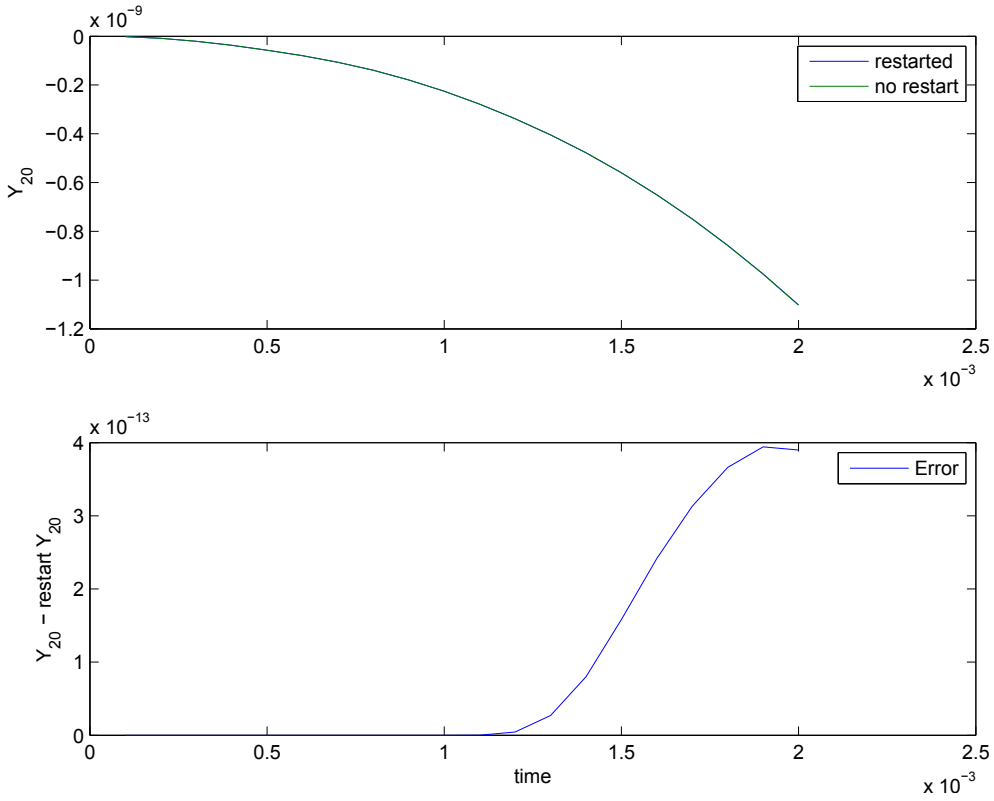

Figure 4-11. – Comparison between truth model and restart

In Figure 4-11 the 20th node in the y direction was compared between the two cases. The error is on the magnitude of $10^{-}13$ which is expected due to the solvers, therefore, validating transient restart capability in Sierra-SD.

2.4.1. Eigen Restart

This model was also analyzed using an eigen restart capability. The difference in this model is that there are no infinite elements only superelements and tied joints. This model

was compared to a truth model and is showing accurate results. The transient and eigen restart tests were created and run in serial and in parallel.

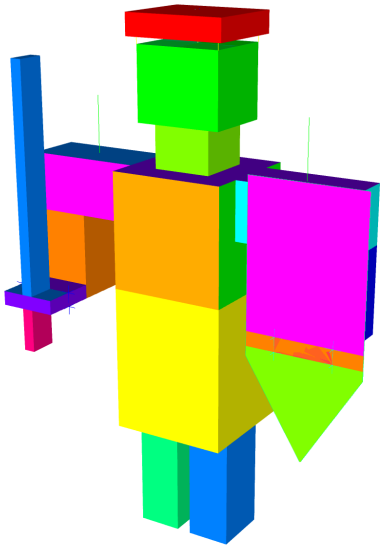

Figure 4-12. – Restart Model Geometry. “Ninjabot”

For input deck see Appendix 11.25.

2.5. Filter Rigid Modes from Loads

2.5.1. Introduction and Purpose

For some analyses, it is advantageous to remove the rigid body component of a solution. This is the case for a reentry body for example, which may have a static preload followed by a transient response with applied random pressures. The static preload is a singular system if the force is not properly self-equilibriated. The transient response is also troublesome. The true physics is complicated and includes a fluid structure interaction with random pressures as well as flight dynamics which stabilize the structure from rotation. The numerical analyst may represent that physics by a random pressure load. Unfortunately, that load can cause the body to rotate wildly, which is both nonphysical and distracting. As a solution, we filter the input forces to the body so that only self-equilibriated forces are applied. Because of the singularity, and small contributions to various linear solvers, a rigid body displacement may be generated. This component is filtered out after the solve, leaving a displacement that has no rigid body component.

2.5.2. Description of the Test

In this test, a small beam of Hex8 elements has a load applied transverse to one end. See Figure 5-13. Because there are no boundary conditions, the resulting system is singular for a statics solution. Figure 5-14 indicates the equilibriated forces applied to the structure, and the resulting deformation.

Verification requires determining the following:

1. The loads are properly equilibriated.
2. The output displacement vector contains no rigid body components.

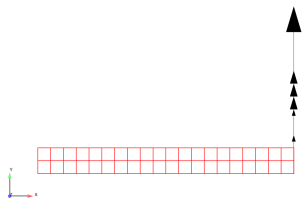

Figure 5-13. – Beam Loading

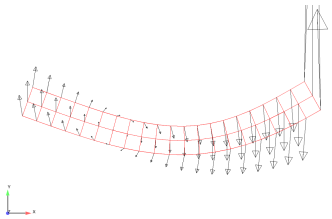

Figure 5-14. – Filtered Beam Forces and Displacements

2.5.3. Evaluation

The verification is done by Matlab. Forces and Displacements are loaded into the Matlab engine and simple calculations are performed.

1. The sum of each force component is zero (1.7e-6). This confirms that the translational portion of the force has been equilibriated.
2. The sum of cross terms is zero (1.25e-5).

$$\sum_{i}^{nodes} \vec{F}_i \times \vec{x}_i = 0$$

   This confirms that the net moments are zero. Thus, the loads have been properly equilibriated.

3. We confirm that the output displacement vector contains no rigid body components as follows.

   The net output translational components are summed for each component.

$$\sum_{i}^{nodes} \vec{u}_i = 0$$

   These components are less than 1e-10.

   We also confirm that the net moment is zero.

$$\sum_{i}^{nodes} \vec{u}_i \times \vec{x}_i = 0$$

   The net moment is less than 1.1e-5.

Thus, we have confirmed that the loads are self equilibriated, and that the resulting displacements are orthogonal to rigid body translation and rotation.

For input deck see Appendix 11.26.

2.6. Sensitivity to Parameters

Sensitivity to parameters is available for multiple solution types. The primary application is in eigen analysis where the semi-analytic solutions can provide significant computation and accuracy benefit over a finite difference approach. A script was developed for testing different parameters using the finite difference method in Sierra-SD. The script checks that, as the step size decreases, the finite difference approximation to the modal sensitivity converges to the value provided in the code. A simple model was developed and analyzed for verification. This model is two hex elements that are connected via a tied joint. The $Kz = elastic1e7 +/- 10$ parameter in the Joint2G block is where the sensitivity analysis is preformed. Figure 6-15 is a plot of the results and shows this capability. The Eigenvalue sensitivity information can be found in the result file and matches the value shown in Figure 6-15.

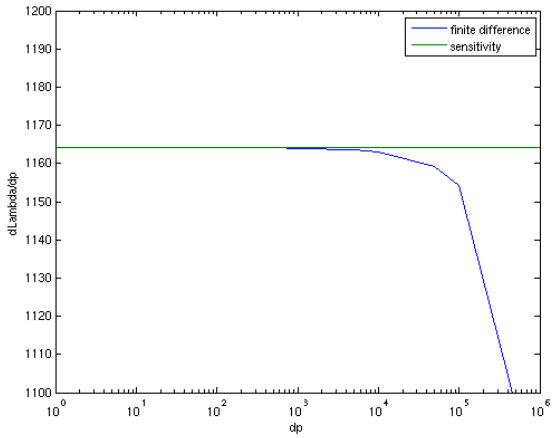

Figure 6-15. – dLambda/dp vs. dp

Figure 6-16 shows the frequency vs. *dp*. For input deck see Appendix 11.28.

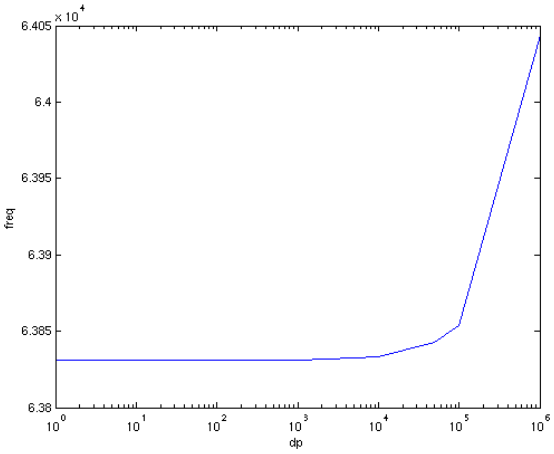

Figure 6-16. – Frequency vs.dp

2.7. Sensitivity Analysis with a Superelement

The goal of the test is to verify both generation of a Craig-Bampton (CB) reduction and associated matrix sensitivities as well as the Taylor series expansion of the resulting matrices to generate a point evaluation of a parameter. In this example, a more complex model is evaluated with two parameters. While the geometry of the model is more complex the structure still is linear in the parameters of interest.

2.7.1. Blade Model

The model is shown in Figure 7-17. The full model (including superelement and residual structure) is shown on the left. The next cut away shows only the residual structure in gray. A portion of that model is provided only for visualization. On the right is the model of the superelement which consists of quadrilateral and triangular shells. The interface nodes are in red. Analysis is performed in two stages. First, the CB reduction is performed and sensitivity matrices dKr/dp and dMr/dp are generated. The reduction is performed in two ways: by constant vector, and by finite difference approaches. Following sensitivity analysis and model reduction, a system analysis is performed where those matrices are used in a Taylor series expansion.

For this analysis, we use the material density and Young's modulus as the sensitivity parameters. There are no repeated frequencies, which avoids any issue of mode mixing for finite difference sensitivity.

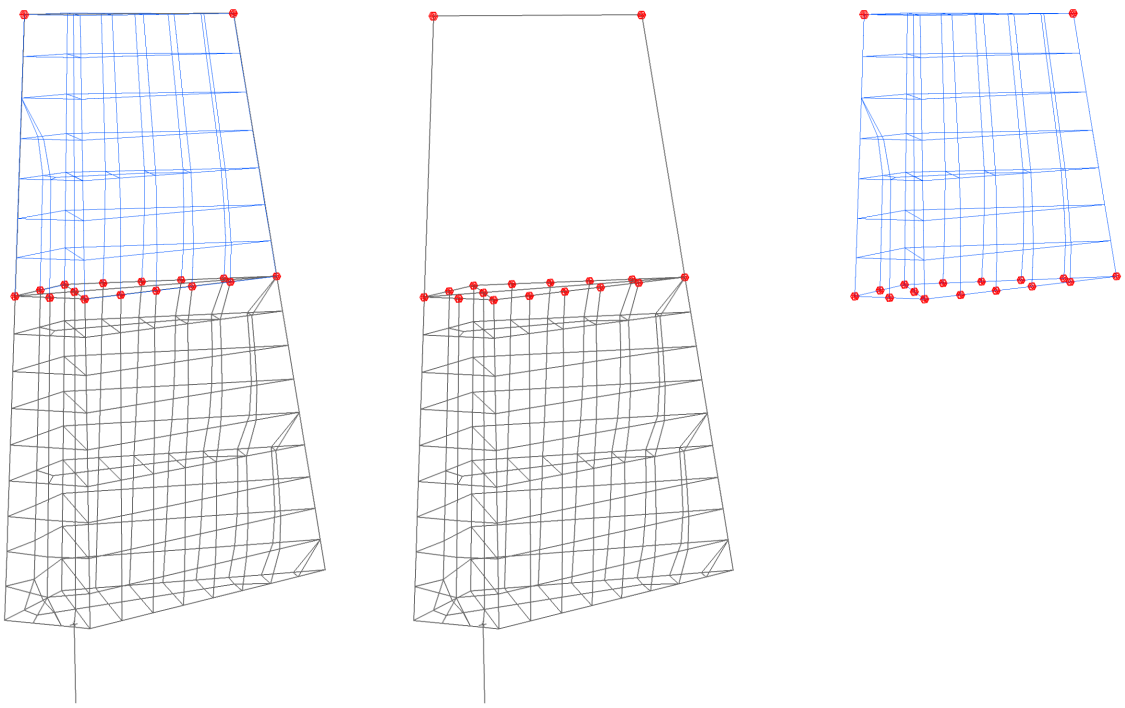

Figure 7-17. – Blade superelement model

2.7.2. Analysis

2.7.2.1. Analytic Analysis

For a constant vector sensitivity analysis, the reduced order matrices are given by,

$$\tilde{k}_o = T_o^T K(p_o) T_o \tag{2.7.1}$$

$$\tilde{k}_1 = T_o^T K(p_o + \Delta p) T_o \tag{2.7.2}$$

$$\frac{d\tilde{k}}{dp} \approx \frac{\tilde{k}_1 - \tilde{k}_o}{\Delta p} \tag{2.7.3}$$

Here,

T_o	is the transformation matrix evaluated at p_o,
p_o	is the nominal value of the sensitivity parameter,
Δp	is the change of the sensitivity parameter,
$\tilde{k}$	is the reduced stiffness matrix, and
$K()$	is the unreduced stiffness matrix.

Identical relations exist for the mass matrix.

For a **finite difference** sensitivity analysis, the relations are somewhat different.

$$\tilde{k}_o = T_o^T K(p_o) T_o \tag{2.7.4}$$

$$\hat{k}_1 = T_1^T K(p_o + \Delta p) T_1 \tag{2.7.5}$$

$$\frac{d\tilde{k}}{dp} \approx \frac{\hat{k}_1 - \tilde{k}_o}{\Delta p} \tag{2.7.6}$$

Here,

T_1 is the transformation matrix evaluated at $p_o + \Delta p$,

Because T_1 depends on the density and Young's modulus, the reduced stiffness matrix is affected by the transformation.

2.7.2.2. Numerical Results

Figure 7-18 shows a comparison of the system level solutions as a function of design parameter. We vary the density and Young's modulus together. Three curves are shown. The exact solution shows results obtained by rebuilding the superelement using the parameter, and without sensitivities. The other two curves evaluate dk/dp at the nominal value, and estimate the superelement contribution using a Taylor series expansion. Results are shown for mode 3. A comparison of the error is shown in Figure 7-19

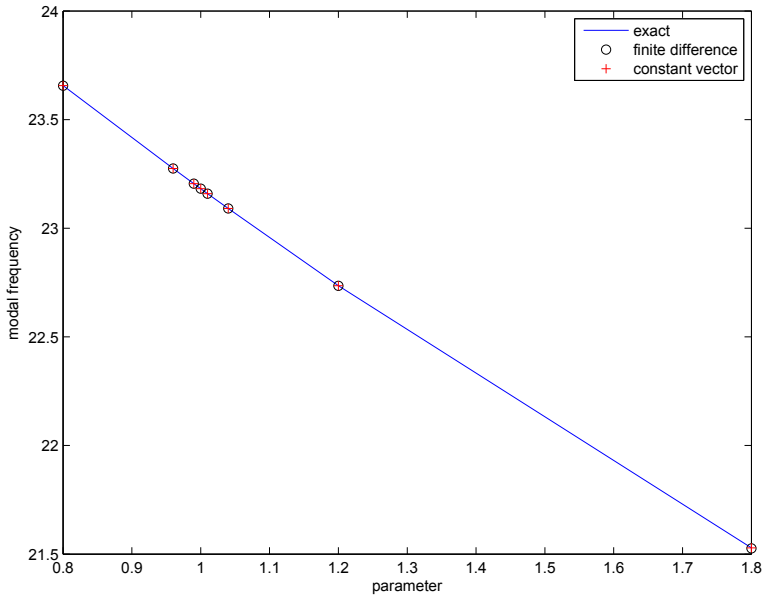

Figure 7-18. – Modal Frequency Variation with Density

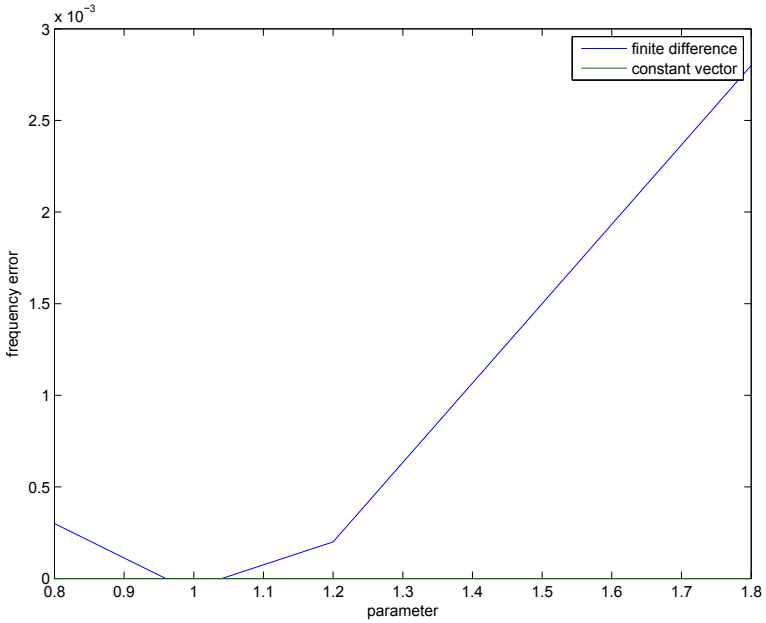

Figure 7-19. – Modal Frequency Error with Density

2.7.3. Summary

These analyses compare results for application of sensitivity matrices to superelement analysis. In this example, for which the superelement matrices vary linearly with the parameter, the constant vector method works extremely well. While not shown here, variations of a single parameter by itself returns very similar results.

One point of interest is that for large variations of the parameter, the finite difference method of computing sensitivities resulted in indefinite matrices that caused the eigensolver to fail. For input deck see Appendix 11.29.

2.8. Shock Tube

Analysis Type	Nonlinear Acoustics
Element Type	Hex8
Boundary Conditions	absorbing, fixed velocity
Keywords	nonlinear acoustics, run time compiler

2.8.1. Problem Description

This is the verification test of nonlinear acoustics.

2.8.2. Verification of Solution

The SierraSD nonlinear acoustics equation is the Kuznetsov equation. In the SierraSD Verification manual, see section 10.2 and specifically the subsection 10.3. Fubini's exact solution to a wave guide is used. A Matlab script, `shocktube_exact_solution.m` generates the exact solution.

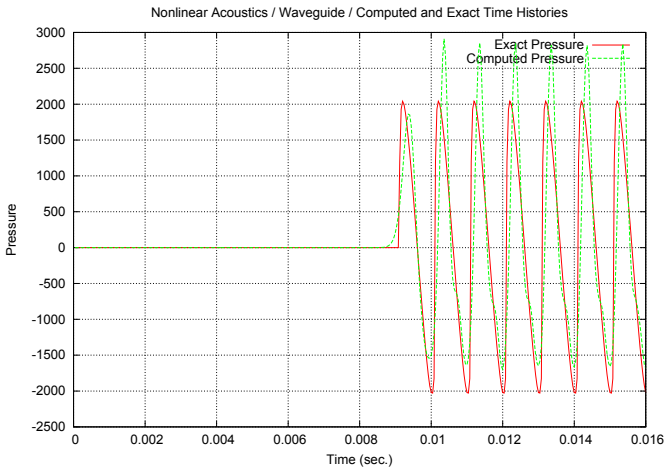

Figure 8-20. – Shock Tube

For input deck see Appendix 11.30.

2.9. Beam-Beam with Craig-Bampton Reduction

This model exercises CBR reductions on a beam. The full model consists of 200 beam elements, each of length 0.01, for a total length of 2 units. The beam is free floating in the X direction, but constrained in all other directions. It is driven by a simple force on the left ($x = 0$) end. The load is a saw tooth force with a period and duration of $1.5\,ms$. The system is integrated with a fixed time step of $0.1\,ms$.

An "equivalent" model is generated by separating the model into two equal sections of 100 elements each. The right hand side segment is converted into a superelement, and then attached to the left hand structure. The superelement includes the single fixed dof on the left end, and 90 internal generalized dofs representing most of the modes of the system. The loading and integration are identical to the full structure.

Figure 9-21 compares the X component of displacement on node 101 of both models. Node 101 is located at the junction of the superelement. Clearly the superelement and residual structure represent the solution very well. Figure 9-22 shows the difference of the solutions.

For comparison, Figure 9-23 compares results with a CBR model that includes no generalized dofs. As anticipated, the results are not nearly as good.

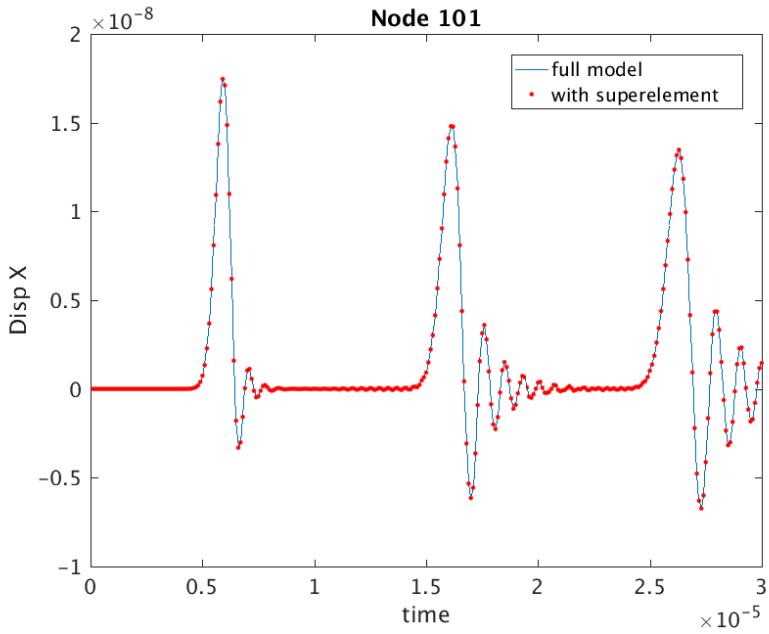

Figure 9-21. – Comparison of Full Model with CBR Reduction

For input deck see Appendix 11.36.

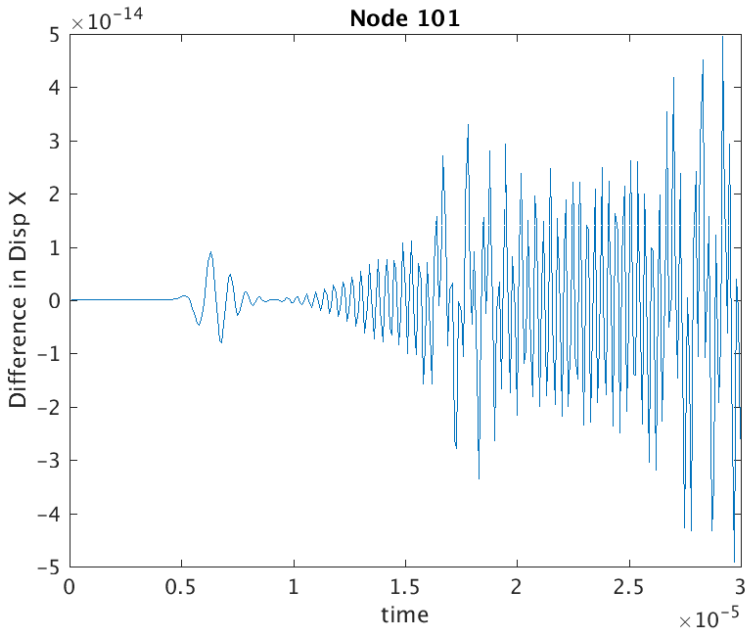

Figure 9-22. – Error in CBR reduction

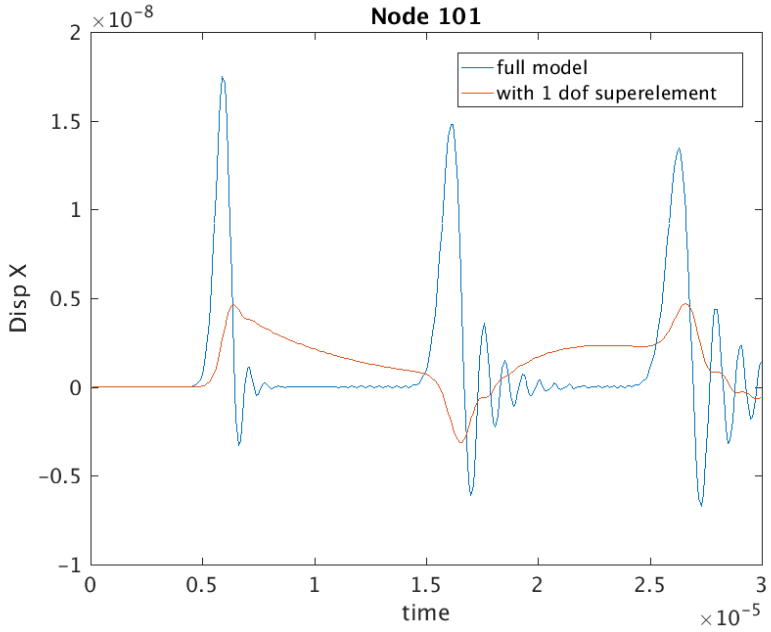

Figure 9-23. – Comparison of Full Model with Guyan Reduction. Without the generalized dofs, the comparison is poor.

2.10. Modal Force Loading

Modal Forces provide an alternative, body-based loading to a structure which can be useful for some solutions. These modal forces are the conjugate of modal force output in the `modaltransient` solution method.

Verification is performed by use of the modal transient method, and is shown in Figure 10-24. The model used is shown in Figure 10-25. The model is first run using physical inputs, and produces two output files: 1) the modal forces, and 2) the output displacements. The second run uses modal force as the input. Finally, the output displacements of the two modal transient runs are compared. Results are identical (except for round-off errors).

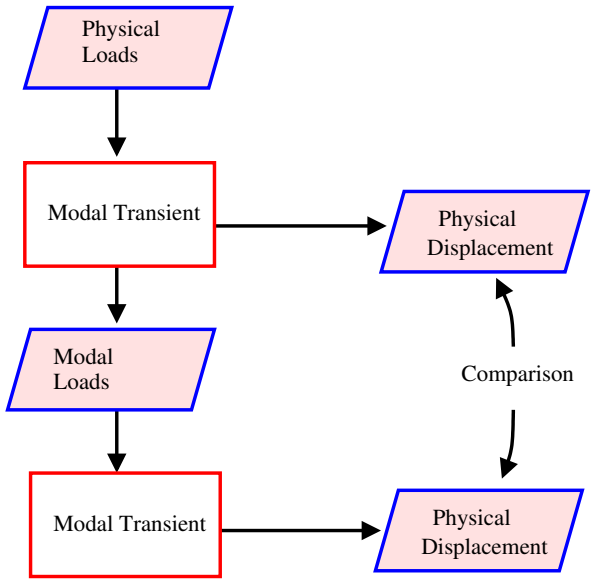

Figure 10-24. – Verification Process for Modal Force

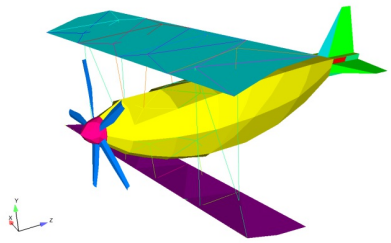

Figure 10-25. – Biplane Model

For input see Appendix 11.39

2.11. Lighthill Analogy - Helmholtz Resonator

The Lighthill tensor provides a source term for noise generation in aeroacoustic simulations. The Lighthill tensor captures noise generated by unsteady convection in flow in a fluids simulation. Sierra/SD produces a source term from the Lighthill tensor that is applied as a nodeset load in the pressure formulation of acoustics. Sierra/SD produces the Lighthill loading by reading in the time varying divergence of the Lighthill tensor using the `readnodalset` function. The divergence of the Lighthill tensor is used to create an equivalent elemental force vector. The divergence of the Lighthill tensor is provided from a Fuego incompressible fluids simulation.

Verification of the Lighthill loading is performed for the Helmholtz resonator shown in Figure 11-26 which has an analytic resonant frequency of 120Hz. The discretized mesh, material properties, initial and boundary conditions used in the Fuego simulation are shown in Figure 11-27. Fuego then calculates the divergence of the Lighthill tensor and writes this out to exodus as nodal data at variable time steps.

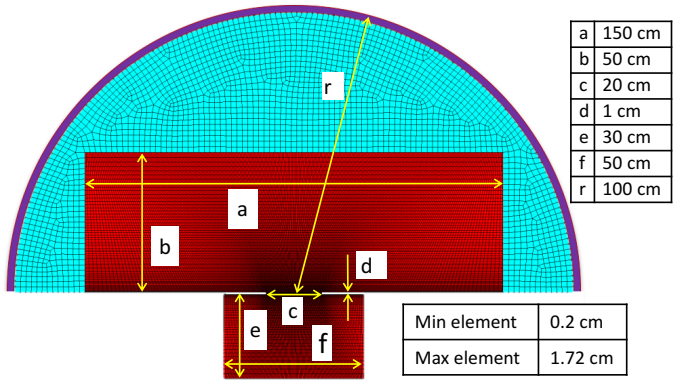

Figure 11-26. – Dimensions of Helmholtz resonator

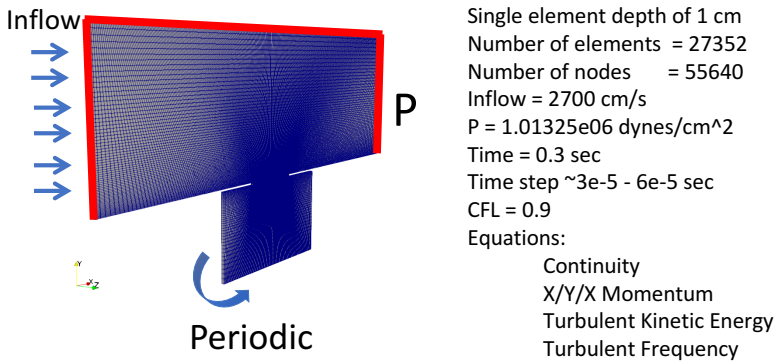

Figure 11-27. – Boundary and initial conditions for Fuego simulation

The Fuego output is used as input in Sierra/SD with the same discretization of the Helmholtz resonator shown in Figure 11-26 with an additional semi-circular domain in order to apply an acoustic boundary condition. Absorbing boundary conditions are applied

to the edge sideset of the semi-circular region, highlighted in red in Figure 11-27. boundary with absorbing boundary conditions eliminate the rigid body modes from the solution which can cause a which linear linear growth in the pressure field. The nodal DivT data on the Fuego domain is converted to nodeset data using the ejoin flag -convert_nodal_to_nodesets. The distribution factors for the new nodeset data are changed from 0 to 1. The Sierra/SD simulation reads in the time varying nodeset data from Fuego and interpolates it to the nearest time step either linearly or using the closest time step. The double divergence of the Lighthill tensor is then calculated and applied as a source term in the Sierra/SD transient acoustic simulation. Results for the Sierra/SD acoustic simulation using Lighthill loading are shown in Figure 11-28 for acoustic pressure versus time. An FFT of the pressure data is shown in Figure 11-29 with peaks at 61, 121, and 183. These resonances were also observed in the pressure data sampled in the rigid chamber of the Fuego simulation. The main peak is close to the analytic resonant frequency of 120Hz.

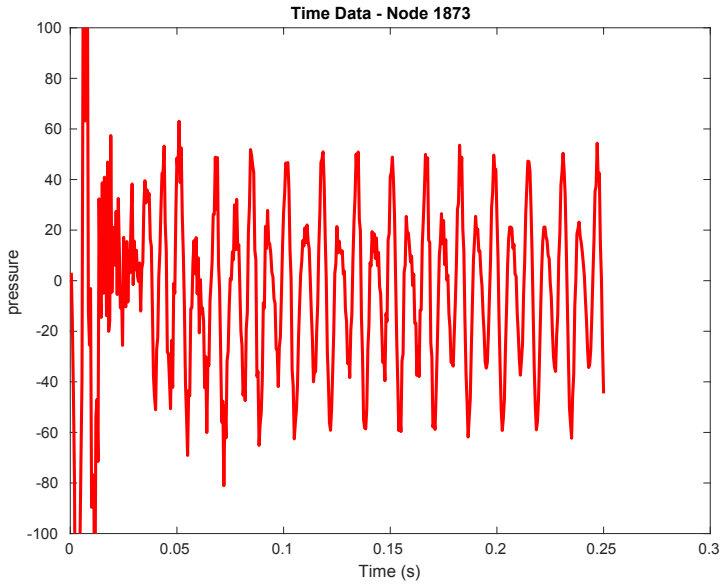

Figure 11-28. – Sierra/SD time history of pressure for Lighthill loading.

For input see Appendix 11.40

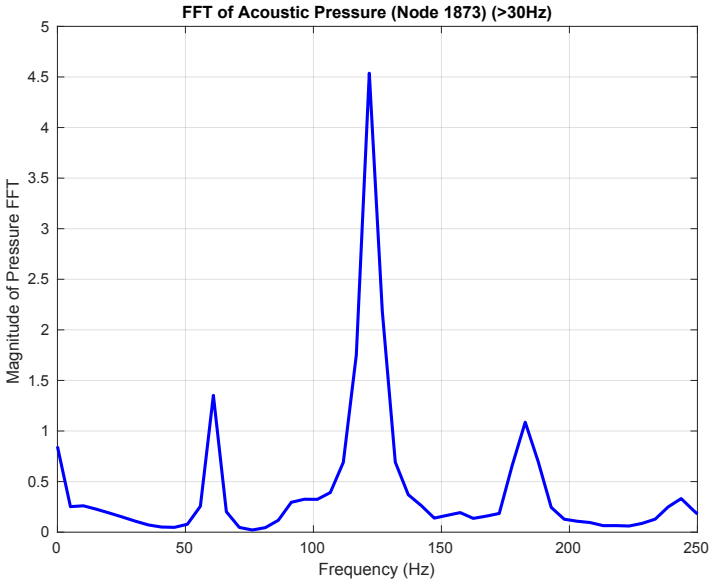

Figure 11-29. – FFT of Sierra/SD pressure data shown in Figure 11-28

2.12. Lighthill Tensor Verification

The Lighthill tensor provides a source term for noise generation in aeroacoustic simulations. The Lighthill tensor, $\mathbf{T}$, captures noise generated by unsteady convection in flow in a fluids simulation. Sierra/SD produces a source term from the Lighthill tensor that is applied as a nodeset load in the pressure formulation of acoustics. Sierra/SD produces the Lighthill loading by reading in the time varying divergence of the Lighthill tensor using the `readnodalset` function. The divergence of the Lighthill tensor, $\nabla \cdot \mathbf{T}$, is used to create an equivalent elemental force vector.

In this verification example we compare Lighthill loading to Point Volume Acceleration loading for a 1-D waveguide shown in Figure 12-30a). The `Lighthill` and `pointVolAcc` load functions are applied to the nodeset indicated by the yellow region. For this example the divergence of the Lighthill Tensor varies only in the x-direction and is given by

$$(\nabla \cdot \mathbf{T})_x = \left(1 + \cos\left(\frac{\pi x}{20}\right)\right) \sin^2\left(\frac{\pi t}{40}\right) \text{ for } t \leq 40\text{s} \tag{2.12.1}$$

where x is the location along the x-axis and t is time. Only a single load pulse is simulated, $t \leq 40$s. The simulation is run for a total time of 550s, giving the pressure pulse time to propagate away from the nodeset. The y and z components of $\nabla \cdot \mathbf{T}$ are zero. This form for Lighthill loading makes $(\nabla \cdot \mathbf{T})_x = 0$ at the end of the nodeset, $x = \pm 20$.

The same pressure response as that given in equation 2.12.1 is produced with a scalar nodal load equal to $\nabla \cdot (\nabla \cdot \mathbf{T})$ properly scaled by the number of nodes and area it is acting over. For the $\nabla \cdot \mathbf{T}$ used in this example,

$$\nabla \cdot (\nabla \cdot \mathbf{T}) = -\frac{\pi}{20}\left(\sin\left(\frac{\pi x}{20}\right)\right) \sin^2\left(\frac{\pi t}{40}\right) \text{ for } t \leq 40\text{s} \tag{2.12.2}$$

and the scalar nodal force applied using Point Volume Acceleration is $\frac{1}{4}\nabla \cdot (\nabla \cdot \mathbf{T})$ for the uniform linear hexahedral mesh shown in Figure 12-30b where each element is 1x1x1.

Figure 12-31 shows the pressure output at t=75s over the length of the waveguide for `Lighthill` and `pointVolAcc` loading given by equations 2.12.1 and 2.12.2, respectively, applied to the uniform mesh shown in Figure 12-30b. These are compared to the analytical result shown by the black line. The results are given after the pressure pulse has been applied, showing the propagation of the pressure wave through the acoustic medium. The percent difference in pressure between the two loading methods and the analytical result is shown in Figure 12-32 at t=75s. The L1 error of the pressure over the domain is shown at each simulation time step in Figure 12-33. This plot shows the L1 error increasing over the duration of the `Lighthill` or `pointVolAcc` load ($t < 40s$) and then remaining steady.

The geometry in Figure 12-30a) was also discretized with an unstructured linear tetrahedral mesh shown in Figure 12-30c) and `Lighthill` loading was applied to the domain. Results for these simulations are also shown in Figures 12-31-12-33 and show the same error as the uniform hexahedral mesh with Lighthill loading.

For input see Appendix 11.41

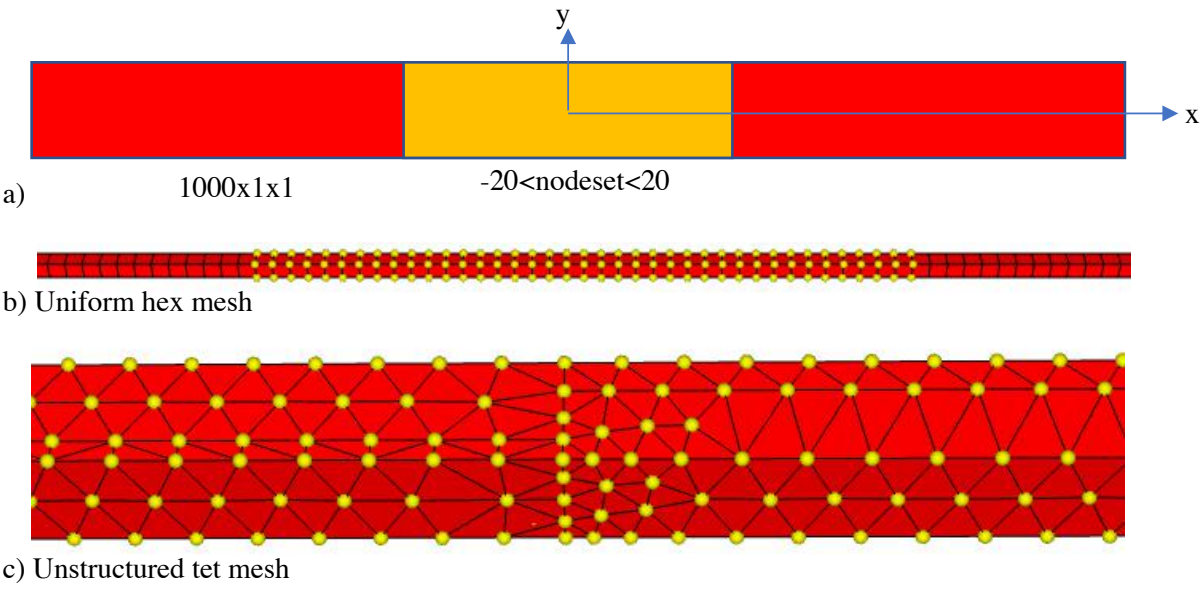

Figure 12-30. – a) Schematic of 1000x1x1 waveguide geometry. Geometry extends from x=±500. Yellow region contains the nodeset being loaded. b) Regular hex mesh used to compare Lighthill and Point Volume Acceleration loading. c) Unstructured tet mesh used for Lighthill loading. Yellow nodes in b) and c) indicate nodes in nodeset being loaded.

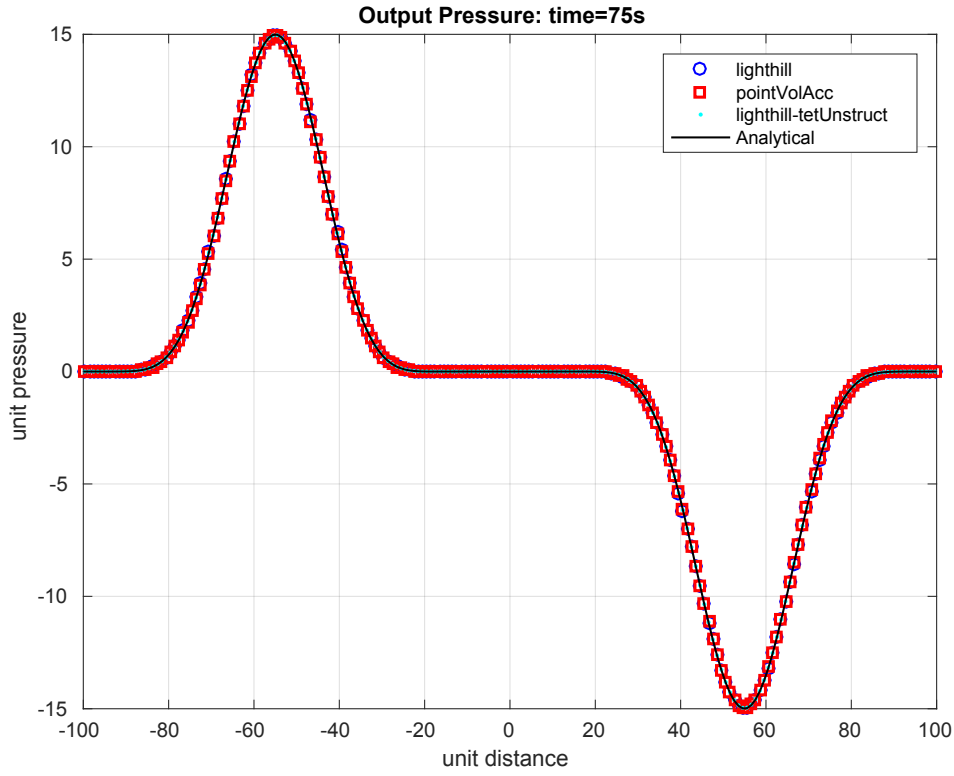

Figure 12-31. – Pressure output for 3 load cases compared to analytical result at t=75s.

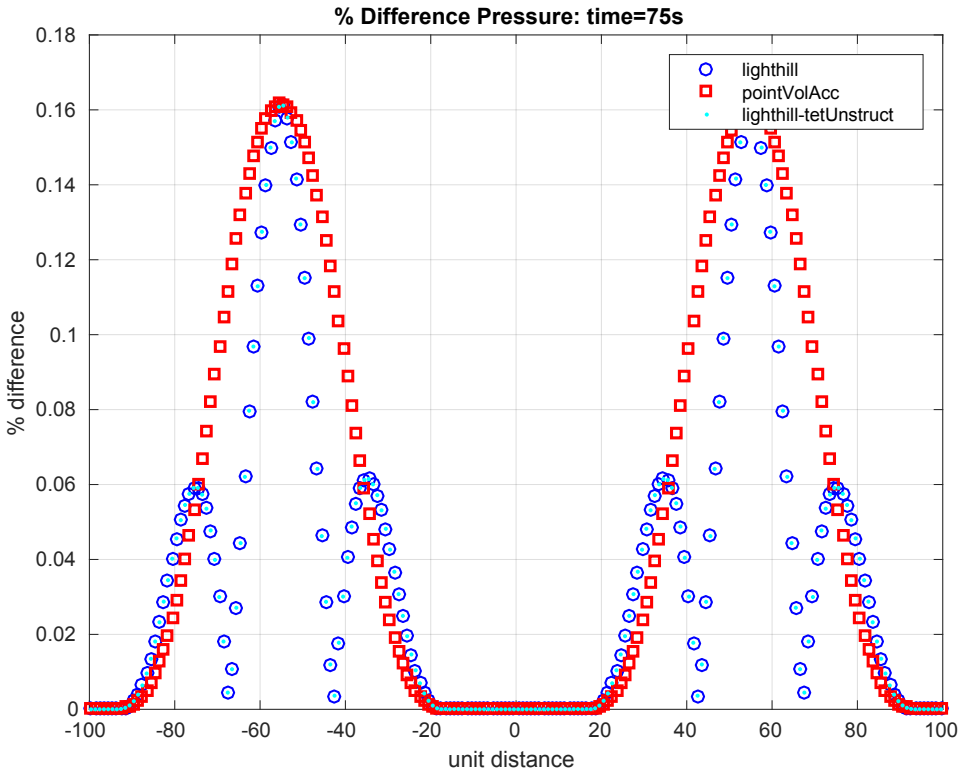

Figure 12-32. – Percent difference in pressure between the three load cases and the analytical pressure for t=75s.

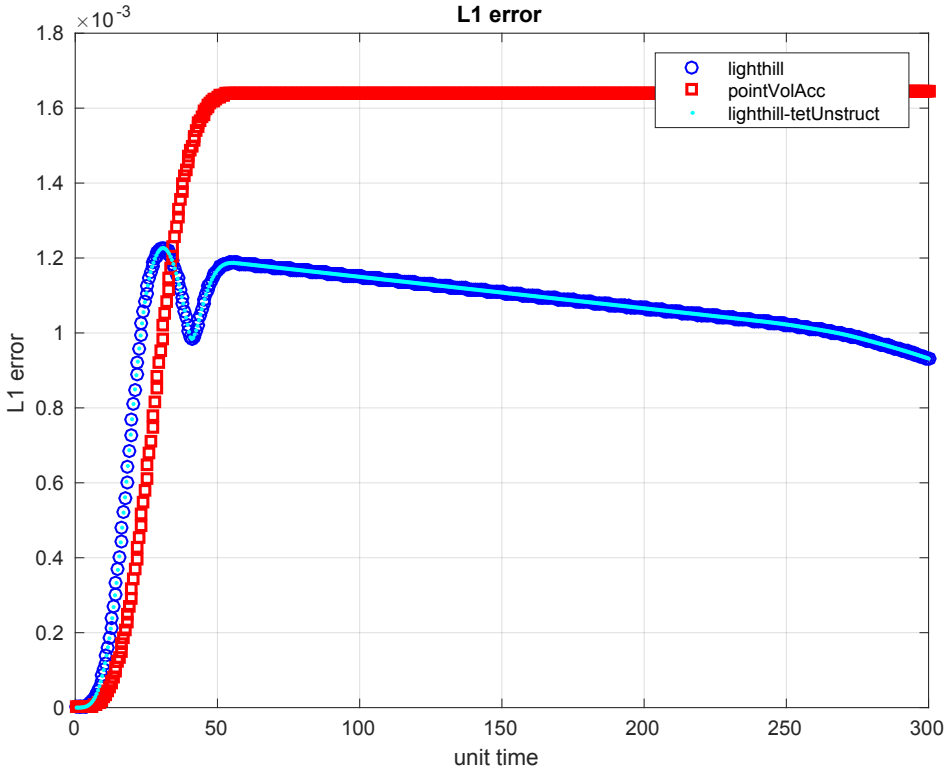

Figure 12-33. – L1 error in pressure for each load type versus time.

2.13. Acoustic Point Source in Frequency Domain

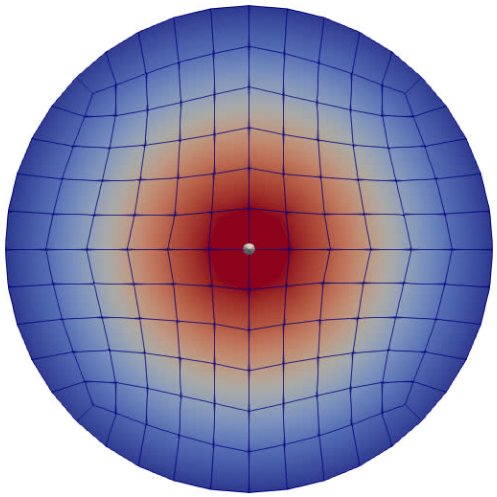

Figure 13-34. – Acoustic Point Source – Coarse Example

Consider an acoustic point source in a sphere of acoustic elements, shown in Figure 13-34. An absorbing boundary condition is applied at radius 2, representing an unbounded acoustic domain. The source is understood as a pulsating sphere with volume V and time derivative $Q = dV/dt$. The value for Q is specified using the keyword **point_volume_vel**.

In the frequency domain, with ω the circular frequency of the wave and $k = \omega/c$ the wave number, the pressure at a distance $r = |x|$ from the source is given by

$$p = i\omega\rho Q\frac{e^{-ikr}}{4\pi r}; \tag{2.13.1}$$

see the section "Point Acoustic Sources" in the theory manual for a detailed explanation.

Figure 13-35 shows a two dimensional slice of the result for a frequency of 91 Hz. At a point on the outside of the sphere, with radius $r = 2$ from the point source, the exact and computed solutions are compared. For the SierraSD solutions, a damping term of $\beta = 1.0e-5$ was added to facilitate solver convergence.

On the boundary of the mesh, with $r = 2$, and a frequency of 91 Hz, the exact answer is Apressure = -5.623 and ImagAPressure = -28.873. For the mesh shown in Figure 13-34, which is relatively coarse, SierraSD calculates Apressure = -4.826 and ImagApressure = -28.600. For the refined mesh shown in Figure 13-35, SierraSD calculates Apressure = -5.513 and ImagAPressure = -28.580.

The verification test suite verifies both nodal point source and element point source options. For input see Appendix 11.42

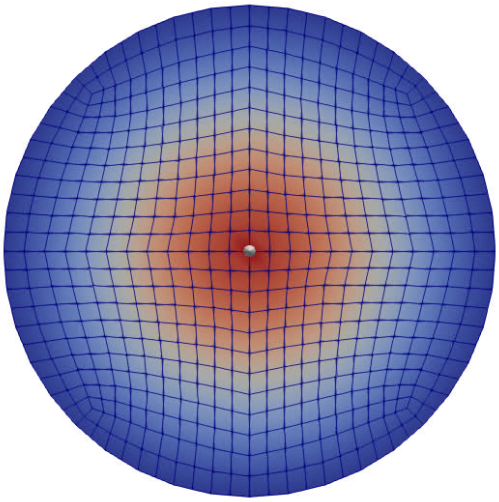

Figure 13-35. – Acoustic Point Source – Refined Example

2.14. Acoustic Point Source in Time Domain

In order to verify the transient acoustic point source (Point_Volume_Vel) in Sierra/SD, we consider a spherical domain with a point source at the center. The spherical domain is given absorbing boundary conditions around its boundary, so as to make the space look infinite in all directions. With this arrangement, we have the problem of a point source in an infinite domain.

The analytical solution to this problem is given by Pierce [41], as follows

$$p(R,t) = \frac{\rho}{4\pi R}\dot{Q}(t-\frac{R}{c})H(t-\frac{R}{c}) \tag{2.14.1}$$

where $p(R,t)$ is the pressure at a distance R from the source and at time t, ρ is the fluid density, c is the speed of sound, $H(t)$ is the Heaviside function, and $Q(t)$ is the time derivative of volume change of the source, i.e.

$$Q = \frac{dV}{dt} \tag{2.14.2}$$

In this problem, we chose $Q(t) = \sin(50\pi t)$, and we examined the solution at the exterior boundary of $R = 2$. Inserting this into Equation 2.14.1 gives

$$p(R,t) = \frac{50\rho}{8}\cos(50\pi(t-\frac{2}{343}))H(t-\frac{2}{343}) \tag{2.14.3}$$

Figure 14-36 shows a comparison of the Sierra/SD results for this problem compared against Equation 2.14.3. Excellent agreement is obtained, except for the initial time where the numerical solution shows some difficulty resolving the abrupt change in the exact solution, which comes from the Heaviside function in Equation 2.14.3. We can also verify the "Point_Volume_Accel" point source with an input of $\dot{Q}(t) = 50\pi\cos(50\pi t)$, and get the same solution.

Two variants of the problem are included in the verification test suite. The first variant uses a node-based point source at a single node at the center of the sphere. The second variant uses a element-based point source at a single element at the center of the sphere. Both variations produce nearly identical results on a relatively coarse mesh and converge to the same analytic solution with refinement. For input see Appendix 11.43

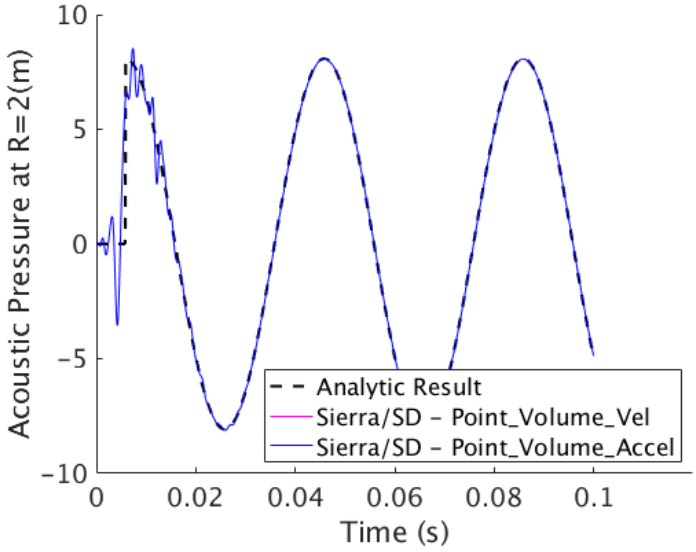

Figure 14-36. – Transient Verification of a PointSource in an Infinite Medium
Comparison of computed and exact solution for a point source in an infinite medium.

2.15. Acoustic Plane Wave Scattering in Frequency Domain

Consider an acoustic plane wave traveling in the $+x$-direction. In the frequency domain, with $\omega = 2\pi f$ describing the angular frequency and $k = \omega/c_0$ describing the wavenumber, the pressure at every point in space is

$$p = p_0 e^{ikx} \,. \tag{2.15.1}$$

Now, consider scattering of a plane wave incident on a steel cylinder in air. Due to the cylindrical symmetry of the problem, it is useful to expand the spatial dependence of the incident plane wave via an infinite series as

$$e^{ikx} = e^{ikr\cos\theta} = \sum_{n=0}^{\infty} i^n \epsilon_n J_n(kr)\cos(n\theta) \,. \tag{2.15.2}$$

where r is the distance from the origin, θ is the azimuthal angle, ϵ_n is the Neumann factor (equal to 1 for $n = 0$ and 2 otherwise), and $J_n(kr)$ are Bessel functions of order n. The scattered pressure field can then be written as

$$p_{\text{sc}} = p_0 \sum_{n=0}^{\infty} i^n \epsilon_n A_n H_n^{(1)}(kr)\cos(n\theta) \,, \tag{2.15.3}$$

where A_n are scattered field coefficients and $H_n^{(1)}(kr)$ are Hankel functions of order n. Hereafter, the superscript will be dropped for notational convenience. Similar expansions can be written for the displacement fields (both longitudinal and transverse) in the cylinder itself, but those are omitted here.

Continuity of radial displacement, continuity of radial stress, and continuity of tangential stress must be enforced at the surface of the cylinder to find A_n. Since fluids cannot support shear stress, the tangential stress must therefore be zero at the boundary. These boundary conditions are straightforward to enforce, but they result in complicated expressions for the scattered field coefficients. While the general expressions can be viewed in `elastic_cylinder_fluid_medium.m`, the scattered field coefficients for a rigid and immovable cylinder are sufficient in this case because steel is acoustically rigid compared with air. These coefficients are

$$A_n = -\frac{J_n'(kR)}{H_n'(kR)} \,. \tag{2.15.4}$$

For a plane wave of frequency $f = 1$ kHz incident on a cylinder of radius $R = 0.1$, the scattered pressure field is shown in Figure 15-37. A PML boundary condition is applied at radius 0.8, representing an unbounded acoustic domain. The pressure amplitude p_0 is specified to be unity. At the point $(x, y) = (0.2, 0)$, the exact solution answer is Apressure = 0.7072 and ImagAPressure = 0.1875, and For a mesh size of 0.01, SierraSD calculates Apressure = 0.7037 and ImagAPressure = 0.1896. For input see Appendix 11.44

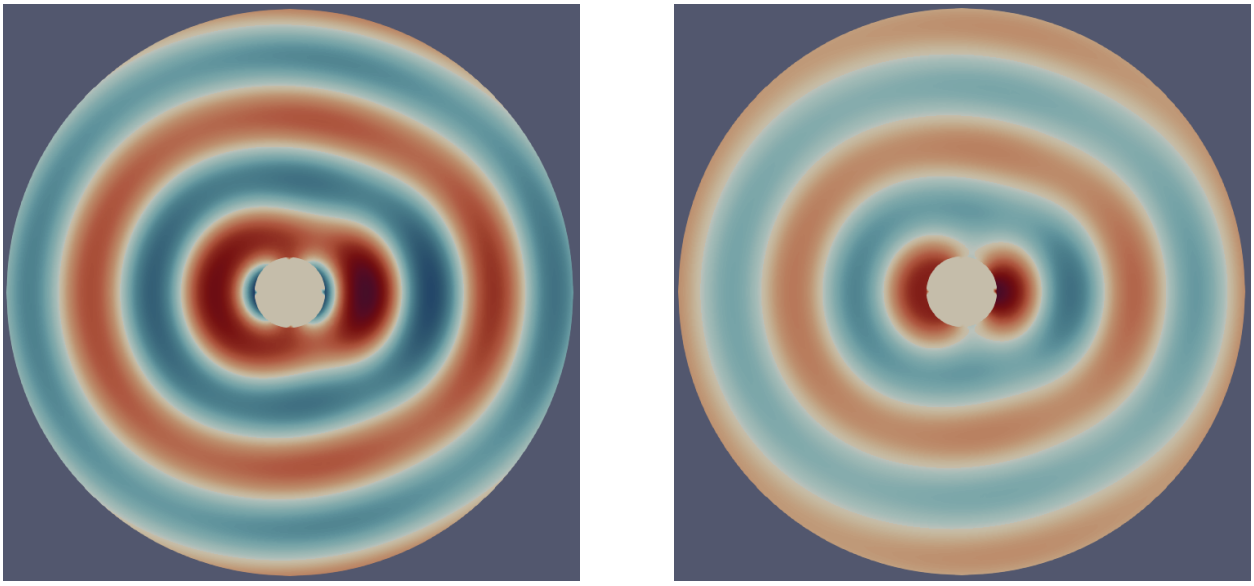

Figure 15-37. – Acoustic Plane Wave Scattering from a Cylinder

2.16. Superelement Superposition

A four truss, 1-D problem provides a simple verification of Craig-Bampton Reduction (CBR) and superposition based reconstruction. As illustrated in Figure 16-38, the model is clamped on the left end, and constrained to admit only translations in the X direction on the remaining four nodes. A transient load acts in the X direction for this problem, so the model is fully one-dimensional.[2] The verification proceeds as follows.

1. Compute the full system (4 element) static load due to a point load on the center node. This is used as the truth model.
2. Split the model into two pieces, each composed of two elements each. The CBR model is floating in the X direction, where load is applied.
3. Approximate solution uses CBR methods to reduce the last two elements (3 nodes) to two dofs.
4. The "residual solution" computes the system statics solution based on the left hand side (unreduced) model connected to the CB reduced right hand side system. Results in the residual are compared with step 1.
5. One output of the system transient solution is "`endtruss-out.ncf`". This file contains the modal amplitudes and the interface amplitudes for the superelement. These amplitudes, together with the modal bases computed in step 2 above, provide the information necessary to compute the physical degrees of freedom in the portion of the structure on the right. The model is generated using the "superposition" solution method. This model is then compared with the results from the right hand portion of the truth model.

Figure 16-39 provides a comparison of the solutions using the full model, and the individual components.

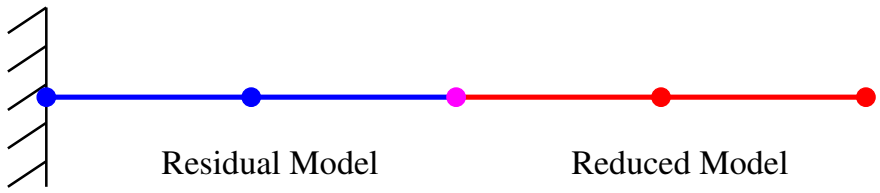

Figure 16-38. – Four Truss Geometry

Theory. A CB model generates a transformation matrix consisting of a combined set of fixed interface and constraint modes. These modes may be stored in an exodus file. We call this "`se-base.exo`". A netcdf file, "`se.ncf`" is also created at this time. Subsequently, this reduced model is inserted into a residual model for superelement analysis, say a transient analysis. That analysis outputs the standard exodus results, "`resid-out.exo`" and results

[2]The CBR reduction must use lumped masses for consistency with the statics solutions.

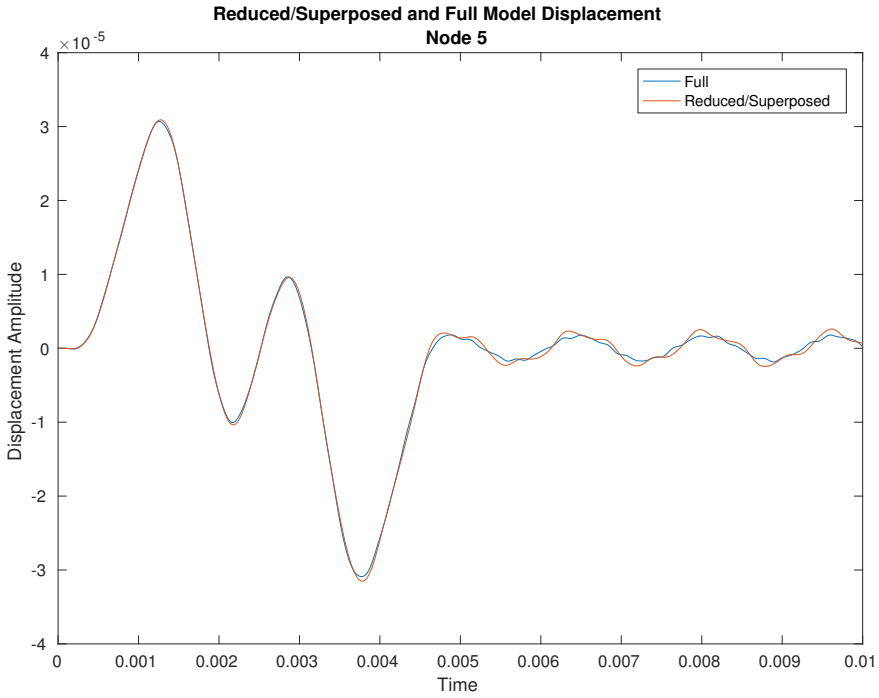

Figure 16-39. – Results of Superposition Problem

on the netcdf file, "`se-out.ncf`". The point is to recover the response on the original interior degrees of freedom of the superelement.

The transient response on the interior degrees of freedom is,

$$u_k(t_n) = \sum_{i}^{nmodes} q_i(t_n)\phi_{ik} + \sum_{j}^{nconstraint} w_j(t_n)\psi_{jk} \tag{2.16.1}$$

where,

$$\begin{aligned} u_k(t_n) &= \text{is the displacement at interior dof } k \\ t_n &= \text{is the time step} \\ q_i &= \text{is the amplitude of a generalized dof for mode } i \\ \phi_{ik} &= \text{is the fixed interface mode } i \text{ at dof } k \\ w_j &= \text{is the amplitude of interface dof } j \\ \psi_{jk} &= \text{is the constraint mode } j \text{ at dof } k \end{aligned}$$

The amplitudes q_i and w_j are found in "`se-out.ncf`", while the mode shapes, ϕ_{ik} and ψ_{jk} are found in "`se-base.exo`". Super_superp simply combines these results and writes a new output file containing the results.

For input see Appendix 11.45

2.17. Superelement Inertia Tensor and Mass Inertia Matrix

The inertia tensor provides a means of applying initial conditions to the interior dofs of a superelement. General boundary conditions are not supported, but initial conditions that include linear combinations of rigid body motion can be readily managed. As these are the most common boundary conditions, there is great utility in computing the inertia tensor as part of the Craig-Bampton (CB) reduction process.

There are two matrices associated with CB reduction and rigid body applications. The inertial tensor, $I_v = T^T R$, is used to establish initial velocity. Here T is the CB reduction matrix and R is a six column rigid body vector in the physical space. The mass inertia matrix, $I_m = T^T M R$, can be used to apply gravity or other body loads. M is the mass matrix in the physical system.

2.17.1. Inertia Tensor, $I_v = T^T R$

The development of the inertia tensor was used for use in LS-Dyna. LS-Dyna also has the reduction process. Verification involves comparison of the output of the two codes. The LS-Dyna output is in DMIG format. We compare with a previous Matlab output from Sierra/SD which was compared by hand with the LS-Dyna results. Also, Sierra/SD outputs the fixed interface modes first, while LS-Dyna puts them last. The model is shown in Figure 17-40.

The overall comparison of the values is very good with a relative L2 norm about 6%. Figure 17-41 compares the values of the matrix. There are 3 rigid body modes (corresponding to each of the three translations). There are 10 fixed interface modes and 12 constraint modes, for a total of 22 columns in the inertia tensor. There is significant difference for mode 10, but that is expected because it is the last mode, and the next mode is very near in frequency.

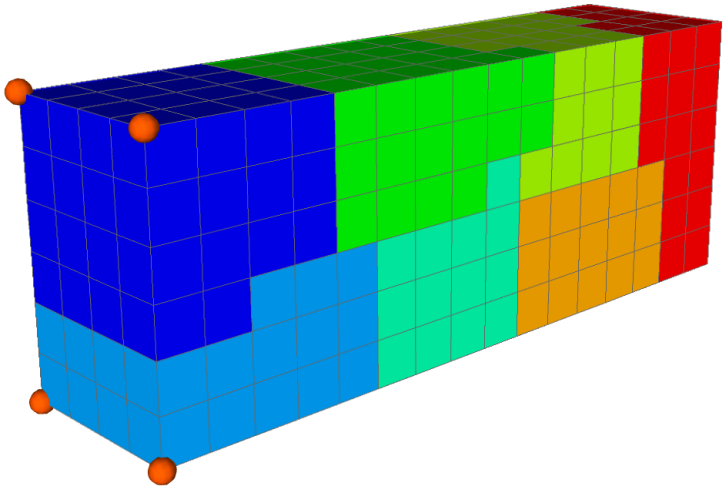

Figure 17-40. – LS-Dyna and Sierra/SD Inertia Tensor Model. The model is colored by the parallel decomposition.

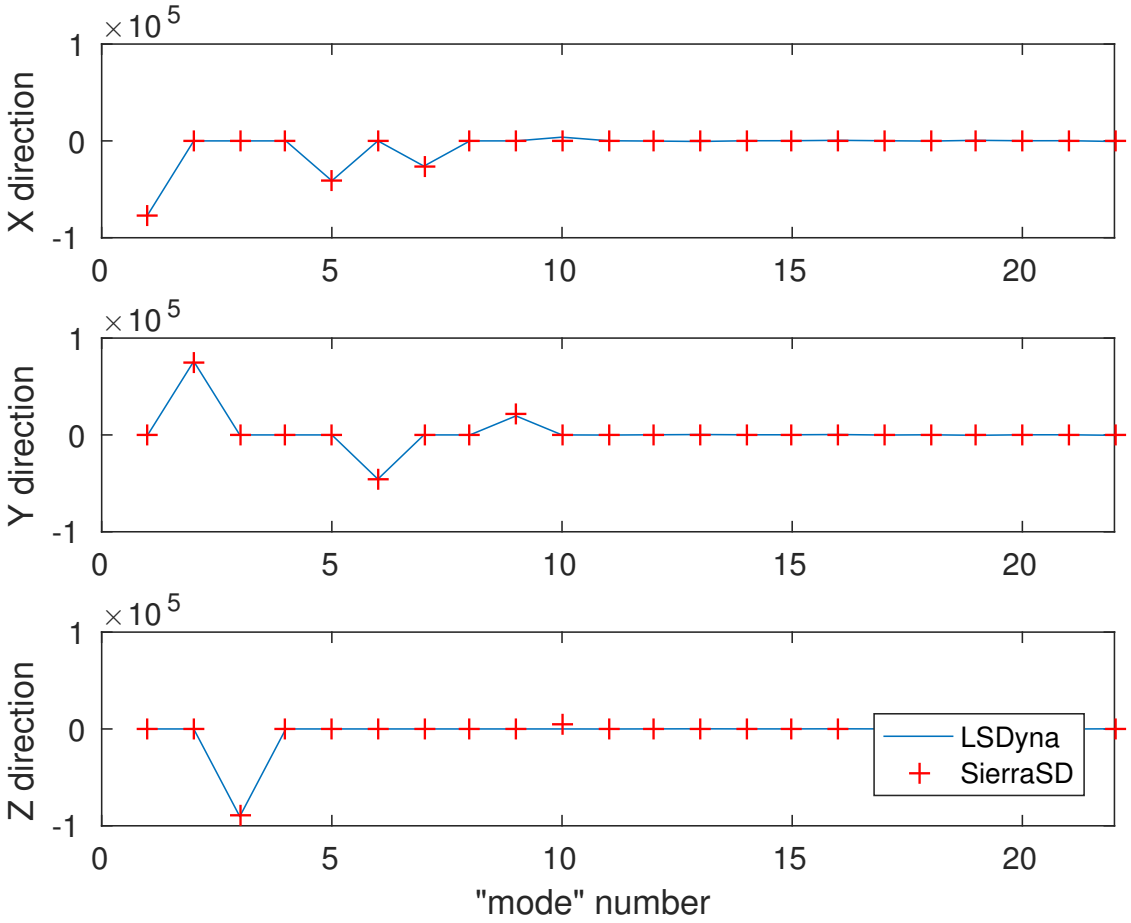

Figure 17-41. – LS-Dyna and Sierra/SD Inertia Tensor Terms

2.17.2. Mass Inertia Matrix, $I_m = T^T M R$

The Mass Inertia matrix, I_m, is determined by a comparison with an independent MATLAB^{TM} calculation, using the following steps.

1. Use the single processor input, and enable "mfile" output.
2. Run Sierra/SD to reduce the model and generate the mass inertia matrix.
3. Read in the fixed interface modes, ϕ, and constraint modes, ψ, from Sierra output.
4. Form the transformation matrix.

$$T = \begin{pmatrix} \phi & \psi \\ 0 & I \end{pmatrix}$$

5. Read the partitioned components of the mass matrix (M_{vv}, M_{cc}, and M_{cv}) from Sierra output. Generate a mass matrix that includes all dofs of interest.

$$M = \begin{pmatrix} M_{vv} & M_{vc} \\ M_{cv} & M_{cc} \end{pmatrix}$$

6. Compute and compare the reduced mass matrix computed by the two methods. $\hat{M} = T^T M T$.
7. Compute the Nx3 rigid body matrix. Only translational components are included.
8. Compare the Sierra computed Inertia Tensor, $I_v = T^T R$, with the LS-Dyna stored values. This is a code-to-code comparison. This is also compared with a Matlab solution.
9. Compute the Mass Inertia matrix, $Iv = T^T M R$, and compare results with those output from Sierra. A comparison of the results is shown in Figure 17-42.
10. Results are compared in serial and in parallel.

These steps found in the Matlab script, `massInertiaTensorCompare.m`.

For input see Appendix 11.46.

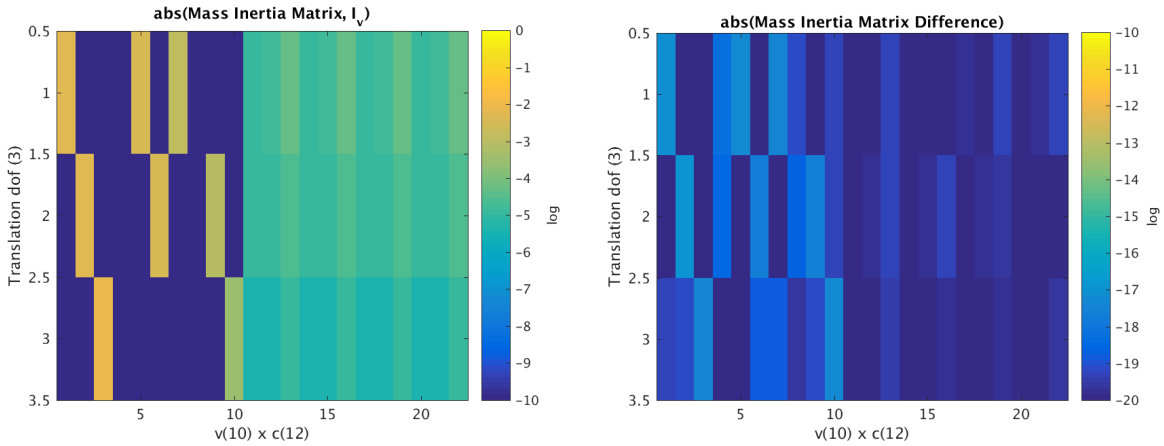

Figure 17-42. – Mass Inertia Matrix. Values (left) and Differences (right).

2.18. Nastran/Sierra/SD Interoperability with Superelements

2.18.1. Needs and Requirements

There is often a need to exchange data with external collaborators. Most often these collaborators use commercial products for finite element analysis. One of the varieties of NASTRAN is the most commonly used exchange format. Sierra/SD has been designed to interface to these formats through its superelement capability. Export through a NASTRAN superelement may be done directly in Sierra/SD as part of the CBR method,or it may be accomplished through the "ncfout" application which translates the model into either DMIG or output4 format. In addition, Sierra/SD may import certain DMIG formatted models using Nasgen.

Such export/import capabilities provide the basis of interaction with collaborators, and it is important that the process be simple and accurate. However while significant effort has been put into these tools, testing has been rather limited because of challenges in running NASTRAN in the Sierra test harness. Without regular testing, capabilities can not be trusted for crucial collaborations. The intent of this verification is to provide a well defined testing strategy to ensure persistent capability. These tests may need to be run manually, but the tests should ensure capability.

> This test does NOT regularly run NASTRAN. Section 2.18.7 contains instructions for running NASTRAN by hand to fully verify current analysis. The nightly test runs Sierra, and compares results carefully with previously completed analyses which had been compared with NASTRAN.

2.18.1.1. Scope of Evaluation

The focus of these tests is evaluation of the CBR exchange capability. In particular, we focus on the following.

1. Compatibility of the data format for exchange of reduced order stiffness and mass matrices.
2. Bi-directional capability, i.e. output of superelements from Sierra/SD in DMIG format, and input through Nasgen.
3. A clear, well defined process for generating and using these reduced order models (or ROM).
4. Support for damping matrices, and output transfer matrices (OTM).
5. Support for inertia mass matrix export. The inertia mass matrix is not currently supported for boundary conditions in Sierra/SD. As such, it cannot be tested for import.

To keep the focus, we explicitly limit the following.

- No element comparisons. NASTRAN element formulations clearly differ from Sierra/SD capabilities. That is expected, and not tested here. Convergence of these elements to proper solutions is performed elsewhere.
- Nasgen translation of most data. There are extensive tests for translation of the model. With the exception of the superelement capabilities, these lie outside the scope of this set of testing.

2.18.2. Model Evaluation

The model must be evaluated for suitability for comparison. In particular, the solutions of the unreduced models (NASTRAN and Sierra), must be close enough to allow code to code comparison of reduced models.

The model is illustrated in Figure 18-43. There are three primary areas of consideration.

Base The support at the base provides the fixed boundary condition and the attachment location for the two tuning tines. It is part of the residual.

Load Tine The leftmost tine (red) is also part of the residual. Force/Pressure boundary conditions may be applied to this tine.

ROM Tine The rightmost tine (yellow) is the portion of the model to be reduced. The interface to the residual is the element at the base of the tine. There is a single point on the end of the tine that serves as a location for OTM evaluation.

All sections of the model use the same material properties (aluminum), and all use Hex20 elements, as these are expected to be very similar between the two applications. We evaluate the model for lowest eigenvalues and for a modal frequency response function (FRF) to an impulse on the side of the loading tine. The FRF provides a useful comparison, even when the time history data would suffer from phase errors introduced by small differences in the element formulations.

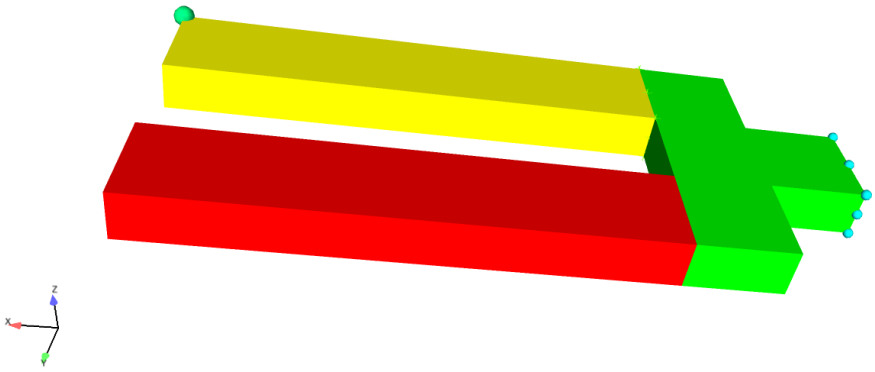

Figure 18-43. – Tuning Fork Model

Table 18-7 provides a comparison of the frequencies for vibration of the structure.

#	Description	Sierra/SD	NASTRAN	Diff %
1	base bending	532.07	527.84	0.8%
2	symmetric bending	937.07	926.53	1.1%
3	asymmetric bending	2956.4	2891.84	2.2%
4	symmetric 2nd bending	4733.4	4630.10	2.2%

Table 18-7. – Vibrational Frequency Comparison

Figure 18-44 compares the modal FRF solutions for the Sierra and NASTRAN solutions.

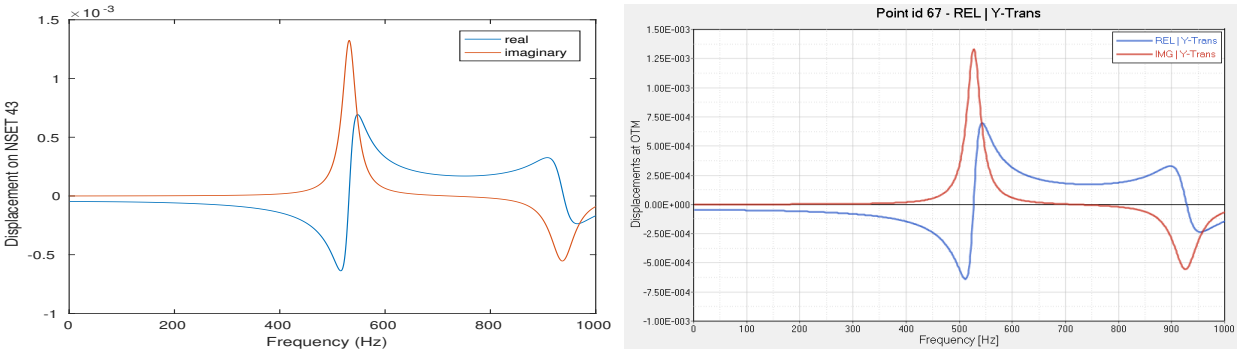

Figure 18-44. – FRF Solutions with 3% damping. Sierra/SD and NASTRAN.

The model is considered suitable for evaluation.

2.18.3. Superelement Reduction and Insertion

2.18.3.1. Sierra/SD Model reduction and Insertion

In Sierra/SD, the following steps are followed to compute the system response by superelement reduction techniques.

1. The ROM section of the exodus model is pulled out separately. This can be accomplished using grepos.
2. The CB reduction input is generated. This is similar to the full system model, with additions of a CB section.
3. Sierra/SD is run on the CBR input. This generates a netcdf output.
4. The residual model is generated. Like step 1, we use grepos and delete the block associated with the ROM.
5. A "socket" is created for the superelement, using "mksuper".
6. A residual input is created. This is very similar to the original full system model, but now contains entries for the new superelement block.
7. Sierra/SD is run on the residual input.

Commands for some of these operations are shown in Figure 18-45. A comparison of the eigenvalues with the full system eigenvalues is shown in Table 18-8. With no internal modes, significant errors are introduced. Four modes in the ROM represents the system well.

Mode	Full Model	4-Mode ROM	0-Mode ROM
1	532.065	532.066	551.163
2	937.066	937.066	1107.19
3	2956.37	2956.87	3758.39
4	4733.4	4734.76	6022.09

Table 18-8. – Eigen Value Comparison - SierraSD full model and with ROM

1. *The ROM section of the exodus model is pulled out separately.*

```
grepos tuningforkx.exo rom.exo « EOF
   delete block 11
   delete block 31
EOF
```

2. *The CB reduction input is generated. The solution and cbmodel sections look like the following.*

```
SOLUTION
   CBR
     nmodes=4
END
cbmodel
   nodeset 41
   format=netcdf
   file=rom.ncf
   inertia_matrix=yes
end
```

3. *Sierra/SD is run on the CBR input. This generates a netcdf output.*

4. *The residual model is generated. This is identical to step 1, but deletes block 21.*

5. *A "socket" is created for the superelement, using "mksuper".*

```
mksuper tmp.exo « EOF
   add nodeset
   41
   write residual.exo
   quit
EOF
```

6. *A residual input is created. Copy full model input to residual.inp. Comment out block definition for block 21, and add definition for block 32.*

7. *Sierra/SD is run on the residual input, and compared with original model.*

Figure 18-45. – Running Sierra/SD solution with Superelement

2.18.3.2. NASTRAN Model reduction and Insertion

In MSC or NX NASTRAN, one approach to compute the system response by superelement reduction techniques is described in the following steps.

1. The ROM section of the NASTRAN mesh file is pulled out separately. This was accomplished using the Altair HyperMesh preprocessor. The residual structure's node and element definition are saved as a separate bulk data file `residual_struct.bulk`.
2. The CB reduction input is generated in `cbr.bdf`. This requires using the `EXTSEOUT` card in the case control section. Also required is the definition of a `BSET` card that contains the interface nodes (a-set dofs) to be constrained during the dynamic reduction step. A `QSET` card is used to define the generalized dofs (q-set) to be used for the reduction. Lastly, a `SPOINT` card is necessary to define scalar points for the generalized dofs. Note that the number of generalized dofs requested should not be excessive – otherwise, the reduced matrices will have null columns for unused q-set dofs and may result in a performance degradation.
3. NASTRAN solves the eigenvalue problem (`SOL 103`). The `EXTSEOUT` card in the case control section has many options for the type and format of superelement information generated. In this example, the `EXTSEOUT` card was specified to request a punch (.pch) file `cbr.pch` that contains the reduced stiffness and mass DMIG matrices. Additional superelement information (e.g., DMI matrices and DTI tables that are associated with the OTM) which may not be necessary for subsequent use is also generated by default.
4. The resulting punch file `cbr.pch` is then cleaned up by removing all the information within it except the stiffness and mass DMIG matrices. The names of the DMIG matrices were also renamed to something more convenient. This updated punch file can be saved as `cbr_dmig.pch`.
5. The residual (residual structure with the superelement attached) input is created. This is very similar to the original full system model, but contains additional cards that insert the superelement via DMIG input. The stiffness and mass DMIG matrices are called in using the K2GG and M2GG cards, and the `SPOINT` card must be included to define the generalized dofs.
6. NASTRAN is run on the residual input.

Additional details of NASTRAN's superelement functionality can be found in Reference [51] (MSC NASTRAN 2017 Superelements User's Guide). Eigenvalues of the full model and the residual model with superelement are shown in Table 18-9. The results are practically identical.

Figure 18-46 compares the input displacement of the Sierra/SD and MSC/NASTRAN ROM on a Sierra/SD residual. Data on the output (ROM) tine is not available with these methods because the basis vectors of the ROM are available only internal to NASTRAN.

	MSC NASTRAN 2016 (full Model)	MSC NASTRAN 2016 (NASTRAN based DMIG)	
Mode	Natural Frequency [Hz]	Natural Frequency [Hz]	Difference [%]
1	528	528	0.00
2	927	927	0.00
3	2,892	2,892	0.00
4	4,630	4,630	0.00
5	6,078	6,078	0.00
6	6,446	6,446	0.00
7	8,118	8,119	0.01
8	12,863	12,864	0.01
9	14,426	14,427	0.01
10	17,672	17,681	0.05

Table 18-9. – : Eigenanalysis Comparison – MSC NASTRAN Full Model with ROM

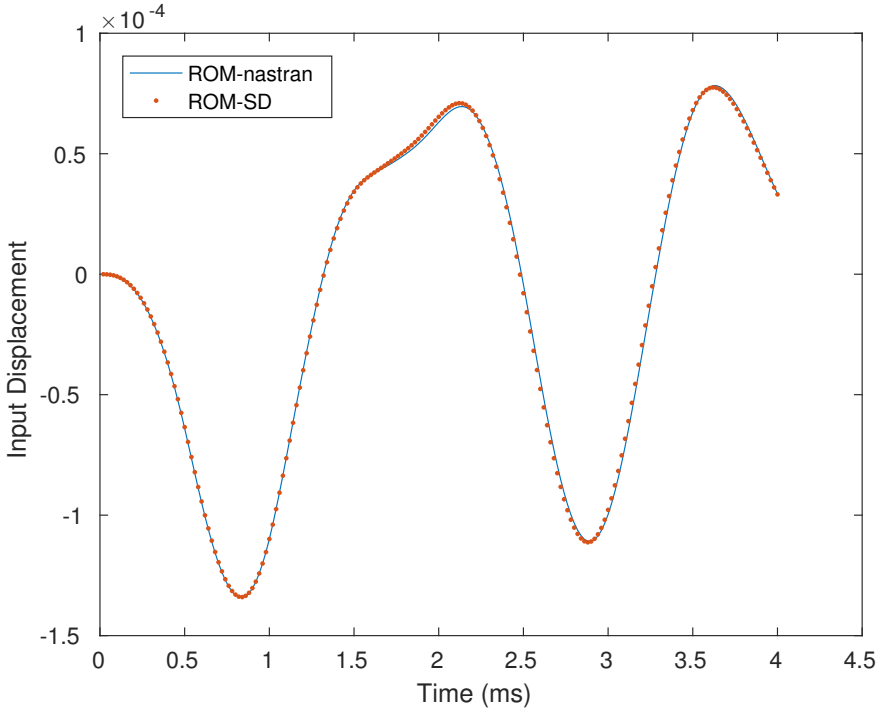

Figure 18-46. – Modal Transient Comparison. The input displacement of the Sierra/SD and MSC/NASTRAN ROM on a Sierra/SD residual

2.18.4. Using Sierra/SD Superelements in NASTRAN

It is also informative to compare the eigenvalues to assess the equivalence of the DMIG matrices generated by Sierra/SD and NASTRAN. In one case, DMIG matrices are exported by Sierra/SD and then used within NASTRAN to attach to the residual structure for an eigenvalue problem. In the second case, DMIG matrices are generated entirely within NASTRAN. These results, shown in Table 18-10, indicate that within practical frequencies of interest, Sierra/SD produces very similar reduced matrices to NASTRAN. Results of a modal frequency response analysis for the full NASTRAN model and the residual model with superelement are shown in Figure 18-47. The output is located at node 14, which lies at the boundary between the residual mesh and the superelement. The results are practically identical.[3]

Mode	MSC NASTRAN 2016 (Sierra/SD based DMIG) Natural Frequency [Hz]	MSC NASTRAN 2016 (NASTRAN based DMIG) Natural Frequency [Hz]	Difference [%]
1	528	528	-0.04
2	931	927	-0.52
3	2,916	2,892	0.84
4	4,675	4,630	0.95
5	6,144	6,078	1.07
6	6,499	6,446	0.83
7	8,292	8,119	2.09
8	13,209	12,864	2.62
9	14,972	14,427	3.64
10	17,796	17,681	0.65

Table 18-10. – Eigenanalysis Comparison – Sierra/SD -generated DMIG and NASTRAN-generated DMIG. Residual and Superelement are employed in each analysis.

Sierra/SD computes a superelement using a Craig-Bampton reduction. That reduced order model may be written in several formats. For use in Sierra/SD, we write this as a netcdf/exodus file. It may alternatively be written as a DMIG[4] compatible with NASTRAN. More flexibly, we can convert the netcdf/exodus file to several formats (including DMIG and Output4) using the `ncfout` application.

For application of a DMIG to a NASTRAN model, the interface node numbers must be consistent. Figure 18-48 illustrates the nodes on an interface, together with the first few lines of the DMIG, which define a portion of the reduced stiffness matrix. Each row and column is indicated by the GRID/CID pair.

The original BDF file must be modified as follows.

1. Copy original, and remove the five elements in the ROM region.

[3] Sierra/SD has recently added a higher precision DMIG output. This uses 16 character "long" format NASTRAN fields, and is selected with the "FMT=dmig*" option.

[4] Direct Matrix Input at Grid points

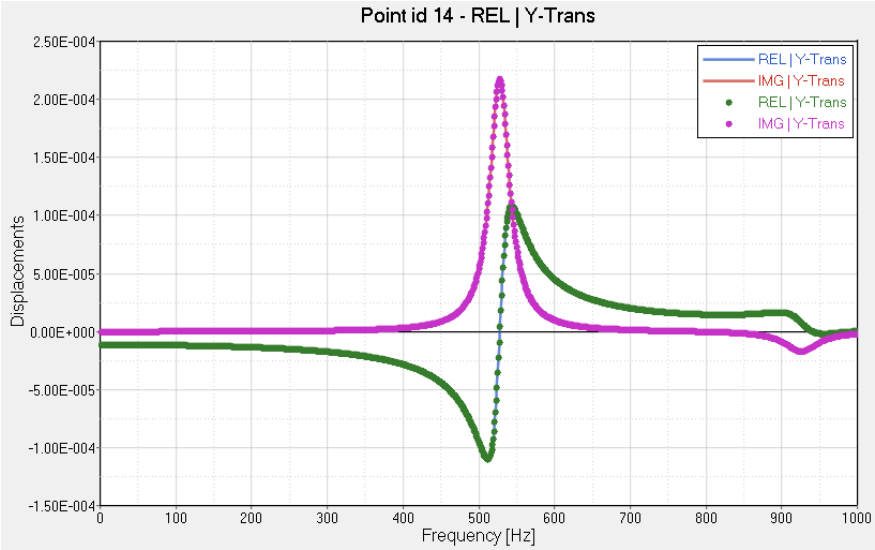

Figure 18-47. – Modal FRF Comparison: Full Model (solid line) and Residual Model with Superelement (solid markers)

```
DMIG    K2GG          6     1                6     1  1.6896+6
                      6     2  -197648.       14     1   726510.
                     14     2   36078.7       47     1   899966.
                     47     2   63681.1       47     3   90702.2
                     55     1   750185.       55     2   58875.3
                     55     3  -67421.3       97     1  -2.141+6
                     97     2  -115178.       97     3  -275194.
                    111     1  -454831.      111     2   45753.7
                    113     1  -1.028+6      113     2   156507.
                    113     3  -587.767      116     1  -442113.
                    116     2  -48070.2      116     3  -202927.
DMIG    K2GG          6     2                6     2  2.0542+6
                     14     1  -36078.7       14     2  1.0384+6
```

Figure 18-48. – DMIG example. On the left, the interface nodes and orientation from the model is shown. The extract from the DMIG on the right illustrates the first row of the stiffness matrix. The index to each value is the GRID and CID pair for that column.

2. Add SPOINTS corresponding to the DMIG
3. Include the new DMIG data.
4. Add commands to include K2GG and M2GG in the case control.

Table 18-11 compares the eigenvalues of the full NASTRAN model to the eigenvalues of the reduced order model from Sierra/SD. The solution with four fixed interface modes provides good accuracy.[5]

Mode	Full Model	4-Mode ROM	0-Mode ROM
1	527.842	528.046	546.461
2	926.535	931.379	1098.845
3	2891.837	2916.451	3681.061
4	4630.102	4674.563	5980.433

Table 18-11. – Eigen Value Comparison - NASTRAN full model and with Sierra/SD ROMs.

2.18.5. Using NASTRAN Superelements in Sierra/SD

The NASTRAN superelement model is translated using `Nasgen`. This tool translates the model and superelement simultaneously, with the superelement written to a netcdf file. NASTRAN uses a different element formulation, and orders the modes differently from Sierra/SD, so we may not reasonably directly compare the matrices output in the translation. It is possible to simply run the translated analysis using Sierra/SD. The compared eigenvalues are shown in Table 18-12. The results are very reasonable.

Mode	Sierra/SD (Hz)	NASTRAN (Hz)
1	530.594	527.8421
2	932.069	926.5357
3	2930.28	2891.865
4	4692.38	4630.148

Table 18-12. – Comparison of NASTRAN and Sierra/SD Eigenvalues using NASTRAN Superelement

2.18.6. Superposition Methods for Output of Internal Data

The Craig-Bampton method necessarily removes internal physical degrees of freedom from the superelement. Sometimes results on those internal dofs are required. The

[5]The default data width for a DMIG is 8 characters. There may be a significant loss of accuracy in truncating data to this size. We have recently added the option to output 16 character DMIG using the DMIG* format.

displacements, accelerations and velocities on these locations may be readily obtained through post-processing using the `super_superp` tool.

Figure 18-49 compares the output of the sample on nodeset 41, at the tip of the unloaded tine, from the full model with the results obtained using the reduced model. Both models are run in Sierra/SD for consistency. The left tine is loaded with an impulse. Figure 18-50 illustrates the deformation of the full model, compared with the residual and superimposed superelement.

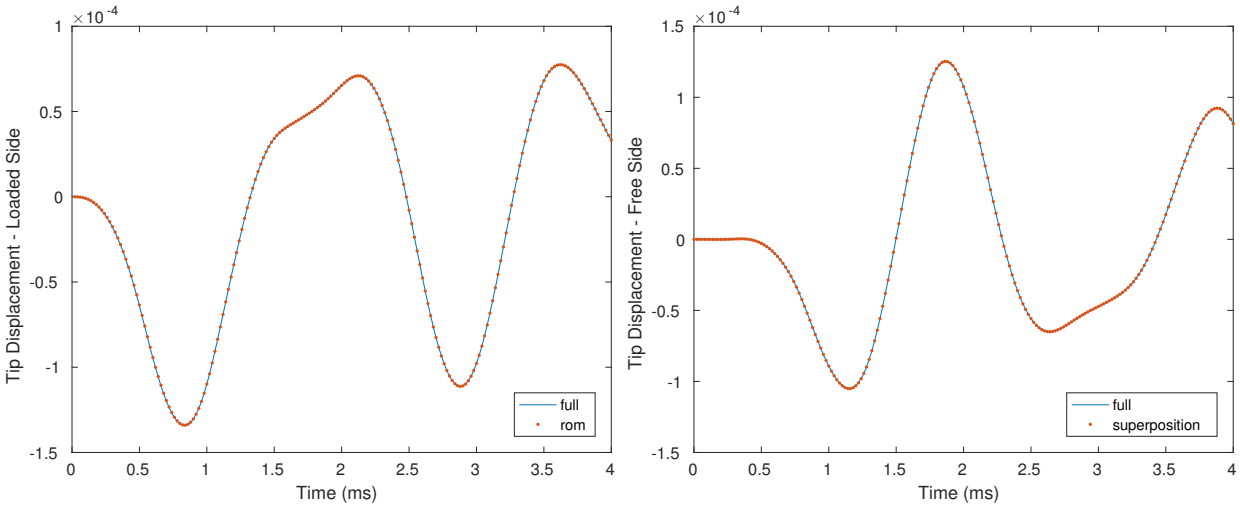

Figure 18-49. – Comparison of Output Displacements. The plot on the left compares displacements of the full and reduced order models at the input location. The plot on the right compares displacements on the unloaded tine after the `selem_superp` tool is used to extract the displacement from the reduced model.

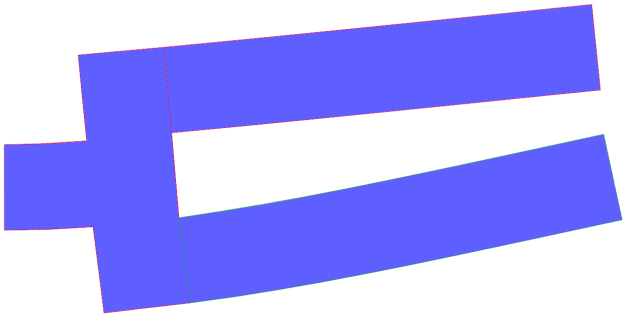

Figure 18-50. – Superposition Solution and Full Deformation, $t = 2\,ms$. The full model (in blue background) is compared with the residual and the post-processed superelement.

2.18.7. Related NASTRAN Analyses Required for Verification

The NASTRAN inputs for these analyses are included in the test repository, but are not run as part of the nightly test process. To evaluate these models, the following steps may be followed.

2.18.7.1. Eigen Problem

NASTRAN approximates the eigenvalues of the entire model by running:

```
workstation> nastran tuningfork.bdf
```

The resulting output in `tuningfork.f06`, may be evaluated for the appropriate normal mode frequencies.

2.18.7.2. Modal FRF

The analysis may be modified to run a modal frequency response. Most modifications are in the case control section. Analyze with,

```
workstation> nastran tuningforkfrf.bdf
```

Output analysis is a relatively easy using NASTRAN aware tools, or the PCH file may be mined to garner the data.

2.18.7.3. Insertion of a ROM from Sierra/SD

There are relatively few changes required to the original BDF file required to include a DMIG from Sierra/SD. See the example in `se.bdf`, which includes the DMIG for the rightmost tine.

```
workstation> nastran se.bdf
```

Output of this analysis is the normal modes solution (as in section 2.18.7.1), but with the ROM of the right tine. Comparison of the modal frequencies provides validation of the analysis.

2.18.7.4. Insertion of a ROM from NASTRAN

The `eigen_se.bdf` file provides the input for NASTRAN analysis using the NASTRAN generated superelement. The superelement (in DMIG format) is read using an 'include' command. Analysis is performed using this command.

```
workstation> nastran eigen_se.bdf
```

The eigenvalues are found in the `.f06` output file and may be compared with the Sierra/SD results of section 2.18.5.

For input see Appendix 11.47.

2.19. Sierra/SD Superelement File Formats

In this section, we consider the tuning fork model (figure 18-43) described in section 2.18. We modify the workflow shown in figure 18-45 so as to compare the full model (without CB reduction) against the superelement results using both `format=netcdf` and `format=dmig*`: for each file format, the superelement is written to disk and read back in to be used in the analysis. The results (c.f. table 18-7) are shown in table

#	Description	Full Model	Rel. Diff. (netcdf)	Rel. Diff. (DMIG)
1	base bending	532.07	1.69649e-08	1.60495e-08
2	symmetric bending	937.07	4.47213e-09	4.36792e-09
3	asymmetric bending	2956.4	4.08084e-06	4.08064e-06
4	symmetric 2nd bending	4733.4	6.50282e-06	6.50278e-06

Table 19-13. – Vibrational Frequency Comparison

For input see Appendix 11.48.

2.20. Transient Reaction Forces

The response of a simple transient system is demonstrated. This test is used in particular to verify the transient time integrator, output of kinematic quantities from transient solution, and output of reaction force quantities from transient solution. A through derivation of expected quantities is provided in the Mathematica input file included in the test directory.

2.20.1. Finite Element Model

The model consists of four Spring-Dashpot elements connected to a central concentrated mass as shown in Figure 20-51.

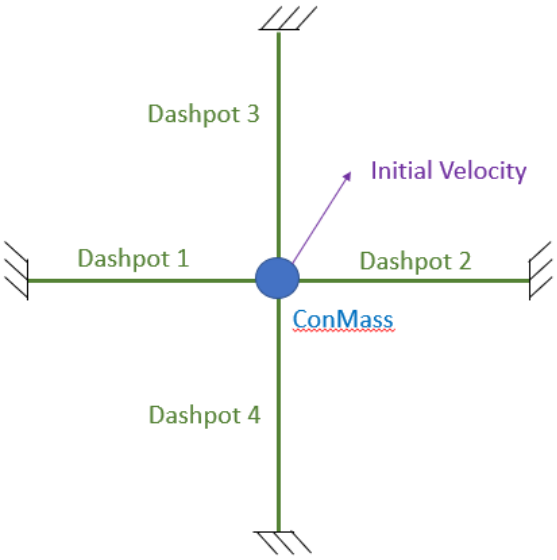

Figure 20-51. – Reaction Force Model

Dashpots 1 and 2 act only in the X direction. Dashpots 3 and 4 act only in the Y direction. Each Dashpot has a unique stiffness and damping coefficient given by Table 20-14. The central conmass has a mass of 2.5.

Block	Stiffness	Damping
1	1.1	0.7
2	1.2	0.8
3	1.3	0.9
4	1.4	1.0

Table 20-14. – Dashpot Element Properties

The model can be treated as two independent single degree of freedom systems. One system involving the sum of the stiffness and damping of Dashpots 1 and 2 acting in the X

direction and a second system involving the sum of stiffness and damping of Dashpots 3 and 4 acting in the Y direction. The Z degree of freedom of all nodes is fixed as is the far end of each Dashpots.

2.20.2. Damped Vibration Due to Initial Conditions

The input deck 'initCond.inp' applies an initial velocity (10, 20, 0) to the conmass and then solves for the resultant system response. At standard textbook response is used for vibration of a single degree of freedom damped system given in the equations 2.20.1 to 2.20.4. K is the stiffness given by the sum of the two Dashpot stiffness. M is the mass of the concentrated mass. C is the sum of the two Dashpot damping coefficients. Initial conditions of displacement are given by d_0 and velocity by v_0

$$\omega = \sqrt{\frac{K}{M}} \tag{2.20.1}$$

$$\zeta = \frac{C}{2 * M * \omega} \tag{2.20.2}$$

$$\omega_{damped} = \omega\sqrt{1-\zeta^2} \tag{2.20.3}$$

$$d(t) = e^{-\zeta\omega * t}(d_0 cos(\omega_{damped} t) + sin(\omega_{damped} t)\frac{v_0 + \zeta\omega d_0}{\omega_{damped}}) \tag{2.20.4}$$

In Sierra/SD the dynamics are integrated through time using the Newmark-Beta time integrator. A small time step is used so that the results have a high degree of time accuracy. The tests checks equivalence between the analytic and Sierra/SD results kinematic quantities at specific time steps in the solution.

The expected reaction forces can be found by considering the fundamental system equation given in 2.20.5.

$$Ku + C\dot{u} + M\ddot{u} = f \tag{2.20.5}$$

2.20.3. Prescribed Acceleration

A second tested case involves constant prescribed acceleration on the central node. The velocity and displacement of the central node can be found via integration of the acceleration. Based on the kinematic motion the forces are given 2.20.5. For the prescribed acceleration case the total damping matrix is formed from the C of the Dashpot and mass proportional (0.1) and stiffness proportional (0.2) damping coefficients.

For input see Appendix 11.49.

2.21. Relative Displacement PSD

A common requirement for random vibration analysis is understanding the probability of interference of two nodes. This use case is discussed in subsubsection RMS Output, subsection Random Vibration, section Solution Procedures of the Theory Manual, and details about usage can be found in the *User's Manual*, in the Outputs section in the Relative_Disp subsection.

In the following examples, we consider a 1D problem. Specifically, we investigate the relative displacement output of a joint2G element in response to two conmass nodes.

2.21.1. In Phase Response

In this example, the motion of both nodes is precisely in phase (see figure 21-52). In that case, the difference of the two nodes should report no response, as seen in figure 21-53. This test verifies that the gap differencing element does not report the rigid motion of the element.

Figure 21-52. – Both nodes moving in phase: diagram

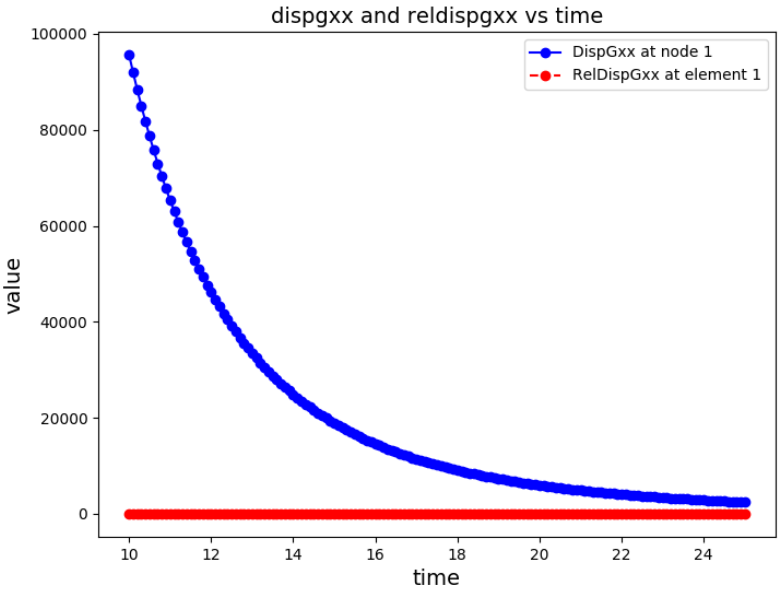

Figure 21-53. – Both nodes moving in phase: results

2.21.2. Opposite Phase Response

In this example, the motion of the two nodes are precisely out of phase with each other (see figure 21-54). This is a direct test of the gap differencing element's measurement of the difference in motion between two points. In the time domain, this condition would result in the gap element reporting twice the response at each node. Likewise, in the frequency domain the gap element should report 4 times the response. This relation is seen in figure 21-55.

Figure 21-54. – Nodes moving exactly out of phase: diagram

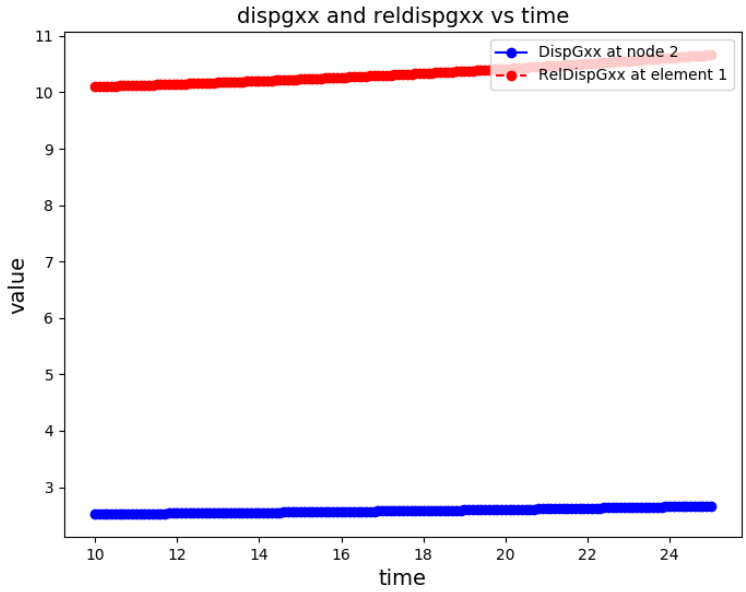

Figure 21-55. – Nodes moving exactly out of phase: results

2.21.3. One Node Fixed Response

In this example, one node is fixed, and the other is free (see figure 21-56). The expected behavior in this case is that the difference in motion between two nodes is equal to the motion of the free node, which can be seen in figure 21-57.

Figure 21-56. – Left node fixed; right free: diagram

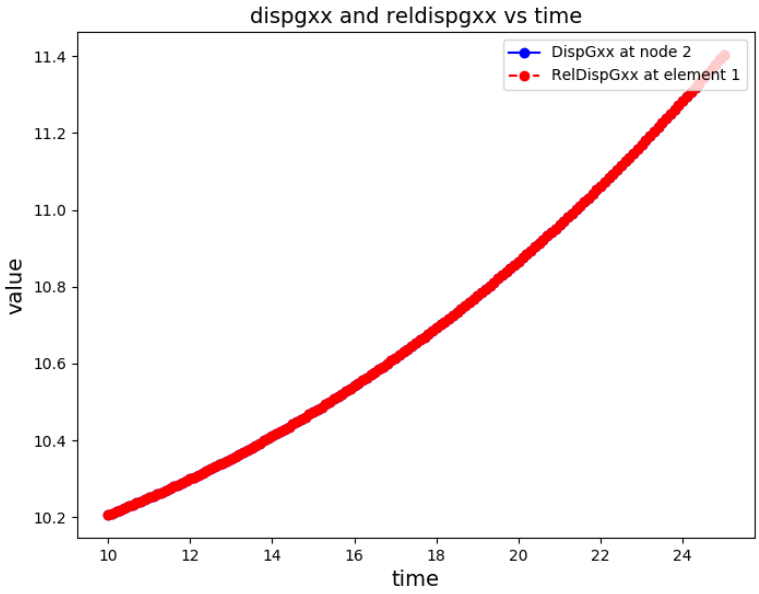

Figure 21-57. – Left node fixed; right free: results

2.21.4. Tuning fork response

In this test, we verify the gap calculation from **Sierra/SD** by directly computing the expected gap PSD from modal displacements. This test also involves several overlapping tied joints, as shown in figure 21-58.

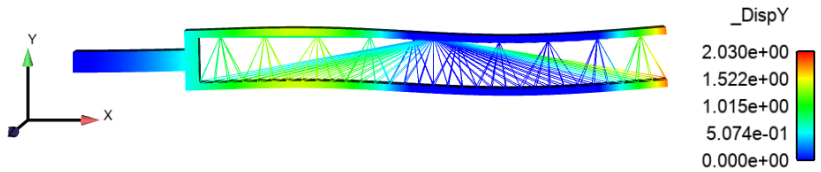

Figure 21-58. – Tuning fork with multiple overlapping tied joints

The PSD, $G(\omega) \in \mathbb{R}^{34\times34}$, is given by

$$G = H\, S_{ff}\, H^* \tag{2.21.1}$$

where $S_{ff}(\omega) \in \mathbb{R}^{34\times34}$ is the forcing PSD, and the transfer function $H(\omega) \in \mathbb{R}^{34\times34}$ is given by

$$H = \Phi\, \widetilde{H}\, \Phi^T \tag{2.21.2}$$

where $\Phi \in \mathbb{R}^{34\times12}$ is the matrix of mode shapes (dofs x mode shapes), and the modal transfer function $\widetilde{H}(\omega) \in \mathbb{R}^{12\times12}$ is a diagonal matrix given at each mode n as

$$\widetilde{H}_{nn} = \frac{1}{\omega_n^2 + 2i * \omega\gamma\omega_n - \omega^2} \tag{2.21.3}$$

For input see Appendix 11.50.

3. CONTACT, CONSTRAINTS AND MPCS

3.1. Parallel Distribution of Load through Rbars

The purpose of the verification is to ensure that loads may be properly distributed through a "spider" collection of Rbar elements onto a concentrated mass. The model is shown in Figure 1-1. This is a model of a conmass connected to a hex by spiders using Rbars. Verification that the model works the same running with one processor or six processors.

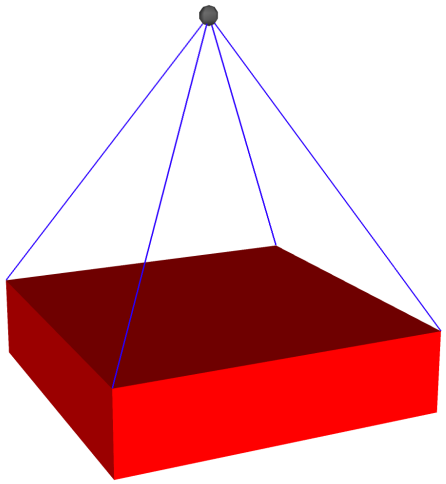

Figure 1-1. – Model for Parallel Distribution of Load through Rbars

For input deck see Appendix 11.1.

3.2. Rigidset Compared to Rbar

The purpose of this test is to verify Rigidsets. Verification means that the Rigidsets do the same thing as an equivalent block of Rbars.

A Rigidset is a tool to define a set of nodes as completely Rigid. It is done by creating a sideset (or a nodeset, but sidesets are preferred) and defining that sideset as a Rigidset in the input deck. While Rbars can be used to produce the same rigidity, the process with Rigidsets is much easier. Setting up an equivalent block of Rbars involves creating a block of beams that are not redundant, which gets trickier with more nodes. This step can take more time than desired. Then the block is defined with Rbars in the input deck. Rigidsets are much easier to use and produce similar results.

While the results are the same, the means of obtaining them are different. This can be seen through the MPCs (Multi-Point Constraint equations). Consider the single hex model in Figure 2-2. Since this meshed model contains only a single hex, it only has eight nodes. A sideset has been assigned to one of the hex surfaces, shown in green in Figure 2-2. This sideset is used to define the Rigidset. Rbars are defined by three of the edges on this surface, constrained as a block of BEAM elements.

As previously mentioned, the Rigidset is defined by a sideset. A wireframe of the single hex's Rigidset can be seen in Figure 2-3. There are 18 MPCs and three node connections that are used in the constraint equations. The node connections here are between nodes 3 and 4, 2 and 1, 3 and 1, as represented by the dashed red lines in Figure 2-3. There are 6 constraint equations for each of these connections. Together, these constraint equations make a perfectly rigid surface.

The MPCs for the block of Rbars also create a perfectly rigid surface, but the equations and node connections differ from those used in the Rigidset. Figure 2-4 shows the block of Rbars created from three edges of the surface. Notice that there cannot be a connection between nodes 3 and 4. A connection between nodes 3 and 4 would require an Rbar there, which would cause redundancy in the constraint equations. One of the difficulties in creating a block of Rbars is making sure there are no redundancies. As shown by the dashed red lines, the connected nodes here are 4 and 1, 1 and 2, 2 and 3. Each connection still has 6 constraint equations, making 18 MPCs in all. The result is the same as Rigidsets, but the means of getting there is different.

Rigidsets and Rbars use different constraint equations, but both can create a rigid set of nodes with the same eigenvalues. This means that Rigidsets can be verified by comparing the results to Rbars. For input deck see Appendix 11.2.

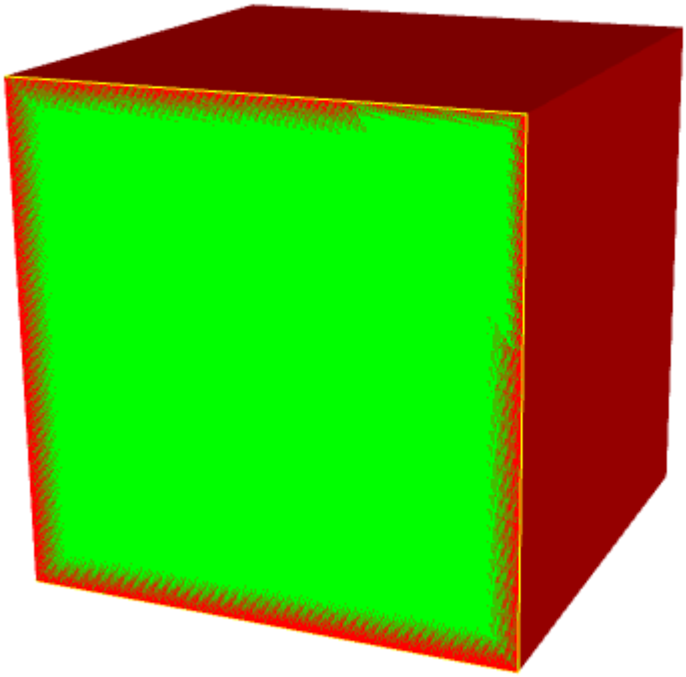

Figure 2-2. – A model of a single hex.

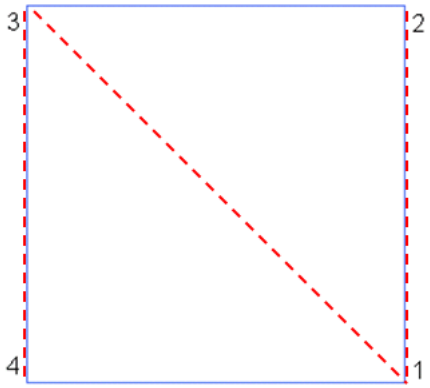

Figure 2-3. – A wireframe view of the sideset used for the Rigidset in Figure 2-2.

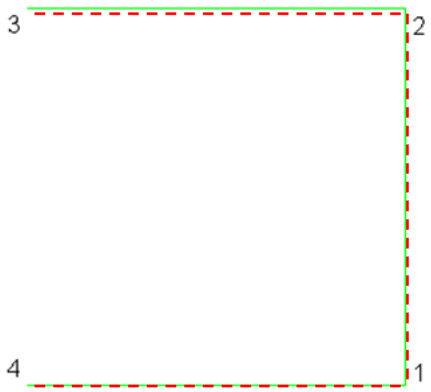

Figure 2-4. – A wireframe view of the block of beams used for the Rbar collection in Figure 2-2.

3.3. Multiple Tied-Surfaces and Curved Surfaces

The purpose of this test is to verify the behavior of multiple tied surfaces. The model is shown in Figures 3-5 through 3-12. Included are several figures that show the model broken down into blocks and the relationships between the surfaces and blocks. Note that Block 3 is actually Block 10 in the input files.

We verify that the eigen analysis retains 6 rigid body modes, and that the structure is appropriately tied on the planar and curved surfaces. Note that 6 rigid body modes are not calculated due to poor conditioning of the constraint matrix if con_tolerance 1e-3 is commented out in the GDSW solver block. Figure 3-13 shows mode 15 of the solution, with a large degree of deformation.

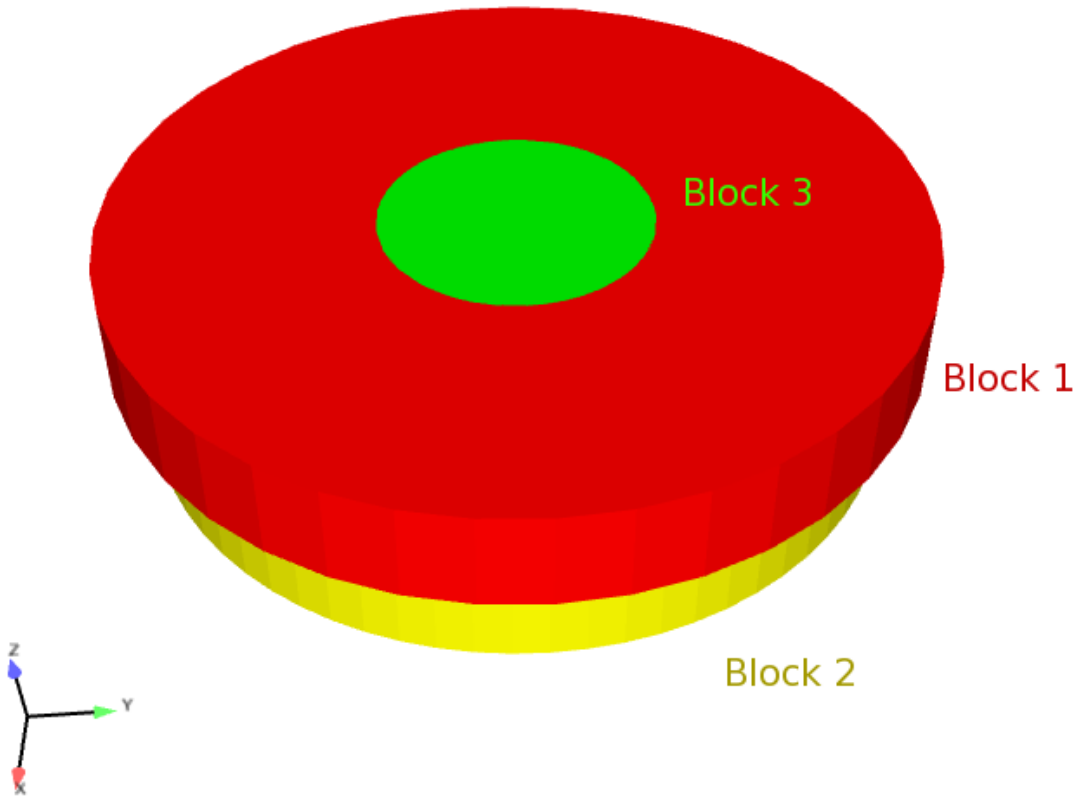

Figure 3-5. – All three blocks from an above angle.

For input deck see Appendix 11.3.

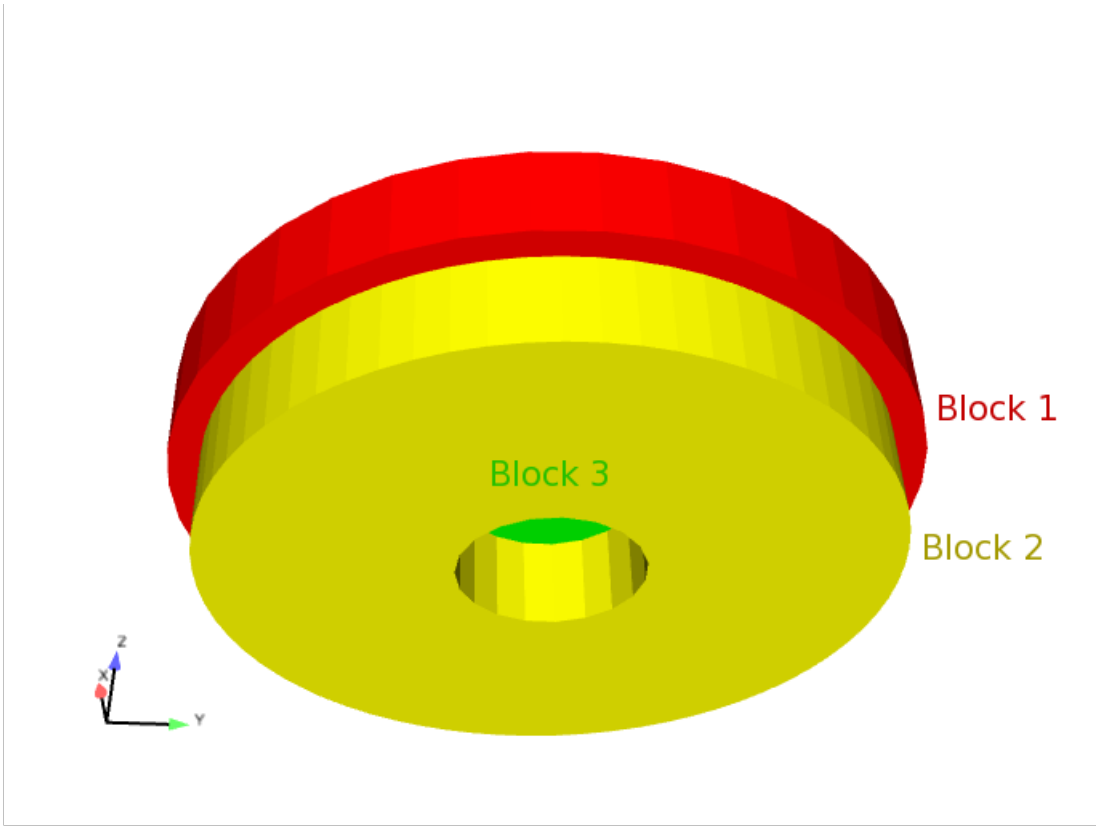

Figure 3-6. – All three blocks from a below angle.

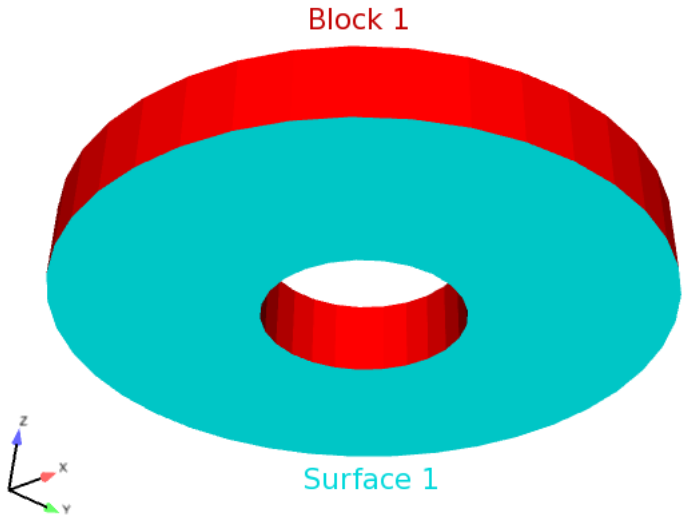

Figure 3-7. – Block 1 and Surface 1.

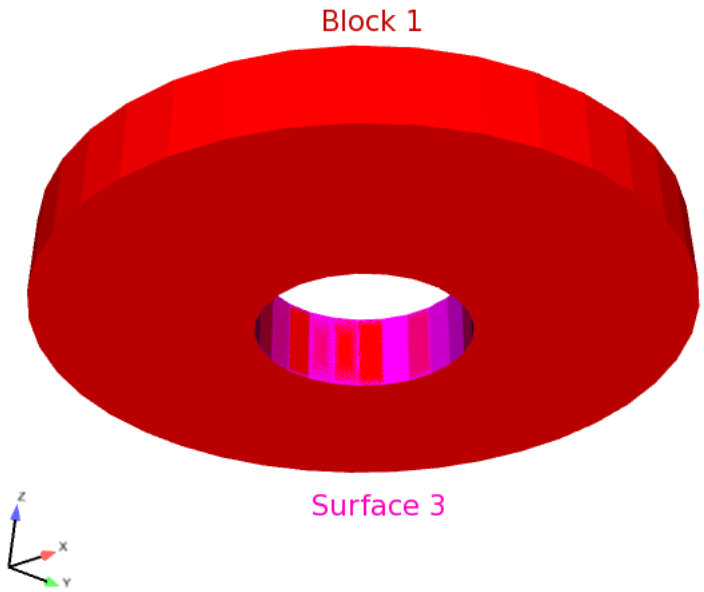

Figure 3-8. – Block 1 and Surface 3.

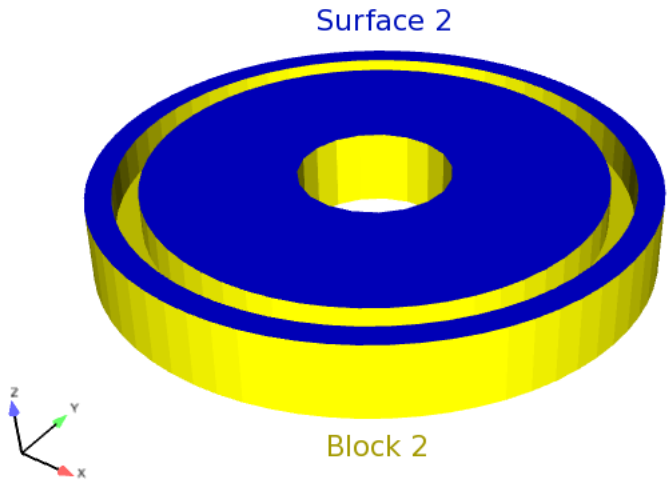

Figure 3-9. – Block 2 and Surface 2.

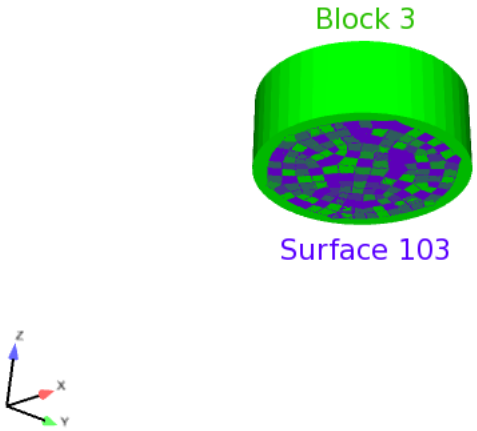

Figure 3-10. – Block 3 and Surface 103.

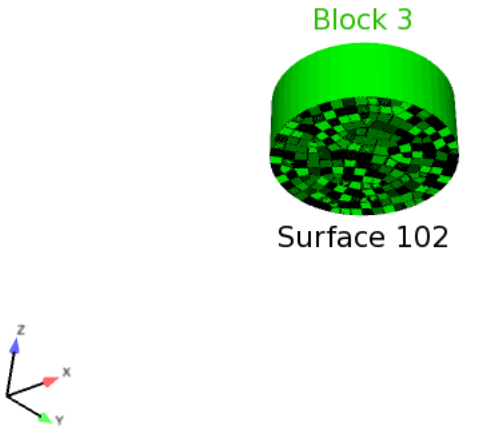

Figure 3-11. – Block 3 and Surface 102.

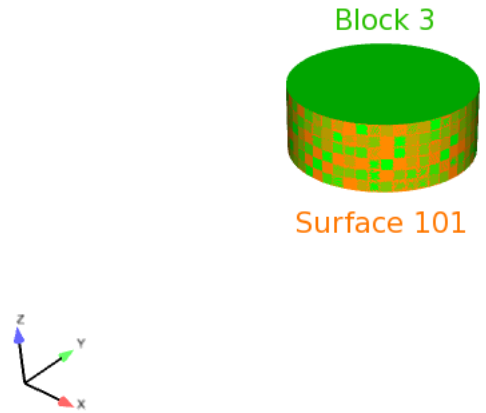

Figure 3-12. – Block 3 and Surface 101.

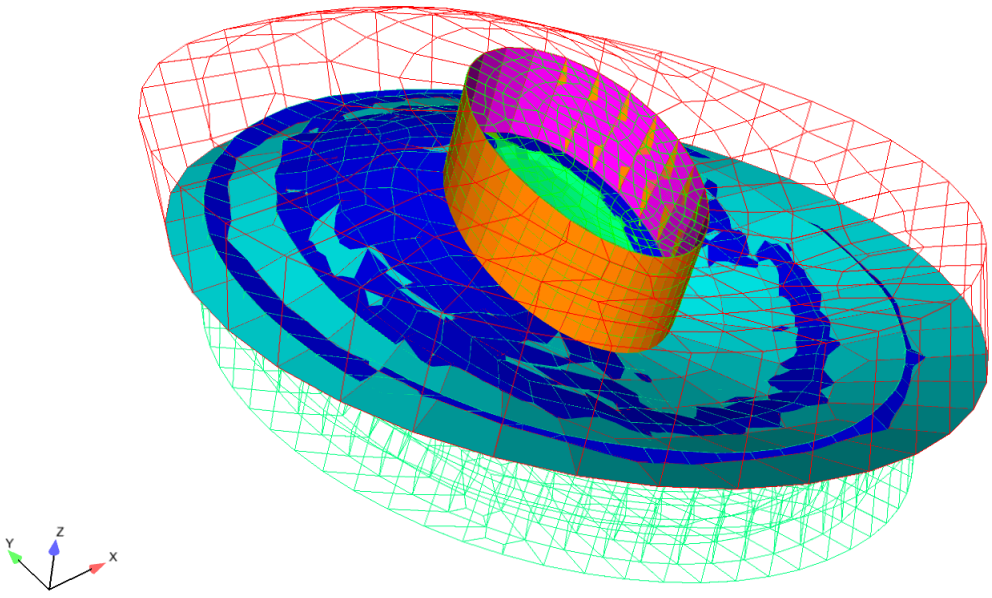

Figure 3-13. – Mode 15. Showing sideset Tying

3.4. Contact Verification

In this section we provide a series of verification tests for a conceptually monolithic bar created by tying together separate element blocks. This verification test documents the solution convergence rate for a contiguous mesh versus a discontinuous mesh tied along planar or curved boundaries. Additionally the test investigates the effect of tied data gap removal and face/node pairings. Evidence based usage guidelines for tied data are provided based on the results.

3.4.1. Description of the Test

Three load cases are considered: A gravity load on a cantilever beam (Figure 4-14(a), a bar fixed at one and with a traction load on the other (Figure 4-14(b), and free-free eigen. To ensure planar notionally 2D results, the Poisson's ratio of the material is set to zero and boundary conditions constrain motion to the xy plane.

The mesh is generated with Hex8 elements. The geometries used are pictured in figure 4-15. The top mesh is a contiguous mesh to be used as a comparison baseline, and refined significantly for a "truth" solution. The middle mesh uses straight interfaces between the block partitions. The bottom mesh uses curved interfaces between the block partitions.

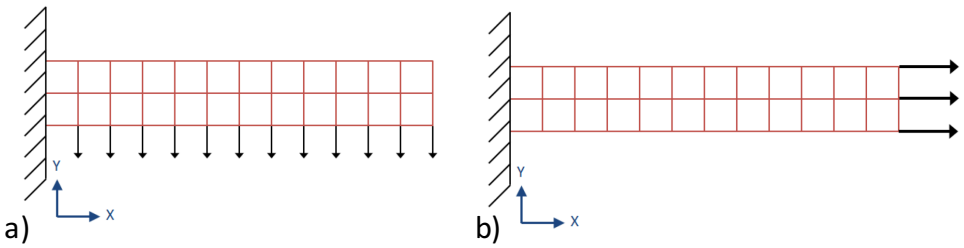

Figure 4-14. – Beam under (a) gravity loading and (b) traction loading.

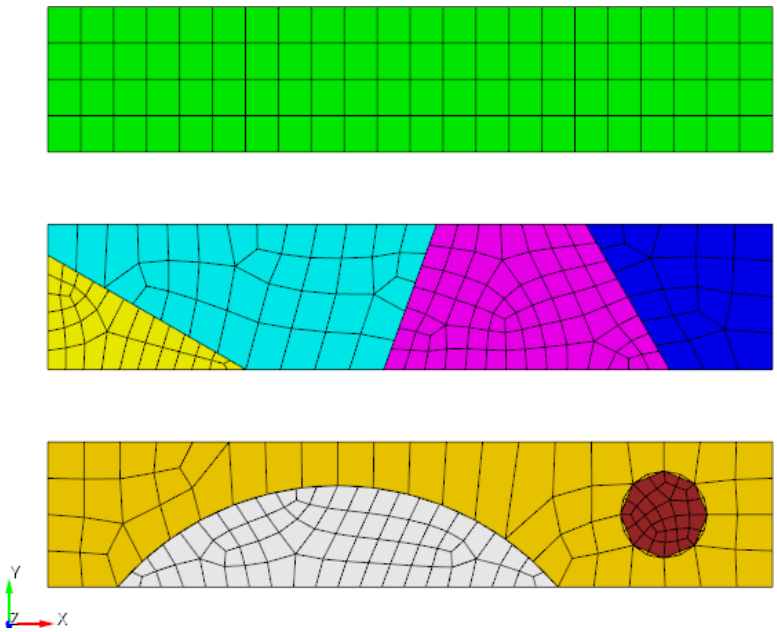

Figure 4-15. – Mesh Geometry

3.4.2. Expected Results

The eigen modes, cantilever beam displacement, and axial pull solution all have approximate solution based on beam theory. However, as the meshed beam has finite thickness, ultimate verification is done against a "truth" solution generated by a highly refined contiguous mesh.

For the free-free eigen case, the first three modes should be rigid body modes. These tests investigate the preservation of rigid body modes with tied data and the convergence of the first three flexible modes. For the cantilever beam problem, the quantity of interest is tip displacement and total strain energy, again compared versus a highly refined contiguous truth solution. For the axial bar pull analysis the quantity of interest is maximum stress, which is expected to be artificially high when tied interfaces are used. The axial bar pull analysis is effectively a patch test that should produce an exactly known uniform stress state. Any deviation from this expected stress state is considered error.

3.4.3. Evaluation of Free-Free Eigen Load Case

The bar is constrained to deform in plane only. Thus, the bar should have three rigid body modes: two translational, and one rotational. The expected mode shapes for the first three flexible modes are shown in Figures 4-16(a) (535.5 Hz), (b) (1272.6 Hz), and (c) (1453.9 Hz).

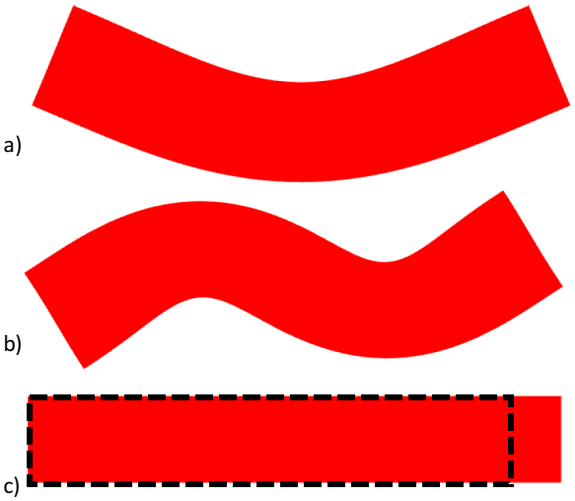

Figure 4-16. – Flexible mode shapes (a) mode 1 (b) mode 2 and (c) mode 3 (non-uniform axial elongation)

3.4.3.1. Convergence Rate for Eigen Values

The mesh convergence for the first three flexible modes are shown in Figures 4-17(a)-(c). Note the third flexible mode is the axial bar extension mode. This mode approaches the correct solution with very few elements due to the complete lack of any bending in the mode shape. As a result, the convergence plot is not particularly informative, but is shown here for completeness. Generally second order convergence rates are achieved with or without contact. The contiguous mesh tends to have moderately less absolute error at any given refinement.

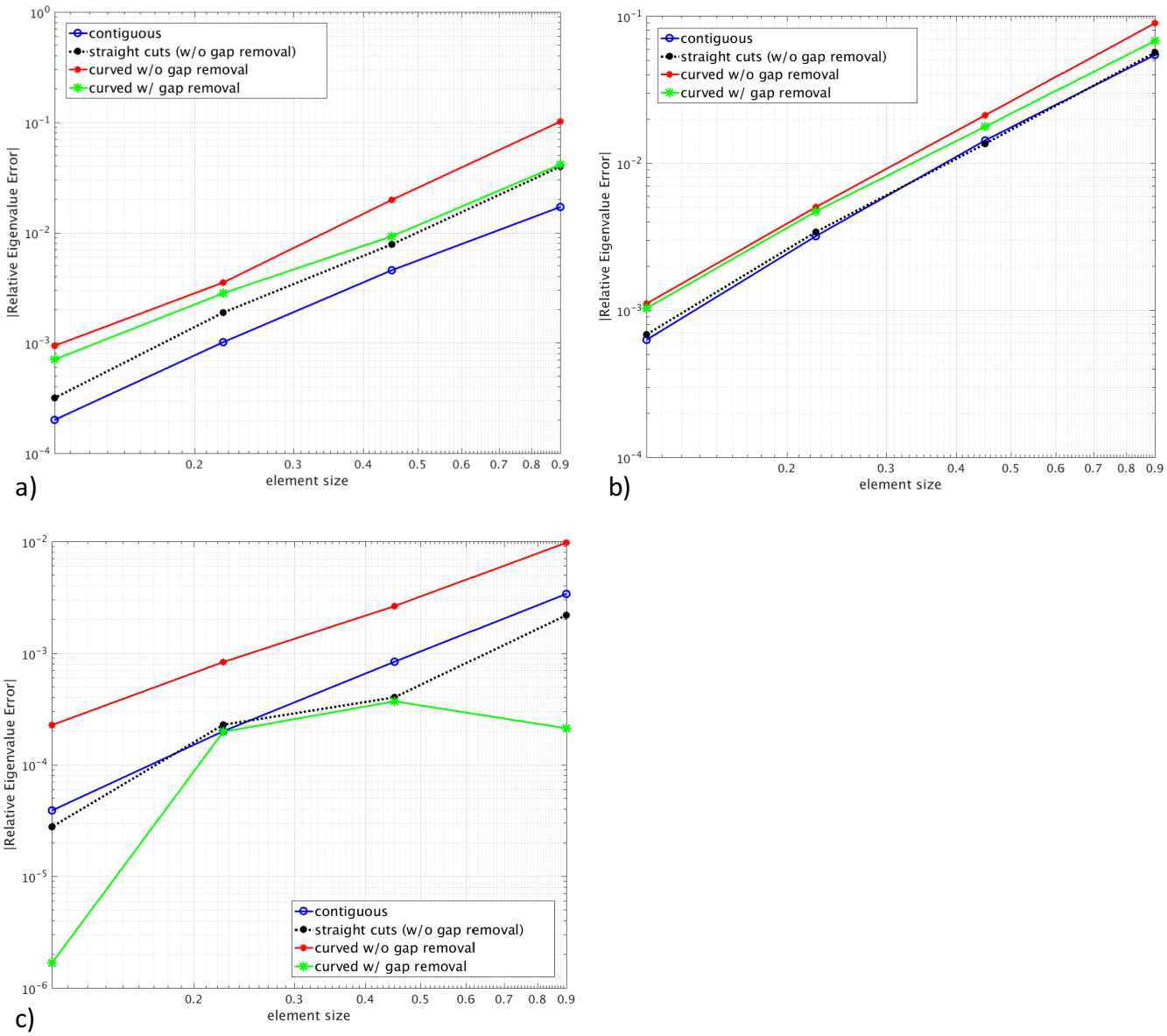

Figure 4-17. – Convergence rates for flexible modes. (a) First elastic mode converges to 534.5 Hz (b) Second elastic mode converges to 1272.6 Hz (c) Third elastic mode converges to 1453.9 Hz.

3.4.3.2. Invariance to Rigid Body Rotation

Figure 4-18 shows how accurately the rigid body rotation mode is preserved. Ideally, this rigid body rotation mode will have zero stiffness. In practice there is a very small stiffness due to round-off errors and finite solver convergence tolerance. However, for the curved contact case with gap removal off there is a very significant error in the rigid body rotation mode. Using the faceted curved cuts, there are finite gaps between the nodes and faces on the two sides of the contact interface. When tied contact constraints are defined across finite gaps, the constraints artificially constrain rotations. The smaller the gap, the less artificial constraint is produced. As the mesh is refined the node to face gap shrinks, and the solution converges toward the exact solution. However, as seen in both the rigid body rotation mode, and the results for the flexible modes, the error from these constraints with gaps is large.

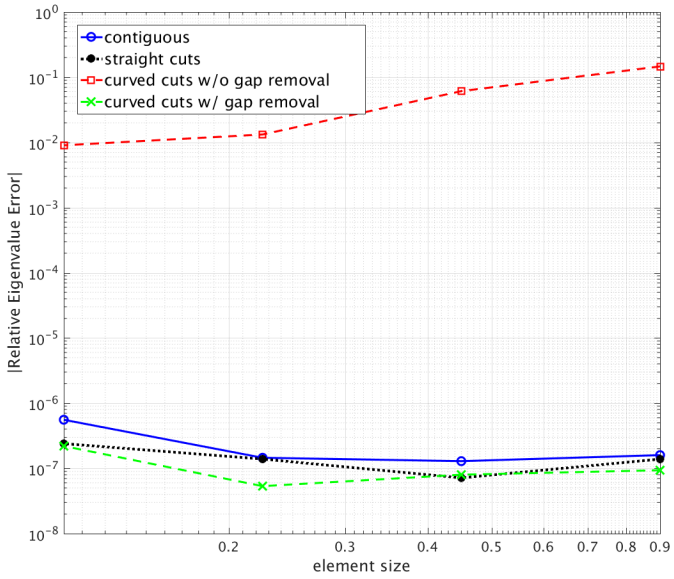

Figure 4-18. – Error in rigid body rotation mode relative to first flexible mode

3.4.3.3. Effect of Node Face Interaction Pairing

For optimal accuracy, it is imperative to chose the correct surface for tied data interactions. The previous results were made with the recommended setting of using the finer meshed surface as the node surface, and the coarser surface as the face (faces). The face and node surfaces are selected by the order of surfaces in the tied data section of te input deck. As an example, the below syntax selects the nodes of surface 101 as the nodes and the faces of surface 100 as the face.

```
TIED DATA
```

```
  SURFACE 100, 101
END
```

The opposite face node pairing is given by:

```
TIED DATA
  SURFACE 101, 100
END
```

If face and node surfaces are selected properly, MPC_Status, which is specified by the constraint_info output option, will appear as shown in figure 4-19(a). If the wrong surface is chosen as face, then the results appear as shown in figure 4-19(b). Notice that many nodes on the tied surfaces have begun to separate from, or penetrate into, the opposing surface. This is a result of the relative refinements between the two surfaces. In the incorrect example, the more refined surfaces were chosen as the face surface, and many interactions were missed.
The reason for this lies in the way that tied data functions; specifically, tied data requires that all nodes on the node surface lie on the faces of the face surface, but does not impose the same requirement on the nodes of the face surface. If both surfaces are at approximately the same refinement, it does not matter which side is the face surface, but when the face surface is at a significantly higher refinement than the node surface, there will be some faces of the face surface which are not constrained to any nodes, and are allowed to move without any stiffness contribution from the node surface.
Note that the MPC_Status variable is not a foolproof check of correct interactions. It clearly shows the issues on the small circular region, but is not a sufficient check on the larger arc.

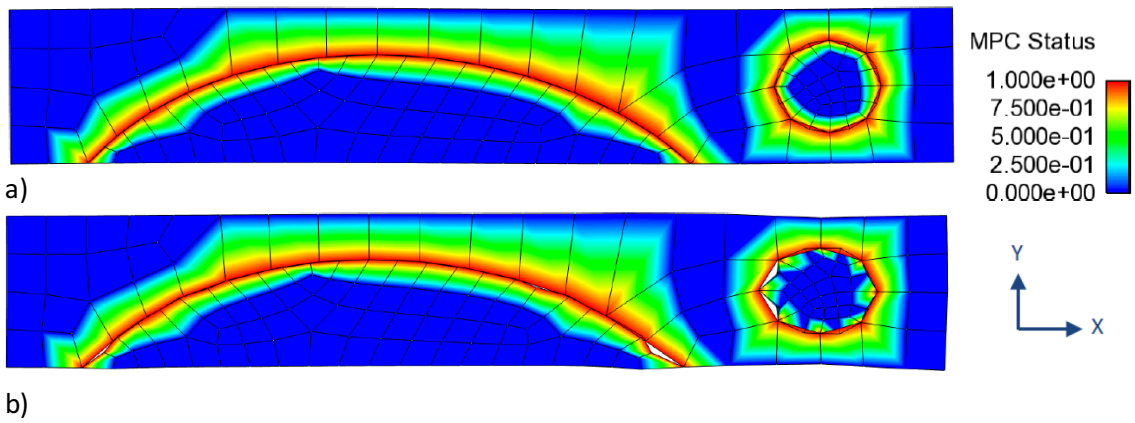

Figure 4-19. – MPC Status (a) correct and (b) incorrect.

The eigen mode convergence with reversed face/node interactions is shown in Figure 4-20(a)-(c). With the non-recommended face/node pairing the convergence rate becomes sporadic. The eigen shape solution will contain obvious errors local to the contact interface. A decent eigen value solution can sometimes be obtained when these errors cancel. On the whole though, the eigen value solutions are much worse with the non-recommended face/node pairings.

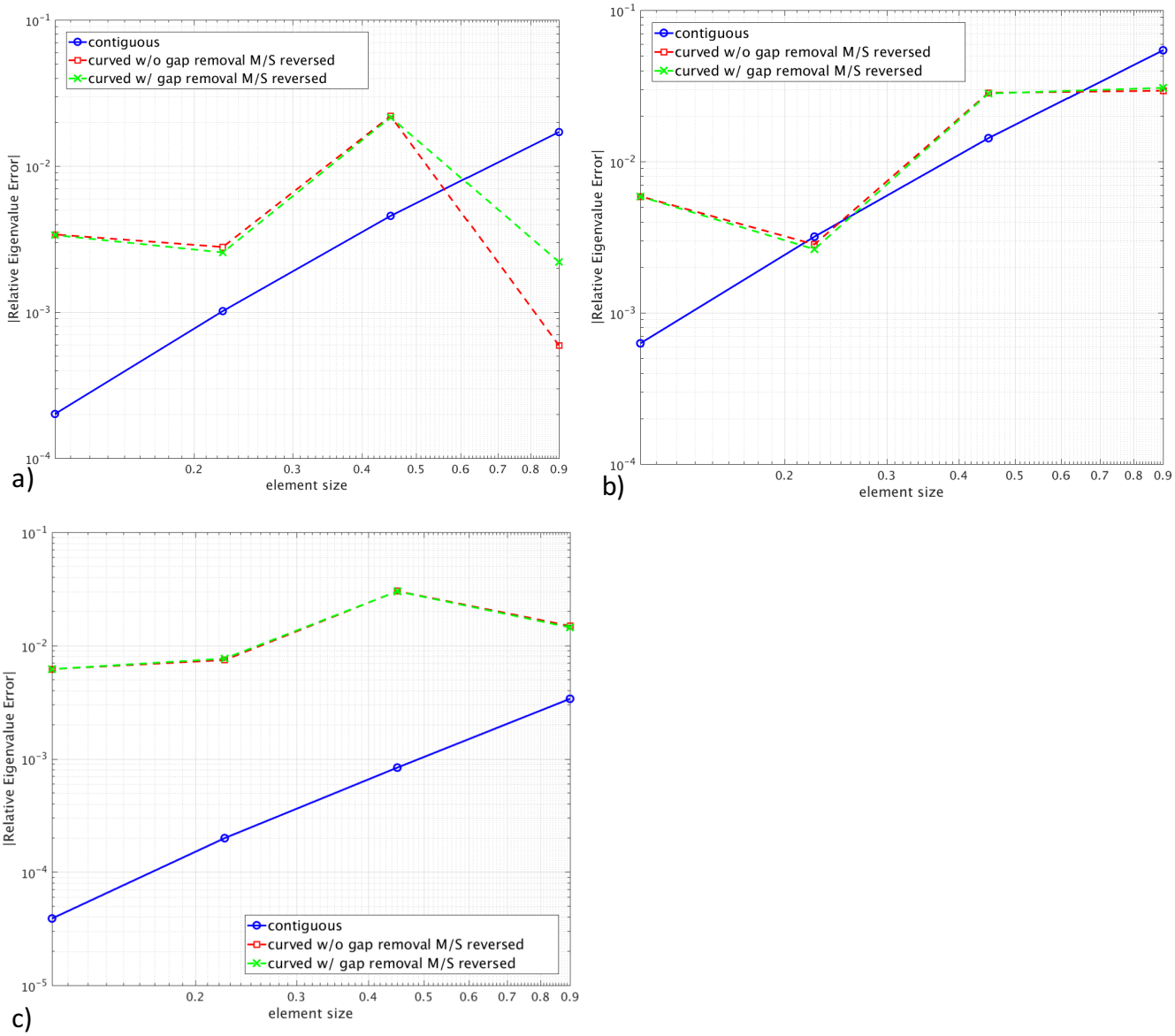

Figure 4-20. – Flexible mode convergence rates with reversed face/node. (a) First flexible mode converged to 534.5 Hz. (b) Second flexible mode converged to 1272.6 Hz. (c) Third flexible mode converged to 1453.9 Hz.

3.4.4. *Evaluation of Cantilever Beam Static Results*

The result for contiguous cantilever beam is shown in Figure 4-21.

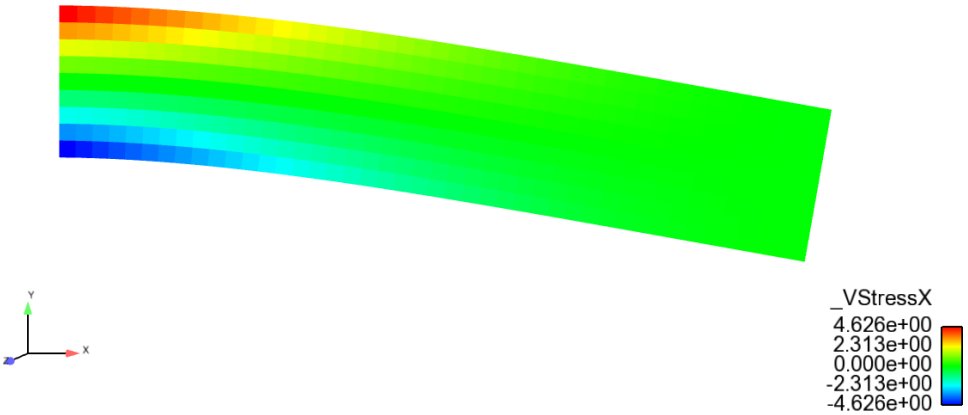

Figure 4-21. – Cantilever Beam Deformed result (greatly magnified)

3.4.4.1. Convergence Rate

The mesh convergence of tip displacement for the cantilever beam is shown in Figure 4-22. Convergence is quadratic with or without contact. As in the eigen mode solution, addition of contact does add some error for a given mesh density. Likewise, the presence of finite gap constraints introduces additional error into the solution.

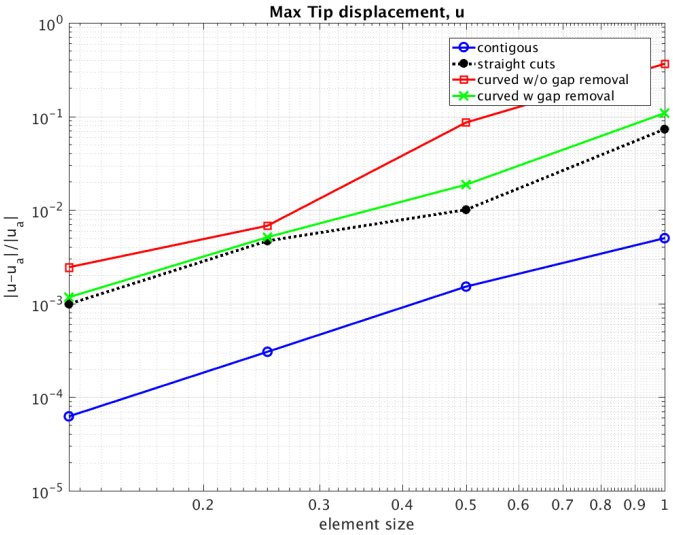

Figure 4-22. – Cantilever Beam Convergence For Tip Displacement

3.4.4.2. Symmetric Contact

It is possible to inadvertently add symmetric contact to a model. In symmetric contact the nodes of surface one are constrained to the faces of surface two while simultaneously the nodes of surface two are constrained to the faces of surface one. For example, including both the following tied data sections in an input deck would add symmetric contact to a model:

```
TIED DATA
  SURFACE 101, 100
END
TIED DATA
  SURFACE 100, 101
END
```

Symmetric contact is not expected to work correctly. Symmetrically constrained interfaces are over constrained. Such interfaces can rotate, stretch, and shear, but they cannot bend. The convergence of the cantilever bar with symmetric constraints is shown in Figure 4-23. With symmetric constraints there is no convergence to the correct solution. As seen in Figure 4-24 the symmetric contact interfaces cannot bend, leading to a completely spurious displacement and stress result.

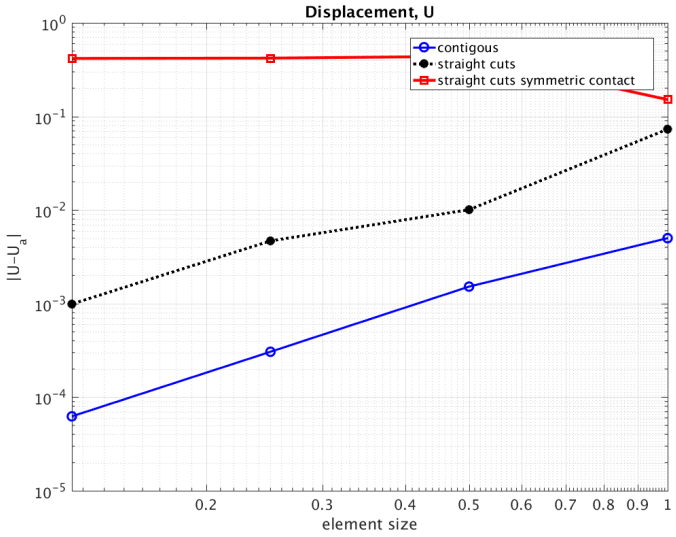

Figure 4-23. – Cantilever Beam Convergence with Symmetric Constraints

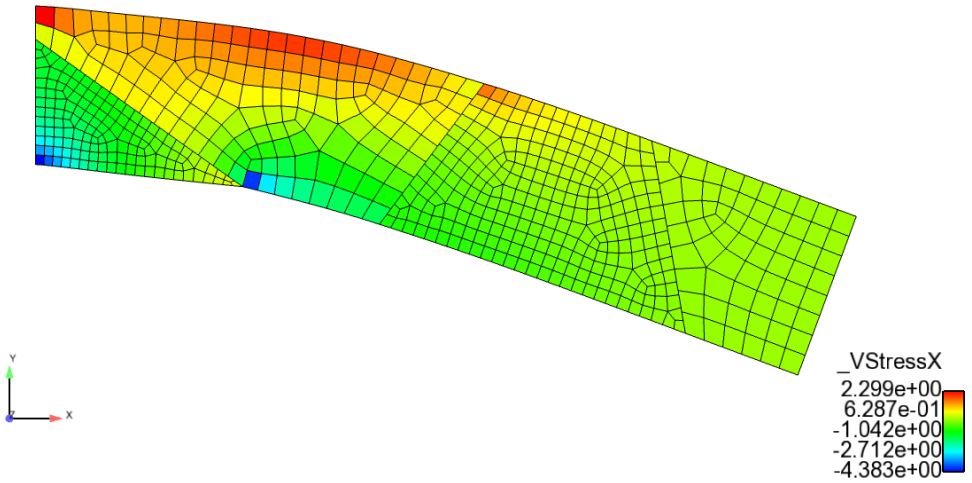

Figure 4-24. – Incorrect Cantilever Beam Result with Symmetric Contact

3.4.5. Evaluation of Axial Pull Results

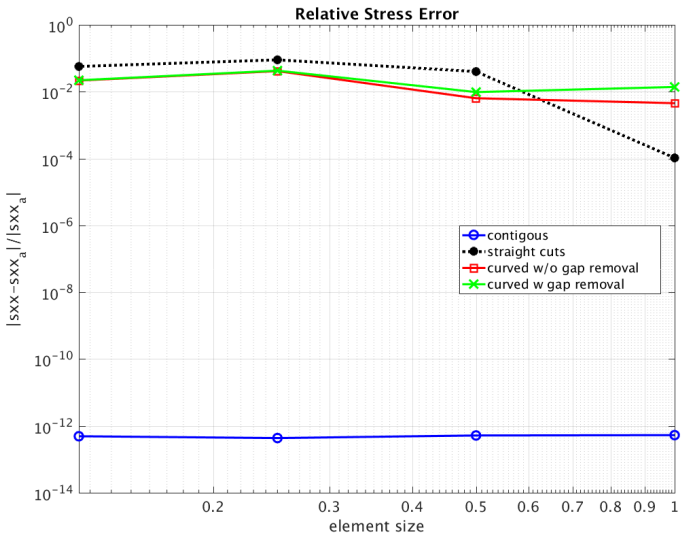

Figure 4-25. – Axial Pull Convergence for Maximum Stress

The axial pull results should produce an exact uniform XX direction stress of 1000, however the nature of tied contact constraints produces artificial stress concentrations at the contact interface. The convergence of stress is shown in Figure 4-25 and the distribution of stress on two mesh resolutions shown in Figure 4-26. The magnitude of tied data stress concentrations are not remedied by mesh refinement. The stress concentrations do become somewhat more localized with mesh refinement.

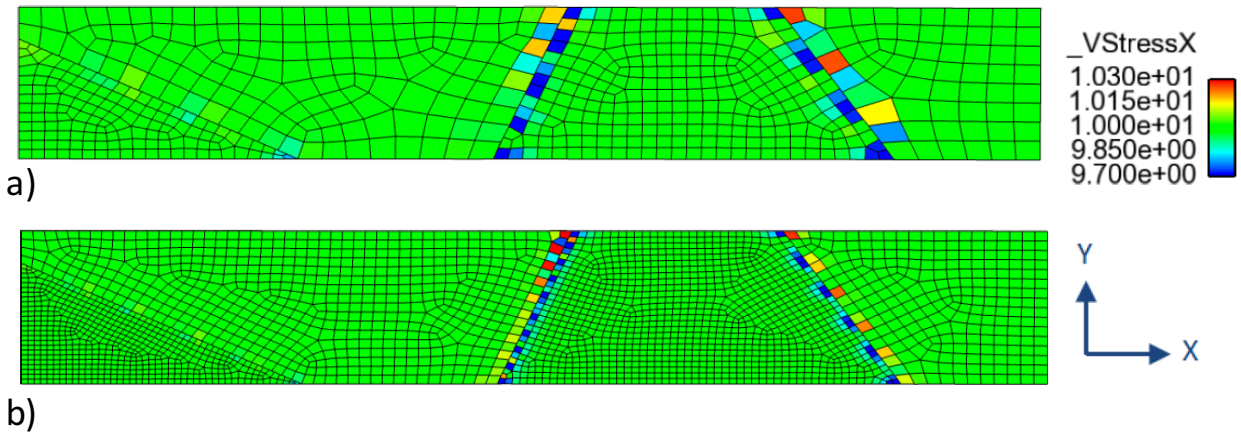

Figure 4-26. – Spurious Local Stress Concentrations with (a) coarse and (b) fine meshes.

3.4.6. Usage Guidelines

Used carefully, tied data can greatly simplify the model creation process by eliminating the need for contiguous meshes. However, there are a number of significant areas for concern when setting up tied data.

- Models using tied data can achieve quadratic convergence for both eigen modes and static displacement. However, results will generally by at least mildly inferior to a contiguous mesh at the interface.
- Using gap removal will significantly improve the accuracy of contact at curved interfaces.
- For optimal accuracy, the finer meshed surface should be used as the 'nodes' of tied data interactions and the coarser surface the 'faces'.
- Symmetric contact constraints should always be avoided as they lead to major errors and a non-convergent solution.
- Tied contact introduces irresolvable local stress concentrations at the tied interface. If an accurate stress is needed near the tied interface, a contiguous mesh should be used.

For input see Appendix 11.51

3.5. Periodic Boundary Conditions

In material characterization through simulation of representative volume elements, periodic boundary conditions are needed on the opposite faces, with imposed stretch and/or distortion. Similarly, in the context of phononic crystals and acoustic/elastic metamaterials, imposing periodic boundary conditions is a key functionality needed for computation of dispersion curves and band structure. Sierra-SD facilitates the imposition of such periodic boundary conditions.

In this section, we provide the verification of the capability by simulating an infinite bar with linear array of spherical voids, with imposed overall tensile strain. We do not attempt to compare with any analytical/reference solutions, but confirm the consistency of results from applying periodic boundary conditions in two different ways. Specifically, we consider an infinite bar of unit (1x1) square cross-section, with spherical voids of radius 0.4, dispersed uniformly with unit spacing. A global strain of 0.015 is applied along the axis (x direction), and the resulting stresses are to be analyzed (the Young's modulus is 1e4). Such an analysis can be carried out by modeling a periodic cell, which can be any 1x1x1 block along the length of the bar. Correctly implemented periodic boundary conditions must give the same results independent of the choice of the periodic cell. Given this, we compare the results from analyses of two separate periodic cells, one with the spherical void at the center of the periodic cell, and the other with the periodic cell boundaries on both ends cutting through the centers of two adjacent voids. A differential x-displacement of 0.015 units is applied between two edges of the periodic cells to simulate the global strain of 0.015. Rigid body displacements are eliminated through appropriate statically determinate boundary conditions on the center section of the cell. Figure 5-27 contains the meshes for the two periodic cells. Note that each half has identical meshes, indicating that identical discrete systems are being solved, thus eliminating the role of the discretization error and leading to the expectation of almost exact match.

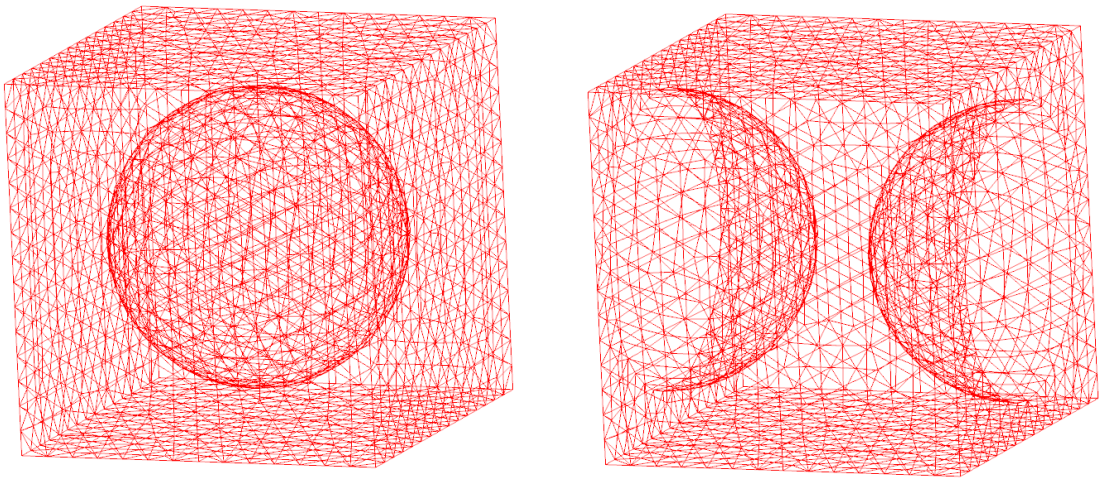

Figure 5-27. – Meshes for two different periodic cells

The stresses are examined at three different locations on the surface of the spherical void, at the intersection with x,y and z axes respectively. To be precise, the results are obtained at element centroids closest to the three locations, which are shown in table 5-1. Only one set of results is shown since the computed stresses are identical between the two models, up to 10 significant digits, clearly verifying the implementation of periodic boundary conditions.

Table 5-1. – Stresses near the surface at points cutting various axes

Stress	y axis	z axis	x axis
σ_{xx}	281.0494288	273.0301545	-1.7271636
σ_{yy}	-8.0119751	0.5224045	-0.2133664
σ_{zz}	-0.2935124	23.5932137	-0.8396841
σ_{xy}	14.8824683	14.2929051	-9.3081820
σ_{yz}	-0.3275614	0.3518104	2.0719204
σ_{xz}	16.8660510	28.2491021	-9.8072644

In addition to the above example, we tested the implementation on homogeneous block with straight and curved surfaces under uniform stretch, resulting in expected uniform stress state with correct values. The details are not presented in this document, but can be found in the test repository. For input see Appendix 11.73

3.6. Multi-directional Periodic BC: Periodic Volume Elements

Representative volume element (RVE) modeling is a standard approach in computing macroscopic materials properties from materials with microstructure. In the context of regular periodic microstructure, RVE reduces to a periodic unit cell of the microstructure, referred to as the periodic volume element (PVE). The boundary conditions for modeling a PVE of a 3D solid would be periodic boundary conditions in all three directions, or in all the directions in which the PVE repeats. This requires multiple begin-periodic blocks, each connecting the faces on the opposite surfaces. The surfaces in one begin-periodic would intersect with surfaces in other periodic blocks, thus testing the associated functionality in Salinas.

We consider the example in Section 3.6, and expand to 3D setting. Specifically, we consider a homogeneous matrix with regularly spaced spherical inclusions in all three directions. There are multiple ways to defined a PVE, and we consider two such PVEs, both cubic in shape. In the first PVE, the void is at the center of the cube, while in the second, the void is split into eight quarters, each centered at each of the vertices of the cube. The schematic of the idea, in 2D settings, is illustrated in Figure 6-28. The actual, discretized PVEs are shown in Figure 6-29, where the meshing is done in a consistent way to eliminate the differences due to discretization.

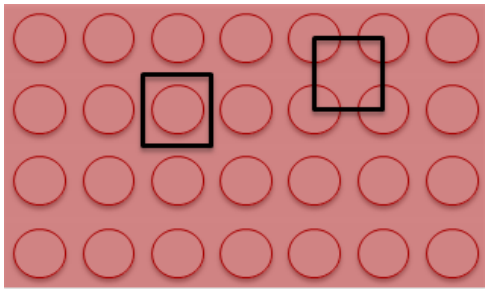

Figure 6-28. – 2D schematic of the two simulated periodic volume elements (PVEs)

Both PVEs are subjected to the same global strain, or equivalently symmetric deformation gradient:

$$\epsilon = \nabla \mathbf{u} = \begin{bmatrix} -1.50 & 1.00 & 0.50 \\ 1.00 & -1.00 & 0.25 \\ 0.50 & 0.25 & -0.50 \end{bmatrix} \tag{3.6.1}$$

Note that since the entire strain is associated with deformation gradient, implicitly, there is no (global) rotation of the PVE. Relative displacement *vector* for each begin-periodic block is determined by the above tensor applied on the geometric offset vector. Since the geometric offsets are unit vectors in x, y and z directions for each of the three begin-periodic blocks, the relative displacements are essentially the three columns of the deformation gradient (see the input file). Note that the imposition periodic BC in three different directions automatically prevent rigid body rotations, but the translation is not restrained. We eliminate the rigid body translations by fixing the center in the second PVE (and correspondingly vertex in the first PVE), in all three directions.

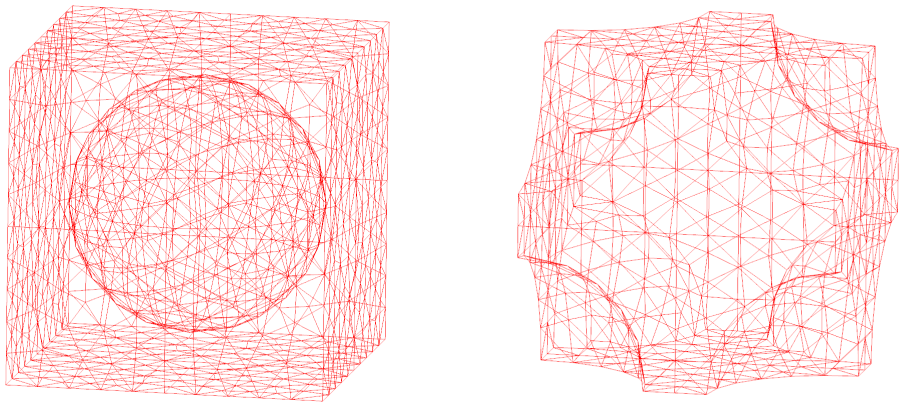

Figure 6-29. – Meshes for two different periodic volume elements

The deformed shape, along with contours of von Mises stresses are shown in Figure 6-30, which visually confirm that the results are the same between the two PVEs.

For quantitative comparison, the stresses are examined at three different locations: at -(0.1,0.5,0.5), -(0.5,0.1,0.5), -(0.5,0.5,0.1), relative to the center of the spherical inclusion. To be precise, the results are obtained at element centroids closest to the three locations, which are shown in table 6-2. Only one set of results is shown since the computed stresses are identical between the two models, clearly verifying the efficacy of the PVE modeling in Salinas.

Table 6-2. – Stresses computed from PVE model

Location	-(0.1,0.5,0.5)	-(0.5,0.1,0.5)	-(0.5,0.5,0.1)
σ_{xx}	114.9294	92.5208	112.5307
σ_{yy}	75.9910	77.9703	7.0164
σ_{zz}	37.4338	0.2489	41.6507
σ_{xy}	-48.9834	-79.2754	-101.6064
σ_{yz}	2.5491	20.0710	16.3110
σ_{xz}	-7.1000	-75.8791	-43.3911

In addition to the above example, we tested the implementation on homogeneous block under specified deformation gradient, resulting in expected uniform stress state with correct values (including Poisson's effect). The details are not presented in this document, but can be found in the test repository. For input see Appendix 11.76

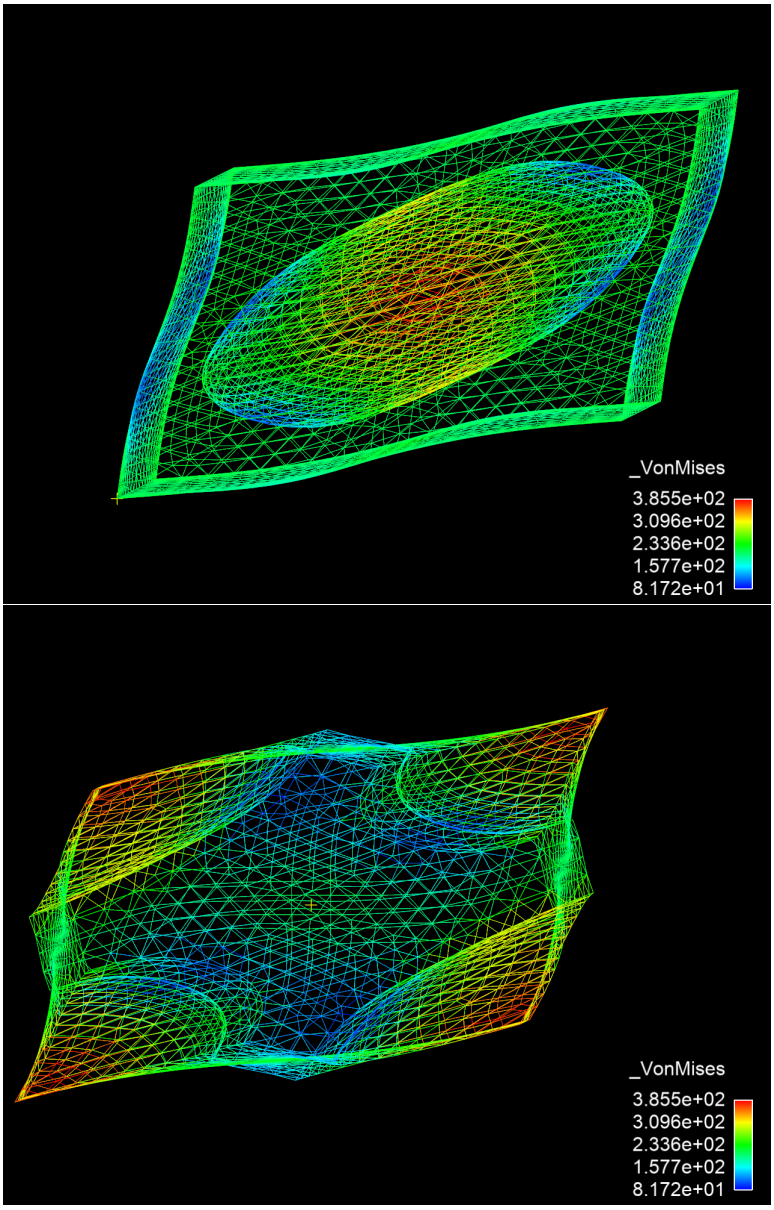

Figure 6-30. – Meshes for two different periodic volume elements

3.7. Moving Mesh MPCs: 1D Balloon Pop waveguide

This verification test demonstrates the use of acoustic multipoint constraints (MPC) to tie together two waveguides at different pressures. The waveguide configuration and boundary and initial conditions used in this test mimic a balloon popping in 1D. The purpose of this test is to verify the correction used to equilibriate a multipoint constraint as described in the theory document. This test will verify that the pressure jump between the two structures is in equilibrium after three steps and equilibriates to the average pressure of the two domains. This is verified in the test file by using compare values to ensure both nodes across the interface are equal after three time steps.

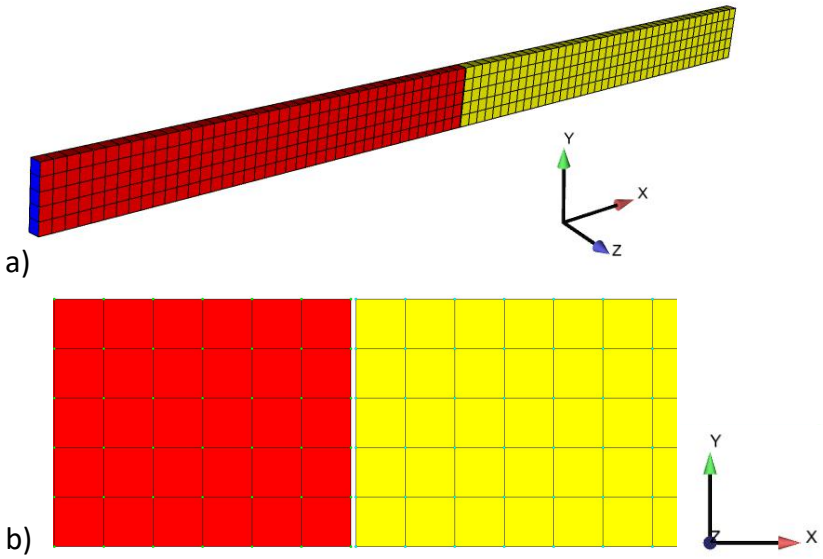

Figure 7-31. – a) Schematic of two 4.0 x 0.5 x 0.1m wave guides with block 1 in red at 4Pa and block 2 in yellow at 2Pa. (b) Close-up of the gap where constraints will tie together the pressure across the interface.

The waveguide configuration shown in figure 7-31 represents a 1-D equivalent of a balloon popping with mirror symmetry at the centerline of the balloon. The over pressured block in red represents the balloon containing air at a high pressure and the surrounding lower pressure atmosphere is shown in yellow. A free surface boundary condition is used on the end of the red domain and absorbing conditions are placed on the end of the yellow domain. The initial conditions for the red block is 4Pa and the yellow block is at 2Pa. At time t=0, the balloon is popped and the pressure waves will propagate away from the red-yellow interface. When the pressure waves reach the end of the red domain they will reflect with opposite phase.

Each block of the wave guide in figure 7-31 is 4.0 x 0.5 x 0.1 meters meshed with 0.1m Hex8 elements. The blocks are separated by a 1cm gap. The purpose of the gap is for visualization only, it has no effect on how the inhomogeneous MPCs tie together the two domains. By including the gap, it is clear that no nodes are being shared between the blocks. The initial pressure of block 1 is set to 4 Pa and block 2 is set to 2 Pa using an

`initial-conditions` block with `acoustics = by_block` in the input file. The `acoustics` initial condition refers to applying an initial condition on the primary variable. For the pressure form of the acoustic equation used in this test, the primary variable is pressure. A block by block application of the initial conditions is set using `by_block`, and each block in the input file that an initial condition is applied to must have the keyword `acoustics` followed by its value. The `LOAD` block is used to apply an `acoustic_accel` that is zero for all time. This switches the acoustics formulation to use pressure as the primary variable instead of the velocity potential. A similar two block conformally meshed waveguide using the same input file is used to verify the results.

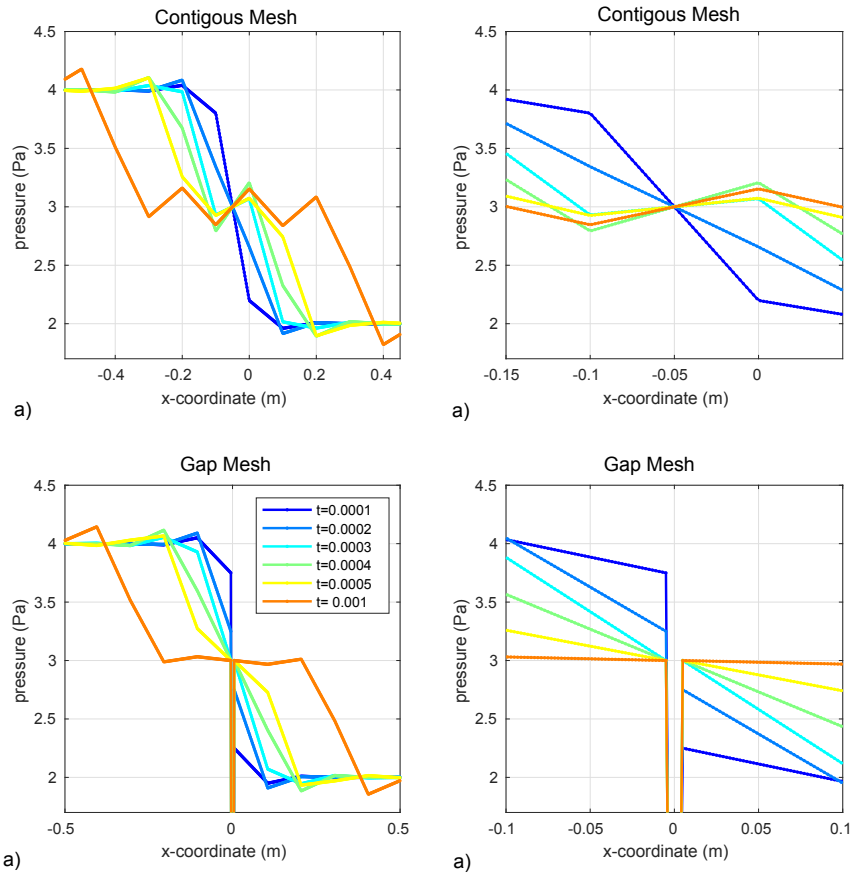

Figure 7-32. – Pressure profiles measured across the length of the waveguide are shown at the times given in the legend shown in (c). (a) and (b) show far and near field pressure profiles for the contiguously/conformally meshed waveguide. (c) and (d) show pressure profiles for the mesh containing a gap and constraints.

Figure 7-32 shows the first time steps after the balloon is popped for the conformal mesh and mesh containing a gap with constraints. Data for these plots is obtained using `linesample` with 1000 sample points taken between $-1 \leq x \leq 1$. The location of the interface is shifted by half an element (0.05m) for the conformal mesh because of where the nodal pressure initial conditions are applied. The pressure profiles for the conformal mesh

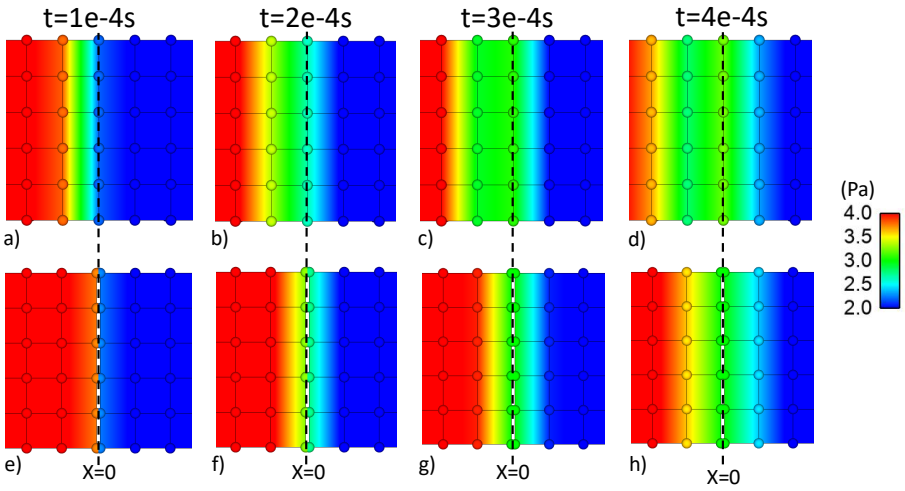

Figure 7-33. – Nodal pressure output shown on the meshed geometry for the time steps plotted in figure 7-32. (a)-(d) are for the conformal mesh and (e)-(f) are for the constrained mesh containing a gap. The dashed line indicates x=0 for both meshes.

are shown in figure 7-32 (a) and (b). For the conformal mesh, the nodal pressure at x=0 is initially 2Pa and increases to 3Pa over 3 time steps while the nodal pressure at x=0.1m is initially at 4Pa and drops to 2Pa. The interpolated pressure in the element at x=-0.05 is held constant at 3Pa for the time steps shown. Nodal pressures for the conformally meshed geometry are shown visually in figure 7-33 (a)-(d).

The nodal pressures for the gap mesh with MPCs is shown visually in figure 7-33 (e)-(h). The different nodal pressure across the gap can be seen for (e)t=1e-4s and (f)2e-4s. The blue pressure profiles for t=1e-4s and 2e-4s in figure 7-32 (d) show the size of the pressure jump across the interface. The MPC correction brings the nodal pressures into equilibrium across the interface in three steps as shown by the nodes being the same color in figure 7-33 (g) for t=3e-4s. Pressure equilibrium is shown by the continuity of the cyan line in figure 7-32 (c) and (d).

The pressure profiles between the two meshes in figure 7-32 are nearly identical once equilibrium is enforced. The delayed enforcement of equilibrium caused by the MPC correction leads to smaller pressure oscillations at later times. The delay in pressure enforcement also causes a small delay in the pressure pulse. The delay can be reduced by reducing the time step as shown in figure 7-34. The peak of the pressure profiles for the conformally meshed waveguide at t=0.015s is approximately at x=-2.6m. This is nearly the same value for dt=5e-5 and is 0.1m ahead of dt=1e-4 and 0.3m ahead of dt=2e-4.

Increasing the time step is also shown to smooth out the profile of the wave. For the largest time step of dt=1e-3 shown in figure 7-34, the wave would travel nearly 1m or 10 elements over the three steps required by the MPC's to reach equilibrium.

For input see Appendix 11.74

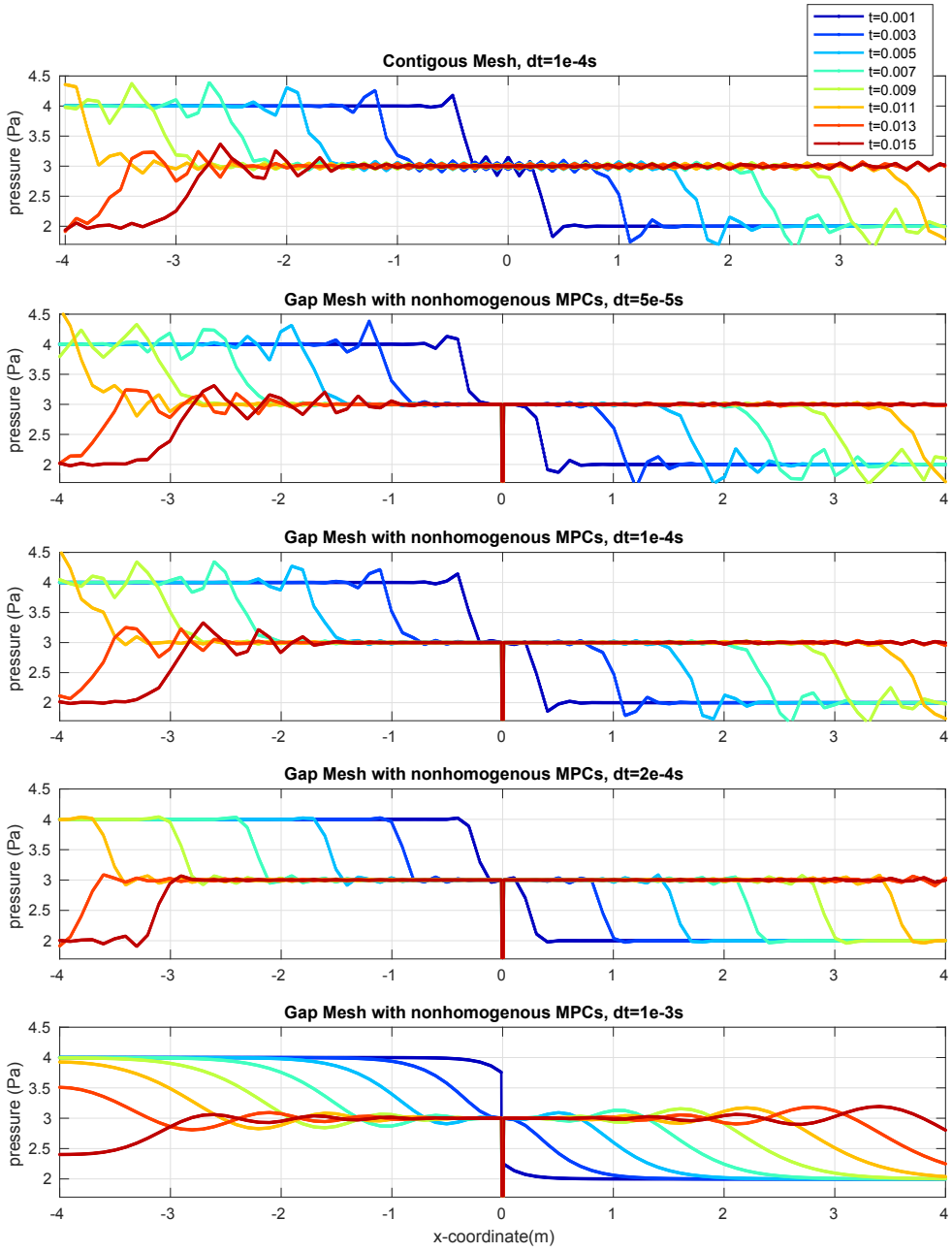

Figure 7-34. – Effect of time step on the pressure profile for the MPC mesh containing a gap compared to the contiguous/conformal mesh at the top.

4. SOLUTIONS

4.1. Waterline of a ship

A code to code comparison was performed between Sierra-SD and the Navy's finite element code Float. This is a ship model, that utilizes the waterline solution case in Sierra-SD. An image of the model is shown in Figure 1-1. Three key parameters were analyzed between

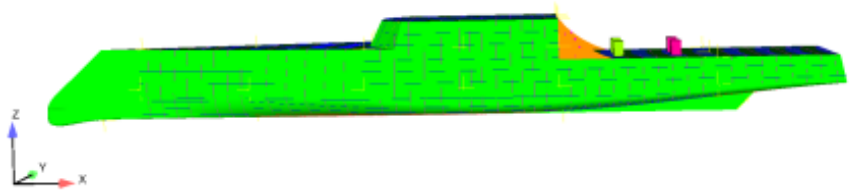

Figure 1-1. – uhwmGeometry

the two codes the draft which is the distance from the bottom of the ship to the waterline, the pitch which is the rotation about the y-axis, and the roll which is the rotation about the x-axis. The results can be seen in Table 1-1. For input deck see Appendix 11.21.

Table 1-1. – Sierra-SD solution vs. Float (Navy code)

	Sierra-SD	Float
Draft	187.0580	187.0579
Pitch (about y-axis)	0.0503	0.0497
Roll (about x-axis)	-0.0001	0.0000

4.2. Transient Convergence

A verification test was created for temporal convergence of the transient solution. A vertical load was applied at the end of a cantilever beam, and the vertical displacement at the end of the beam after 4.5 seconds was calculated.

Figure 2-2 shows the final displacement of the deformed beam.

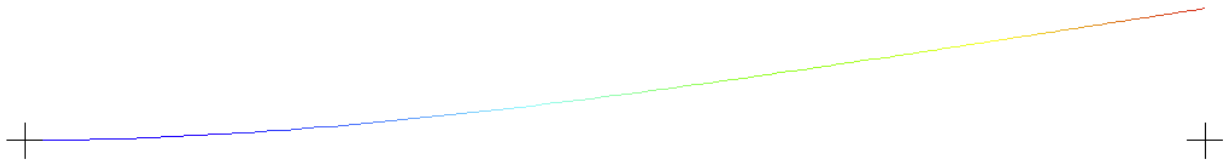

Figure 2-2. – Verification Problem - Beam

Figure 2-3 shows the time history result for the problem, solved at three different time-steps.

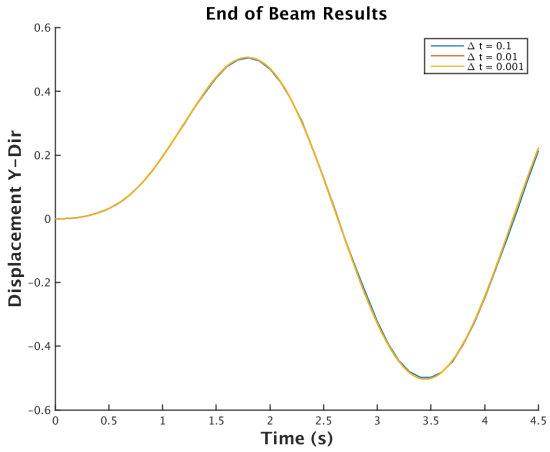

Figure 2-3. – Time History of Transient Verification Problem

Figure 2-4 shows the Richardson Convergence of the problem. Convergence values $n = 2$ implies second order convergence.

For input deck see Appendix 11.22.

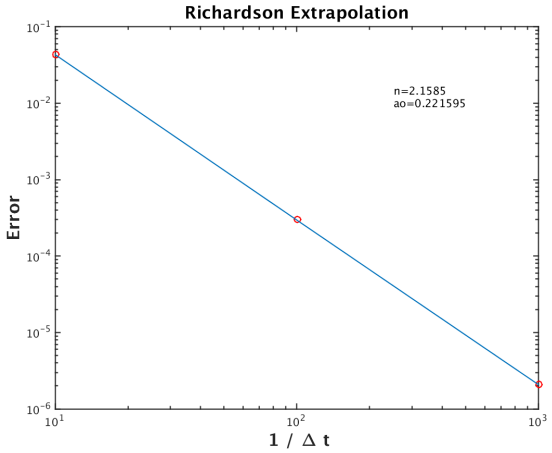

Figure 2-4. – Richardson Extrapolation of Transient Verification Problem

4.3. Modal Transient Temporal Convergence

The modal transient temporal convergence The test consists of a 100 element cantilevered beam that is loaded using a triangle pulse function. The modal transient test was run using 3 different time steps, and the results of these tests are compared to the results obtained from the same tests run using the direct transient method.

Figure 3-5 shows the plot of the deformed beam. The loading for the three tests is the same and it consists of a ramp load applied at the free end of the beam. The load has a duration of 2 seconds and a max value of 1 at 1 second.

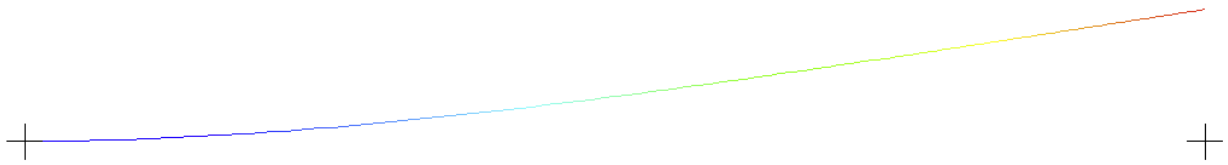

Figure 3-5. – Verification Problem - Beam

Figure 3-6 shows the time history of the beam end point for the problem for three time steps.

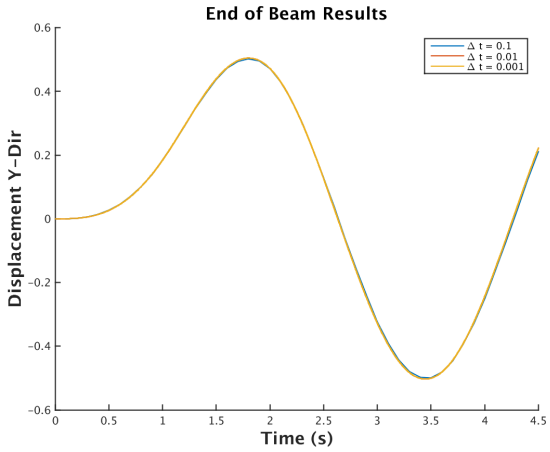

Figure 3-6. – Time History of Modal Transient Verification Problem

The Richardson convergence was used as a means of determining the order of convergence for the modal transient method. Figure 3-7 shows the Richardson Convergence of the problem. Convergence values $n = 2$ implies second order convergence. This results is very similar to the Richardson convergence obtained from the direct transient method.

The modal transient tests were run using only 3 modes for verification purposes. Figure 3-8 shows the difference in displacement at the end of the beam between the direct transient method and the modal transient method for $\Delta t = 0.001$.

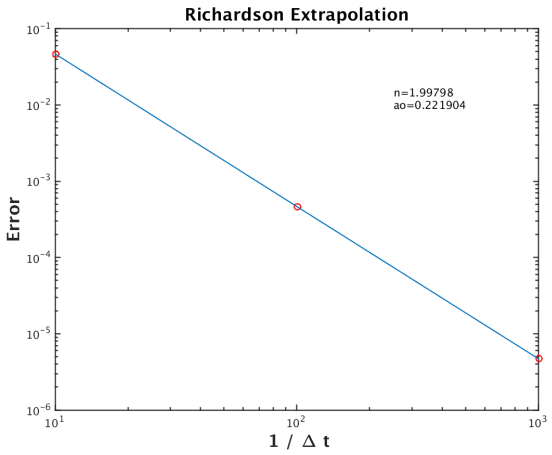

Figure 3-7. – Richardson Extrapolation of Modal Transient Verification Problem

It should be noted that this difference decreases as the number of modes used in the modal transient method are increased. The three modes retained are sufficient to approximate most of the solution for this low frequency loading. This corresponds well to the analysis use case where modal transient is used to represent the lower frequency response of complex systems. Temporal convergence depends on adequate modal basis. A similar study with high frequency input could not be expected to converge without a much larger modal basis.

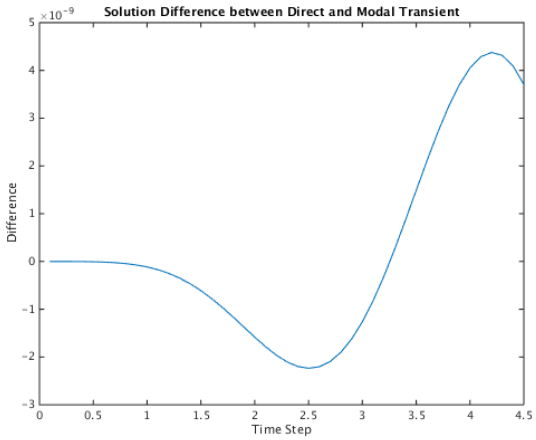

Figure 3-8. – Displacement Difference for Modal and Direct Transient Solutions

For input deck see Appendix 11.23.

4.4. Transient Restart

Analysts should be able to restart from any of the transient analysis capabilities into any of the others. Of course, there are differences in the solutions with respect to accuracy, and output quantities. For example, the nonlinear transient integrator outputs the number of nonlinear steps as a global output variable. This is unavailable for modal transient. In addition, there are internal variables associated with nonlinear elements and viscoelastic materials which may not be propagated across the restart boundary.

Verification of this use case involves the following steps.

1. Computation of 40 normal modes.
2. Computation and output of 30 ms of time history with the first integrator.
3. Exit **Sierra/SD**, and start a new **Sierra/SD** analysis.
4. Restart read the previous normal modes.
5. Restart read the previous time history data, and computation of the next $10\,ms$ of data.
6. Check of the .rslt to ensure that the time history data was restarted (as opposed to recomputed from scratch).
7. Check the history file for accuracy. Note that the tolerances are loose on this check. Each integrator provides a somewhat different solution (as expected).
8. Visual comparison of the results.

Table 4-2 indicates the tests that have been performed. Nonlinear transient as the first integrator is not currently tested. Figure 4-9 provides the data for the second row of Table 4-2, which includes all cases where the direct transient was the first integrator. Likewise, figure 4-10 shows data for modaltransient as the initial integrator.

Integrator	NLtransient	transient	modaltrans	Explicit	modaltrans
NLtransient	Untested	Untested	Untested	Untested	NA
transient	TESTED	TESTED	TESTED	TESTED	NA
modaltransient	TESTED	TESTED	TESTED	TESTED	NA
Explicit	TESTED	TESTED	Untested	TESTED	NA
modaltrans	NA	NA	NA	NA	NA

Table 4-2. – Tested restart capabilities for transient integrators in **Sierra/SD**.

For example inputs, see Appendix 11.24. The model is shown in Figure 4-12.

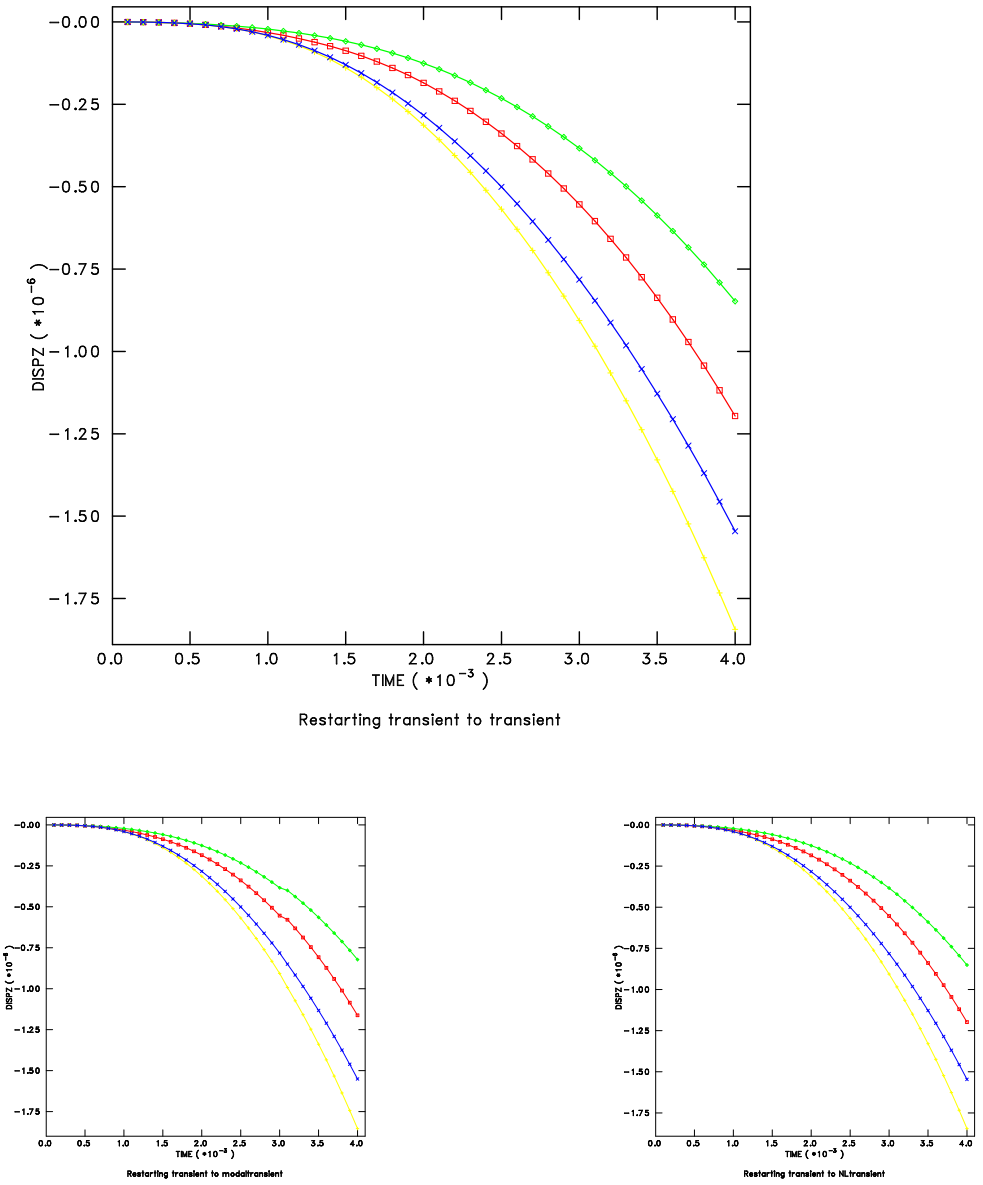

Figure 4-9. – Restart from Direct Transient Analysis. In each case, $30ms$ of analysis is completed using a direct transient run, and is followed by a restart.

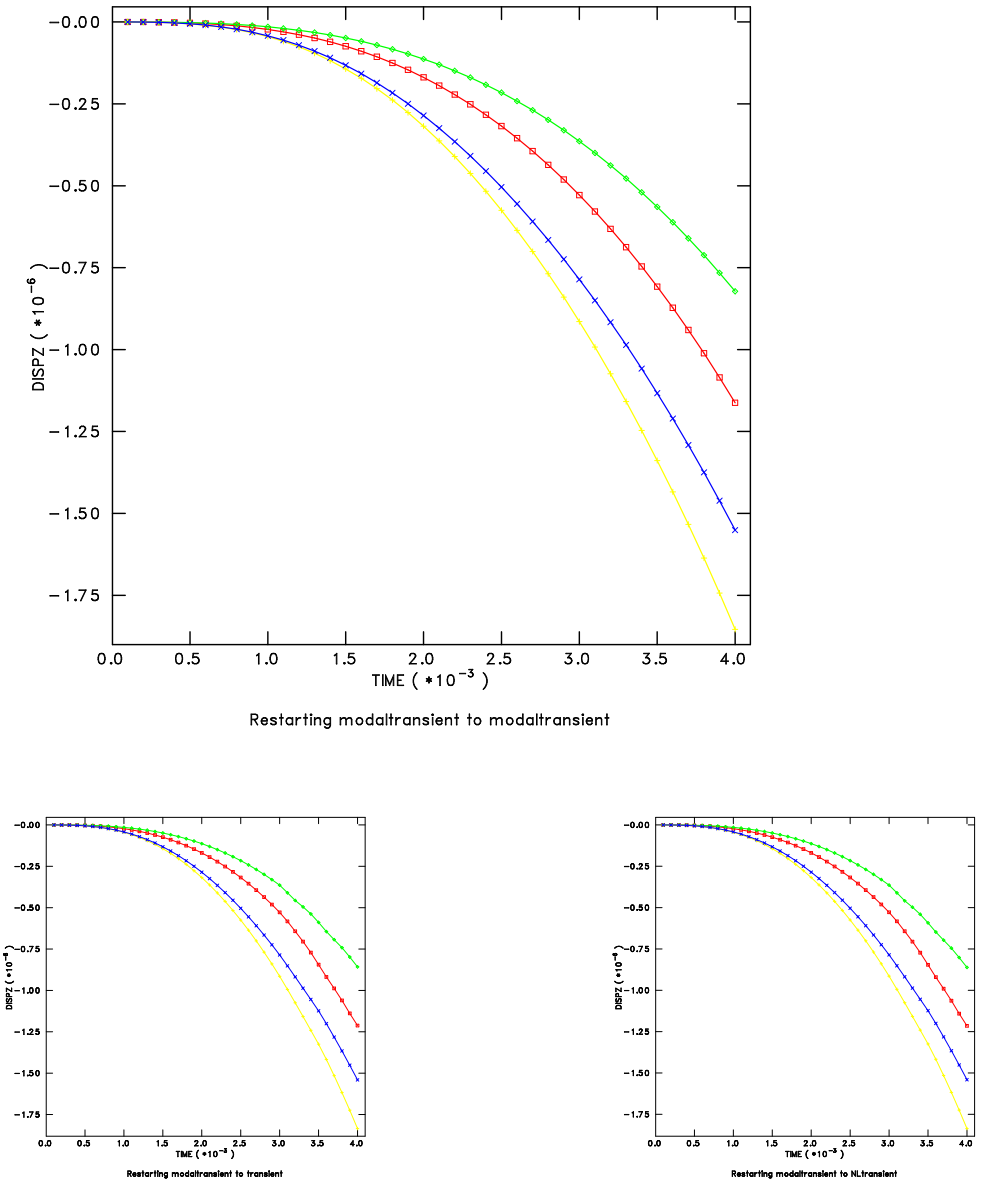

Figure 4-10. – Restart from Modal Transient Analysis. In each case, $30\,ms$ of analysis is completed using a Modal transient run, and is followed by a restart.

4.5. Modal Transient

The modal solution method is a standard Newmark-beta integrator that is applied in parallel on the modal space. It is limited to boundary conditions that are space/time separable, and all outputs must fit on single processor. Verification is applied to four cases.

1. Constant force on a floating body, with limited modal interaction. The behavior is rigid body only, and analytic solutions are trivial.
2. Repeat the above, but eliminate the rigid body motion. A comparison with the standard modal solution provides the verification.
3. We repeat case 2, but add modal damping. Again, the analytic solution is straightforward.
4. A complex loading.

The above examples exercise the primary elements of the software. All are run in parallel. The model is shown in Figure 5-11. It consists of a thin cylinder with beams on one end attaching to a large mass. The loading is applied to the mass.

Figure 5-11. – Q Modal Verification Model

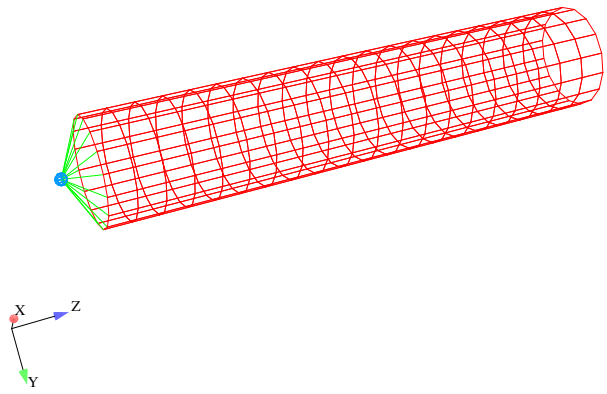

4.5.1. Constant Force Applied to Floating Structure

In this example the load activates only a rigid body mode, and the body behaves as a point mass. The analytic solution for a constant force applied to a point mass is,

$$a(t) = \frac{F_o}{m} \tag{4.5.1}$$

$$v(t) = \int_o^t a(t')dt' \tag{4.5.2}$$

$$= \frac{F_o}{m}t \tag{4.5.3}$$

$$d(t) = \int_o^t v(t')dt' \tag{4.5.4}$$

$$= \frac{F_o}{2m}t^2 \tag{4.5.5}$$

The dimensionless load is set to 10^5 in the input file, and the result file indicates that the total dimensionless mass of the structure is $1001.25 \cdot wtmass$=2.5932375.

Figure 5-12 compares the analytic and numerical solutions for displacement. Figure 5-13 provides similar results for acceleration. While the agreement is excellent, a small discrepancy is observed if differencing the solutions. This occurs because the numerically integrated solution tends to lag the analytic solution by a half step.

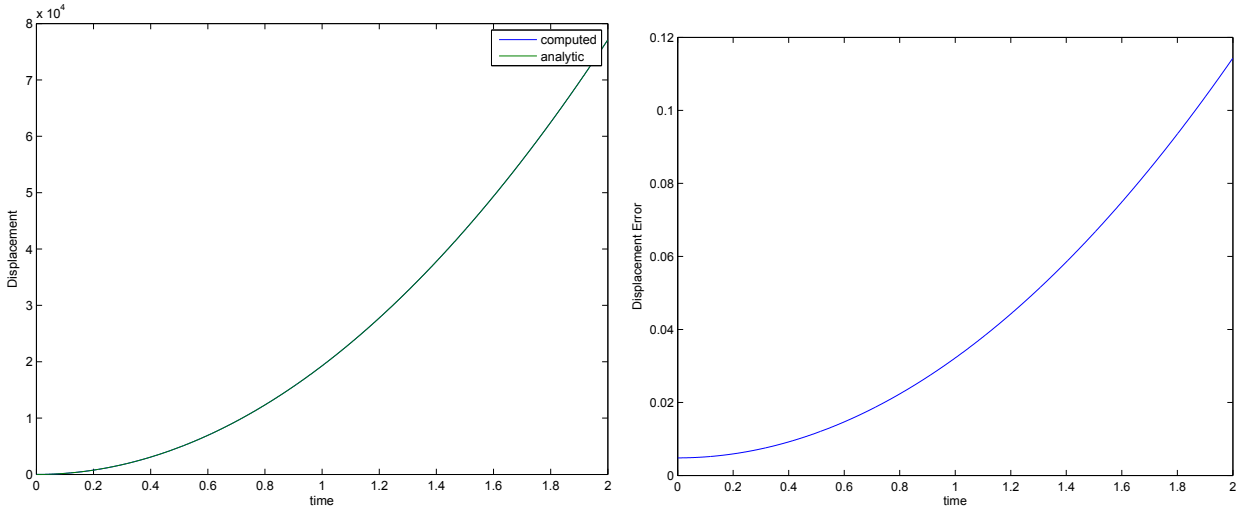

Figure 5-12. – Response of Rigid Body Mode

This example ensures that the modal force is being computed properly for rigid body modes. As they are identical to elastic modes, that follows as well. It verifies the behavior of the integrator, except that there are contributions from the damping matrix which are not considered.

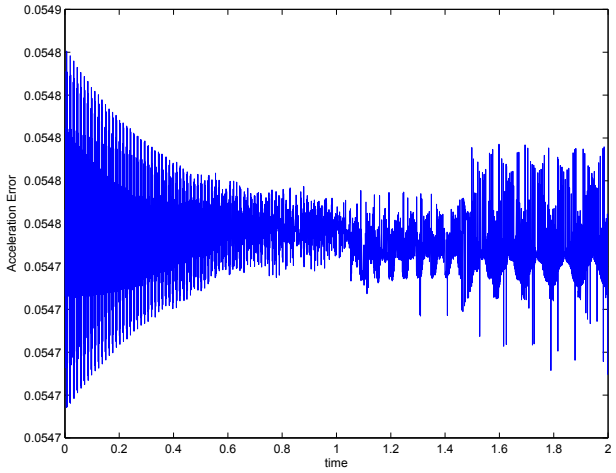

Figure 5-13. – Acceleration Response of Rigid Body Mode. The analytic acceleration is a constant of $F/m \approx 38561.8$. The error in the figure is much smaller than this, and represents the elastic response of higher frequency elastic modes, that are just slightly active in the analysis.

4.5.2. A single Elastic Mode

While the analytic expression for an analytic mode is not quite as complete as for a rigid body response, we may still proceed with verification. We assume that the eigenvalues are computed correctly. We also assume that the modal force, $f_q(t) = \phi^T f(x,t)$, has been verified. The previous example addresses this. Then, the analytic response may be computed.

$$
\begin{aligned}
a(t) &= F_o \alpha \cos(\omega_i t) && (4.5.6)\\
v(t) &= \int_o^t a(t')dt' && (4.5.7)\\
&= F_o \omega_i \alpha \sin(\omega_i t) && (4.5.8)\\
d(t) &= \int_o^t v(t')dt' && (4.5.9)\\
&= \frac{F_o}{\omega_i^2}\alpha(1-\cos(\omega_i t)) && (4.5.10)
\end{aligned}
$$

where α represents the modal contribution from mode i at natural frequency ω_i, i.e. $\alpha = \phi_{ij}^2$. The analytic and numeric results for this case are shown in Figure 5-14.

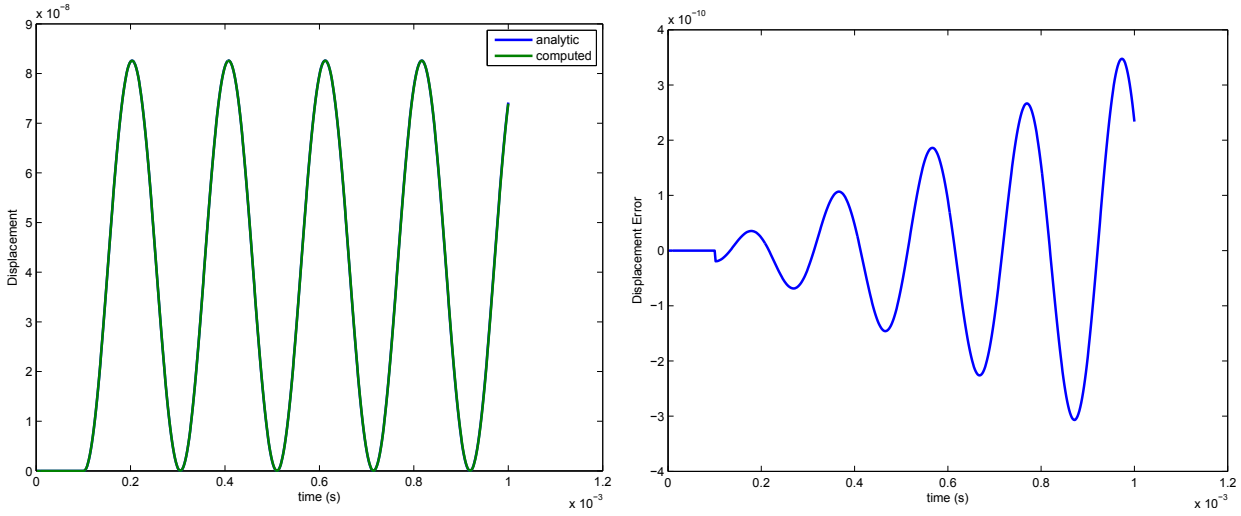

Figure 5-14. – Step Function response of Undamped Oscillator

4.5.3. Damped Simple Harmonic Oscillator

The solution of the previous solution can be neatly modified by applying damping. The phase ϕ satisfies $\cos\phi = \zeta$. The analytic solution is,

$$x(t) = A\left(1 - e^{-\zeta\omega_i t}\frac{\sin\left(\sqrt{1-\zeta^2}\right)\omega_i t + \phi}{\sin(\phi)}\right) \tag{4.5.11}$$

Results for the analytic and numeric solutions are shown in Figure 5-15.

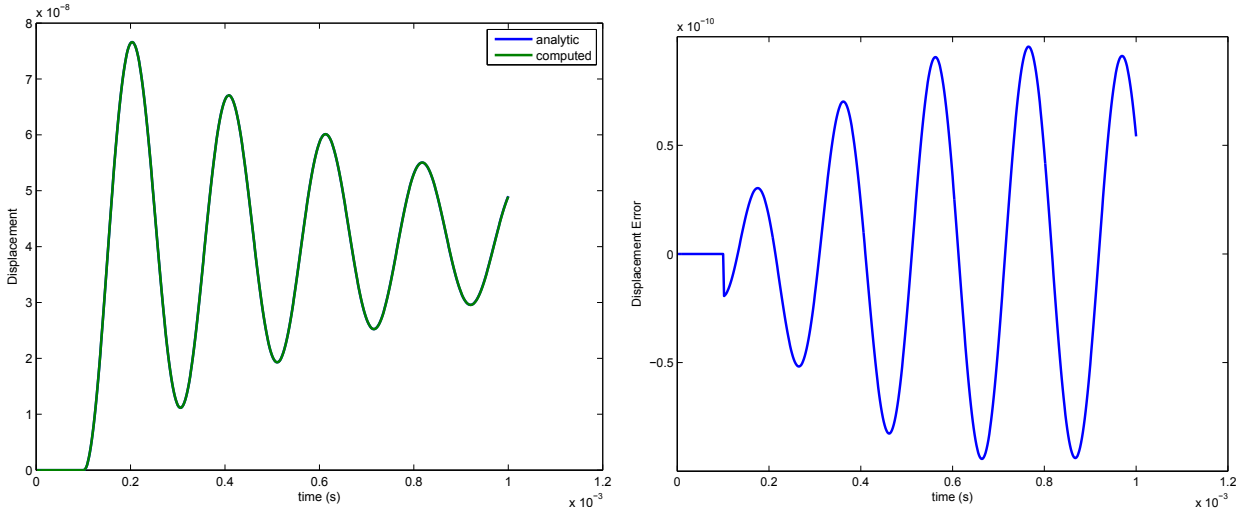

Figure 5-15. – Step Function response of Damped Oscillator

4.5.4. Complex Loading

The last verification example (case 4) utilizes code to code comparison. We apply a triangle pulse of unit amplitude and duration 1 ms. Comparison is with the standard modaltransient method. This boundary condition is essentially an impulse which causes a linear increase in displacement. There is no difference between the modaltrans and modaltrans solutions.

For input deck see Appendix 11.27.

4.6. Fluid Structure Interaction Added Mass

The following test is used to determine to what extent that SierraSD accounts for an added fluid mass to a structure when computing the angular frequencies. The test consists of a hollow steel sphere with a spring attached to the outer surface. Tests were run with the steel sphere submerged in water as shown in Figure 6-16 and a steel sphere with no added mass. The fluid is an acoustic medium.

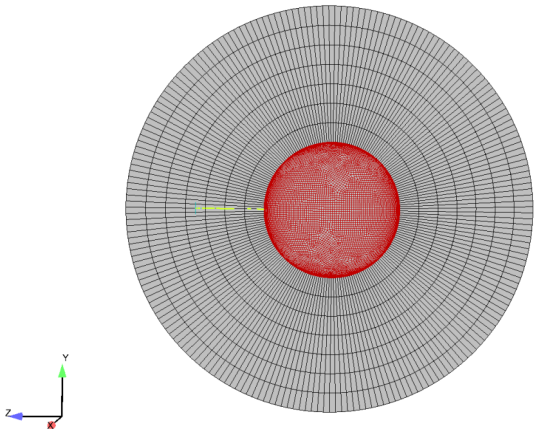

Figure 6-16. – Model of the hollow sphere and spring submerged in water

4.6.1. Analytical solution

The analytical solution for this test is based on the natural frequency equation of an object attached to an oscillating spring. Assuming that the spring is ideal and massless with no damping $\omega =$:

$$\omega = \sqrt{\frac{K}{m}} \tag{4.6.1}$$

When the fluid is added around the sphere and is submerging the spring, the added mass must be accounted for. This changes ω to:

$$\omega = \sqrt{\frac{K}{m + m_a}} \tag{4.6.2}$$

The formulas for various shapes are documented[10]. In the case of a spherical structure, the added mass is given by:

$$m_a = \frac{2}{3}\pi\rho a^3 \tag{4.6.3}$$

The first mode computed in SierraSD should match the analytical solution.

There are several parameters for this test. The steel sphere is fixed in the x and y direction so that displacements were only allowed in the z direction (direction of the spring). Also, the steel sphere is constrained from rotating. The outer surface of the fluid region follows the Dirichlet boundary conditions where p=0. The node attached to the end of the spring is fixed for no translation. The only displacement allowed in the system is in the direction of the spring. As a result the global structure has no rigid body modes. The steel sphere has a high modulus of elasticity to ensure a very stiff structure. For this verification problem the steel sphere is essentially rigid.

4.6.2. Computational Approach

The eigenfrequencies of the coupled structural acoustic system require computation of a quadratic eigenvalue problem (QEVP).

$$(K + C\lambda + \lambda^2 m)u = 0 \tag{4.6.4}$$

where K is the stiffness matrix, m the mass matrix, and C is the gyroscopic coupling matrix. The solutions to the equation include only purely imaginary eigenvalues $\lambda = i\omega$. Two methods for computing QEVP are applied. SA_eigen uses a modal projection to reduce the dimension of the problem and solve dense QEVP using LAPACK routines. The QEVP/Anasazi method is a custom solution solving the full problem without the approximation of a modal projection.

Shell elements were investigated in particular detail. When analyzing shell elements the thickness of the inner sphere was as thin as 0.0001. The test was run using SA-eigen and Anasazi. The number of modes, refinements, and test parameters varied to maximize accuracy of the results. A collection of results using SA-eigen and Anasazi with various thicknesses is shown in Table 6-3.

Table 6-3. – Frequency results for SA-eigen, Anasazi, and analytical results

Model	**Frequencies**									
Sphere size	0.1	0.05	0.025	0.01	0.005	0.0025	0.001	0.0005	0.00025	0.0001
analytic	0.1529	0.1945	0.2385	0.2881	0.3136	0.3293	0.3400	0.3438	0.3458	0.3470
sa-eigen	0.1522	0.2040	0.2628	0.3381	0.3825	0.4123	0.4340	0.4419	0.4459	0.4480
anasazi	0.1477	0.1934	0.2412	0.2955	0.3237	0.3412	0.3532	0.3574	0.3595	0.3605

A visual representation of the frequencies in SierraSD using SA-eigen and Anasazi compared to the analytical solution is shown in Figure 6-17. For Anasazi, when the shell begins to get thick (above 0.010), the parameters have to be changed in order for the test to converge. The conditioning of the matrices begins to act up, so changing parameters such as young's modulus will help this. SA-Eigen will work for all models and parameters.

This figure shows that the impact of the fluid loading is largest for thin shells. The QEVP/Anasazi method tracks the analytical solution very well. The QEVP/SA_eigen solution is not as accurate, but the solution is still much better then the coupled solution.

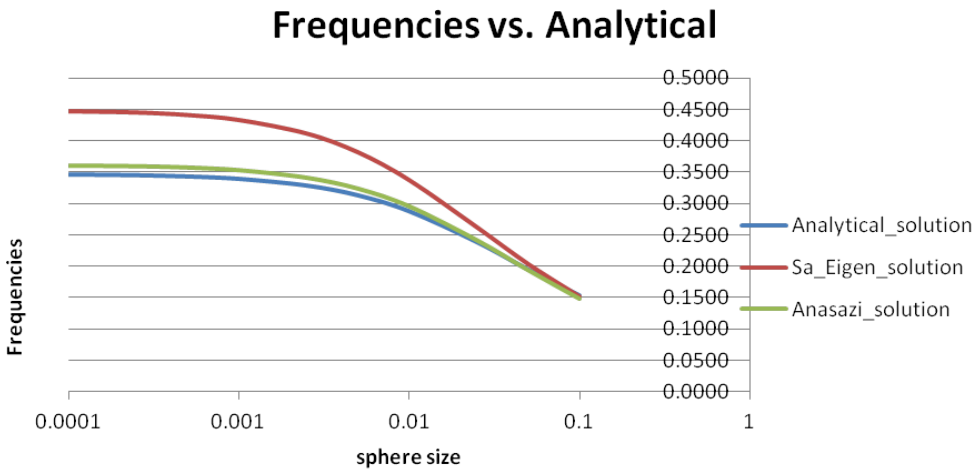

Figure 6-17. – Frequencies in SierraSD compared to the analytical solution.

Validation of the SierraSD code is most visible when the size of the inner steel sphere is the thinnest. When the steel sphere is very thin the added mass has a greater impact on the results. The weight of the steel sphere will be considerably less then the weight of the surrounding fluid and the ratio between the mass added and the mass of the structure has an immense impact on the frequencies of the system. Figure 6-18 shows the comparison of having an added mass to your system and shows the results between SierraSD and the analytical solution.

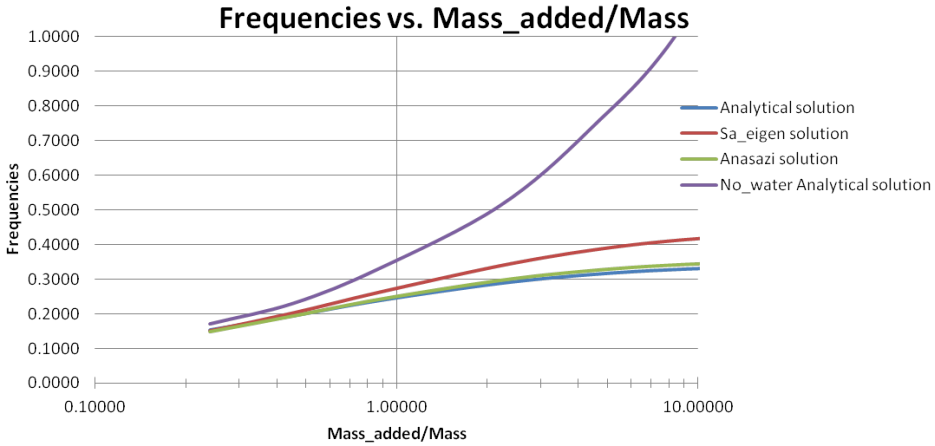

Figure 6-18. – Frequencies in SierraSD vs the mass ratio of the system.

This model was also investigated using using hexahedral and tetrahedral solid elements with a QEVP/SA-eigen solution case. For thicker models using either solid element produced more accurate results. However, the overall system was to be modeled as a rigid body and when using the solid elements this process increased complexity as the steel sphere became increasingly thin. The number of elements increased exponentially with the thinner the structure. Also, adjustments to the parameters of the model had to be

constantly maintained to ensure a stiff structure. For the shell elements, the thickness is defined in the input deck and the stiffness is easily accounted for. For input deck see Appendix 11.31.

4.7. Fluid Structure Cavitation

An important class of fluid-structure interaction (FSI) problems involve the numerical calculation of the response of a structure that is excited by a transient acoustic pressure wave. These complex models have been created and well represented with the development of the doubly asymptotic approximations that describe the fluid-structure interaction in terms of a radiation boundary that truncates the fluid-volume mesh to finite extent. In Sierra-SD we do not use the DAA, but apply a volumetric acoustic mesh with infinite elements representing the radiation boundary. A model was created in Sierra-SD that represents a solution that has already been obtained[9]. This is a one-dimensional problem, which involves a flat plate initially resting on the surface of a half space of fluid. An acoustic pressure wave is prescribed on the plate causing excitations that consist of a step-exponential plane wave superimposed upon an ambient hydrostatic pressure field. Figure 7-19 is an illustration of the model.

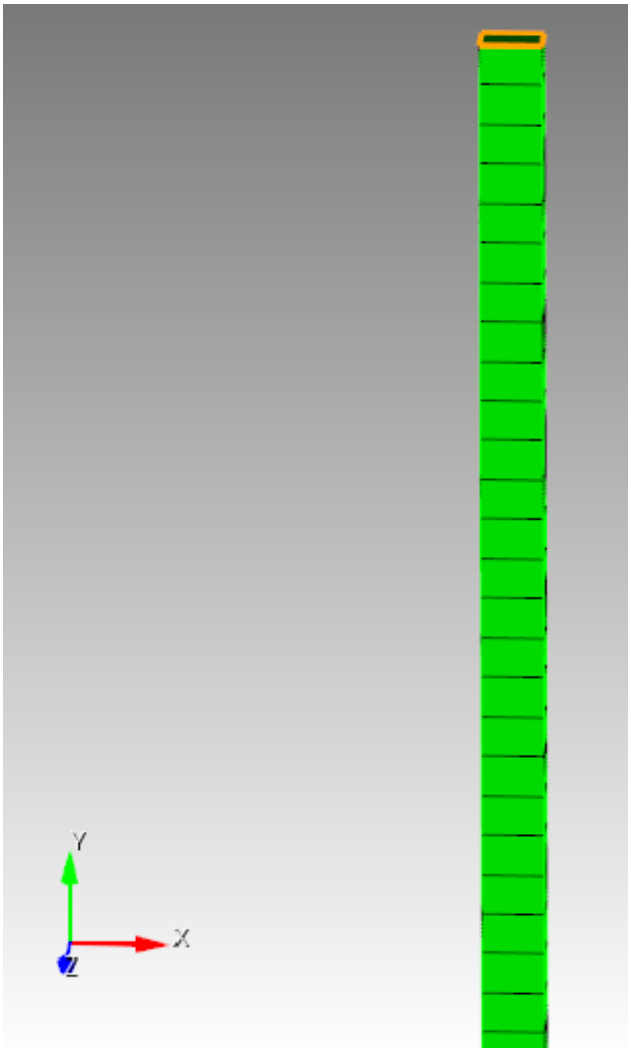

Figure 7-19. – 1D FSI Plate Shell Model in SD

This model consists of a single structural rectangular plate 1.5 in by 1 in. The plate consists of a QuadT shell element with a thickness of one. The fluid volume is 300 hex elements of similar rectangular dimensions. The boundary of the fluid mesh has infinite elements to serve as absorbing boundary conditions, as well as far-field calculators. The physical properties used for the analysis were in imperial units. The mass density of the plate was 5.329686e−4 lb $sec^2 in^4$, while that of the fluid was 9.3455e−5 lb $sec^2 in^-4$. The speed of sound of the fluid was 57120 in/sec.

A peak pressure of the incident wave that is applied to the plate is 103 psi with a decay time of 0.9958e−3 sec. For the transient analysis, 1200 time steps were used, with an intergration time step of 1.313e−5 sec.

The Sierra-SD results were compared to and verified against published results [21]. Figure 7-20 of the y component of velocity versus time reproduces the published results.

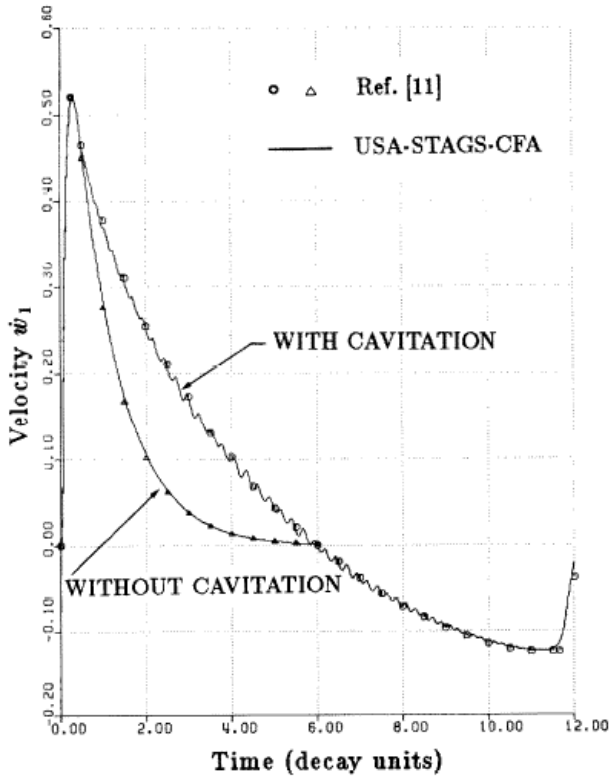

Figure 7-20. – Velocity vs Time, Results from Felippa and DeRuntz

The model without cavitation was reproduced in Sierra-SD and compared to [21]. This is shown in Figure 7-21. The actual velocities in in/sec can be obtained by multiplying by 57.12, while the time scale is given in decay time units. The decay time units can be expressed as $t = 1/\lambda * (time)$. The velocity of the plate is essentially zero by six decay times.

Comparisons of the models is very good. For input deck see Appendix 11.32.

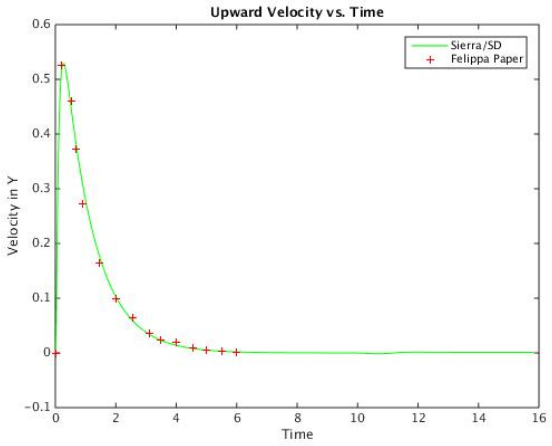

Figure 7-21. – Velocity vs Time, Results from Sierra-SD

4.8. Buckling of Constant Pressure Ring

Most analytic solutions for linear buckling are derived using Euler-Bernoulli beam theory. These solutions are ideal for meshes built with beam and shell elements, but are only approximate verification examples for 3D solid meshes. In this section we present the buckling analytic solution of buckling of a circular ring. We only present the results using 3D solid elements. The model is shown in Figure 8-22.

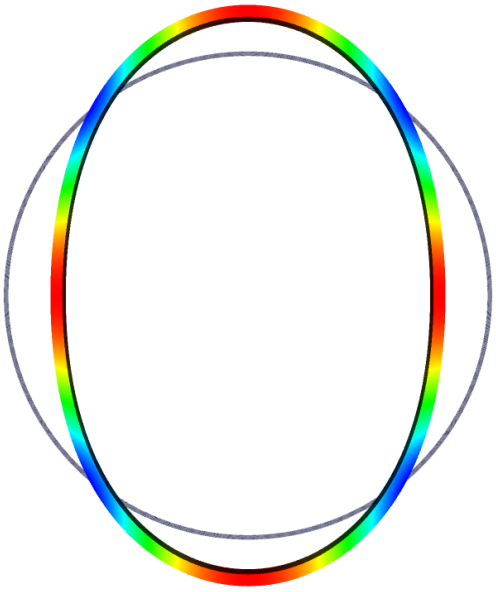

Figure 8-22. – Buckling Ring Example. Model parameters

Diameter: 40

Material: aluminum

Cross Section I: 1/12

Cross Section Area: 2.0

Cross Section Thickness: 1.0

In this example, we consider buckling of a circular ring subjected to a uniform, external pressure. The critical buckling pressure is given [54] as

$$P_{cr} = \frac{3EI}{R^3} \tag{4.8.1}$$

For the geometry of the problem, the critical buckling load is predicted to be

$$P_{cr} = \frac{3 \times 10^7 \times \frac{1}{12}}{20^3} = 312.5 \tag{4.8.2}$$

The computed buckling load was 395.408. Since the exact solution is for Euler-Bernoulli beam theory we expect some difference, however this may be a little too high. We will re-try with beam elements once they are on-line for buckling.

For input see Appendix 11.52

4.9. Buckling of a Cantilever Beam

The buckling of a cantilever beam modeled using solid elements is verified. The geometry for this example consists of a cantilever beam with one end clamped, and with the other subjected to a compressive load P. Euler-Bernoulli beam theory predicts the critical buckling load to be

$$P_{cr} = \frac{2.4674EI}{L^2} \tag{4.9.1}$$

A simple mesh of this example was created, consisting of a $2 \times 2 \times 20$ hex elements. The critical buckling load is predicted to be

$$P_{cr} = \frac{2.4676 \times 30 \times 10^6 \times \frac{1}{12}}{10^2} = 61675 \tag{4.9.2}$$

The computed buckling load was 61370.1. The model is shown in Figure 9-23.

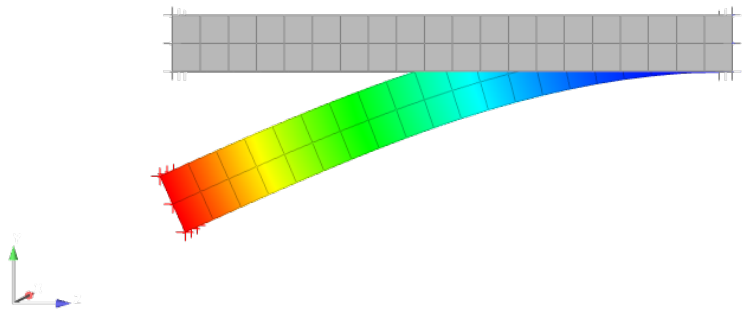

Figure 9-23. – Buckling Cantilever Beam Example. Model parameters

Material: steel

Length: 20

Area: 2×2

For input see Appendix 11.53

5. ELEMENTS

5.1. Euler Beam Bending

The Beam2 element is a simple Euler Beam. The beam bending equation for a point load, P, on the end of a cantilever beam of length, L, is,

$$w(x) = \frac{Px^2(3L - x)}{6EI}$$

Figure 1-1 shows the comparison with the analytic solution for a beam of length $L = 1$, $E = 10e6$, and bending moment $I1 = 0.2$ for a 100 element beam. Figure 1-2 shows the convergence as a function of the number of elements in the beam. The solutions here are performed with a direct solver, sparsepak, and with the GDSW solver with 2 processors. The lack of convergence to the analytic solution is expected, and indicates the increased numerical error as the matrices become more ill conditioned. As the number of elements increases, the matrix condition worsens. Even the serial solver accuracy suffers, but parallel iterative solvers are particularly vulnerable to reduced accuracy for poorly conditioned systems.[1]

In some sense, the lack of convergence is pathological in this example. The exact solution is a cubic, which can be met exactly by a single element of the beam. Thus, increasing the beam count is not required to improve accuracy. The example illustrates both the correctness of the solution for a low element count, and the effect of matrix condition and solver on the solution.

For input deck see Appendix 11.6.

[1] Note that for this example we have used standard solver parameters for GDSW. With care, the solution can be forced to be more accurate.

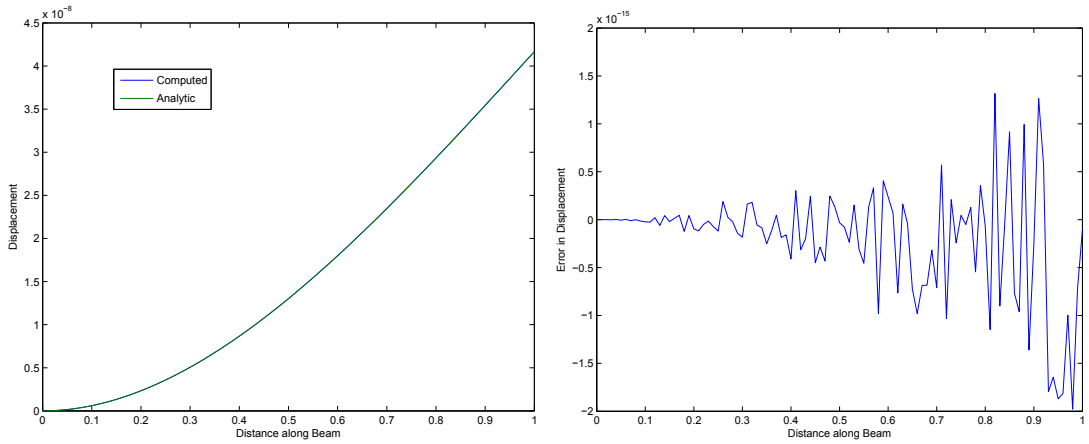

Figure 1-1. – Comparison of Beam2 Bending

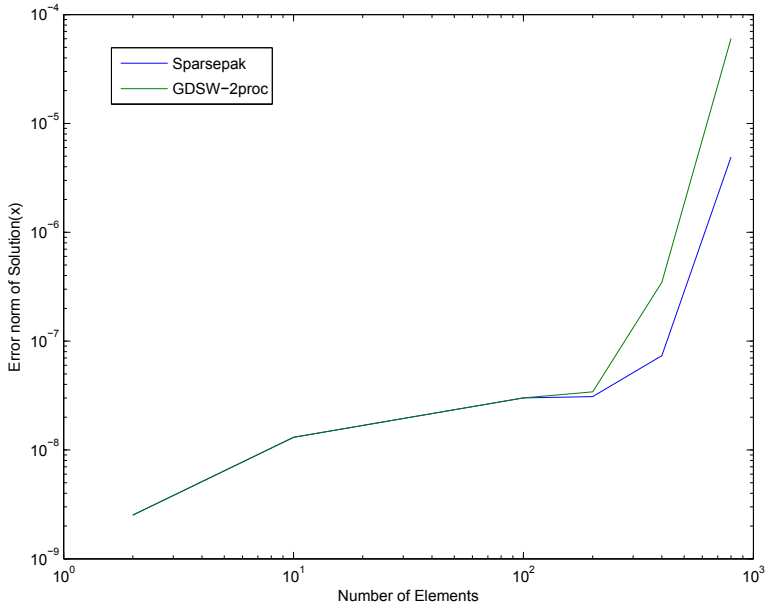

Figure 1-2. – Beam2 Bending "Convergence". The plot shows the L_2 Norm of the error in w, divided by the L_2 norm of w as a function of the number of elements. Properly convergent solutions would decrease as the number of elements increase. While this solution is very accurate, it is not converging to the analytic solution as the number of elements increases.

5.2. Euler Beam Properties

The following test verifies that Sierra SD uses the I1 and I2 properties defined in the input deck in the manner outlined by the user's documentation. The problem was analyzed using a thin long cantilevered beam with a rectangular cross-section made up of 100 Beam2 elements with the following geometry:

Figure 2-3. – Geometry of Beam

Table 2-1. – Beam Cross-Sectional Properties

Width	0.1	Height	0.3
Length	100	Area	0.03
I1	0.09	I2	0.01

The beam's cross-sectional properties were chosen to give a very long slender beam with a good separation between bending axes.

5.2.0.1. Analytical Solution

A MATLAB script was created to calculate the modal frequencies for a single span cantilevered beam using the following formula from Blevins:

$$f_i = \frac{\lambda_i^2}{2\pi L^2}\left(\frac{EI}{m}\right)^{\frac{1}{2}} \tag{5.2.1}$$

f_i Natural Frequency
λ_i Natural Frequency Parameter (Tabular Values)
E, I, m, A, and L are the usual physical properties of the beam

5.2.0.2. Computational Approach

The beam was analyzed using both Sierra-SD and NASTRAN. The NASTRAN results were used as a reference for comparison along with the analytical solution results obtained previously. It is important to note that both the analytical solution and the NASTRAN solution do not calculate twisting modes, while the Sierra-SD model did. These modes were not compared.

The natural frequencies for all 3 modes are shown in Table 2-2

Table 2-2. – Natural Frequency [Hz] results for Analytical, Sierra-SD and NASTRAN models, Displacement Axis Comparison for NASTRAN and Sierra-SD models

Mode	Analytical	NASTRAN	Sierra-SD	NASTRAN	Sierra-SD
1	0.1022	0.1021669	0.102161	Z-Axis	Z-Axis
2	0.3065	0.3065007	0.306484	Y-Axis	Y-Axis
3	0.6403	0.640269	0.640129	Z-Axis	Z-Axis
4	1.7928	1.792772	1.79205	Z-Axis	Z-Axis
5	1.9208	1.920807	1.92039	Y-Axis	Y-Axis
6	3.5131	3.513118	3.51092	Z-Axis	Z-Axis
7	N/A	N/A	4.90285	N/A	N/A
8	5.3783	5.378316	5.37615	Y-Axis	Y-Axis
9	5.8074	5.807436	5.80229	Z-Axis	Z-Axis
10	N/A	7.905694	7.90561	Z-Axis	Z-Axis

Natural frequencies that show N/A are twisting modes. Figure 2-4 shows the differences in calculated natural frequencies.

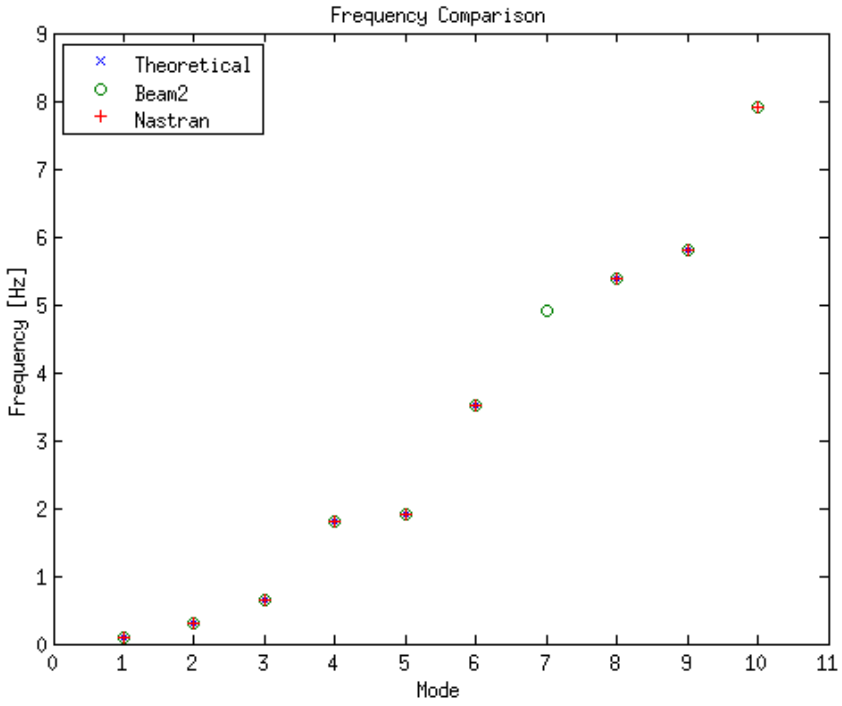

Figure 2-4. – Frequency Comparison

5.2.0.3. I1 and I2 Verification

After testing that natural frequencies were in agreement for all three models, the displacements of the Sierra-SD model were compared to the displacements of the NASTRAN model to confirm that the orientations of I1 and I2 were correct. The following table 2-2 shows the comparison results.

5.2.0.4. References

Blevins, Robert D. “Formulas for Natural Frequencies and Mode Shape “, Krieger Publishing Company, 1984

For input deck see Appendix 11.7.

5.3. A Navy Beam

The following test was used to verify that Sierra SD is using the I1 and I2 properties defined in the input deck in the manner outlined by the user's documentation. The problem was analyzed using a thin long cantilevered beam with a rectangular cross-section made up of 100 Nbeam elements with the following geometry:

Figure 3-5. – Geometry of Beam

Table 3-3. – Beam Cross-Sectional Properties

Width	0.1	Height	0.3
Length	100	Area	0.03
I1	0.09	I2	0.01

The beam's cross-sectional properties were chosen to give a very long slender beam with a good separation between bending axes.

5.3.0.1. Analytical Solution

A MATLAB script was created to calculate the modal frequencies for a single span cantilevered beam using the following formula [10]

$$f_i = \frac{\lambda_i^2}{2\pi L^2}\left(\frac{EI}{m}\right)^{\frac{1}{2}} \tag{5.3.1}$$

f_i Natural Frequency
λ_i Natural Frequency Parameter (Tabular Values)
E, I, m, A, and L are the usual physical properties of the beam

5.3.0.2. Computational Approach

The beam was analyzed using both Sierra-SD and NASTRAN. The NASTRAN results were used as a reference for comparison along with the analytical solution results obtained previously. It is important to note that both the analytical solution and the NASTRAN solution do not calculate twisting modes, while the Sierra-SD model did. These modes were not compared.

Table 3-4. – Natural Frequency [Hz] results for Analytical, Sierra-SD and NASTRAN models, Displacement Axis Comparison for NASTRAN and Sierra-SD models

Mode	Analytical	NASTRAN	Sierra-SD	NASTRAN	Sierra-SD
1	0.1022	0.1021669	0.102161	Z-Axis	Z-Axis
2	0.3065	0.3065007	0.306484	Y-Axis	Y-Axis
3	0.6403	0.640269	0.640129	Z-Axis	Z-Axis
4	1.7928	1.792772	1.79205	Z-Axis	Z-Axis
5	1.9208	1.920807	1.92039	Y-Axis	Y-Axis
6	3.5131	3.513118	3.51092	Z-Axis	Z-Axis
7	N/A	N/A	4.90285	N/A	N/A
8	5.3783	5.378316	5.37615	Y-Axis	Y-Axis
9	5.8074	5.807436	5.80229	Z-Axis	Z-Axis
10	N/A	7.905694	7.90561	Z-Axis	Z-Axis

The natural frequencies for all 3 modes are shown in Table 3-4

Natural frequencies that show N/A are twisting modes. Figure 3-6 shows the differences in calculated natural frequencies.

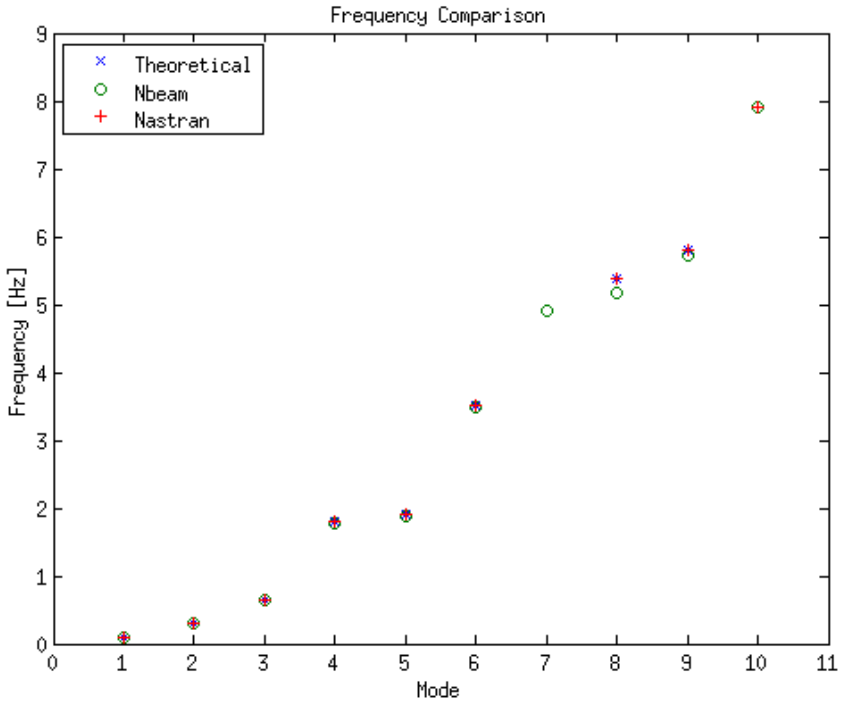

Figure 3-6. – Frequency Comparison

5.3.0.3. I1 and I2 Verification

After testing that natural frequencies were in agreement for all three models, the displacements of the Sierra-SD model were compared to the displacements of the NASTRAN model to confirm that the orientations of I1 and I2 were correct. The following table 3-4 shows the comparison results. For input deck see Appendix 11.8.

5.4. Two Layered Hexshell

5.4.1. Problem Description

This example demonstrates that the automatic verification documentation is viable. Static analyses of a sequence of layered plates problems are solving using the hexshell element

Analysis Type	Statics
Element Type	Hexshell
Dimensions	$[-1/2, 1/2] \times [-1/2, 1/2] \times [-5/2, 5/2]$
Keywords	layered

5.4.2. Verification of Solution

The mesh consists of a hexahedron of dimension $[-1/2, 1/2] \times [-1/2, 1/2] \times [-5/2, 5/2]$. The example is a step in a study of deflection versus layer thickness. Results have been compared to documented results [23],[22] in the past. For input deck see Appendix 11.9.

5.5. Preloaded Beam

5.5.1. Beam Elements

The following test was used to verify that Sierra SD accurately accounts for an axial preload on a beam. This test was verified using three different references, two different analytical solutions (Shaker, 1975), (Carne, 1982), and an Abaqus benchmark problem. The problem was first analyzed with no preload using the same analytical solution and then modeled to verify that the system is functioning appropriately.

We use an Abaqus verification problem for the modes of a prestressed beam. A cantilever beam, one hundred elements, is on the x axis. An axial force is applied in the x direction.

The beam was analyzed with and without the static preload. Figure 5-7 shows the geometry of the model.

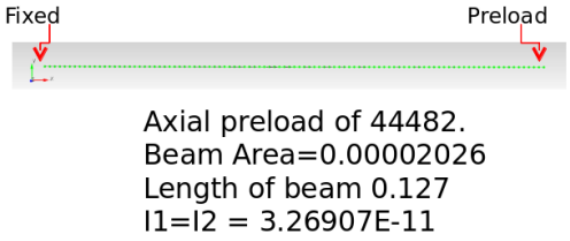

Figure 5-7. – Geometry of Beam

An equivalent test was created and analyzed in Sierra-SD. The test had three solution cases static, tangent, and eigen analysis. The cantilever beam is partitioned into one hundred beam elements. The frequencies were compared between Abaqus and Sierra-SD and shown in table 5-5.

Table 5-5. – Results Abaqus vs. Sierra-SD (beam elements)

	Abaqus	Sierra-SD
Without Preload		
Mode 1	212.4	212.818
Mode 2	1330.8	1333.49
Mode 3	3727.2	3733.11
With Preload		
Mode 1	1137.9	1136.8
Mode 2	3624.4	3616.07
Mode 3	6694.1	6667.12

The results are consistent for the benchmark problem.

5.5.2. References

Carne, Thomas G., Donald W. Lobitz, Arlo R. Nord, and Robert A. Watson. "Finite Element Analysis and Modal Testing of a Rotating Wind Turbine." (1982): 8-9. Sandia Report. Web.
Shaker, Francis J. "Effect of Axial Load on Mode Shapes and Frequencies of Beams." Lewis Research Center (1975): 1-9. Web.
For input deck see Appendix 11.12.

5.5.3. Prescribed displacement

The following test was used to verify that Sierra SD accurately accounts for an axial preload on a beam. This test was verified using three different references, two different analytical solutions (Shaker, 1975), (Carne, 1982), and an Abaqus benchmark problem. The problem was first analyzed with no preload using the same analytical solution and then modeled to verify that the system is functioning appropriately.

5.5.4. Test One

Test one is a verification of the analytical solution using beam elements. All parameters were incorporated using SI units. The beam parameters are:

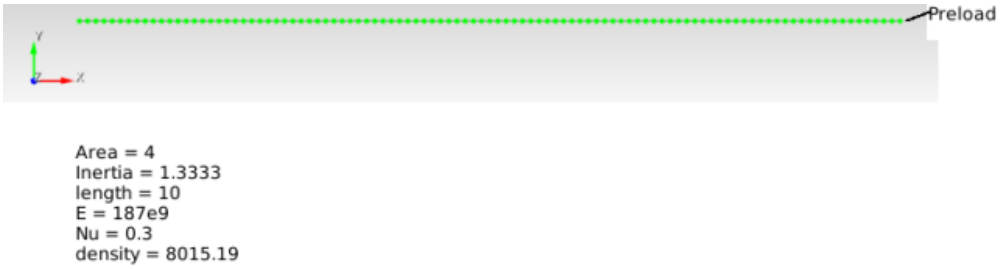

Figure 5-8. – Geometry of Beam

The beam is pinned on both ends (pinned pinned), with an axial preload in the x direction. This test was analyzed using a tensile and compressive preload.

5.5.4.1. Analytical Solution

An axial preload has limited verification due to lack of closed form solutions, however; in the paper (Carne, 1982) an analytical solution can be used. Assuming pinned pinned constraints on the beam the natural frequencies are:

$$V_n = \left(\frac{n\pi}{L}\right)^2 \left(\frac{EI}{\rho A}\right)^{\frac{1}{2}} \left[1 - \frac{PL^2}{EIn^2\pi^2}\right]^{\frac{1}{2}} \tag{5.5.1}$$

n represents the mode number;
P is the axial load;
E, I, ρ, A, and L are the usual physical properties of the beam

A similar analytic solution for non dimensional natural frequency of a pinned pinned beam under axial preload can be found at (Shaker, 1975). Also, a Matlab file is in the test repository under beam preload verification that solves the two analytical solutions.

5.5.4.2. Computational Approach

This test case was modeled using Sierra SD.The eigenfrequencies of a beam under an axial preload require a multicase solution set including static, tangent, and eigen. The static case applies the preload. The tangent case is used following the linear solution step, where the stiffness matrix is recomputed based on the current value of displacement. Finally, the eigen case is used to output eigenfrequencies. The beam was partitioned into one hundred elements.

There are several parameters for this test. In order to model the beam with pinned pinned constraints and an axial displacement due to preload the beam was treated with pin roller constraints (where y=0) first. The preload was applied in the x direction at the roller and the max displacement was found. This Max displacement was then used in the pin pin model as a boundary condition of x at the location of the pin and preload.This extra step needs to be done for a pin pin case because an axial preload is being applied at the pin where x=0 as a boundary condition, so the beam has zero displacement in the x direction. Also, the length of the beam had the following constraints: z = 0, rotx = 0, and roty = 0. These constraints are used to ensure that the appropriate bending modes are analyzed.

A summary of the results where compared and shown in Table 5-6.

Table 5-6. – Natural Frequency results for Analytical and Sierra SD solution

	Sierra SD				Analytical			
#	P=N/A	P = 1e3	P = 1e7	P = 1e10	P=N/A	P = 1e3	P = 1e7	P = 1e10
1	43.8041	43.8041	43.8041	51.3605	43.8048	43.805	43.805	51.948
2	175.207	175.207	175.207	181.575	175.219	175.220	175.220	183.905
3	394.18	394.18	394.18	397.775	394.244	394.244	394.244	403.046
4	700.677	700.677	700.677	700.268	700.878	700.878	700.878	709.723
5	1094.63	1094.63	1094.63	1089.04	1095.122	1095.122	1095.122	1103.987
6	1575.96	1575.96	1575.96	1564.04	1576.976	1576.976	1576.976	1585.852
7	2144.55	2144.55	2144.55	2125.15	2146.439	2146.44	2146.44	2155.322
8	2800.29	2800.29	2800.29	2772.26	2803.512	2803.513	2803.513	2812.399
9	3543.03	3543.03	3543.03	3505.24	3548.196	3548.196	3548.196	3557.085
10	4372.62	4372.62	4372.62	4323.94	4380.489	4380.489	4380.489	4389.381

All modes are within 1.5 percent error between the analytical solution and Sierra SD.

5.5.5. References

Carne, Thomas G., Donald W. Lobitz, Arlo R. Nord, and Robert A. Watson. "Finite Element Analysis and Modal Testing of a Rotating Wind Turbine." (1982): 8-9. Sandia Report. Web.

Shaker, Francis J. "Effect of Axial Load on Mode Shapes and Frequencies of Beams." Lewis Research Center (1975): 1-9. Web.
For input deck see Appendix 11.12.1.

5.6. Partial Cylinder Patch

This verification example checks the strain output on shell elements. The model is a partial cylinder under axial stretch, with a radius $r = 2.0$, height $h = 1.0$ and thickness $t = 0.01$, shown in Figure 6-9. The material has a Young's modulus of $E = 10^6$ and a Poisson's ratio of $\nu = 0.3$. An axial displacement of $d_{axial} = 0.01$ is applied to the cylinder.

The analytical axial strain and hoop strains are:

$$\epsilon_{axial} = 0.010 \tag{5.6.1}$$

$$\epsilon_{hoop} = 0.003. \tag{5.6.2}$$

The analytical axial stress and hoop stress are:

$$\sigma_{axial} = \epsilon_{axial} * E = 10^4 \tag{5.6.3}$$

$$\sigma_{hoop} = 0.0. \tag{5.6.4}$$

The analytical strain energy density and total strain energy are:

$$SE_{density} = 0.5 * \sigma_{axial}\epsilon_{axial} = 50 \tag{5.6.5}$$

$$SE = SD_{density} * \frac{2ht\pi * r}{4} = 1.570754. \tag{5.6.6}$$

Post processing scripts are used to transform the shell strain results to the hoop and axial directions. Special care has been taken to ensure that the mesh is general, and to verify strain output for arbitrary shape elements. Figure 6-10 shows the axial strain for each element type. Figure 6-11 shows the strain energy density for each element type. Figure 6-12 shows the axial stress for each element type. For input deck see Appendix 11.13.

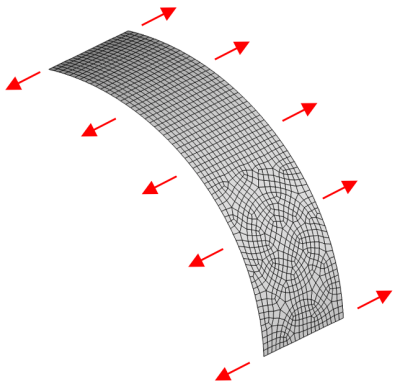

Figure 6-9. – Partial Cylinder under Axial Stretch

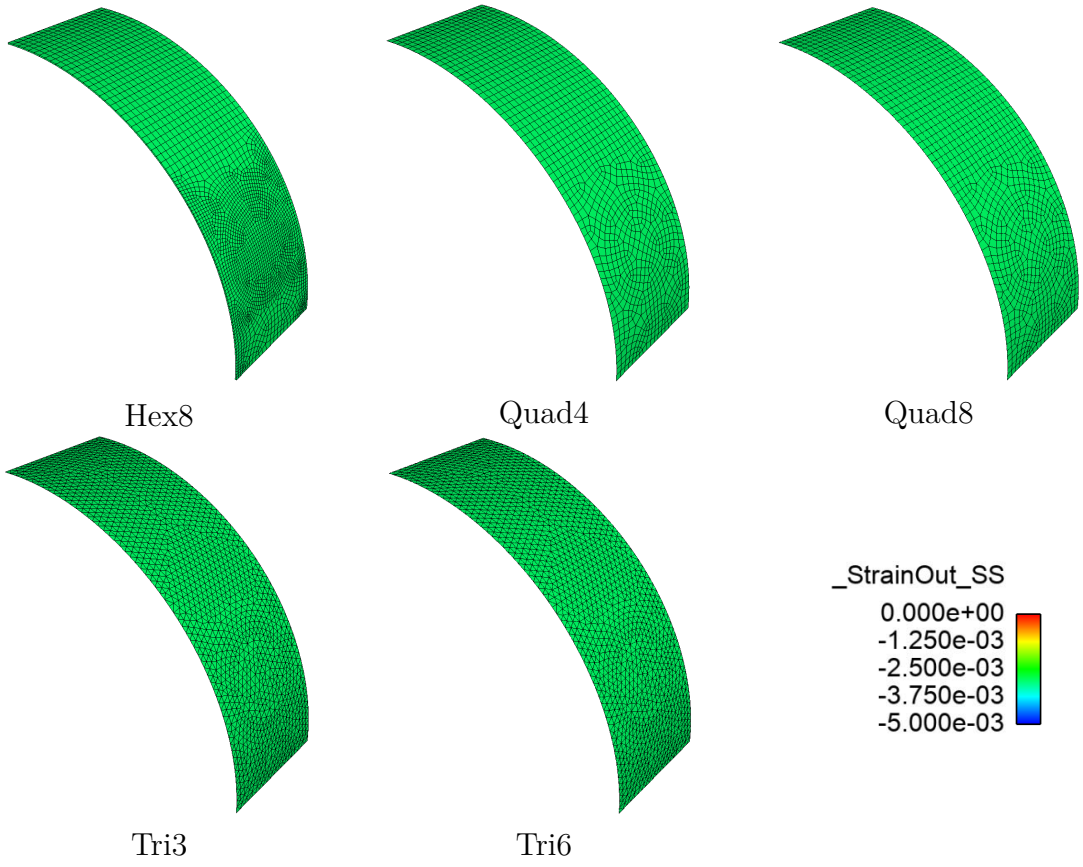

Figure 6-10. – Axial Strain for Partial Cylinder

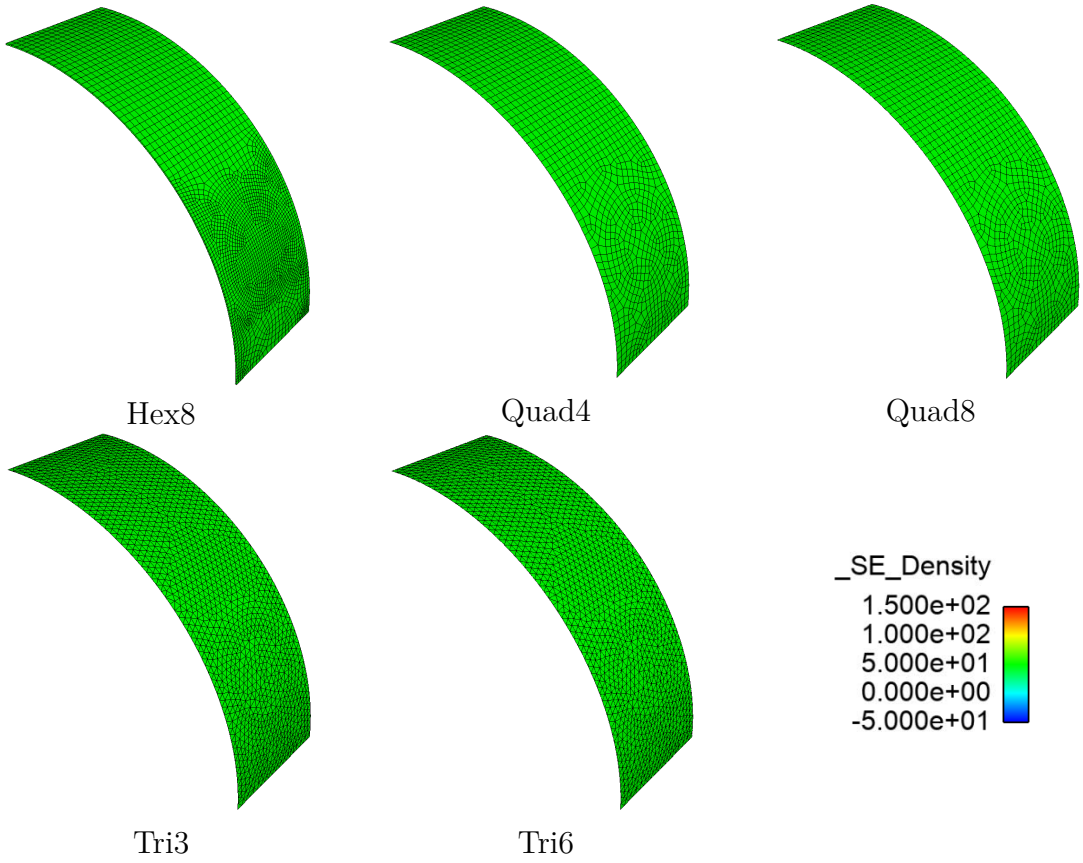

Figure 6-11. – Strain Energy Density for Partial Cylinder

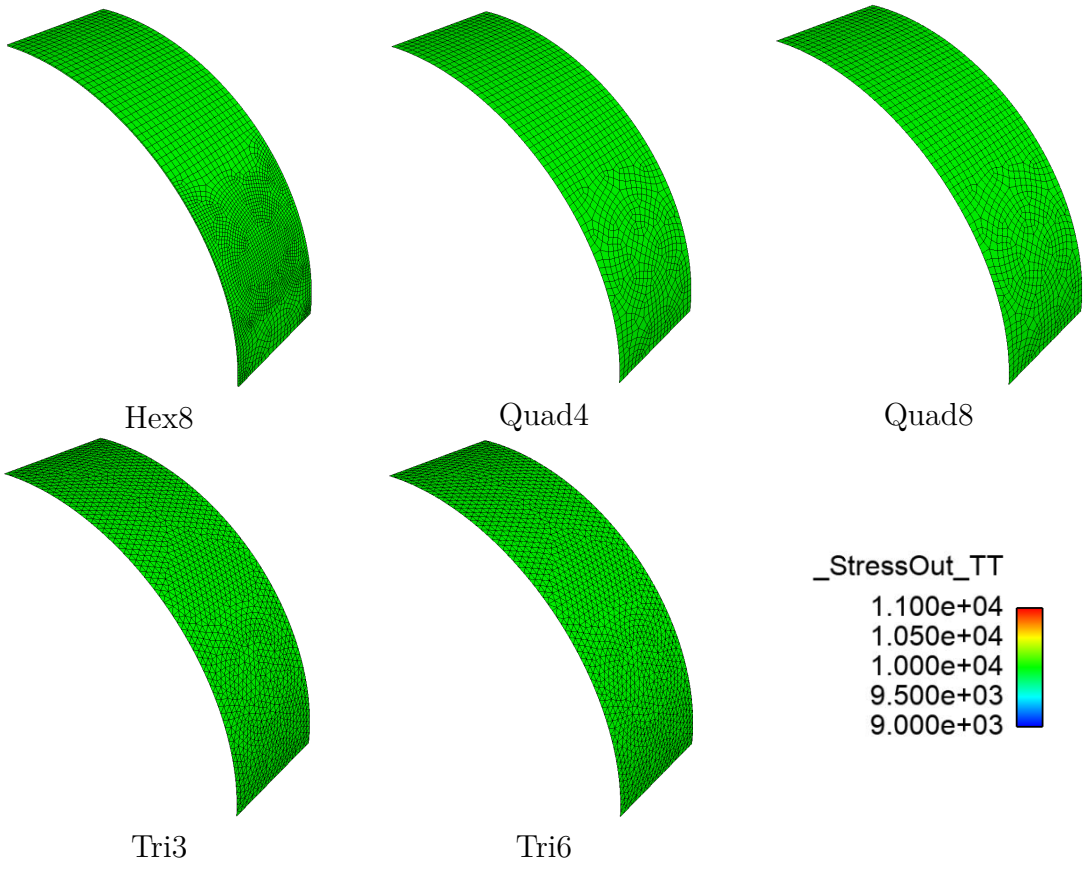

Figure 6-12. – Axial Stress for Partial Cylinder

5.7. Membrane Geometrical Stiffness

We wish to evaluate the geometric stiffness for a simple unit square, with pre-stress in the Y direction. As described in the theory manual, the geometric stiffness is given by,

$$E_g = t\int_A \sigma_{lm}\left[\left(\frac{\partial\delta\boldsymbol{u}}{\partial x_m}\right)^T\frac{\partial\boldsymbol{u}}{\partial x_l} - \frac{1}{2}\sum_{\gamma=1}^{2}\left(\boldsymbol{e}_\gamma\frac{\partial\delta\boldsymbol{u}}{\partial x_l}+\boldsymbol{e}_l\frac{\partial\boldsymbol{u}}{\partial x_\gamma}\right)\left(\boldsymbol{e}_\gamma\frac{\partial\delta\boldsymbol{u}}{\partial x_m}+\boldsymbol{e}_m\frac{\partial\boldsymbol{u}}{\partial x_\gamma}\right)\right]dA \tag{5.7.1}$$

5.7.1. Development

Let nodes 1, 2, 3 and 4 have coordinates (0,0), (1,0), (0,1), and (1,1). The shape functions for the nodes are given by

$$N_1 = (1-x)(1-y) \tag{5.7.2}$$
$$N_2 = x(1-y) \tag{5.7.3}$$
$$N_3 = (1-x)y \tag{5.7.4}$$
$$N_4 = xy. \tag{5.7.5}$$

The shape function derivatives are then

$$N_{1,x} = y-1 \tag{5.7.6}$$
$$N_{1,y} = x-1 \tag{5.7.7}$$
$$N_{2,x} = 1-y \tag{5.7.8}$$
$$N_{2,y} = -x \tag{5.7.9}$$
$$N_{3,x} = -y \tag{5.7.10}$$
$$N_{3,y} = 1-x \tag{5.7.11}$$
$$N_{4,x} = y \tag{5.7.12}$$
$$N_{4,y} = x \tag{5.7.13}$$

We have

$$\boldsymbol{u} = \sum_{i=1}^{3}(u_{1,i}N_1 + u_{2,i}N_2 + u_{3,i}N_3 + u_{4,i}N_4)\boldsymbol{e}_i, \tag{5.7.14}$$

where $\boldsymbol{e}_i$ is a unit vector in global direction i. We then obtain

$$\boldsymbol{u}_{,x} = \sum_{i=1}^{3}(u_{1,i}N_{1,x} + u_{2,i}N_{2,x} + u_{3,i}N_{3,x} + u_{4,i}N_{4,x})\boldsymbol{e}_i \tag{5.7.15}$$

$$\boldsymbol{u}_{,y} = \sum_{i=1}^{3}(u_{1,i}N_{1,y} + u_{2,i}N_{2,y} + u_{3,i}N_{3,y} + u_{4,i}N_{4,y})\boldsymbol{e}_i \tag{5.7.16}$$

When $\sigma = \sigma_{22}$, and all other components are zero, we can write,

$$E_g = t\int_A \sigma_{22}\boldsymbol{u}_{,y}^T\boldsymbol{u}_{,y} +$$

$$-\frac{1}{2}t\int_A \sigma_{22}\left[(\boldsymbol{e}_1\boldsymbol{u}_{,y}+\boldsymbol{e}_2\boldsymbol{u}_{,x})(\boldsymbol{e}_1\boldsymbol{u}_{,y}+\boldsymbol{e}_2\boldsymbol{u}_{,x})+(\boldsymbol{e}_2\boldsymbol{u}_{,y}+\boldsymbol{e}_2\boldsymbol{u}_{,y})(\boldsymbol{e}_2\boldsymbol{u}_{,y}+\boldsymbol{e}_2\boldsymbol{u}_{,y})\right]dA \tag{5.7.17}$$

or,

$$\frac{E_g}{t\sigma_{22}} = \int_A \boldsymbol{u}_{,y}^T\boldsymbol{u}_{,y}dA \tag{5.7.18}$$

$$-\frac{1}{2}\int_A(\boldsymbol{e}_1\boldsymbol{u}_{,y})^2dA \tag{5.7.19}$$

$$-\int_A(\boldsymbol{e}_1\boldsymbol{u}_{,y})(\boldsymbol{e}_2\boldsymbol{u}_{,x})dA \tag{5.7.20}$$

$$-\frac{1}{2}\int_A(\boldsymbol{e}_2\boldsymbol{u}_{,x})^2dA \tag{5.7.21}$$

$$-2\int_A(\boldsymbol{e}_2\boldsymbol{u}_{,y})^2dA \tag{5.7.22}$$

5.7.1.1. $K_{1,1}$ entry

We will examine the 1,1 entry of the stiffness matrix first. This can be found by setting $\boldsymbol{u}_{j,i}=0$ unless $i=j=1$, and $\boldsymbol{u}_{1,1}=1$. This is often called "probing". Then,

$$\boldsymbol{u}_{,x} = N_{1,x}\boldsymbol{e}_1 \tag{5.7.23}$$

$$\boldsymbol{u}_{,y} = N_{1,y}\boldsymbol{e}_1 \tag{5.7.24}$$

Then,

$$\frac{E_g}{t\sigma_{22}} = \int_A \frac{N_{1,y}^2}{2}dA \tag{5.7.25}$$

$$= \int_A \frac{(x-1)^2}{2}dx\,dy \tag{5.7.26}$$

$$= \left.\frac{(x-1)^3}{6}\right|_0^1 \tag{5.7.27}$$

$$= \frac{1}{6} \tag{5.7.28}$$

5.7.1.2. Other Entries

Computing the remaining terms in the matrix is tedious, but straightforward. A maple script can be used to accomplish this. From that script, we determine the following.

$$K_{11} = t\sigma_{22}/6 \tag{5.7.29}$$

$$Kg_{22} = -t\sigma_{22}/2 \tag{5.7.30}$$

$$Kg_{33} = t\sigma_{22}/3 \tag{5.7.31}$$

$$Kg_{12} = t\sigma_{22}/8 \tag{5.7.32}$$

$$\tag{5.7.33}$$

The maple script is available.

5.7.1.3. Rotations

The test in this directory runs only on a unit square in the xy plane. However, a related verification test rotates that structure generally, and compares eigen responses for that rotation with an unrotated square. Having identical eigenvalues assures us that rotations are an issue. For input deck see Appendix 11.14.

5.8. Membrane Quad

A verification test was created for membrane elements in Sierra-SD. The geometry of this test is shown in Figure 8-13.

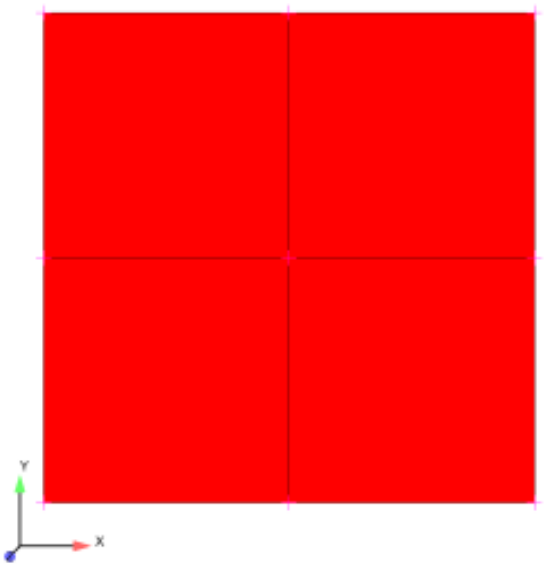

Figure 8-13. – membraneGeometry

There is a total of four membrane elements in the model with the following boundary conditions. The three bottom and top nodes are fixed in the x and y direction. This is an eigen solution case with a total of fourteen modes. For verification the test in Sierra-SD was compared to the Abaqus finite element code. The Eigenvalue results are shown in Table 8-7. All modes are compared. There are nine rigid body modes in the model.

For input deck see Appendix 11.15.

Table 8-7. – Sierra-SD and Abaqus Eigenvalue Comparison

Mode Number	Sierra-SD	Abaqus
1	-6.70788E-09	0.0
2	-6.70788E-09	0.0
3	0.0	0.0
4	0.0	0.0
5	0.0	0.0
6	0.0	3.7945E-08
7	6.70788E-09	3.7945E-08
8	9.48637E-09	8.8049E-05
9	1.16184E-08	1.1743E-04
10	2607.7	2607.7
11	4237.42	4237.4
12	4723.49	4723.5
13	4723.49	4723.5
14	5164.01	5164.0

5.9. QuadM membrane Patch

A patch test that was created for a SierraSD membrane element. The geometry of this test is shown in Figure 9-14. There are a total of five boundary conditions constraining the

Figure 9-14. – Patch Test Geometry

model. First, all nodes are fixed in the z direction, which is the direction normal to the plane of the model. Second, the top left corner node is fixed in all directions. Third, the nodes on the left side of the geometry are constrained in the x direction. Fourth, the nodes on the top of the geometry are constrained in the y direction. Finally, the nodes on the far right side of the geometry have a prescribed displacement of 0.1 in the positive x direction. The test was analyzed by verifying constant strain throughout the geometry. The results from this test can be seen in Table 9-8.

Table 9-8. – Strain for Membrane Elements

Node Number	Strain
1	Fixed = 0
2	0.0250
3	0.0250
4	Fixed = 0
5	0.0250
6	Fixed = 0
7	0.0250
8	Fixed = 0
9	0.0250
10	0.0250
11	0.0250
12	0.0250
13	0.0250

5.9.1. Eigen

The model was also tested using an eigen solution. In this case only the out-of-plane boundary conditions were applied, resulting in a model that should have three rigid body modes. The number of rigid body modes was to be verified in accordance with the boundary conditions. The test case outputs three rigid body modes as expected.

5.9.2. Rotated Patch Test

Further verification was performed using the same patch test by rotating the test out of the XY plane, shown in Figure 9-15.

Figure 9-15. – Test Geometry

The model is constrained by MPC's to impose exactly the same boundary conditions as were described in the previous section, except that they were defined with respect to the rotated coordinate system. With these boundary conditions the model has no rigid body modes. The first 10 modes for the rotated test are compared to the in plane patch test. The Eigenvalue results are shown in Table 9-9. As expected, the modes are the same in both cases and are invariant with respect to the rotation of the model.

Table 9-9. – Rotated Patch Test

Mode Number	No-rotation	Rotated
1	627.172	627.172
2	818.997	818.997
3	924.864	924.864
4	1471.59	1471.59
5	1869.91	1869.91
6	2187.29	2187.29
7	2429.53	2429.53
8	2574.91	2574.91
9	2931.04	2931.04
10	3073.42	3073.42

5.9.3. Hex Elements

For verification, the model was also created using the default hex8 elements. The same geometry was used as the membrane element, but the surface was extruded with a thickness of 1. The same boundary conditions were used as well. The results can be seen in table 9-10. The strain is constant for every node through out the model, therefore, verifying the patch test is working.

Table 9-10. – Strain for Hex Elements

Node Number	Strain
1	Fixed = 0
2	Fixed = 0
3	0.0250
4	0.0250
5	Fixed = 0
6	Fixed = 0
7	0.0250
8	0.0250
9	0.0250
10	Fixed = 0
11	0.0250
12	Fixed = 0
13	Fixed = 0
14	Fixed = 0
Nodes 15-26	0.0250

5.9.4. Orthotropic Material Properties

In this test, we consider a 2×2 mesh of an orthotropic membrane model where the material elasticity tensor only provides stiffness in the x direction, with zero stiffness in the remaining directions. In addition, we constrain the out-of-plane motion to be zero. With these conditions, we expect 12 rigid body modes, since each of the nodes in the mesh is free to move in the y direction with no resistance. This test involves a coupled Sierra-SM and Sierra-SD analysis, where Sierra-SM produces an output exodus file that contains the necessary material properties. Sierra-SD uses this output exodus file and performs a modal analysis. For verification, the first 18 modes are compared to the Abaqus finite element code. The eigenvalue results are shown in Table 9-11. There are 12 rigid body modes in the model, and the remaining modes show an acceptable comparison of the two codes.

The direction of the fibers in the material properties were also changed from the y direction to the x direction. The modes were verified to match exactly and were independent of the fiber direction as expected. For input deck see Appendix 11.16.

Table 9-11. – Orthotropic Material Patch Test

Mode Number	Abaqus	Sierra-SD
1	0.0000	-3.63305E-03
2	0.0000	-2.86194E-03
3	2.18886E-03	-2.33876E-03
4	4.74120E-02	-9.21049E-04
5	6.70089E-02	9.91374E-05
6	6.70388E-02	5.23966E-04
7	6.70477E-02	9.29529E-04
8	6.70864E-02	1.14456E-03
9	6.71252E-02	1.45159E-03
10	8.20846E-02	1.71789E-03
11	8.20859E-02	2.19313E-03
12	9.47649E-02	2.70663E-03
13	1.08203E+05	1.08184E+05
14	1.53022E+05	1.52995+05
15	1.53022E+05	1.52995+05
16	1.87413E+05	1.87379+05
17	2.16406E+05	2.16367+05
18	2.65042E+05	2.64994+05

5.10. QuadS_GY Shear Membrane Shell

Verification of the QuadS_GY Element. The existing Salinas membrane element used for eigenmode/linear analysis is a quad with three extensional degrees of freedom: u, v, and w. The new shell finite element draws on the Reissner-Mindlin plate theory, as described in Chapter 5 of Ref.[31]. This element has six degrees of freedom per node; three infinitesimal displacements: u, v, w; and three infinitesimal rotations: θ_x, θ_y, and θ_z. Selective reduced integration is used in this bilinear element. Bending and membrane strains are integrated with the 2-by-2 Gauss rule. Shear deformation is integrated with the 1-by-1 Gauss rule. Under integration avoids locking attributed to the shear interpolation. Uncoupled drilling stiffness is added to curb in-plane rotation θ_z. This stiffness is set internally and prevents the solution from containing meaningless null eigenvalues.

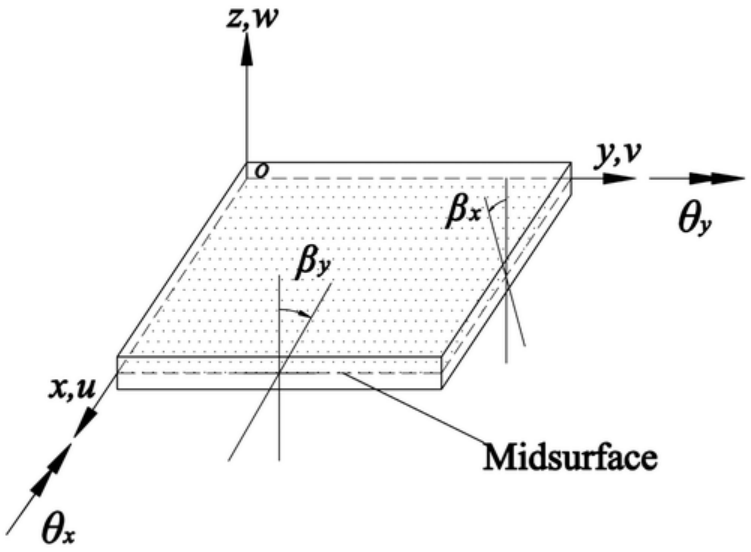

Figure 10-16. – Transverse shear strains β_x and β_y allow cross sections to not remain on a plate perpendicular to fiber direction. This relaxation of the Kirchhoff hypothesis enables accurate study of thick plates and shells.

5.10.1. Eigenvalue analysis: Verification on a flat shell

In this section, we verify the new element using two procedures: a) The existing Salinas element QuadT is used to generate reference data; b) Analytical solutions are used. Note that whereas the element QuadT captures only bending, the new QuadS_GY captures bending and shear deformations, in addition to membrane modes. The shell used for verification has dimensions of 1 m by 1 m, the modulus of elasticity is $E = 30$ MPa, the Poisson ration is 0.3, and density is 0.288 kg/m^3.

5.10.1.1. Isotropic

In this subsection, the behavior of Quad_T (bend. + memb.) and QuadS_GY (bend. + memb. + shear) are compared to bending analytical results (Kirchhoff-Love). A general formula for obtaining the natural frequencies of a flat plate for various boundary conditions is as follows

$$f_{ij} = \frac{\lambda_{ij}^2}{2\pi a^2}\left[\frac{Eh^3}{12\gamma(1-\nu^2)}\right]^{\frac{1}{2}}, \tag{5.10.1}$$

where λ is a parameter that depends on the shell dimensions and its boundary conditions, a is the first dimension of the rectangular shell, E is the isotropic modulus of elasticity, h is the thickness, γ is the mass per unit area of the shell, and ν is the Poisson ration. The λ_{ij} values for specific boundary conditions, relative dimensions, and mode number are given in the literature (see Ref. [10]).

5.10.1.1.1. Fixed-Fixed-Fixed-Fixed (FFFF) The bending eigenfrequencies of the plate for two different thickness values are reported in Tables 10-12 and 10-13. The shear-deformable shell element (QuadS_GY) results naturally diverge from bending theory for increasingly thicker sections.

Table 10-12. – Eigenfrequencies for FFFF flat shell of thickness 0.001 m. Frequencies are in Hertz and discrepancies from theory are given in percentage between parenthesis.

	Analytical	QuadT	QuadS_GY
1st mode	347.620	347.466	347.669
	(Ref.)	(0.04)	(0.01)
2nd mode	709.052	708.562	709.363
	(Ref.)	(0.07)	(0.04)
3rd mode	709.052	708.579	709.406
	(Ref.)	(0.07)	(0.05)
4th mode	1046.048	1044.239	1045.507
	(Ref.)	(0.17)	(0.05)
5th mode	1271.098	1270.185	1272.846
	(Ref.)	(0.07)	(0.17)
6th mode	1276.893	1276.245	1278.894
	(Ref.)	(0.05)	(0.15)

Table 10-13. – Eigenfrequencies for FFFF flat shell of thickness 0.01 m. Frequencies are in Hertz and discrepancies from theory are given in percentage between parenthesis.

	Analytical	QuadT	QuadS_GY
hline 1st mode	3476.203	3474.659	3463.921
	(Ref.)	(0.04)	(0.35)
2nd mode	7090.527	7085.620	7048.431
	(Ref.)	(0.07)	(0.60)
3rd mode	7090.527	7085.790	7048.851
	(Ref.)	(0.07)	(0.59)
4th mode	10460.48	10442.393	10361.58
	(Ref.)	(0.17)	(0.94)
5th mode	12710.98	12701.847	12598.886
	(Ref.)	(0.07)	(0.88)
6th mode	12768.93	12762.453	12661.539
	(Ref.)	(0.05)	(0.84)

5.10.1.1.2. Free-Free-Free-Free(FrFrFrFr) Tables 10-14 and 10-15 show natural frequency results of the same plate with the four edges free. Rigid body motion has been disregarded. Only deformation modes are reported in this subsection.

Table 10-14. – Eigenfrequencies for FrFrFrFr flat shell of thickness 0.001 m. Frequencies are in Hertz and discrepancies from theory are given in percentage between parenthesis.

	Analytical	QuadT	QuadS_GY
1st mode	130.297	129.818	129.919
	(Ref.)	(0.37)	(0.29)
2nd mode	191.147	188.996	189.086
	(Ref.)	(1.12)	(1.08)
3rd mode	235.964	233.438	234.240
	(Ref.)	(1.07)	(0.73)
4th mode	338.251	333.017	335.625
	(Ref.)	(1.54)	(0.78)
5th mode	338.251	335.954	335.756
	(Ref.)	(0.68)	(0.74)
6th mode	594.306	582.394	589.133
	(Ref.)	(2.00)	(0.87)

5.10.1.1.3. Simply supported-Free-Free-Free (SFrFrFr) The natural frequencies associated with the lowest-frequency deformation modes are shown in Tables 10-16 and 10-17.

Table 10-15. – Eigenfrequencies for FrFrFrFr flat shell of thickness 0.01 m. Frequencies are in Hertz and discrepancies from theory are given in percentage between parenthesis.

	Analytical	QuadT	QuadS_GY
1st mode	1302.97	1316.80	1263.69
	(Ref.)	(1.06)	(3.01)
2nd mode	1911.48	2167.89	1938.90
	(Ref.)	(13.41)	(1.43)
3rd mode	2359.65	2353.98	2632.25
	(Ref.)	(0.24)	(11.55)
4th mode	3382.51	3359.54	3331.60
	(Ref.)	(0.68)	(1.50)
5th mode	3382.51	4489.73	3331.81
	(Ref.)	(32.73)	(1.50)
6th mode	5943.06	5891.27	5873.92
	(Ref.)	(0.87)	(1.16)

Table 10-16. – Eigenfrequencies for SFrFrFr flat shell of thickness 0.001 m. Frequencies are in Hertz and discrepancies from theory are given in percentage between parenthesis.

	Analytical	QuadT	QuadS_GY
1st mode	64.212	64.152	64.177
	(Ref.)	(0.09)	(0.05)
2nd mode	145.075	143.874	143.905
	(Ref.)	(0.83)	(0.81)
3rd mode	246.203	244.989	244.650
	(Ref.)	(0.49)	(0.63)
4th mode	252.384	250.912	249.830
	(Ref.)	(0.58)	(1.01)
5th mode	470.480	467.576	467.594
	(Ref.)	(0.62)	(0.61)
6th mode	491.150	488.143	487.013
	(Ref.)	(0.61)	(0.84)

Table 10-17. – Eigenfrequencies for SFrFrFr flat shell of thickness 0.01 m. Frequencies are in Hertz and discrepancies from theory are given in percentage between parenthesis.

	Analytical	QuadT	QuadS_GY
1st mode	642.117	641.523	635.558
	(Ref.)	(0.09)	(1.02)
2nd mode	1450.752	1438.741	1437.167
	(Ref.)	(0.83)	(0.94)
3rd mode	2462.029	2449.891	2426.925
	(Ref.)	(0.49)	(1.42)
4th mode	2523.845	2509.117	2486.897
	(Ref.)	(0.58)	(1.46)
5th mode	4704.803	4675.760	4639.690
	(Ref.)	(0.62)	(1.38)
6th mode	4911.501	4881.430	4841.552
	(Ref.)	(0.61)	(1.42)

5.10.1.2. Orthotropic

For an orthotropic material model, we use a clamped-clamped shell with the following arbitrary orthotropic properties: $E_x = 30\,\text{MPa}$, $E_y = 0.5\,\text{MPa}$, $\nu_{xy} = 0.3$, $G_{xy} = 0.5\,\text{MPa}$, $\rho = 7.46\ \text{g/m}^3$, and thickness is 1 mm. It is assumed that the fiber is aligned with the element frame of reference, i.e., fiber angle $\alpha = 0\,\text{deg}$. Both analytical and QuadT results disregard shear dynamics, whereas shear is present in the computations of the QuadS_GY. The effect of transverse shear tends to be negligible for small relative thickness values. Analytical results are obtained by applying a similar expression to 5.10.1, also provided in Ref. [10]. Results are summarized in Table 10-18. A graphical comparison of the (32) mode for two SD elements is shown in Fig. 10-17.

Table 10-18. – Eigenfrequencies for clamped-clamped orthotropic flat shell of thickness 0.001 m. Frequencies are in Hertz and discrepancies from theory are given in percentage between parenthesis.

	Analytical	QuadT	QuadS_GY
11 mode	209.022	210.144	210.365
	(Ref.)	(0.54)	(0.64)
12 mode	226.154	226.862	227.138
	(Ref.)	(0.31)	(0.43)
13 mode	266.218	266.395	266.738
	(Ref.)	(0.06)	(0.19)
21 mode	572.750	571.523	572.802
	(Ref.)	(0.21)	(0.01)
22 mode	585.382	583.755	585.204
	(Ref.)	(0.28)	(0.03)
23 mode	611.422	609.315	611.004
	(Ref.)	(0.34)	(0.07)
31 mode	1118.82	1115.867	1120.096
	(Ref.)	(0.26)	(0.11)
32 mode	1130.410	1126.535	1131.111
	(Ref.)	(0.34)	(0.06)
33 mode	1152.056	1147.003	1152.097
	(Ref.)	(0.43)	(0.00)

For input deck see Appendix 11.17.

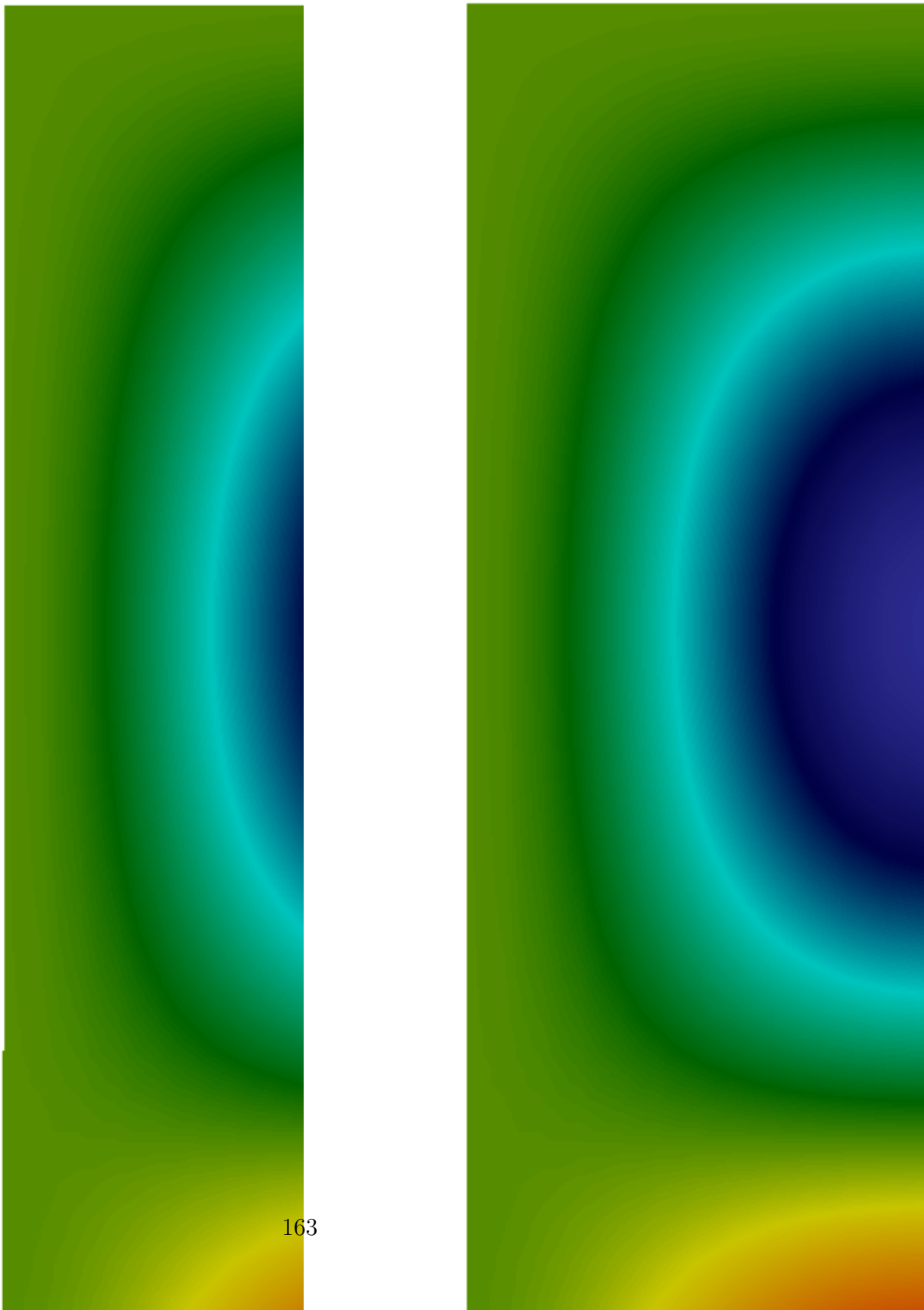

5.11. QuadS_GY Shear Membrane Shell - Geometric Stiffness and Preload

Verification of the QuadS_GY Geometric Stiffness matrix and SierraSM Preload.

5.11.1. Verification of geometric stress stiffness matrix

A cantilever beam modeled by shear-deformable shell elements used to test other Sierra-SD shell elements is used here too. One end of the beam is clamped. An axial pressure is applied to the other end. The beam is 0.127 m (length) by 0.0044504 m (width) by 0.0044504 m (thickness). The modulus of elasticity is 187 GPa, $\nu = 0.3$, and $\rho = 8015.19\,\mathrm{kg/m^3}$. A linear pressure of -2245852908.28 N/m is applied to the free end, which yields an axial displacement of 1.5656243 mm. The effect of an axial load stiffens the system thus increasing the beam's natural frequencies. The following table summarizes the behavior of the new element:

Table 11-19. – First three natural frequencies of a beam with applied axial pressure.

	Abaqus	SD shell	QuadS_GY	Difference (%)
Without Preload				
Mode 1	212.4	212.793	215.574	1.49
Mode 2	1330.8	1327.73	1345.831	1.12
Mode 3	3727.2	3689.86	3740.46	0.36
With Preload				
Mode 1	1137.9	1141.66	1111.647	2.31
Mode 2	3624.4	3621.86	3536.431	2.42
Mode 3	6694.1	6636.30	6507.385	2.79

Two methods are used to obtain the eigenfrequencies reported in Table 11-19:

- **SD shell**. In Sierra-SD, the pressure load is applied to the shelled beam and, with the resulting displacements, the system stiffness is updated. After that, eigenvalue analysis on the beam is performed considering the updated stiffness.
- **QuadS_GY**. The eigenfrequencies of the preloaded system is computed in a two-step process. First, we applied a prescribed displacement in Sierra-SM to achieve a beam stress state analogous to the SD shell. Then we write those stress to an Exodus output file. This file is used in Sierra-SD to read the geometry of the system and its stresses, which are then used to compute the natural frequencies of the preloaded beam.

This difference in methodology is justified by the way tire eigenanalysis is performed: First a complex nonlinear system is solved in Sierra-SM. With the resulting stresses, a geometric stress stiffness matrix is built to account for the preloaded state of the tire. Finally eigenvalue analysis is performed in Sierra-SD. Note that the process used for the QuadS_GY shell involves some approximation: Only one integration point is used to carry

stresses from Sierra-SM to Sierra-SD, whereas membrane and bending deformation is spatially integrated on a 2-by-2 grid – this may be the reason for the slight discrepancies reported in Table 11-19.

5.11.2. Verification Sierra-SM–Sierra-SD for small deformation

This section compares small deformation results between Sierra-SM and Sierra-SD. For the GY fiber shell, several fiber angles are chosen in order to verify that element frames of reference and orientation match.

5.11.2.1. Isotropic shell

A clamped shell on one edge, of dimensions 150 mm by 100 mm is used to compare the displacement results of Sierra-SM and Sierra-SD for small deformation. The shell thickness is 0.4409 m, its modulus of elasticity is 187 MPa, and its Poisson ration, 0.3. One of the short edges is fully clamped and a force of 200 N/node is applied on the other short edge. The same shell is defined in both, the quasistatic nonlinear code Sierra-SM and the linear solver Sierra-SD. Results in terms of axial and lateral displacements may be observed in Figs. 11-18 and 11-19. The axial displacement on the solicited edge center for Sierra-SM is $5.9924 \cdot 10^{-5}$ mm, whereas for Sierra-SD is $5.9908 \cdot 10^{-5}$ mm. Similarly, for lateral displacement, the values are $1.0332 \cdot 10^{-6}$ mm for Sierra-SM, and $1.0409 \cdot 10^{-6}$ mm for Sierra-SD.

For input deck see Appendix 11.18.

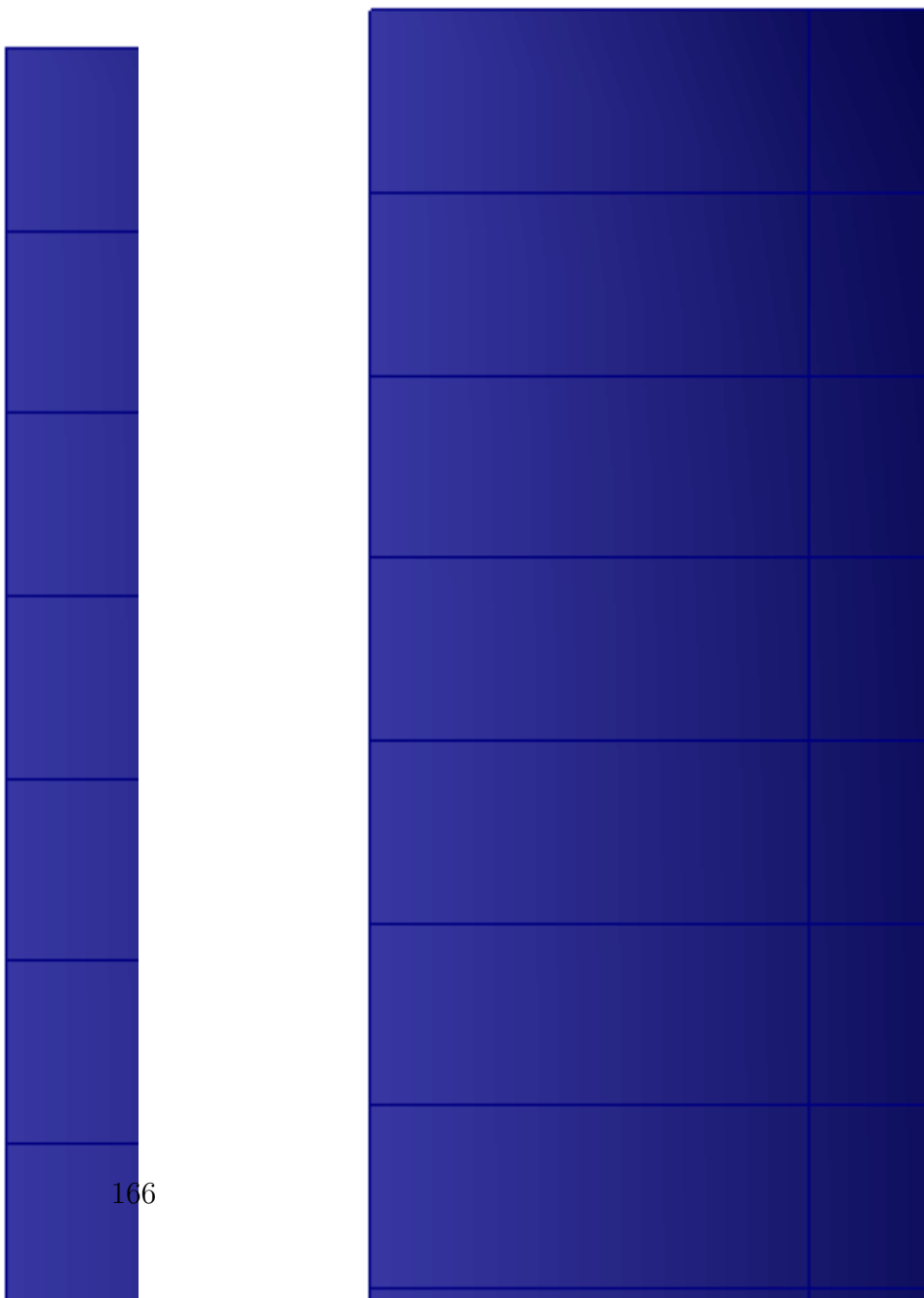

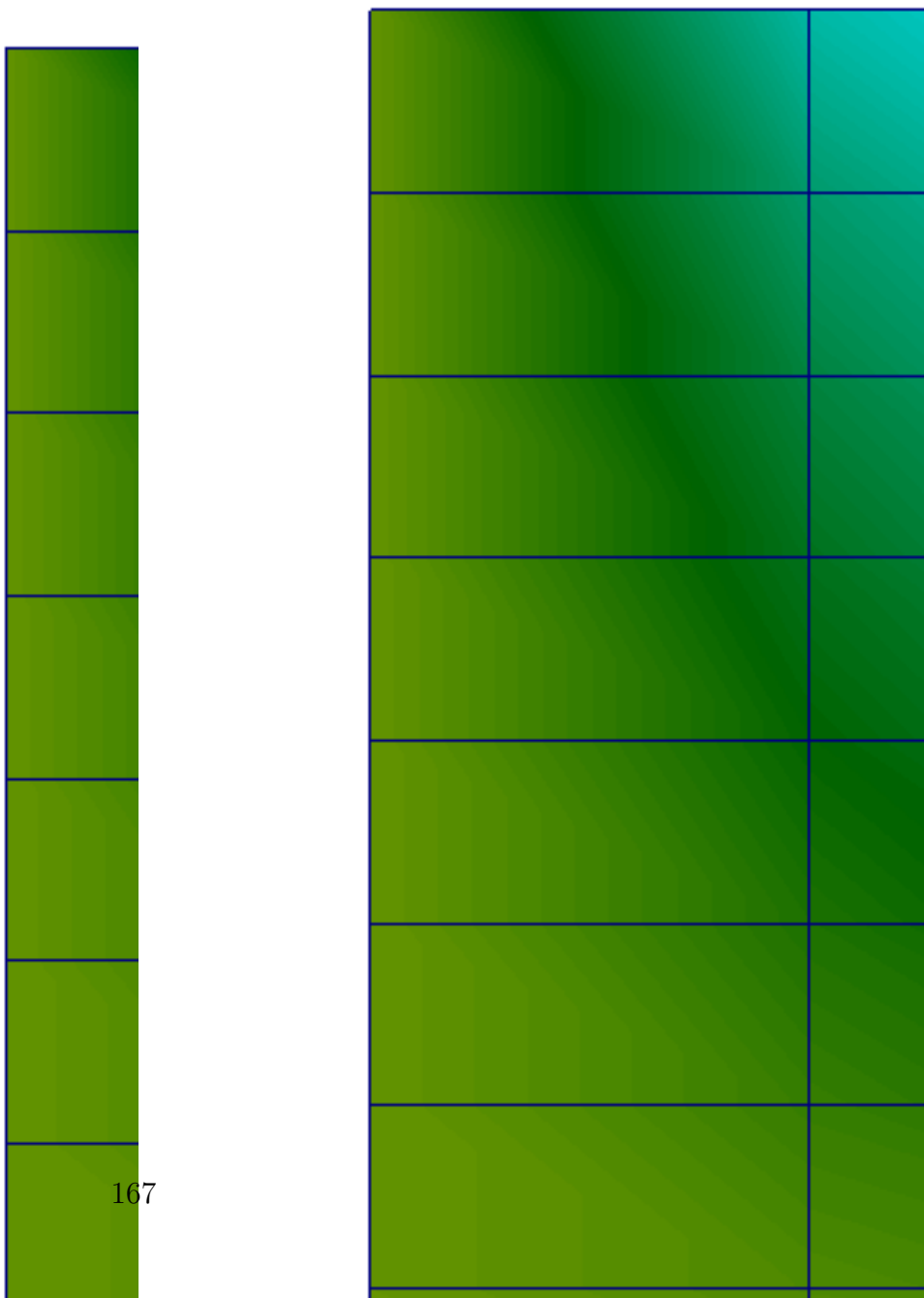

5.12. Hex Membrane Sandwich

5.12.1. Isotropic Material

A simple plate model was constructed and analyzed using hex and membrane elements, shown in Figure 12-20.

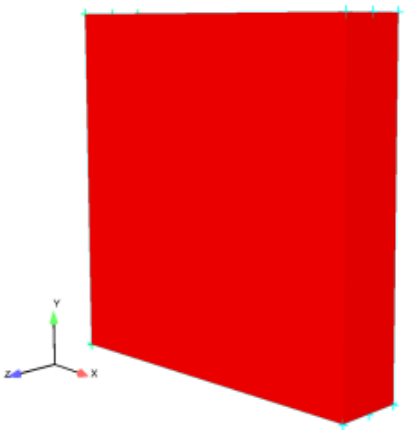

Figure 12-20. – Test Geometry

The first test using this plate model had no preload. It consisted of isotropic membrane elements sandwiched in between hex elements. The model is fixed on one end and constrained in the Y and Z direction on the other end. The Eigenvalue results are shown in Table 12-20.

Table 12-20. – Isotropic-Nopreload

Mode Number	Abaqus	Sierra-SD
1	1472.5	1472.46
2	1994.5	1994.48
3	5231.2	5231.19
4	6787.4	6787.39
5	8958.0	8957.96
6	11674.0	11674.2

For a preloaded model, this test was stretched with large deformations in Sierra-SM and a representative Exodus file was outputted. This Exodus file was used in Sierra-SD for a subsequent eigen analysis. For verification, all modes were compared to the Abaqus finite element code. As in the first case, the plate is fixed on one end and is constrained in the Y and Z direction on the other end. The Eigenvalue results are shown in Table 12-21.

Table 12-21. – Isotropic-Preload

Mode Number	Abaqus	Sierra-SD
1	1420.8	1410.79
2	1798.3	1808.77
3	5212.8	5208.10
4	6765.5	6765.63
5	8914.0	8911.89
6	11638	11636.50

5.12.2. Orthotropic Material

The same plate model was tested using orthotropic material properties. The material elasticity tensor only provides stiffness in the x direction, with zero stiffness in the remaining directions. The first test had no preload. The modal results are shown in Table 12-22.

Table 12-22. – Orthotropic-Nopreload

Mode Number	Abaqus	Sierra-SD
1	4776.10	4772.99
2	5231.20	5231.19
3	8152.20	8149.91
4	8958.00	8957.96
5	10998	10970.90

For the second test, the same model was used, except that a uniaxial preload in the x-direction was applied using Sierra-SM. An output Exodus file was then passed to Sierra-SD for the modal analysis. For verification, all modes were compared to the Abaqus finite element code. The Eigenvalue results are shown in Table 12-23.

Table 12-23. – Orthotropic-Preload

Mode Number	Abaqus	Sierra-SD
1	4600.30	4451.72
2	5212.80	5208.10
3	7821.60	7919.50
4	8914.00	8911.89
5	9878.40	9227.89

For input deck see Appendix 11.19.

5.13. Higher Order Hex Acoustic Element Convergence

This section demonstrates a convergence study for the phex element, up to order 4. We verify that the convergence rates approach the theoretically predicted ones in the limit of small enough element size.

The geometry of the model is shown in Figure 13-21. It consists of an acoustic waveguide of length $L = 10.0(m)$, and cross sectional dimensions of $1.0(m)$. The walls were assigned as rigid around the boundaries of the waveguide, including the endcaps. The speed of sound was given as $c = 332.0\frac{m}{s}$. With these parameters, the exact frequencies of vibration of the air in the waveguide are given as

$$f_n = \frac{nc}{2L} = 16.6, 33.2, ... \tag{5.13.1}$$

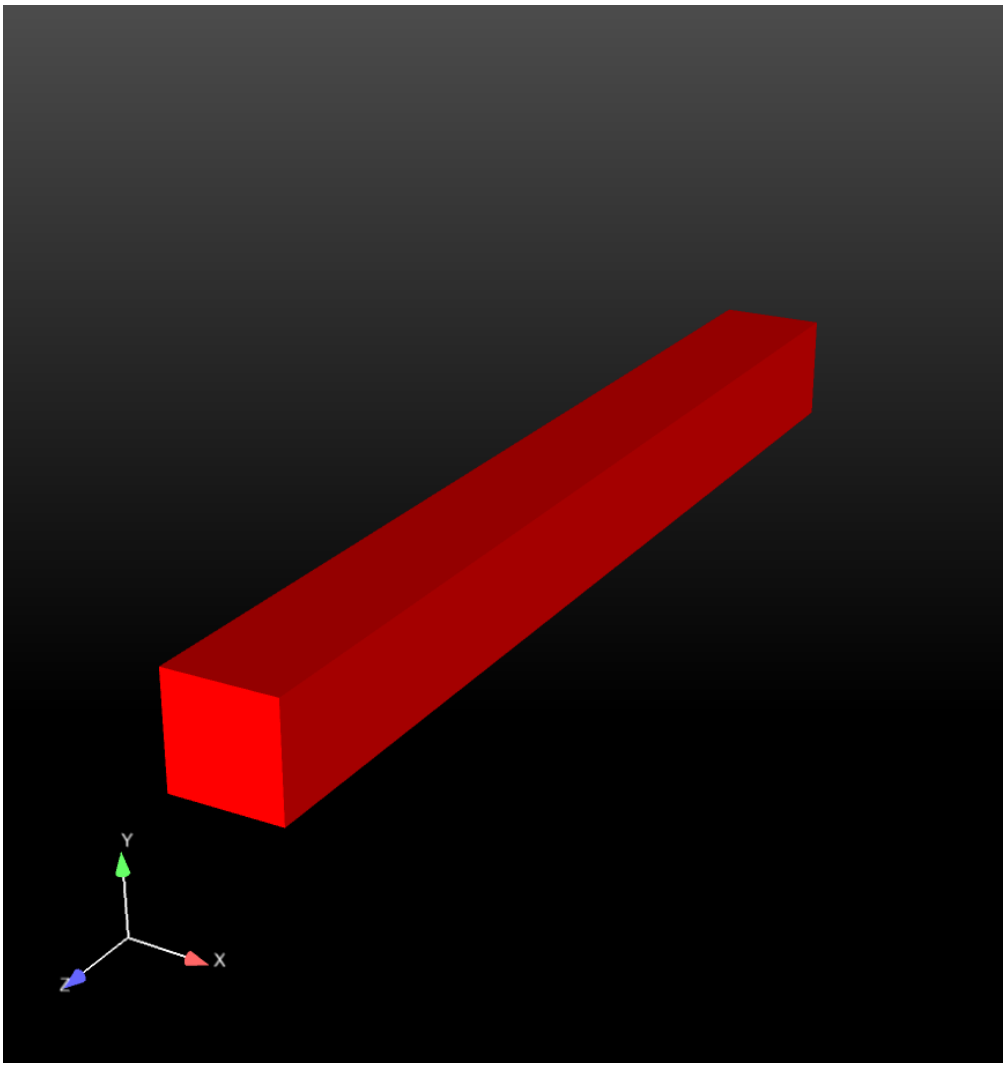

Figure 13-21. – Waveguide Model for Convergence Study of P-hex elements.

Figure 13-22 shows the convergence plot for the hex element for orders $2-4$. The theory predicts that the modal frequencies should converge at a rate of h^{2p}, where h is the element size, and p is the order. Thus, on a log-log plot, the slopes of the convergence lines should be 4, 6, and 8, respectively. In Figure 13-22 we show the relative errors in the 10^{th} modal frequency. Similar results were obtained for the other modes, and so we only show the 10^{th} modal frequency for brevity. In addition to the errors, we show lines that have slopes of 4, 6, and 8, respectively for comparison with the error curves. As seen, for each order, the correct slope is obtained in the limit of small h, (or large $\frac{1}{h}$).

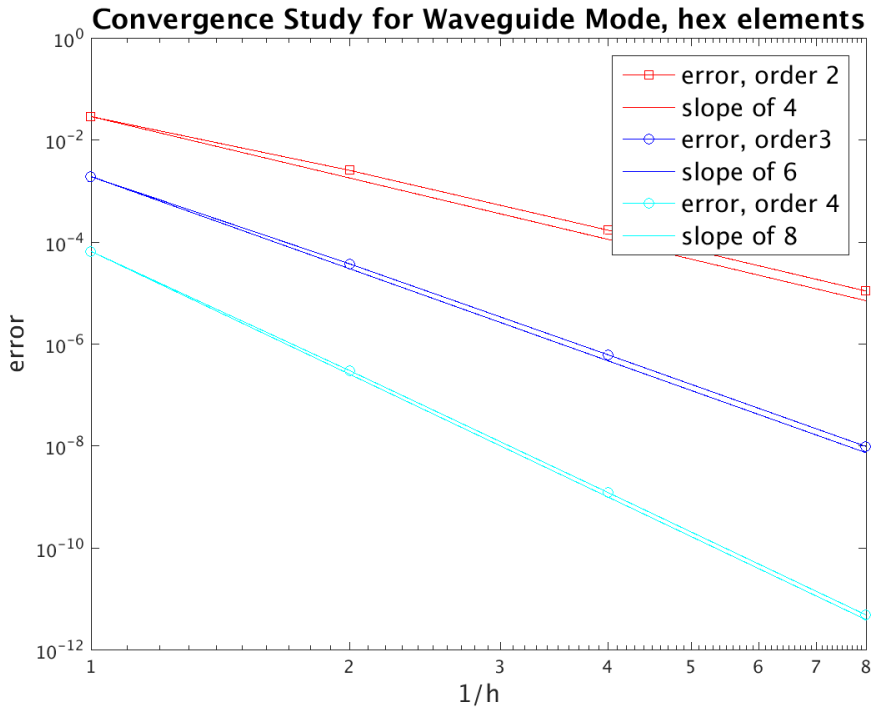

Figure 13-22. – Convergence Study of P-hex elements.

For input deck see Appendix 11.33.

5.14. Higher Order Tet Acoustic Element Convergence

This section demonstrates a convergence study for the ptet element, up to order 4. We verify that the convergence rates approach the theoretically predicted ones in the limit of small enough element size.

The geometry of the model is shown in Figure 14-23. It consists of an acoustic waveguide of length $L = 10.0(m)$, and cross sectional dimensions of $1.0(m)$. The walls were assigned as rigid around the boundaries of the waveguide, including the endcaps. The speed of sound was given as $c = 332.0\frac{m}{s}$. With these parameters, the exact frequencies of vibration of the air in the waveguide are given as

$$f_n = \frac{nc}{2L} = 16.6, 33.2, ... \tag{5.14.1}$$

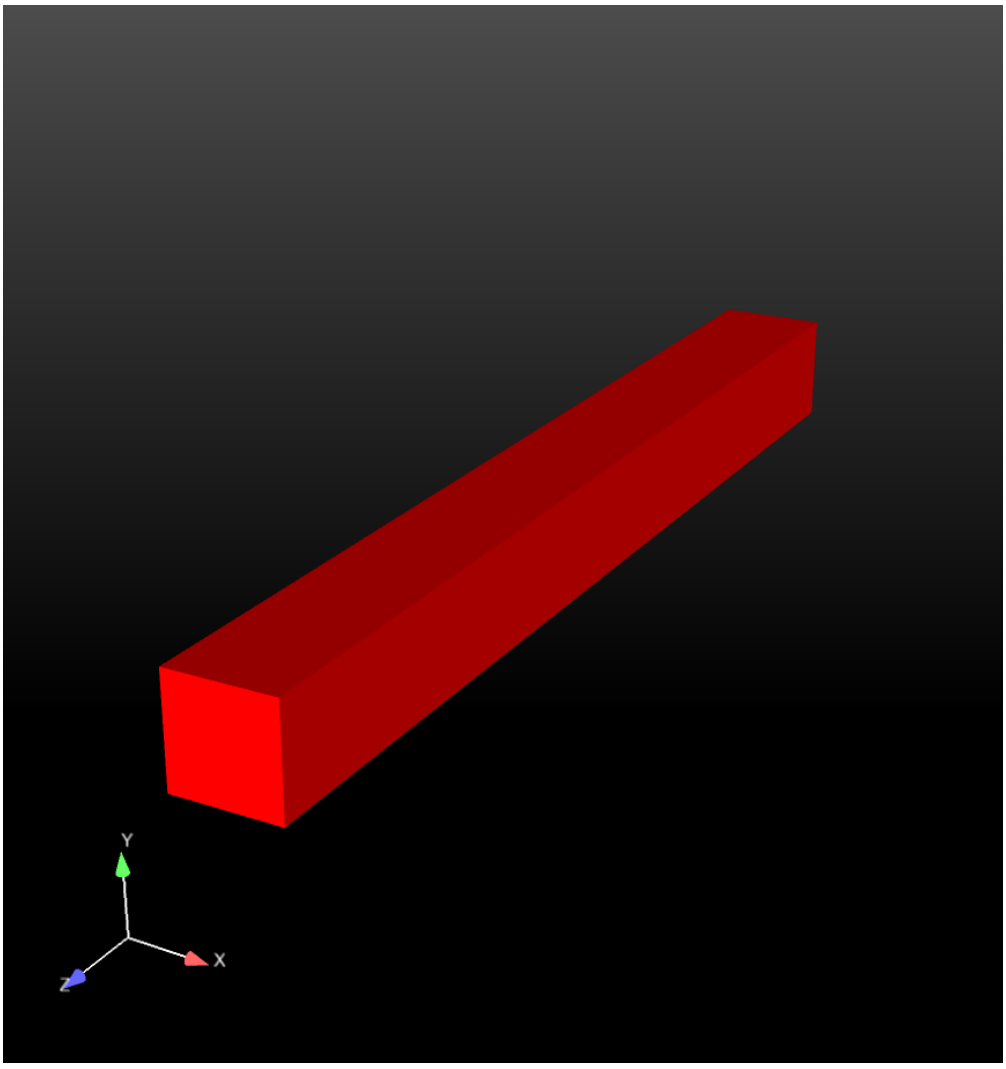

Figure 14-23. – Waveguide Model for Convergence Study of P-tet elements.

Figure 14-24 shows the convergence plot for the tet element for orders $2-4$. The theory predicts that the modal frequencies should converge at a rate of h^{2p}, where h is the element size, and p is the order. Thus, on a log-log plot, the slopes of the convergence lines should be 4, 6, and 8, respectively. In Figure 14-24 we show the relative errors in the 10^{th} modal frequency. Similar results were obtained for the other modes, and so we only show the 10^{th} modal frequency for brevity. In addition to the errors, we show lines that have slopes of 4, 6, and 8, respectively for comparison with the error curves. As seen, for each order, the correct slope is obtained in the limit of small h, (or large $\frac{1}{h}$).

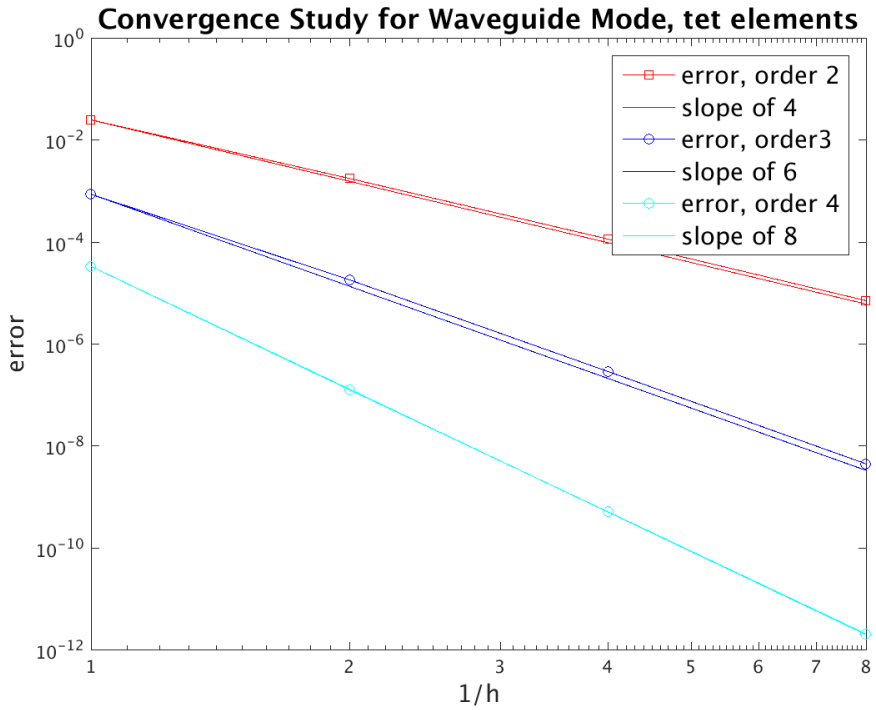

Figure 14-24. – Convergence Study of P-tet elements.

For input deck see Appendix 11.34.

5.15. Tied-Joint with Joint2G and Spring. Slip and Rigid

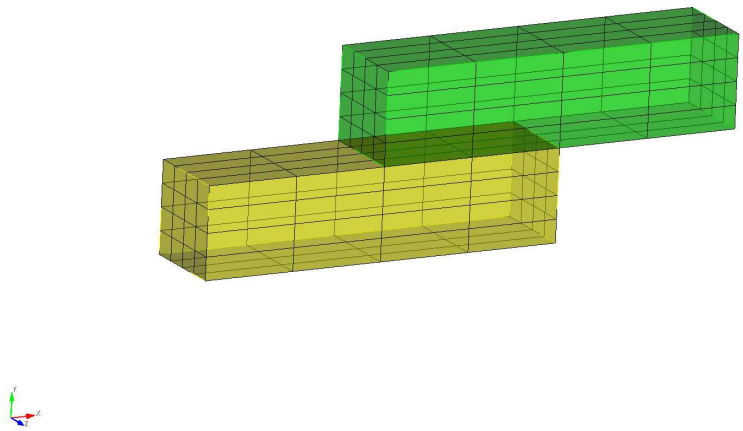

Figure 15-25. – Tied-Joint Model Geometry

5.15.1. Purpose

The "Tied Joint" structure is a meta structure that provides an efficient and robust means of modeling a joint structure. The purpose of this document is to verify that both the tied-joint and conventional methods produce the same solution. Showing the results are the same encourages the use of tied-joints rather than the more tedious conventional method which involves replicating nodes and the use of multi-point constraints (MPCs). Generally, the input file for the tied-joint method is much simpler since all of the constraints are accounted for, rather than having to list them by hand. Also, for the tied-joint input files the necessary constraints become included in the method itself, resulting in a simpler model for the input geometry file.

5.15.2. Lap Joint Comparison

5.15.2.1. Model Geometry

The lap joint model used for both the conventional and tied-joint tests consists of two partially overlapping rectangular blocks, as seen in Figure 15-25. The end of one of the blocks is fixed, while the opposite end of the other block is loaded with a constant applied force. The particular model seen here and used in the following results was created using Cubit and exported as an exodus file.

5.15.2.2. Building the Tied-Joint model

5.15.2.3. Non-slip

```
Tied Joint
        Normal Definition = none
                surface 1,2
        Shear Definition
                side = rigid
                connect to Block 33
end

Block 33
        Spring
                Kz = Elastic 1e9
                Kx = Elastic 1e9
                Ky = Elastic 1e9
end
```

Figure 15-26. – Tied-Joint Non-Slip Input

The exodus file of the original model as described in 5.15.2.1 is the geometry file used for the tied-joint input. The non-slip tied joint model requires the use of a new block. The relevant portions of the input file for the Tied-joint model are seen in Figure 15-26. Using the tied-joint model results in two virtual nodes being created. The exodus output file obtained from using the tied-joint approach is then used as the input geometry file for the conventional non-slip method, and the extra nodes are included using MPCs as explained later.

5.15.2.4. Slip

The geometry file used for the tied-joint slip input is also the original exodus file created from Cubit. However, some changes to the Sierra/SD input file are made in order to incorporate slipping. In the Tied-Joint block the normal definition is set to slip and the side is set equal to "rrod" under the shear definition. Everything else in the file is kept the same, as seen in Figure 15-27. The output of the tied-joint slip file creates two extra blocks that constrain the overlapping surfaces from stretching, allowing the surfaces to move together as one. This output is in turn used in the input file of the conventional slip model, as described later.

```
Tied Joint
        Normal Definition = slip
                surface 1,2
        Shear Definition
                side = rrod
                connect to Block 3
end

Block 3
        Spring
                Kx = Elastic 1e9
                Ky = Elastic 1e9
                Kz = Elastic 1e9
end
```

Figure 15-27. – Tied-Joint Slip Input

5.15.3. Building the Conventional Model

5.15.3.1. Non-slip

The input model used for the conventional approach is the output of the tied-joint model. The tied-joint model produces an additional block to connect the virtual nodes that are created internally, and thus an additional block with spring or joint2g properties is explicitly added to the input file of the conventional method. The difference between the joint2g and the spring properties, is that the joint2g includes rotational degrees of freedom, everything else within the input file remain the same. The input file requires rigidsets and MPCs linking the duplicate nodes that the tied-joint model creates to the "original" nodes on the corresponding faces. The rigidset input section with the spring connection is seen in Figure 15-28.

```
Rigidset
        sideset 1
end
Rigidset
        sideset 2
end

Block 33
        Spring
                Kz = Elastic 1e9
                Kx = Elastic 1e9
                Ky = Elastic 1e9
end
```

Figure 15-28. – Conventional Non-Slip Input

5.15.3.2. Slip

The geometry file used for the conventional slip input is the output from the tied-joint slip input. The extra blocks created from the tied-joint slip output are defined "dead" for this input file when using a spring. In their place, a new section called Tied Data is added in order to incorporate slipping. When a joint2g is used, these extra blocks are defined as "rbe3", replacing the use of MPCs. This can be seen in Figure 15-29. The Tied Data is specified to be a transverse slip that applies to the overlapping surfaces. Rrodsets are also added instead of the rigidsets that are seen in the conventional non-slip input file. Figure 15-30 shows a section of the input file when using a spring connection for conventional slip.

```
Rrodset
        sideset 1
end
Rrodset
        sideset 2
end

Block 3
        Joint2G
                Kx = Elastic 1e9
                Ky = Elastic 1e9
                Kz = Elastic 1e9
                Krx = Elastic 1e9
                Kry = Elastic 1e9
                Krz = Elastic 1e9
end
Block 4
                rbe3
                method=new
end
Block 5
                rbe3
                method=new
end

Tied Data
        surface 1,2
        transverse slip
end
```

Figure 15-29. – Conventional Slip Input with Joint2G

```
Rrodset
        sideset 1
end
Rrodset
        sideset 2
end

Block 3
        Spring
                Kx = Elastic 1e9
                Ky = Elastic 1e9
                Kz = Elastic 1e9
end

Tied Data
        surface 1,2
        transverse slip
end
```

Figure 15-30. – Conventional Slip Input with Spring

5.15.4. Comparison of Results

Exodiff was used to compare the tied-joint and the conventional model for both the slip and non-slip models. While the results from using the tied-joint method and the conventional method were not exactly the same, they were extremely close. These results show that the tied-joint method is just as accurate as the conventional approach. This, in addition to the previously mentioned advantages of offering the user a simpler input and model definition, make the case for the continued use of Tied-Joints in Sierra/SD.

For input deck see Appendix 11.35.1 and Appendix 11.35.2.

5.16. Slide RBE2. Selected DOFS

This test exercises the RBE2 element as a slider. The model and results are shown in Figure 16-31. The base plate is clamped. The perpendicular plate is clamped on the left, and pulled from the right. We are interested in the behavior of the RBE2 links that connect the two plates.

In this example, the RBE2 (which are translated as RBARS in Nasgen) provide a connection in only selected dofs. In particular, the 13456 dofs are constrained, while the 2 is left free. This leaves translation in the Y axis unconstrained.

Figure 16-31 indicates a uniform displacement in the Y direction on the loaded side of the perpendicular plate. This is in agreement with the NASTRAN results. NASTRAN results indicate a maximum displacement of 0.00213, while the QuadT displacement is 0.0023220022994. The discrepancy is expected based on the difference in element formulations. The results indicate that the plate is free to translate, but constrained in the other directions.

Figure 16-32 uses an identical geometry but the load is augmented with a Z component of load. As can be seen in the example, addition of an orthogonal loading does not restrict the sliding behavior.

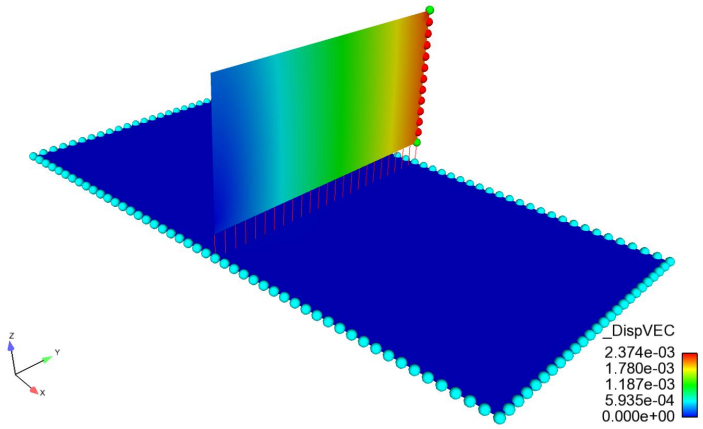

Figure 16-31. – Model and Results of Selective DOF RBE2 Test

For input see Appendix 11.37

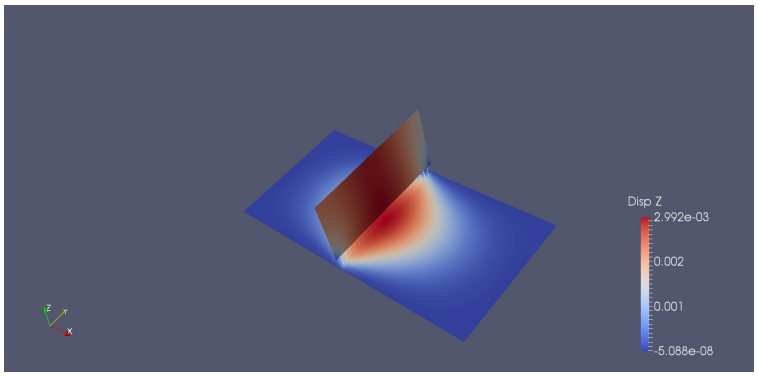

Figure 16-32. – Model and Results of Orthogonally loaded Test

5.17. Thin Plate Bending

The model, shown in Figure 17-33, is a flat rectangular plate of dimension 48×24×0.5. The normal is in the Z coordinate direction. A uniform pressure is applied to the plate. Analytic expressions for the maximum displacement are found in Roark for the thin plate approximation, to which this should apply. The edges are clamped (no rotations for translations).

Table 17-24 compares the solutions from various methods and elements for this example.

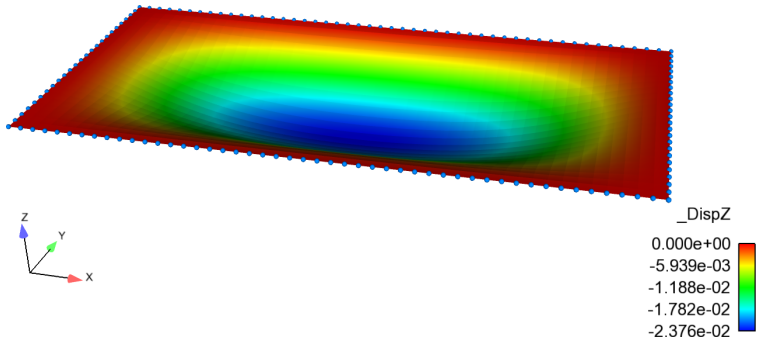

Figure 17-33. – Thin Plate Bending. Geometry and Deformation

Roark	NASTRAN	%error	NQuad	%error	QuadT	%error
0.02451	0.02459	-0.33	0.02376	3.05	0.024497	0.05

Table 17-24. – Thin Plate Bending Center Point Solutions

For input see Appendix 11.38

5.18. Perfectly Matched Layers: Offset Sphere

In this section, we describe the verification of the offset sphere problem for the Ellipsoidal PML formulation. Further background, verification, results, and implications are available in [12]. An acoustic source is placed asymmetrically in a spherical domain.

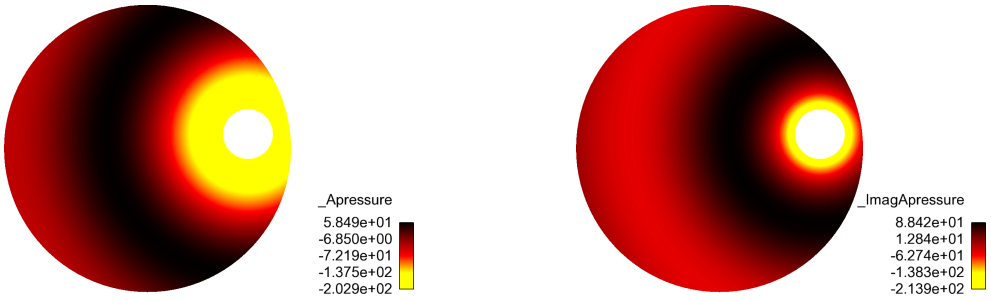

Figure 18-34. – Solution for Offset Sphere (50 Hz)

Figure 18-34 shows the numerical solution for the offset sphere problem. The radius of the outer sphere is 5 meters, and the radius of the inner sphere is 1 meter. An acoustic velocity of $V_0 = 1$ is applied to the normal surface of the inner sphere, to create a monopole excitation. The sphere is composed of 850,000 TET4 elements, and 145,000 nodes. The material modeled is air, where $\rho = 1.293 \frac{\text{kg}}{\text{m}^3}$, $c_0 = 332.0 \frac{m}{s}$.

A 2D representation of the spherical result cut along the plane y=0 is shown. Note that the solution is spherically symmetric about the acoustic source. The exact solution is given as

$$P(r) = \frac{iV_0\Omega\rho a^2}{r(1+ika)} e^{ik(r-a)} \tag{5.18.1}$$

where r is the distance from the center of the inner sphere to a point in the mesh, and a is the radius of the inner sphere.

The relationship between the thickness of the PML boundary, the discretization of the elements within the PML boundary, and the selection of loss parameters is investigated on the Offset Sphere example. The discrete L^2 error norm of the solution at every degree of freedom is compared between the PML formulations, the absorbing boundary conditions, and infinite elements of various orders. We also examine the performance of the iterative solver on these problems, and compare the effects of PML and infinite elements on linear solver performance.

Figure 18-35 shows the results for the offset sphere at a frequency of 50Hz. For this case, the outgoing waves are not perpendicular to the boundary surface, and the spherical wave absorbing boundary condition gives very inaccurate results. The infinite element solution has converged around order 4, and the remaining error compared to the analytic solution corresponds to the discretization error for the mesh. Both the ellipsoidal and spherical PML formulations converge to the discretization error of the mesh. The PML layer

converged with 12 layers of elements, a loss parameter of 600, and a thickness of 2 meters. Figure 18-36 shows the magnitude of acoustic pressure in the PML layer of the offset sphere, showing the rapid decay to zero magnitude towards the outer-most boundary of the PML layer. Note that the ellipsoidal PML formulation is the only supported or accessible formulation in SierraSD.

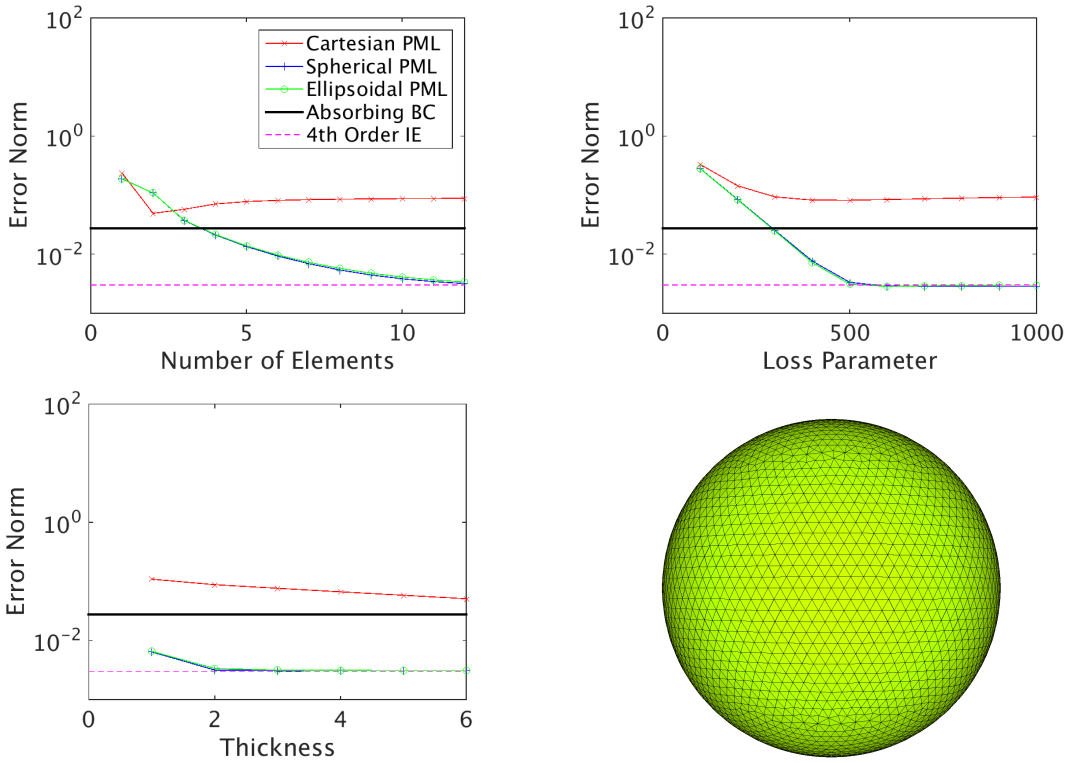

Figure 18-35. – Parameter Studies for OffsetSphere (50 Hz). Note: Ellipsoidal PML is the only supported capability, Cartesian and Spherical have been removed.

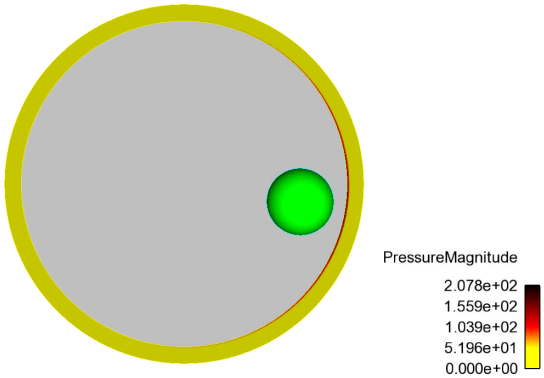

Figure 18-36. – Acoustic Pressure in PML Layer for offset sphere, showing the rapid decay to zero magnitude near the outermost boundary of the PML layer.

For input deck see Appendix 11.10.

5.19. Thermally Induced Elastic Waves: Hollow Sphere

This test compares thermally induced elastic vibrations in a hollow sphere with an analytic solution from the 1965 paper *Thermal Stress-Wave Propagation in Hollow Elastic Spheres* by Tsui and Kraus. The inner surface is heated suddenly while the outer surface is held at the initial temperature, causing an elastic wave to propagate from the inner surface to the outer surface. It should be noted that the properties chosen are implausible for real materials: the elastic wave speed is unphysically low, and the thermal diffusivity is unphysically high. Thus, the time required for the temperature to reach equilibrium is on the order of the time required for the elastic wave to travel to the outer surface. This results in a more challenging dynamic test because the quasi-static approximation is not valid.

Table 19-25. – Parameter Definitions in Tsui and Kraus

a	sphere inner radius
b	sphere outer radius
μ	shear modulus
ν	Poisson ratio
β	density
α	coefficient of thermal expansion
κ	thermal diffusivity

We begin by describing the solution found in the paper, with key parameter definitions given in table 19-25. The temperature $T(r,t)$ solves the heat equation

$$\frac{\partial T}{\partial t} = \kappa \nabla^2 T \tag{5.19.1}$$

$$T(a,t) = T_a \tag{5.19.2}$$

$$T(b,t) = 0 \tag{5.19.3}$$

$$T(r,0) = 0, \tag{5.19.4}$$

where κ is the thermal diffusivity. The Sierra code Aria is used to compute T, but it solves an energy conservation equation which reduces to the heat equation provided that the specific heat capacity C_p, density β, and thermal conductivity k are related to the thermal diffusivity κ in the heat equation as follows:

$$\kappa = \frac{k}{\beta C_p}. \tag{5.19.5}$$

The change from zero temperature induces a thermal strain $\epsilon_{ii} = \alpha T$, which drives the elastodynamic equations.

Tsui and Kraus introduce a dimensionless "inertia" parameter

$$\gamma = \frac{\kappa}{ca}, \tag{5.19.6}$$

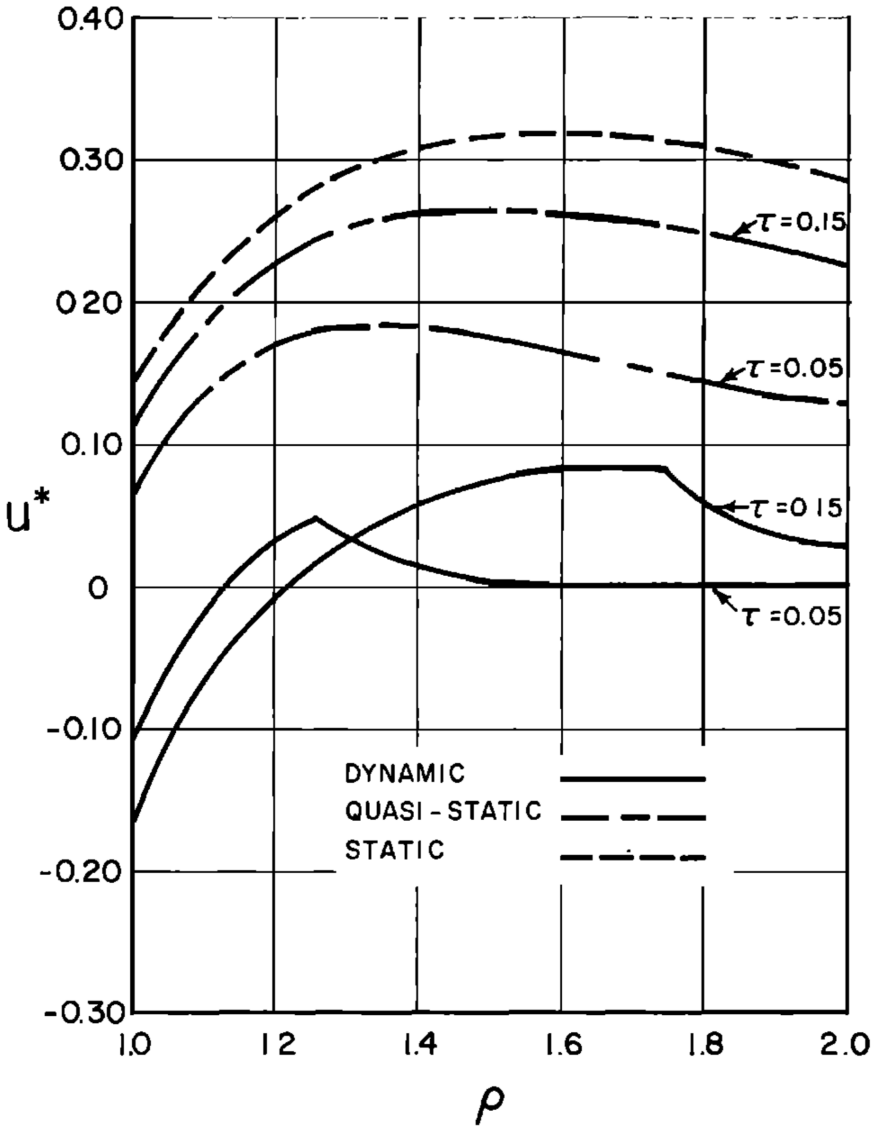

Figure 19-37. – This is figure 1 from Tsui and Kraus. Plotted are the dimensionless radial displacement u^*, which is related to the physical displacement by $u^* = [(1-\nu)/(a\alpha T_a*(1+\nu))]u$ against the dimensionless radius $\rho = r/a$. We are interested in the dynamic case (solid line) at dimensionless times $\tau = 0.05, 0.15$, where $\tau = \kappa t/a^2$.

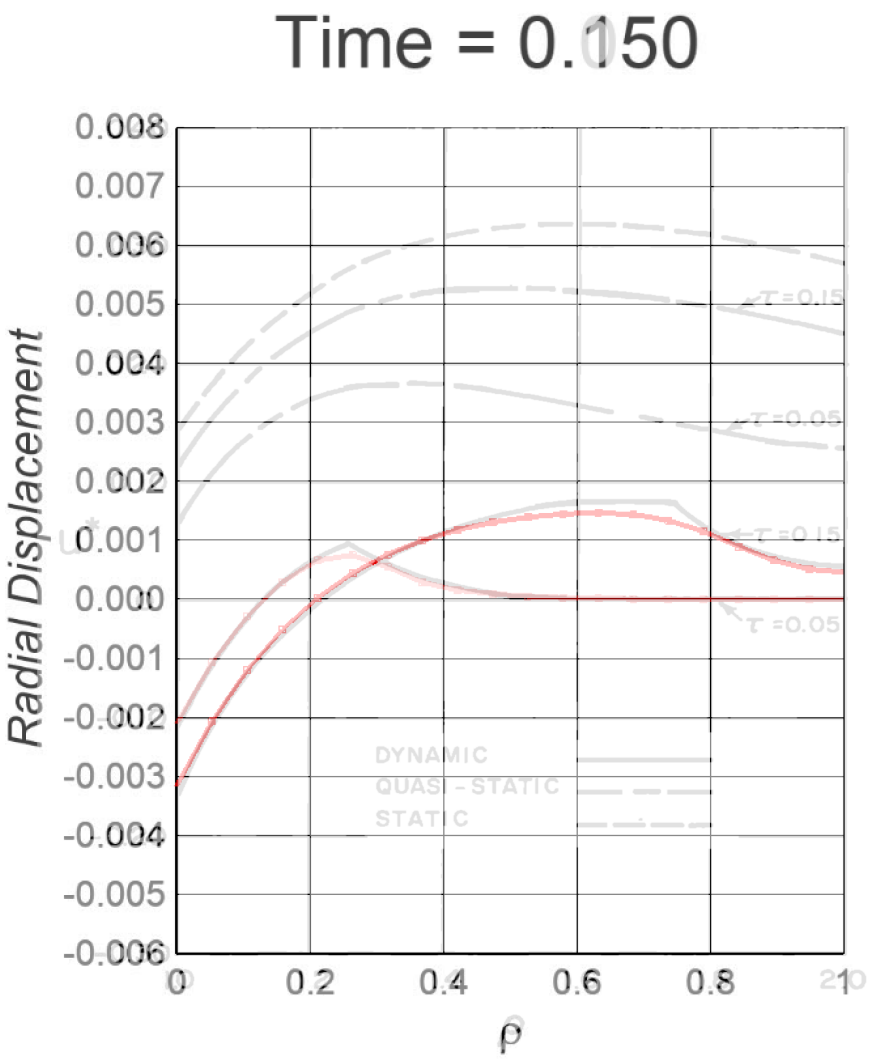

Figure 19-38. – Overlay of Sierra SD results on figure 19-37.

where the propagation speed of elastic pressure waves is given by

$$c = \sqrt{\frac{2(1-\nu)\mu}{\beta(1-2\nu)}}. \tag{5.19.7}$$

In figure 19-37, the analytic solution of Tsui and Kraus is plotted for $\gamma = 1/5$, $b/a = 2$, and $\nu = 1/3$. Note that values of γ are much smaller than this for real materials, e.g., approximately 10^{-8} for steel. We choose $a = 1$, $\kappa = 1$, and $c = 5$ so that $\gamma = 1/5$ as in the paper. We set $c = 5$ by choosing $\mu = 25/4$, and $\beta = 1$. The temperature parameters are chosen with $\alpha = 10^{-2}$, and $T_a = 1$. These choices imply (see the definitions in the caption of figure 19-37) that $\rho = r$, $\tau = t$, and $u^* = 50u$.

Results using Sierra SD are shown in figure 19-38. We do not make a direct numerical comparison for two reasons: the analytical formula in Tsui and Kraus is based on series

solutions, and is very challenging to evaluate. Furthermore, they provide no table of the values computed using the analytic solution, so the best that we can do is scale the graphs by hand to line up the axes. Agreement is excellent, except for the kink at the propagating wavefront, which could presumably be better resolved with a finer mesh or finer initial timesteps.

For input deck see Appendix 11.11

6. SOLUTIONS IN ROTATING COORDINATE FRAMES

Sierra/SD supports solutions in a rotating coordinate frame. Tests in this section address this verification.

6.1. Rotating Dumbbell Statics

6.1.1. Model Description and Purpose

The model consists of a symmetric bar 6 units long with equal masses on either end. The bar is stationary in a rotating coordinate frame. To avoid singularities, the center point of the bar is clamped. The bar is massless. See Figure 1-1.

The test evaluates a very simple geometric problem, and insures that centrifugal forces are correctly applied to concentrated masses. It insures that rotations will work properly about the default coordinate axis.

Figure 1-1. – Dumbbell Geometry

Analysis Type	linear statics
Element Type	Hex8
Loading	centrifugal
Keyword	centrifugal force

6.1.2. Analytic Results

Each mass on either end of the rotating bar should experience only centrifugal boundary conditions. The left hand side includes the centrifugal softening matrix (but no geometric stiffening). The magnitude of the loading is,

$$F_{axial} = \Omega \times (\Omega \times \vec{r}) \, \Delta M$$

where,

Ω = 1.1 in the Z direction.

$\vec{r}$ is 3.0, radial direction.

ΔM is 2.0

The resulting force is 7.26 units in the radial direction. It is applied only at the end nodes where the concentrated masses are located, as the other points are massless. For input deck see Appendix 11.54.

6.2. Rotating Beam Statics

Consider a beam of length L with constant cross-sectional area A, elastic modulus E, and mass density ρ. The root of the beam is at $x = 0$ and its tip at $x = L$. The axis of rotation passes through the origin and is in the z-direction. Further, the angular velocity is constant and denoted by Ω.

With the assumption of all mass being concentrated along the axis of the beam, the net force in the x-direction at radial position r is given by

$$\begin{aligned} F &= \Omega^2 \int_r^L x \, dm \\ &= \Omega^2 \int_r^L x \rho A \, dx \\ &= \rho A \Omega^2 (L^2 - r^2)/2. \end{aligned} \tag{6.2.1}$$

Thus, the axial stress at r is

$$\sigma(r) = F/A = \rho \Omega^2 (L^2 - r^2)/2. \tag{6.2.2}$$

The axial strain is assumed constant across each cross section and given by

$$\epsilon(r) = \sigma(r)/E = \rho \Omega^2 (L^2 - r^2)/(2E). \tag{6.2.3}$$

The axial displacement is obtained by integrating the axial strain. Since the axial displacement vanishes at $x = 0$, we obtain

$$\begin{aligned} u(r) &= \int_0^r \epsilon(x) \, dx \\ &= \rho \Omega^2/(2E) \int_0^r (L^2 - x^2) \, dx \\ &= \rho \Omega^2/(2E)(L^2 x - x^3/3)|_0^r \\ &= \frac{\rho \Omega^2 L^3}{6E} [3(r/L) - (r/L)^3]. \end{aligned} \tag{6.2.4}$$

For input deck see Appendix 11.55.

6.3. Rotating Shell Statics

The rotating shell example is similar to the rotating beam 6.2 with $E = 19.5 \times 10^{10}$, $L = 10$, $\rho = 7700$, $A = 1$, and $\Omega = 5$. Three different finite element meshes of the beam were constructed. The first one is a `HEX8` mesh with 50 elements in the x-direction and 5 elements in both the y and z-directions (the dimensions of the beam in the three coordinate directions are 10, 1, and 1). The second one is a quadrilateral shell mesh with 50 elements in the x-direction and 5 elements in the y-directions. The third one is a mesh of beams with 50 elements in the x-direction. Comparisons of axial deformations for three finite element analyses are shown in Figures 3-2 and 3-3. Notice that all three finite element results are close to the exact solution, with the `QUADT` results being the least accurate. We note that much more accurate results were obtained when the `QUADT` elements were replaced by `NQUAD` elements. We think that the less accurate predictions for the mesh of `QUADT` elements is caused by anisotropies introduced by representing each quadrilateral element as the union of two triangular elements.

For input deck see Appendix 11.56.

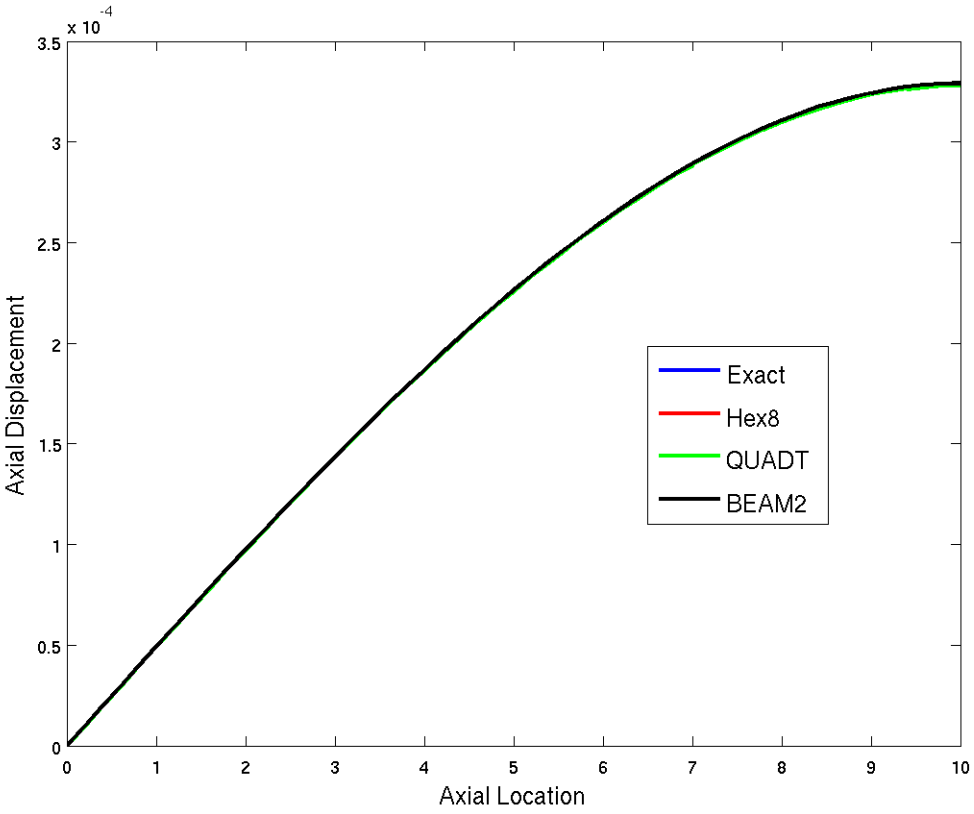

Figure 3-2. – Comparisons of axial deformations with exact solution for a beam.

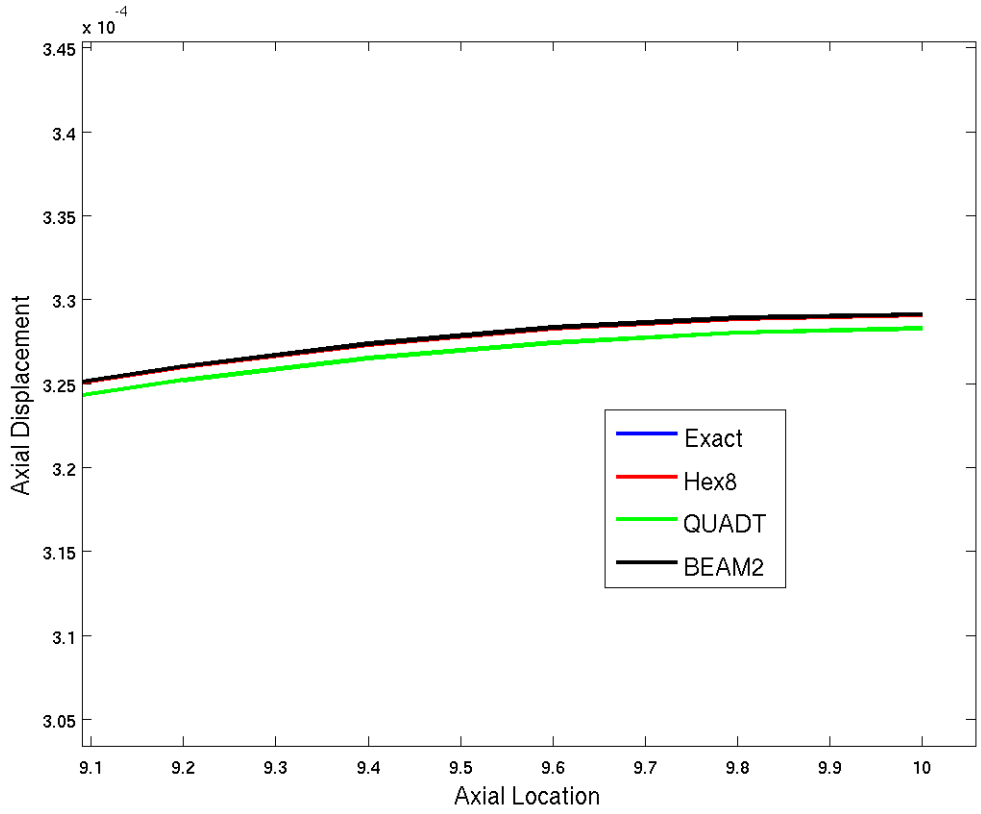

Figure 3-3. – Zoomed in view of Figure 3-2 showing differences for QUADT elements.

6.4. Rotating Ring Statics

6.4.1. Introduction and Purpose

This test examines a simple ring in a rotating frame. Verification of the *forces* is made here. We intentionally do *not* verify displacements as these depend on the element formulation.

The ring, shown in Figure 4-4 is a two unit radius thin structure. A constant angular velocity, $\vec{\Omega}$, is applied at 1.1 radians per second in the Z direction. The ring is not centered on the origin, but is centered on a user defined coordinate system.

6.4.1.1. Analytical Results

The resulting forces are given by,

$$\vec{F} = \int \rho \vec{\Omega} \times \vec{\Omega} \times \vec{r} dV \tag{6.4.1}$$

$$= 1.1^2 2.0 \left(\rho V_n\right) \hat{r} \tag{6.4.2}$$

Where ρV_n represents the mass associated with a node. For this model, there are 148 nodes on the ring which each share equally the total ring mass of 12.5626 units. The resulting force is 0.2054 units outward.

For the Euler force,

$$\vec{F} = \int \rho \frac{d}{dt} \vec{\Omega} \times \vec{r} dV \tag{6.4.3}$$

$$= 1.12.0 \left(\rho V_n\right) \hat{r} \tag{6.4.4}$$

and the resulting force is 0.2054/1.1 units outward.

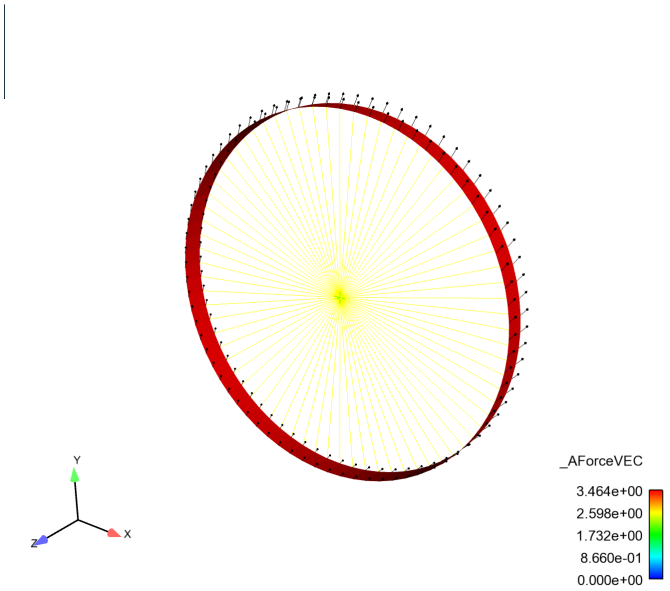

Figure 4-4. – Rotating Ring Geometry and Results

6.4.2. What is tested

The test evaluates the following:

- The centrifugal force in a rotating system.
- The force on shells with rotational degrees of freedom. The moment should be zero.
- A coordinate translation.

It does *not* test,

- Coordinate rotation.
- Solid or point mass elements.
- Solution when there is no symmetry.

For input deck see Appendix 11.57.

6.5. Rotating Ring Acceleration

This is a variation on the static analyses of a rotating ring described in section 6.4. Here an angular acceleration is applied instead of the angular velocity in 6.4. By hand, the angular acceleration is .2054/1.1 force units. For input deck see Appendix 11.58.

6.6. Rotating Superelement Statics

Models (including superelements) must be loaded by centrifugal forces if they are to be analyzed in a rotating coordinate frame. However, as discussed in the analysis section, there are inherent problems in loading a superelement with a centrifugal force. In this test, we examine one case where the loading is exact.

The model is a single hex element which is rotated about an edge. The unreduced model force may be computed as,

$$F_{centrifugal} = \vec{\Omega} \times (\vec{\Omega} \times \vec{r}) \quad (6.6.1)$$

$$= [\Omega]^T [M][\Omega][r] \quad (6.6.2)$$

where $\vec{\Omega}$ is the angular velocity vector, $[\Omega]$ is a rotation matrix, $[M]$ is the mass matrix and $[r]$ represents the position coordinates. This solution is as accurate as possible for a finite element representation of the continuous model. See details in the theory manual.

The geometry is shown in Figure 6-5.

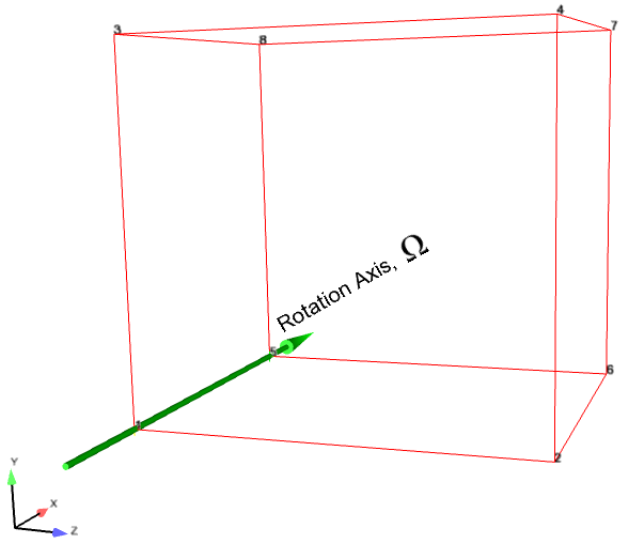

Figure 6-5. – Rotating Hex Geometry

6.6.1. Tests

We evaluate several steps of the test.

1. We look at the loading of a single hex in rotation. This is our truth model.
2. We insure that the model reduction process is consistent.

3. We examine the loading of a superelement equivalent to the single hex element.

Each of these tests is described in a little more detail in what follows.

Single Hex Rotation

Equation 6.6.2 describes the load calculation for a single hex in a coordinate frame rotating at a constant angular velocity. The results of the loading have been examined visually for reasonable response, but no strict verification of these results are available. The loading vectors are not entirely radial (as expected).

The analysis is singular, i.e. the body has a zero energy mode and is free to rotate about the axis of rotation. Because of this, only the forces are evaluated - comparison of displacements could result in errors from inaccurate solution of the singular system. The force response is shown in Figure 6-6.

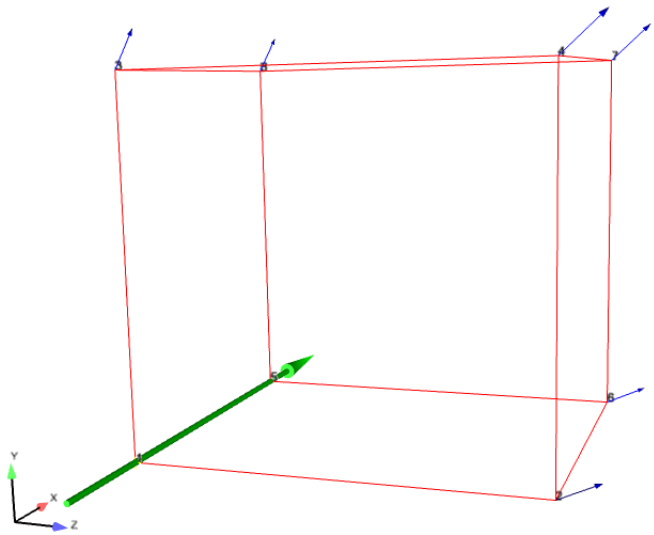

Figure 6-6. – Rotating Hex Response

6.6.1.1. Superelement Reduction

A critical part of this evaluation is "reduction" of the hex to a superelement. In most such reductions, a combination of interior "fixed interface" modes are combined with interface or "constraint" modes to generate a reduced basis. Here we have no interior modes and all the interface nodes are retained. One of those nodes has only 2 degrees of freedom, so there is a slight reduction. As a consequence, the superelement model is of dimension 23, while the original hex has 24 degrees of freedom. The most important point is that the superelement

model may now be run through the software, which follows an entirely different path from the original.

6.6.1.2. Loading of a Superelement

In the final stage, the superelement is inserted into a new model. In this case, we re-use the original mesh. However, the block definitions are those of a superelement. The superelement is loaded using the centrifugal force routines. The result *must* be identical to the original test.

6.6.2. Analysis

Superelements are problematic for computation of internal integrals. Typically, all the internal shape functions and data are available *only* during the superelement reduction stage. During subsequent analyses, only the interface information and reduced order matrices are retained.

For computation of the centrifugal force, an integral must be evaluated over the volume of the element.

$$\vec{f} = \rho \int_{element} \vec{\Omega} \times (\vec{\Omega} \times \vec{r})\, dV$$

When the full shape functions are available, this can be evaluated as a discretized linear algebra system (equation 6.6.2). However, the model reduction process condenses out information from the interior of the superelement to the nodes of the interface. The total mass is conserved, but information required to compute the interior integrals is no longer available. This verification test is structured so that no internal information is lost and the integrals may be computed exactly.

This set of tests insures the following:

- The software can successfully exercise a superelement.
- Identical results are obtained to the original hex, indicating no transposing of degrees of freedom.
- All of the nodes on the interface are being exercised.
- Superelements are supported with other than 3 dofs on a node. Node 1 has 2 degrees of freedom, and there are 23 degrees of freedom total.

However, because of the details of the test, we do not evaluate the following:

- Superelements with internal degrees of freedom.
- Superelements with a reduced set of interface nodes.

For input deck see Appendix 11.59.

6.7. Rotating Superelement Beam Statics

We build on the analysis of a rotating hex beam. As shown in the hex beam example, the analytic solution can be written,

$$\begin{aligned} u(r) &= \int_0^r \epsilon(x)\,dx \\ &= \rho\Omega^2/(2E)\int_0^r (L^2 - x^2)\,dx \\ &= \rho\Omega^2/(2E)(L^2x - x^3/3)|_0^r \\ &= \frac{\rho\Omega^2 L^3}{6E}[3(r/L) - (r/L)^3]. \end{aligned} \tag{6.7.1}$$

We next consider an example with $E = 19.5 \times 10^{10}$, $L = 10$, $\rho = 7700$, $A = 1$, and $\Omega = 5$. A superelement is generated by extracting all the nodes down the center of the beam. There are 101 nodes retained in the superelement, with 40 generalized degrees of freedom associated with fixed interface modes. Comparison of axial deformations for the finite element analysis is shown in Figure 7-7. Finite element results are close to the exact solution, but there differences because the superelement integration is not fully accurate for computation of centrifugal force moments.

For input deck see Appendix 11.60.

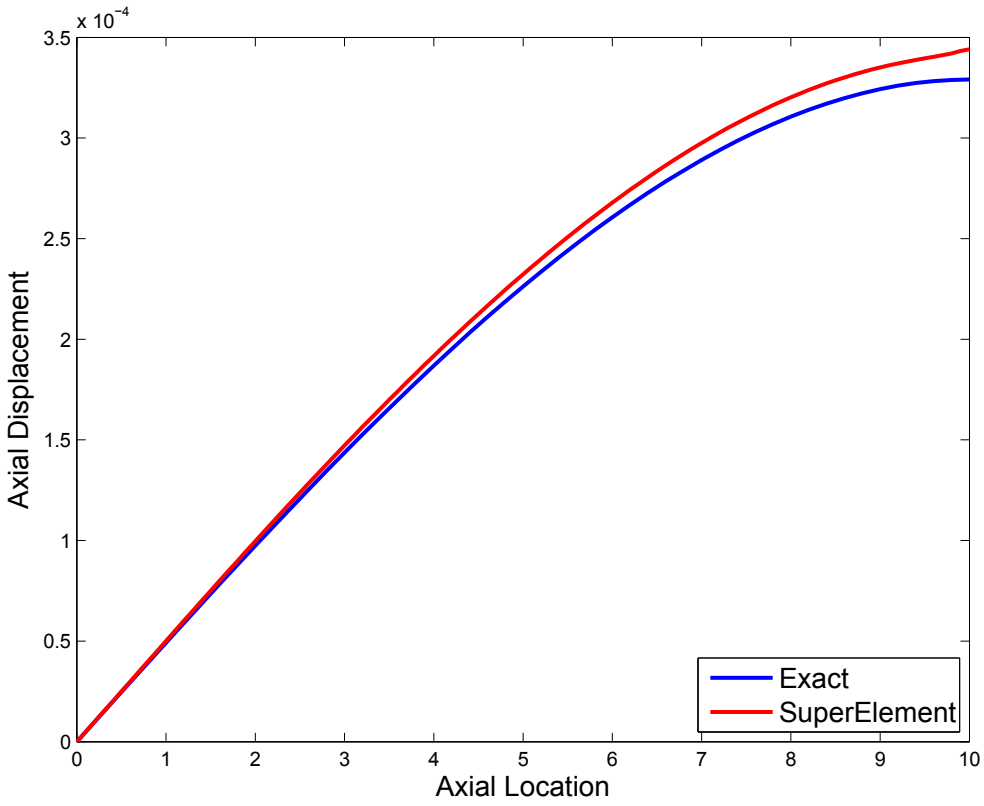

Figure 7-7. – Comparisons of axial deformations with exact solution for a beam.

6.8. Point Mass in a Rotating Frame

It is useful to verify a simple point mass in a rotating frame. We consider a system rotating at a constant angular velocity $\vec{\Omega} = \Omega\hat{k}$. The angular acceleration is zero. A single point mass, m, is observed in the rotating frame. The point mass is frictionless. The geometry is illustrated in Figure 8-8.

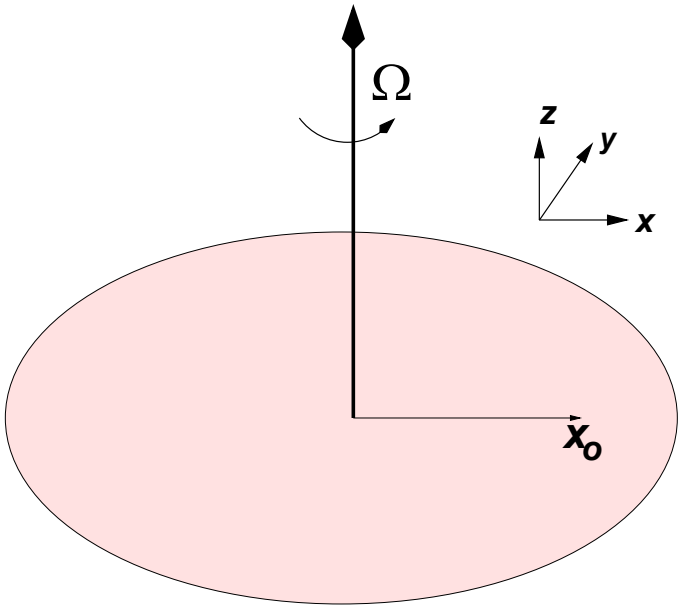

Figure 8-8. – Rotating Frame Geometry

6.8.1. Mass at Rest in Inertial Frame

This is by far, the simplest case. In the inertial frame we have a mass located at $(x_o, 0)$. It does not move. In the rotating frame, $r = x_o$ and $\theta' = -\Omega t$', or in the Cartesian rotating frame,

$$x' = x_o \cos(-\Omega t) \tag{6.8.1}$$
$$y' = x_o \sin(-\Omega t) \tag{6.8.2}$$

6.8.2. Mass Initially at Rest in Rotating Frame

We consider a mass initially at the point $(x_o, 0)$ with an initial velocity of $\vec{v} = \Omega x_o \hat{e}_y$. In the rotating frame this mass appears initially at rest at location $(x'_o, 0)$. However, because of the rotation of the frame, the mass will begin to move away from the center of the rotating frame.

6.8.2.1. Without Coriolis Contribution

In the rotating frame, the only force acting on the body is the centrifugal force, $\vec{\Omega} \times (\vec{\Omega} \times \vec{r})$. As all the forces are in the radial direction, the differential equation reduces to a single degree of freedom system.

$$m\ddot{r} = \Omega^2 r$$

This equation is very similar to that of a harmonic oscillator. With the given initial conditions the solution is,

$$r = x_o cosh(\Omega t)$$

where $cosh()$ is the hyperbolic cosine.

This solution is not physical, as there is no Coriolis force. At time progresses, the velocity continues to grow unbounded, but the angular position remains zero.

6.8.2.2. With Coriolis Contribution

We solve this by computing the solution in the inertial coordinate system, and transforming back to the rotating frame.

In the inertial frame, there are no forces acting on the body. The solution in Cartesian frame is,

$$\begin{aligned} x &= x_o && (6.8.3)\\ y &= v_o t && (6.8.4)\\ &= x_o \Omega t && (6.8.5) \end{aligned}$$

This may be transformed to polar coordinates, still in the inertial frame.

$$\begin{aligned} r &= \sqrt{x^2 + y^2} && (6.8.6)\\ &= x_o \sqrt{1 + (\Omega t)^2} && (6.8.7)\\ \theta &= \tan^{-1}(y/x) && (6.8.8)\\ &= \tan^{-1}(\Omega t) && (6.8.9) \end{aligned}$$

We use the relation that $\theta' = \theta - \Omega t$ and $r' = r$. Then,

$$\theta' = \tan^{-1}(\Omega t) - \Omega t$$

This solution may then be transformed to rotating cartesian frame in the usual way.

Small Angle Approximations

For solutions with $\Omega t << 1$ the solutions in this section may be compared with the previous section. We use,

$$\tan^{-1}(\theta) \approx \theta - \frac{\theta^3}{3} + \frac{\theta^5}{5} + ... \tag{6.8.10}$$

$$\sqrt{1+\epsilon^2} \approx 1 + \frac{\epsilon^2}{2} \tag{6.8.11}$$

$$\tag{6.8.12}$$

For both solutions,

$$r' \approx x_o \left(1 + \frac{(\Omega t)^2}{2}\right),$$

while $\theta' = 0$ with no Coriolis term. Including the Coriolis term we obtain,

$$\theta' \approx \frac{-(\Omega t)^3}{3}$$

Figure 8-9 shows the solution to this problem. Both analytic and finite element solutions are shown. A good degree of agreement is obtained even for a very large displacement.

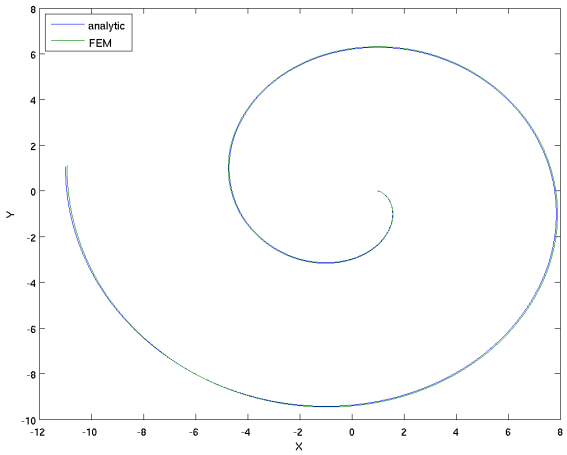

Figure 8-9. – Point Mass initially at rest in rotating frame

6.8.3. Mass Moving in the X axis

This example starts at the same location, i.e. $(x_o, 0)$ in the inertial frame, but the initial velocity in the inertial frame is $-2x_o\Omega/\pi\hat{e}_x$. Thus, at time $\Omega t = \pi/2$, the mass will be at the origin. At time $\Omega t = \pi$, the particle will be located at $(-x_o, 0)$. In the inertial frame,

$$y = 0 \tag{6.8.13}$$

$$x = x_o(1 - 2\Omega t/\pi) \tag{6.8.14}$$

or,

$$r = x_o(1-2\Omega t/\pi) \tag{6.8.15}$$
$$\theta = 0 \tag{6.8.16}$$

In the rotating frame, $r' = r$ and $\theta' = -\Omega t$. The Cartesian description is therefore,

$$x' = x_o(1-2\Omega t/\pi)\cos(\Omega t) \tag{6.8.17}$$
$$y' = x_o(1-2\Omega t/\pi)\sin(\Omega t) \tag{6.8.18}$$

For input deck see Appendix 11.61.

7. INVERSE METHODS

7.1. Force Identification from Structural Acoustic Frequency Responses

The structural-acoustic frequency domain force identification capability is demonstrated using the synthetic response at three frequencies. The geometry of this test is shown in Figure 1-1.

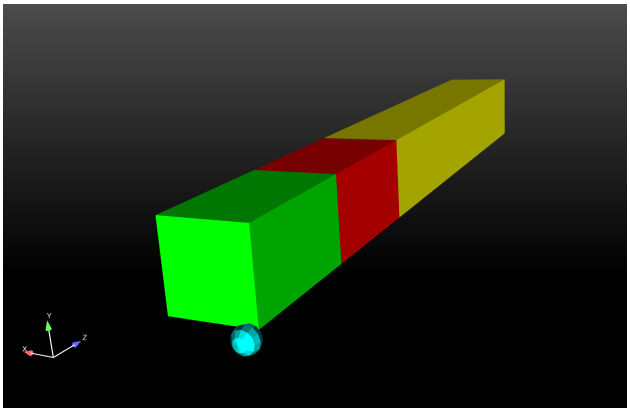

Figure 1-1. – Force Inversion Test Geometry

The model contained three regions, as shown in Figure 1-1: two steel regions, represented by the red and green blocks, and a region of air, represented by the yellow block. Tied constraints were assigned at the steel-steel and steel-air interfaces to connect these regions. A concentrated mass, represented in cyan, was placed at one end of the model and was connected with a spring connection. Acoustic loading was applied to one side of the air region, shown in blue in Figure 1-2. The frequency of the acoustic loading was varied between 10 Hz, 20 Hz, and 30 Hz.

Synthetic input data was generated by performing a forward problem on the coupled air-steel model using known acoustic velocity amplitudes for two loading functions, F_1 and F_2. Displacement values were determined for a node set on the end of the green steel block, while acoustic pressure values were determined for a node set on the side of the air region. The data was then used in the inverse problem to verify that the code could recover the original acoustic velocity inputs for the two acoustic loading functions. The test, which used a full Newton algorithm with analytic Hessians, was analyzed by comparing the obtained acoustic velocity amplitudes to the expected values. Table 1-1 compares the expected acoustic velocity values to values obtained through the inverse problem (Exp/Obt).

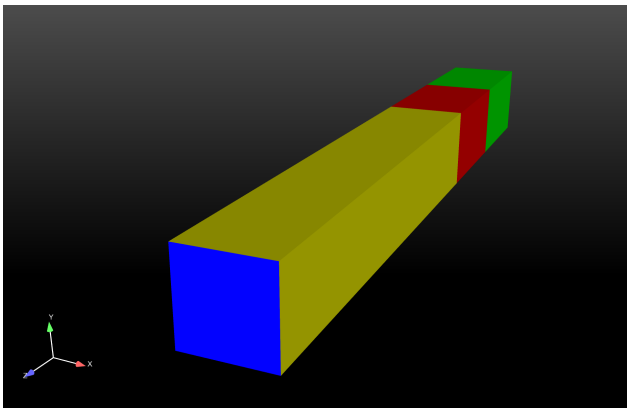

Figure 1-2. – Side of model with applied acoustic loading represented in blue

Table 1-1. – Acoustic Velocity Values

Frequency (Hz)	F_1 (*Exp/Obt*)	F_2 (*Exp/Obt*)
10	4.0/4.0	5.0/5.0
20	4.0/4.0	5.0/5.0
30	4.0/4.0	5.0/5.0

At each frequency tested, acoustic velocity values obtained in the inverse problem matched expected values of 4.00 and 5.00 for forcing functions F_1 and F_2, respectively. The test was performed both in serial and parallel. For each run, the ROL optimization performed three iterations, providing appreciable convergence for the objective function and gradient.
Figure 1-3 shows the convergence behavior of the objective function and gradient values for the serial run; optimization results for the parallel run matched the serial run results.

For input deck see Appendix 11.62.

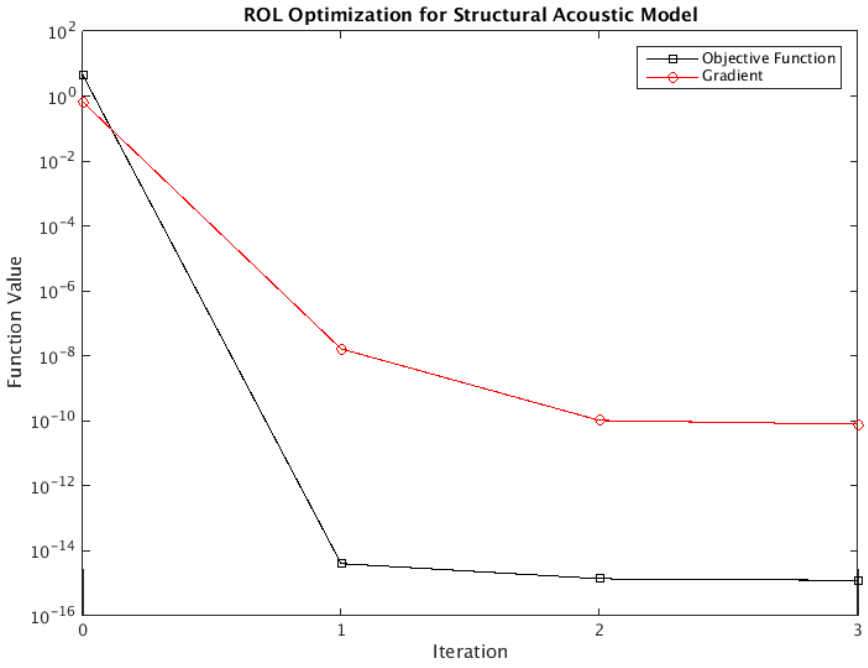

Figure 1-3. – ROL Optimization of Objective Function and Gradient

7.2. Force Identification from Frequency Responses

The frequency domain force identification capability is demonstrated using the synthetic response and three frequencies. The cubic geometry of this test is shown in Figure 2-4.

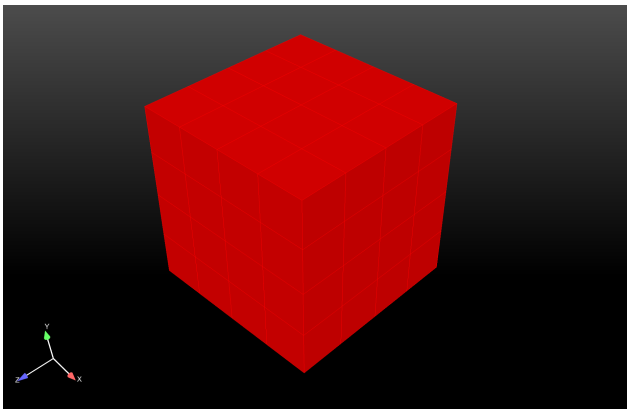

Figure 2-4. – Force Inversion Test Geometry

One boundary condition constrained the model. An absorbing boundary was specified on one side, emulating a non-reflecting condition. Acoustic loading was applied to the opposite side, applied at frequencies of 1, 2, and 3 Hz. Figure 2-5 indicates sides of the model with specified boundary conditions:

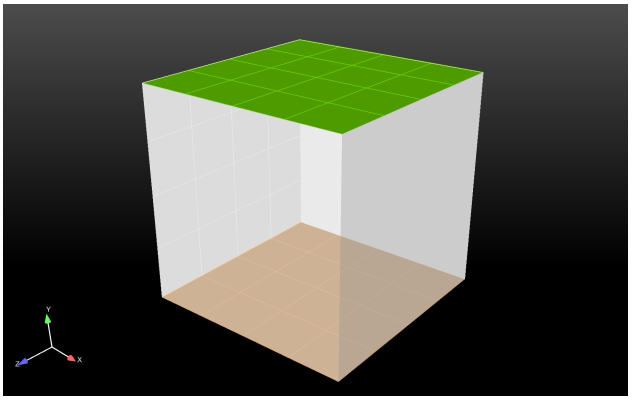

Figure 2-5. – Sides with absorbing boundary side (green) and with acoustic loading (orange)

The model was discretized using 64 Hex-8 elements, arranged in a 4×4×4 cube. Synthetic input data for the inverse problem was generated by running a forward problem with the amplitudes shown in Table 2-2, and was comprised of acoustic pressure values specified at element nodes. This data was then used in the inverse problem to verify that the code could recover the original acoustic velocity inputs. The test, which used a full Newton algorithm with analytic Hessians, was analyzed by comparing obtain acoustic velocity amplitudes of three loading functions–F_1, F_2, and F_3– to the expected values. The expected values and obtained results (*Exp/Obt*) for the acoustic loading functions are shown in Table 2-2.

Table 2-2. – Acoustic Velocity Values

Frequency (Hz)	F_1 (*Exp/Obt*)	F_2 (*Exp/Obt*)	$F_3 1$ (*Exp/Obt*)
1	10.0/10.0	5.0/5.0	1.0/1.0
2	10.0/10.0	5.0/5.0	2.0/2.0
3	10.0/10.0	5.0/5.0	3.0/3.0

Acoustic velocity for loading functions F_1 and F_2 matched the expected values of 10.0 and 5.0, respectively. The acoustic velocity of loading function F_3 demonstrated linear dependence on frequency, also as expected. Optimization using ROL allowed for appreciable convergence of the objective function and gradient; the convergence history of the objective function and gradient, minimized in three iterations, is illustrated in Figure 2-6:

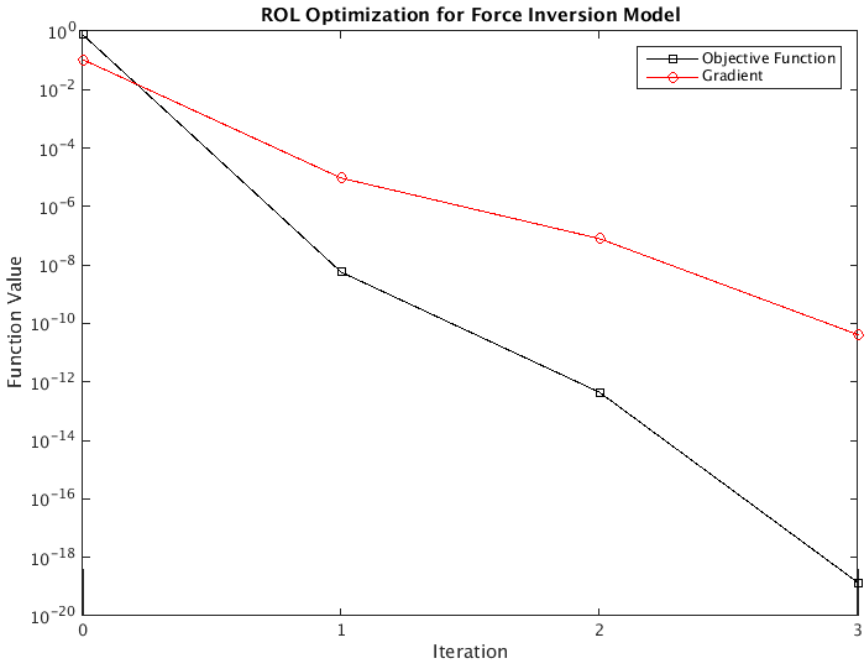

Figure 2-6. – ROL Optimization of Objective Function and Gradient

For input deck see Appendix 11.63.

7.3. Force Identification from Temporal Pressures

The temporal force identification capability is demonstrated using synthetic displacement data generated from a 1 Hertz pressure field. The cubic geometry of this test is shown in Figure 3-7.

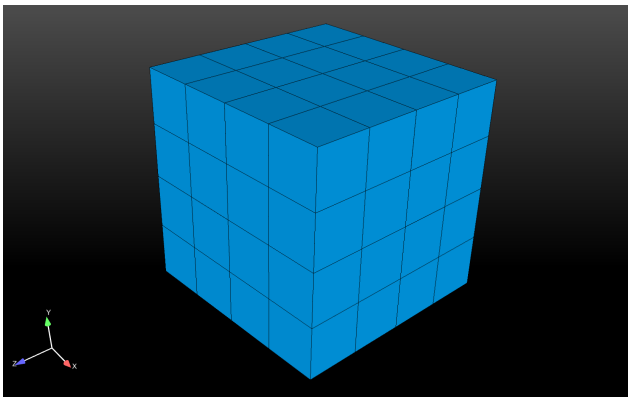

Figure 3-7. – Pressure Inversion Test Geometry

The model consists of 64 Hex-8 elements, arranged in a 4×4×4 cube , and was assigned as a solid material. One boundary condition constrained the model, with one side assigned as a fixed boundary. A distributed pressure load acted normal to the side opposite of the fixed side. Figure 3-8 shows the sides with boundary (yellow) and loading (pink) conditions.

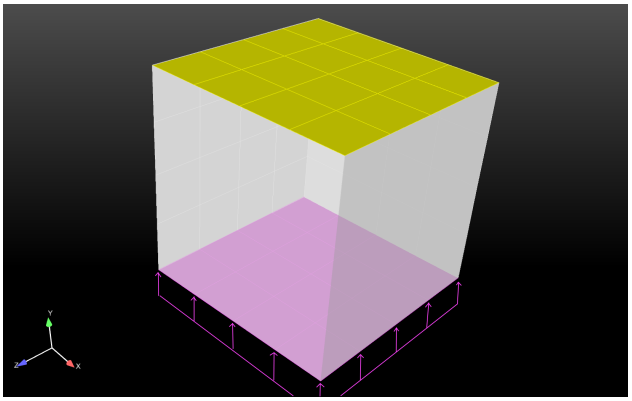

Figure 3-8. – Fixed (yellow) and pressure-loaded (pink) sides in model

Synthetic input data was generated by performing a forward problem on the model, using a periodic distributed pressure load function with a known magnitude of 1 and frequency of 1 Hz. The data generated represented elastic displacements measured at element nodes. The data was used in the inverse problem to verify that the code could recover the original time history of the pressure loading. The test, which used a full Newton method with cubic interpolation linesearch, was analyzed by comparing the obtained pressure loading time-history with the original loading function. Figure 3-9 compares the inverse-problem results with the original function.

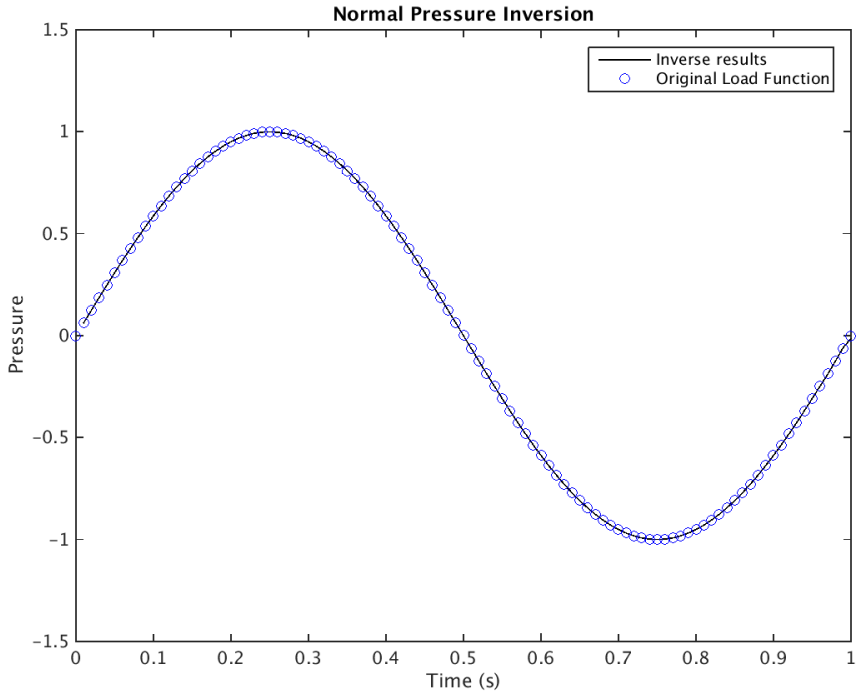

Figure 3-9. – Inverse-problem results for elastic pressure loading time-history

As shown in Figure 3-9, the inverse problem results nearly exactly matched the original forcing function. The optimization method ran through four iterations and achieved significant convergence for the objective function and gradient. The test was conducted in both series and parallel; Figure 3-10 shows the convergence history for the serial run, though parallel results essentially matched the serial results.

For input deck see Appendix 11.64.

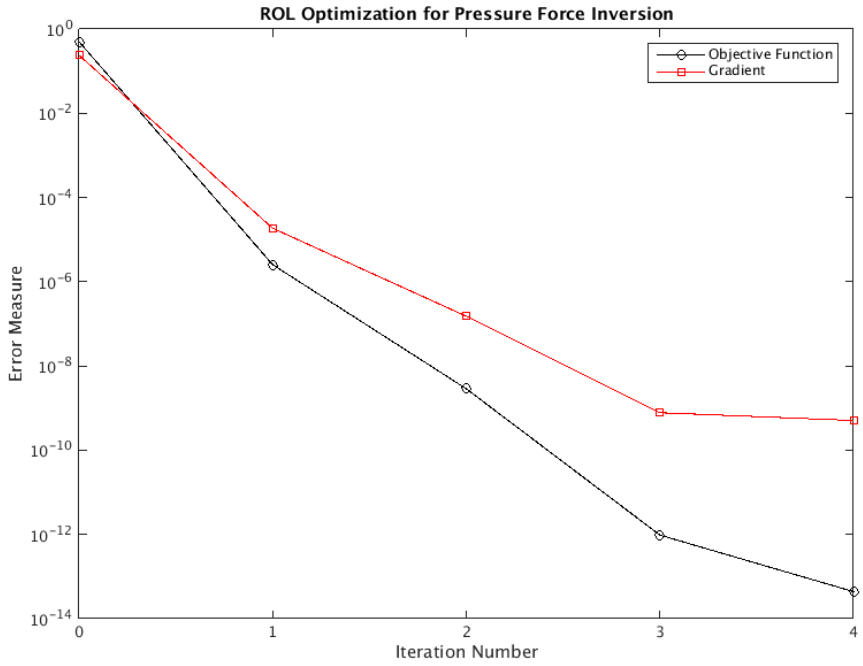

Figure 3-10. – ROL Optimization of Objective Function and Gradient

7.4. Force Identification from Temporal Tractions

The temporal force identification capability is demonstrated using synthetic displacement data generated from a 1 Hertz traction field. The cubic geometry of this test is shown in Figure 4-11.

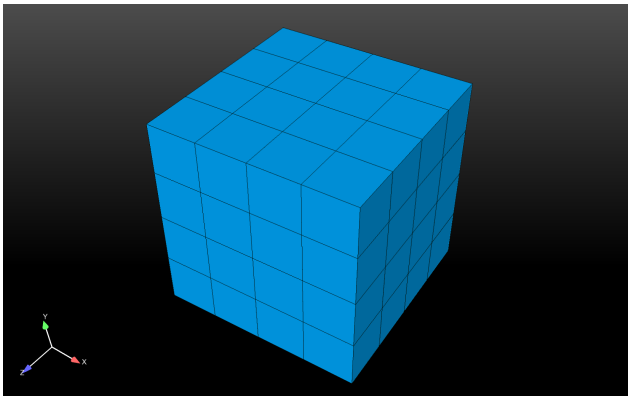

Figure 4-11. – Force Inversion Test Geometry

The model consists of 64 Hex-8 elements, arranged in a 4×4×4 cube , and was assigned as a solid material. The model was constrained by one boundary condition, one side assigned as a fixed boundary. A traction load, including a normal component and two orthogonal shear components, acted on the side opposite of the fixed side and had a direction of $(x = 1, y = 2, z = 3)$. Figure 4-12 shows the sides with boundary (green) and loading (orange) conditions.

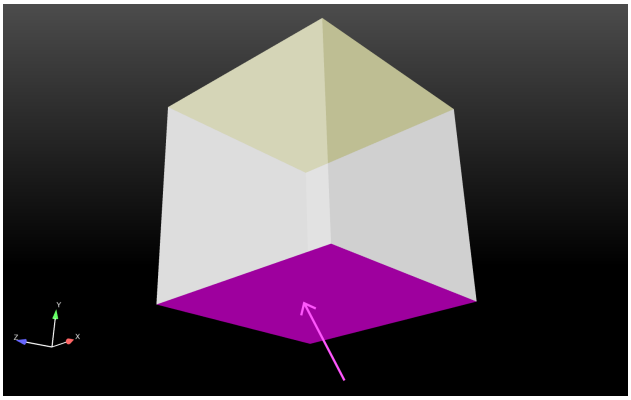

Figure 4-12. – Fixed boundary (yellow) and traction loaded (pink) sides in model

Synthetic input data was generated by performing a forward problem on the model, using a periodic traction load with a known magnitude of 1 and frequency of 1 Hz. The data generated represented displacements measured for element nodes. The data was then used in the inverse problem to verify that the code could recover the original time history of the traction load. The test, which used a full Newton method with analytic Hessians, was analyzed by comparing the obtained traction load time-history with the original loading function. Figure 4-13 compares the inverse-problem results with the original function:

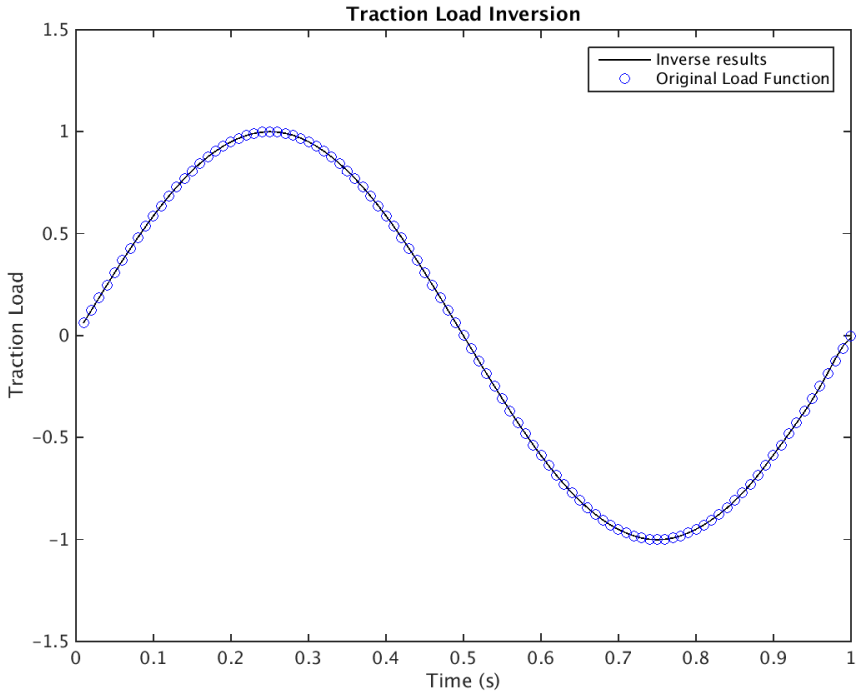

Figure 4-13. – Inverse-problem results for traction loading time-history

As shown in Figure 4-13, the inverse problem results exactly matched the original forcing function. Optimization using ROL provided for significant convergence of the objective function and its gradient. The test was conducted in both series and parallel, each run undergoing three iterations; Figure 4-14 shows the convergence history for the serial run.

For input deck see Appendix 11.65.

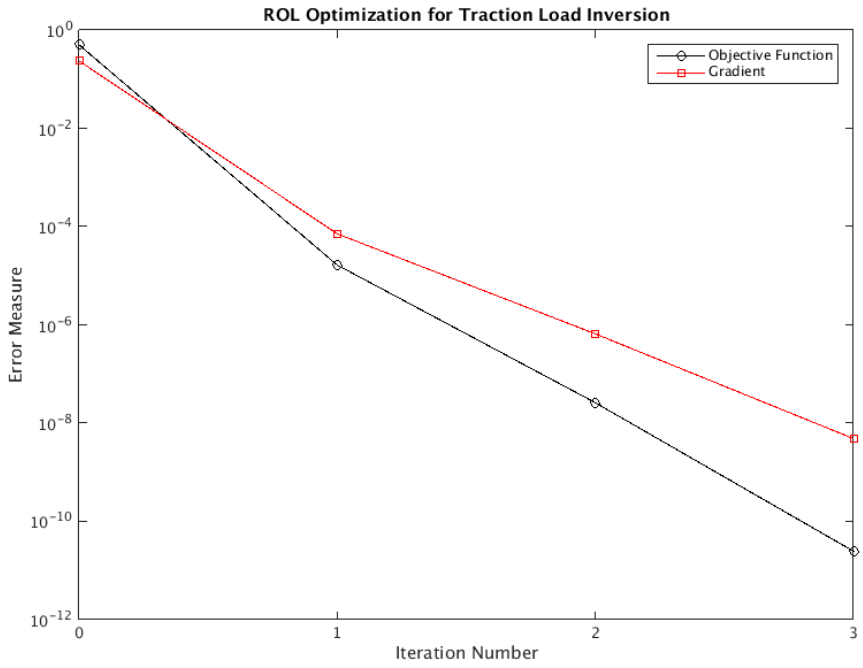

Figure 4-14. – Convergence History for ROL Optimization of Transient Traction Load Inversion

7.5. Force Identification from Temporal Acoustic Pressures

The temporal force identification capability is demonstrated using synthetic displacement data generated from a 1 Hertz acoustic pressure field. The cubic geometry of this test is shown in Figure 5-15.

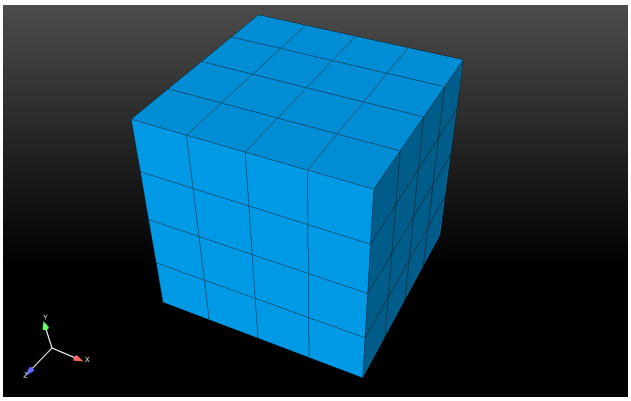

Figure 5-15. – Force Inversion Test Geometry

The model consists of 64 Hex-8 elements, arranged in a 4×4×4 cube, and was specified as air for its material. One boundary condition constrained the model: one side was assigned with an absorbing boundary, creating a non-reflecting condition. Acoustic loading was applied to the opposite side, and consisted of one forcing function. Sides with boundary (green) and loading (orange) conditions are shown in Figure 5-16.

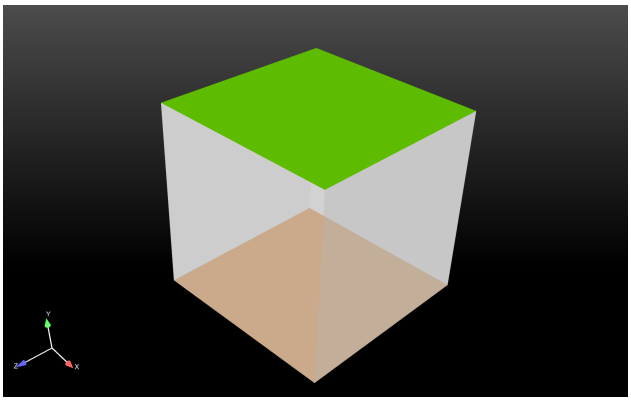

Figure 5-16. – Side of model with applied acoustic loading represented in blue

Synthetic input data was generated by performing a forward problem on the model, using a forcing function with a known amplitude of 1 and frequency of 1 Hz. The data generated represented acoustic pressures measured for element nodes. The data was then used in the inverse problem to verify that the code could recover the original time history of the acoustic loading. The test, which used a full-Newton method with analytic Hessians, was analyzed by comparing the obtained acoustic loading time-history with the original loading function. Figure 5-17 compares the inverse-problem results with the original function:

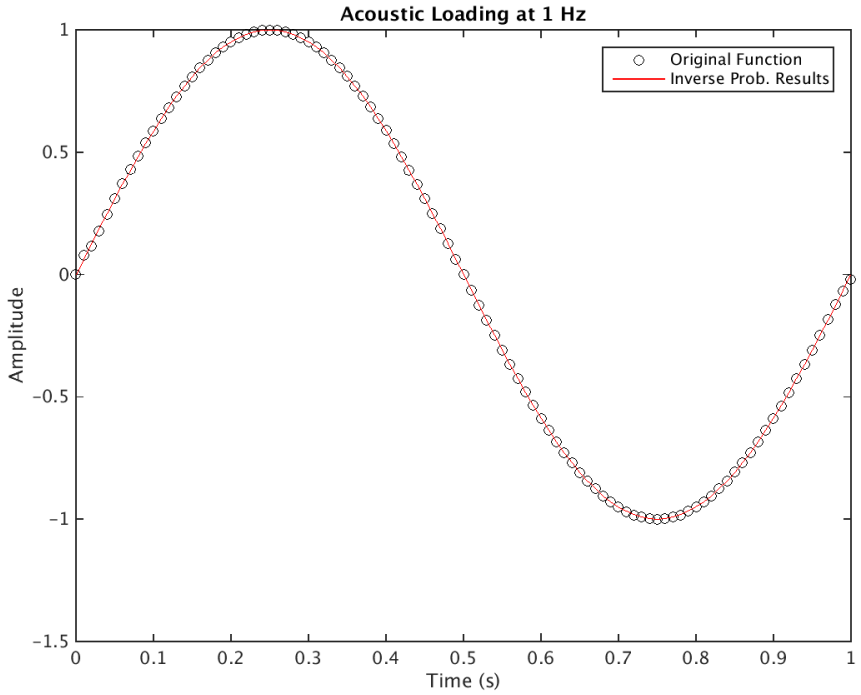

Figure 5-17. – Transient Acoustic Pressure Identification

As shown in Figure 5-17, the inverse problem results exactly matched the original forcing function. The optimization of the objective function and gradient, run in both serial and parallel, performed four iterations and achieved appreciable convergence in both runs. Figure 5-18 shows the convergence history for the serial run.

For input deck see Appendix 11.66.

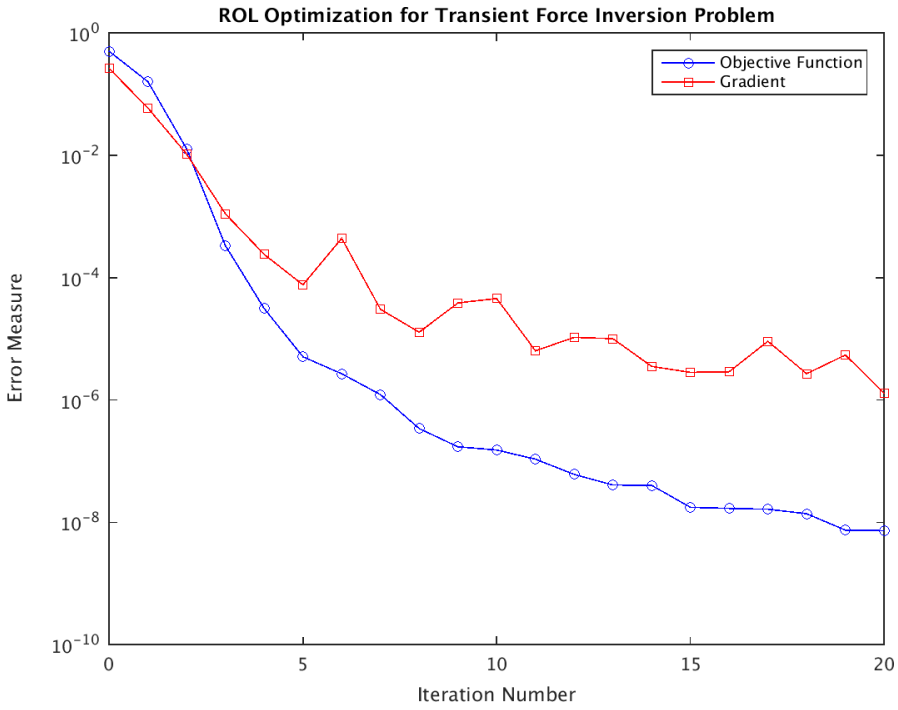

Figure 5-18. – ROL Optimization of Objective Function and Gradient

7.6. Force Identification using Modal Transient

The temporal force identification capability for modal transient is demonstrated using synthetic displacement data generated from a 1 Hertz traction field, using the direct transient forward solution method. The cubic geometry of this test is shown in Figure 6-19.

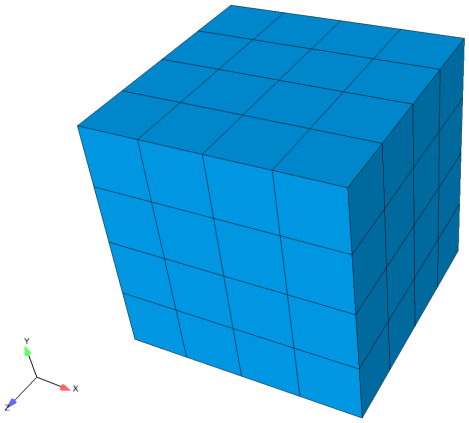

Figure 6-19. – Force Inversion Test Geometry

The model consists of 64 Hex-8 elements, arranged in a 4×4×4 cube , and was assigned as a solid material. The model was constrained by one boundary condition, one side assigned as a fixed boundary. A traction load, including a normal component and two orthogonal shear components, acted on the side opposite of the fixed side and had a direction of $(x = 1, y = 2, z = 3)$. Figure 6-20 shows the sides with boundary (yellow) and loading (pink) conditions.

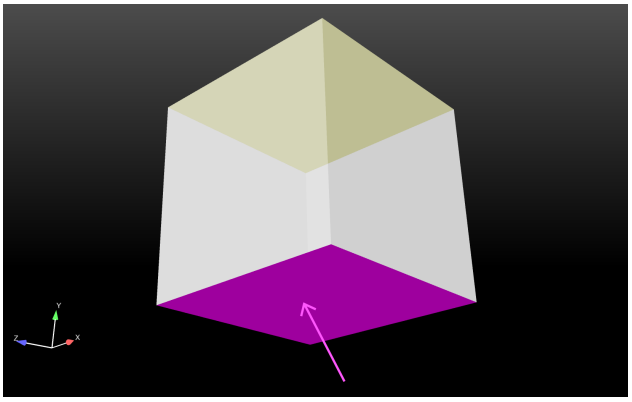

Figure 6-20. – Fixed boundary (yellow) and traction loaded (pink) sides in model

Synthetic input data was generated by performing a forward problem (direct transient) on the model, using a periodic traction load with a known magnitude of 1 and frequency of 1 Hz. The data generated represents displacements measured for element nodes. The data is then used in the modal-transient inverse problem to verify that the code can recover the

original time history of the traction load. The test, which used a full Newton method with analytic Hessians, was analyzed by comparing the obtained traction load time-history with the original loading function. Figure 6-21 compares the inverse-problem results with the original function, with increasing numbers of modes. Note that as the number of modes increase the ability for the modal transient solution to match the direct transient solution increases, and the magnitude of the objective function drops.

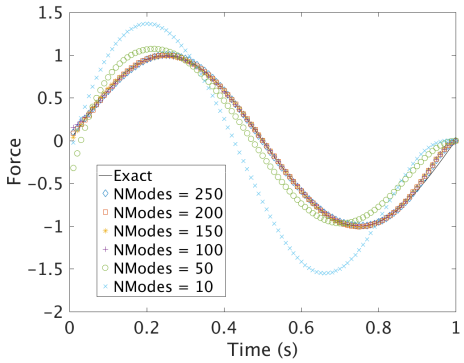

Figure 6-21. – Inverse-problem results for traction loading time-history

Figure 6-22 shows the convergence of the final objective function with increased number of modes. Note that for this case, the objective function does not converge to zero, as not all of the modes can be calculated, so some truncation error exists in the problem. One possible solution is to use the modal transient optimization solution as the initial guess for a direct transient run. Figure 6-22 shows the convergence for the serial run. Note that the Tikhonov Parameter is used to maintain stability in the early time period.

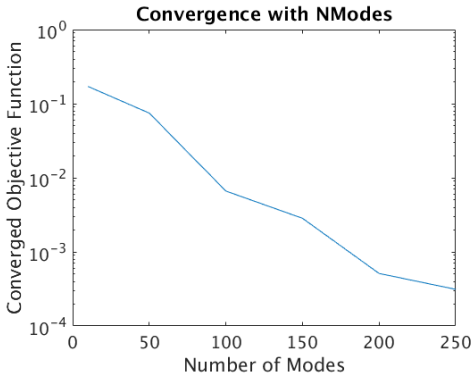

Figure 6-22. – Convergence of Final Objective Function with Increasing Number of Modes

For input deck see Appendix 11.67.

7.7. PSD Identification using Modal FRF

To verify the implementation of PSD inversion, we consider a dynamical system that is simple yet captures the essential complexities of a general PSD inversion problem: (a) coupling between degrees of freedom, and (b) complex-valued PSD and dynamic stiffness matrices arising from real (damped) dynamical systems. The system includes a unit mass supported by a generalized (coupled) spring. All three transnational degrees of freedom are active. The stiffness elements are chosen to be $K_{xx} = 10$, $K_{yy} = 20$, $K_{zz} = 40$, $K_{xy} = 5$, $K_{xz} = 10$, and $K_{yz} = 15$. Damping is introduced through mass and stiffness proportional damping that exists in Sierra-SD, i.e.

$$\mathbf{C} = \alpha\mathbf{K} + \beta\mathbf{M}, \tag{7.7.1}$$

where,$\mathbf{K}, \mathbf{M}$ are stiffness and mass matrices, and α and β are chosen as 0.5.

For this system, the frequency-dependent dynamic stiffness matrix is given by:

$$\mathbf{H} = \begin{bmatrix} 10+4.5i\omega-\omega^2 & 5+2.5i\omega & 10+5i\omega \\ 5+2.5i\omega & 20+9.5i\omega-\omega^2 & 15+7.5i\omega \\ 10+5i\omega & 15+7.5i\omega & 40+19.5i\omega-\omega^2 \end{bmatrix} \tag{7.7.2}$$

The system is subjected to random excitaton with load PSD of,

$$\mathbf{S_{ff}} = \begin{bmatrix} 1.0 & 0.5i & 0.25i \\ -0.5i & 1.0 & -0.5i \\ -0.25i & 0.5i & 1.0 \end{bmatrix}, \tag{7.7.3}$$

which is Hermitian positive definite matrix. The corresponding response PSD is computed using,

$$\mathbf{S}_{rr} = \mathbf{H}\mathbf{S}_{ff}\mathbf{H}^*. \tag{7.7.4}$$

Specifically, the response PSD matrices for $\omega = 1.0$ is given by:

$$\begin{aligned} \mathbf{S_{rr}} = & \begin{bmatrix} 5.80518248610408 & -0.20186636551875 & -0.94581281856099 \\ -0.20186636551875 & 2.93198109071619 & -1.81697259423814 \\ -0.94581281856099 & -1.81697259423814 & 1.71390964877432 \end{bmatrix} \\ + \quad i & \begin{bmatrix} 0 & 1.03255582876588 & -0.12062608555571 \\ -1.03255582876588 & 0 & -0.31481273538822 \\ 0.12062608555571 & 0.31481273538822 & 0 \end{bmatrix} \end{aligned} \tag{7.7.5}$$

And for $\omega = 2$, the response PSD is given by:

$$\begin{aligned} \mathbf{S_{rr}} = & \begin{bmatrix} 0.40600284323792 & -0.01261108737714 & -0.01763921194869 \\ -0.01261108737714 & 0.23973256506857 & -0.15691809860232 \\ -0.01763921194869 & -0.15691809860232 & 0.19193866893329 \end{bmatrix} \\ + \quad i & \begin{bmatrix} 0 & 0.09743252750327 & 0.00483348116274 \\ -0.09743252750327 & 0 & -0.05282964809931 \\ -0.00483348116274 & 0.05282964809931 & 0 \end{bmatrix} \end{aligned} \tag{7.7.6}$$

The above response PSD matrices are in turn is used as an input into a PSD inversion algorithm implemented in Sierra-SD, and is verified that inverted load PSD matches with the expected load PSD in Equation 7.7.3.

For input deck see Appendix 11.68.

7.8. Orthotropic Material Identification

To verify orthotropic elastic material-id in fully three-dimensional setting, we consider a $2 \times 3 \times 4$ deep beam that is fixed on one edge. The beam is excited on one of the side faces with Heaviside force that is uniformly distributed in space. The traction has equal components in all three directions, thus exciting in all directions, making the response sensitive to all of the material parameters. The material properties are chosen as:

$$\mathbf{E}_{actual} = \begin{bmatrix} 4 & 1 & 2 & 0 & 0 & 0 \\ 1 & 5 & 3 & 0 & 0 & 0 \\ 2 & 3 & 6 & 0 & 0 & 0 \\ 0 & 0 & 0 & 2 & 0 & 0 \\ 0 & 0 & 0 & 0 & 2 & 0 \\ 0 & 0 & 0 & 0 & 0 & 2 \end{bmatrix} \tag{7.8.1}$$

The synthetic data is taken as the three displacement components computed on the free end of the cantilever beam. The data is in turn used to perform inversion using Sierra-SD. The initial estimate of the modulus matrix assumed to be invariant to the three directions and is chosen as,

$$\mathbf{E}_{initial} = \begin{bmatrix} 3 & 1 & 1 & 0 & 0 & 0 \\ 1 & 3 & 1 & 0 & 0 & 0 \\ 1 & 1 & 3 & 0 & 0 & 0 \\ 0 & 0 & 0 & 1 & 0 & 0 \\ 0 & 0 & 0 & 0 & 1 & 0 \\ 0 & 0 & 0 & 0 & 0 & 1 \end{bmatrix} \tag{7.8.2}$$

Sierra-SD implementation of the above problem converges to the expected orthotropic material modulus shown in Equation 7.8.1. For input deck see Appendix 11.69.

8. HIGH CYCLE FATIGUE AND DAMAGE

8.1. Fatigue Output of Single DOF in Random Vibration

A single hex (and single degree of freedom) model is used to verify the computations of the random vibration problem. Four nodes of the 8 node brick are clamped. The remaining nodes are constrained to move in only the X direction. In addition, multipoint constraints tie three nodes to a single master node. The model has only one active degree of freedom, and a single element. Each of the results may be examined individually without a need for a summation over mode shapes.

Comparison is made to a Matlab^{TM} calculation found in "byhand.m". Each result is listed in following paragraphs.

8.1.1. Ensure Normalization of Eigenvectors

From the output of `Maa.m`, the mass is 8.6333e-5. The eigenvector, ϕ, is of length 1, and value 107.6244. Then,

$$\phi^T m \phi = 107.6244 \cdot 8.6333\text{e-}5 \cdot 107.6244 = 1$$

The eigenvalues and vectors may be compared with results in `onehex-eig.exo`.

8.1.2. Determine the modal transfer functions, H_i

The physical force, F, is transformed to modal space by premultipling by ϕ^T. The modal transfer function at frequency ω describes the contribution of one mode to the resulting displacement.

$$u = \sum_{i}^{Nmodes} H_i(\omega) F_i(\omega) \tag{8.1.1}$$

where (8.1.2)

$$H_i(\omega) = \frac{1}{\omega^2 - \omega_i^2} \tag{8.1.3}$$

In our example the sampling frequency is 10:100 Hz, while the modal frequency is 62,846. Thus $\omega_i >> \omega$. We can approximate,

$$H_i = 1/(2\pi \cdot 62846)^2 \approx 6.4133\text{e-}12$$

Thus, the modal amplitude, u_i, is given by $u_i = H_i F_i \approx \phi^T F/\omega_i^2 \approx$6.2121e-9. The modal amplitude for FRF is not directly output, but the physical amplitude is output.

8.1.3. Determine the physical transfer function, H(ω) and Displacement

Physical space is simply related to modal space, $x = \phi q$. Likewise,

$$U = HF$$

or,

$$H(\omega) = \phi H_i \approx \phi^2/(2\pi f)^2$$

Thus, the physical transfer function, $H \approx 7.4286\text{E-}8$. Likewise, the amplitude is the transfer function multiplied by the force. $U(\omega) = H(\omega) * Force \approx \phi F \phi^T/\omega_i^2 \approx 6.6857\text{E-}7$ and is essentially independent of frequency. This physical amplitude may be compared with results in `onehexran-frf.frq`.

Salinas computes: 6.6857E-07.

Likewise the acceleration response can be predicted. The acceleration is simply ω^2 times the displacement. At $f = 10$, $\ddot{U} = 4\pi^2\phi^2 F/\omega_i^2$. At $f = 10$, $\ddot{U}(10) = 0.0026394$. At the the top end of frequency band, $\ddot{U}(100) = 0.26394$.

Salinas computes 0.0026394 and 0.26394.

8.1.4. Determine the Displacement and Acceleration Spectral Density

The output is generated by a computation of a modal sum.

$$X_{rms} = \sqrt{\sum_{i,j}^{Nmodes} \phi_i \phi_j \Gamma_{ij}}$$

Here Γ contains the integral of the frequency component of the load.

$$\Gamma_{ij} = \int_0^\infty H_i(\omega) H_j(\omega) S(\omega) d\omega$$

And, S is the PSD of the input force. A similar relation exists for acceleration, but the integration includes ω^4, i.e.

$$\Gamma A_{ij} = \int_0^\infty \omega^4 H_i(\omega) H_j(\omega) S(\omega) d\omega$$

We use a simple trapezoidal integration strategy. Thus, we can weight the final and initial intervals at half the value of the central intervals.

$$\begin{aligned}
\Gamma &\approx 2\pi \sum_f H_q^2 S \Delta f w_i && (8.1.4)\\
&\approx 2\pi H_q^2 9.0[5\,10\,10\,10\,10\,10\,10\,10\,10\,10\,5] && (8.1.5)\\
&\approx 2\pi(2.7249\text{e-}8)^2(9.0)(90) && (8.1.6)\\
&\approx 3.7789\text{e-}12 && (8.1.7)
\end{aligned}$$

Likewise

$$\begin{aligned}\Gamma_A &\approx (2\pi)^5 \sum_f H_q^2 S f^4 \Delta f w_i && (8.1.8)\\ &\approx (2\pi)^5 H_q^2 9.0[10\,20\,30\,40\,50\,60\,70\,80\,90\,100]^4[5\,10\,10\,10\,10\,10\,10\,10\,10\,10\,5] \\ &\approx (2\pi)^5 (2.7249\text{e-}8)^2 (9.0) 2.0332\text{e}9 \\ &\approx 0.13306 && (8.1.9)\end{aligned}$$

The ratio of GammaA/Gamma is 3.5211e10. This same ratio should be found in the square of A_{rms}/X_{rms} found in the random vibration output of `onehex-ran.exo`.

Salinas has: $X_{rms} = 1.4799\text{E-}5$. $A_{rms} = 2.7770$. These are found in onehex-ran.exo. The ratio $(A_{rms}/X_{rms})^2 = 3.5212\text{E}10$.

8.1.5. Fatigue Parameters

For fatigue life predictions, we are interested in several parameters. The first of these is the stress moments, M_o, M_2 and M_4. These are important as the ratios of these moments provide information on the rate of zero crossing, ν_o^+, and the number of zero crossings, $n_c = \nu_o^+ \tau$.

The ratio of `Vrms2/Vrms` is related to ratios of moments. In particular, $VRMS2/VRMS = \sqrt{M_2/M_o}$. These are related to the ratios of Γ_v/Γ.

$$\begin{aligned}\Gamma_V &\approx (2\pi)^4 \sum_f H_q^2 S f^2 \Delta f w_i && (8.1.10)\\ &\approx (2\pi)^3 H_q^2 9.0\,[10\,20\,30\,40\,50\,60\,70\,80\,90\,100]^2[5\,10\,10\,10\,10\,10\,10\,10\,10\,10\,5] \\ &\approx 5.5447\text{E-}7 && (8.1.11)\end{aligned}$$

Salinas has $VRMS = 1.1384\text{E}2$ and $VRMS2 = 4.3607\text{E}4$. Therefor $(VRMS2/VRMS)^2 = 1.4673\text{E}5$, which can be compared to the closed form ratio 5.5447E-7 / 3.7789E-12 = 1.4673E5.

This is `Salinas_rtest/verification/fatigue/onedof/onehexran.test`.

8.1.6. Fatigue Solution

We verify the fatigue analysis on a single, 1x1x1 Hex8 element. This is an entirely contrived example, with material properties invented to simplify the calculation. Results from within Sierra/SD are compared to independent Matlab computations.

Variable	Value
Vrms	113.8421029
Vrms2	4.360736489E+04
Vrms4	2.136176695E+07

Table 1-1. – Input Moments

8.1.6.1. Assumptions

We begin the solution with a previously verified random vibration solution with results in Table 1-1.

We also *construct* a fictitious material with fatigue parameters (i.e. S-N curves) that make computation simple. The S-N curve is represented in Figure 1-1. It is constructed such that with an RMS value of stress equal to 113.8421029, a solution of N of 1 million is obtained. The associated material parameters are listed in Table 1-2.

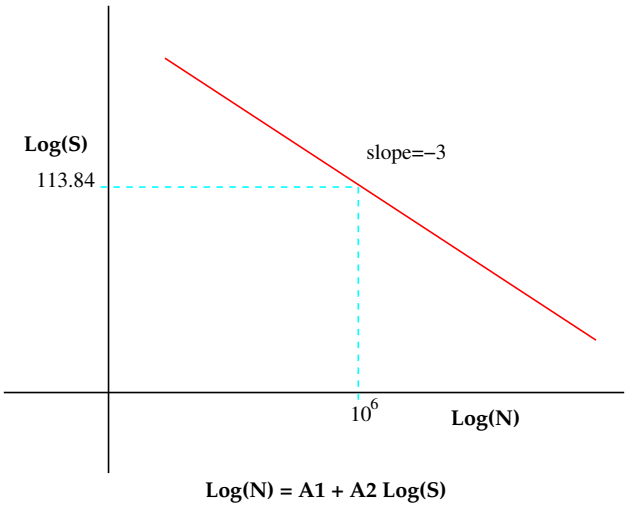

Figure 1-1. – S-N Curve for Fictitious Material

Variable	Value
A2	-3
m	3
A1	Log(N)-A2*Log(113.84) $\approx$ 12.1

Table 1-2. – Fatigue Material Parameters

8.1.6.2. Damage Rate Calculation

The narrow band damage rate is,

$$D_{NB} = \frac{\nu_o^+}{10^{A_1}} \left(\sqrt{2} V_{rms}\right)^m \Gamma\left(1 + m/2\right)$$

This may be evaluated in terms of the above parameters.

$$\begin{aligned} \nu_o^+ &= \tfrac{V_{rms2}}{2\pi V_{rms}} && \approx 61.0 \\ 10^{A_1} & && \approx 1.475 \times 10^{12} \\ (\sqrt{2} V_{rms})^m & && \approx 4.173 \times 10^{6} \\ \Gamma\left(1 + m/2\right) &= \Gamma(2.5) && \approx 1.3293 \end{aligned}$$

For which we have $D_{NB} \approx 2.2919 \times 10^{-4}$.

This is the test `Salinas_rtest/verification/fatigue/onedof/onehexfatigue.test onehexran.test`. For input deck see Appendix 11.70.

8.1.7. Fatigue Stress Scaling

We verify the fatigue analysis scaling on a single, 1x1x1 Hex8 element. This is an entirely contrived example, with material properties invented to simplify the calculation. The model is identical to a fatigue example previously verified, we simply scale the geometry and loads, and verify the solution. The experimental material data is unchanged.

8.1.7.1. Model Definition and Scaling

- The model is a 1x1x1 in^3 cube. It is scaled to SI units 0.0254 meters on a side.
- Input pressure is 7 psi, multiplied by a frequency function. In SI units, this becomes $7 \times 6894.76 = 48263.32$ pascals, multiplied by the same function.
- Young's Modulus of 1e7 psi becomes 68.947573e9 pascals. Handbook value is 69 GPa.
- Density of 0.000259 slinch/in^3 (0.1000776 lbm/in^3) becomes 2770.138 kg/m^3. Handbook values of 2700 kg/m^3.

8.1.7.2. Results

The damage rate and stress must be independent of units. This is ensured by using the same comparison file for both. In addition, we have the following correspondence.

Result	**English Units**	**SI Units**	**Status**
Eigen Frequency	62846.1 Hz	62820.8 Hz	✓
max(Axrms)	2.7770 $\mathrm{in/s^2}$	0.070537 $\mathrm{m/s^2}$	✓
Vrms	113.84 psi	0.78492×10^6 Pa	✓
ZeroCrossingRate	60.965	60.965	✓
PeakFrequency	77.965	77.965	✓
NbDamageRate	2.2923E-13	2.2923E-13	✓
DamageRate	1.9324E-13	1.9324E-13	✓

8.2. Fatigue Output of Dogbone Test

8.2.1. Scope:

Verification of **Sierra/SD** in the frequency domain builds upon a verification of "Siesta", a python post-processing tool for evaluation of high cycle fatigue damage. These solutions represent evaluation of the same damage quantities through a variety of means. Sierra/SD will evaluate the damage using frequency domain methods only.

Siesta has been evaluated using both the time domain and frequency domain. Computations were performed to individually compare both domains to an analytical solution for the simple case of a 5 Hz sine wave input. Two additional computations were conducted with the same model verifying that time domain and frequency domain both result in the same solution when provided more complex inputs. These evaluations were conducted on an element by element basis, and so some discrepancies to the single DOF analytical solution are expected.

8.2.2. Methodology:

The dog-bone specimen described by Anes et al.[4] was chosen as a sufficiently simple model to solve damage analytically, with the additional benefit that experimentally derived results were available for our load case. Note that calculations were done using English units: IPS in Salinas, converted to Ksi during import into Siesta.

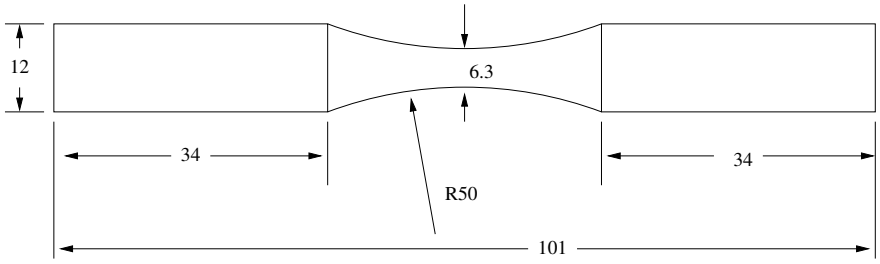

Figure 2-2. – Dog-bone Specimen Dimensions (mm)

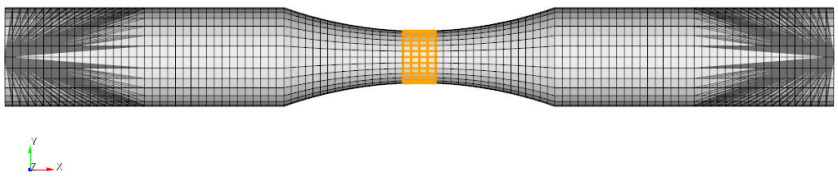

Figure 2-3. – Boundary conditions of mesh

For all tests, the mesh is constrained via two points at either end of the specimen. Both points are fixed in all degrees of freedom except axial translation, and affixed to the mesh

by rigid elements to the surfaces of the mesh near the ends. Results are output only for the narrow highlighted potion at the center of the model. Forces are applied at the end points with equal and opposite magnitudes. There are no point masses in the system; frequency domain input PSDs are truly provided as force squared per Hz.

To verify the results in both time domain and frequency domain, three test scenarios were evaluated, as illustrated by the PSDs shown in Figure 2-4, with details in Tables 2-3 through 2-5. The first was a 5 Hz fully reversed sine wave with 3141 lbf peak magnitude, the second was an example input matching a test specification with relatively narrow band frequency content, and the third was an example test specification with a wide band of frequency content. Note that the first elastic mode of the system occurs at 929 Hz, and modal random vibration solves included calculation of 150 modes to capture what is effectively a static solution at 5 Hz. Modes are computed to about 340 KHz.

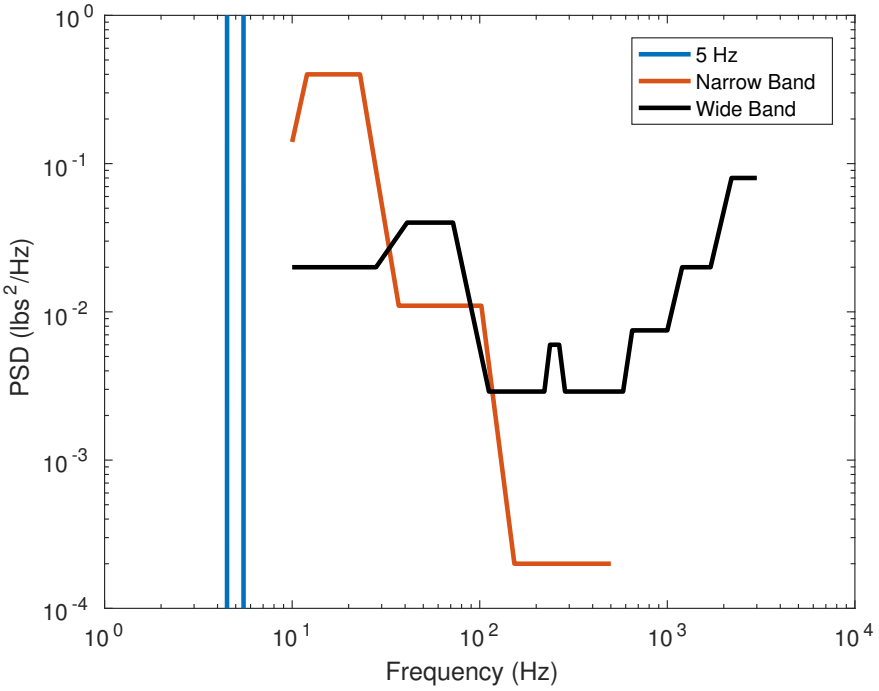

Figure 2-4. – Power Spectral Density of Input Force

In the absence of an easy way to define a single-frequency PSD, the 5 Hz test was represented in the frequency domain using a PSD with the appropriate RMS magnitude, centered around 5 Hz, and with a band width of 1 Hz. Time domain realizations of the wide and narrow band test PSDs were generated such that their RMS values could not differ from the specification by more than 1 dB, the PSD of the generated signals could not differ by more than 6 dB at any frequency, and could not differ by more than 3 dB over 80% of the frequency range.

Table 2-6 shows the preliminary results of the 5 Hz test of frequency and time domains. Sierra/SD and Siesta results are very close for this model. However, it is important to note

Frequency (Hz)	PSD (lbs^2/Hz)
4.00	1e-13
4.49	1e-13
4.50	4.93128e6
5.50	4.93128e6
5.51	1e-13
6.00	1e-13

Table 2-3. – 5 Hz PSD representation

Frequency (Hz)	PSD (lbs^2/Hz)
10	0.1400
12	0.4000
23	0.4000
37	0.0110
102	0.0110
153	0.0002
500	0.0002

Table 2-4. – Narrow-Band PSD

Frequency (Hz)	PSD (lbs^2/Hz)
10	0.0200
28	0.0200
41	0.0400
72	0.0400
112	0.0029
221	0.0029
237	0.0060
265	0.0060
285	0.0029
581	0.0029
650	0.0075
1000	0.0075
1200	0.0200
1700	0.0200
2200	0.0800
3000	0.0800

Table 2-5. – Wide-Band Force PSD

Domain	Damage Model	Vrms (ksi)	Cycling Rate (Hz)	Damage Rate
Time	Minor's Rule	44.3-47.1	4.17	1.8E-6 - 4.2E-6
Frequency	Steinberg	42.9-46.3	5.01	3.0E-3 - 8.7E-3
	Narrow Band			9.4E-3 - 2.7E-2
	Wirsching-Light			4.8e-3 - 1.4e-2
Documentation	Experiment	46.36	5.00	5.0E-6

Table 2-6. – Preliminary 5 Hz Results. Ranges indicate spatial changes.

that neither domain's damage formulations are intended to be used on a sine input. Because this is a sine input, three adjustments must be made to the raw data.

1. The rainflow algorithm consistently misses one half cycle on the input, and interprets a 0.6 second 5 Hz tone as a 4.17 Hz tone instead. As the time history in increased in length, the recorded cycling rate converges to 5 Hz, so we will act as though it detected 5 Hz. It is recommended that you use the longest time history feasible, preferably 50-100 cycles of the lowest frequency.
2. Narrow band damage, and Wirsching-Light by extension, includes a scale factor of $\Gamma(1+m/2)$ on the damage, where Γ is the gamma function, and m is the fatigue exponent. For a sine input, this is not appropriate, as it makes the calculated damage wildly conservative, so we will reduce the damage by this same factor.
3. The Steinberg method for calculating damage includes the assumption that the magnitude of Vrms is a one sigma event, and adjusts the damage to reflect the influence of 2-sigma and 3-sigma events as well. These cycles do the majority of the damage on a system, and so this approach is not appropriate for modeling a strictly controlled experiment with 100% of the cycles at the same value.

After adjusting the results and removing Steinberg from the chart, we are left with Table 2-7. It is worth noting that the Wirsching-Light damage metric is intended to compensate for conservatism on wide-band signals; as this signal is very narrowband, the correction is unnecessary. In summary, the narrow band results are as expected.

- ✓ The preliminary results for Siesta and Sierra/SD agree very well.
- ✓ With appropriate corrections, these results are consistent with both rainfall computations and with experiment.

Domain	Damage Model	Vrms (ksi)	Cycling Rate (Hz)	Damage Rate
Time	Minor's Rule	44.3-47.1	5	2.2E-6 - 5.0E-6
Frequency	Narrow Band	42.9-46.3	5.01	1.7E-6 - 5.0E-6
	Wirsching			0.9E-6 - 2.5E-6
Anes	Experiment	46.36	5.00	5.0E-6

Table 2-7. – 5 Hz test after adjustments. Ranges indicate spatial variation.

8.2.2.1. Narrowband and Wide-Band Evaluation

Tables 2-8 and 2-9 show the results under representative wide and narrow-band PSD inputs. Narrow band damage represents the time domain solution well, and is strictly conservative in our selected band of elements, but the wide band test revealed that the frequency domain is only an estimate of damage expected from the time domain analysis under wide-band loading. Why this discrepancy exists is not well understood, but may be caused by the shape of the wide-band PSD used. It may be possible to better represent the wide-band test with 2-3 narrow band tests under the order-independent assumption of Minor's rule, but this was not tested.

As with the 5 Hz test, the rainflow algorithm used in the time domain calculated an inaccurate cycling frequency when provided with a narrow-band signal. This is not considered to be a problem because the overall damage appears to be well accounted for.

Domain	Damage Model	Vrms (ksi)	Cycling Rate (Hz)	Damage Rate
Time	Minor's Rule	0.046-0.049	532	5.6E-43 - 1.7E-42
Frequency	Steinberg	0.051-0.055	47	2.0E-43 - 5.8E-43
	Narrow Band			6.3E-43 - 1.8E-42
	Wirsching			2.9E-43 - 8.4E-43

Table 2-8. – Narrow-Band Test Results. Ranges indicate spatial variation.

Narrow-band and Wide-band results are very similar for Siesta and Sierra/SD, but they are not identical. We expect that there are round off errors and integration differences leading to those differences. These are particularly difficult in an undamped system with numerical integration crossing peak resonance. Table 2-10 compares these results. Overall, the comparison is good, and well within the differences of the other methods.

Domain	Damage Model	Vrms (ksi)	Cycling Rate (Hz)	Damage Rate
Time	Minor's Rule	0.22 - 0.24	2486 - 2487	21E-33 - 56E-33
Siesta results				
Frequency	Steinberg	0.20 - 0.22	2293	2.2E-33 - 6.3E-33
	Narrow Band			6.8E-33 - 20E-33
	Wirsching			3.1E-33 - 9.0E-33
Sierra/SD results				
Frequency	Narrow Band	0.201 - 0.217	2293	6.5E-33 - 19E-33
	Wirsching			3.0E-33 - 8.6E-33

Table 2-9. – Wide-Band Test Results. Ranges indicate spatial variation.

Parameter	Narrow-Band			Wide-Band		
	Siesta	Sierra	Diff	Siesta	Sierra	Diff
Vrms (psi)	55	55.45	0	220	220	0%
ν_o^+	47	47	0	2293	2293	0%
NB Damage	1.8e-42	1.74-e42	3%	2.0e-32	1.9E-32	5%

Table 2-10. – Maximum of Siesta and Sierra/SD Computations

8.2.2.2. Integration and Damping

The PSD spectrum is integrated through frequency to determine the RMS stress and the stress moments. For undamped systems, that function is singular at the resonance points. Two factors influence the accuracy of that solution. First, damping removes the singularity in the solution. Second, the size of the frequency step addresses the accuracy of the integral.

Figure 2-5 provides some information on the convergence of the solution as these parameters are varied. The figure on the left shows variation of the narrowband damage, D_{NB}, as damping is increased. For damping below 1%, there is no significant impact on the solution. The graphic on the right illustrates the same data, sliced another way. We observe that the frequency step, ΔF, has a significant affect on the solution. For our problem, independent of damping, the frequency step should be below 1 Hz. However, with no damping and a small frequency step, very different (non-convergent) results are obtained. This is consistent with numerical integration across a singularity. For input deck see Appendix 11.71.

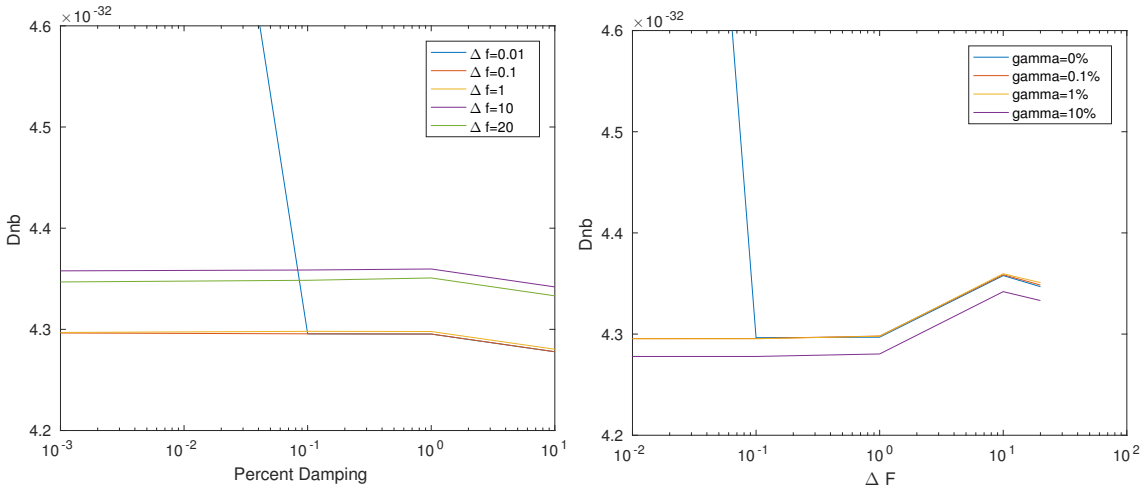

Figure 2-5. – Convergence of PSD Integration

8.3. Fatigue Output of Pinned Shell

Both a narrowband and wideband example are evaluated. The verification test ensures the following.

- The stress is evaluated at all three surfaces (top, middle, bottom), and the *larger* of these values is used for evaluation of damage.
- The zero crossing and peak frequency make sense in the context of the PSD inpt. This is easier to evaluate for narrowband processes.
- Von Mises stress is consistent between `modalranvib` and `FRF` solutions.
- The von Mises stress is consistent with a static solution.
- Damage Rate is consistent with independent Matlab calculations.

We do not have a comparison with time domain rain fall calculations. We also have no convergence study, either with mesh, or with modes.

8.3.1. Narrow Band Pinned Plate

The model is a simple rectangular plate, shown in Figure 3-6. The plate is 10 units in X, 1 unit in Y, 0.01 units thick, and all deformation is in the Z direction. In modal analysis, only the first mode is retained, which is a bending mode, shown in the lower portion of Figure 3-6. The +/- X surfaces are pinned, with no other Dirichlet boundary conditions. Loading is a uniform pressure in the $-Z$ direction. The narrowband loading in shown in Figure 3-7, where the entire loading is in the 4 Hz to 5 Hz range. The first mode is at about 8.9 Hz, so this loading is below that first mode.

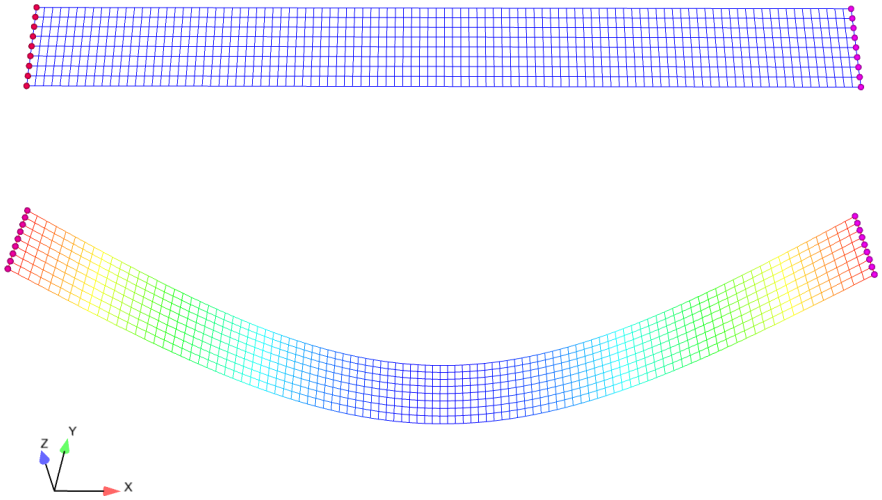

Figure 3-6. – Pinned Plate Geometry, and First Mode

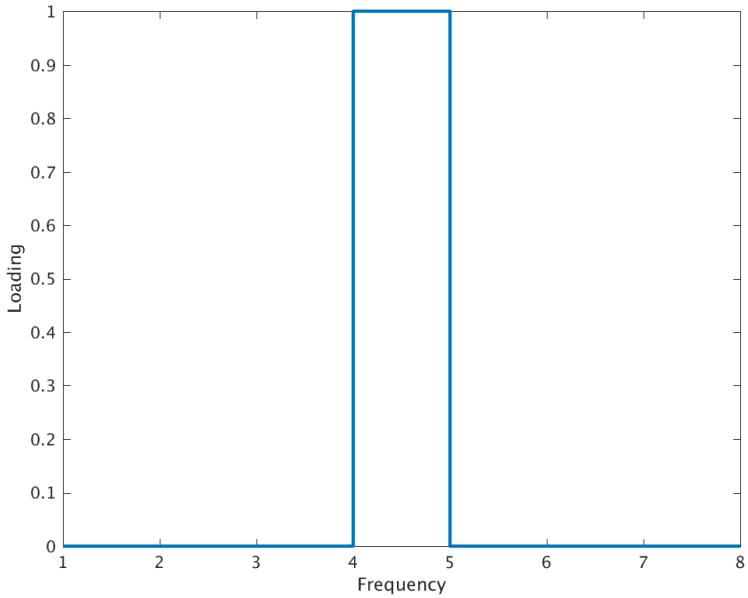

Figure 3-7. – Pinned Plate. Random Vibration Loading

8.3.1.1. Statics:

The static response on the bottom surface, to a uniform pressure load is shown in Figure 3-8. Stress on the top surface is the negative of this, and there is no stress on the midplane.

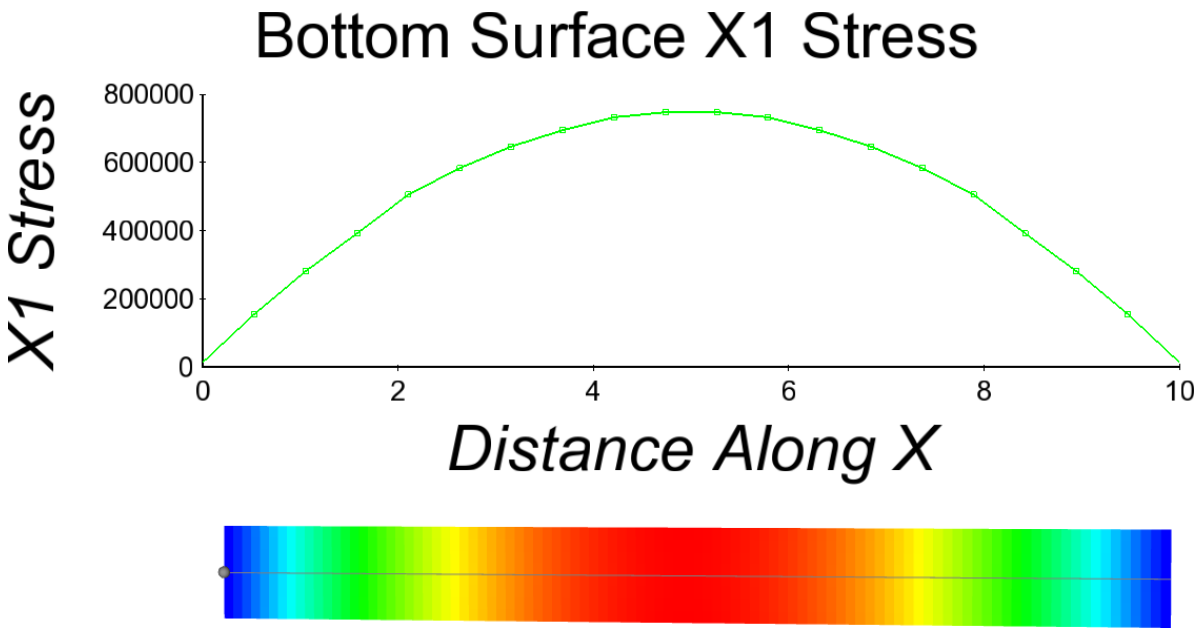

Figure 3-8. – Pinned Plate. Statics Response

8.3.1.2. FRF:

The input is modified, and a modal FRF computed from 0.01 to 8 Hz, as shown in Figure 3-9. The stress response is very similar to the static solution, as evidenced in Figure 3-10. There are expected deviations, as the FRF response includes only a single mode. However, the stresses are as expected, and they increase at the sample frequency of 4.55 Hz, as the solution approaches resonance.

✓ FRF and Statics displacements and stresses are consistent.

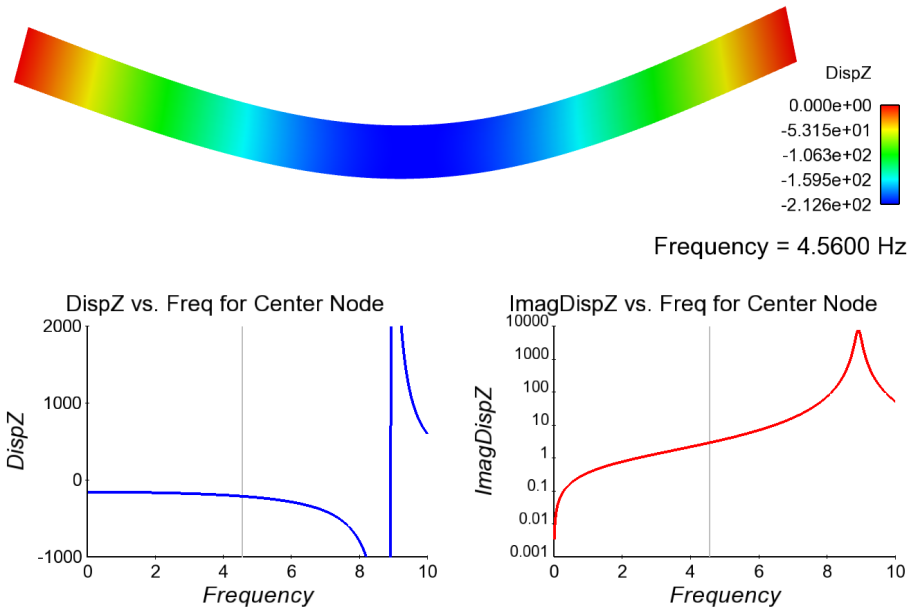

Figure 3-9. – Pinned Plate. Modal FRF Response

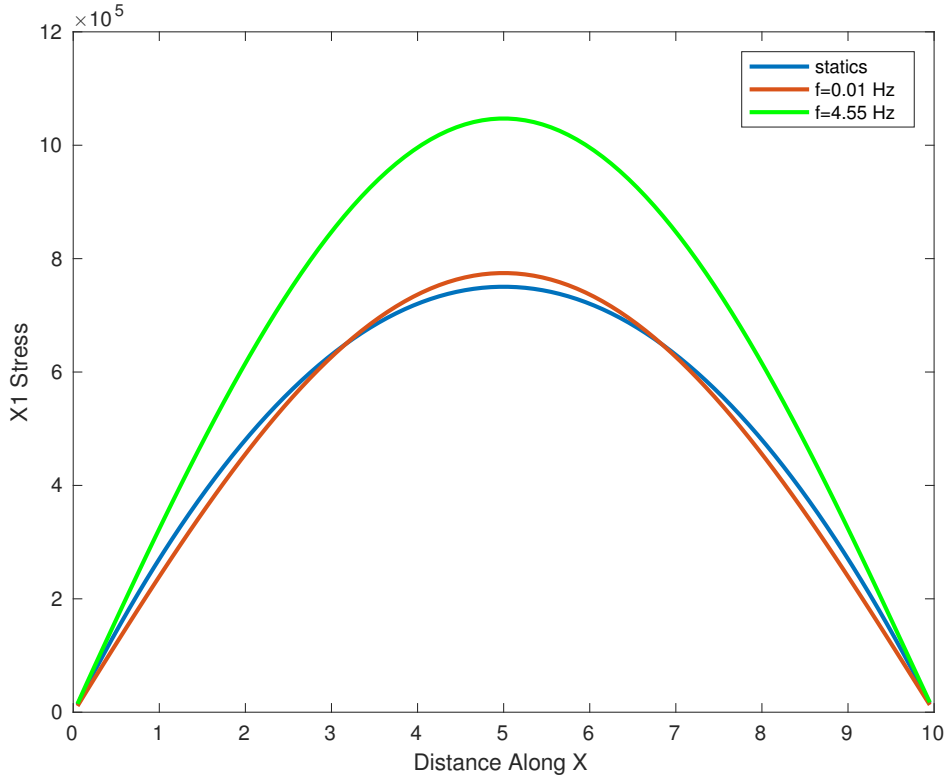

Figure 3-10. – Pinned Plate. Comparison of Static and FRF Solutions

8.3.1.3. Random Vibration Analysis:

The next step of the computation is evaluation of the RMS von Mises stress through the modal random vibration analysis. The peak value of this stress is 1.037×10^6, which occurs in the center of the structure. This value is consistent with the stresses computed in the FRF and Statics portions of the analysis. The following are confirmed.

- ✓ The zero crossing and peak frequency, determined from Vrms_i, are both about 4.5 Hz, consistent with the narrow band sweep in this analysis.
- ✓ RMS stresses are consistent with the FRF values. Note however, that these are all axial stresses.

8.3.1.4. Fatigue Damage Analysis:

The final step is the fatigue analysis. Output of this analysis confirms,

- ✓ The zero crossing and peak frequency are correct.
- ✓ Damage rates are consistent with hand calculations.

$$D_{NB} = \frac{\nu_o^+}{A}(\sqrt{2}\sigma_s F_{SS})^m \Gamma\left(\frac{m}{2}+1\right)$$

For our structure, $D_{NB} \approx 5$ in the center of the plate.

$$\begin{aligned}
A_1 &= 12.1689 \\
A &= 10^{A_1} = 1.475\times10^{12} \\
m &= 3 \\
F_{SS} &= 0.0001 \\
\nu_o^+ &= 4.534 \\
\Gamma(5/2) &= 1.3293 \\
\sigma &\approx 1.0377\times10^6 \\
D_{NB} &= 1.2911\times10^{-5} \qquad \text{(from hand calcs)}
\end{aligned}$$

The value from the output is $D_{NB} = 1.291125933\times10^{-5}$.

8.3.2. Wideband Calculations

Wideband calculations use the same model as narrowband. Only a single mode is retained as shown in Figure 3-6, however the band selected is from 10 -100 Hz. Figure 3-11 shows the displacement response over this band, with a 1% damping. Above the 8.9 Hz mode, the response rolls off.

For this model, the zero crossing rate at all locations is $\nu_o^+ = 12.351$. The peak frequency is somewhat higher (as expected), at $\nu_p = 20.115$ Hz. Both reflect the much higher energy at lower frequency because the dominant mode is at 8.9 Hz.

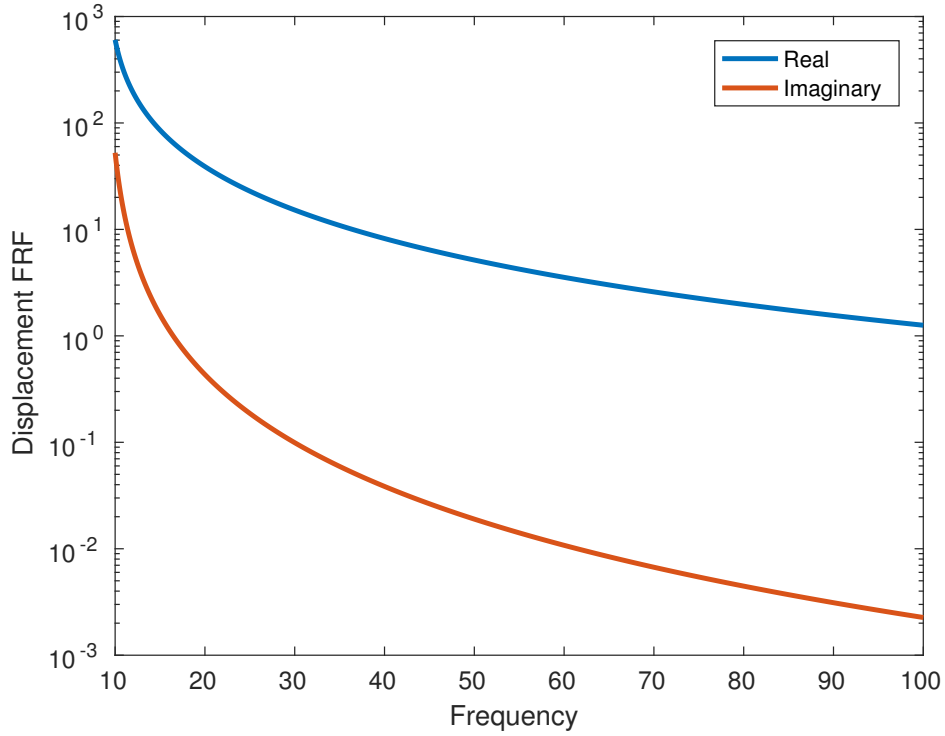

Figure 3-11. – Pinned Plate. Wide Band FRF Response

✓ The zero crossing and peak frequency are reasonable.

The peak Damage occurs in the middle of the plate. Peak values for `NbDamageRate` and `DamageRate` are 6.8259×10^{-4} and 5.6715×10^{-4} respectively.

The RMS von Mises stress can be computed in two ways. First, the modal random vibration method can be used. Second, a frequency response method is used. Each of these methods is applied here for the element 51, which is found at the center of the plate where the stress is maximum.

ModalRanVib: This method, described in the Sierra/SD manuals, computes the RMS von Mises stress. The value from the method is $\hat{V}_{RMS} = 2.7886 \times 10^6$.

FRF: This method uses the transfer functions. From the output of the modalFRF calculation,

$$\bar{V}^2_{RMS} = \int_0^\infty H^\dagger(\omega) S_{FF}(\omega) H(\omega) d\omega$$

where $H(\omega)$ is a stress transfer function, and S_{FF} is the force input power spectral density. For element 51, $\bar{V}_{RMS} = 2.8695 \times 10^6$. Here we assume that the stress is uniaxial, and H applies to σ_{xx}, the axial portion of the stress. The Matlab code to approximate this integral is,

```
h1  =  evar23(51,:) + sqrt(-1)*evar01(51,:);
h1  = h1.';
df  =  0.1;
```

```
 Sff   = 1;
Vrms2 =  h1'*Sff*h1*df;
Vrms  = sqrt(Vrms2)
```

The difference between these two values is about 3 percent. That would appear to be too large. However, evaluation of convergence as the frequency step is decreased indicates much less error in the modal random vibration solution. See Figure 3-12. The RMS stress depends on damping. Setting the damping ratio to 50%, results in stresses of 1.2721e6 and 1.262251e6 using an FRF and random vibration method respectively. As expected, the integration error is lower for these values, and relative error is about 0.8%.

✓ Computation of the RMS stress is consistent between the two methods.

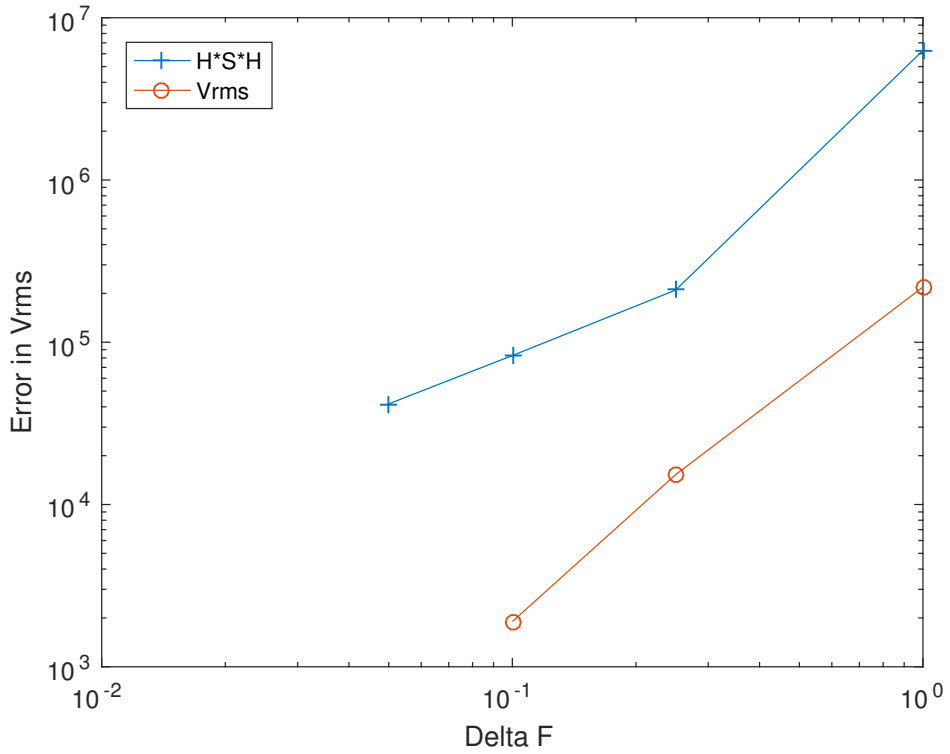

Figure 3-12. – Convergence of Frequency Integrals

For input deck see Appendix 11.72.

8.4. Nodal Loading vs Sideset Loading for Modal Random Vibration

Modal random vibration verification test of the flat plate of hexshells is shown in Figure 4-13 for pressure loading on the top surface. The plate is fixed at nodeset 3 and nodeset 4 and is fixed in the "z" direction at nodeset 1 and 2.

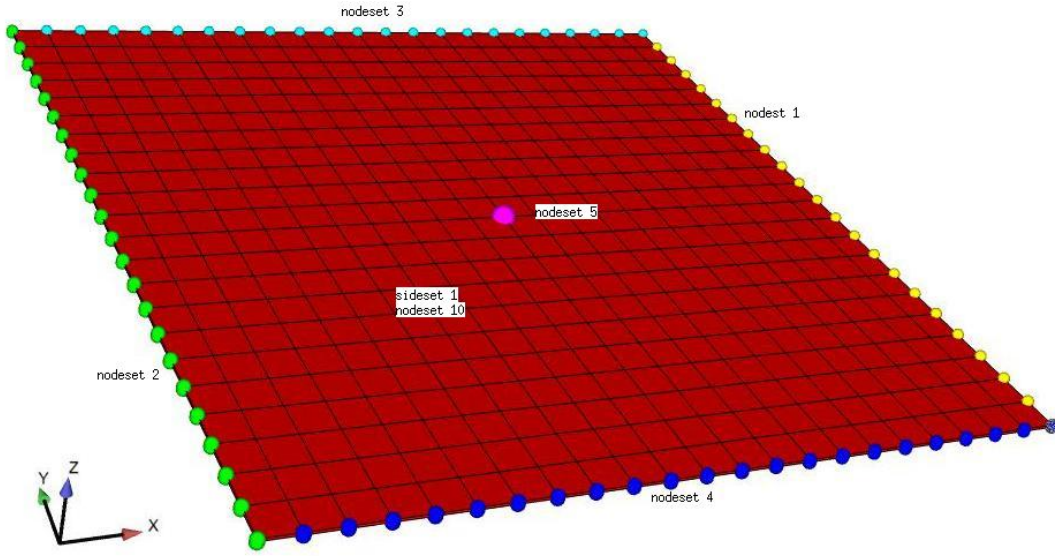

Figure 4-13. – Schematic of flat plate geometry with nodesets and sidesets labeled. A pressure load is applied to the top surface on sideset 1 and a force load is applied to the top surface on nodeset 10. Frequency output shown in Figure4-14 is taken at nodeset 5.

The pressure loading is compared to three other loading scenarios for verification. The four solutions to this problem are presented in Figure 4-14 for measurements taken at the center node of the plate, nodeset 5 in Figure 4-13.

The four solutions are:

1) Modalranvib with pressure applied to the top surface of the plate, sideset 1 in Figure 4-13. Results are shown in blue in Figure 4-14.

2) Modalranvib with nodal forces applied to the entire top surface, nodeset 10 in Figure 4-13. The load is scaled to be equivalent to the pressure load in case 1. Note that the exodus mesh for nodeset 10 has a distribution factor of 0.5 so the force load is scaled by 2 in the input file. Results are shown in red in Figure 4-14. Note that their are no noticeable differences for cases 1 and 2.

3) A time history solution post-processed to give the power spectral density shown in red.

4) NASTRAN solution for modalranvib shown in green.

All of the input files and matlab scripts required to run these simulations are in the test directory.

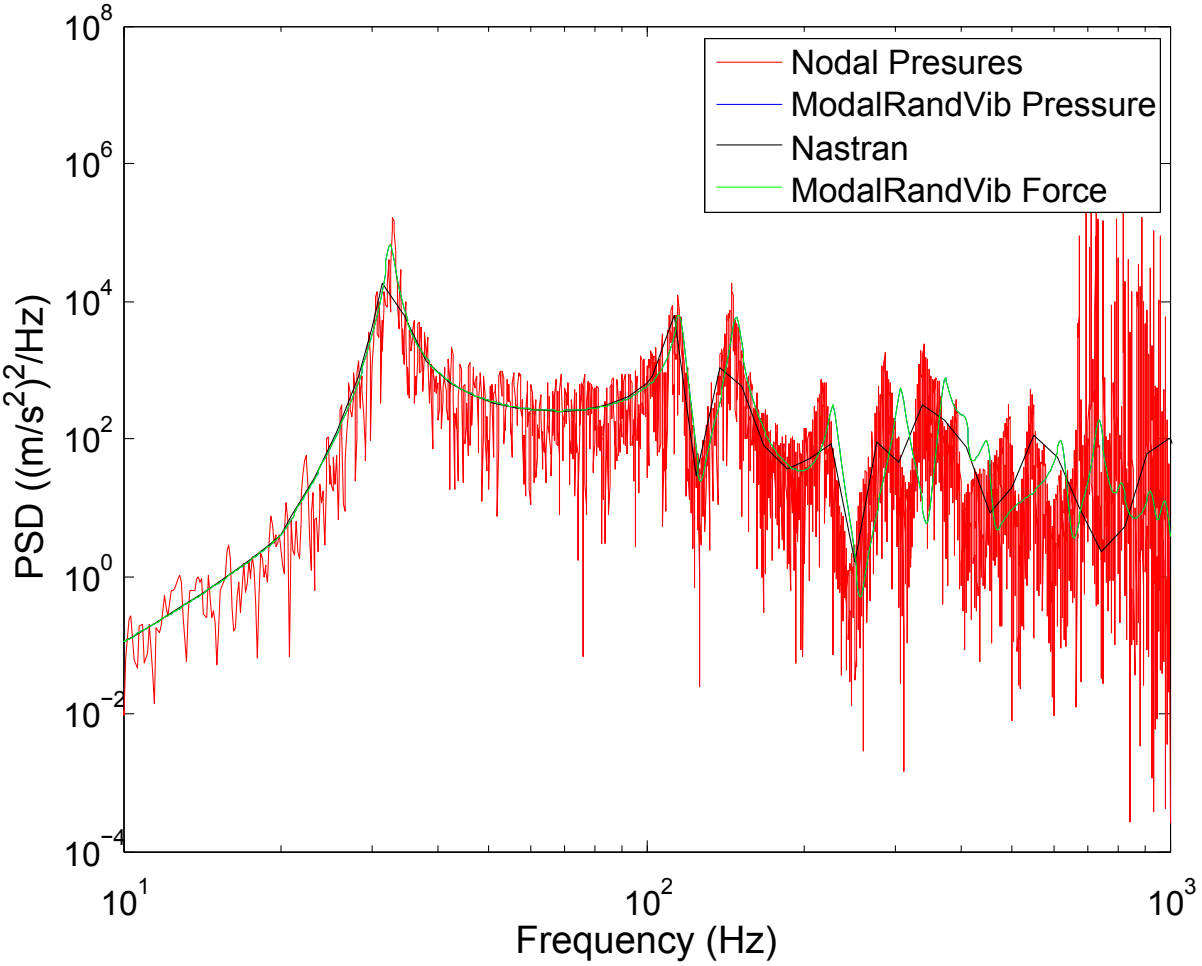

Figure 4-14. – PSD Comparison of modalranvib, nodal transient, and NASTRAN modalranvib.

The Salinas results for pressure loaded modalranvib are the same as the other solution methods.

For input deck see Appendix 11.75.

9. COUPLED ELECTRO-MECHANICAL PHYSICS

9.1. Static Response for Electric Field Induced Beam Deformation

In this section, we verify the electro-mechanical coupling in the stiffness matrix using the static response of two bimorph beam models (1-1) that were presented in work by X.D. Zhang and C.T. Sun [59]. The first test verifies the part of the stiffness matrix that couples the electric field to transverse strain, and the second verifies the coupling of the electric field to shear strain. To verify, we compared the transverse displacements generated from **Sierra/SD** with the analytic solutions derived in the referenced paper [59].

9.1.1. Bimorph Beam in Bending

The first model is an aluminum cantilevered beam pressed between two piezoelectric strips (Figure 1-1a). The piezoelectric strips are PZT5H and are polarized in the direction parallel to their thickness (z-axis). The constitutive properties of the piezoelectric and aluminum materials are presented in Table 1-1. Ten volt voltages ($V_{in} = V_{out} = 10$) are prescribed to the outermost surfaces parallel to the length of the beam and the aluminum core is grounded ($V_g = 0$). Figure 1-2 presents the analytic and **Sierra/SD** generated transverse displacements over the length of the beam.

Table 1-1. – Material Properties for PZT5H [59]

PZT5H								Al	
GPa					C/m^2			GPa	
c_{11}	c_{12}	c_{13}	c_{33}	c_{44}	e_{31}	e_{33}	e_{15}	E	ν
126	79.5	84.1	117	23	-6.5	23.3	17	70.3	0.345

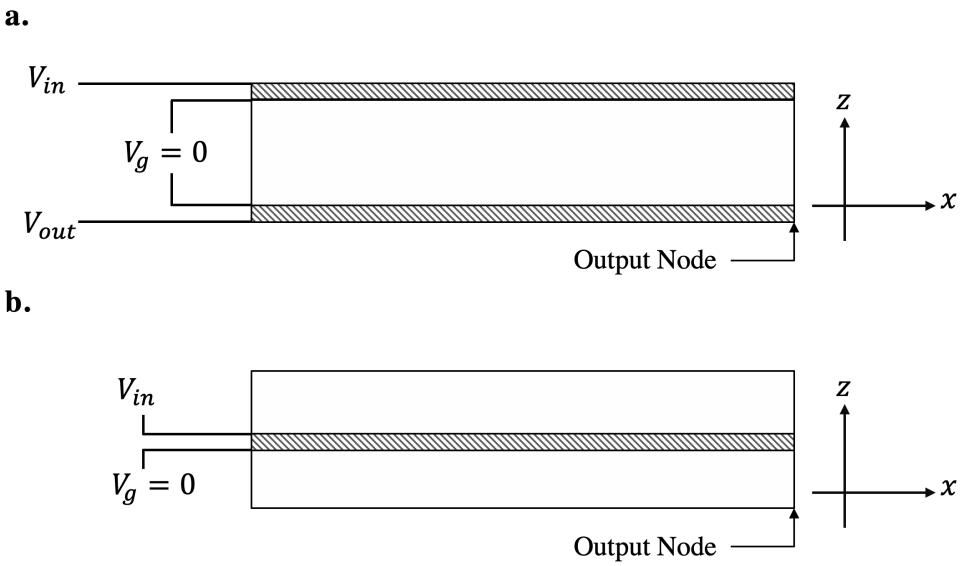

Figure 1-1. – Cantilevered bimorph beams with piezoelectric layer (hatch) and aluminum layer (solid). Model (a) verifies the electric field transverse strain coupling, and model (b) verifies the electric field shear strain coupling

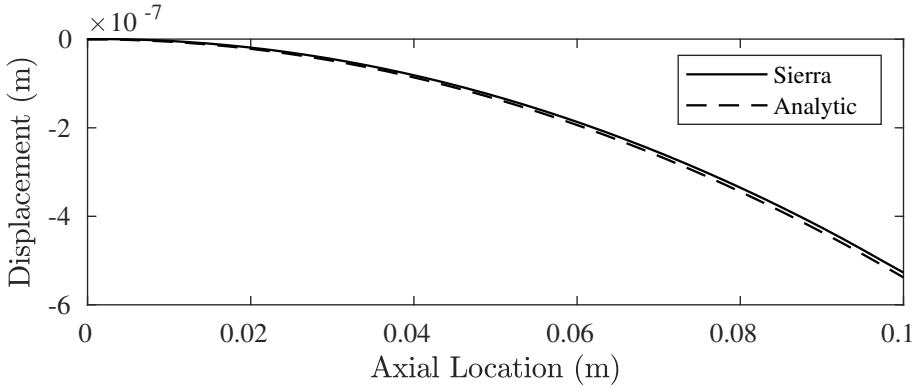

Figure 1-2. – The FE and analytic transverse displacements along the length of the bimorph beam from Figure 1-1a

9.1.2. Sheared Bimorph Beam

The second model is a piezoelectric cantilevered beam pressed between two aluminum strips (Figure 1-1b). The piezoelectric material is PZT5H and it is polarized in the direction parallel to the length of the beam (x-axis). A twenty volt voltage ($V_{in} = 20$) is prescribed to the upper interface between the aluminum and piezoelectric strip, while the lower interface is grounded ($V_g = 0$). Figure 1-3 presents the analytic solution superimposed over the transverse displacements generated from **Sierra/SD** over the length of the beam.

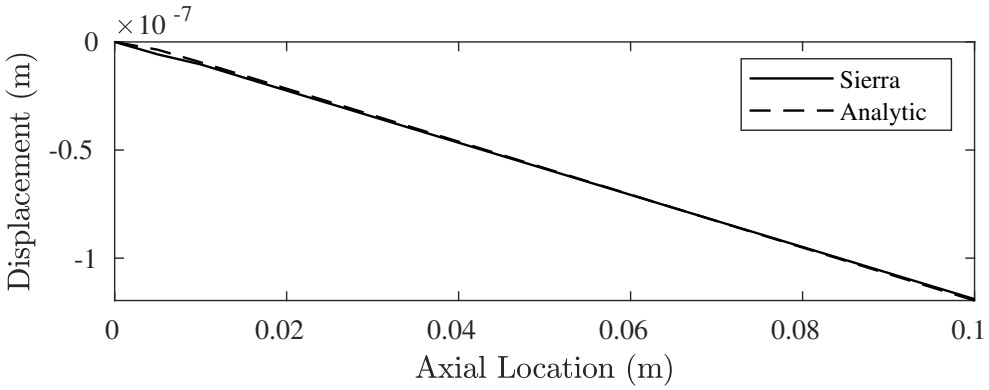

Figure 1-3. – The FE and analytic transverse displacements along the length of the shear beam from Figure 1-1b

9.2. Transient Response for Electric Field Induced Beam Deformation

In this section, we verify the transient solution method for a piezoelectric model subject to prescribed time-varying voltage boundary conditions. The details of the bimorph beam are provided in Figure 1-1a and section 9.1. A constant voltage of 20 volts ($V_{in} = 20$) is prescribed to the top surface, and the aluminum core is grounded. An equipotential surface is enforced at the bottom surface (V_{out}) with a voltage rigid set. In other words, the voltage is spatially constant along the equipotential surface. The piezoelectric material is isotropic in permittivity where its permittivity is set to the permittivity of free space.

To verify the transient solution method, we performed a transient solve using an identical model with the FE software COMSOL [14] and compared its generated time-histories with those generated from **Sierra/SD**. Figure 2-4 presents the displacement time-history of the output node (see Figure 1-1a) in the transverse direction (z-axis) and the axial direction (x-axis). Figure 2-5 presents the voltage time-history at (V_{out}). We observe excellent agreement between **Sierra/SD** and COMSOL.

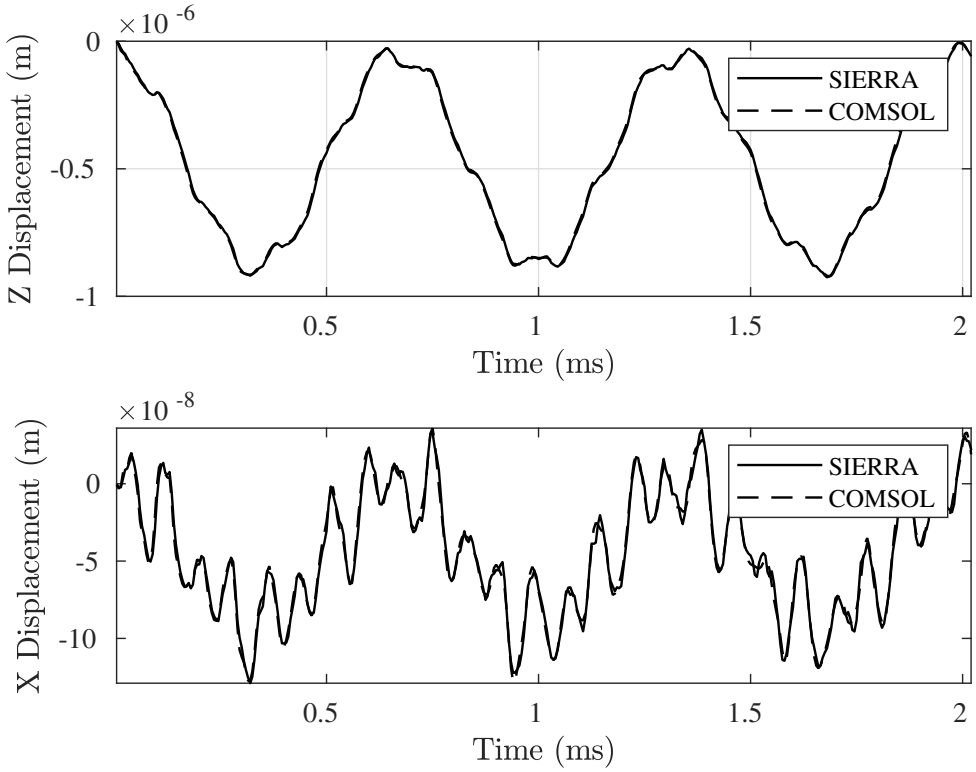

Figure 2-4. – Time-histories of transverse (z) and axial (x) displacements generated from COMSOL (dashed) and **Sierra/SD** (solid)

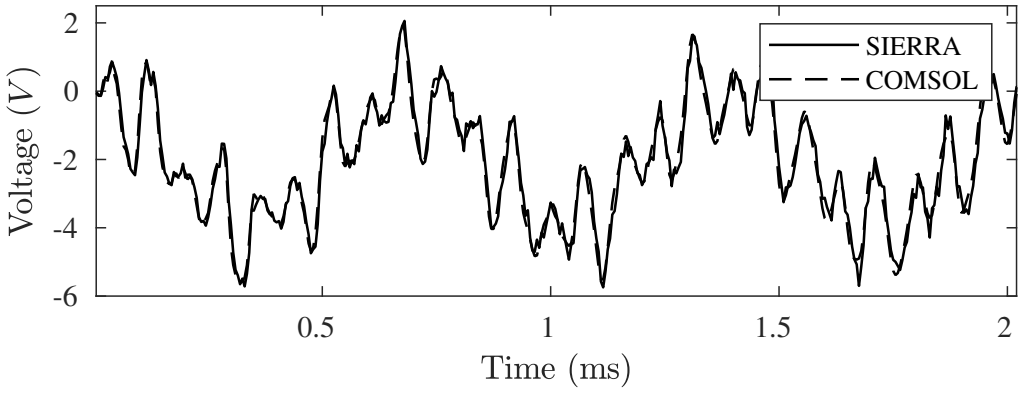

Figure 2-5. – Voltage time-history of V_{out} generated from COMSOL (dashed) and **Sierra/SD** (solid)

9.3. Frequency Response for Electric Field Induced Beam Deformation

The frequency response of the bimorph beam subjected to a prescribed frequency dependent voltage boundary condition is verified. The details of the bimorph beam are provided in Figure 1-1a and section 9.1. In this example, a voltage of 20 volts is prescribed to the top surface of the beam ($V_{in} = 20$) and the aluminum core is grounded. Like the transient example, we enforce an equipotential surface at the bottom surface of the beam (V_{out}) using a voltage rigid set. Stiffness proportional damping, with coefficient $\beta = 8e-7$, is prescribed to the piezoelectric blocks. The aluminum core is undamped.

To verify the direct frequency response solution method, we performed a frequency domain solve using an identical model with the FE software COMSOL [14] and compared its solution with the solution generated from **Sierra/SD**. Figure 3-6 presents the response amplitudes of the output node (see Figure 1-1a) for the following: 1) the transverse direction (z-axis), 2) the axial direction (x-axis), and 3) the voltage at V_{out}. We observe excellent agreement between **Sierra/SD** and COMSOL.

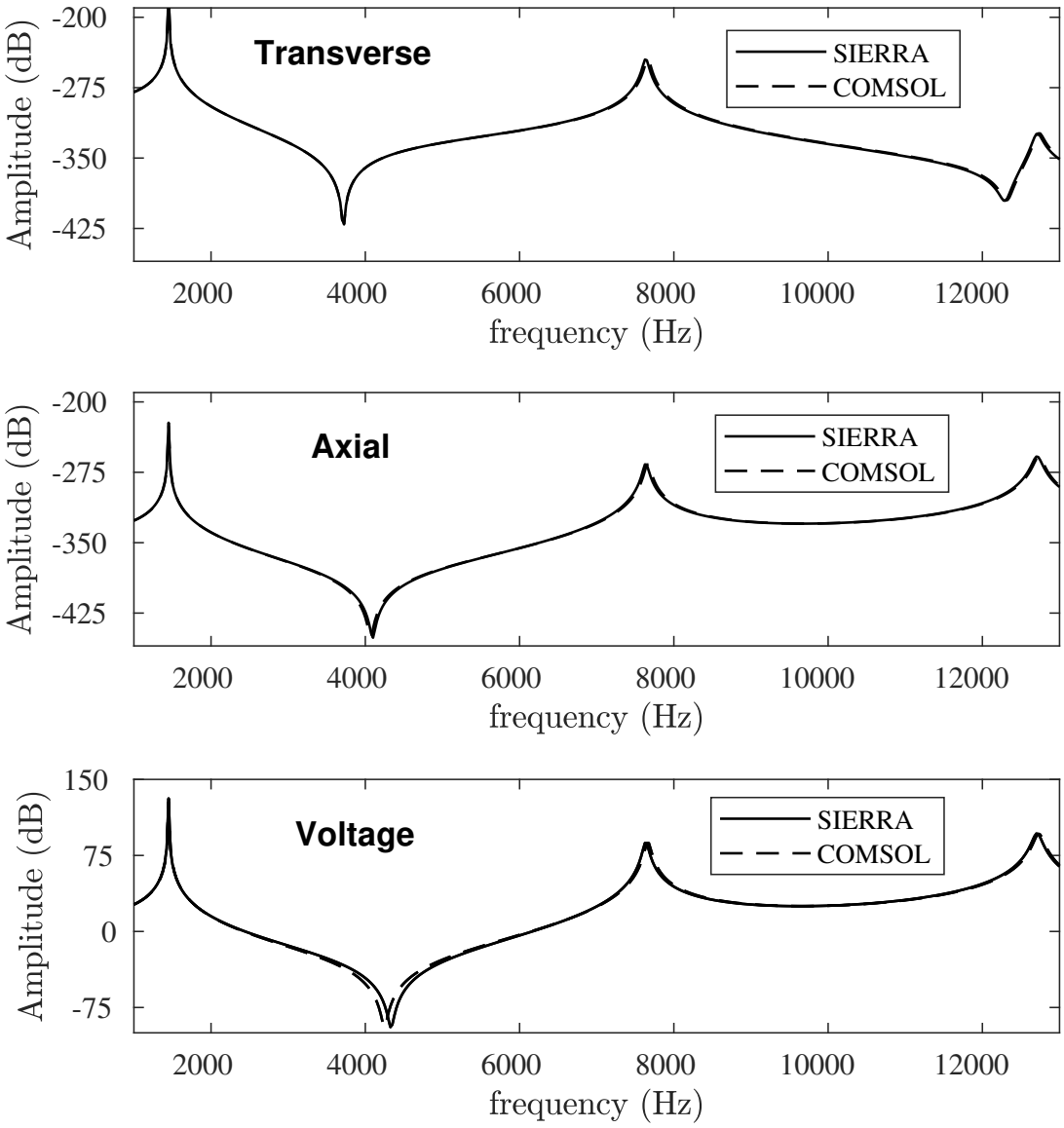

Figure 3-6. – The frequency response amplitudes generated from **Sierra/SD** and COMSOL for 1) the transverse direction (z-axis), 2) the axial direction (x-axis), and 3) the voltage at V_{out}

9.4. Eigenvalue Verification of a PZT5A Disc

This section verifies eigen-analysis for coupled electro-mechanical physics. The following verification is based on the example available in the referenced paper by Guo, Cawley, and Hitchings [25]. The specified problem is a PZT5A disc with D/T ratio of 20. The properties used are in Table 4-2. The disc is $40.10mm$ in diameter and $2.03mm$ thick, giving it a D/T ratio of 20, which is the same ratio as many transducers. The piezoelectric material is polarized in the Z (or 3) axis.

Table 4-2. – Properties of PZT-5A [25]

Property	Units	PZT-5A
ε_0	F/m	8.854×10^{-12}
$\varepsilon^S_{11}/\varepsilon_0$		916
$\varepsilon^S_{33}/\varepsilon_0$		830
c^E_{11}	$10^{10}N/m^2$	12.1
c^E_{33}	$10^{10}N/m^2$	11.1
c^E_{12}	$10^{10}N/m^2$	7.54
c^E_{13}	$10^{10}N/m^2$	7.52
c^E_{44}	$10^{10}N/m^2$	2.11
c^E_{66}	$10^{10}N/m^2$	2.26
e_{31}	C/m^2	-5.4
e_{33}	C/m^2	15.8
e_{15}	C/m^2	12.3
ρ	$10^3kg/m^3$	7.75

Thus the elasticity matrix:

$$C^E = 10^{10} \times \begin{bmatrix} 12.1 & 7.54 & 7.52 & 0 & 0 & 0 \\ 7.54 & 12.1 & 7.52 & 0 & 0 & 0 \\ 7.52 & 7.52 & 11.1 & 0 & 0 & 0 \\ 0 & 0 & 0 & 2.11 & 0 & 0 \\ 0 & 0 & 0 & 0 & 2.11 & 0 \\ 0 & 0 & 0 & 0 & 0 & 2.26 \end{bmatrix} N/m^2 \quad (9.4.1)$$

the dielectric matrix:

$$\varepsilon^S = 8.854 \times 10^{-12} \times \begin{bmatrix} 916 & 0 & 0 \\ 0 & 916 & 0 \\ 0 & 0 & 830 \end{bmatrix} F/m \quad (9.4.2)$$

and the piezoelectric coupling matrix:

$$e = \begin{bmatrix} 0 & 0 & 0 & 0 & 12.3 & 0 \\ 0 & 0 & 0 & 12.3 & 0 & 0 \\ -5.4 & -5.4 & 15.8 & 0 & 0 & 0 \end{bmatrix} C/m^2 \quad (9.4.3)$$

Figure 4-7. – PZT5A disc verification problem

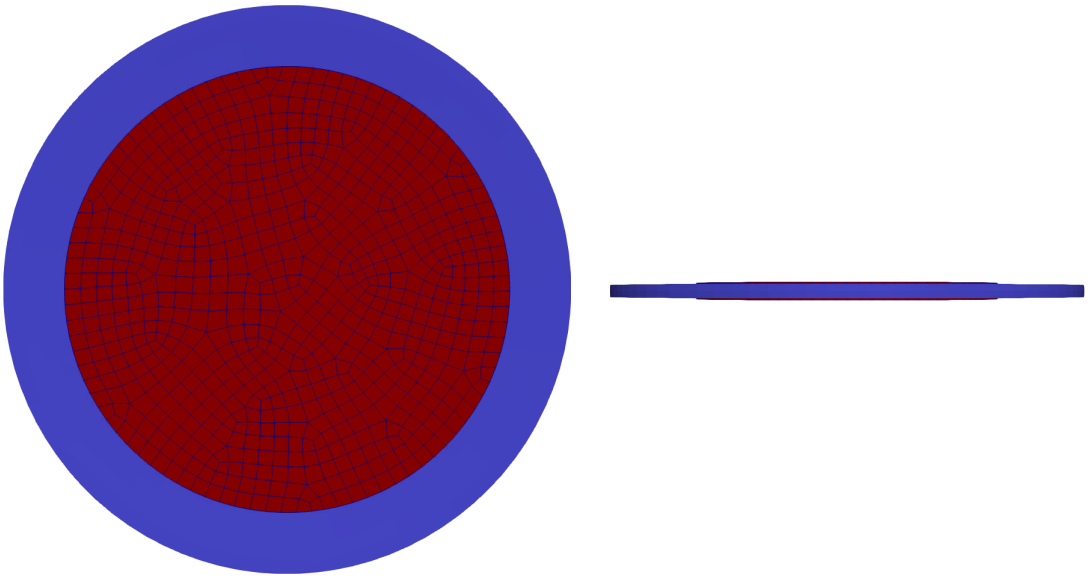

Figure 4-8. – First Radial Model of PZT-Disk. Literature 49.56 kHz, Sierra/SD 49.603 kHz. Red shows undeformed disk, blue shows radial extension mode shape.

The referenced paper [25] uses radially symmetric elements, thus only the radially symmetric modes are presented. Additionally, the authors claim that the bending modes can not be used to excite the mechanical system, so only the radial extension modes are presented [25] . **Sierra/SD** calculated all modes, including radially symmetric bending modes, as well as non-symmetric modes. In the referenced paper[25], the first two radial extensional modes occur at 49.56 kHz and 128.1 kHz. From the **Sierra/SD** runs, the first radial mode is represented by the 35th eigenpair, and has a natural frequency of 49.603 kHz. The second radial mode is represented by the 104th eigenpair, and has a natural frequency of 128.757 kHz. It should be noted that when the material is modeled as a purely elastic orthotropic material, with no consideration of the piezoelectric effect, these modes also appear at the same frequencies. In the pure elastic-orthotropic case, other modes change frequency, ordering and numbering, but the radial modes remain at the same frequency. Figure 4-8 shows the first radial extension mode calculated in **Sierra/SD**, and Figure 4-9 shows the second radial extension mode calculated in **Sierra/SD**.

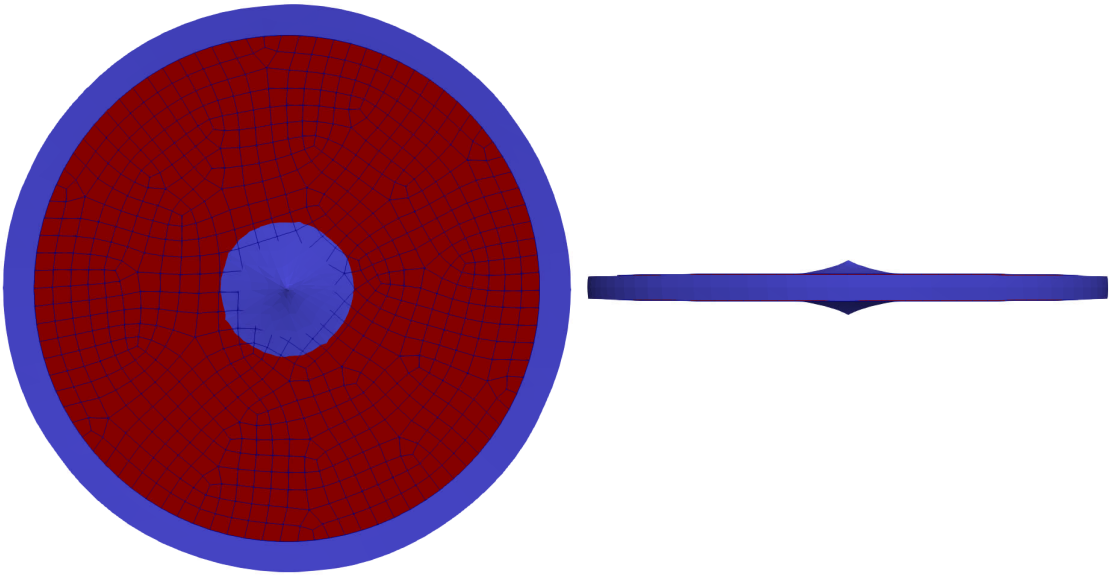

Figure 4-9. – First Radial Model of PZT-Disk. Literature 128.1 kHz, Sierra/SD 128.757 kHz. Red shows undeformed disk, blue shows radial extension mode shape.

10. LEGACY TESTS

10.1. Element Verification Tests

The purpose of this section is to report the verification calculations that have been performed on the **Sierra/SD** software. Test models and calculations were performed to ensure that **Sierra/SD** performs as required. Element patch tests are described, convergence studies for the elements are performed, and code to code comparisons are made to ensure that the software meets the requirements for analysis of hypersonic vehicles used in *Sandia National Labs*'s nuclear weapons program.

The tests described in this document were performed in support of release 1.1 of **Sierra/SD**. This covers capabilities for linear structural dynamics, linear statics, and linear transient dynamics. Specifications and requirements for this release are identified in the Requirements document,[36] and summarized in a technical report.[43]

Verification tests can never cover the full aspects of the software. Analysis shows that there are too many paths through the software to ever adequately cover all such paths (see *Beizer*[6] or *Myers*[40]). However, these tests are essential to provide confidence that with proper input, solutions to the fundamental equations of mechanics are solved properly.

Note that verification tests address mesh discretization indirectly.

10.1.1. Element Patch Tests

The element patch tests in this study are derived from MacNeal's monograph.[34] These tests are designed to ensure that the element formulations are independent of element orientation, and that the elements are capable of solving exactly the equations on which they are based. As a minimum, elements should be able to represent a constant strain field exactly since the linear shape functions of the elements are the minimum required to do this exactly.

All of the 2D and 3D elements in the **Sierra/SD** element library are tested. The 2D elements are: QuadT, Tria3, TriaShell, and Tria6. The 3D elements are Hex8b, Hex8, Hex20, Wedge6, Tet4, and Tet10. The 2D elements are tested using a membrane patch test and a bending plate patch test. The 3D elements are tested using the solid patch test. These patch tests are defined in *MacNeal*.[34]

All the 2D elements pass the membrane and bending patch tests. All the 3D elements pass the solid patch test. These patch test problems are located in the Salinas_test repository

in the Salinas_test/patch_tests subdirectory. The results for the patch tests are shown in Table 1-1.

Table 1-1. – Patch Test Results.

Element Type	Patch Test		
	Membrane	Bending	Solid
QuadT	Passed	Passed	N/A
Tria3	Passed	Passed	N/A
TriaShell	Passed	Passed	N/A
Tria6	Passed	Passed	N/A
Hex8	N/A	N/A	Passed
Hex8b	N/A	N/A	Passed
Hex20	N/A	N/A	Passed
Wedge6	N/A	N/A	Passed
Tet4	N/A	N/A	Passed
Tet10	N/A	N/A	Passed

10.1.2. Element Accuracy Tests

Accuracy tests are designed to stress test elements. These are not convergence tests. The purpose of the test is to provide information about how badly the element performs in common (but under meshed) environments. It can be noted in the results below that `Tet4` elements are way too stiff in almost all loadings. This is expected, and the test results are provided to help analysts determine the applicability of this element for their analysis. Below are test results for the accuracy tests (Tables 8 through 15 of *MacNeal* [34]). All tabulated results are the ratio of the numerical solution to the exact solution, i.e. a value of 1.00 is a perfect result. The test problems are described and illustrated in the reference, Figures 4 through 10.

The first test from *MacNeal* is a straight beam with a length of 6.0, an in-plane cross sectional dimension of 0.2 and an out of plane cross sectional dimension of 0.1. There is a single element at any given point along the length of the beam and total of 6 elements along the length of the beam. The Young's Modulus, $E = 10^7$, the Poisson ratio, $\nu = 0.30$, and the loading is a unit force at the free end of the beam. Reported table values refer to displacement at the loaded tip of the beam. Tables 1-2, 1-3 and 1-4 show results for rectangular, trapezoidal, and parallelogram shaped elements, respectively.

In the tables Hex8 denotes the Hex8U element.

Table 1-5 below shows results for a curved beam, also with a 6 by 1 element mesh. The inner radius is 4.12, the outer radius 4.32, the arc 90 degrees, and the thickness 0.1. The Young's Modulus is $E = 10^7$, the Poisson ratio is 0.25. The tip load is of unit magnitude.

Table 1-2. – Straight Beam – *Rectangular* Elements.

Element Type	Extension	In Plane	Out of Plane	Twist
Hex20	0.994	0.970	0.961	0.904
Hex8b	0.988	0.978	0.973	0.892
Hex8	0.986	9.22	2.50	89.2
Tet10	0.998	0.960	0.959	0.910
Tet4	0.979	0.0219	0.0119	0.00264
Wedge6	0.991	0.0326	0.0882	0.0257
QuadT	0.839	1.05	0.979	0.704
Tria6	0.999	1.00	0.988	0.716
Tria3	1.01	1.06	0.978	0.704
TriaShell	0.966	0.224	.0978	0.720

Table 1-3. – Straight Beam – *Trapezoidal* Elements.

Element Type	Extension	In Plane	Out of Plane	Twist
Hex20	0.977	0.731	0.714	0.863
Hex8	0.988	0.734	0.307	51.4
Hex8b	1.009	0.0475	0.03	0.623
Tet10	0.999	0.277	0.208	0.667
Tet4	0.978	0.0144	0.00691	0.00755
Wedge6	0.992	0.0187	0.0302	0.0546
QuadT	1.00	0.559	0.980	0.0226
Tria6	0.999	1.00	0.988	0.716
Tria3	0.999	0.733	0.980	0.705
TriaShell	0.996	0.208	0.979	0.721

Table 1-6 shows results for a cantilever beam that twist a total of 90 degrees along the length of the beam. The beam length is 12.0, the in-plane cross sectional dimension 0.32 and the out of plane cross sectional dimension is 1.1. The Young's Modulus is 29.0e6 and the Poisson ratio 0.22. The tip load is of unit magnitude.

Tables 1-7 through 1-10 show results for a rectangular plate with either simply supported or clamped boundary conditions and either a point load of $4x10^4$ at the center of the plate or a uniform pressure of $1x10^4$ over the plate. The plate has either a width-to-height aspect ratio of 1.0 or 5.0. The plate height is 4.0. The plate thickness is 0.01 for solid elements (Hex20, Hex8, Hex8b, Tet10, Tet4, and Wedge6) and 0.0001 for shell elements (QuadT, Tria6, Tria3, and TriaShell). The Young's Modulus is $1.7472x10^7$ and the Poisson ratio 0.3. The quantity N in these tables denotes the number of node spaces on half the edge of the plate. If the element has midside nodes, e.g., the Hex20, Tet10, or Tria6, then the number of elements along this portion of the edge of the plate is half the value of N. These tests are unsuitable for the Tet elements (Tet10 and Tet4) as the aspect ratios of the elements is

Table 1-4. – Straight Beam Tests – *Parallelogram* Elements.

Element Type	Extension	In Plane	Out of Plane	Twist
Hex20	1.01	0.404	0.280	0.758
Hex8	0.983	1.60	0.943	38.68
Hex8b	0.977	0.623	0.528	1.27
Tet10	0.998	0.289	0.213	0.744
Tet4	0.981	0.0122	0.00708	0.00779
Wedge6	0.991	0.0148	0.0558	0.154
QuadT	0.985	0.407	0.981	0.141
Tria6	0.998	0.816	0.988	0.716
Tria3	1.00	0.535	0.978	0.702
TriaShell	0.996	0.190	0.978	0.720

Table 1-5. – Curved Beam Tests.

Element Type	In Plane	Out of Plane
Hex20	0.874	0.937
Hex8	7.06	22.8
Hex8b	0.879	0.952
Tet10	0.839	0.776
Tet4	0.0174	0.00738
Wedge6	0.0255	0.0557
QuadT	1.09	0.867
Tria6	.167	0.276
Tria3	1.07	0.864
TriaShell	0.185	0.895

large due to the small thickness. Nastran's Tet10 performs in a similar fashion to **Sierra/SD**'s Tet10 on the remaining problems in this section.

Table 1-11 shows the results for the Scordelis-Lo Roof tests. This test involves a curved plate. The radius of curvature is 25.0 and the associated arc 80 degrees. The length of the plate is 50.0 and the thickness 0.25. The straight edges of the plate are free and the curved edges are constrained to not to move in the plane in which the curved edge is contained. The loading is a traction in the z-direction on the face of the plate of magnitude 90.0 per unit area. The Young's Modulus is 4.32e8 and the Poisson ratio 0.0. The quantity N still represents the number of node spaces along half of one of the edges of the plate.

Table 1-12 gives the results for the spherical shell tests. This is a semi-spherical shell with a hole cut out of the top. The angular size of the hole is 36 degrees. The radius is 10.0. The thickness is 0.04. The Young's Modulus is 6.825e7. The Poisson ratio is 0.3. The loading is made up of four equally spaced radial point loads of magnitude 2.0 at the equator. Two of these point loads are radial inward and two are radially outward. The quantity N

Table 1-6. – Twisted Beam Tests.

Element Type	In Plane	Out of Plane
Hex20	.996	0.987
Hex8	14.3	11.0
Hex8b	0.744	0.740
Tet10	1.01	1.01
Tet4	0.0949	0.162
Wedge6	0.0846	0.243
QuadT	.998	1.01
Tria6	19.7	15.5
Tria3	30.9	24.6
TriaShell	11.4	8.99

Table 1-7. – Rectangular Plate with Simple Supports and Uniform Pressure Load, Aspect Ratio 1.0

Element Type	N=2	N=4	N=6	N=8
Hex20	0.0167	0.691	0.831	0.976
Hex8	0.220	0.904	2.02	3.11
Hex8b	0.04	0.412	0.782	0.92
Tet10	0.00116	0.00331	0.00752	0.015
Tet4	4.42e7	8.00e6	4.10e5	1.29e4
Wedge6	0.228	0.0824	0.0568	0.0543
QuadT	0.966	0.922	0.997	0.998
Tria6	1.01	0.974	0.987	0.992
Tria3	0.978	0.992	0.997	0.998
TriaShell	0.958	0.987	0.994	0.997

represents the number of node spaces along a quarter of one of the edges of the shell.

The next table (Table 1-13) shows the results for the thick walled cylinder tests. This is a donut shaped, thick plate of thickness 1.0, inner radius 3.0, and outer radius 9.0. The Young's Modulus is 1000, and the Poisson ratio is either 0.49, 0.499, or 0.4999. The loading is a unit radial pressure on the inner radius. The mesh has five elements along the radius at 10 degree intervals and one element through the thickness, for a total of 180 elements.

Table 1-8. – Rectangular Plate with Simple Supports and Uniform Pressure Load, Aspect Ratio 5.0

Element Type	N=2	N=4	N=6	N=8
Hex20	0.503	0.649	1.04	1.02
Hex8	0.130	0.515	19.21	2.03
Hex8b	0.024	0.302	1.10	0.917
Tet10	0.000702	0.00181	0.00424	0.00852
Tet4	1.57e7	2.52e6	1.28e5	4.05e5
Wedge6	0.179	0.0977	0.0474	0.0470
QuadT	0.978	0.993	0.994	0.999
Tria6	0.658	1.02	1.01	1.00
Tria3	0.945	0.991	0.997	0.999
TriaShell	0.960	0.995	0.999	0.999

Table 1-9. – Rectangular Plate with Clamped Supports and Concentrated Load, Aspect Ratio 1.0

Element Type	N=2	N=4	N=6	N=8
Hex20	0.00106	0.072	0.553	0.822
Hex8	0.120	0.578	1.33	2.36
Hex8b	0.0195	0.246	0.614	0.824
Tet10	0.00110	0.00329	0.00624	0.0109
Tet4	1.46e6	2.31e5	1.15e4	3.52e4
Wedge6	0.0037	0.0186	0.0373	0.0561
QuadT	1.08	1.03	1.02	1.01
Tria6	1.06	1.17	1.01	1.01
Tria3	0.778	1.03	1.02	1.01
TriaShell	0.860	1.02	1.01	1.01

Table 1-10. – Rectangular Plate with Clamped Supports and Concentrated Load, Aspect Ratio 5.0

Element Type	N=2	N=4	N=6	N=8
Hex20	8.51e4	0.0396	0.220	0.374
Hex8	0.0362	0.138	0.551	0.992
Hex8b	0.00585	0.083	0.247	0.415
Tet10	3.39e4	0.00141	0.00282	0.00475
Tet4	2.26e7	3.60e6	1.80e5	5.61e5
Wedge6	0.00320	0.0181	0.0241	0.0297
QuadT	0.613	0.919	1.00	1.01
Tria6	0.606	0.910	0.998	1.01
Tria3	0.603	0.915	1.00	1.01
TriaShell	0.666	0.945	1.01	1.02

Table 1-11. – Scordelis-Lo Roof Tests.

Element Type	N=2	N=4	N=6	N=8	N=10
Hex20	0.0583	0.276	0.645	0.870	0.956
Hex8	.563	1.43	2.17	2.73	3.16
Hex8b	0.125	0.574	0.889	0.967	0.981
Tet10	0.0198	0.0526	0.0770	0.101	0.149
Tet4	0.00599	0.0108	0.0196	0.0333	0.0472
Wedge6	0.017	0.0289	0.0642	0.08	0.093
QuadT	1.58	1.13	1.06	1.02	1.00
Tria6	1.45	1.13	1.06	1.02	1.00
Tria3	1.45	1.13	1.06	1.02	1.00
TriaShell	1.35	1.04	1.01	0.995	0.984

Table 1-12. – Spherical Shell Tests.

Element Type	N=2	N=4	N=6	N=8	N=10	N=12
Hex20	–	0.00129	0.00662	0.0209	0.0500	0.0974
Hex8	0.00573	0.0547	0.133	0.238	0.371	0.531
Hex8b	.000303	0.0104	0.056	0.162	0.319	0.491
Tet10	–	2.21e4	3.83e4	6.73e4	0.00107	0.00167
Tet4	2.22e5	3.18e5	3.78e5	4.46e5	5.62e5	6.94e5
Wedge6	0.0153	0.00447	0.00645	0.00660	0.00708	0.00781
QuadT	0.0423	0.0834	0.263	0.502	0.697	0.820
Tria6	0.0194	0.0879	0.263	0.502	0.697	0.819
Tria3	0.0445	0.0891	0.266	0.499	0.693	0.816
TriaShell	0.436	0.199	0.226	0.378	0.560	0.708

Table 1-13. – ThickWalled Cylinder Tests.

Element Type	$\nu = .4900$	$\nu = .4990$	$\nu = .4999$
Hex20	1.03	1.04	1.04
Hex8	0.445	0.437	0.406
Hex8b	0.437	0.437	0.437
Tet10	0.444	0.442	0.442
Tet4	0.393	0.356	0.349
Wedge6	0.408	0.399	0.398
QuadT	0.416	0.414	0.413
Tria6	0.438	0.436	0.436
Tria3	0.419	0.417	0.417
TriaShell	0.425	0.423	0.423

10.1.3. Element Convergence Tests

Mesh convergence studies establish confidence that the accuracy of the solution increases as the mesh is refined. They also establish the rate of convergence of the solution. They may be performed with or without a known analytical solution for the problem. Fortunately, for many structural dynamics problems, analytic solutions are available.

In structural dynamics, unstructured grids are necessarily used. While standard Richardson extrapolation[44] is not directly applicable to unstructured meshes, related methods can be used to determine truncation error (see *Alvin*[3] for example). Some detail is provided in Appendix 13.

Convergence testing is used either to explore the properties of newly designed elements or to assure the adequacy of a candidate mesh. Use of it to verify the correct implementation of an element is not universally done; instead the patch test and the accuracy tests are considered sufficient. Convergence testing is performed as part of this verification suite to provide consistency with verification efforts in other *Sandia National Labs* codes.

In its simplest form, convergence analysis involves performing an analysis with at least three levels of mesh fineness and assessing the rate at which the error goes to zero. For the elements under consideration, convergence is known to be geometric: quadratic for the low order elements and quartic for the high order elements once the elements are small enough.

The convergence tests for the Hex8 elements was the static deformation of a cantilevered beam. The meshes employed are shown in Figure 1-1 and the appropriate plot of convergence error is show in Figure 1-2. It was seen that the convergence slope increased in magnitude as the meshes were refined and that for both the fully integrated and the selectively integrated element, the slopes found through this numerical experiment approximate the theoretical value of -2. Fine meshes are required to achieve this geometric convergence. Requiring convergence at a single point was a mistake.

Element convergence for Hex20 and Tet10 elements was preformed focusing on the calculated first eigenvalues. The resulting convergence plot for the Hex20 is shown in Figure 1-3. Here we see that the convergence rate is -3.8, close to the theoretical value.

Refining a general mesh through sectioning to create new elements all of approximately the same size increases the aspect ratios compared to the coarser mesh. This prevents standard convergence tests of Tet elements. A BCC mesh can be uniformly refined, but it was too difficult to implement. Instead several independent meshes were created. The resulting slope of the log-log error plot (shown in Figure 1-4 is the theoretical value, -4.

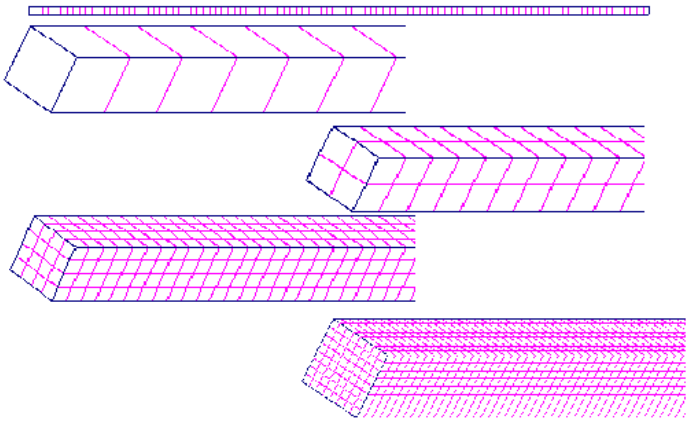

Figure 1-1. – Meshes for convergence test for Hex8 elements.

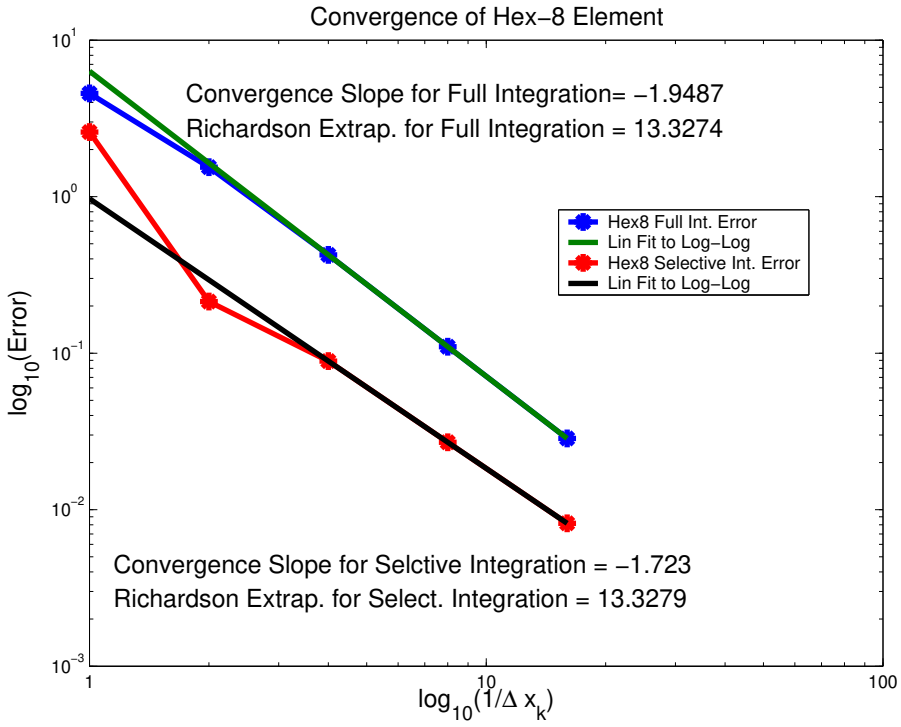

Figure 1-2. – As the meshes are progressively refined, the slope of the log-log plot of the error approaches -2, as predicted by theory.

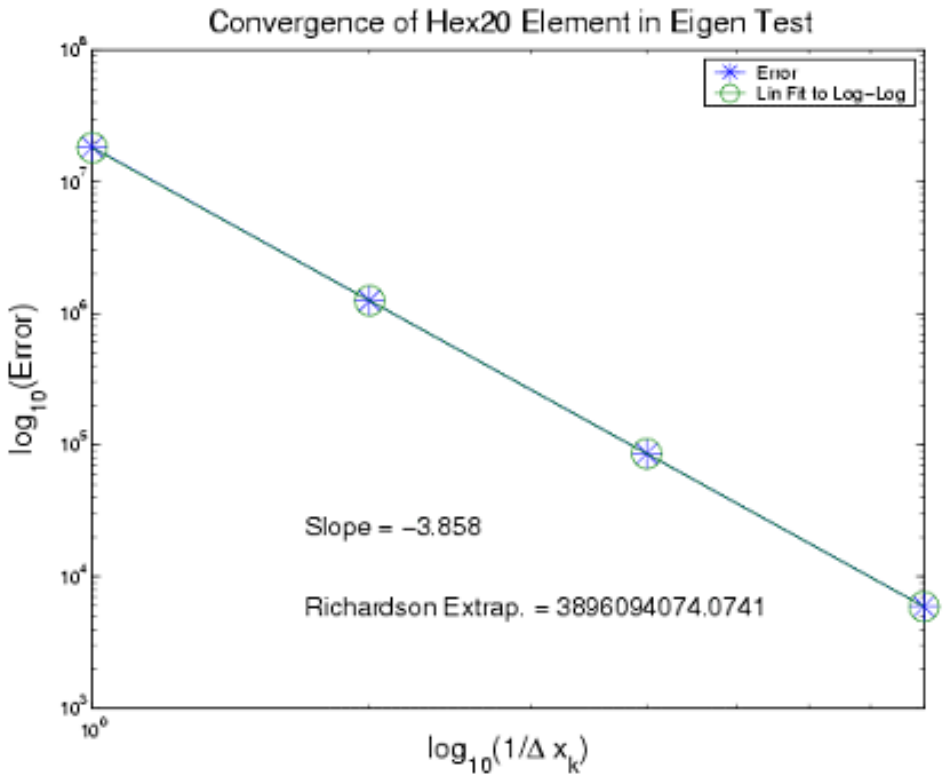

Figure 1-3. – The convergence plot of the Hex20 element for the first eigenvalue shows a slope close to the theoretical value of -4.

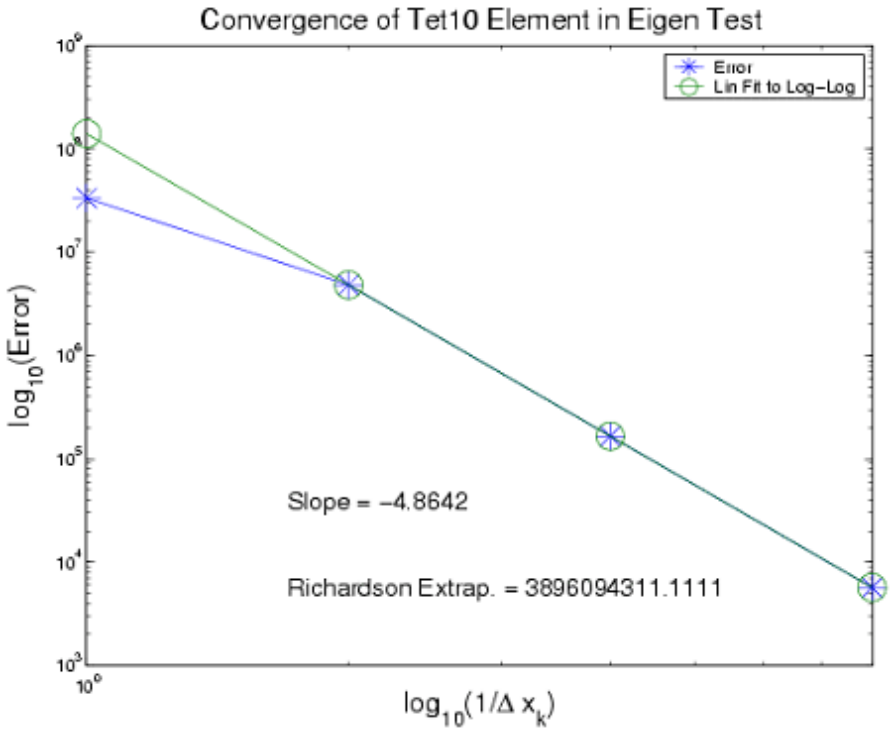

Figure 1-4. – The convergence plot of the Tet10 element for the first eigenvalue shows a slope close to the theoretical value of -4

The convergence rates of the various elements are listed in Table 1-14.

Table 1-14. – Element Convergence Rates.

Element Type	Ideal Rate	Measured Rate	Comments
Hex8	2	2	Beta=1.0, Alpha=$1-\sqrt{1-2\nu}$
Tria3	2		
TriaShell	2		
QuadT	2		derived from Tria3
Quad8T	2		derived from Tria3. First order.
Beam2	2		
Tet4	2		
Hex20	4	4	using eigen analysis
Tet10	4	4	using eigen analysis
Tria6	2		derived from Tria3. First order.

10.1.4. RBE3 - comparison with Nastran

Verification of the RBE3 pseudo-element necessarily requires comparison with Nastran, because no physical model exists. The RBE3 is designed to function like the Nastran pseudo element. A simple model was constructed for evaluation of an RBE3 link. The structure consisted of a cube placed on the end of a beam. The beam terminates in the center of the cube, and is connected to the eight corners of the cube with an RBE3 as illustrated in Figure 1. The model is named `BoxOnBarRbe3.inp`. The test is `Salinas_rtest/test_tool/fast_regression_tests/mpc/BoxOnBarRbe3.test`.

There are slight differences in the beam models used by Nastran and by **Sierra/SD**. A summary of the modes is included in the table. As can be seen in the table, the agreement is good. All the modes of the structure are preserved by the RBE3.

#	Nastran Frequency	**Sierra/SD** Frequency	Description
1	2354.8	2354.4	1st bending
2	2354.8	2354.4	1st bending
3	6833	6832.7	Pogo Stick, axial mode
4	9942	9939.4	2nd bending
5	9942	9939.4	2nd bending
6	13697	13335	torsion
7	22367	22365	hex deformations
	$> 20,000$	$> 20,000$	hex deformations

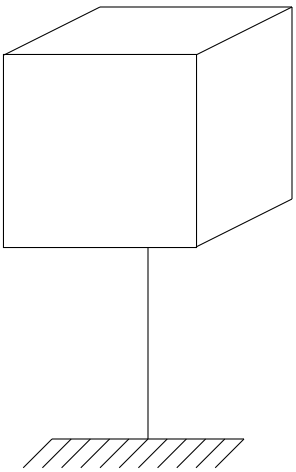

Figure 1-5. – Box on a Bar test object.

10.1.5. Verification of hexshells

In this section we list the results of several verification examples for hexshell elements. These verification examples were taken from Professor Carlos Felippa, the developer of the element, (see reference[23]). The goal here was to reproduce the results obtained in that report.

10.1.5.1. Example 1

This example corresponds to section 9.5 in the report,[23] and consists of a circular ring subjected to equal and opposite forces acting along the vertical direction. The exact solution for this problem is given in both reference[57] and reference[53] as

$$\frac{\pi^2 - 8}{4\pi} \frac{PR^3}{EI} \tag{10.1.1}$$

We note that this solution is the total change in diameter for the ring.

By symmetry a quarter ring with appropriate boundary conditions suffices. We note three details for comparing the results to the exact solution. First, the exact solution as given is for the total change in diameter for the ring. For a quarter ring, this result is halved. Second, since the ring is cut at the top surface and we are applying a point load on the symmetry plane, the applied load P will produce twice the deflection in a quarter ring as in the full ring. This is explained in more detail in reference.[53] However, since there is a need to both divide by two and multiply by two, these factors effectively cancel one another out, and thus equation 10.1.1 is the solution for comparison in the case of a quarter ring.

The results obtain by **Sierra/SD** are compared with those of Dr. Felippa in Table 1-15.

For this example, Dr. Felippa also reported results for a two-ply case. Since we do not have an analytical solution to compare with, and since the reported results are normalized by

Table 1-15. – Normalized Deflections for the Pinched Composite Ring.

N_e	$\frac{R}{h} = 20$ Felippa	$\frac{R}{h} = 20$ **Sierra/SD**	$\frac{R}{h} = 100$ Felippa	$\frac{R}{h} = 100$ **Sierra/SD**
4	.5746	.5771	.0062	.062
6			.4322	.4376
8	.9582	.9631	.7813	.7971
16	.9896	.9947	.9659	.9886
32	.9955	1.00072	.9753	.9981

the exact solution, we have no reference point and thus we did not run the two-ply case. We did, however, run a two-ply example where the modulus and Poisson's ratio were the same in both plies. The results were the same as running a single ply with those same material properties. This provided a weak verification of the multi-ply implementation.

10.1.5.2. Example II

This was the pinched cylindrical shell example (section 9.6). Only one eighth of the shell was considered. The computed results were divided by four to account for the fact that the load was applied to a quarter section. The results are shown in Table 1-16.

Table 1-16. – Normalized Deflections for the Pinched Cylindrical Shell.

mesh	Felippa	**Sierra/SD**
4x4	.0762	.1
8x8	.2809	.45
16x16	.5366	.81
32x32	.8029	.87
128x128		.897

10.1.5.3. Example III. Scordelis-Lo Roof

A quarter of the roof is modeled. The applied load is a gravity load. The boundary conditions at the rigid diaphragms were incorrectly reported in.[23] The correct ones are $u_x = u_z = 0$. With these conditions, the results as shown in Table 1-17 agree well with the expected values.

Table 1-17. – Normalized Deflections for Scordelis-Lo Roof example.

mesh	Carlos	**Sierra/SD**
2x2	1.2928	1.29
4x4	1.0069	1.011
8x8	.9844	.984
16x16	.9772	.979

10.1.5.4. Example IV

This is the twisted beam model. The normalized results, compared with those of Carlos, are given in Table 1-18.

Table 1-18. – Normalized Deflections pretwisted beam example.

mesh	Carlos		**Sierra/SD**	
	in plane	out of plane	in plane	out of plane
1x6	1.0257	.9778	1.014	.929
2x12	1.0041	.9930	.985	.975

10.1.6. Verification of TriaShells for Composite Modeling

Laminate composites modeling in **Sierra/SD** is implemented by coupling Allman's triangle[2] with the DKT triangle.[5] Combining these elements together does not capture the coupling that can occur between bending degrees of freedom and membrane degrees of freedom. An additional stiffness that couples these degrees of freedom is generated as documented in References[19] and.[1]

In the next sections we list the results of several verification examples for composite TriaShell elements.

10.1.6.1. Example 1

The first verification example is taken from Reference.[19] A rectangular plate with dimensions 6" x 1" x 0.005" is modeled using 2 triangular elements (Figure 1-6). In figure 1-6, the left side is clamped (nodes 1 and 3) while node 4 has a unit load in the positive z-direction, and node 2 has a unit load in the negative z direction. Each element is composed of 3 layers. Each layer has the following orthotropic material properties: $E_1 = 10e6$, $E_2 = 0.3e6$, $\nu_{12} = 0.25$, and $G_{12} = 4e6$. The fiber orientation for each layer is $45°, 0°$, and $-45°$, respectively.

This mesh is refined 6 times to create 6 other test cases. The convergence of the displacements and rotations at nodes 2 and 4 is compared with the STRI3 element in

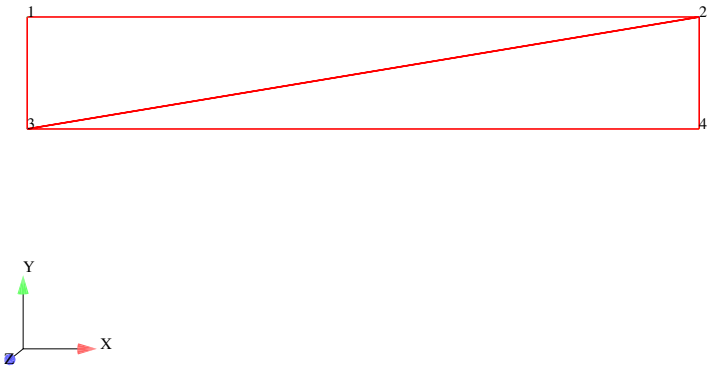

Figure 1-6. – Two Element Test.

ABAQUS as shown in figures 1-7 through 1-12 These figures show that the convergence of the Allman/DKT element is good. Both elements have similar convergence rates as the mesh is refined with the exception of the drilling degree of freedom. Figures 1-13 and 1-14 compare the x, y, z, θ_x, θ_y, and θ_z displacements at nodes 2 and 4 (see figure 1-6. Again, the Allman/DKT element compares well with the STRI3 element as the mesh is refined. The exception is the drilling degree of freedom.

The 4th mesh refinement model is stored as a test in the "`Salinas/test_tool/fast_regression_tests/triashell`" subdirectory, and is named "`mesh4_test`".

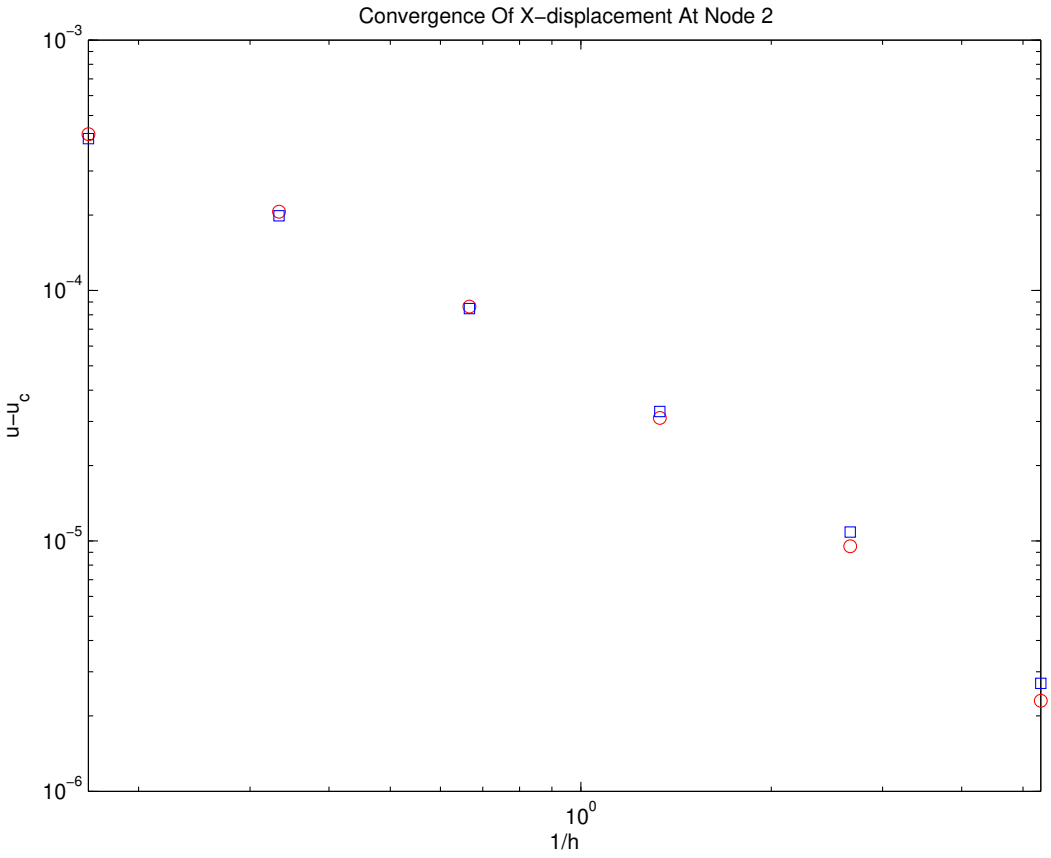

Figure 1-7. – Comparison Of X-displacement Between **Sierra/SD** and ABAQUS

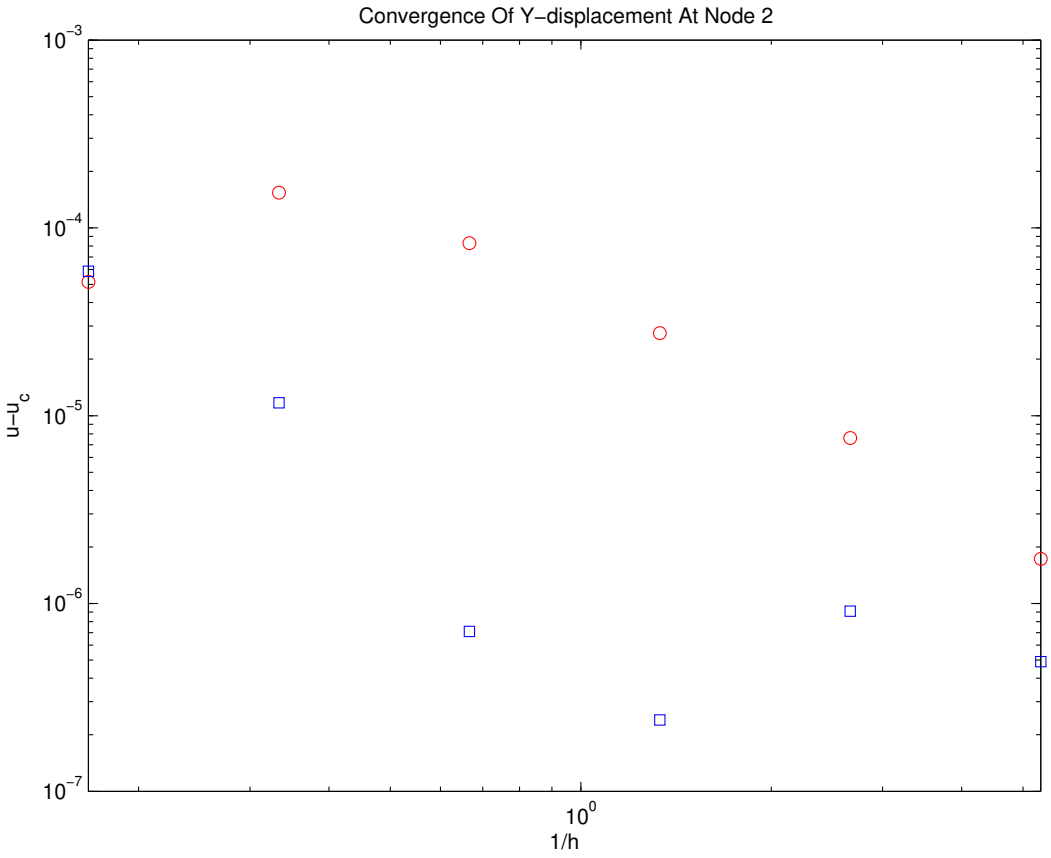

Figure 1-8. – Comparison Of Y-displacement Between **Sierra/SD** And ABAQUS

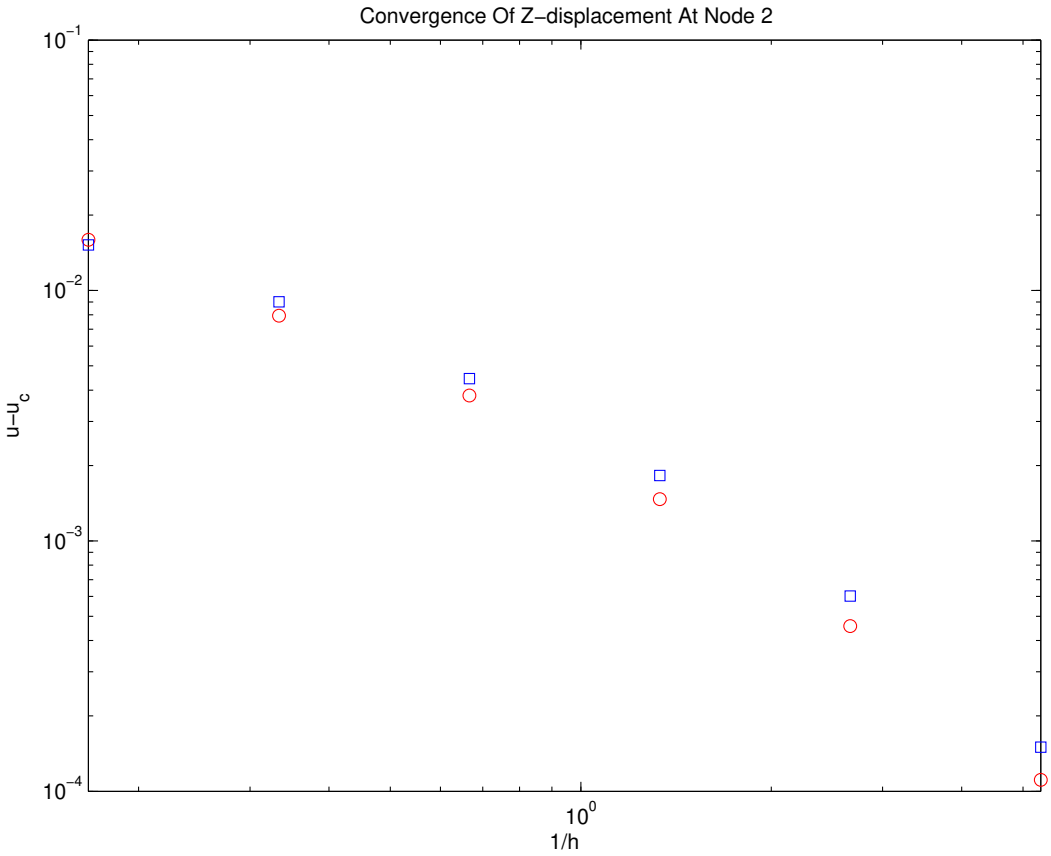

Figure 1-9. – Comparison Of Z-displacement Between **Sierra/SD** And ABAQUS

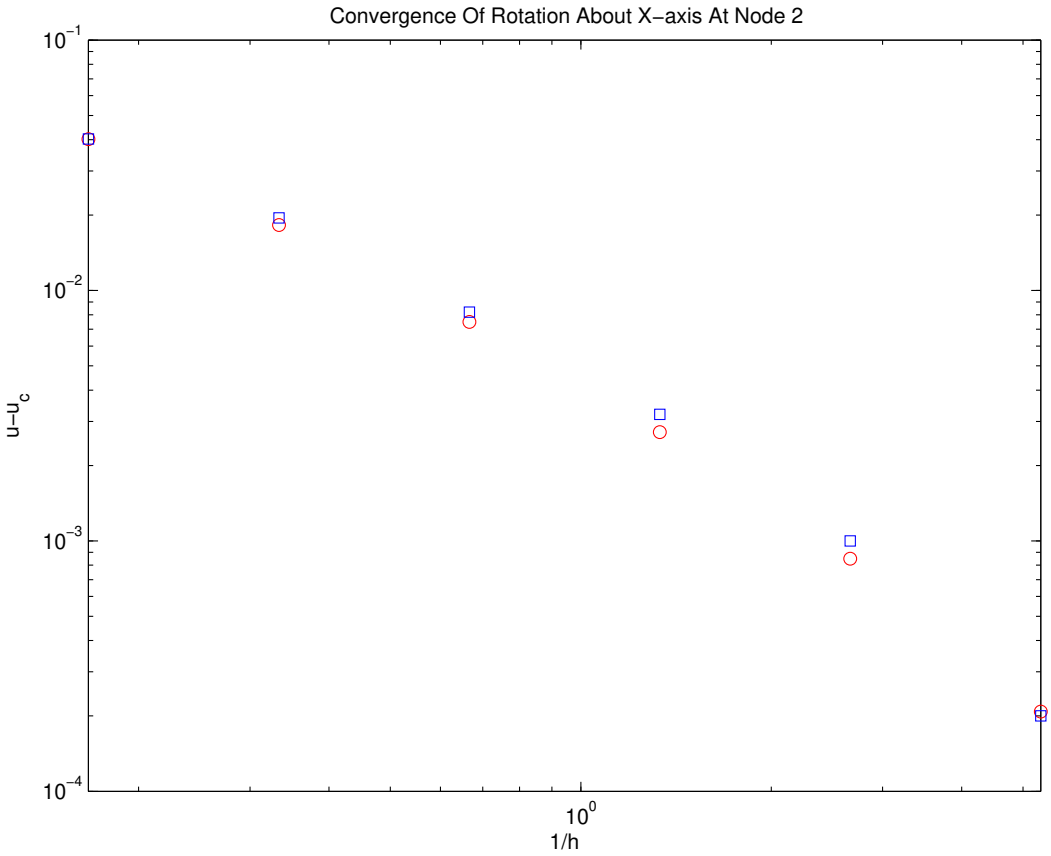

Figure 1-10. – Comparison Of Rotation About X-axis Between **Sierra/SD** And ABAQUS

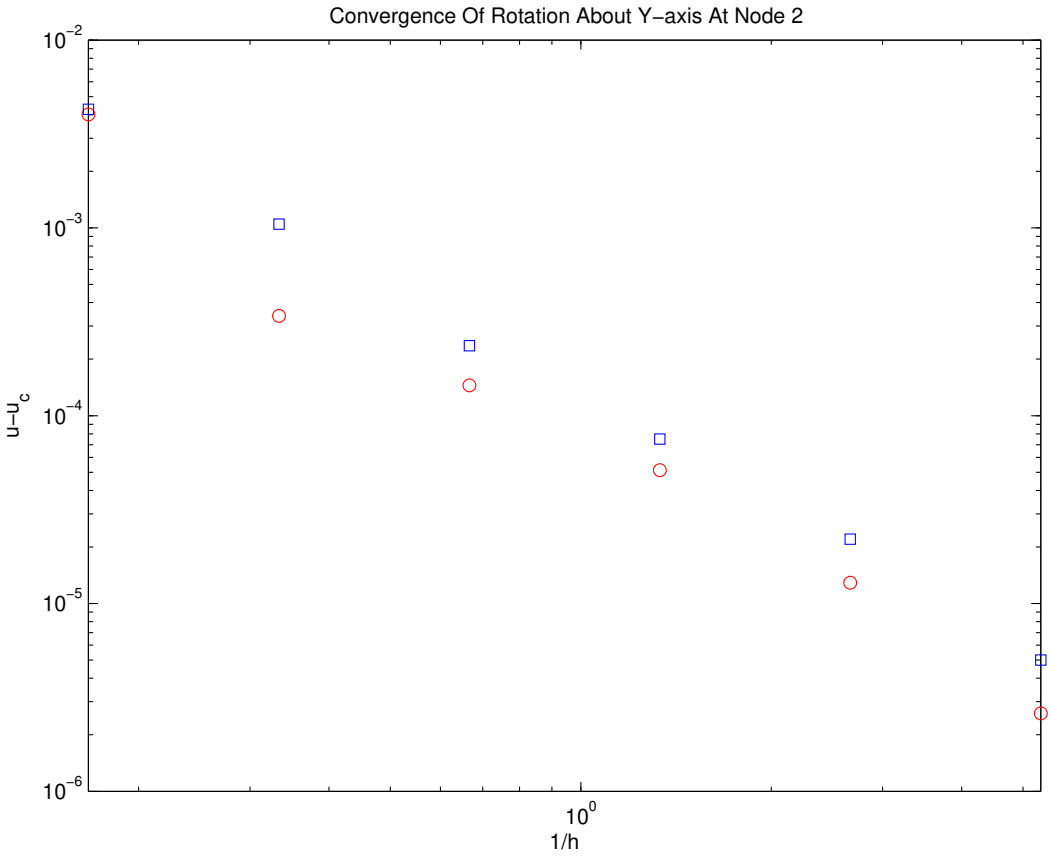

Figure 1-11. – Comparison Of Rotation About Y-axis Between **Sierra/SD** And ABAQUS

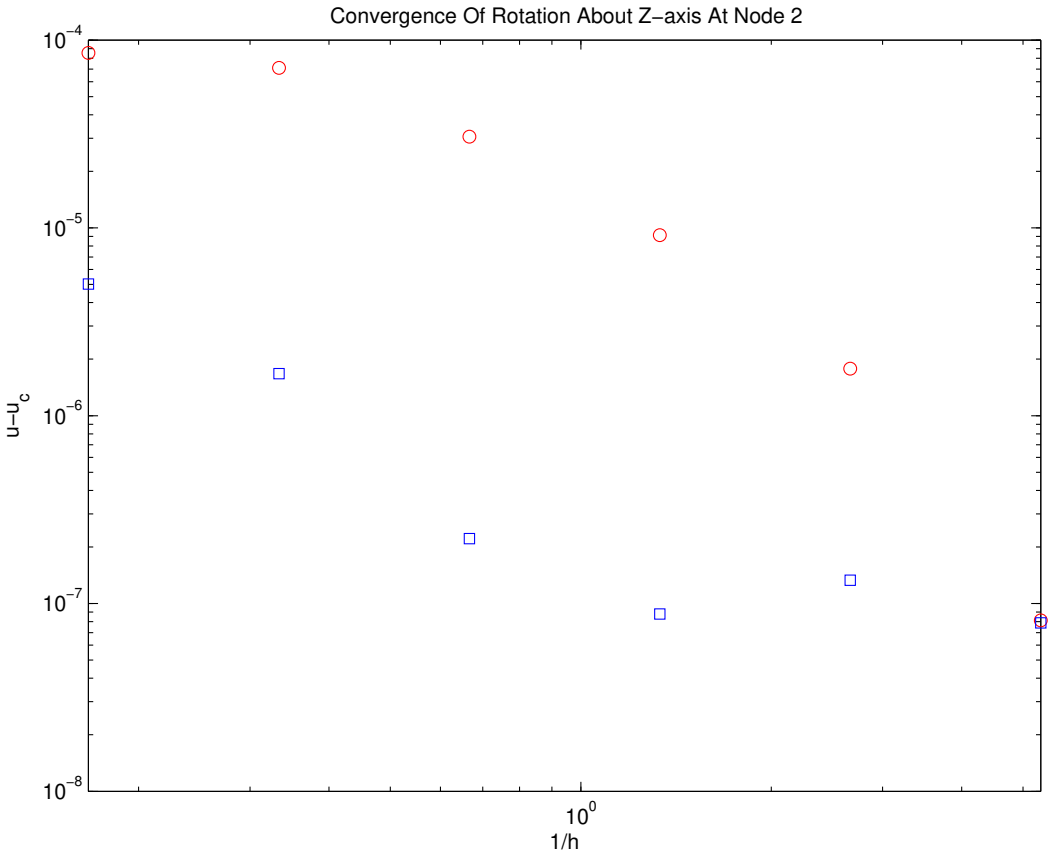

Figure 1-12. – Comparison Of Rotation About Z-axis Between **Sierra/SD** And ABAQUS

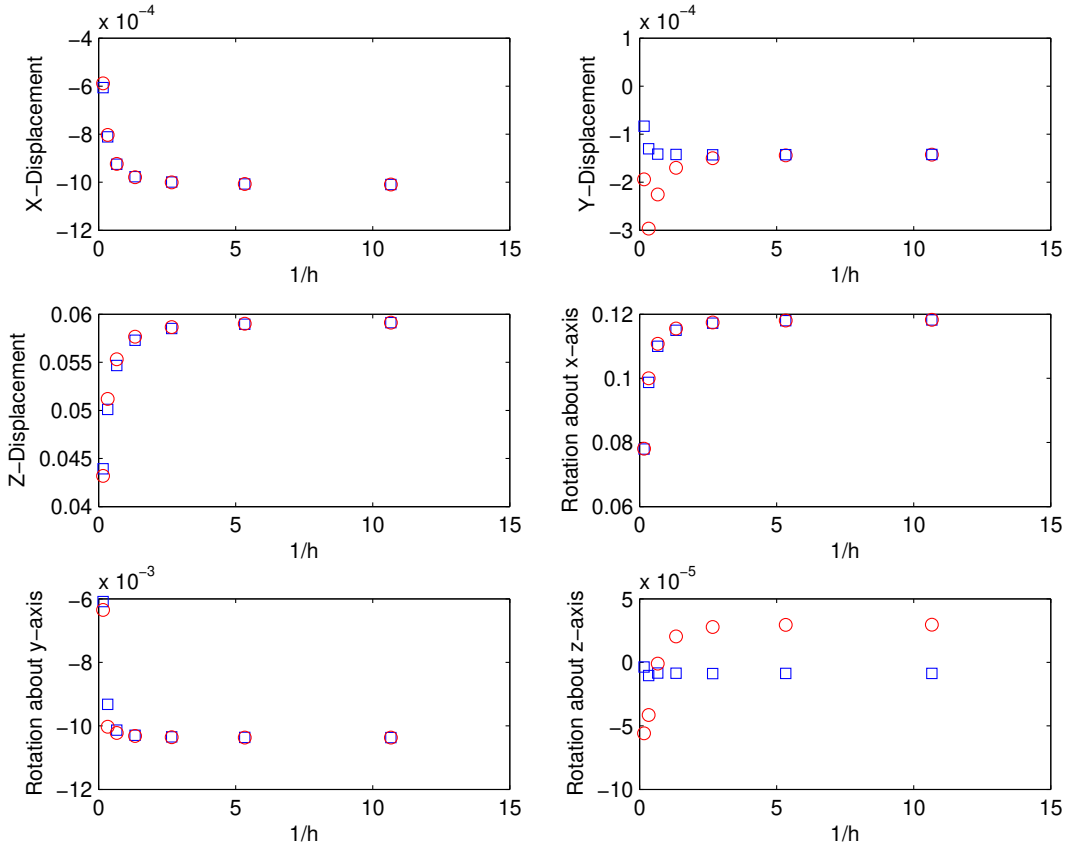

Figure 1-13. – Convergence Of Displacements and Rotations At Node 2.

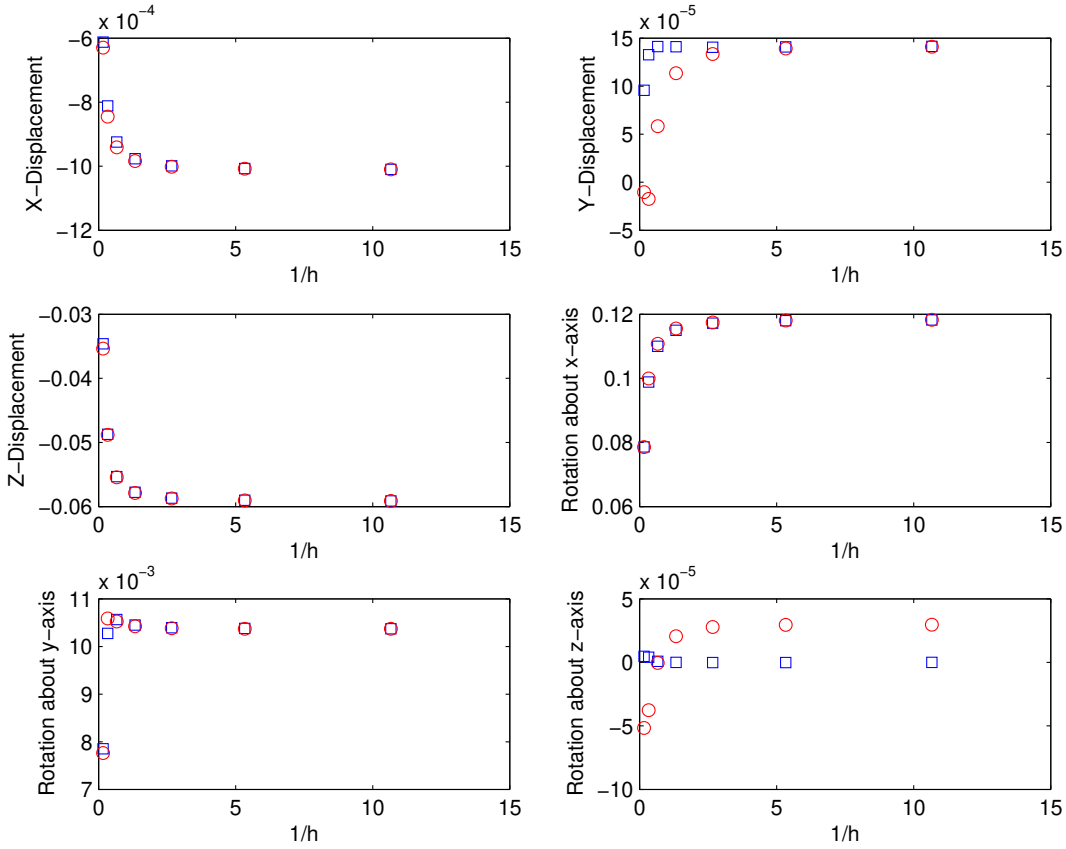

Figure 1-14. – Convergence Of Displacements And Rotations At Node 4.

10.1.6.2. Example II

The second verification example for laminate composite modeling is taken from Reference.[27] A rectangular plate is subjected to a uniform pressure load of q = 0.003 psi. The plate, shown in figure 1-15 has dimensions 12 in. x 8 in. and is simply supported on each edge. The antisymmetric angle-ply stacking sequence is [-30/30 -30/30 -30/30 -30/30]. Each layer has a thickness of 0.01 in. The orthotropic material properties for each layer are: $E_1 = 26.25e6psi$, $E_2 = 1.49e6psi$, $nu_{12} = 0.28$, and $G_{12} = 1.04e6$ psi.

The transverse displacement at the center of the plate is compared with the analytical solution developed in reference.[27] **Sierra/SD** calculates a value of -2.377e-4, while the analytical solution is -2.38e-4. Again, the DKT/Allman triangle produces a good comparison with the analytical solution.

This test is kept in the Salinas_test repository in the verification/composite subdirectory and is named plate_test.

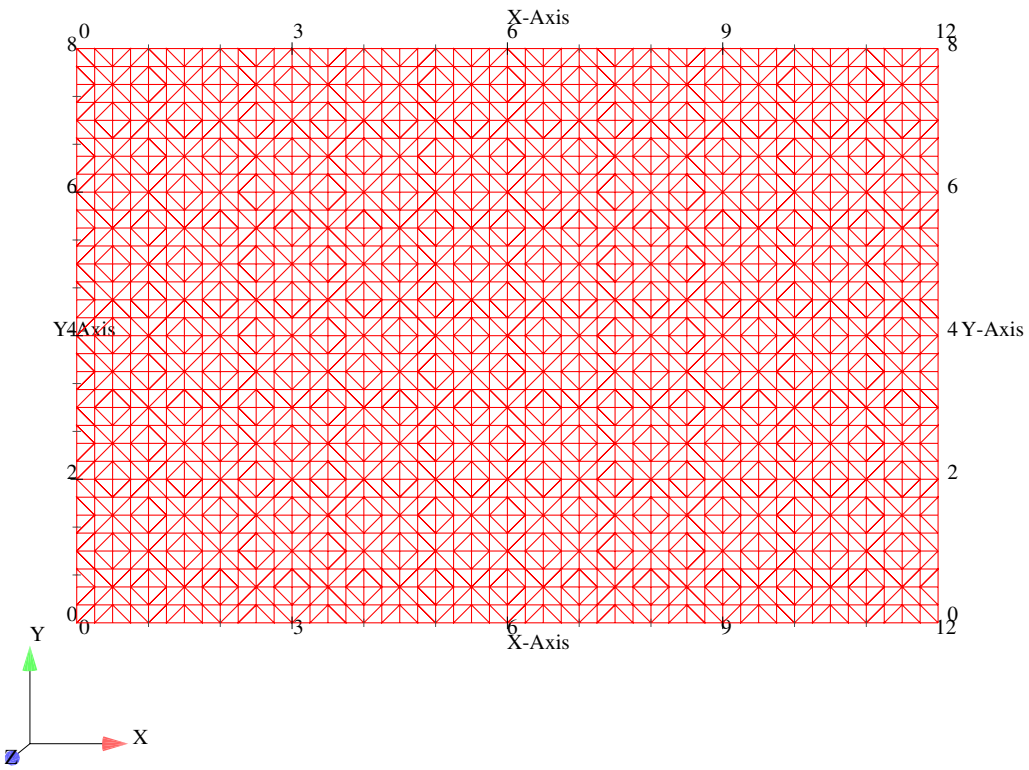

Figure 1-15. – Finite Element Model Of A Flat Plate.

10.1.6.3. Example III

This verification example for laminate composite modeling is also taken from Reference.[27] A cylindrical panel is subjected to a uniform pressure load of q = 0.003 psi. The cylindrical panel ($\frac{1}{4}$ of model is shown in figure 1-16) has a length of 80 in., while the arc length of the other side is 41.89 in. corresponding to an angle of $\phi = 24^\circ$ and radius of 100 in. The stacking sequence is [0/90/90/0]. Each layer has a thickness of 0.08 in. The orthotropic material properties for each layer are: $E_1 = 18e6psi$, $E_2 = 1.4e6psi$, $nu_{12} = 0.34$, and $G_{12} = 0.9e6$ psi.

The transverse displacement of the free corner is compared with the analytical solution developed in reference.[27] **Sierra/SD** calculates a value of 6.958e-4, while the analytical solution is 6.945e-4. Again, the DKT/Allman triangle produces a good comparison with the analytical solution.

This test is kept in the Salinas_test repository in the verification/composite subdirectory and is named cyl_panel_test.

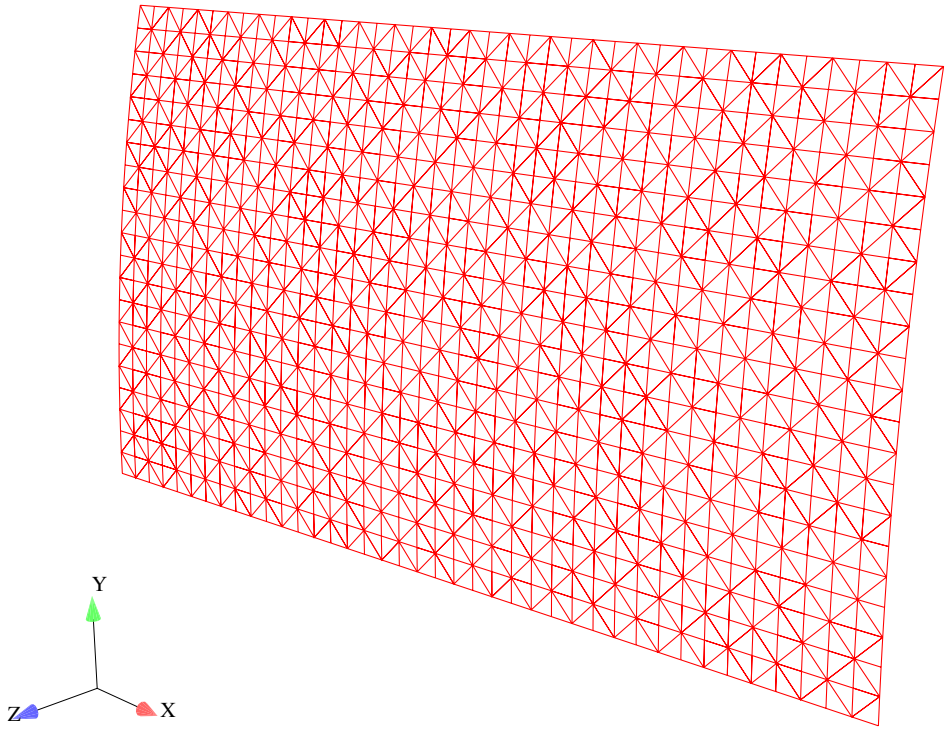

Figure 1-16. – Finite Element Model Of A Cylindrical Panel.

10.1.7. Joint Modeling: Joint2g Element with Iwan Constitutive Model

The Joint2g element permits independent specification of the constitutive relations between each of the relative displacements. Currently, the most prominent of the constitutive equations employed for the "whole joint" modeling approach is the 4 parameter Iwan model. The Joint2g element and the Iwan constitutive model are documented in *User's Manual* and *Sandia National Labs* reports specifically addressing the 4 parameter model.

There exists a closed form expression for the energy dissipation per cycle resulting from harmonic excitation imposed on a joint of this nature. That expression (presented in *SAND2002-3828*[49]) is,

$$D = r^{\chi+3} \frac{4F_s\phi_{max}(\chi+1)}{(\beta+\frac{\chi+1}{\chi+2}(\chi+2)(\chi+3)} \tag{10.1.2}$$

where β, χ, ϕ_{max}, and F_s are model parameters, and r satisfies

$$\frac{F_o}{F_s} = r\frac{(\beta+1)-r^{\chi+1}/(\chi+2)}{\beta+(\chi+1)/(\chi+2)}, \tag{10.1.3}$$

where F_o is the amplitude of the harmonic excitation. Comparison of the exact solution and **Sierra/SD** predictions is presented in Figure 1-17.

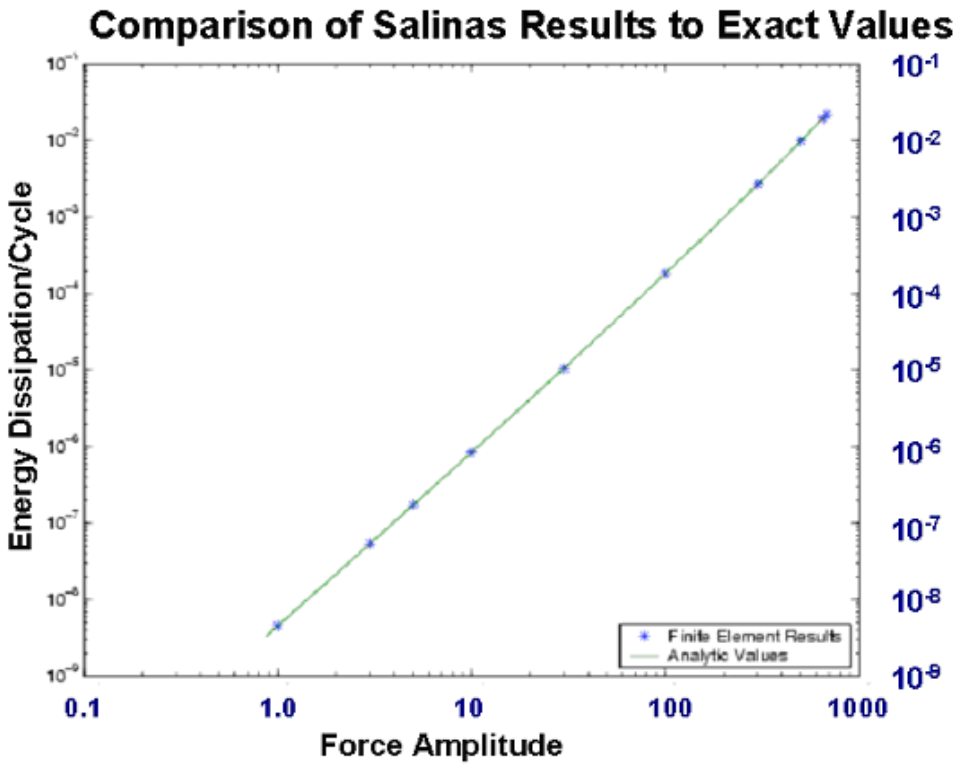

Figure 1-17. – **Sierra/SD** Iwan Element: Comparison to Analytic Solution.
The **Sierra/SD** predictions for unidirectional load on a simple joint agrees with the exact solutions.

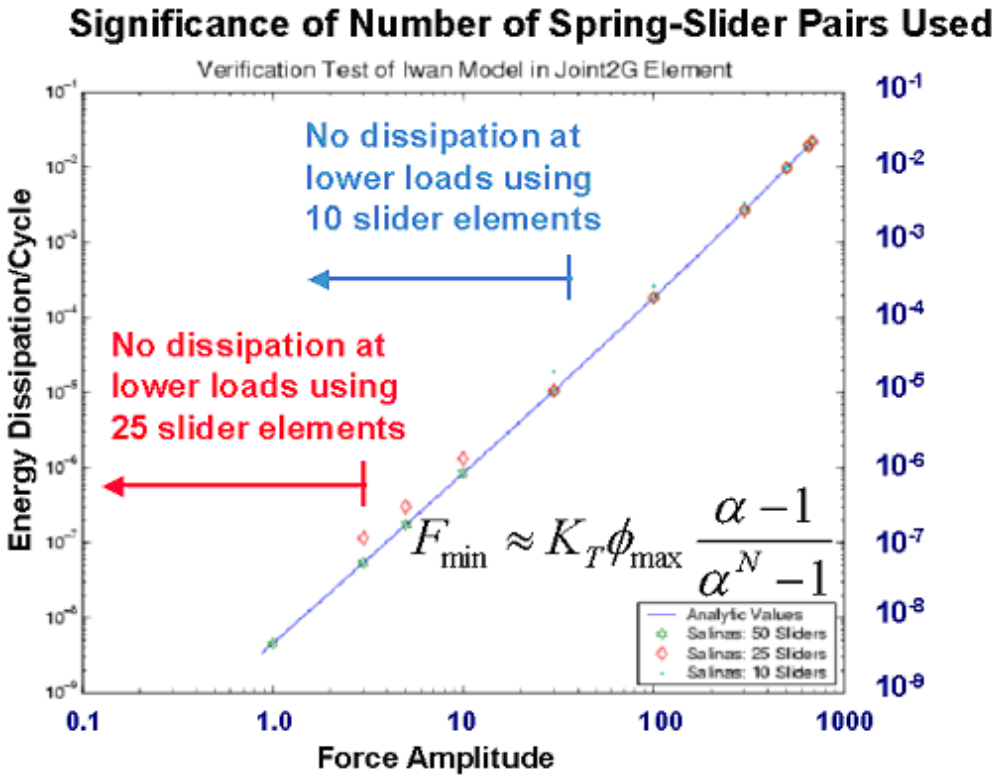

Figure 1-18. – Significance of Number of Spring-Slider Pairs Used.
The number of spring-slider pairs necessary to demonstrate sensitivity to given levels for load in **Sierra/SD** is that predicted by theory.

$$F_{min} \approx K_T \phi_{max} \frac{\alpha - 1}{\alpha^N - 1}$$

There is one integration parameter in **Sierra/SD**, the number of spring-slider pairs used to approximate the continuous distribution of Jenkins elements. The relevant SAND report provides guidance as to the number of elements necessary to manifest proper dissipative response to loads of given size. Figure 1-18 shows that desired accuracy is achieved with the number spring slider pairs predicted by theory.

10.1.7.1. Iwan Macroslip

To evaluate the Iwan model in **Sierra/SD** when it hits macro-slip, a 1D MATLAB test case involving macro-slip and simple dynamics was developed. It was compared with the results of the corresponding 1D Sierra/SD analysis. Here is a sketch of the model.

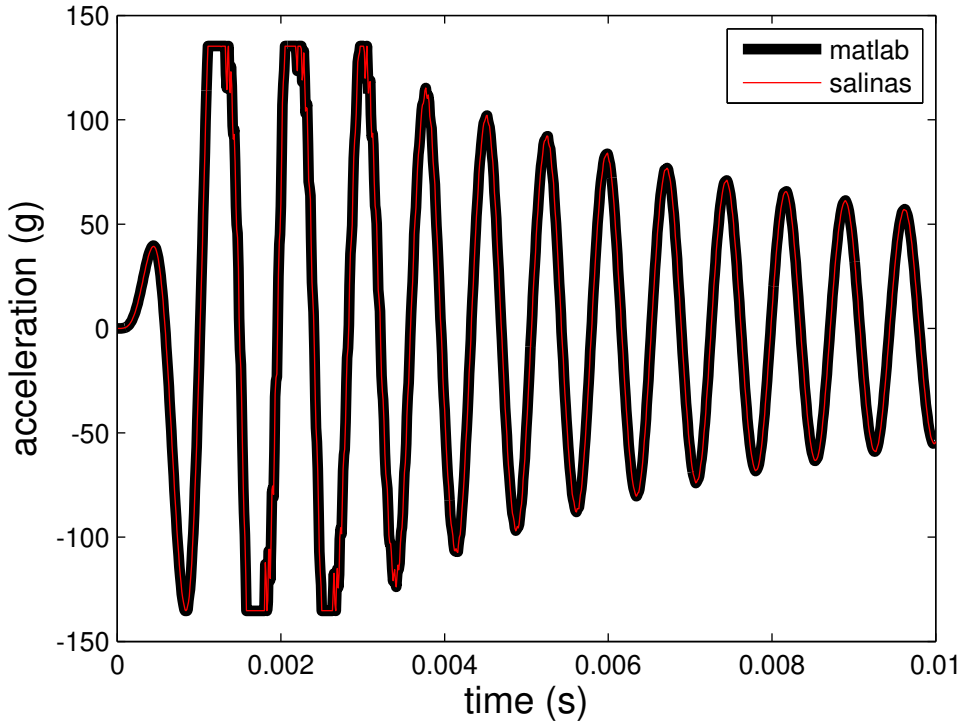

Figure 1-19. – MATLAB and **Sierra/SD** calculation of M_2 acceleration.

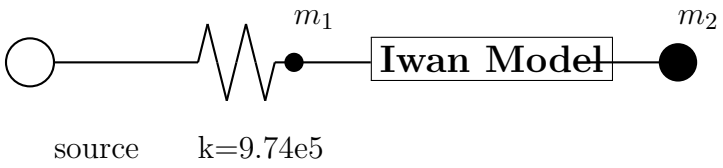

Here the source is a 100g wavelet base excitation, $m_1 = 0.05\,lb$, and $m_2 = 4\,lb$.

Analysis is performed both within **Sierra/SD** and MATLAB. The acceleration of the four pound mass for each analysis method is compared in figure 1-19. We see agreement, though the MATLAB result better resolves macro-slip.

The stretch of the Iwan joint is another good indicator of agreement, and is shown in figure 1-20. The stretch is the relative displacement across the *Iwan* element. Again, the agreement is good, but not perfect.

In both analyses, the acceleration of the spring mass shows significant high frequency response (or hash) as shown in figure 1-21. The high frequency noise is undesirable, but is a feature of the model constructed of a finite number of slider/spring elements. As the elements begin to slide, high frequency noise is generated.

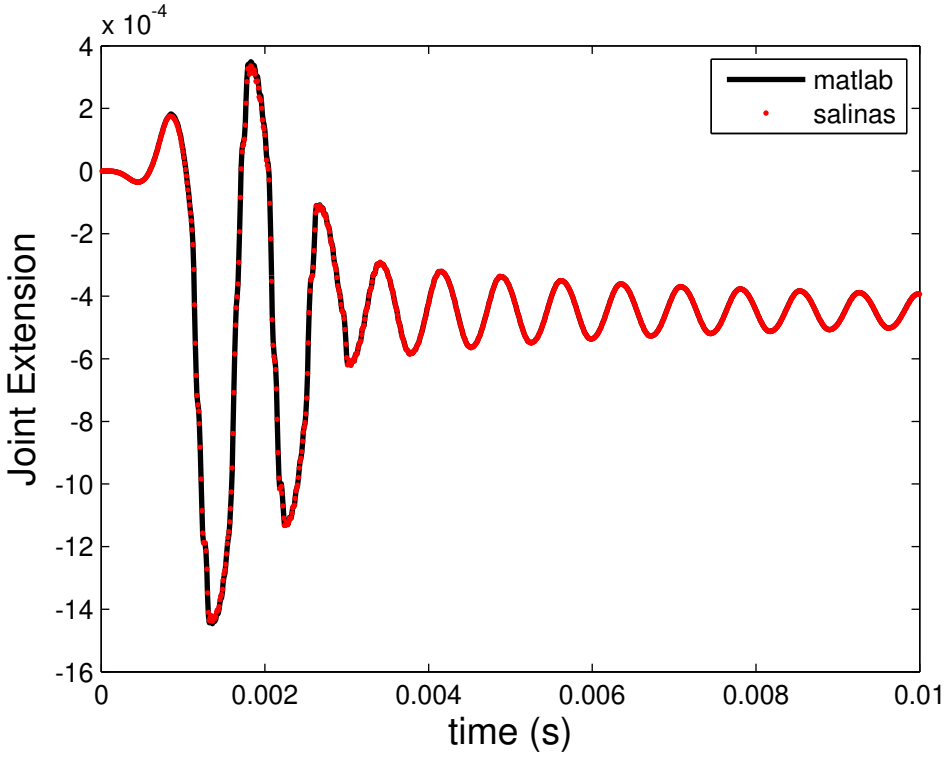

Figure 1-20. – MATLAB and **Sierra/SD** calculation of joint extension.

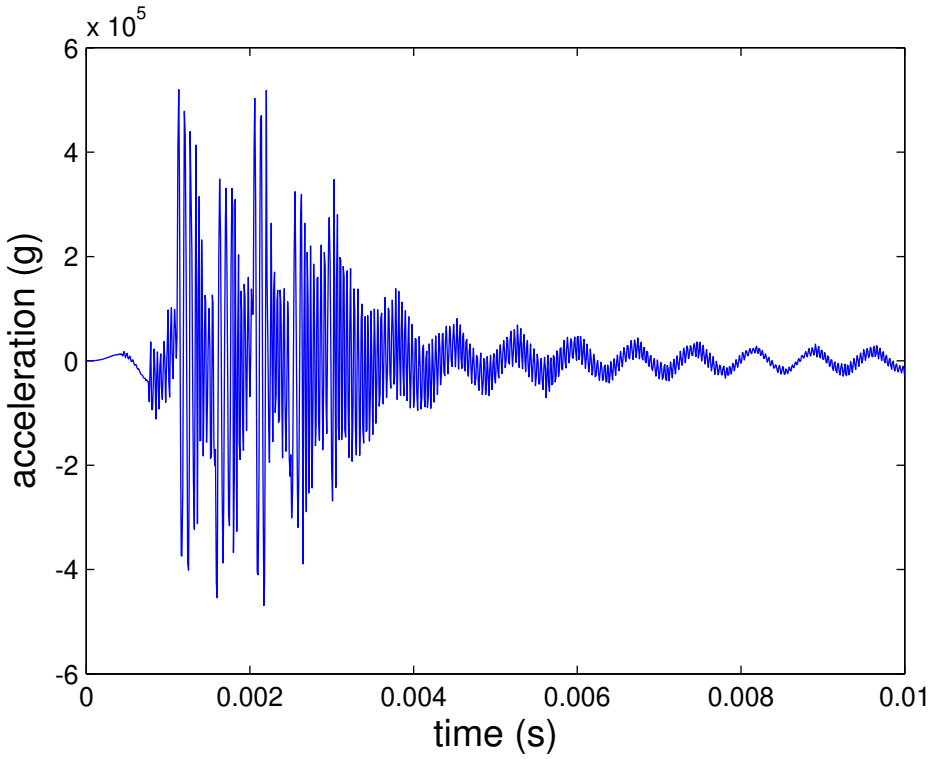

Figure 1-21. – **Sierra/SD** calculation of M_1 acceleration.

10.1.8. Verification of Membrane Elements

Membrane elements are similar to shells, except that they have no rotational degrees of freedom, and have no out-of-plane stiffness in the unstressed state. When they are pulled in tension, an out-of-plane stiffness appears, and takes the form of a geometric stiffening. In the following test cases, we examine the response of the membrane element to both in-plane and out-of-plane deformation. We consider these two loading cases separately.

The first example consists of a square membrane of dimension $1x1$, which is subjected to a uniform tension T in both in-plane directions. After the application of the tension, the membrane boundaries are either fixed, or placed on rollers, and an modal analysis is performed about the stressed state. Since these elements are intended to be used in transfers between Adagio and **Sierra/SD**, we perform the static preload in Adagio, and then transfer the stresses and displacements to **Sierra/SD**. In this way, we also exercise the transfer capabilities for these elements.

The exact eigenvalues for stretched square membranes are given in.[32] In the case of a membrane that is clamped along all boundaries, the frequencies are

$$f_{nm} = \frac{\omega_{nm}}{2\pi} = \frac{c}{2}\sqrt{\left(\frac{n}{L_x}\right)^2 + \left(\frac{m}{L_y}\right)^2} \tag{10.1.4}$$

where $c = \sqrt{\frac{T}{\rho_s}}$ is the speed of sound in the membrane, T is the tension per unit length in the membrane, and ρ_s is the surface density. Note that in the case of a square membrane $L_x = L_y$. Also, the indices $m = 1, 2, 3, ...$ and $n = 1, 2, 3, ...$ In the case of a free-free membrane, the expression for the frequencies is the same, except that both m and n start at 0. In this way, they allow for a rigid body mode.

Table 1-19 shows a comparison of the first three exact and computed eigenvalues of the square clamped membrane, and Table 1-20 shows the same for the free-free membrane. In both cases, good agreement is seen. For the free-free case, we do not compare rigid body modes in the table, but we verified that they came out to be numerically zero. Note that for both cases, repeated modes are observed.

Since they are coupled tests, they have to be located in the tempo test are under sierra. In a tempo project checked out under sierra, these tests are located in the following directories

exact (Hz)	computed
13.178	13.230
20.83	21.126
20.83	21.126

Table 1-19. – Eigenvalue convergence for a fixed-fixed, prestressed membrane. The values given are the natural frequencies, in Hz.

exact (Hz)	computed
9.3169	9.3553
13.178	13.230
18.634	18.941
18.634	18.941

Table 1-20. – Eigenvalue convergence for a free-free, prestressed membrane. The values given are the natural frequencies, in Hz.

```
tempo/tempo/rtest/tempo/membrane_free_free
tempo/tempo/rtest/tempo/membrane_free_free_par
tempo/tempo/rtest/tempo/membrane_clamped
tempo/tempo/rtest/tempo/membrane_clamped_par
```

For in-plane loading, there are 2 verification tests located at

```
Salinas_test/patchtests/quadt/quadt-patch8_test
Salinas_test/patchtests/quadt/quadt-patch9_test
```

These tests use in-plane tension, and verify the corresponding deformation of the membrane.

10.1.9. Verification of Tangent Stiffness Matrix for Sierra Transfers

In this section, we present numerical experiments to confirm the implementation of the tangent stiffness matrix following a Sierra transfer. We note that the tangent stiffness matrix is the sum of contributions from internal and external forces. In some texts, the contributions from the former is referred to as the material/geometric stiffness, while the former is referred to as the follower stiffness. In the following experiments, all components of the stiffness matrix are being exercised.

10.1.9.1. A Cantilever Beam Subjected to Large Deflection Via End Load

In this example we consider a cantilever beam that is subjected to a large deflection from a concentrated end load. We note that in this case, the follower stiffness is zero, since the load does not depend on the deformation. In this example, Adagio was used to model the deformation of the beam to the large deflection state, and then the results were passed to **Sierra/SD** for modal analysis. Table 1-21 shows the modal frequencies of the beam in the deformed state, compared with those obtained from Abaqus. Excellent agreement is seen between the two codes.

Table 1-21. – Comparison of **Sierra/SD** and Abaqus modal results for a cantilever beam subjected to large deflection via point load.

mode	Abaqus	**Sierra/SD**	% difference
1	56.219	56.236	0.029
2	245.720	246.106	0.154
3	274.010	274.159	0.054
4	358.280	358.316	0.010
5	400.030	399.916	0.028
6	630.540	630.113	0.058
7	649.890	650.113	0.034
8	803.580	803.389	0.024
9	933.100	933.198	0.011
10	1069.80	1070.180	0.036

10.1.9.2. A Cantilever Beam Subjected to Large Deflection Via Pressure Load

In this section, we consider the same cantilever beam as in the previous example, except in this case the beam is loaded with a distributed pressure load. Since the pressure will follow the beam's deformation, we expect a contribution from the follower stiffness in this case. Table 1-22 shows the comparison of **Sierra/SD** with Abaqus for the first ten modes of the pressure-loaded beam. In this case, follower stiffness was not included in the **Sierra/SD** results. Some significant differences in the frequencies is observed.

Including the follower stiffness matrix in the **Sierra/SD** tangent stiffness matrix calculation (table 1-23) agrees with Abaqus. We note that this example is included in the **Sierra/SD** test suite, in the following location

`Salinas_test/verification/follower/beam_test`

Table 1-22. – Comparison of **Sierra/SD** and Abaqus modal results for a cantilever beam subjected to large deflection via pressure load, with no follower stiffness in the **Sierra/SD** tangent matrix.

mode	Abaqus	**Sierra/SD**	% difference
1	59.015	57.019	3.382
2	60.472	59.858	1.015
3	252.140	230.927	8.413
4	306.200	304.988	0.396
5	322.590	322.217	0.116
6	493.650	492.184	0.297
7	742.200	736.837	0.723
8	770.830	769.096	0.225
9	773.340	771.410	0.250
10	1230.500	1227.530	0.241

Table 1-23. – Comparison of **Sierra/SD** and Abaqus modal results for a cantilever beam subjected to large deflection via pressure load, with follower stiffness in the **Sierra/SD** tangent matrix.

mode	Abaqus	**Sierra/SD**	% difference
1	59.015	59.053	0.064
2	60.472	60.470	0.003
3	252.140	252.194	0.021
4	306.200	306.141	0.019
5	322.590	322.651	0.018
6	493.650	493.719	0.013
7	742.200	742.064	0.019
8	770.830	771.112	0.036
9	773.340	773.366	0.003
10	1230.500	1230.25	0.020

10.1.10. Tied Joint

The tied joint provides a means of connecting two surfaces together while allowing compliance in the shear behavior. The tied joint allows more flexibility in the specification of the normal behavior than previous methods that required a fully rigid surface pair to which a whole joint model (such as a Joint2g) is attached.

A first step in developing the tied joint is replicating the old model behavior. This is done with the two test cases “2x2tied” and “2x2whole”. The first of these couples a block of elements using the new methodology. The “2x2whole” example uses the old approach. The solutions are shown to be identical.

Next, we present transient simulations on a single-leg model. This single leg model was taken from a more complicated three-leg model. The surfaces that join the two pieces are modeled with a tied joint, and then we compare those results with a truth model where the constraints on the interface were implemented manually using the “old" approach of an RBE3 element.

The first example compares the two approaches in the case when the tied joint model is modeled with the following block

```
TIED JOINT
    normal definition = slip
    side = free
         . . .
END
```

Figures 1-22, 1-23, 1-24 shows the comparison of the X, Y, and Z displacements as a function of time, for the tied joint and truth models. Excellent agreement is observed.

The second example compares the tied joint and truth model approaches when the tied joint model is modeled with the following block

```
TIED JOINT
     normal definition = none
     side = rigid
        . . .
END
```

Figures 1-25, 1-26, 1-27 shows the comparison of the X, Y, and Z displacements as a function of time for this case, for the tied joint and truth models. Excellent agreement is observed.

These tests are located in the verification test suite in the directory

```
Salinas_rtest/verification/tiedjoint
```

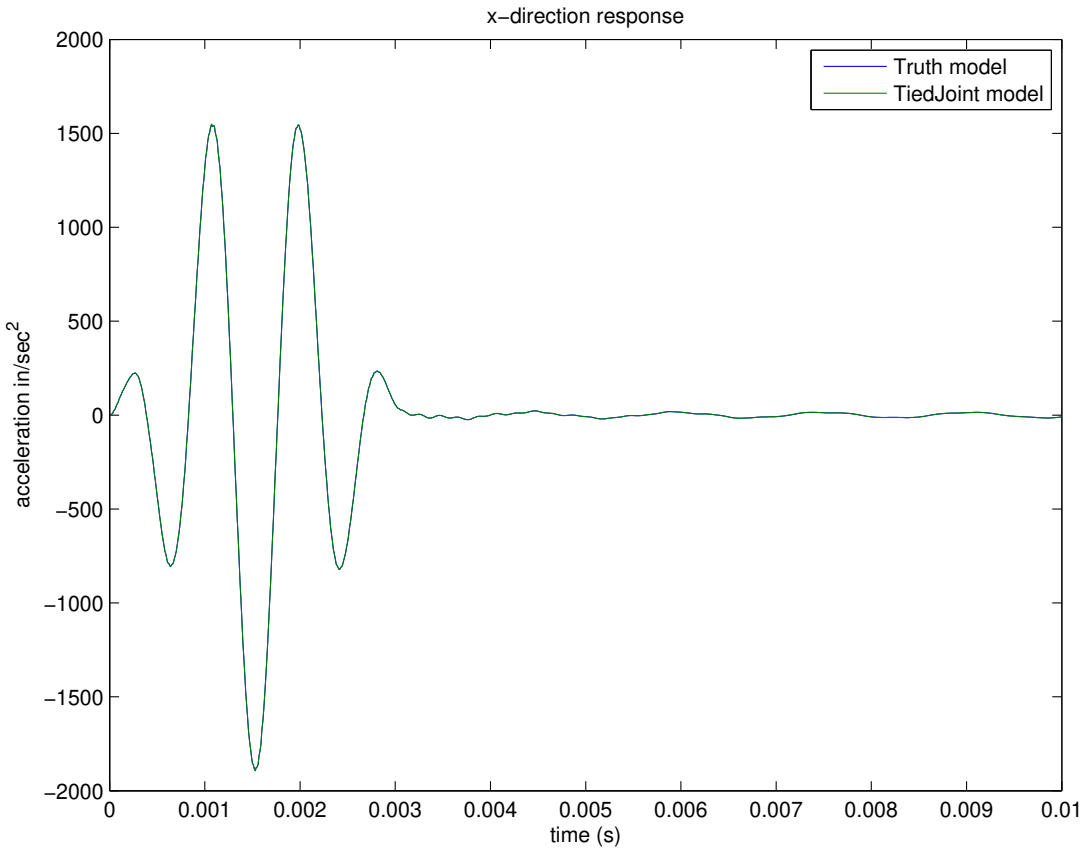

Figure 1-22. – X displacement comparison for tied joint versus truth model, tied=slip, side=free

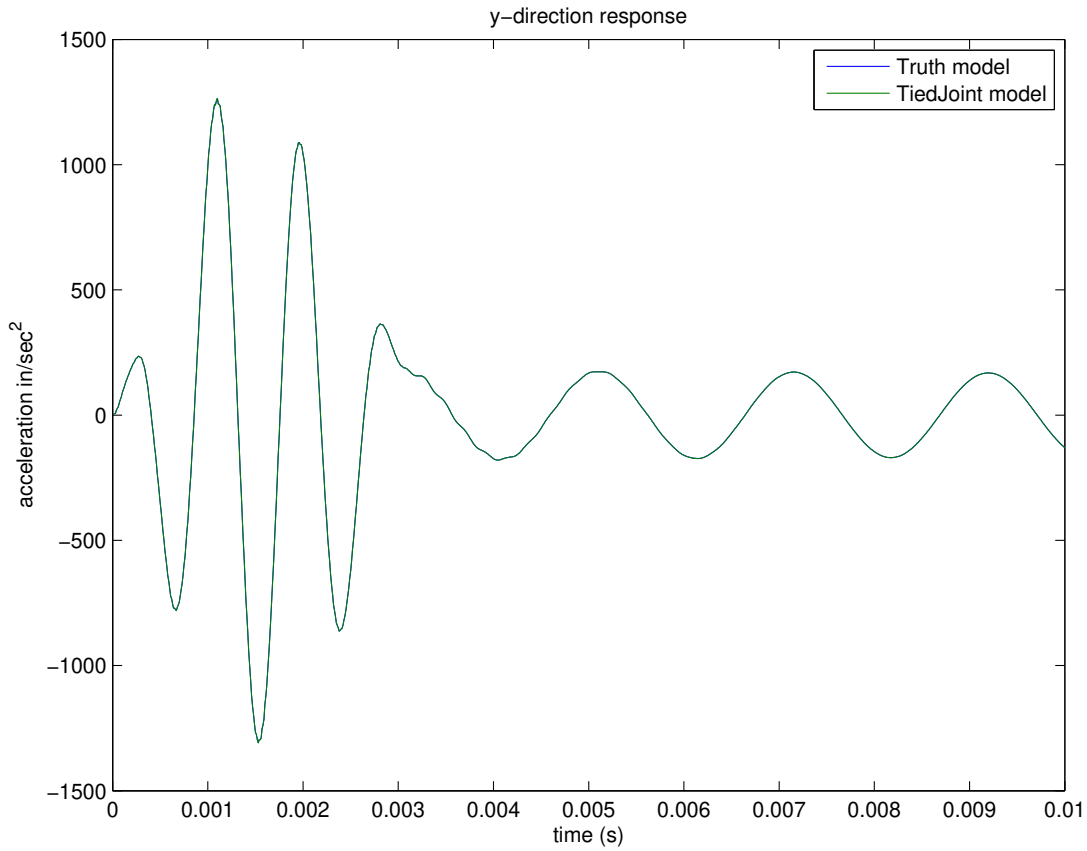

Figure 1-23. – Y displacement comparison for tied joint versus truth model, tied=slip, side=free

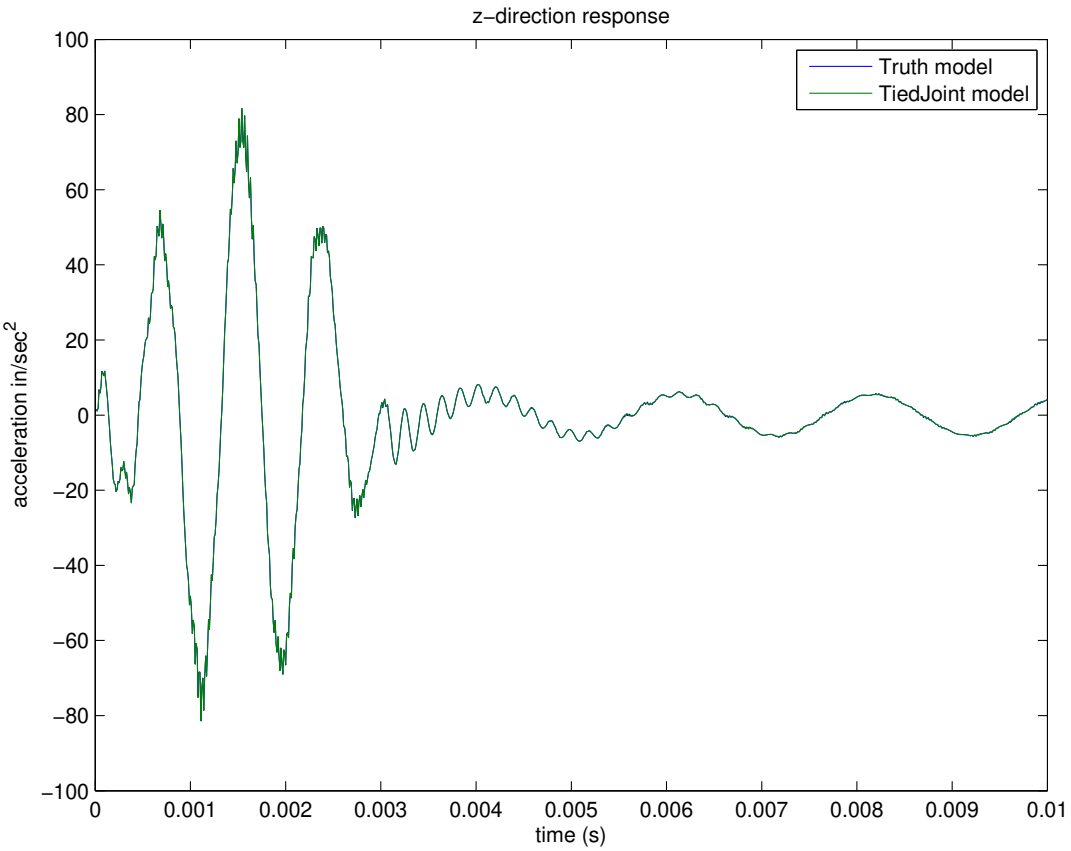

Figure 1-24. – Z displacement comparison for tied joint versus truth model, tied=slip, side=free

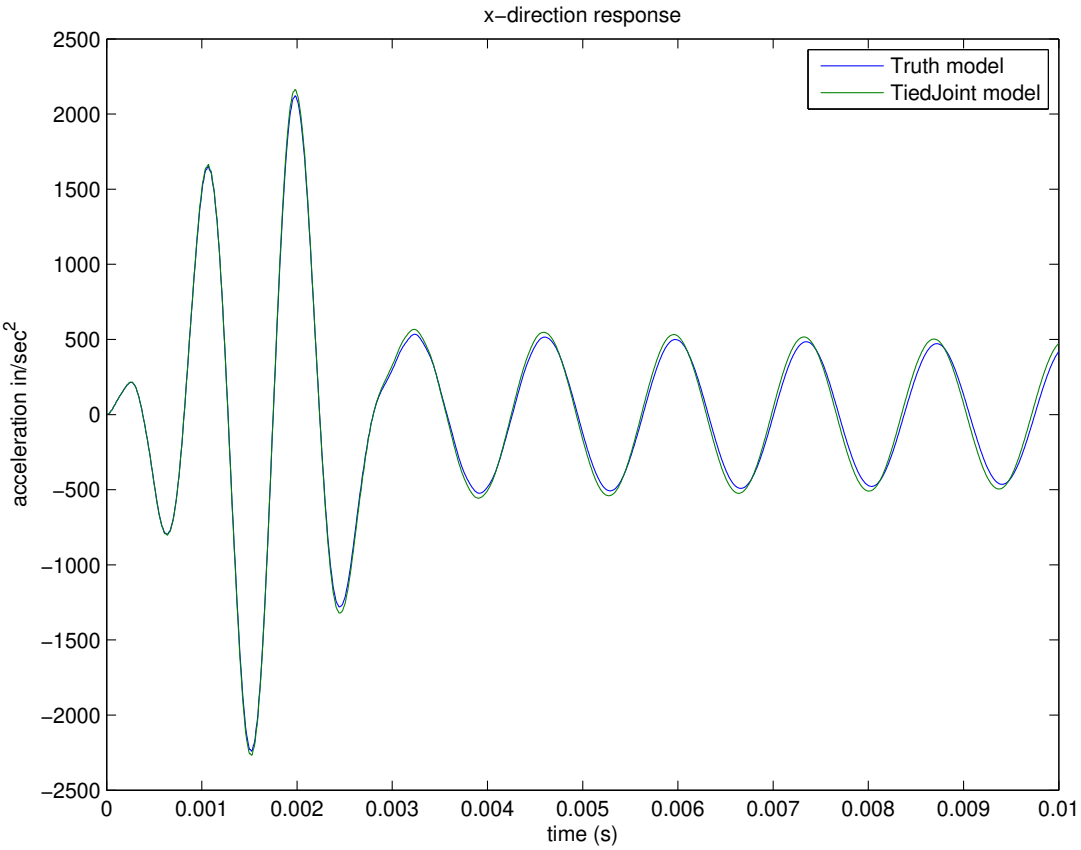

Figure 1-25. – X displacement comparison for tied joint versus truth model, tied=none, side=rigid

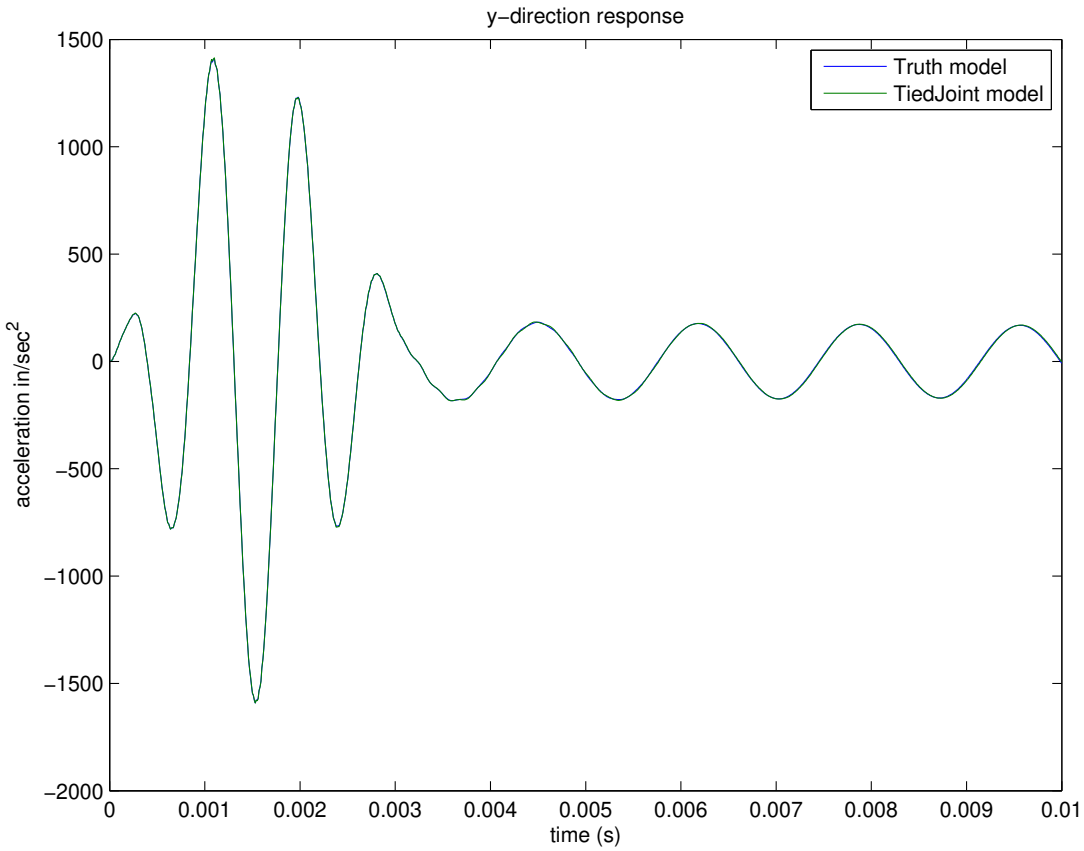

Figure 1-26. – Y displacement comparison for tied joint versus truth model, tied=none, side=rigid

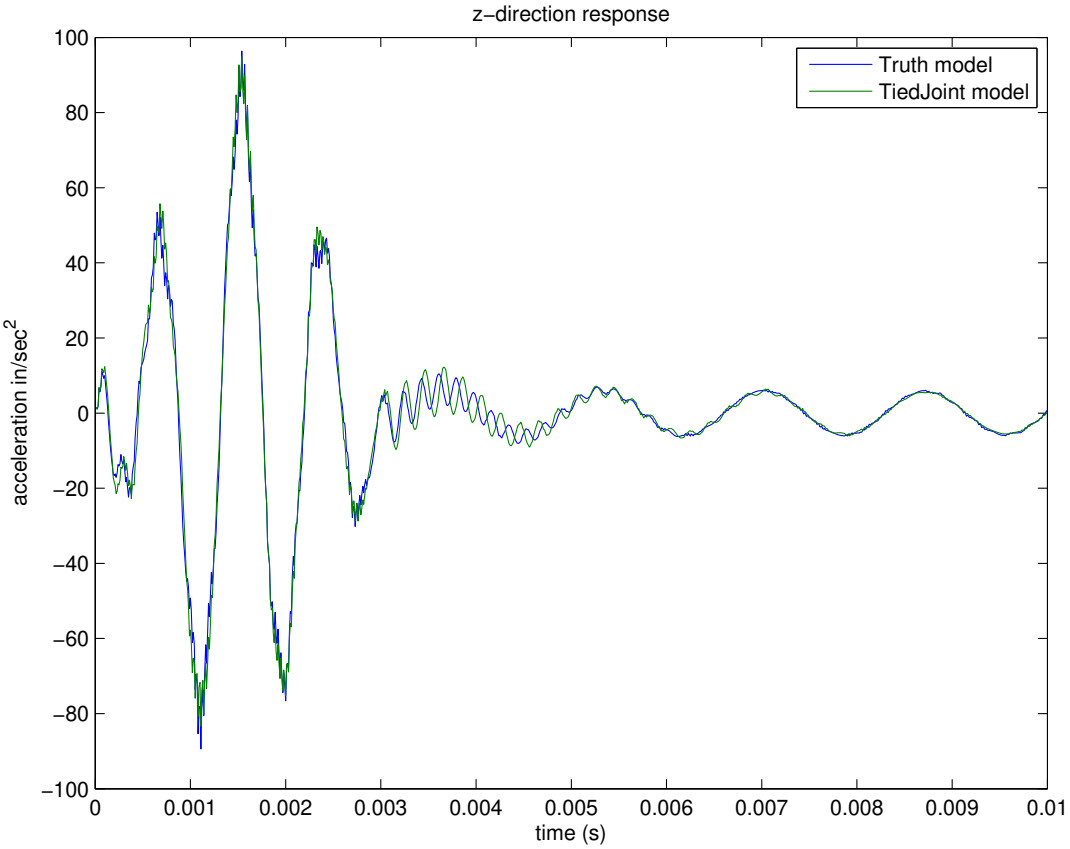

Figure 1-27. – Z displacement comparison for tied joint versus truth model, tied=none, side=rigid

10.1.11. Rrodset

The Rrodset mimics a kevlar type material in that in does not oppose bending in any way, but it does oppose tension. Fundamentally, it is identical to placing a collection of Rrods along every edge of a surface. One use is to distribute the shear loading of a tied joint.

To verify that it does not oppose bending, a simple example with 2 connected plates on top of each other was created. The left side was fixed and the right side had loads applied. The top plate was pulled while the bottom plate was pushed with equal force, causing a pivot around the center where the Rrodset can be placed. It was shown that a statics solution produced the same results whether or not an Rrodset was placed in the middle. The test is in the fast regression tests suite and is called `Rrodset.` The test is `Salinas_rtest/test_tool/fast_regression_tests/traction/rrodset.test`.

10.1.12. Elements Provided by the Navy

As part of the Navy/CREATE program,[39,42] various elements are being introduced to **Sierra/SD**. These elements fall into two categories: specialty connector element and legacy elements pulled from Nastran.

The legacy elements are designed to exactly mimic elements in the Nastran capabilities. Typically these come from the open literature. Because of the nature of these elements, verification is naturally a code to code comparison.

Connector elements are all two node elements provided to enhance special Navy needs. For example, connection of rafts to a hull is best defined using a nonlinear spring dashpot.

The names for all Navy provided elements begins with "N". For example, the navy beam element is the "NBeam".

10.1.12.1. NBeam

The **NBeam** is both a connector and a legacy element. The **Beam2** element has most of the same functionality, but does not include offset moments (I12) or shear factors. The static tests included are detailed in Table 1-24. Table 1-25 summarizes some of the results of the tests. In this section of tests, the Nastran results are treated as the truth model. Models were translated using "Nasgen".

Test	Section	Description
btest1	rectangular	simple test of end loaded cantilever
btest2	rectangular	tests rotational invariance
btest3	rectangular	tests beam tower
btest4	channel	tests I_{12}
btest5	channel	rotational invariance of I_{12}
btest6	I-beam	end loaded offset
btest7	rectangular	one element test
btest8	C	offset, rotated C beam

Table 1-24. – Static Tests for NBeam.

Test	Maximum Error
btest1	0.02%
btest2	0.01%
btest3	0.05%
btest4	%
btest5	%
btest6	%
btest7	%
btest8	%

Table 1-25. – Results of Static Tests for NBeam. The maximum error in deflection is shown.

The tests are `Salinas_rtest/test_tool/navy/nbeam/btest1.test`,...,
`Salinas_rtest/test_tool/navy/nbeam/btest8.test`.

10.2. Acoustics

In the following examples computational results are compared to analytic solutions.

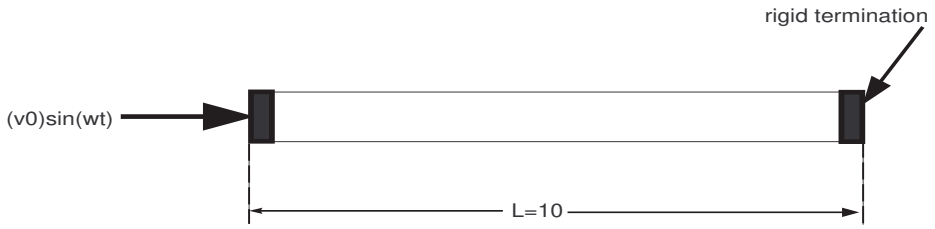

Figure 2-28. – Acoustical waveguide with rigid end cap.

exact (Hz)	80 elements	640 elements	5120 elements	40960 elements
16.6	16.61707	16.60426	16.601065	16.600265
33.2	33.33669	33.23414	33.20853	33.20213
49.8	50.26197	49.9153	49.828799	49.8072

Table 2-26. – Eigenvalue convergence for a piston-driven tube with rigid cap at end. The values given are the natural frequencies, in Hz.

10.2.1. Eigen Analysis of Wave Tube

The first example consists of a convergence study for the natural frequencies of an acoustical tube that is driven at the left end and has a rigid cap the right end, as shown in Fig. 2-28. The eigenvalue problem for this configuration was solved by uniformlly refining a linear hexahedron mesh.

Table 2-26 shows the numerical results, and demonstrates that the first three natural frequencies approach the exact values. Table 2-27 demonstrates quadratic convergence for the natural frequencies, as expected for linear elements.

80 elements	640 elements	5120 elements	40960 elements
.0103	.0257	6.415e-3	1.596e-3
.4117	.10283	.0257	6.416e-3
.9277	.2315	.05783	.01446

Table 2-27. – Relative error in computation of natural frequencies for a piston-driven tube with rigid cap at end. The reduction by a factor of 4 each time the element size is halved demonstrates quadratic convergence in natural frequencies.

10.2.2. Eigen Analysis with Multiple Fluids

A subtlety when working with fluids of spatially varying properties is that the linear wave equation, which is typically written in the form

$$\frac{1}{c^2}\ddot{p} - \Delta p = 0 \tag{10.2.1}$$

is no longer valid. Assumptions were made in the derivation of this equation that restricted its applicability to a homogeneous fluid. When density and speed of sound change with position in the fluid, the linear wave equation takes the form[41]

$$\nabla \cdot \left(\frac{1}{\rho}\nabla p\right) - \frac{\ddot{p}}{B} = 0 \tag{10.2.2}$$

where ρ is the fluid density, B is the fluid bulk modulus, and p is the acoustic pressure. If we assume that the speed of sound is $c = \sqrt{\frac{B}{\rho}}$, then this equation can also be written as

$$\rho\nabla \cdot \left(\frac{1}{\rho}\nabla p\right) - \frac{\ddot{p}}{c^2} = 0 \tag{10.2.3}$$

Next, we consider how the heterogeneous wave equation is implemented in **Sierra/SD**. We note that **Sierra/SD** uses the form in equation 10.2.3. Since we want to allow the density to vary with position, we have to first divide by density before multiplying by a test function and integrating by parts. This is because the factor of ρ in front of the first term in equation 10.2.3 varies with position, and thus we will not be able to move the ∇ symbol over to the test function. Thus, we have

$$\nabla \cdot \left(\frac{1}{\rho}\nabla p\right) - \frac{\ddot{p}}{\rho c^2} = 0 \tag{10.2.4}$$

We solve for the time derivative of pressure in **Sierra/SD**. Thus, we substitute $p = \dot{\phi}$ into equation 10.2.4, and then integrate in time to obtain

$$\nabla \cdot \left(\frac{1}{\rho}\nabla \phi\right) - \frac{\ddot{\phi}}{\rho c^2} = 0 \tag{10.2.5}$$

The gradient ∇ can be moved to the test function in equation 10.2.5. Thus, this is the formulation that is used in **Sierra/SD** to construct the finite element implementation.

In deriving the analytic solution, we note that the analytical solutions to equations 10.2.2, 10.2.3, 10.2.4, and 10.2.5 will all be the same (assuming we converted the final analytic solution from equation 10.2.5 into pressure), since these equations differ by a scale factor. Thus, we use equation 10.2.2 to derive the analytical solution. If we consider the eigenvalue problem, equation 10.2.2 becomes

$$\nabla \cdot \left(\frac{1}{\rho}\nabla p\right) + \lambda\frac{p}{B} = 0 \tag{10.2.6}$$

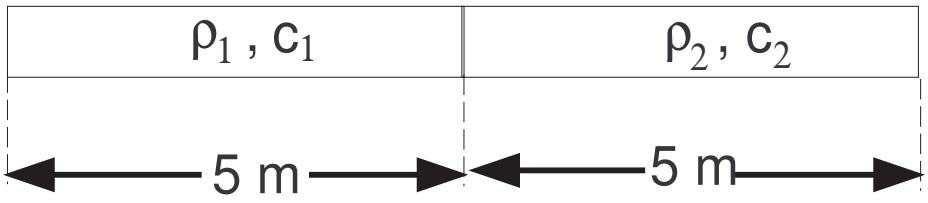

Figure 2-29. – Acoustical waveguide containing two fluids.

This equation will serve as the basis for deriving the analytical solution.

We consider three cases. All three cases involve the geometry shown in Figure 2-29. An exact solution for the eigenvalues of the geometry in Figure 2-29 can be derived by considering each fluid separately and applying appropriate compatibility conditions on the fluid-fluid interface. The equations are as follows

$$\frac{d^2p_1}{dx^2}+\lambda\frac{\rho_1}{B_1}p_1=0 \quad 0\le x\le\frac{L}{2} \tag{10.2.7}$$

$$\frac{d^2p_2}{dx^2}+\lambda\frac{\rho_2}{B_2}p_2=0 \quad \frac{L}{2}\le x\le L \tag{10.2.8}$$

$$\tag{10.2.9}$$

$$p_1=p_2 \quad x=\frac{L}{2} \tag{10.2.10}$$

$$\frac{1}{\rho_1}\frac{dp_1}{dx}=\frac{1}{\rho_2}\frac{dp_2}{dx} \quad x=\frac{L}{2} \tag{10.2.11}$$

$$\tag{10.2.12}$$

where B_1 and B_2 are the bulk moduli of the two fluids. At the endpoints, there are two options. Either we could have rigid caps ($\frac{dp}{dx}=0$), or we could have pressure release boundary conditions ($p=0$). The solution will have the form

$$p_1(x)=C_1\cos\left((x-\frac{L}{2})\sqrt{\frac{\lambda\rho_1}{B_1}}\right)+C_2\sin\left((x-\frac{L}{2})\sqrt{\frac{\lambda\rho_1}{B_1}}\right) \quad 0\le x\le\frac{L}{2} \tag{10.2.13}$$

$$p_2(x)=C_3\cos\left((x-\frac{L}{2})\sqrt{\frac{\lambda\rho_1}{B_1}}\right)+C_4\sin\left((x-\frac{L}{2})\sqrt{\frac{\lambda\rho_1}{B_1}}\right) \quad \frac{L}{2}\le x\le L \tag{10.2.14}$$

$$\tag{10.2.15}$$

Inserting these into equations 10.2.8, applying the compatibility conditions 10.2.11, and using the appropriate boundary conditions at the endpoints, we get two transcendental equations that give the exact eigenvalues. For the pressure release (Dirichlet) end cap case,

exact (Hz)	computed, h=1	computed, h=0.5
17.7322	17.7505	17.7333
34.1990	34.3411	34.2079
53.1689	53.6642	53.1998

Table 2-28. – Eigenvalue convergence for a two-fluid system with rigid cap at end. The values given are the natural frequencies, in Hz.

exact (Hz)	computed, h=1	computed, h=0.5
17.0965	17.1143	17.0976
35.4575	35.6039	35.4666
51.3135	51.7932	51.3435

Table 2-29. – Two-fluid eigenvalue convergence with pressure release BC.

we obtain

$$\cos\left(\frac{L}{2}\sqrt{\frac{\lambda\rho_1}{B_1}}\right)\sin\left(\frac{L}{2}\sqrt{\frac{\lambda\rho_2}{B_2}}\right) = -\sqrt{\frac{\rho_1 B_1}{\rho_2 B_2}}\cos\left(\frac{L}{2}\sqrt{\frac{\lambda\rho_2}{B_2}}\right)\sin\left(\frac{L}{2}\sqrt{\frac{\lambda\rho_1}{B_1}}\right) \tag{10.2.16}$$

(10.2.17)

For the rigid (Neumann) case, we obtain

$$\sin\left(\frac{L}{2}\sqrt{\frac{\lambda\rho_1}{B_1}}\right)\cos\left(\frac{L}{2}\sqrt{\frac{\lambda\rho_2}{B_2}}\right) = -\sqrt{\frac{\rho_1 B_1}{\rho_2 B_2}}\sin\left(\frac{L}{2}\sqrt{\frac{\lambda\rho_2}{B_2}}\right)\cos\left(\frac{L}{2}\sqrt{\frac{\lambda\rho_1}{B_1}}\right) \tag{10.2.18}$$

(10.2.19)

Equations 10.2.16 and 10.2.18 can be solved to obtain the exact eigenvalues of the system shown in Figure 2-29.

First, we consider the case $\rho_1 = 1.293$, $\rho_2 = 2.5860$, $c_1 = 332.0$, $c_2 = 366.0$. Table 2-28 shows the comparison when rigid walls are placed at either end of the tube, and Table 2-29 shows the comparison with pressure release conditions at both ends. Convergence is seen in all cases.

The next case is an impedance matching condition, in which $\rho_1 c_1 = \rho_2 c2$. In this case, we take $\rho_1 = 2\rho_2$, and $c_1 = 0.5c_2$. Thus, the parameters are different but the impedances are

exact (Hz)	computed, h=1	computed, h=0.5
11.0667	11.0797	11.0675
22.1333	22.2632	22.1414
33.2000	33.6067	33.2256

Table 2-30. – Eigenvalue convergence for a two-fluid system with rigid cap at end. The values given are the natural frequencies, in Hz.

exact (Hz)	computed, h=1	computed, h=0.5
33.1974	33.3341	33.206
66.3825	67.4755	66.4506

Table 2-31. – Eigenvalue convergence for an air/water system with rigid cap at ends. The values given are the natural frequencies, in Hz.

the same. The computed and theoretical results are shown in Table 2-30. Again, good convergence behavior is observed.

Finally, we consider a case with air and water. The same two-fluid case from the previous example was used, with rigid boundary conditions. The comparison between theoretical and computed eigenvalues is shown in Table 2-31.

10.2.3. Eigen Analysis of Elliptic Tank

This section written by Jerry Rouse.
The acoustic modal analysis capability of **Sierra/SD** was further verified using a three dimensional elliptic cylindrical tank. The dimensions of the tank are shown in Figure 2-30. The verification involved two boundary condition configurations. For the first configuration all boundaries of the enclosure were rigid, which requires the normal component of acoustic velocity be zero at all points along the boundary. For the second configuration, the end caps of the tank were rigid, and the sidewall of the tank was a pressure release surface. A pressure release boundary requires that the acoustic pressure be zero at the boundary.

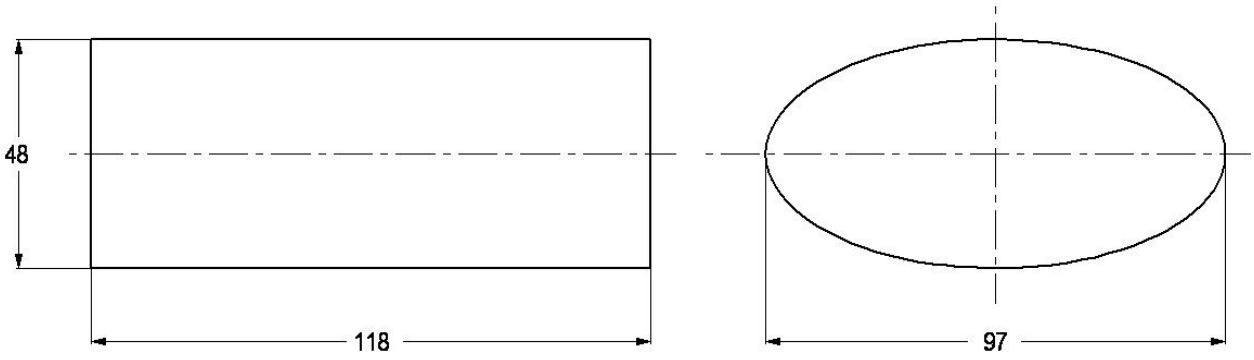

Figure 2-30. – Dimensions of the elliptic cylindrical tank model. All dimensions in inches.

To determine theoretically the resonance frequencies for the elliptic cylindrical tank, the linear wave equation was solved in elliptic cylindrical coordinates. The coordinate system is illustrated in Figure 2-31. This coordinate system is not commonly encountered, and therefore the solution of the wave equation is described. The linear wave equation in terms of acoustic pressure is given by

$$\nabla^2 p + \frac{1}{c^2}\frac{\partial^2 p}{\partial t^2} = 0. \tag{10.2.20}$$

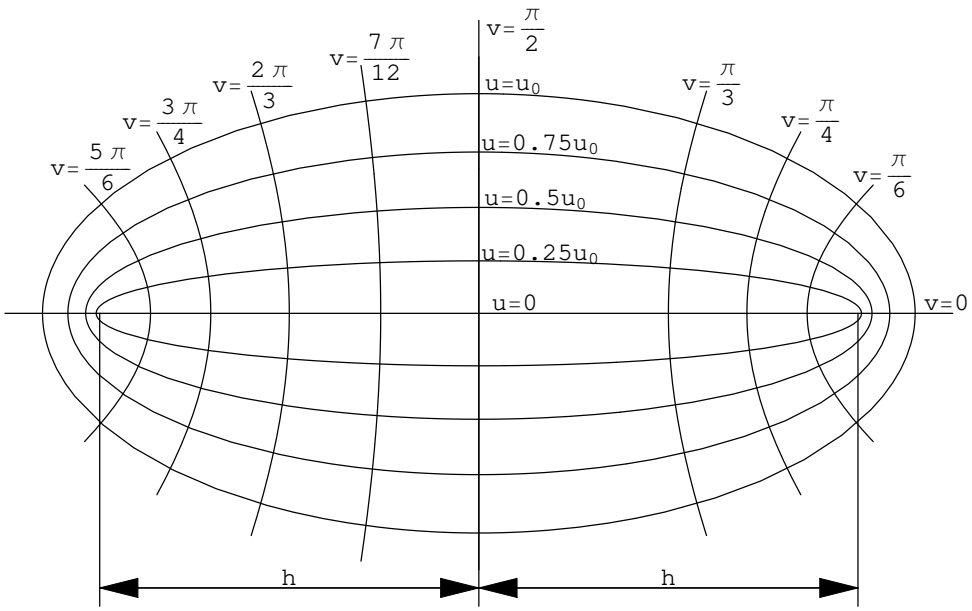

Figure 2-31. – The elliptic cylindrical coordinate system.

In elliptic cylindrical coordinates the Laplacian has the form

$$\nabla^2 = \frac{1}{h^2(\sinh^2(u)+\sin^2(v))}\left(\frac{\partial^2 p}{\partial u^2}+\frac{\partial^2 p}{\partial v^2}\right)+\frac{\partial^2 p}{\partial z^2} \tag{10.2.21}$$

where $x = h\cosh(u)\cos(v)$, $y = h\sinh(u)\sin(v)$, and $h = \sqrt{a^2-b^2}$ with a equal to half the major axis, and b equal to half the minor axis. For the tank dimensions shown in Figure 2-30 $a = \frac{97}{2}$, $b = 24$, $h = \frac{7\sqrt{145}}{2}$, and $u_0 = \sinh^{-1}\left(\frac{48}{7\sqrt{145}}\right)$. Assuming the acoustic pressure p to be harmonic in time $p = P(u,v,z)e^{i\omega t}$, which upon substitution into Eq. (10.2.20) produces the Helmholtz equation:

$$\nabla^2 P + k^2 P = 0, \tag{10.2.22}$$

where $k = \omega/c$ with ω the angular frequency, and c the phase speed. Using separation of variables $P(u,v,z) = U(u)V(v)Z(z)$. Substituting this expression into the Helmholtz equation and dividing the result by UVZ gives

$$\frac{1}{h^2(\sinh^2(u)+\sin^2(v))}\left(\frac{1}{U}\frac{d^2U}{du^2}+\frac{1}{V}\frac{d^2V}{dv^2}\right)+\frac{1}{Z}\frac{d^2Z}{dz^2}+k^2 = 0. \tag{10.2.23}$$

Equating the term containing U and V to the separation constant $-m^2$ and the term containing Z to $-k_z^2$ gives the system dispersion relation

$$k^2 = k_z^2 + m^2. \tag{10.2.24}$$

The differential equation for Z,

$$\frac{d^2Z}{dz^2}+k_z^2 Z = 0, \tag{10.2.25}$$

has solution

$$Z(z) = A_n \cos(k_z z) + B_n \sin(k_z z). \tag{10.2.26}$$

Simplifying the differential equation for U and V gives:

$$\left[\frac{1}{U}\frac{d^2U}{du^2} + m^2h^2\sinh^2(u)\right] + \left[\frac{1}{V}\frac{d^2V}{dv^2} + m^2h^2\sin^2(v)\right] = 0. \tag{10.2.27}$$

The first term is independent of v and the second term is independent of u, therefore each term must equal a constant. Letting c represent this constant:

$$\frac{1}{U}\frac{d^2U}{du^2} + m^2h^2\sinh^2(u) = c \rightarrow \frac{d^2U}{du^2} - \left[c - m^2h^2\sinh^2(u)\right]U = 0 \tag{10.2.28}$$

$$\frac{1}{V}\frac{d^2V}{dv^2} + m^2h^2\sin^2(v) = -c \rightarrow \frac{d^2V}{dv^2} + \left[c + m^2h^2\sin^2(v)\right]V = 0 \tag{10.2.29}$$

The trigonometric relations

$$\sinh^2(u) = \frac{1}{2}(\cosh(2u) - 1) \tag{10.2.30}$$

$$\sin^2(v) = \frac{1}{2}(1 - \cos(2v)) \tag{10.2.31}$$

are used to Eq. (10.2.28) and Eq. (10.2.29). Substitution of these relations into the differential equations for U and V gives:

$$\frac{d^2U}{du^2} - \left[\left(c + \frac{m^2h^2}{2}\right) - \frac{m^2h^2}{2}\cosh(2u)\right]U = 0 \tag{10.2.32}$$

$$\frac{d^2V}{dv^2} + \left[\left(c + \frac{m^2h^2}{2}\right) - \frac{m^2h^2}{2}\cos(2v)\right]V = 0. \tag{10.2.33}$$

Letting $a \equiv c + \frac{m^2h^2}{2}$ and $q \equiv \frac{m^2h^2}{4}$ gives:

$$\frac{d^2U}{du^2} - [a - 2q\cosh(2u)]U = 0 \tag{10.2.34}$$

$$\frac{d^2V}{dv^2} + [a - 2q\cos(2v)]V = 0 \tag{10.2.35}$$

These are the canonical forms of the differential equations Mathieu obtained solving for the vibration of an elliptical membrane. The solution to the differential equation for V is given by

$$V = C_r ce_r(a, q, v) + D_r se_r(a, q, v), \tag{10.2.36}$$

where the Mathieu function of the first kind ce has been termed the 'cosine-elliptic' and the Mathieu function of the first kind se has been termed the 'sine-elliptic' by E. T. Whittaker. The solution to the differential equation for U is

$$U = E_r Ce_r(a, q, u) + F_r Se_r(a, q, u), \tag{10.2.37}$$

where Ce and Se are termed the modified Mathieu functions of the first kind. The following relates the Mathieu functions to the modified Mathieu functions:

$$Ce_r(a,q,z) = ce_r(a,q,iz) \tag{10.2.38}$$

$$Se_r(a,q,z) = -ise_r(a,q,iz), \tag{10.2.39}$$

where $i = \sqrt{-1}$.

For the majority of the physical problems encountered, the solution in v is periodic by either π or 2π. This periodicity requires that a relationship exist between q and a for each ce_r and se_r, such that for each non-zero value of q a characteristic value of a exists allowing for a periodic solution in v. Common among authors today is to denote the characteristic values for ce_r by a_r, and the characteristic values for se_r by b_r. Methods for determining a_r and b_r based on q are presented in McLachlan, and Gradshteyn and Ryzhik, with formulas for r up to 8 given in Abramowitz and Stegun. For the two cases described here, *Mathematica* was used to determine the characteristic values.

For both boundary condition configurations considered, the ends of the elliptical tank were rigid, i.e. acoustic velocity is zero at $z = 0$ and $z = L$. The solution obtained above gives the acoustic pressure in the tank. To apply the zero velocity boundary condition, the momentum equation was used to relate acoustic pressure to acoustic velocity. The momentum equation is

$$\rho_0 \frac{\partial \vec{u}}{\partial t} = -\vec{\nabla} p, \tag{10.2.40}$$

where $\vec{u} = \vec{e}_u u_u + \vec{e}_v u_v + \vec{e}_z u_z$. The gradient operator in elliptic cylindrical coordinates takes the form

$$\vec{\nabla} = \frac{1}{h\sqrt{\sinh^2(u) + \sin^2(v)}} \left(\vec{e}_u \frac{\partial}{\partial u} + \vec{e}_v \frac{\partial}{\partial v} \right) + \vec{e}_z \frac{\partial}{\partial z}. \tag{10.2.41}$$

Substitution of the z component of pressure in Eq. (10.2.26) into Eq. (10.2.40), and applying the $u_z = 0$ boundary condition gives

$$Z(z) = \sum_{n=0}^{\infty} A_n \cos(k_z z), \tag{10.2.42}$$

where $k_z = \frac{n\pi}{L}$.

The boundary condition configuration having rigid boundaries on all sides of the elliptic cylindrical tank requires the $\vec{e}_u$ acoustic velocity component be 0 at $u = u_0$. Substitution of Eq. (10.2.37) into Eq. (10.2.40) and applying this boundary condition gives

$$\sum_{r=1}^{\infty} \left[E_r \left. \frac{\partial Ce_r(a,q,u)}{\partial u} \right|_{u=u_0} ce_r(a,q,v) + F_r \left. \frac{\partial Se_r(a,q,u)}{\partial u} \right|_{u=u_0} se_r(a,q,v) \right] = 0, \tag{10.2.43}$$

where $\frac{\partial Ce_0(a,q,v)}{\partial u} = 0$. To satisfy this equation requires each term of the series equal zero, giving

$$\left.\frac{\partial Ce_r(a_r,q_r,u)}{\partial u}\right|_{u=u_0} = 0 \tag{10.2.44}$$

$$\left.\frac{\partial Se_r(b_r,q_r,u)}{\partial u}\right|_{u=u_0} = 0, \tag{10.2.45}$$

where the resonance frequencies are determined from the values of q which satisfy Eqs. (10.2.44) and (10.2.45). The complete set of resonance frequencies for the elliptic cylindrical tanker having all boundaries rigid is determined from the dispersion relation using the values of k_z in Eq. (10.2.42) and $m = \frac{4\sqrt{q_r}}{h}$ obtained from Eqs. (10.2.44) and (10.2.45)

$$f = \frac{c}{2\pi}\sqrt{\left(\frac{n\pi}{L}\right)^2 + \frac{4q_r}{h^2}}, \tag{10.2.46}$$

where $c = 58724$ in/s. Table 2-32 compares the first 24 resonance frequencies between the exact determination and the **Sierra/SD** prediction for the case of rigid boundary conditions.

The boundary condition configuration having pressure release boundaries $p = 0$ on the sidewall of the elliptic cylindrical tank (and rigid end caps) requires the acoustic pressure be zero at $p(u_0, v, z)$. Applying this condition to Eq. (10.2.37) gives

$$\sum_{r=0}^{\infty} [E_r Ce_r(a,q,u_0)ce_r(a,q,v) + F_r Se_r(a,q,u_0)se_r(a,q,v)] = 0. \tag{10.2.47}$$

As before, to satisfy this condition each term of the series must equal zero, giving

$$Ce_r(a_r,q_r,u_0) = 0 \tag{10.2.48}$$

$$Se_r(b_r,q_r,u_0) = 0, \tag{10.2.49}$$

where the resonance frequencies are obtained from the values of q which satisfy Eqs. (10.2.48) and (10.2.49). The complete set of resonance frequencies for the elliptic cylindrical tanker having rigid end caps and pressure release sidewalls is determined from Eq. (10.2.46) with $c = 58724$ in/s. Table 2-33 compares the first 24 resonance frequencies between the exact determination and the **Sierra/SD** prediction for this boundary condition configuration. Note that since $Ce_0 \neq 0$ the modes cut-on at a higher frequency compared to the rigid boundaries configuration.

Exact (Hz)	**Sierra/SD**	Percent Error
248.832	248.832	0
361.1	361.1	0
438.532	438.533	2.28e-4
497.664	497.665	2.00e-4
614.868	614.87	3.25e-4
659.152	659.156	6.07e-4
687.876	687.879	4.36e-4
704.556	704.56	5.68e-4
731.499	731.503	5.47e-4
746.497	746.501	5.36e-4
825.925	825.932	8.48e-4
829.247	829.253	7.24e-4
849.025	849.035	1.18e-3
900.831	900.843	1.33e-3
934.566	934.58	1.50e-3
950.48	950.495	1.58e-3
982.512	982.529	1.73e-3
995.329	995.346	1.71e-3
995.861	995.878	1.71e-3
1015.1	1015.12	2.00e-3
1029.16	1029.18	1.94e-3
1058.81	1058.83	1.89e-3
1072.88	1072.91	2.80e-3
1130.71	1130.74	2.65e-3

Table 2-32. – Comparison between the exact analytical resonance frequencies and **Sierra/SD** predictions for the elliptic cylindrical tank with rigid boundary boundaries.

Exact (Hz)	**Sierra/SD**	Percent Error
733.807	733.811	5.45e-4
774.849	774.853	5.16e-4
886.647	886.657	1.13e-3
970.884	970.898	1.44e-3
1002.26	1002.28	2.00e-3
1046.77	1046.8	2.86e-3
1224.69	1224.75	4.90e-3
1225.4	1225.45	4.08e-3
1236.59	1236.65	4.85e-3
1250.41	1250.47	4.80e-3
1322.61	1322.68	5.29e-3
1332.8	1332.89	6.75e-3
1355.83	1355.92	6.64e-3
1390.43	1390.53	7.19e-3
1422.68	1422.81	9.14e-3
1434.88	1434.99	7.67e-3
1444.44	1444.57	9.00e-3
1491.07	1491.19	8.05e-3
1511.69	1511.82	8.60e-3
1527.61	1527.8	1.24e-2
1550.06	1550.23	1.10e-2
1569.9	1570.08	1.15e-2
1571.93	1572.09	1.02e-2
1578.15	1578.34	1.20e-2

Table 2-33. – Comparison between the exact analytical resonance frequencies and **Sierra/SD** predictions for the elliptic cylindrical tank having rigid end caps and pressure release boundary conditions on the sidewall.

10.2.4. Direct Frequency Response

Next direct frequency response is determined for the previous configuration. The boundary condition is either the rigidly capped configuration of the previous example (a Neumann boundary condition), or a pressure release condition (a Dirichlet condition). For the two types of boundary conditions on the right end,[41] gives the exact resonance frequencies. When the tube is rigidly capped, they are

$$f_n = \frac{nc}{2L} \quad n = 0, 1, 2, 3, ... \tag{10.2.50}$$

and when the tube is open (pressure release) they are

$$f_n = \frac{(n + \frac{1}{2})c}{2L} \quad n = 0, 1, 2, ... \tag{10.2.51}$$

where f_n is in Hz, c is the speed of sound, and L is the length of the tube. In this example, $c = 332.0m/s$, and $L = 10.0m$, which results in the frequencies

$$f_n = 0.0, 16.6, 33.2, 49.8, ... \tag{10.2.52}$$

and

$$f_n = 8.3, 24.9, 41.5, ... \tag{10.2.53}$$

Figures 2-32 and 2-33 show the direct frequency response computations, and it is seen that the peaks in these plots correspond to the natural frequencies given above, for both types of boundary conditions.

The pressure at the piston, as a function of frequency, is given in[32] as

$$p = -j\rho c V_0 cot(kL) \tag{10.2.54}$$

In Figure 2-34, we plot the computed and exact pressure at the piston, as a function of frequency. The two curves are virtually identical, except at the point of resonance. At resonance, however, the computed solutions are known to be inaccurate, and thus some difference there is expected.

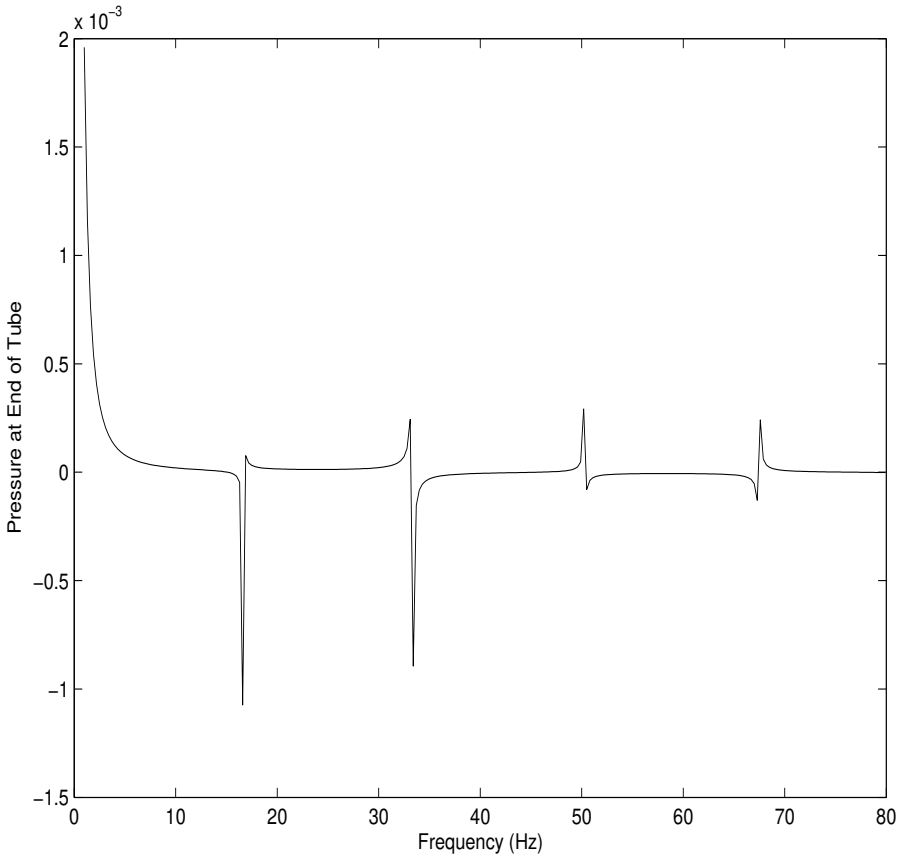

Figure 2-32. – Direct frequency response of an acoustical waveguide with rigid end cap.

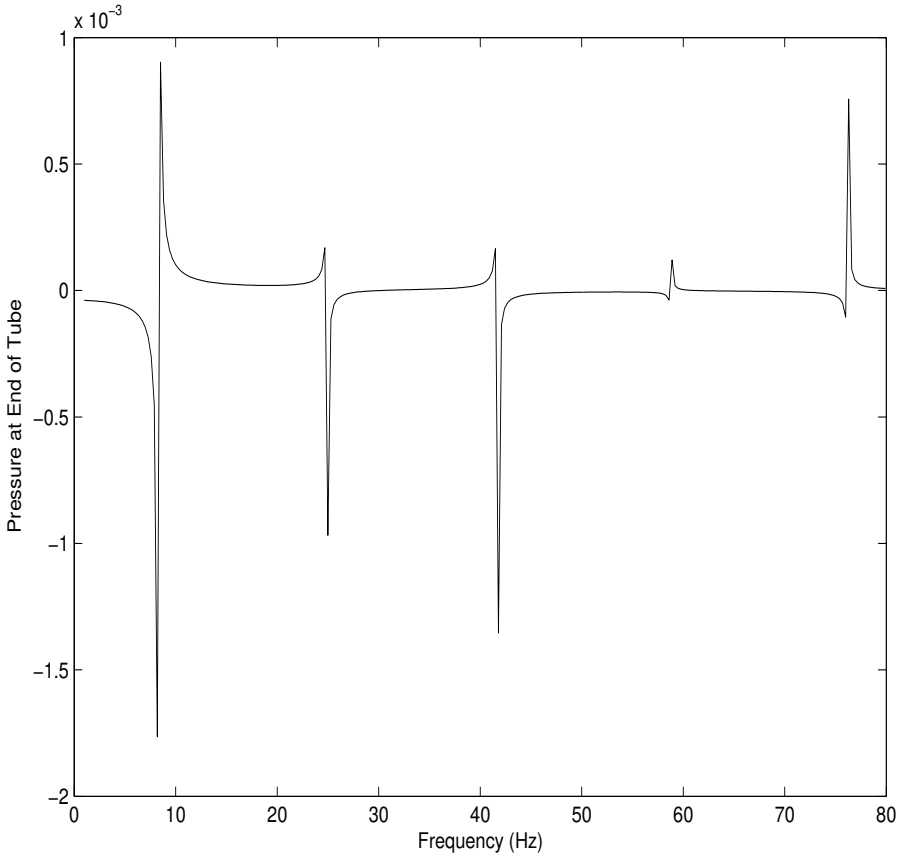

Figure 2-33. – Direct frequency response of an acoustical waveguide with pressure release end.

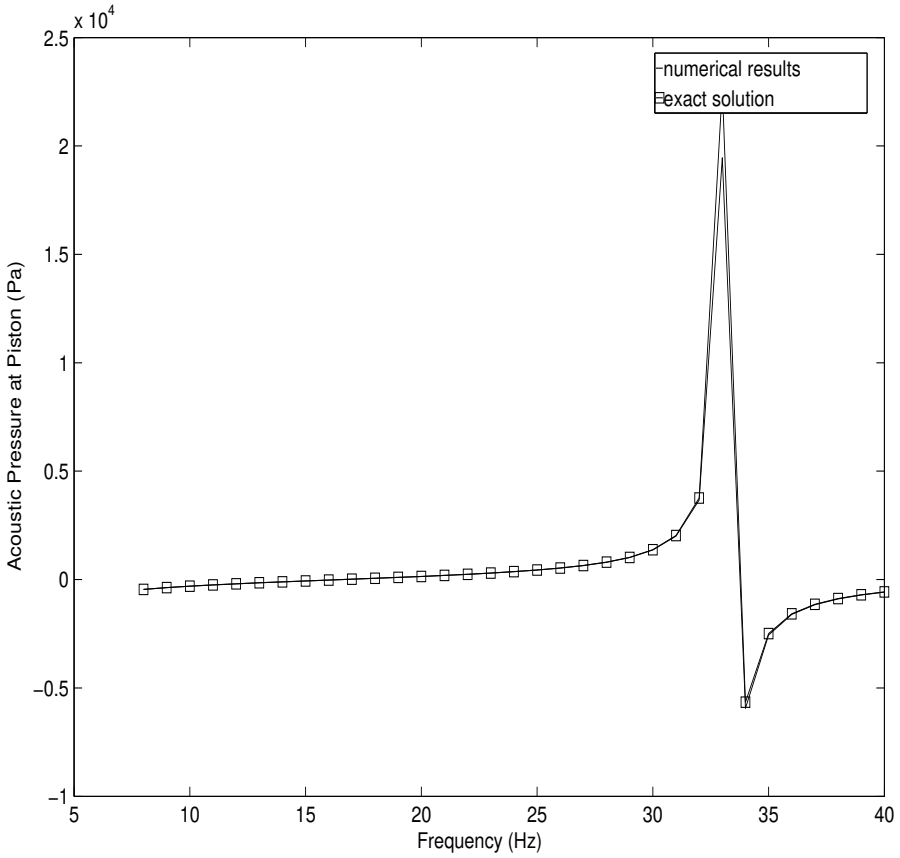

Figure 2-34. – Direct frequency response of an acoustical waveguide with rigid end cap. A comparison of computed and exact acoustic pressure at the piston.

10.2.5. Transient Acoustics with Pressure Release

This example was similar to the previous case, except that the far end of the tube was assigned a pressure release boundary condition. Also, in this case the velocity of the piston was assigned as

$$v(0,t) = v_p(t) = \sin(\omega t) \tag{10.2.55}$$

where $\omega = 60\pi$. The exact solution is given in[41] as

$$p(0,t) = \rho c \left[v_p(t) + 2 \sum_{n=1}^{\infty} (-1)^n v_p(t - \frac{2nL}{c}) \right]. \tag{10.2.56}$$

The terms in the summation become nonzero if their arguments are positive. This behavior was implemented in MATLAB using Heaviside functions, and the results were compared with **Sierra/SD**. Figure 2-35 shows the results. Excellent agreement between exact and computed solutions is observed.

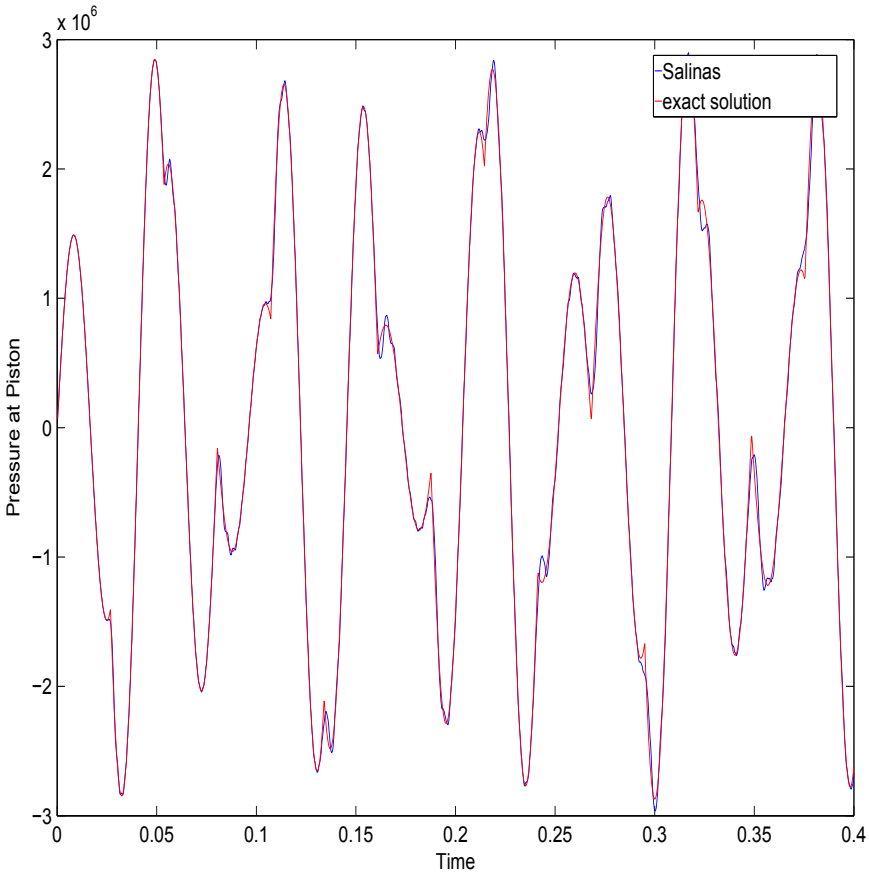

Figure 2-35. – Transient simulation of an acoustical waveguide with pressure release end condition.

10.2.6. Nonconforming Acoustic-Acoustic Discretizations

In this example, we test our simple method for coupling two acoustic domains that have mismatched meshes on the interface between them. In this case we chose an acoustic eigenvalue analysis, since the resulting eigen frequencies can be conveniently used in a convergence analysis. A three-dimensional example consisting of two adjacent acoustic domains with different discretization densities was investigated, as shown in Fig. (2-36). The nearly cubic volume having dimensions $L_x = 5$ m., $L_y = 10\sqrt{2}/3$ m., and $L_z = 15/(2\sqrt{2})$ m. was used to avoid repeated eigenvalues. The model was divided in half by an xy-plane located at $L_z/2$, as shown in Fig. (2-36), and the two halves were connected together using the inconsistent tied contact approach described in the previous section. This configuration was chosen to investigate the convergence of inconsistent tied contact for mode shapes having pressure variations in the plane of the interface. The fluid in both regions had sound speed $c = 343$ m/s and fluid density $\rho = 1.20$ kg/m^3. The boundary condition is a rigid wall (Neumann). The equations in subsubsection Coupled Equations and Their Discretizations, subsection Coupled Structural Acoustics, section Acoustics and Structural Acoustics[47] were solved with zero forcing on the right hand side, thus corresponding to the acoustic eigenvalue problem with mismatched meshes on subdomains.

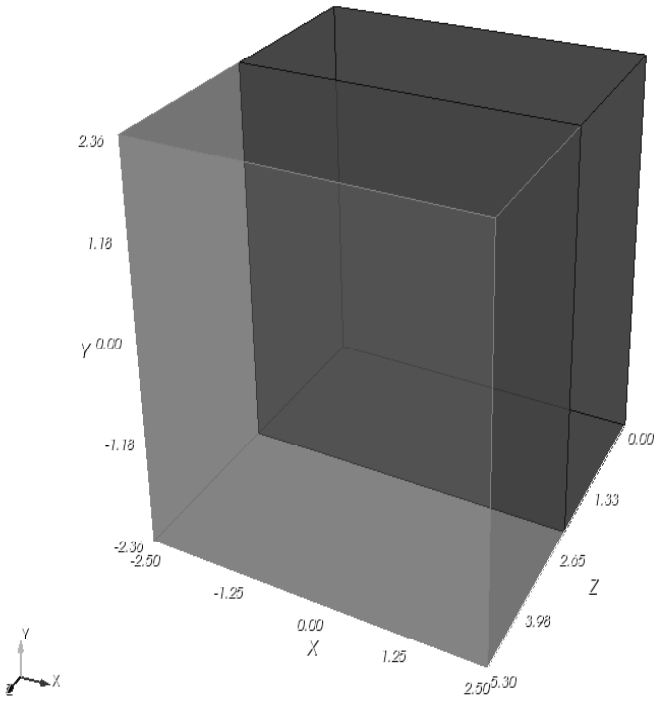

Figure 2-36. – Three-dimensional model.

Four element size ratios at the interface were investigated: 2:3, 2:4, 3:4, and 4:5. Problems with convergence can arise in inconsistent tied contact when the face-surface is more finely discretized than the node-surface, see for example.[17,18] In all cases, the face-surface was chosen as the side with the coarser discretization. The convergence study consisted of uniformly refining the meshes several times, while keeping these discretization ratios (and hence element size ratios) at the nonconforming interface fixed. Only linear hexahedrons were considered. The eigenvalues of the first thirty modes in the model were compared to the theoretical eigenvalues given by

$$f = \frac{c}{2}\sqrt{\frac{N_x^2}{L_x^2} + \frac{N_y^2}{L_y^2} + \frac{N_z^2}{L_z^2}}, \tag{10.2.57}$$

where N_x, N_y, and N_z are non-negative integers. For comparison of the convergence rates, the eigenvalues of a conforming model were also obtained. In Figs. (2-37)-(2-39) the convergence plot for the four discretization ratios are shown along with the conforming case. The horizontal axis is the common logarithm of the largest dimension of the face-surface side elements. The eigenvalue error is given by $100(\lambda^h - \lambda)/\lambda$. Figures (2-37), (2-38), and (2-39) illustrate convergence for an axial, tangential and oblique mode, respectively. For the conforming case, theory predicts that the eigenvalues will converge at a rate of 2.0 for linear elements. For comparison purposes, an additional line with a slope of 2.0 is added to the three previous figures, using the triangle symbol. For all of the cases presented, the convergence rates for the nonconforming meshes are close to those of the conforming meshes. The exceptional the 2:3 case, in which the nonconforming meshes convergence rate is greater than 2, is believed to be an abnormality. The theoretical convergence rate of 2.0 is based on conforming theory, and thus does not apply in the nonconforming case.

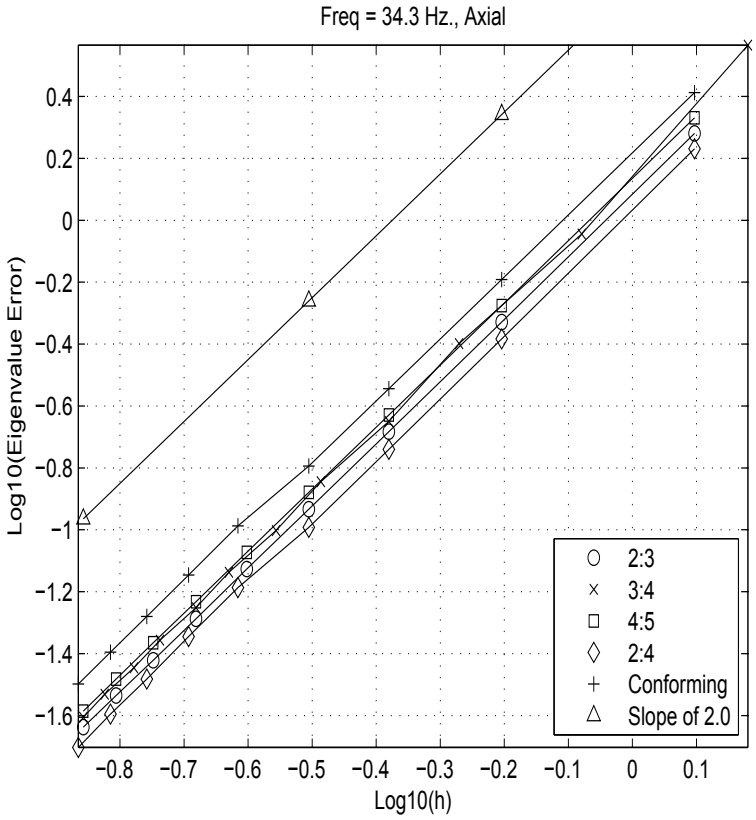

Figure 2-37. – Convergence plot for an axial mode ($N_x = 1, N_y = N_z = 0$).

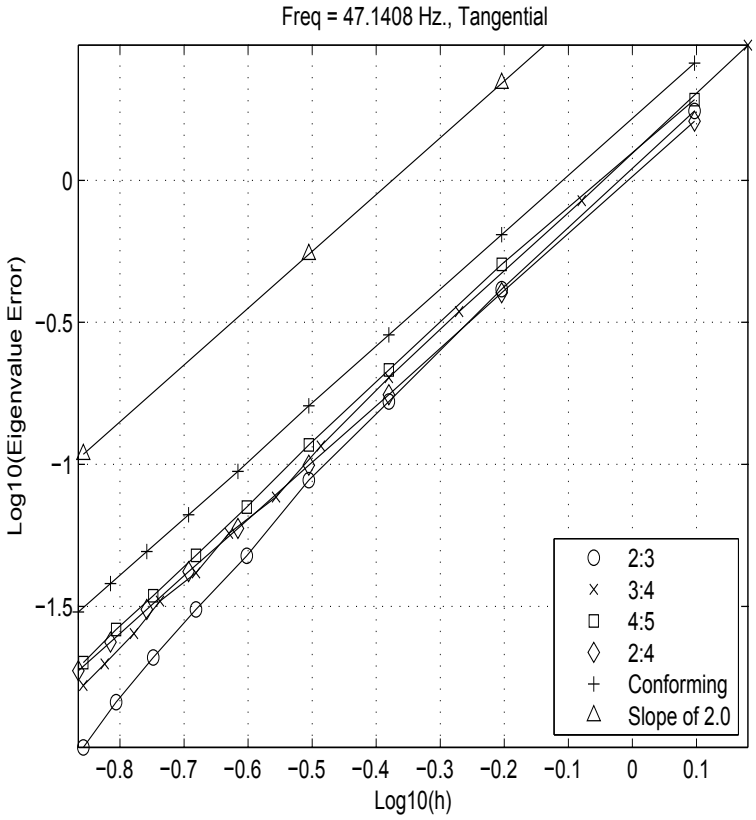

Figure 2-38. – Convergence plot for a tangential mode ($N_x = 1, N_y = 0, N_z = 1$).

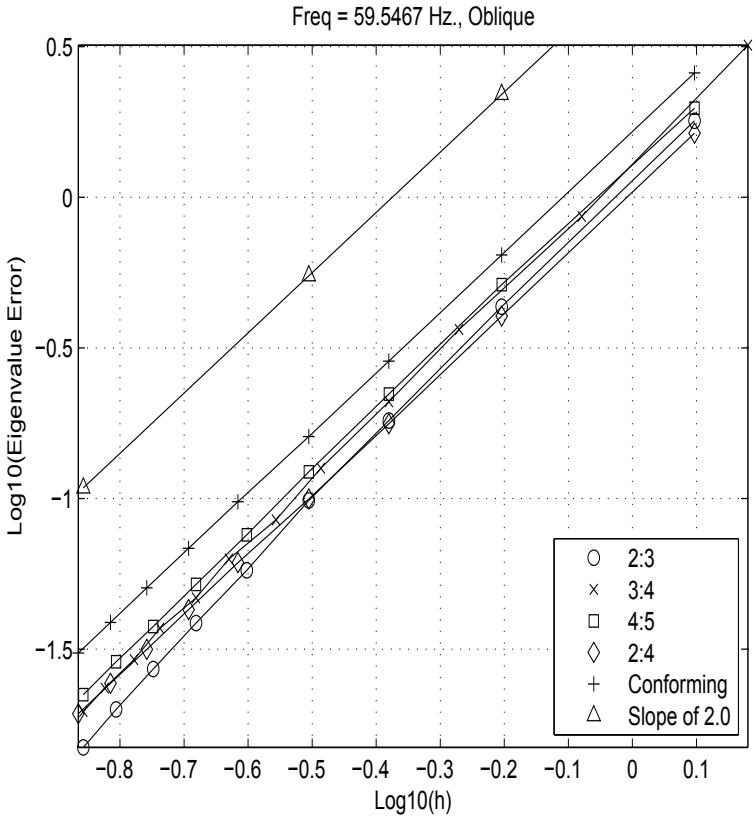

Figure 2-39. – Convergence plot for an oblique mode ($N_x = N_y = N_z = 1$).

10.2.7. Direct Frequency Response of Structural Acoustics with Tied Surfaces

This section written by Jerry Rouse.
In this case, the acoustic pressure and structural particle displacement of a one dimensional structural acoustic model is compared with theory. The model consists of a waveguide of square cross-section, 0.25 meters on a side, having an overall length of 20 meters. The length is equally divided between fluid and structure, each of length 10 meters. To the free end of the fluid is applied a harmonic particle velocity (forcing), and the free end of the structure is fixed. Inconsistent tied contact is used at the solid-fluid interface, where the fluid is treated as the independent surface. The model was investigated using the direct frequency response solution in **Sierra/SD** running in serial. The **Sierra/SD** prediction was verified at the tied interface between the fluid and solid regions.

The theoretical response of the system was obtained by solving the wave equation for longitudinal wave propagation in the solid and acoustic wave propagation in the fluid. The two solutions were coupled at the solid-fluid interface through the continuity of elastic stress and pressure, and the continuity of structural particle displacement and acoustic particle displacement. The longitudinal wave equation for the solid is given by

$$\frac{\partial^2 u}{\partial x^2} - \frac{1}{c_s^2}\frac{\partial^2 u}{\partial t^2} = 0, \tag{10.2.58}$$

where u is the particle displacement, the phase velocity $c_s = \sqrt{\frac{E}{\rho_s}}$, E is Young's modulus, and ρ_s is the material density. The coordinate system for the solid was aligned such that the x_s-axis was the center of the waveguide, with $x_s = 0$ at the fixed end of the solid and $x_s = -L_s$ at the solid-fluid interface. The fixed end boundary condition for the solid is expressed $u(x_s = 0, t) = 0$. Application of this boundary condition to the general solution of Eq. (10.2.58), expressed in terms of left and right traveling waves, gives

$$u = A\sin(k_s x_s)e^{i\omega t}, \tag{10.2.59}$$

where the wave number $k_s = \omega/c_s$, $i = \sqrt{-1}$ and A is a frequency dependent coefficient which shall be determined from the continuity conditions at the solid-fluid interface.

The acoustic wave equation is given by

$$\frac{\partial^2 p}{\partial x^2} - \frac{1}{c^2}\frac{\partial^2 p}{\partial t^2} = 0, \tag{10.2.60}$$

where p is the acoustic pressure, the phase velocity $c = \sqrt{\frac{\gamma P_0}{\rho_0}}$, where P_0 and ρ_0 are the undisturbed atmospheric pressure and density, respectively, and γ is the ratio of specific heats, here equal to 1.4. The coordinate system for the fluid was aligned such that the x_a-axis was the center of the waveguide, with $x_f = 0$ at the forcing end of the fluid and $x_f = L_f$ at the solid-fluid interface. The forcing boundary condition at the free end of the fluid in terms of the applied particle velocity V_0 is expressed

$$V_0 = \frac{i}{\omega\rho_0}\frac{\partial p}{\partial x}\bigg|_{x_f=0}. \tag{10.2.61}$$

Application of this boundary condition to the general solution of Eq. (10.2.60) gives

$$p = \left[\frac{V_0 \omega \rho_0}{k_f} e^{-ik_f x_f} + B \cos(k_f x_f) \right] e^{i\omega t}, \tag{10.2.62}$$

where the wave number $k_f = \omega/c$ and B is a frequency dependent coefficient which shall be determined from the continuity conditions at the solid-fluid interface.

The coupling conditions at the solid-fluid interface ensure no net pressure and no net velocity across the interface. The continuity condition on pressure is given by

$$E \frac{\partial u}{\partial x}\bigg|_{x_s=-L_s} = -p\bigg|_{x_f=L_f}, \tag{10.2.63}$$

where tensile stress in the solid is considered positive, and the continuity condition on velocity is given by

$$\frac{\partial u}{\partial t}\bigg|_{x_s=-L_s} = \frac{i}{\omega \rho_0} \frac{\partial p}{\partial x}\bigg|_{x_f=L_f}. \tag{10.2.64}$$

Substitution of Eqs. (10.2.59) and (10.2.62) into Eqs. (10.2.63) and (10.2.64), and solving for the frequency dependent coefficients A and B finds

$$A = \frac{iV_0 \omega \rho_0}{\omega^2 \rho_0 \sin(k_s L_s)\cos(k_f L_f) + E k_s k_f \cos(k_s L_s)\sin(k_f L_f)}, \tag{10.2.65}$$

and

$$B = \frac{-V_0 c \rho_0 \sin(k_f L_f) e^{-ik_f L_f} \left[\omega^2 \rho_0 + iE k_s k_f \cot(k_s L_s) \right]}{\omega^2 \rho_0 \cot(k_f L_f) + E k_s k_f \cot(k_s L_s)}. \tag{10.2.66}$$

Given these coefficients, the structural particle displacement is

$$u = \frac{iV_0 \omega \rho_0 \sin(k_s x_s) e^{i\omega t}}{\omega^2 \rho_0 \sin(k_s L_s)\cos(k_f L_f) + E k_s k_f \cos(k_s L_s)\sin(k_f L_f)}, \tag{10.2.67}$$

and the acoustic pressure given by

$$p = \frac{iV_0 c \rho_0 \sin(k_f L_f) e^{i\omega t} \left[\omega^2 \rho_0 \sin(k_f (L_f - x_f)) - E k_s k_f \cot(k_s L_s) \cos(k_f (L_f - x_f)) \right]}{\omega^2 \rho_0 \cot(k_f L_f) + E k_s k_f \cot(k_s L_s)}. \tag{10.2.68}$$

The Sierra/SD verification was performed with the following properties for the system. The fluid was modeled as air: $c = 343$ m/s and $\rho_0 = 1.2$ kg/m^3. The solid was modeled as steel: $E = 200$ GPa., $\rho_s = 7850$ kg/m^3, and Poisson's ratio $\nu = 0$. The value of Poisson's ratio was intentional. In Figure 2-40 the **Sierra/SD** prediction of structural particle displacement at the solid-fluid interface is compared to the theoretical result given by Eq. (10.2.67) evaluated at $x_s = -L_s$. The **Sierra/SD** prediction was obtained over the frequency range 1 to 60 Hz. using a frequency step of 1 Hz. In Figure 2-41 the **Sierra/SD** prediction of acoustic pressure at the solid-fluid interface is compared to the theoretical result given by Eq. (10.2.68) evaluated at $x_f = L_f$. In both figures the **Sierra/SD** prediction shows excellent agreement with the theoretical result.

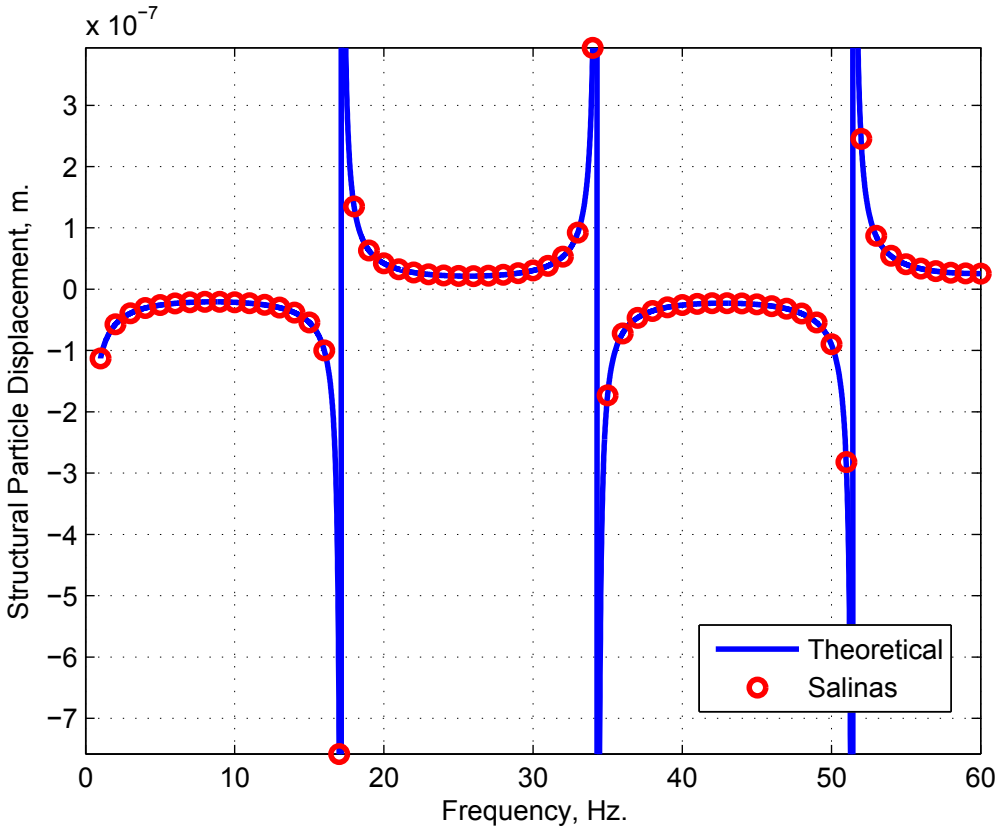

Figure 2-40. – Comparison of the **Sierra/SD** prediction of structural particle displacement at the solid-fluid interface with the theoretical result.

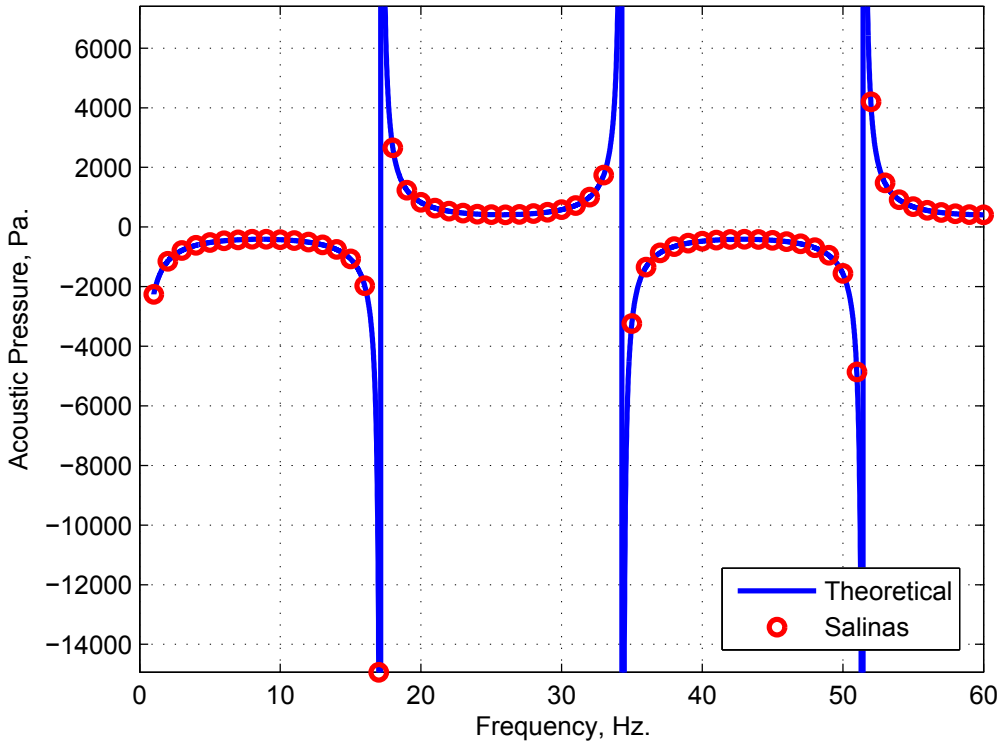

Figure 2-41. – Comparison of the **Sierra/SD** prediction of acoustic pressure at the solid-fluid interface with the theoretical result.

10.2.8. Radiation from a uniformly-driven spherical shell

In this example, we considered a spherical shell that was surrounded by an infinite acoustic fluid. The shell was composed of tria3 elements, and the acoustic fluid was modeled with tet4 elements. On the wet interface, the shell/acoustic meshes were conforming. The radius of the spherical shell was 1.0(m), and the radius of the truncated acoustic domain was 5.0(m). An absorbing boundary condition was applied to the exterior surface of the truncated acoustic domain, to simulate the infinite fluid.

A uniform, periodic pressure was applied to the inside surface of the spherical shell, and the resulting shell displacements and acoustic pressures were measured in the frequency domain. The analytic solution to this problem was derived in.[20] First we define some physical quantities. The impedance of the shell structure is given as

$$Z_s = \frac{i}{\omega}(\omega^2 m_s - k_s) \tag{10.2.69}$$

where $m_s = 4\pi a^2 h$, $k_s = \frac{8\pi E h}{1-\nu}$, h is the thickness of the shell, a is the radius of the shell, E is Young's modulus, and ν is Poisson's ratio. The impedance of the infinite fluid (as seen by the spherical surface that defines the shell) is

$$Z_f = \frac{i\omega\rho 4\pi a^3}{1+ika} \tag{10.2.70}$$

where $k = \frac{\omega}{c}$ is the wavenumber, ρ is the fluid density.

With the above quantities defined, the exact expression for the complex-valued radial displacement is

$$d = \frac{4\pi a^2 p_0}{i\omega(Z_s + Z_f}) \tag{10.2.71}$$

Figure 2-42 shows the comparison of the numerical results and analytic solution, for the real and imaginary components of radial displacement of the shell. The results show good agreement.

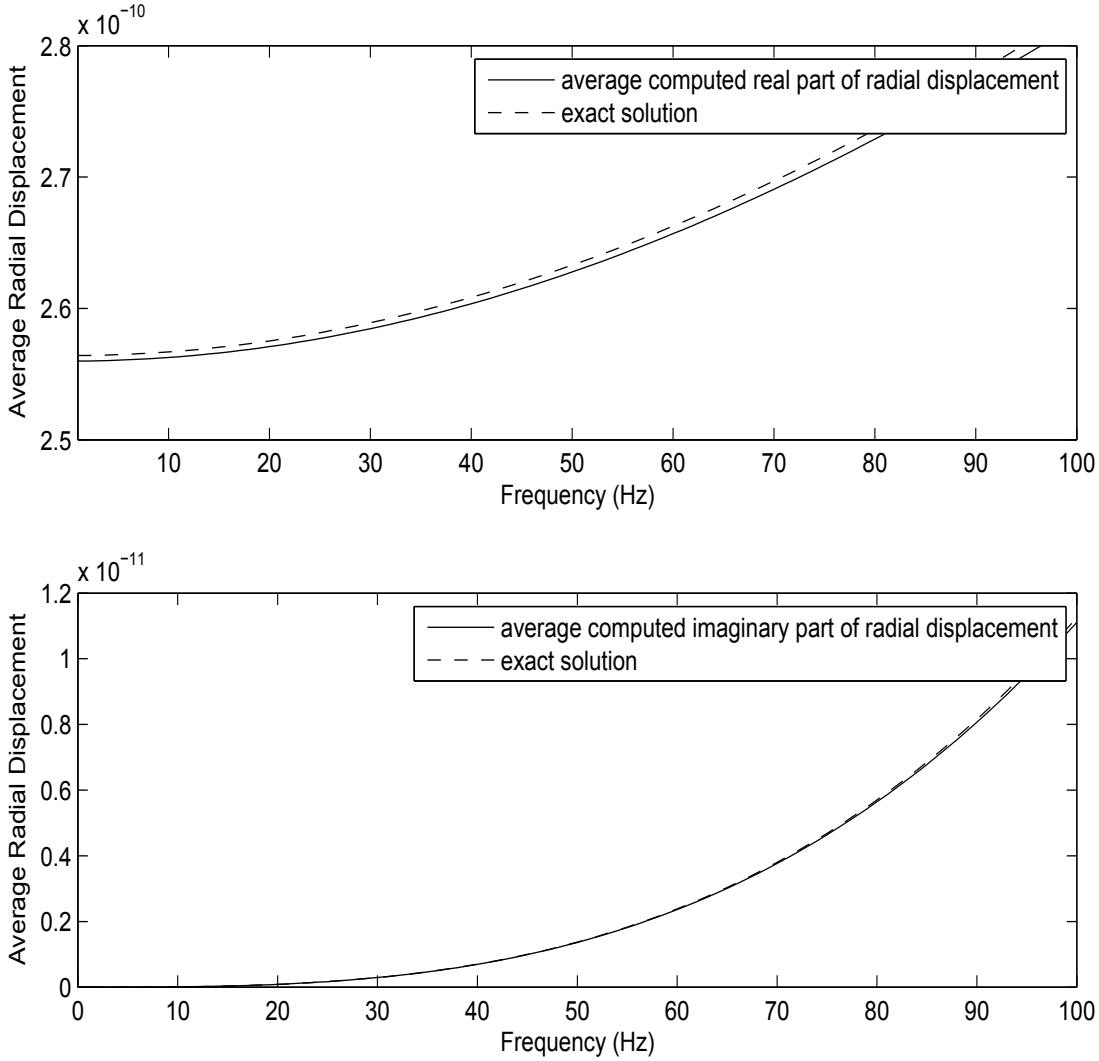

Figure 2-42. – Direct frequency response of a spherical shell immersed in an infinite fluid. The real and imaginary parts of the analytical solution are compared against **Sierra/SD**. The results show good agreement.

10.2.9. Radiation from a uniformly driven spherical acoustic surface

This example is similar to the previous example, except that the shell is removed, and we instead apply a uniform, periodic particle velocity to the inside surface of the spherical acoustic space. As in the previous example, an absorbing boundary condition is applied to the exterior surface of the truncated acoustic space, to simulate the infinite fluid. Once again, the radius of the inner spherical void is 1.0(m).

In this case, the analytic solution for the acoustic pressure on the driven surface is given by[41]

$$P = \frac{iv_0\omega\rho a^2}{r(1+ika)}e^{ik(r-a)} \tag{10.2.72}$$

where v_0 is the amplitude of the imposed particle velocity on the driven surface.

Figure 2-43 shows the comparison of the numerical results and analytic solution, for the real and imaginary components of the acoustic pressure. The results show good agreement.

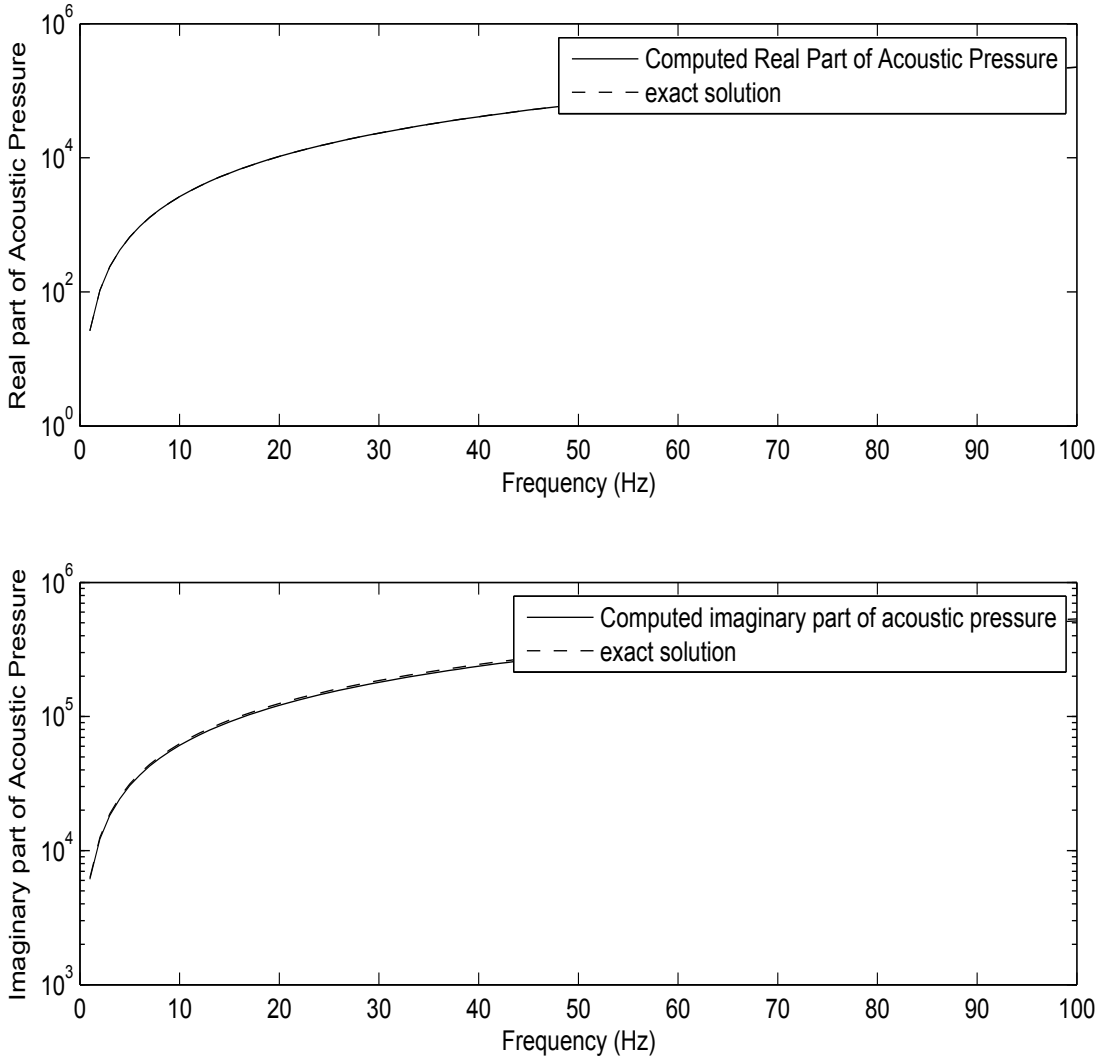

Figure 2-43. – Direct frequency response of a spherical shell immersed in an infinite fluid. The real and imaginary parts of the analytical solution are compared against **Sierra/SD**. The results show good agreement.

10.2.10. Scattering from a Flat Plate

This example involves scattering from a flat plate. The geometry consists of a uniform, acoustic tube of length 10(m), which is terminates by a flat plate. The acoustic tube is discretized with 3D acoustic elements, and the flat plate is discretized with quad shell elements. Plane waves are initiated inside of the acoustic tube, which then scatter off of the flat plate.

There is no analytical solution to this problem. However, we can still verify that the resonances of both the acoustic tube and the plate are excited at the correct excitation frequencies. This checks that the structural acoustic coupling between the plate and acoustic fluid is working correctly.

In the first example, we consider the fluid to be air, and the plate to be composed of steel, with a thickness of 0.1(m). In that case, the plate is a rigid surface to the fluid, and hence the resonance frequencies of the tube should match exactly that of a tube with rigid end caps. Figure 2-44 shows the acoustic pressure in the tube as a function of frequency. It is seen that the first resonance is predicted correctly, which according to theory should be 16.6Hz.

In the second example, we consider a light fluid that has a high speed of sound ($\rho = 1.0$, $c = 1500.0$). We also consider a thin plate, with thickness of 0.001(m). This lowers the natural frequencies of the plate well below those of the previous example. In this case, the fluid imparts no added mass effect onto the plate, since its density is low. Also, due to the high speed of sound, the natural frequencies of the tube are much higher than those of the plate. Consequently, the resonances of the plate should be the first observed resonances of the overall system. The first two exact resonances of the plate are at 3.5Hz, and 4.7Hz. Figure 2-45 shows the displacement of a corner point on the plate as a function frequency. The numerical results correctly predict the first two resonances of the plate.

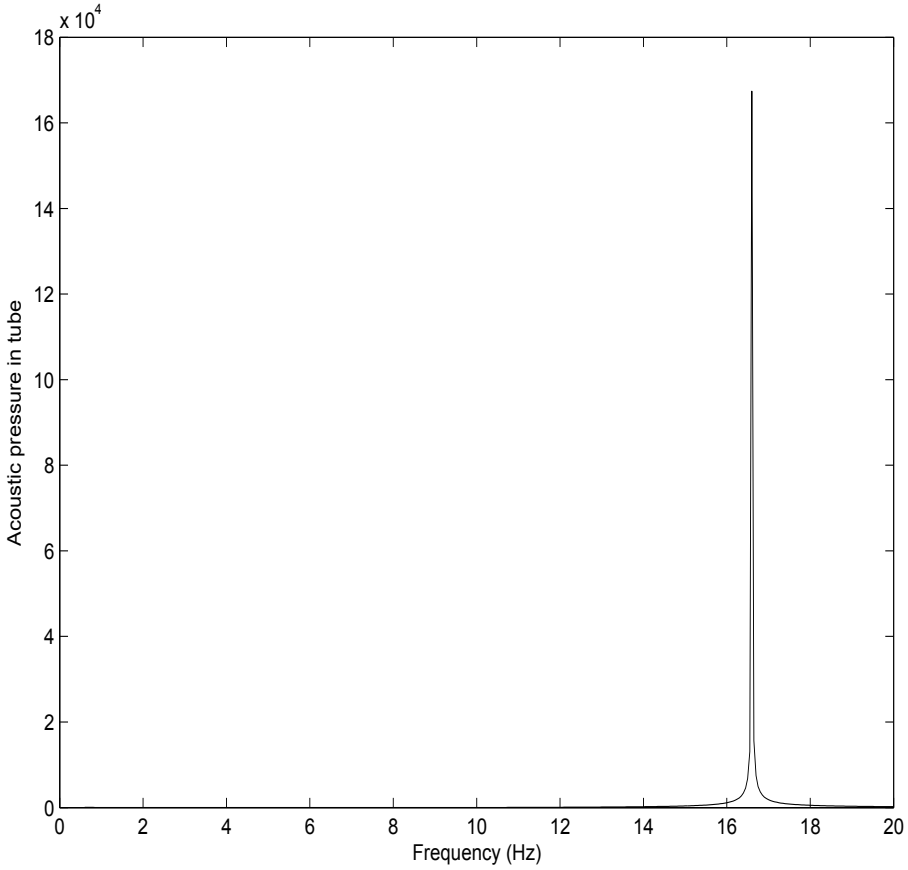

Figure 2-44. – Acoustic scattering from a plate. In the case when the plate is rigid compared with the fluid, the first resonance of the fluid tube, 16.6Hz, is reproduced well.

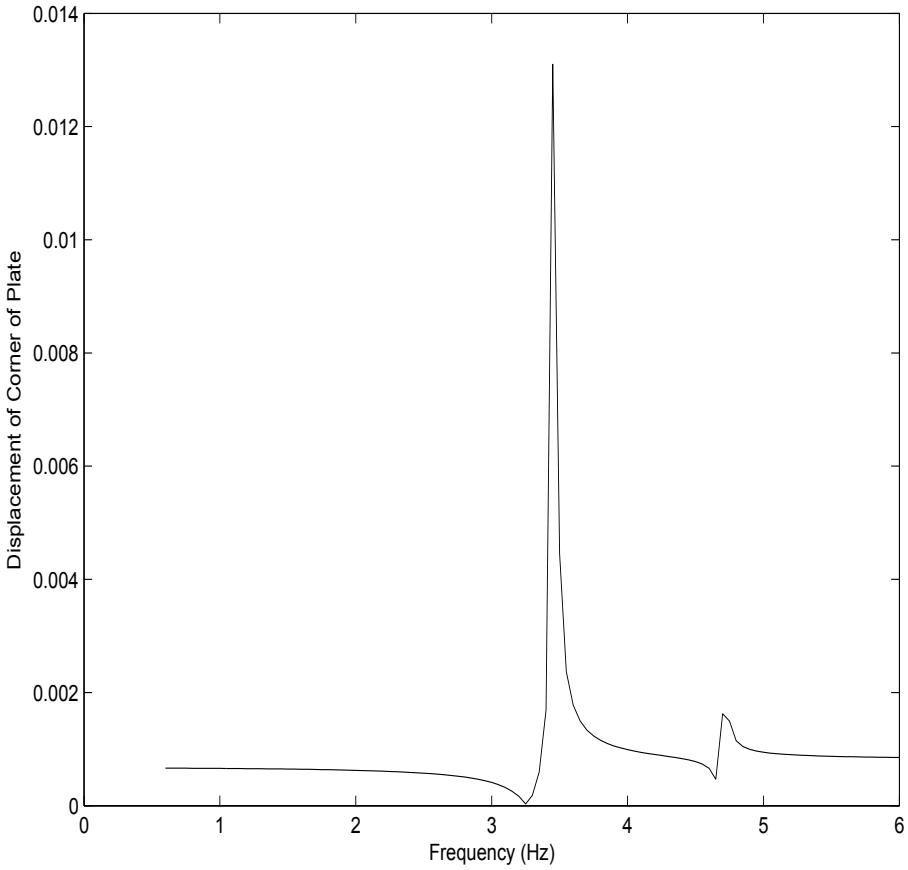

Figure 2-45. – Acoustic scattering from a plate. In the case when the fluid is given a low density and high speed of sound, the first resonance of the plate appears before the acoustic tube resonances. In that case, the first two resonances of the plate, 3.5Hz and 4.7Hz, are reproduced well.

10.2.11. Transient Scattering from a Flat Plate

In this example, we evaluate transient scattering from a flat plate. The test consists of an acoustic domain that is a perfect cube of dimensions $1 \times 1 \times 1$, which is attached with tied surfaces to a flat plate of dimension 1×1. The acoustic domain is given properties of air, and the flat plate is made of steel. Given the material property mismatch between the structural and acoustic domains, the coupling between these domains is negligible. This allows us to test the effect that the scattering waves have on the acoustic and structural components separately, without having to consider coupling.

The structural acoustic system is subjected a harmonic plane wave with frequency of 10Hz. The wet surface is located at the origin, and thus the incident pressure at the wet surface is given by

$$p(t) = \cos(\omega t) \tag{10.2.73}$$

The corresponding velocity input on the acoustic domain is given by

$$v(t) = \frac{1}{\rho c}\cos(\omega t) \tag{10.2.74}$$

An absorbing boundary condition is placed at the far-end of the acoustic domain, and thus the acoustic response should resemble that of an infinite tube. In that case, the acoustic pressure response should be equal to the input velocity times ρc. Figure 2-46 shows a comparison of the analytical and computed acoustic pressure on the wet surface. Excellent agreement is observed.

In the case of the structural response, we can use a simple force balance to determine the acceleration response of the plate, since we are ignoring coupling between the structural and acoustic components. In this case, the total pressure on the plate is equal to the sum of the incident and scattered pressures. The area of the plate is 1.0, and thus the force is equal to the pressure. Thus, we can compute the acceleration of the plate as follows

$$a = \frac{F}{m} = \frac{2\cos(\omega t)}{770} \tag{10.2.75}$$

Figure 2-47 shows the comparison of the analytical and computed acceleration of the plate.

This test case can be found at

`Salinas_rtest/verification/acoustic/hexplane.xml`

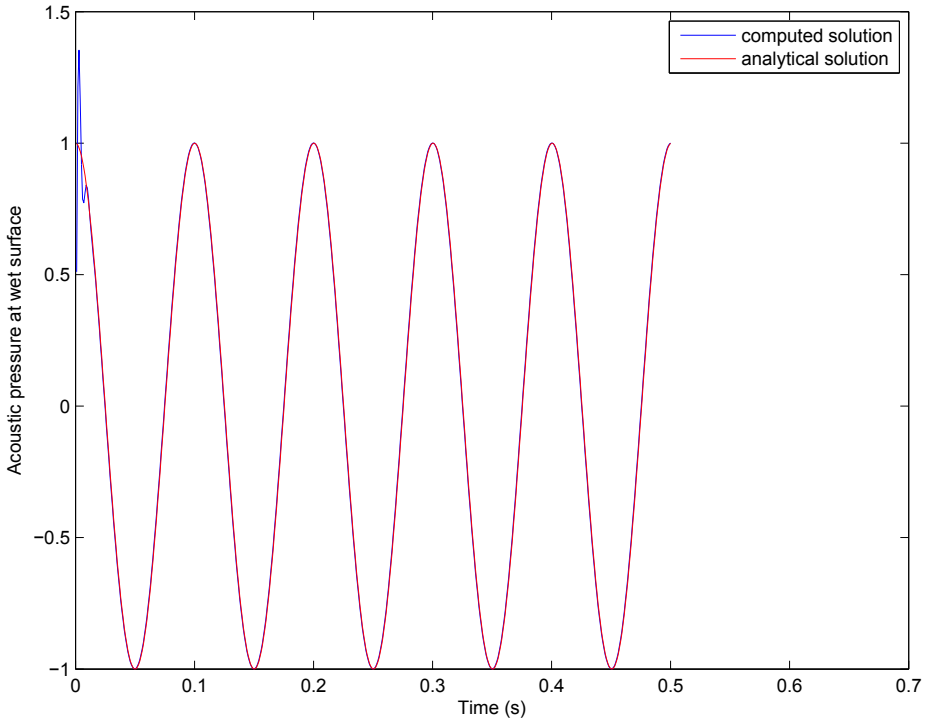

Figure 2-46. – Comparison of **Sierra/SD** result with analytical solution of the scattered acoustic pressure for a simple 1D problem.

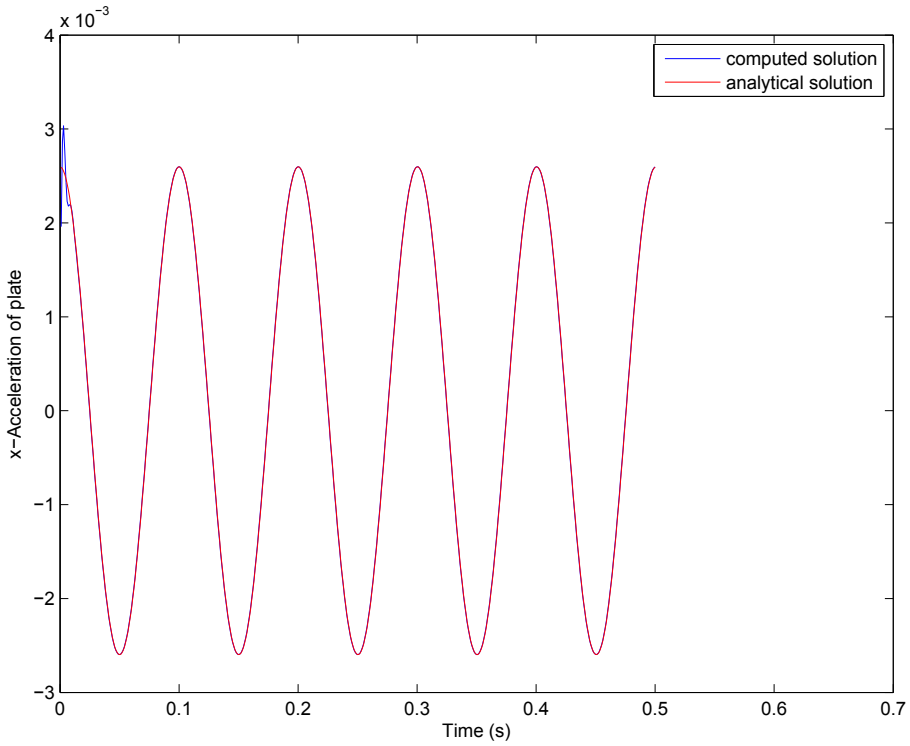

Figure 2-47. – Comparison of **Sierra/SD** result with analytical solution of the acceleration for a simple 1D scattering problem.

10.2.12. Transient Scattering of a Plane Step Wave from a Spherical Shell

Acoustic analysis often includes the concepts of a "scattering" solution. By this, we mean an analysis where it is easy to specify the incident wave at all points in space, and we solve for the reflected wave. Such scattering solutions are useful in a variety of contexts. For example, a submarine in the ocean may be struck by an incident "ping" from a neighboring ship. Such a ping is nearly a plane wave, and calculation of the outbound wave is the item of interest. Because the incident wave is known, we do not need to model the vast region of space between the incident source and the scattering object. This reduces the cost of the computation.

The theory manual details the formulation. Here we address verification of a simple sphere in an infinite medium using a problem from a LS-Dyna Verification Manual that is no longer available. The model includes a steel sphere of radius 10 inches and thickness 0.1 inches immersed in sea water. The parameters of the problem are given in Table 2-34.

parameter	value
shell radius	10.0 in
shell thickness	0.1 in
shell modulus	$0.29e+08\frac{lb}{in^2}$
shell density	$0.732e-03\frac{lb-sec^2}{in^4}$
water density	$0.96e-04\frac{lb-sec}{in^4}$
water speed of sound	$60000\frac{in}{sec}$
step wave amplitude	$100\frac{lb}{in^2}$
hit point	$z=-10in$

Table 2-34. – Parameters from Verification Model of Spherical Shell Subjected to Plane Step Wave

The solution is shown in Figure 2-48. There are discrepancies. The FEM solution excites higher order modes not seen in the analytic solution. There may be reflections from the boundaries of the fluid mesh. The verification example (found in verification/acoustic/scattering), is "quarter-sphere".

We note that the quarter-sphere model described utilized the standard absorbing boundary condition for the exterior surface of the acoustic mesh. Identical results are obtained using infinite elements. The location of the test is

`Salinas_rtest/verification/acoustic/scattering/quarter_sphereIE.inp`

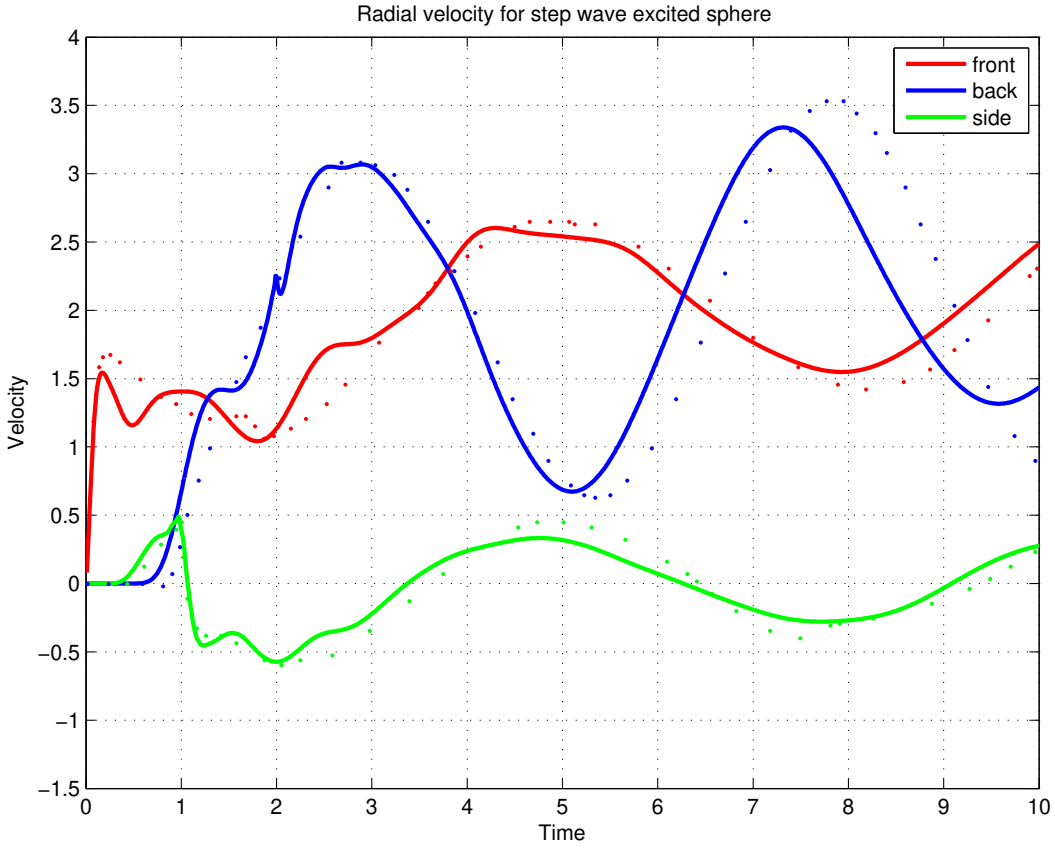

Figure 2-48. – Sphere Impacted by Step Wave. The incoming step wave arrives from the $-Z$ direction. Dashed lines are the analytic solution.

10.2.13. Infinite Elements on an Ellipsoidal Surface - Transient Scattering

It is often advantageous to mesh the area about a structure with an ellipsoidal (or prolate spheroid) mesh, and use infinite elements on the ellipsoidal boundary to model the effects of an infinite fluid. This is the case if a submarine is modeled. A spherical mesh about this long cylindrical structure is larger than an ellipsoidal mesh. To verify the behavior of the infinite elements on this boundary, we use the spherical structure of section 10.2.12 and compare with the closed form solutions obtained by Huang,.[30] This problem came to our attention through an LS-Dyna Verification Manual that is no longer available.

The standard formulation of infinite elements is built on radial basis functions. In the case of a sphere, these basis functions can be defined using a common source location at the origin of the sphere. When the infinite element surface is an ellipsoid, a common source location yields basis functions that are not orthogonal to the infinite element surface, resulting in poor performance and spurious reflections. To alleviate this, the basis functions for an ellipsoidal can be defined using a variable source location, such that each element (each node on the surface) has its own source point for expansions of the basis functions. This ensures that the basis is orthogonal to the ellipsoidal surface.

To evaluate the reflection of the infinite elements, several meshes were composed. Details of the meshes are shown in Table 2-35. All meshes are quarter symmetry models. A representative mesh is shown in Figure 2-49. Results from the analyses are shown in Figures 2-50 through 2-52.

10.2.13.0.1. High Frequencies. There are two reasons why it is necessary to eliminate high frequencies from the comparison. First, the analytic solution is a series summation (see equation 17[30]). It contains the lowest frequency modes in the solution, and filters the higher frequency solution. Second, high frequencies are introduced through of the mesh discretization. We observe that while the frequency of these spurious solutions increases with mesh density, the amplitude typically decreases. It is impractical to refine the mesh sufficiently to eliminate all such mesh dependent responses.

Name	Eccentricity	Acoustic Elements
sphere-m1	1:1	672
sphere-m2	1:1	5088
sphere-m3	1:1	40128
sphere-m4	1:1	323856
ellipse-m1	3:1	672
ellipse-m2	3:1	5088
ellipse-m3	3:1	40128
ellipse-m4	3:1	323856

Table 2-35. – Mesh Parameters of Infinite Elements on Ellipsoidal Surfaces.

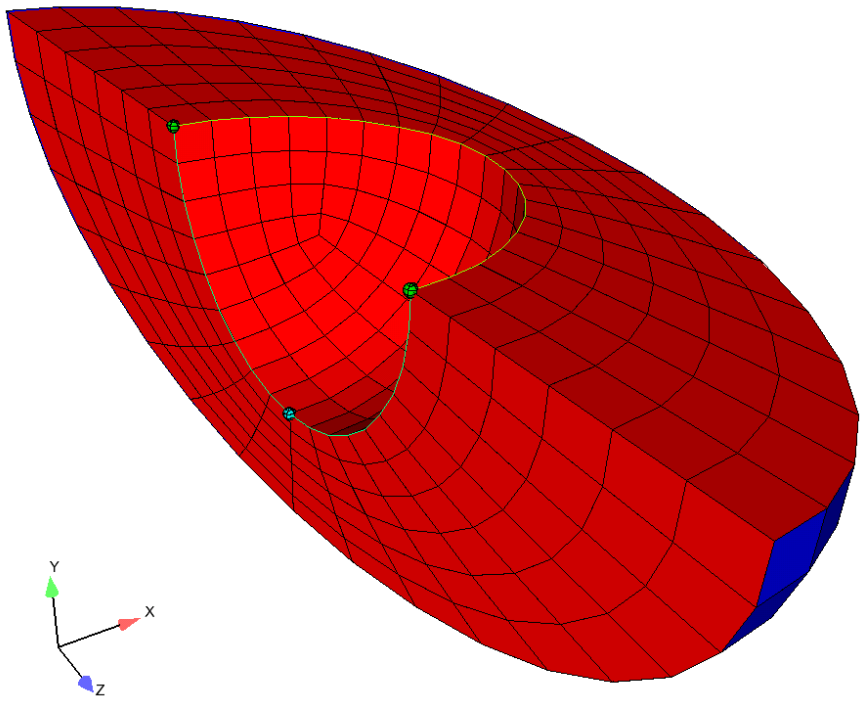

Figure 2-49. – Representative Mesh of Quarter Symmetry Sphere in Ellipse.

The higher frequencies could be eliminated in a variety of ways. The input loading can be filtered to "smooth" the step function and eliminate high frequency excitation. The integrator could introduce artificial numerical damping which removes high frequency energy during the computation. Or, the signal could be post-processed by filtering. We use post-process filtering in this case because it is straightforward to implement and does not introduce unknown phase shifts. We use the MATLAB "filtfilt" function on a Butterworth low pass filter of order 6. The cutoff frequency is 10 kHz.

The radial response of an unfiltered and filtered responses is shown in Figure 2-53. Even with increasing mesh density, high frequency oscillations continue to dominate the response.

10.2.13.0.2. Dependence on Loading Decay. The analytic solution loadings include an exponential decay following a step wave response.[1] The previous analysis was analysis performed with no decay. Figures 2-54 and 2-55 show the response for various decay factors as observed on the leading and trailing edges of the sphere. The analytical solutions for this case were taken from Sprague and Geers.[52]

[1] The pressure can be written as,

$$P = H(t-\tau)\exp\left(-\beta[t-\tau]\right)$$

where $H()$ is the Heavyside step function, t is the measurement time, τ represents the travel time from the source to measurement location and β is the decay constant.

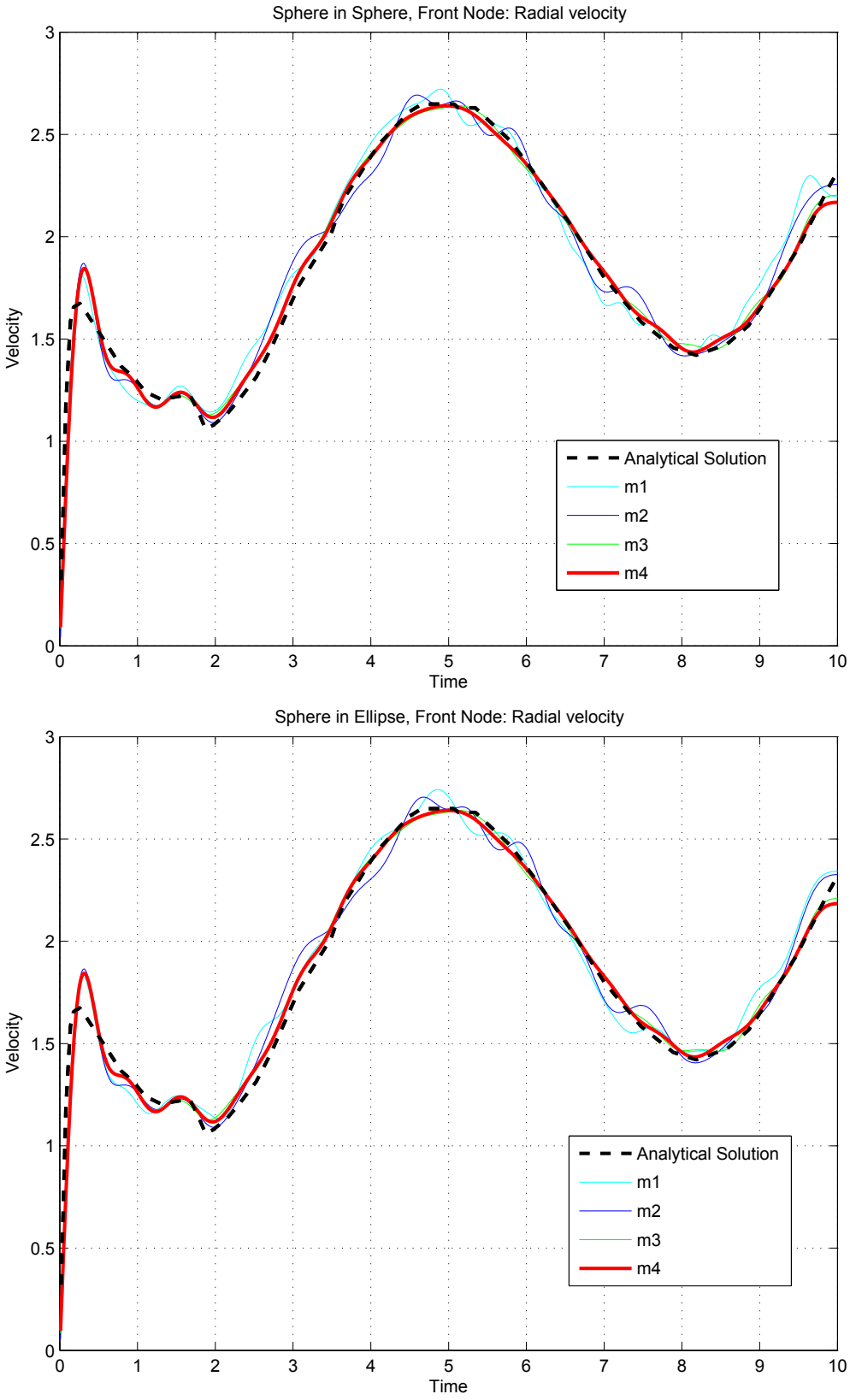

Figure 2-50. – Filtered Front Node Response and mesh convergence for both a spherical and ellipsoidal acoustic region.

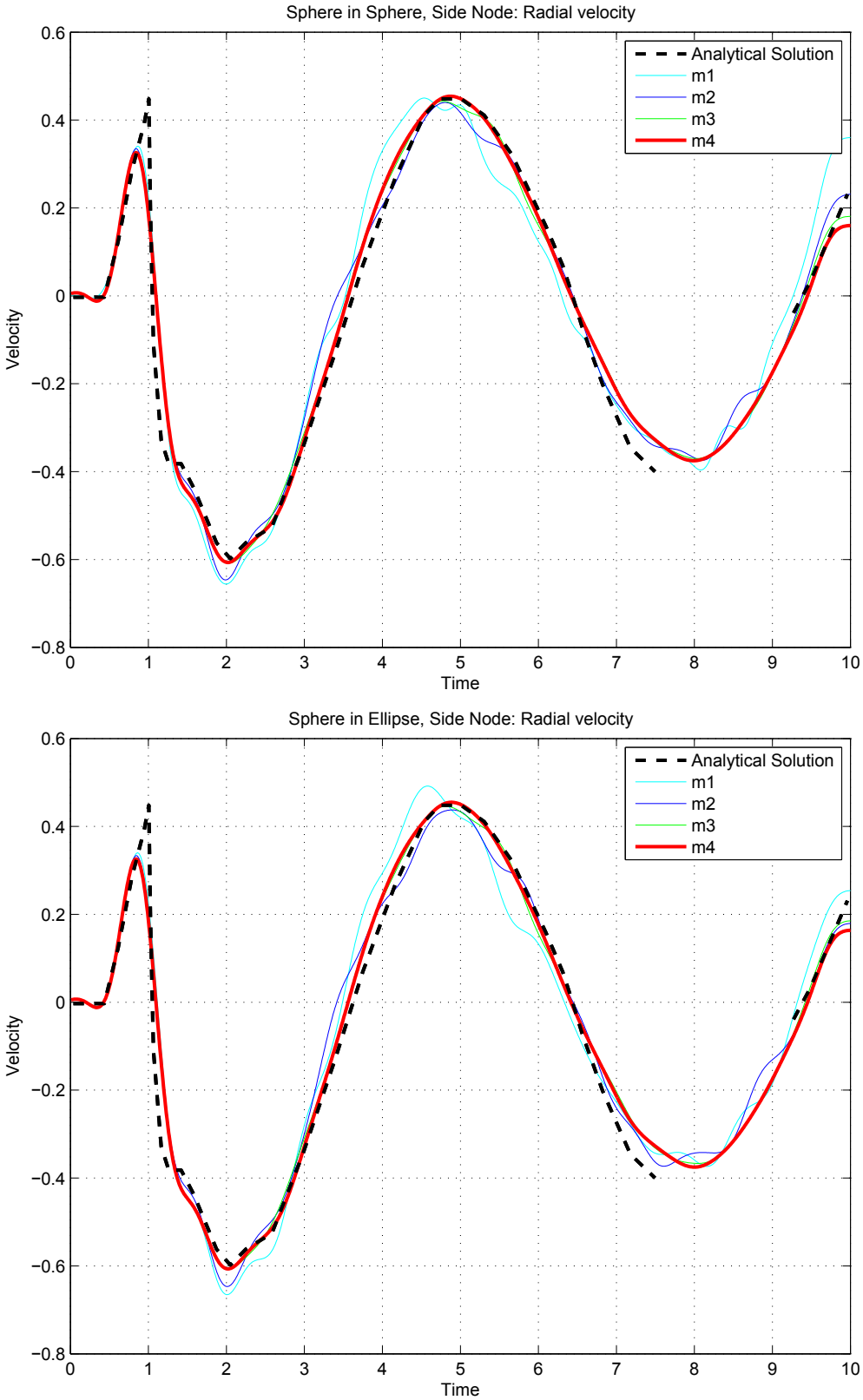

Figure 2-51. – Filtered Side Node Response and mesh convergence for both a spherical and ellipsoidal acoustic region.

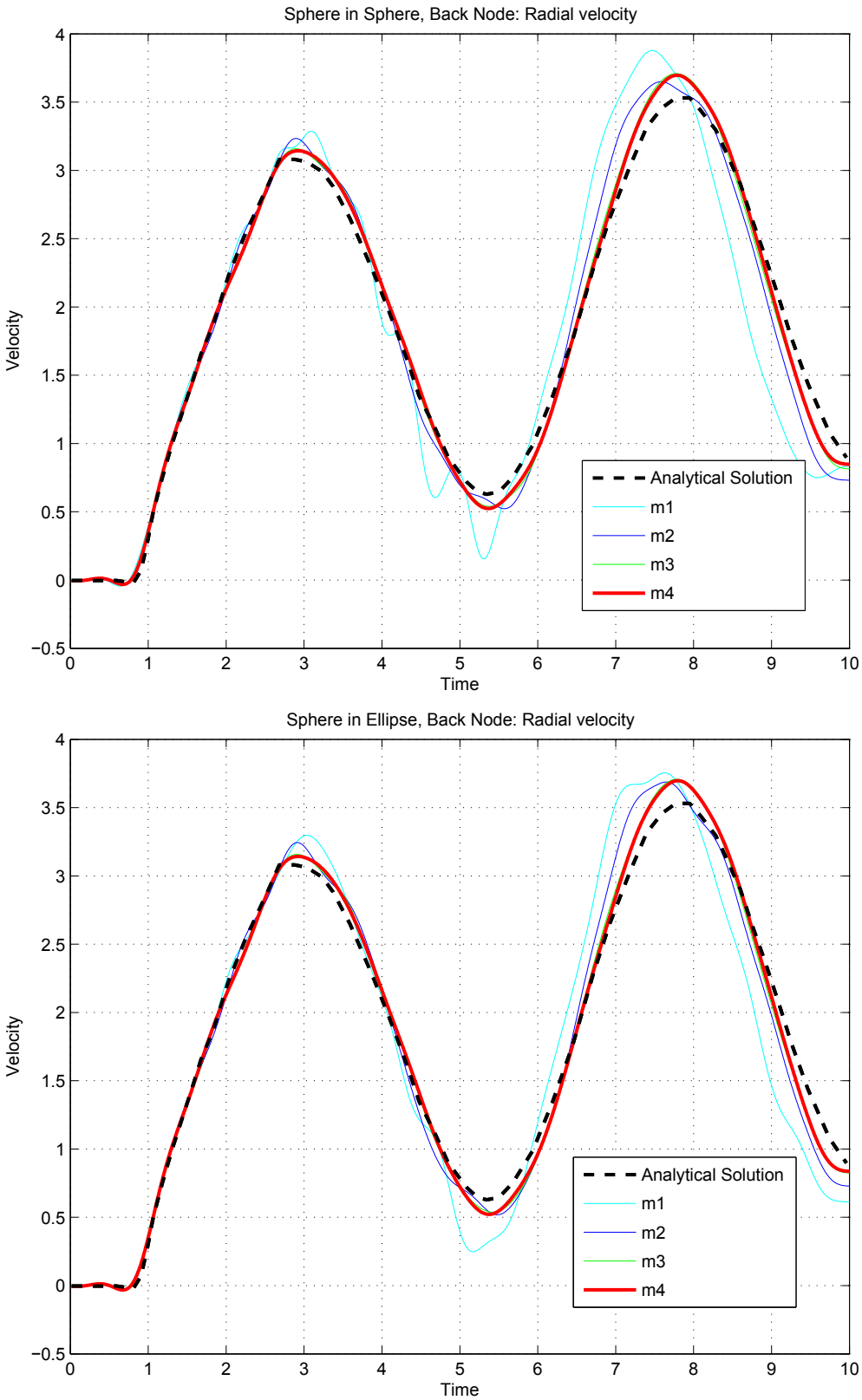

Figure 2-52. – Filtered Back Node Response and mesh convergence for both a spherical and ellipsoidal acoustic region.

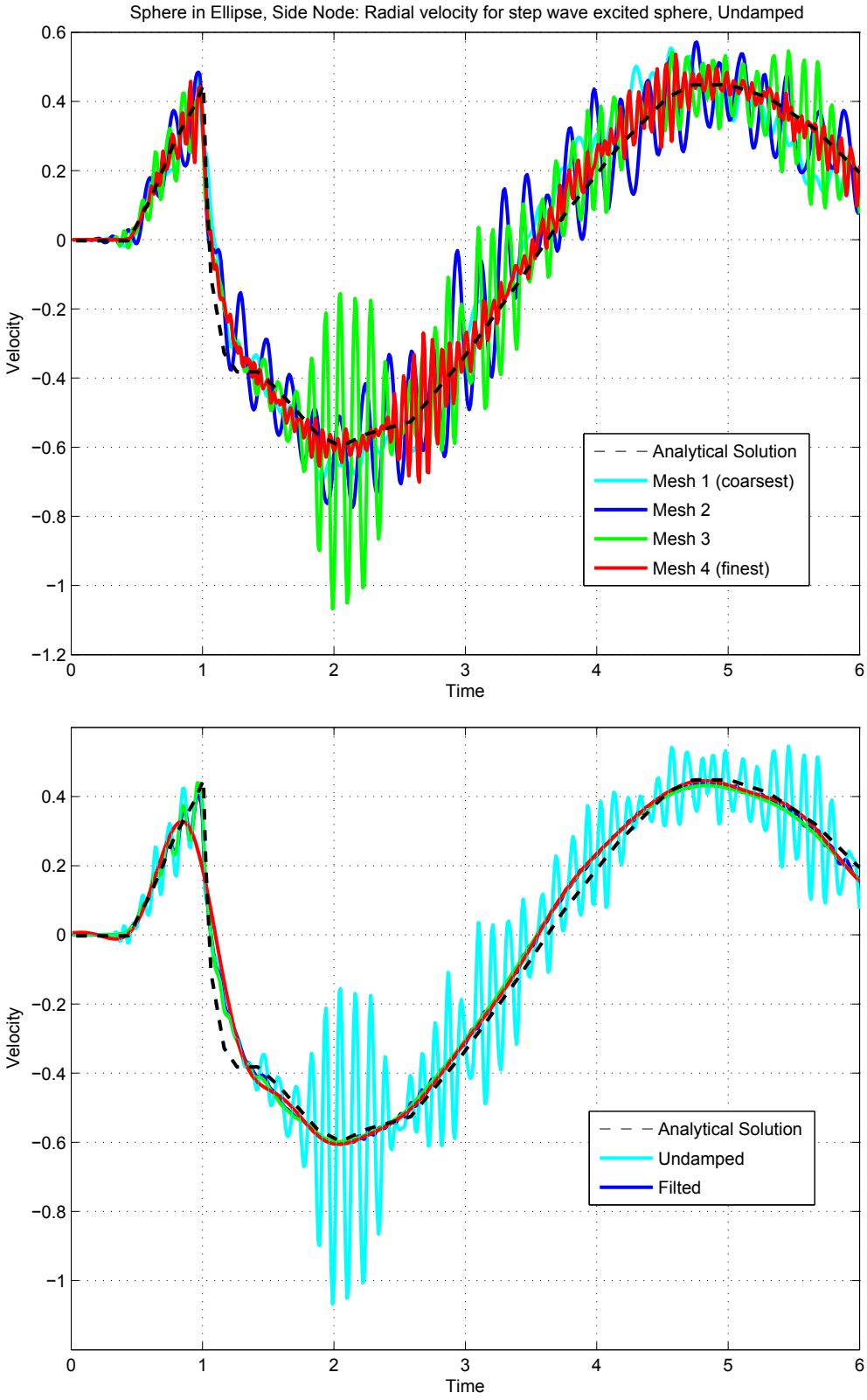

Figure 2-53. – Sphere in Ellipsoid. Unfiltered response at 90^o location.

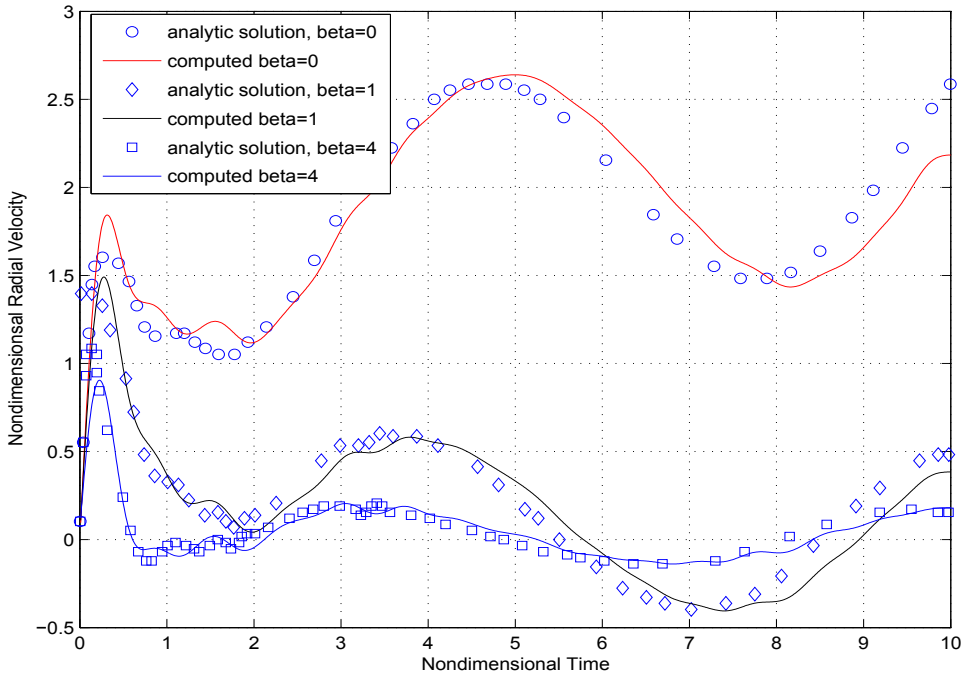

Figure 2-54. – Comparison of **Sierra/SD** result with analytical solution of the scattered acoustic pressure on the leading surface of a sphere. Mesh=m4.

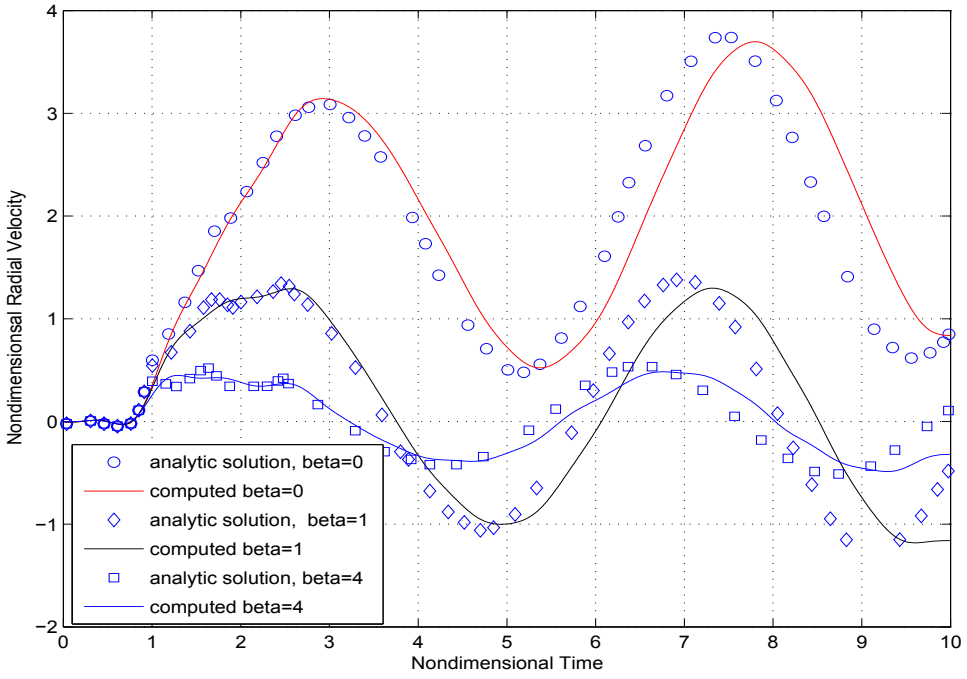

Figure 2-55. – Comparison of **Sierra/SD** result with analytical solution of the scattered acoustic pressure on the back surface of a sphere. Mesh=m4.

The purposes of these plots is to determine the dependence of the solution on the decay parameter "beta". This dependence is in general well represented, but the phase error is significant. Figure 2-56 compares numeric solution with the analytic solution of Geers and the results published in the USA verification manual for the case of $\beta = 0$. The numeric results are much closer to the USA prediction. There are some issues here that have not been identified. The two analytical solutions should be identical, but differ. We can guess that a different number of terms were retained in the series expansion. The USA solution is available for $\beta = 0$ only.

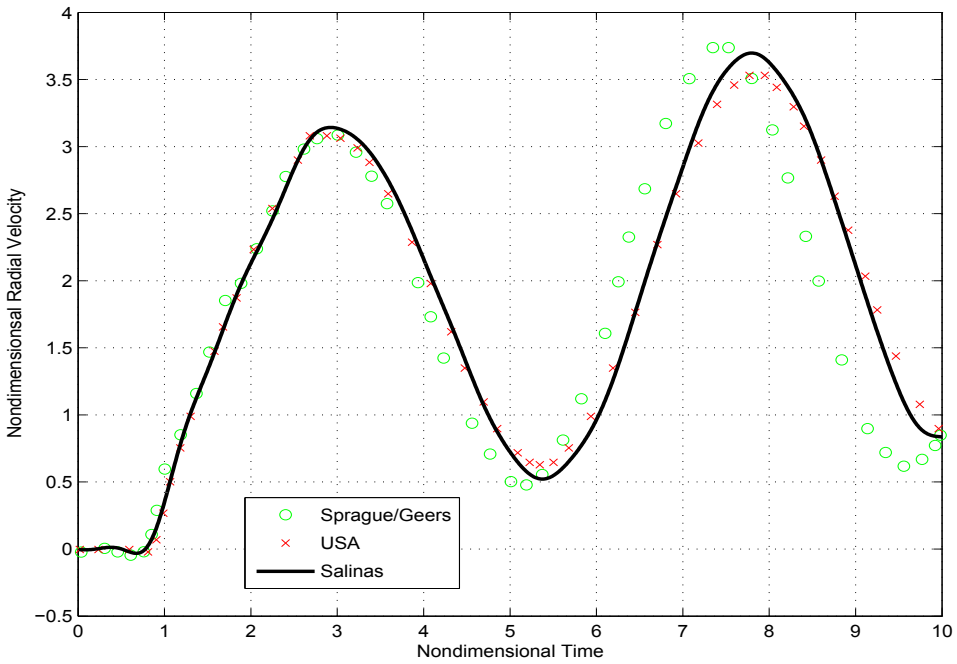

Figure 2-56. – Comparison of **Sierra/SD** numerical result with two differing analytic solutions. Mesh=m4. Prediction on the back surface

10.2.14. A comparison of spherical and ellipsoidal infinite elements on a model problem

In this section we examine the results of a simple test problem designed to compare the results of infinite elements on spherical and ellipsoidal meshes. For the purposes of these comparisons, we will use the results on the spherical meshes as the truth model, and the goal will be to show that for sufficiently fine acoustic meshes and sufficiently high infinite element order, the results on the spherical and ellipsoidal meshes are the same.

Figures 2-57 and 2-58 show the geometry of the test case. In the case of the ellipse, two different aspect ratios were studied, $10:1$ and $3:1$. Figure 2-58 shows the aspect ratio of $10:1$. An acoustic mesh is defined on a spherical (Figure 2-57) and ellipsoidal (Figure 2-58) geometry. In both cases a cylindrical hole is cut out from the mesh, and an applied

acoustic velocity is applied to the outermost surface of the cutout. The applied velocity is the same on the entire surface, and consists of the hat function shown in Figure 2-59.

Figure 2-60 shows the results of acoustic pressure along a 45^o angle relative to the major axis, for a spherical mesh and an ellipsoidal mesh of aspect ratio $3:1$. For the ellipsoidal meshes, results are shown using two different source location algorithms of the plane-line intersect method, and the constant offset method. The results from a previous **Sierra/SD** release that involved a fixed source location is also shown. Both the plane-line intersect and constant offset ellipse algorithms replicate the results produced on the sphere, but the fixed source location algorithm from the previous **Sierra/SD** release shows significant differences. This is expected, since that algorithm required a zero mass matrix even when the mass matrix was non-zero, as in this case. Figure 2-61 shows the same results, but for an ellipsoidal mesh of aspect ratio $10:1$. Similarly, the plane-line intersect and constant offset source location algorithms for the ellipsoidal meshes yield identical results to the sphere.

Figure 2-62 shows the results of acoustic pressure along the major axis, for a spherical mesh and an ellipsoidal mesh of aspect ratio $3:1$. For the ellipsoidal meshes, results are shown using the two different source location algorithms of the plane-line intersect method, and the constant offset method. The results involving a fixed source location that was implemented in a previous **Sierra/SD** release are also shown. Both the plane-line intersect and constant offset ellipse algorithms replicate the results produced on the sphere, but the fixed source location algorithm shows significant differences. This is expected, since that algorithm required a zero mass matrix even when the mass matrix was non-zero, as in this case. Figure 2-63 shows the same results, but for an ellipsoidal mesh of aspect ratio $10:1$. In this case, the initial behavior of the results on ellipsoidal meshes are identical to that of the sphere, but later times show some small discrepancies. Further increases in infinite element order did not resolve these discrepancies. Additional acoustic mesh refinements are necessary for the results to converge.

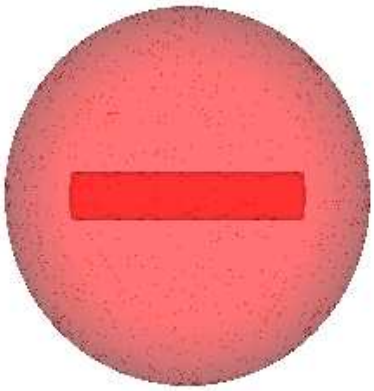

Figure 2-57. – Spherical acoustic mesh for cylindrical cutout problem.

Figure 2-58. – Ellipsoidal mesh with aspect ratio 10:1 for cylindrical cutout problem.

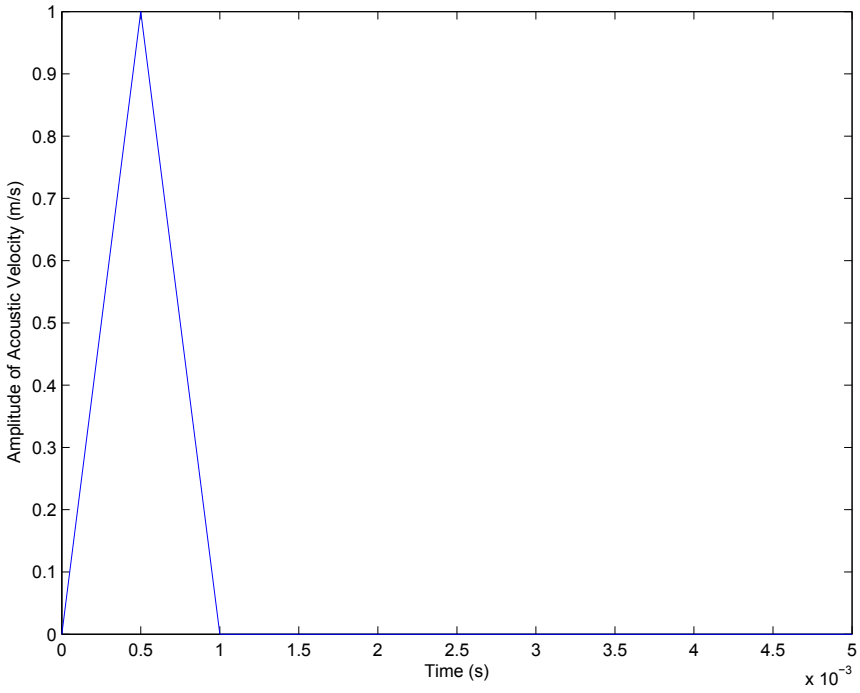

Figure 2-59. – Amplitude function used to scale input acoustic velocity for cylindrical cutout problem.

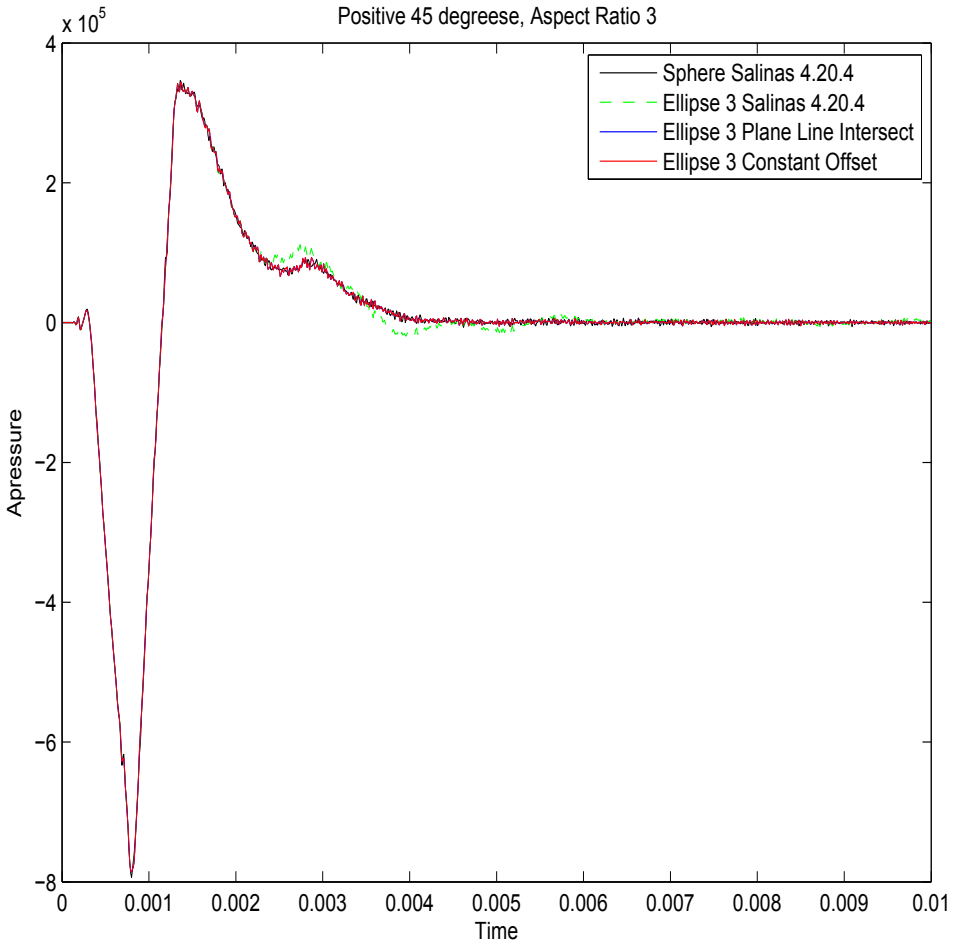

Figure 2-60. – A comparison of results along a 45^o angle from cylindrical cutout problem on spherical and ellipsoidal meshes of aspect ratios 3:1

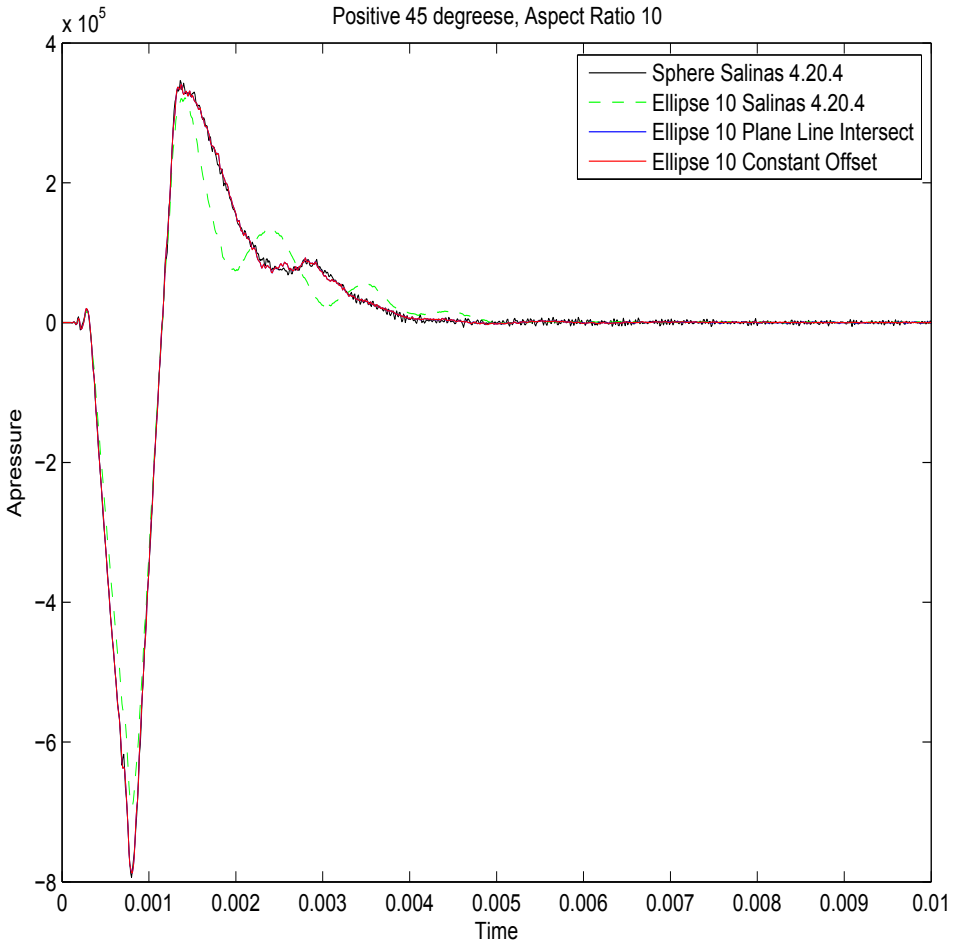

Figure 2-61. – A comparison of results along a 45^o angle from cylindrical cutout problem on spherical and ellipsoidal meshes of aspect ratios 10:1

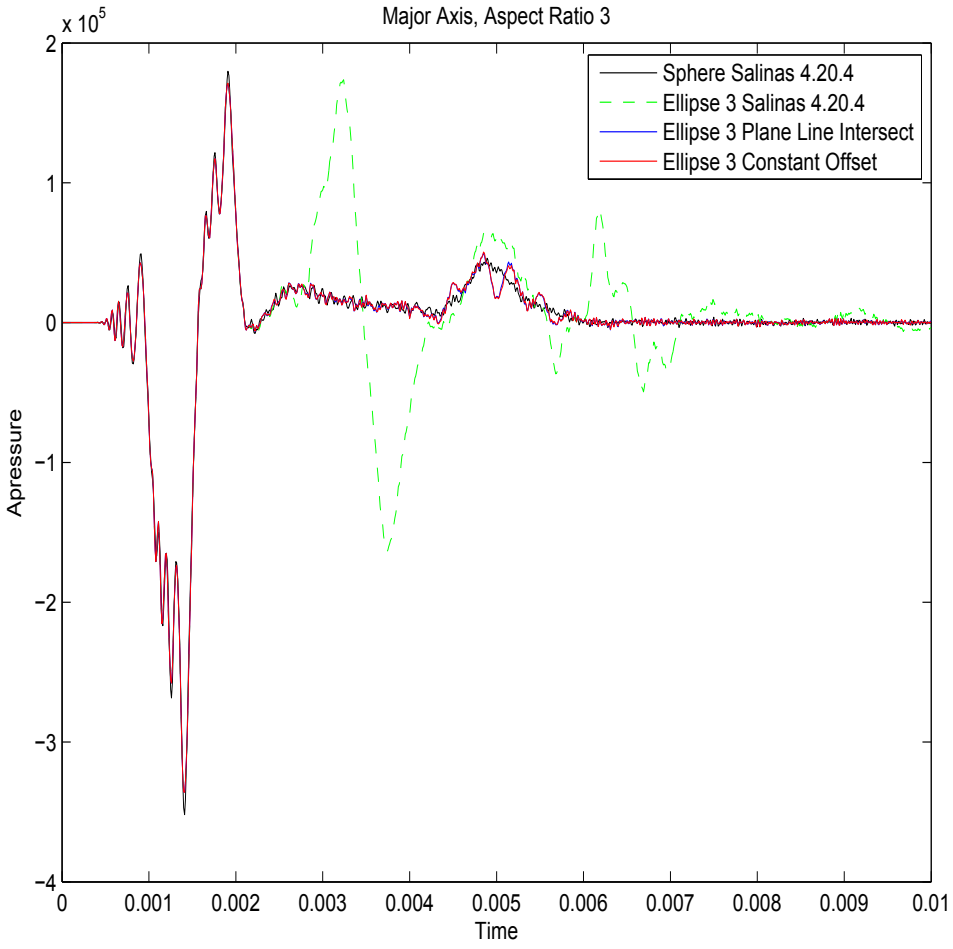

Figure 2-62. – A comparison of results along the major axis from cylindrical cutout problem on spherical and ellipsoidal meshes of aspect ratios 3:1

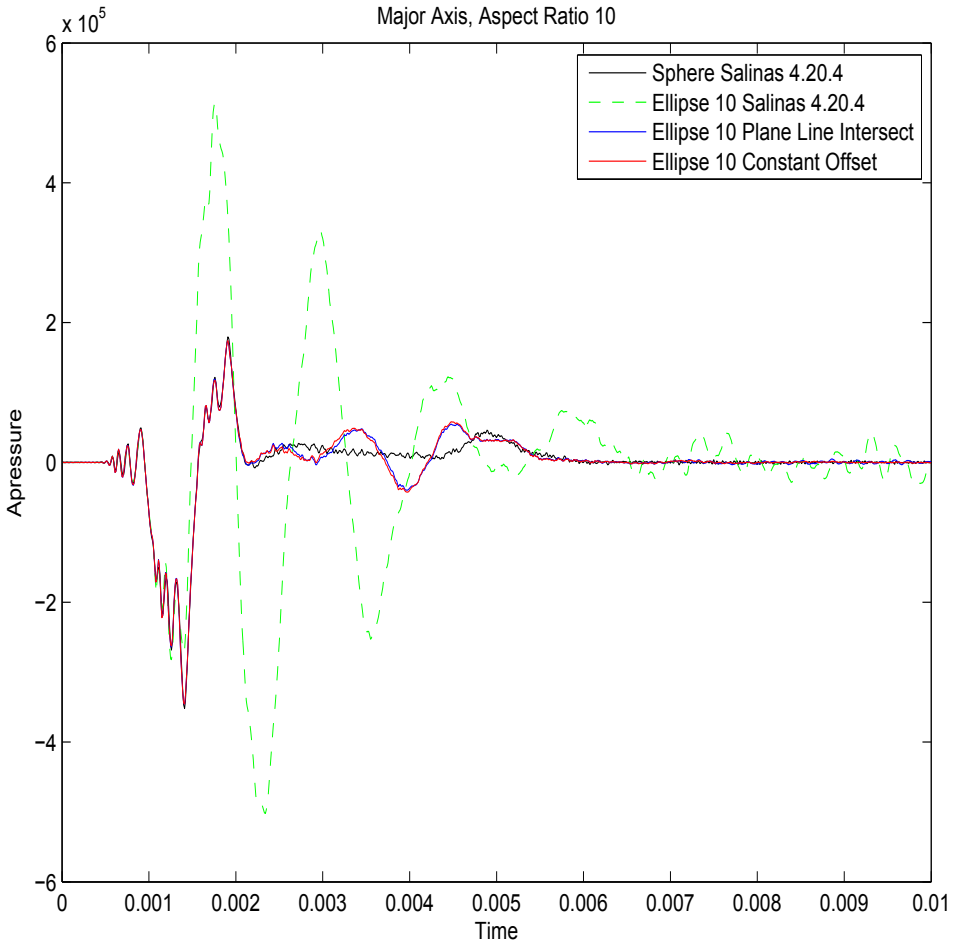

Figure 2-63. – A comparison of results along the major axis from cylindrical cutout problem on spherical and ellipsoidal meshes of aspect ratios 10:1

10.2.15. Absorbing Boundary Conditions for Infinite Elastic Spaces.

In this example we consider a perfect cube, of dimensions $1 \times 1 \times 1$, which is subjected to a pressure wave and a shear wave along one of its faces. The opposing face is designated to be an absorbing boundary condition. In both cases, we apply the loads in the frequency domain, since we have analytical solutions for the corresponding particle displacements. We note that for the shear wave loading, we needed to constrain the motion of the space to be zero in the orthogonal directions in order to match the analytical solution. This is expected, since this solution assumes no rigid body rotation of the space. We note that these tests can be found at

```
Salinas_test/verification/acoustic/infinite_elastic_space_frf_test
Salinas_test/verification/acoustic/infinite_elastic_space_frf2_test
```

In the case of a pressure wave, the amplitude of the particle displacement at the forcing boundary is given by

$$u = \frac{P}{\omega \rho c} \tag{10.2.76}$$

where P is the pressure wave amplitude, ω is the circular frequency, ρ is the material density, and c is the dilatational wave speed in the material. The solution is for the infinite space. It will test the accuracy of the absorbing boundary condition for pressure waves. Figure 2-64 shows the comparison of this exact solution with the displacements obtained by **Sierra/SD**. The results are indistinguishable.

In the case of a shear wave, the amplitude of the particle displacement at the forcing boundary is given by

$$u = \frac{T}{\omega \rho c_s} \tag{10.2.77}$$

where T is the traction wave amplitude, ω is the circular frequency, ρ is the material density, and c_s is the shear wave speed in the material. The solution is for the infinite space. It hence will test the accuracy of the absorbing boundary condition for shear waves. Figure 2-65 shows the comparison of this exact solution with the displacements obtained by **Sierra/SD**. The results are indistinguishable.

We also test the verification of the far-field evaluation. In the frequency domain, the exact solution for an outwardly propagating spherical wave is given by

$$P = \frac{A}{r} e^{-ikr} \tag{10.2.78}$$

If we prescribe the value $P = P_a$ at some value of a, as in the time-domain example described above, then we have

$$P_a = \frac{A}{a} e^{-ika} \tag{10.2.79}$$

This implies that $A = P_a a e^{ika}$, and thus

$$P = P_a \frac{a}{r} e^{-ik(r-a)} \tag{10.2.80}$$

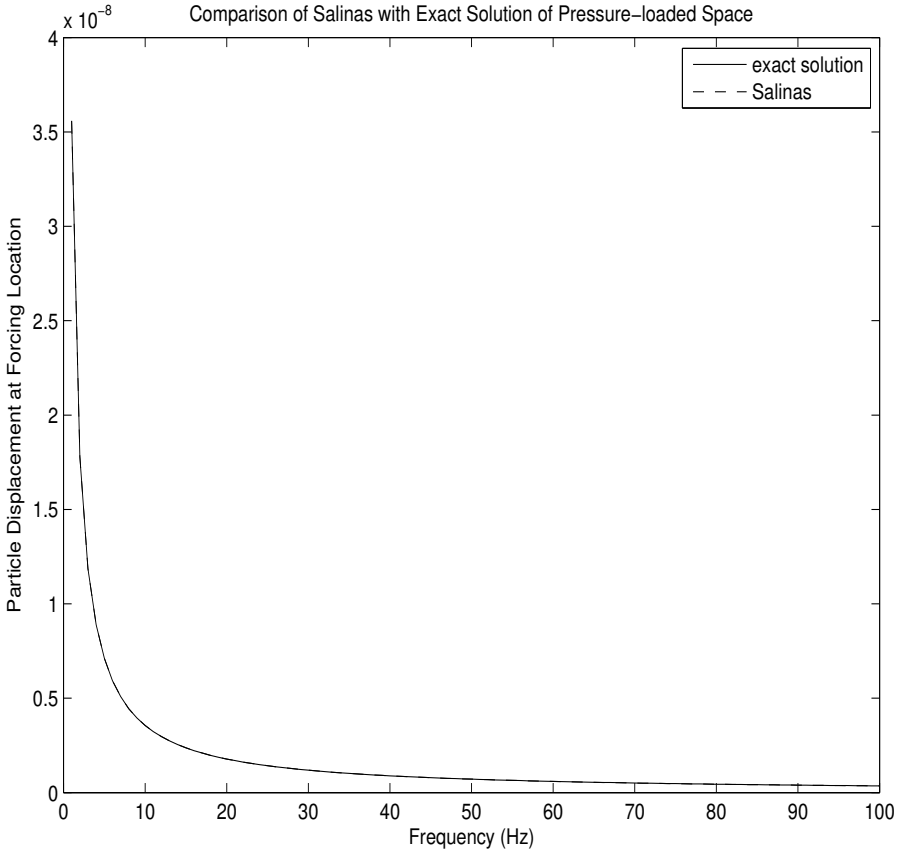

Figure 2-64. – This plot shows the comparison of **Sierra/SD** prediction with the analytical solution of particle displacement at the forcing boundary, for a perfect cube subjected to a pressure load at one end and an absorbing boundary condition at the opposite end.

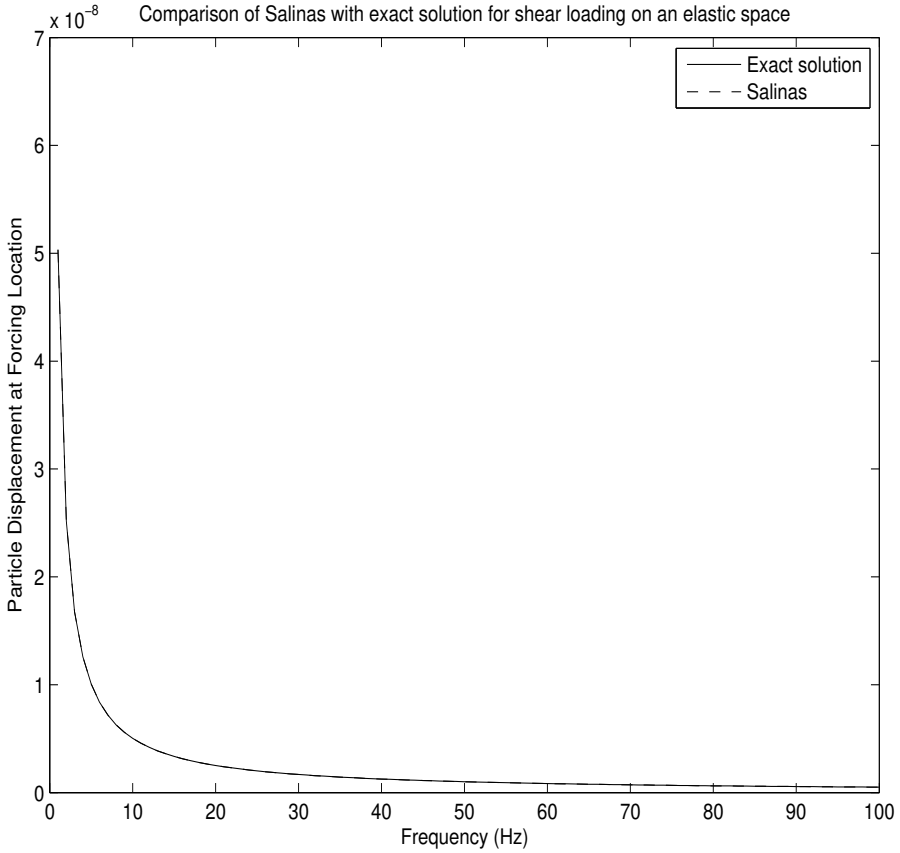

Figure 2-65. – This plot shows the comparison of **Sierra/SD** prediction with the analytical solution of particle displacement at the forcing boundary, for a perfect cube subjected to a shear load at one end and an absorbing boundary condition at the opposite end.

Equation 10.2.80 was used to compute the far-field solution to the frequency-domain version of the

10.2.16. Impedance Boundary Conditions

A simple impedance boundary condition has been implemented in **Sierra/SD**. This boundary condition relates the acoustic pressure and particle velocity on the surface. In the implementation, it results in a damping matrix with a multiplicative coefficient that depends on the impedance. For more details, we refer to the theory notes.

We consider an air-filled acoustic waveguide of length L. At the left end, we apply a prescribed particle velocity V, and at the right end, we apply an impedance boundary condition with an impedance of Z. The exact solution to this problem is given by Kinsler[32] as

$$p = V\rho c * \frac{\frac{Z}{\rho c} + jtan(kL)}{1 + j\frac{Z}{\rho c}tan(kL)} \tag{10.2.81}$$

where p is the acoustic pressure at the left end, ρ is the density, c is the speed of sound, $k = \frac{\omega}{c}$ is the wave number, and j is the imaginary number.

We consider an example with the following properties: $L = 5$, $c = 332.0$, $\rho = 1.293$, and $Z = 0.5\rho c$. Given these parameters, we ran a directfrf analysis in **Sierra/SD** and compared in Figure 2-66 the **Sierra/SD** results against the analytic solution in equation 10.2.81. An excellent agreement is observed.

This example is located in the test suite at

```
Salina_rtest/verification/acoustic/waveguide_impedance.inp
```

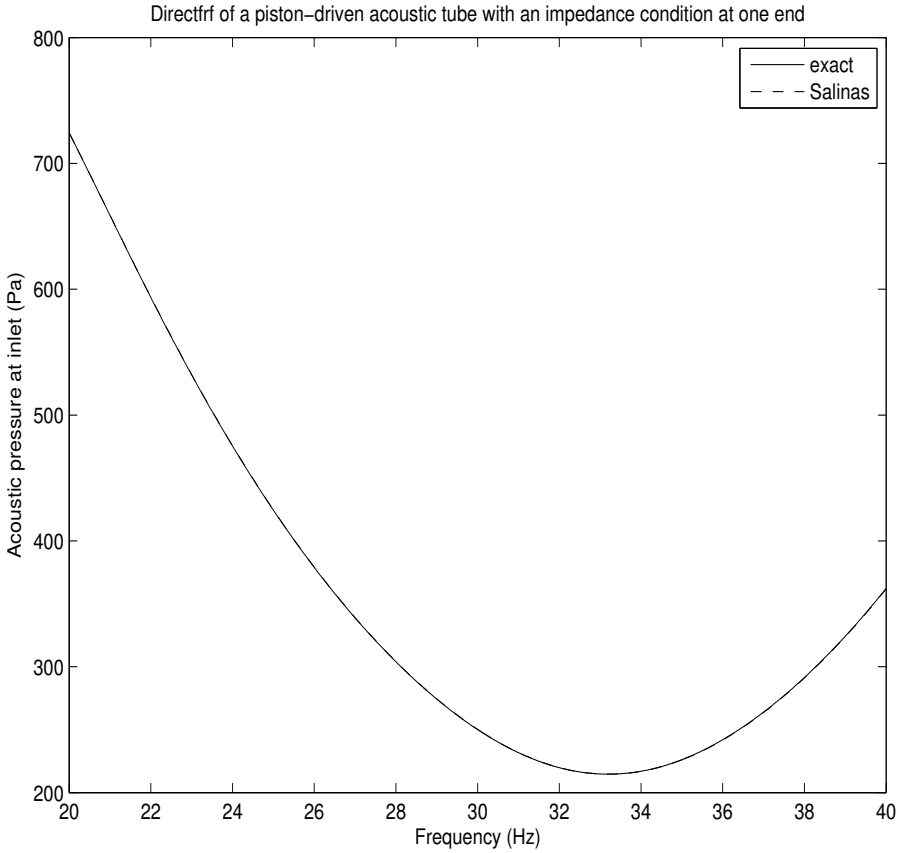

Figure 2-66. – This plot shows the comparison of **Sierra/SD** prediction with the analytical solution of acoustic pressure, for a piston-driven acoustic wave tube with an impedance boundary condition at the opposite end.

10.2.17. Point Acoustic Source

See Section 2.14.

10.2.18. Moving Point Source

In this section, we study a similar example as the previous one, except that the point source has a translation superimposed on the sinusoidal volume change. For simplicity, we assume that the point source is moving in a straight line with velocity V. The exact solution for this problem is given as[38]

$$p(R,t) = \frac{\rho}{4\pi}\frac{\dot{Q}(t-\frac{R}{c})}{R(1-M\cos\theta)^2}H(t-\frac{R}{c}) + \frac{\rho Q(t-\frac{R}{c})}{4\pi}\frac{(\cos\theta - M)V}{R^2(1-M\cos\theta)^2}H(t-\frac{R}{c}) \quad (10.2.82)$$

where Q is the same as the preceding example, $M = \frac{V}{c}$ is the Mach number of the point source, R is a vector going from the field point of interest to the source location, and θ is the angle between the direction of motion of the source and the vector R.

We note that in the case when the velocity $V = 0$ of the source is zero, we have that $M = 0$. In that case, the second term in equation 10.2.82 is zero and equation 10.2.82 reduces to equation 2.14.1. Also, we note that equation 10.2.82 is derived by assuming that the point source is moving subsonically, i.e. that the Mach number $M < 1$. In the case $M > 1$, a similar equation can be derived (see,[38] but we will not consider it here.

Figure 2-67 shows the geometry for the test problem in this case. It consists of a single hex element that moves in the x direction, along the center line of an acoustic half-space. The second time derivative of the volume of this hex element is mapped to the acoustic space, creating an image of a moving source. The hex element moves with a constant velocity. Its volume is given by the equation

$$Q(t) = \frac{8}{3\sqrt{3}}(r_0 + \Delta\sin(\omega t))^3 \quad (10.2.83)$$

where $r_0 = 0.01 * \sqrt{(3)}$, $\Delta = 0.01$, and $\omega = 100 \times 2\pi$. Two subsequent time derivatives of this function give the necessary expressions for $\dot{Q}$ and $\ddot{Q}$ for the time derivatives of volume that are mapped to the acoustic space. Given these, equation 10.2.82 can be used to compute the exact solution.

Figure 2-68 shows the comparison of computed and analytical solutions for the case when the hex is given a velocity of $20\frac{m}{s}$, and the measurement point is at the bottom of the acoustic hemisphere. Generally the agreement is good, with both solutions showing increasing amplitude as the hex approaches the measurement point (at $t = 0.025$), and decreasing amplitude as the hex passes and travels away from the measurement point ($0.025 < t < 0.05$). Better agreement could likely be obtained by refining both the acoustic and hex meshes, but that is not pursued here. We note that this example can be found in the performance test suite (it was too large to be placed in the verification suite) at

`Salinas_rtest/performance/moving_source.inp`

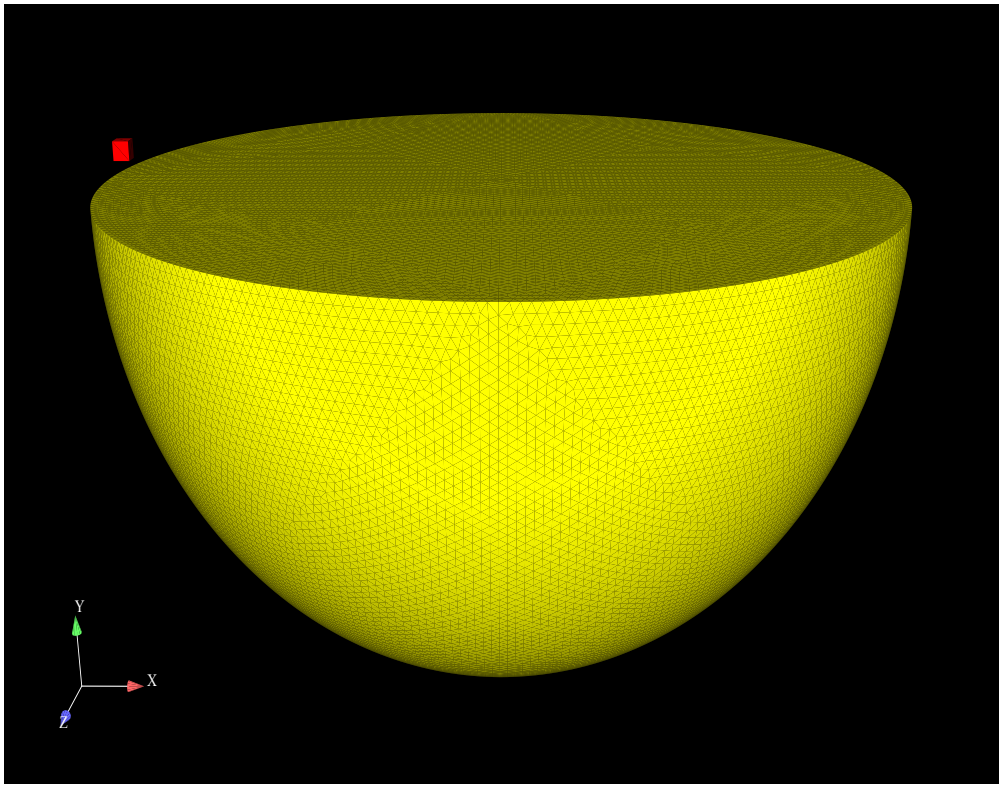

Figure 2-67. – Geometry for verification example of moving point acoustic source in an infinite medium.

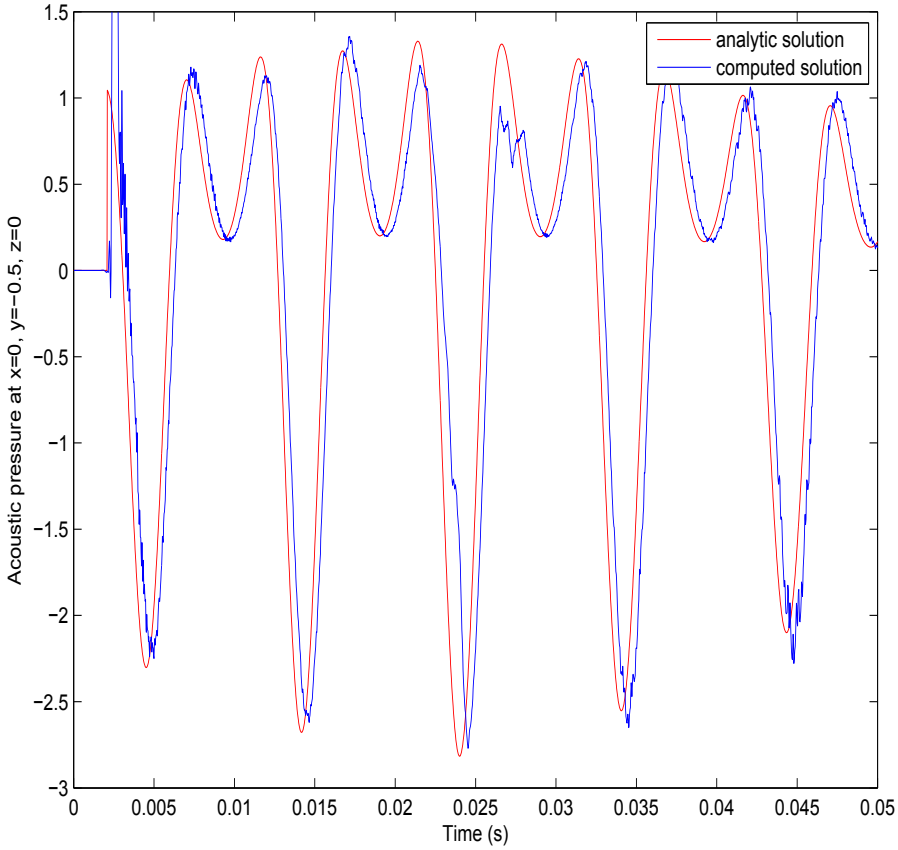

Figure 2-68. – Comparison of computed and analytic solutions for verification example of moving point acoustic source in an infinite medium.

10.2.19. Infinite Elements for Transients

The infinite element implementation was verified on a single element transient example. This element was a hex element that was aligned with a spherical surface of radius $a = 100m$. A surface acceleration excitation of $\sin(2\pi t)$ was applied to the free face of the hex element, and a third order infinite element was defined on the opposite face. Since this element was aligned with a spherical coordinate system, its exact solution should be the same as that of the sound pressure radiated from a pulsating sphere of the same radius. This exact solution is given in[41] as

$$\phi(t) = a\int_{-\infty}^{t} e^{-(c/a)(t-\tau)} v_S(\tau) d\tau \tag{10.2.84}$$

where a is the radius of the sphere, c is the speed of sound, and $v_S(t)$ is the applied surface velocity on the inner surface of the sphere. Once $\phi(t)$ is found, the acoustic pressure can be recovered as follows

$$p(r,t) = \frac{\rho c \dot{\phi}}{r} \tag{10.2.85}$$

If we define an input surface acceleration as

$$a_S(t) = \sin(2\pi t) \tag{10.2.86}$$

Then we have an implied input velocity of

$$v_S(t) = \frac{-1}{2\pi}\cos(2\pi t) + \frac{1}{2\pi} \tag{10.2.87}$$

Substituting this into equation 10.2.84, we obtain

$$\phi = \frac{-a}{2\pi}\int_{-\infty}^{t} e^{-(c/a)(t-\tau)}\left[\frac{-1}{2\pi}\cos(2\pi t) + \frac{1}{2\pi}\right] d\tau \tag{10.2.88}$$

Simplifying, and using the identity

$$\int e^{c_1 x}\cos(c_2 x) = \frac{e^{c_1 x}}{c_1^2 + c_2^2}\left(c_1\cos(c_1 x) + c_2\sin(c_2 x)\right) \tag{10.2.89}$$

we obtain

$$\phi(t) = \frac{-a}{2\pi}\frac{1}{(\frac{c}{a})^2 + (2\pi)^2}\left[\frac{c}{a}\cos(2\pi t) + (2\pi)^2\sin(2\pi t)\right] + \frac{2\pi a^2}{c\left(\frac{c}{a}\right)^2 + c(2\pi)^2} e^{\frac{-ct}{R}} \tag{10.2.90}$$

Inserting this expression into equation 10.2.85, we obtain the exact solution on the surface of the sphere (R=a)

$$p(r,t) = \frac{\rho c}{\left(\frac{c}{a}\right)^2 + (2\pi)^2}\left[2\pi e^{\frac{-ct}{a}} + \frac{c}{a}\sin(2\pi t) - 2\pi\cos(2\pi t)\right] \tag{10.2.91}$$

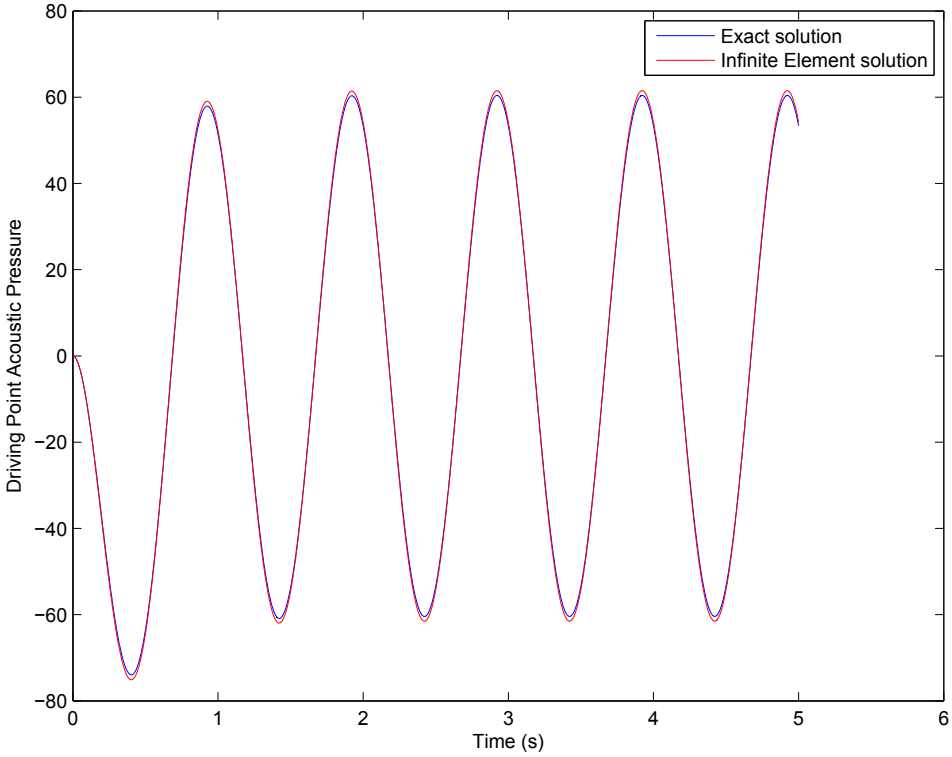

Figure 2-69. – A comparison of an exact solution for spherical wave radiation and the **Sierra/SD** computation using transient infinite elements.

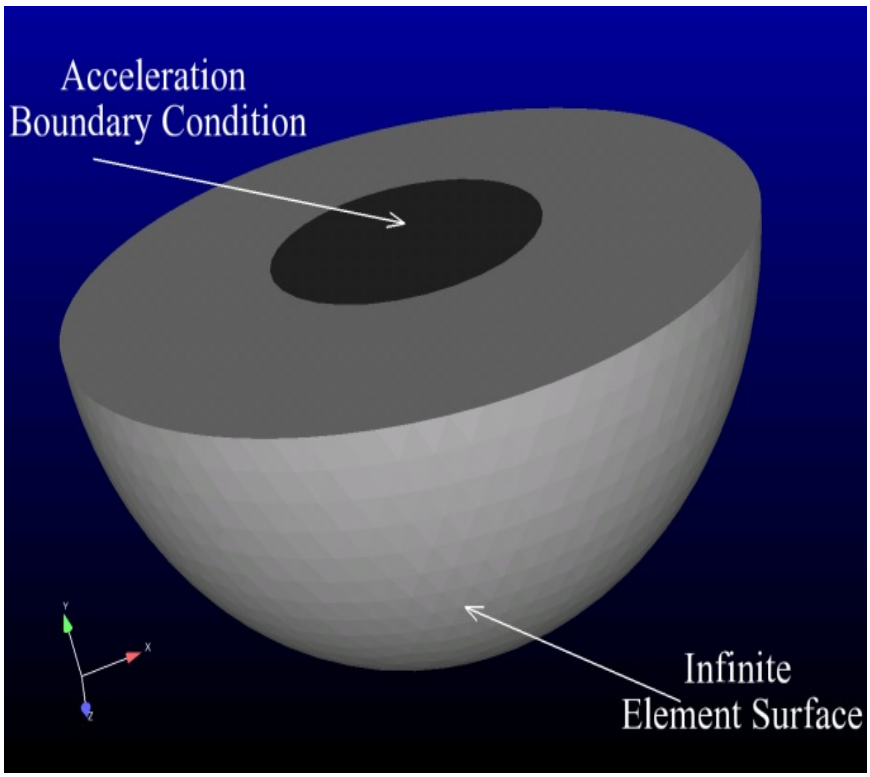

Figure 2-70. – A schematic of the geometry of a piston mounted on an infinite baffle for verification of transient infinite elements.

We note that there is both a transient and a steady-state component to the solution in equation 10.2.91. The transient term dies out after sufficient time, and then the steady terms persist.

Figure 2-69 shows the comparison of the exact solution of equation 10.2.91 and the computed solution using **Sierra/SD**. Excellent agreement is seen between the curves.

A second verification example was considered that consisted of a piston mounted on an infinite baffle. Figure 2-70 shows a schematic of the geometry. A 3D hemispherical domain of radius $0.5(m)$ was constructed and meshed with tetrahedrons. A normal acceleration boundary condition was applied to a circular portion of the flat face, of radius $0.25(m)$. The flat plane of the hemisphere was set at $y = 0$, as shown in Figure 2-70. The remaining part of the flat surface was treated as acoustically rigid (zero particle acceleration). Infinite elements were then applied to the curved surface, thus making the geometry appear to be a semi-infinite space with a piston mounted on the (rigid) baffle.

The analytical solution to this problem is given as[41]

$$p(x,t) = \frac{\rho}{2\pi}\int_S \frac{a_n(x_s, y_x, t - R/c)}{R} dS \tag{10.2.92}$$

where $p(x,t)$ is the acoustic pressure at an arbitrary point x in space and time t, ρ is the fluid density, $a_n(x_s, y_x, t - R/c)$ is the normal acceleration on the piston surface, x_s and y_s

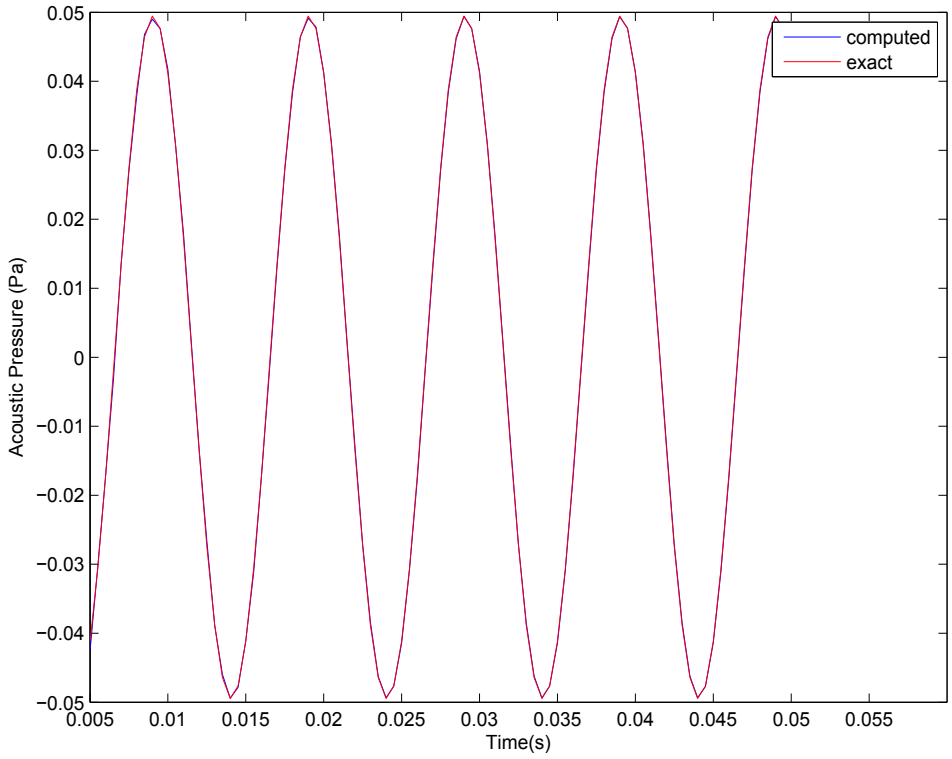

Figure 2-71. – A comparison of computed vs. analytic solution for a piston mounted on an infinite baffle. Field point is at $x = 0$, $y = -0.5$, $z = 0$.

are points on the piston used in the surface integration,
$R = \sqrt{[(x-x_s)^2 + (y-y_s)^2 + (z-z_s)^2]}$ is the distance from a point on the piston surface to the point x where the solution is desired, and c is the speed of sound. Thus, we see that for an arbitrary point in space x, and an arbitrary time history of accelerations a_n, the integral in equation 10.2.92 must be carried out numerically.

We consider 2 points in space for the comparison with analytical solution. The first point (point A) is located along the axis of the piston at $x = 0$, $y = -0.5$, and $z = 0$. The second point (point B) is located off-axis as $x = 0.5$, $y = 0$ and $z = 0$. Figures 2-71 and 2-72 show comparisons of the analytical and computed solutions for the case when $a_n(t) = \sin(200\pi t)$, which corresponds to the case when the piston is rigid and moving harmonically at a frequency of 100Hz.

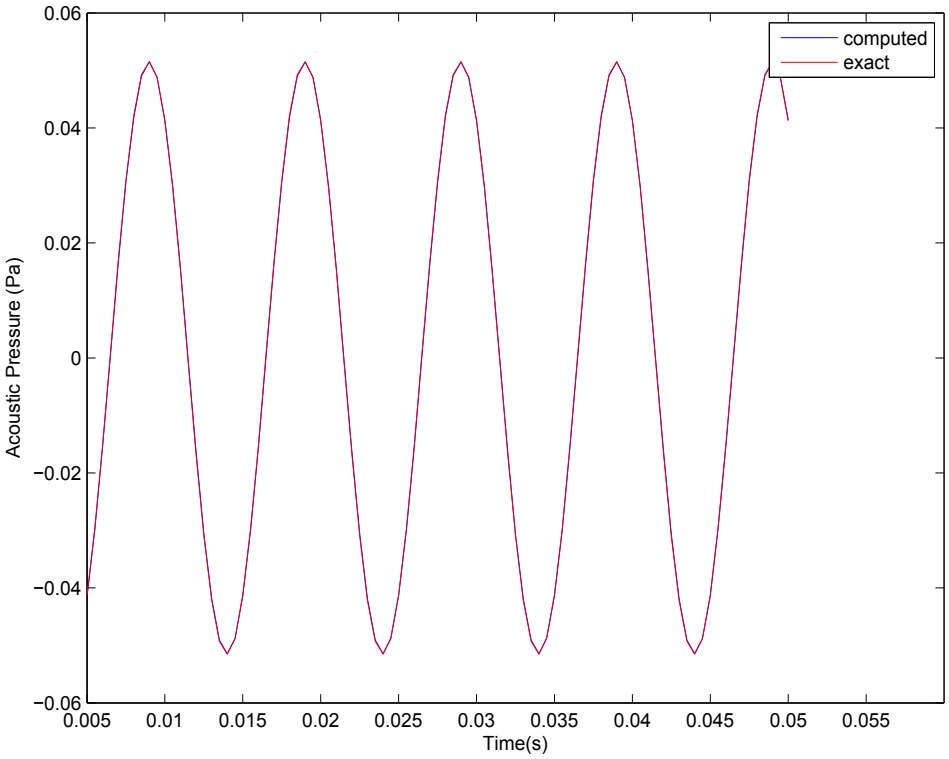

Figure 2-72. – A comparison of computed vs. analytic solution for a piston mounted on an infinite baffle. Field point is at $x = 0.5$, $y = 0.0$, $z = 0$.

10.2.20. Variable Order Infinite Element Implementation

Before making comparisons of the infinite element and Kirchhoff integral approaches, we first examine the dependence of the infinite element approach on the order of the radial expansion used in the approximation. If the implementation is correct, the computed solution should converge to the analytical solution for sufficiently high order of radial expansion in the infinite element approximation.

Figure 2-73 shows the geometry of the mesh used for the baffled piston. It consists of a hemispherical geometry with a circular surface defining the area over which the piston makes contact with the air. An applied acceleration time history is given to the piston, which acts as a Neumann boundary condition. The flat face of the hemisphere is a subset of the infinite baffled plane. The infinite elements are placed on the curved part of the hemispherical surface. The piston is given a uniform, time-dependent acceleration in the direction of its surface normal. We denote this acceleration as $a_P(t)$, and the exact form of the time dependence will take two different forms, as described below.

The exact solution to this problem can be computed from the Kirchhoff integral

$$p(\boldsymbol{x},t) = \frac{\rho}{2\pi}\int_S \frac{a_P(\boldsymbol{x_S},t-\frac{R}{c})}{R}dS \tag{10.2.93}$$

where $p(\boldsymbol{x},t)$ is the acoustic pressure at point $\boldsymbol{x}$ and time t, ρ is the density of the fluid, S is the surface area over which the piston interacts with the fluid, $a_P(\boldsymbol{x_S},t-\frac{R}{c})$ is the normal acceleration of the piston at the point $\boldsymbol{x_S}$, and at the delayed time $t-\frac{R}{c}$, $R=|\boldsymbol{x}-\boldsymbol{x_S}|$ is the distance from the surface point $\boldsymbol{x_S}$ to the far field point $\boldsymbol{x}$, and c is the speed of sound. The evaluation of equation 10.2.93 was carried out numerically, and this provided the exact solution for comparison with the computations.

In all of the following examples, we consider standard conditions for the air surrounding the piston, $\rho = 1.293$, $c = 332.0$. The piston has a radius of 0.25(m). The mesh consists of $1,800,000$ linear tetrahedral acoustic elements with an approximate element diameter of 0.0026 m. For a wave at 2000 Hz, the wavelength is about 0.166 m, and thus this consists of about 50 elements per wavelength. The time step for the transient analysis was taken at $5.0\text{x}10^{-6}$ s, which is much finer than needed to resolve a frequency of 2000 Hz. Thus, we expect both spatial and temporal resolution to be sufficient to capture the wave response, and thus allow the infinite element and Kirchhoff solutions for far-field pressures to be easily compared.

Figure 2-74 shows a comparison of the exact vs. computed transient response at the particular point $x=-0.25$, $y=0$, $z=0$ for increasing order of the infinite element approximation. In this case, the piston was given an acceleration of the form $a_P(t) = \sin(2\pi f t)H(t)$, $f = 2000(\text{Hz})$. As expected, the infinite element solution converges to the exact solution as the order is increased. For the examples that follow, a similar approach was taken in that the order was increased until subsequent increases in the order of the infinite elements made no difference in the obtained results.

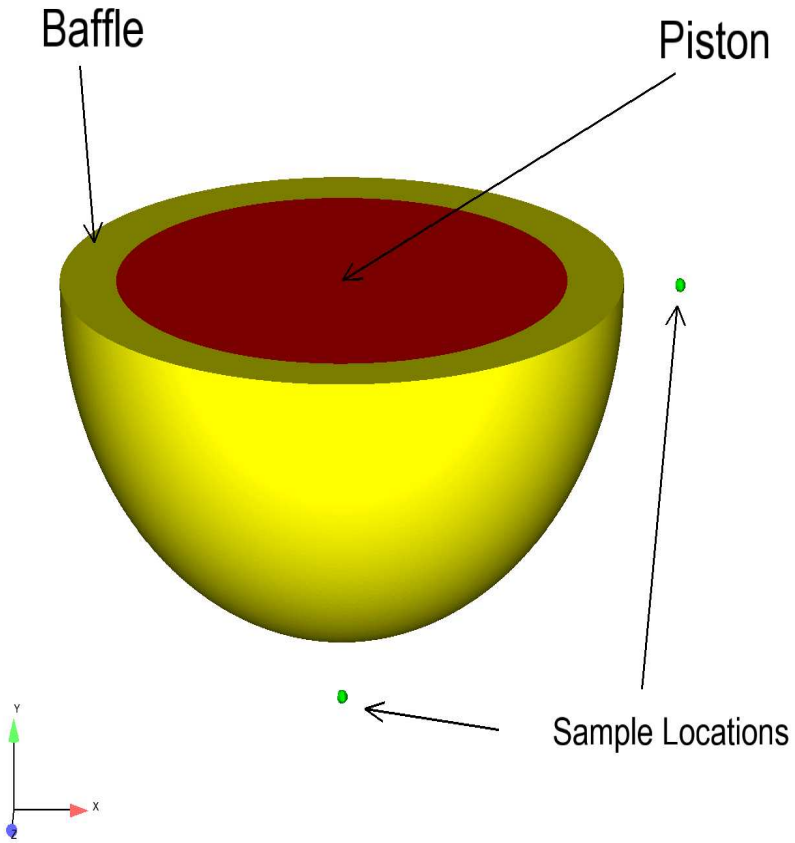

Figure 2-73. – The geometry and mesh of the baffled piston problem.

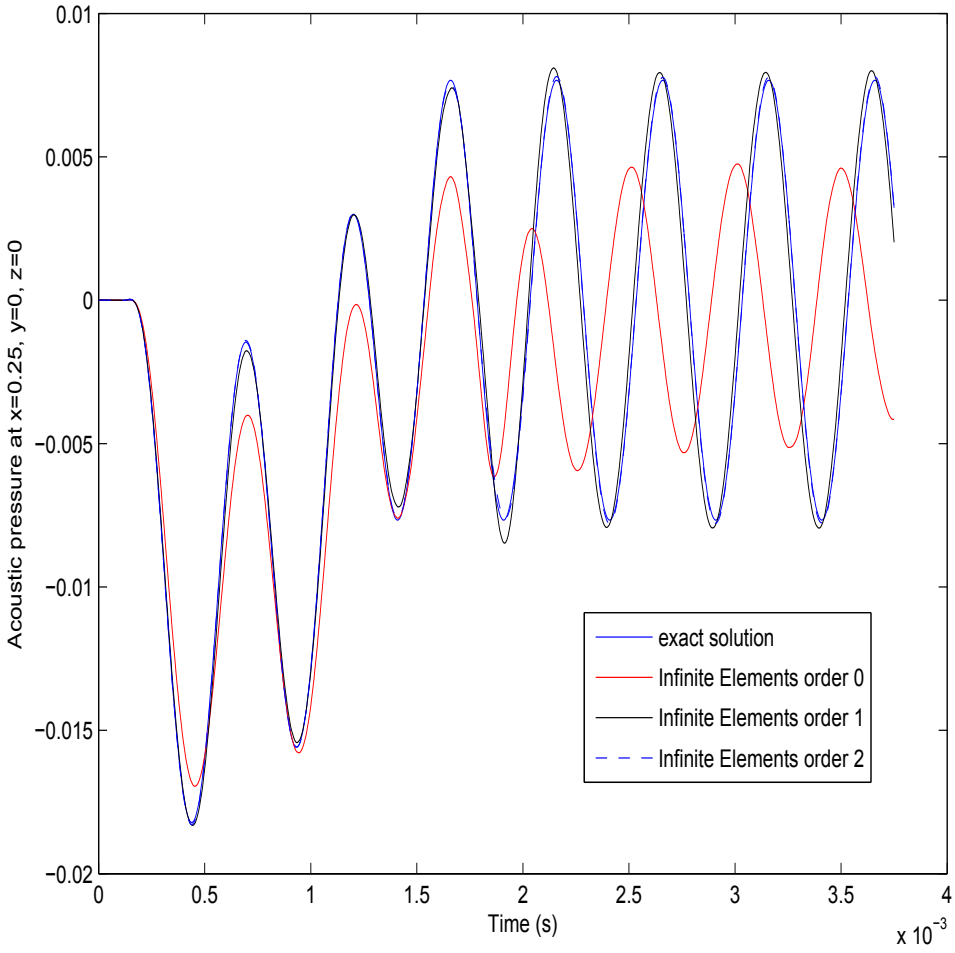

Figure 2-74. – A convergence study for infinite element order, demonstrated on the baffled piston problem

10.2.21. Coupled Acoustic-Structure Directfrf with Viscoelastic Material

This example compares the solution from ABAQUS with that of **Sierra/SD** for a coupled acoustic-structure interaction directfrf problem with a viscoelastic material. The problem consists of a thick plate fixed on the edges and loaded on one face. The opposite side of the solid is coupled a prism with a prescribed acoustic pressure equal to zero on the opposite face. A sketch of the problem domains is shown in Figure 2-75. The pressure contours for both the **Sierra/SD** and ABAQUS outputs are shown in Figures 2-77 and 2-76, respectively, while a comparison of peak values are shown in Table 2-36.

	Peak Pressure (Pa)	Peak Uy (m)
ABAQUS	-10811.5	1.031e-6
Sierra/SD	-10818.16	-1.030e-6

Table 2-36. – . Peak pressure and displacement for coupled acoustic-structure interaction problem with viscoelastic material.

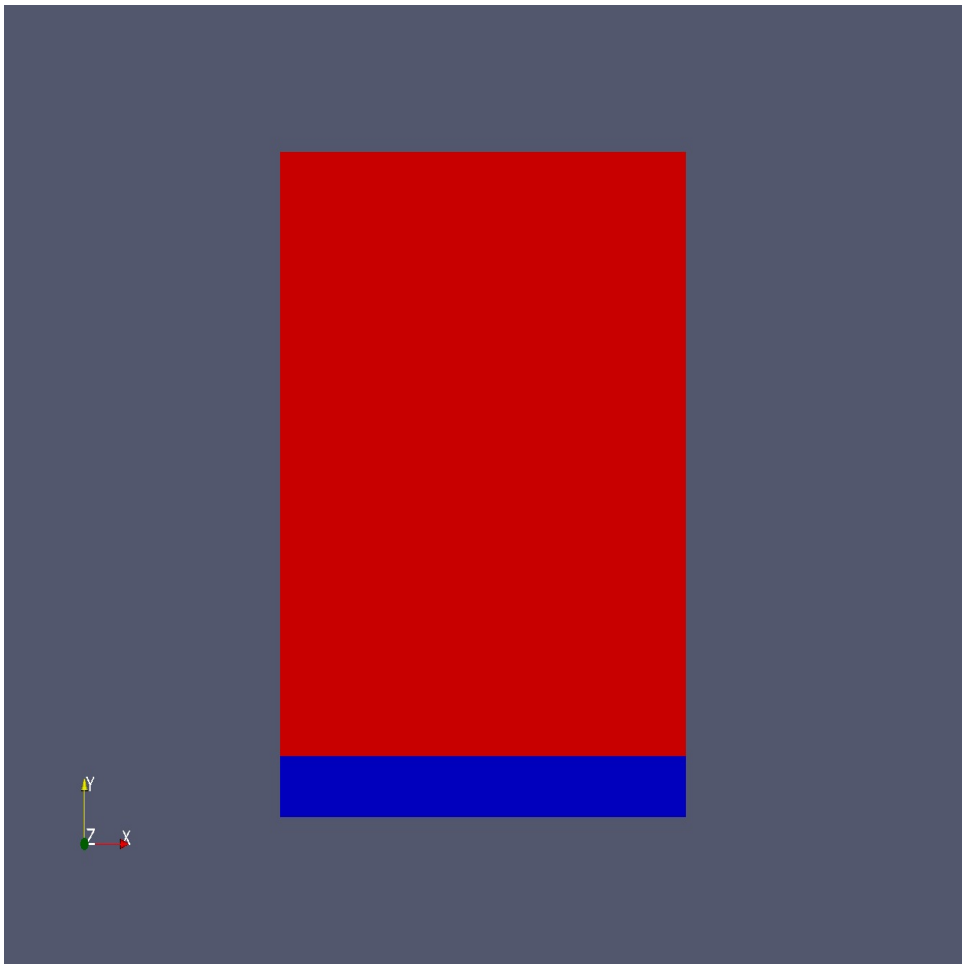

Figure 2-75. – Problem sketch. The bottom part is the solid, the top part is the fluid

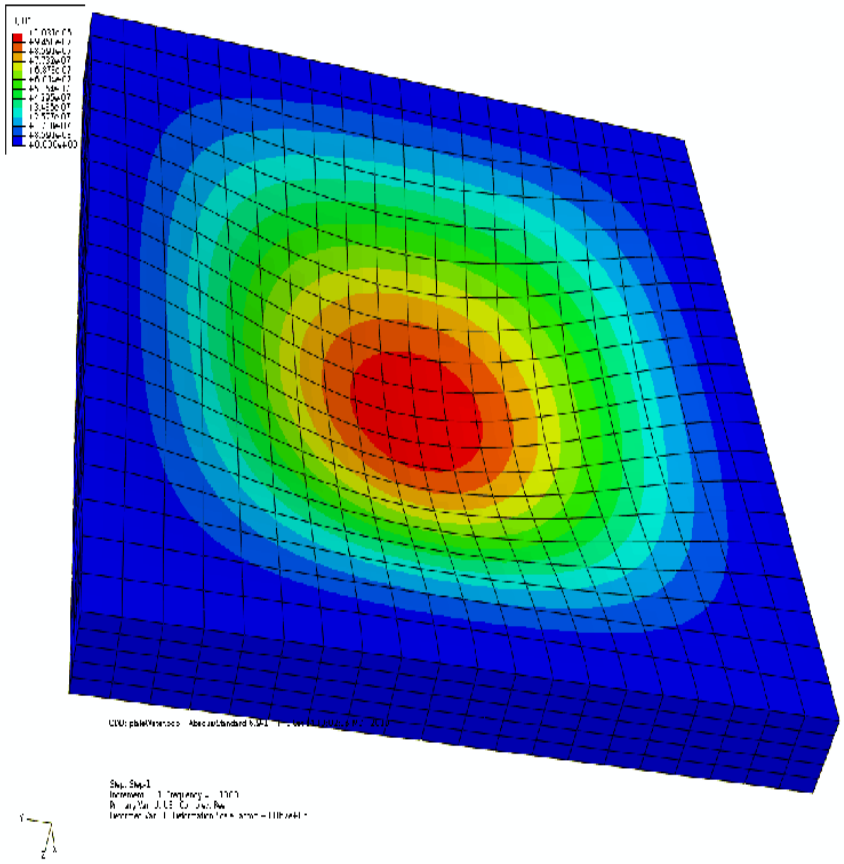

Figure 2-76. – Vertical displacement distribution from ABAQUS.

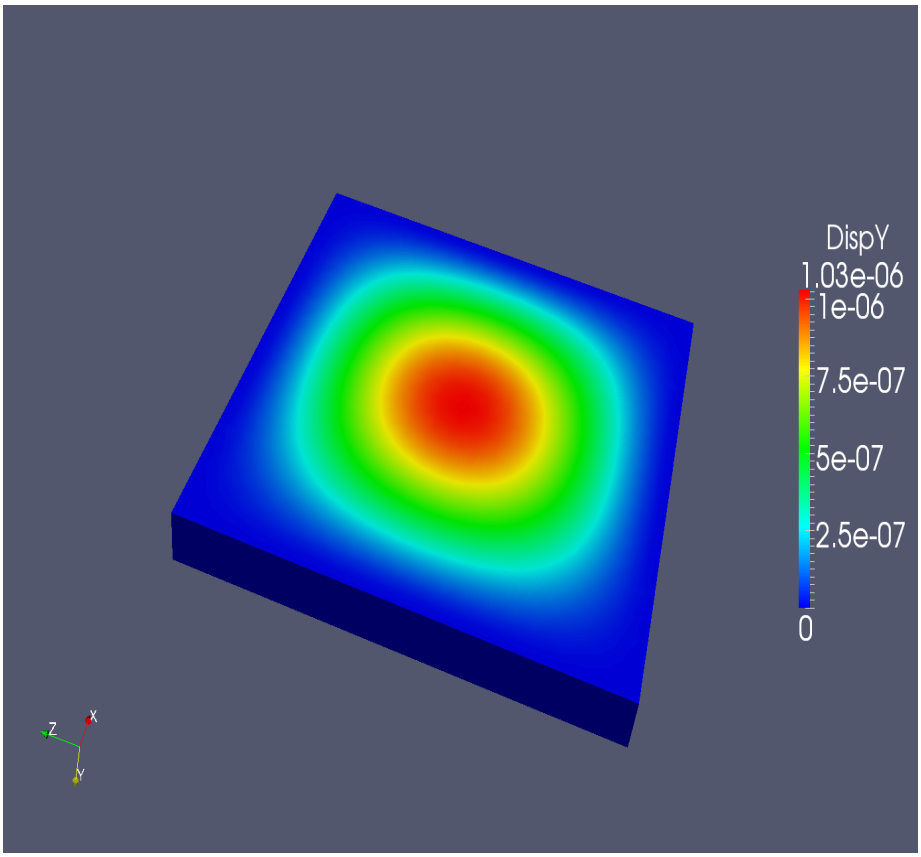

Figure 2-77. – Vertical displacement distribution from **Sierra/SD**.

10.3. Nonlinear Acoustics

In Sierra SD nonlinear acoustics is modeled using the Kuznetsov Equation. For verification purposes, we consider the same sequence of simulations given in[29,28] involving a piston-radiation problem. This example is shown in Figure 3-78. It consists of a long air-filled tube that has a sinusoidal boundary condition at the left end. This boundary condition can either be in the form of a pressure (Dirichlet) condition or a velocity (Neumann) condition, which are given as

$$p(0,t) = p_0 \sin(\omega t) \tag{10.3.1}$$

$$v(0,t) = v_0 \sin(\omega t) \tag{10.3.2}$$

In order to simulate the infinite condition at the right end of the tube, an absorbing boundary condition is used. The exact solution to this problem is given by the Fubini solution (see section 11.2 of[41]) in the pre-shock regime and by the Fay solution in the post-shock regime.

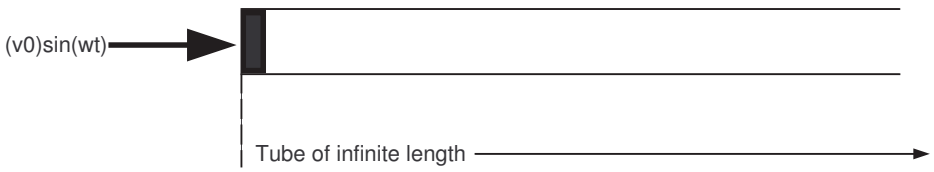

Figure 3-78. – A wave tube example for verification.

In the case of a plane wave, the distance to shock formation is given as

$$\sigma = \frac{c}{\left(1 + \frac{B/A}{2}\right) v_0 k} \tag{10.3.3}$$

where v_0 is the amplitude of the velocity of the source, and k is the wave number. As expected, for larger amplitude sources, and for more nonlinear fluids (larger B/A), the shock forms closer to the source. Interestingly, we see that the shocks also form closer to the source for high frequency waves, since k is in the denominator. In the numerical experiment, we chose $v_0 = 20\frac{m}{s}$, and $k = \frac{100}{332} = .3$, which resulted in a shock formation distance of $\sigma = \frac{332}{1.2*20*.3} = 46.1m$.

The Fubini solution[33,26] is given by

$$p(x,t) = p_0 \sum_{n=1}^{\infty} \frac{2}{n\bar{x}} J_n(n\bar{x}) \sin(n\omega\tau) \tag{10.3.4}$$

where $J_n(x)$ is the Bessel function of order n, $\bar{x} = \frac{x}{\sigma}$, and $\tau = t - \frac{x}{c_0}$. The Fay solution is

$$p(x,t) = p_0 \frac{2}{\Gamma} \sum_{n=1}^{\infty} \frac{\sin(n\omega\tau)}{\sinh\left[n(1+\sigma)\Gamma\right]} \tag{10.3.5}$$

where Γ is the ratio of the absorption length to the shock formation distance (see[26]). The Fubini solution assumes a lossless media, and is valid for $x < \sigma$. For the post-shock regime, $x > 3.5\sigma$, the Fay solution must be used since it accounts for absorption. Transition solutions have been derived[7] that provide exact solutions for $\sigma < x < 3.5\sigma$, but we do not consider those here.

For all of the results presented next, the fluid is air at ambient conditions, with $c = 332.0\frac{m}{s}$, $\rho = 1.293\frac{Kg}{m^3}$. Accounting for viscosity and thermal conductivity loss mechanisms, the absorption parameter can be calculated from the following equation[41]

$$\frac{b}{c^2} = \frac{1}{\rho c^2}\left[\frac{4}{3}\eta + (\gamma - 1)\frac{k}{C_p}\right] \tag{10.3.6}$$

$$= \frac{1}{1.293x332^2}\left[\frac{4}{3}1.846e^{-5} + (0.4)\frac{2.624e^{-2}}{1000}\right] \tag{10.3.7}$$

$$= 7.017e^{-6}x\left[2.461e^{-5} + 1.0496e^{-5}\right] = 2.46e^{-10} \tag{10.3.8}$$

$$\tag{10.3.9}$$

For air, $\frac{b}{c^2}$ is too small to affect the results. Note that this estimate neglects additional loss mechanisms such as molecular relaxation, and wall losses.

Figures 3-79, 3-80, and 3-81 show the solution at $x = 0$, $x = \sigma$, and $x = 4\sigma$, respectively. In all cases, the computed solution is compared with the exact solution, and convergence is obtained. In these results, three- dimensional linear finite elements were used, with element diameters of 0.125(m). The time steps were 1.0×10^{-3}, 2.5×10^{-4}, and 1.25×10^{-4} for Figures 3-79, 3-80, and 3-81, respectively.

In order to demonstrate the significant difference between linear and nonlinear solutions, in Figure 3-82 we show the results for the previous problem using linear and Kuznetsov wave equations. In this case, we plot acoustic pressure with distance along the tube, rather than with time. It is seen that linear theory is not sufficient for capturing the correct response.

Next, we examine the nonlinear convergence properties of the algorithm. Since we are using Newton's method to solve the nonlinear system of equations, we examine the number of iterations required for convergence. The criteria for convergence is based on a relative tolerance of 10^{-6}, e.g.

$$\frac{|Res_f|}{|F_{ext}|} \leq 10^{-6} \tag{10.3.10}$$

Also, we mention that the starting point for the Newton iterations is the value of velocity potential from the previous time step. Figure 3-83 shows the number of Newton iterations required to satisfy the inequality 10.3.10, for various levels of input velocities of the piston. As expected, for larger input velocities, more iterations are required for convergence. The highest level that was considered, $120\frac{m}{s}$, is beyond the limitations of the Kuznetsov equation, but we show it anyway to illustrate the divergence of the Newton scheme. For reasonable levels of piston velocities (i.e. $20\frac{m}{s}$), the Newton iterations converge rapidly, leveling off at about 4 iterations per time step. Interestingly, for source amplitudes that are

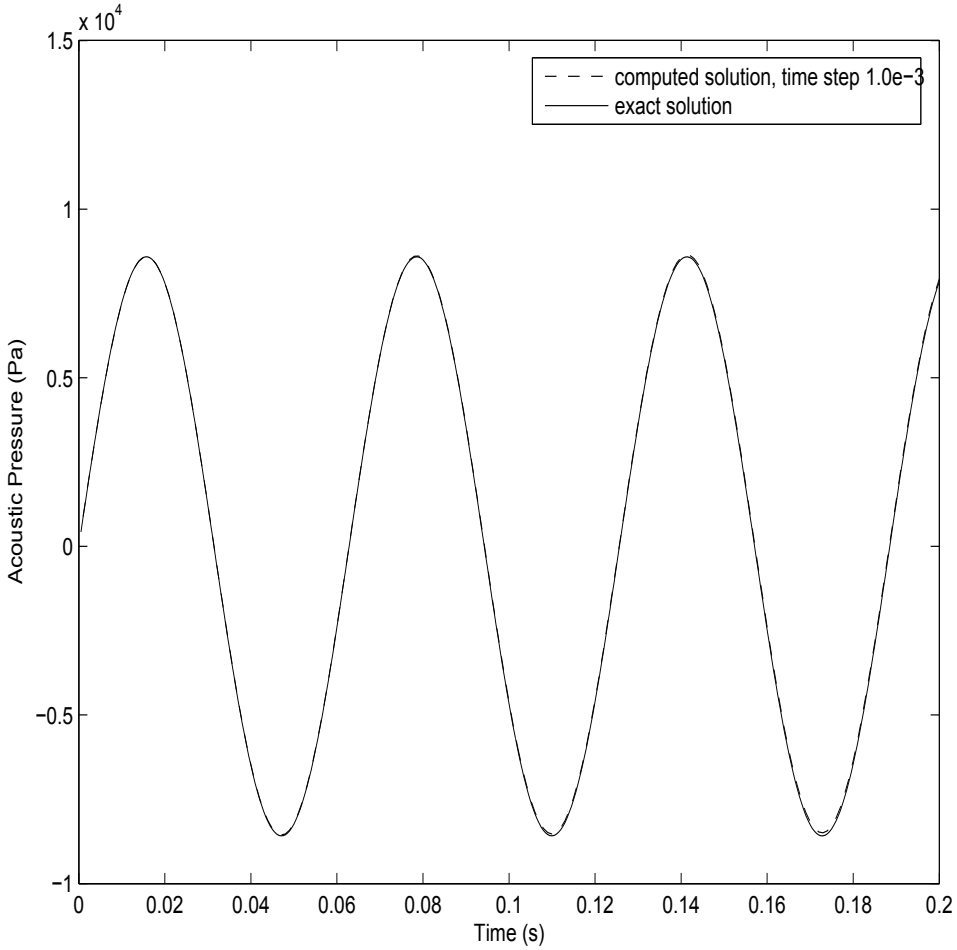

Figure 3-79. – Acoustic radiated pressure at $x = 0$

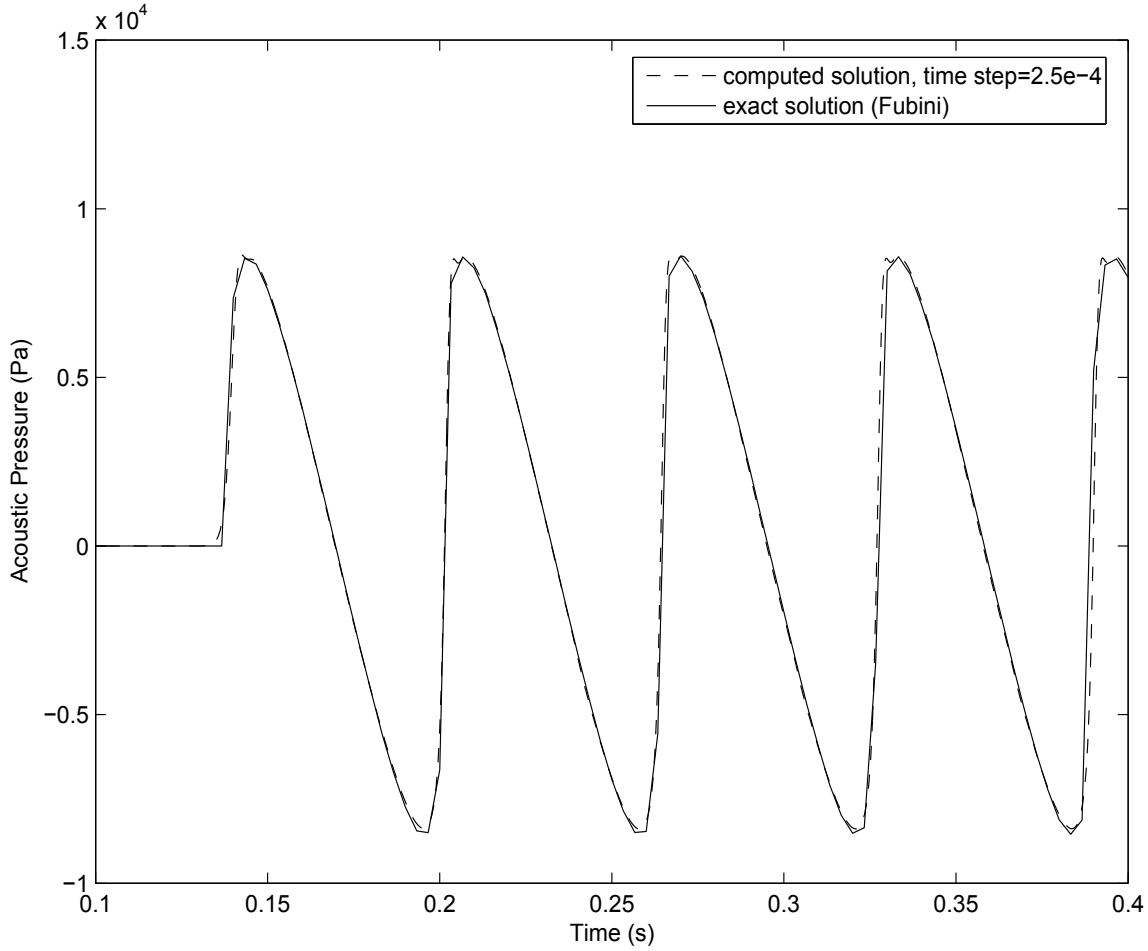

Figure 3-80. – Acoustic radiated pressure at $x = \sigma$.

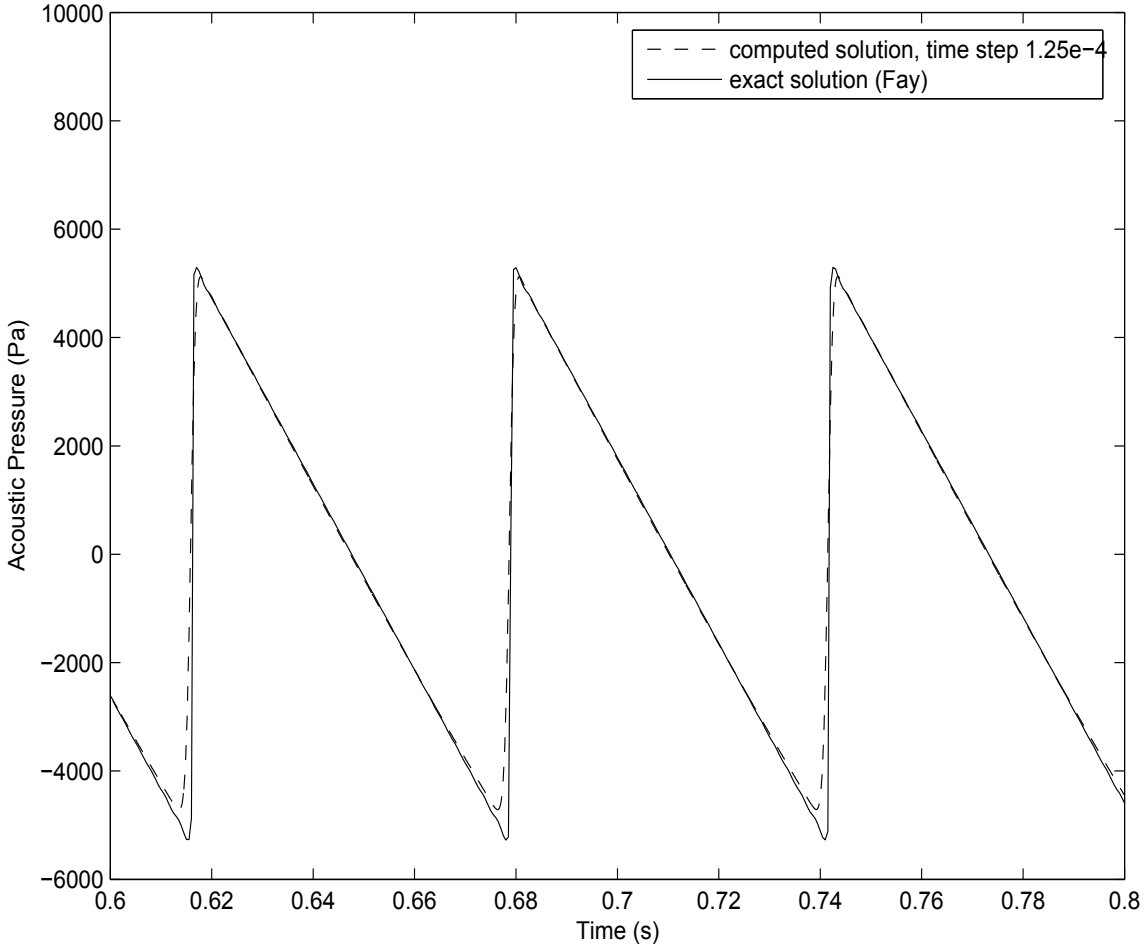

Figure 3-81. – Acoustic radiated pressure at $x = 4\sigma$.

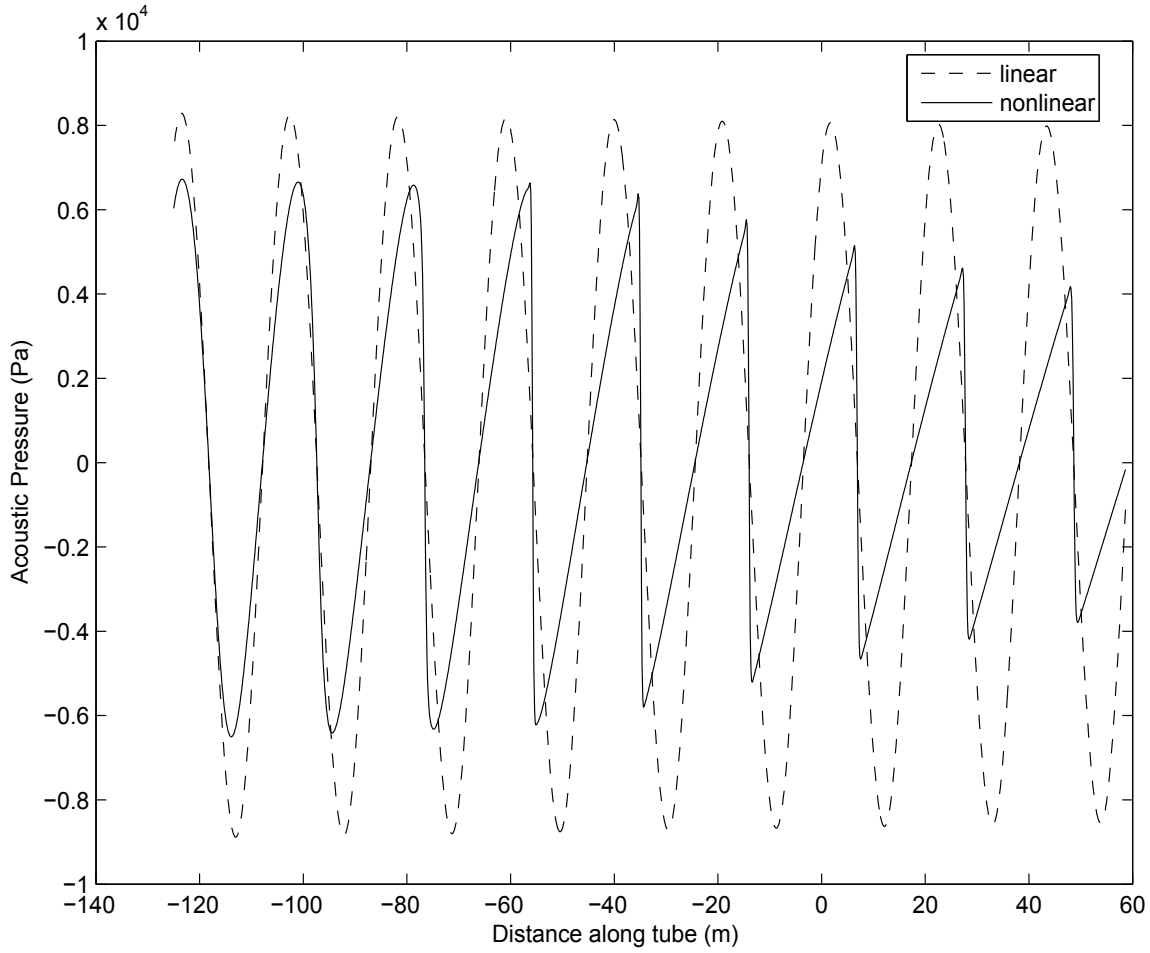

Figure 3-82. – A comparison of radiated pressure using linear and nonlinear acoustic formulations

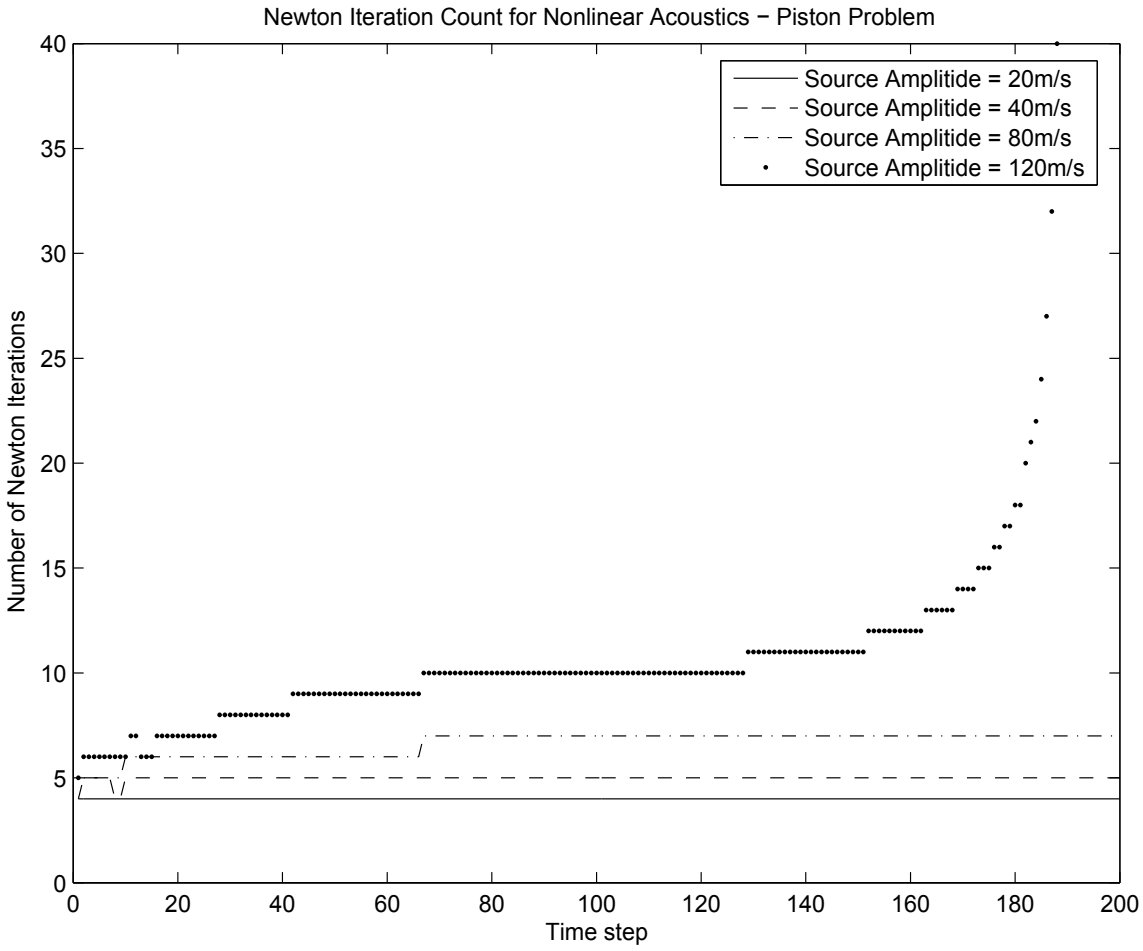

Figure 3-83. – The number of Newton iterations required for convergence of the piston radiation problem.

within the range of validity of the Kuznetsov equation, the formation of shocks does not influence the number of iterations required for convergence.

A test case for the Fubini solution with the shock wave is currently in the verification test suite

`Salinas_rtest/verification/acoustics/shockwave_SI.test for SI units and`
`Salinas_rtest/verification/acoustics/shockwave_english.test for english units`

10.4. Material Identification

These verification problems are too computationally expensive to include in the automatic verification suite.

10.4.1. Elastic Material Inversion for a Tunnel

In this section, we describe a materials inversion test performed on a hemispherical solid containing an embedded cylindrical tunnel of different material. Figure 4-84 shows the geometry of the model.

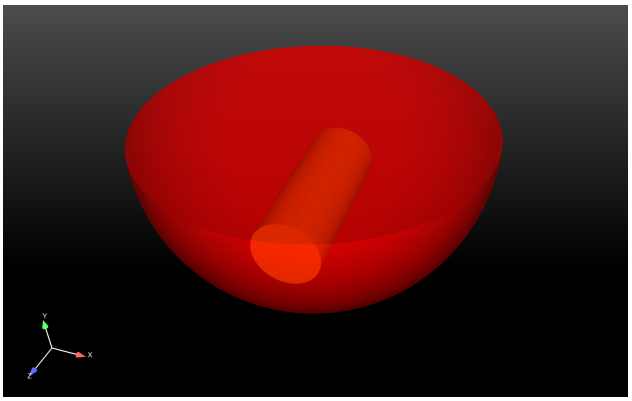

Figure 4-84. – Force Inversion Test Geometry.

In the model, a hemispherical solid contained a cylindrical *tunnel* region of a different solid material. A Dirichlet boundary condition was assigned on the solid, setting a fixed boundary on the hemispherical face of the model. A periodic structural loading was applied to a circular region on the flat face of the model. Figure 4-85 shows the side with the fixed boundary condition (pink) and the region of loading (orange). It was desired to determine the elastic material properties–the shear (G) and bulk (K) moduli– of the two material regions

Synthetic input data for the inverse problem was generated by performing a forward run on the model. The data represented elastic displacements for element nodes caused by the loading on the hemisphere's face. In the forward run, the hemispherical and tunnel regions

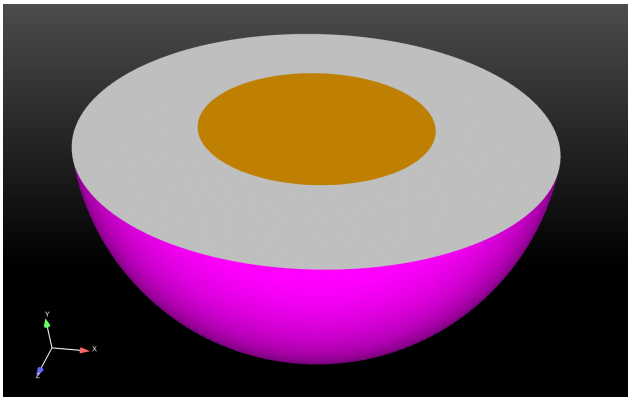

Figure 4-85. – Sides with boundary (pink) and loading (orange) conditions.

were assigned their true material properties, $\{G_h, K_h\}$ and $\{G_t, K_t\}$, displayed in Table 4-37. For the inverse run, initial guesses were chosen for the properties of the two material regions, also shown in Table 4-37. The two regions were designated as having heterogeneous, isotropic elastic materials, allowing the bulk and shear moduli to vary by element. The initial guesses, along with the input data, were used to verify that the true material properties could be recovered by the code. Figures 4-86 through 4-89 show results of the heterogeneous material-identification; cross-sections of the model are colored by the computed results for the shear or bulk moduli of the elements in the model. Figures 4-86 and 4-87 show results using a least-squares objective, while figures 4-88 and 4-89 show results using a Modified Error in Constitutive Equations (MECE) objective functional.

Table 4-37. – True material properties and initial guesses for tunnel-model material identification.

Property	Exact	Initial Guess
G_h	150.0	90.0
K_h	150.0	90.0
G_t	50.0	90.0
K_t	50.0	90.0

As shown in Figures 4-86 and 4-87, the elastic material properties calculated using the least-squares objective generally differentiate the two blocks and recover the blocks' original material properties. Due to the heterogeneous conditions on the block elements, element properties vary through the block volumes and include outliers. The properties recovered using the MECE objective, shown in Figures 4-88 and 4-89, much more closely recovered the original material properties of the two regions, though still demonstrated heterogeneous variations. The least-squares optimization, performed using a BFGS

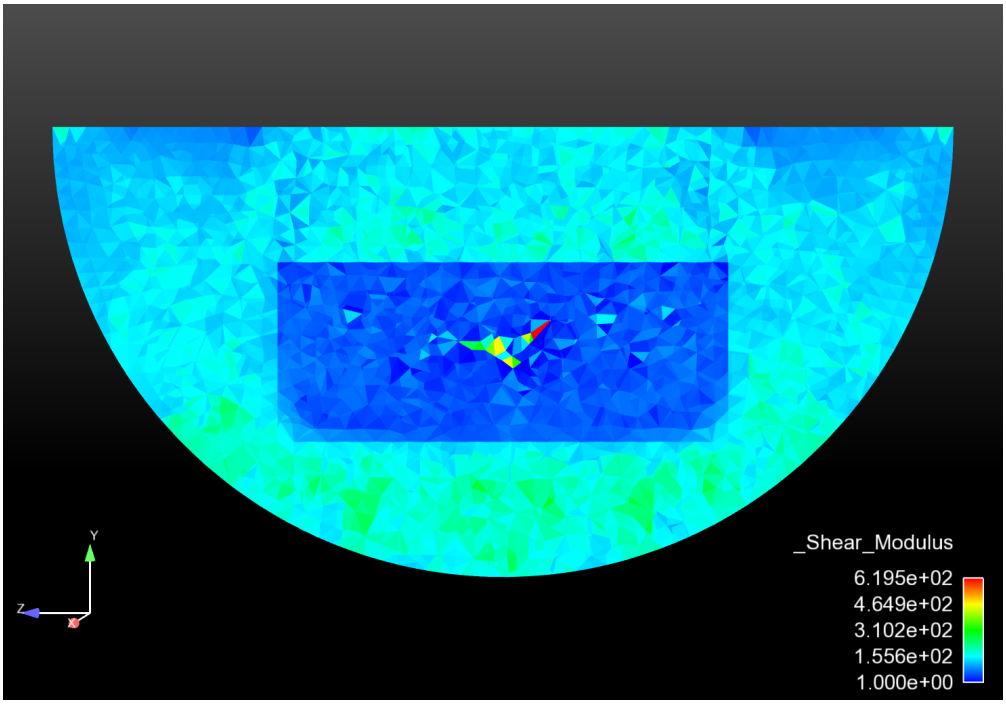

Figure 4-86. – Shear modulus values of model elements, using least-squares objective.

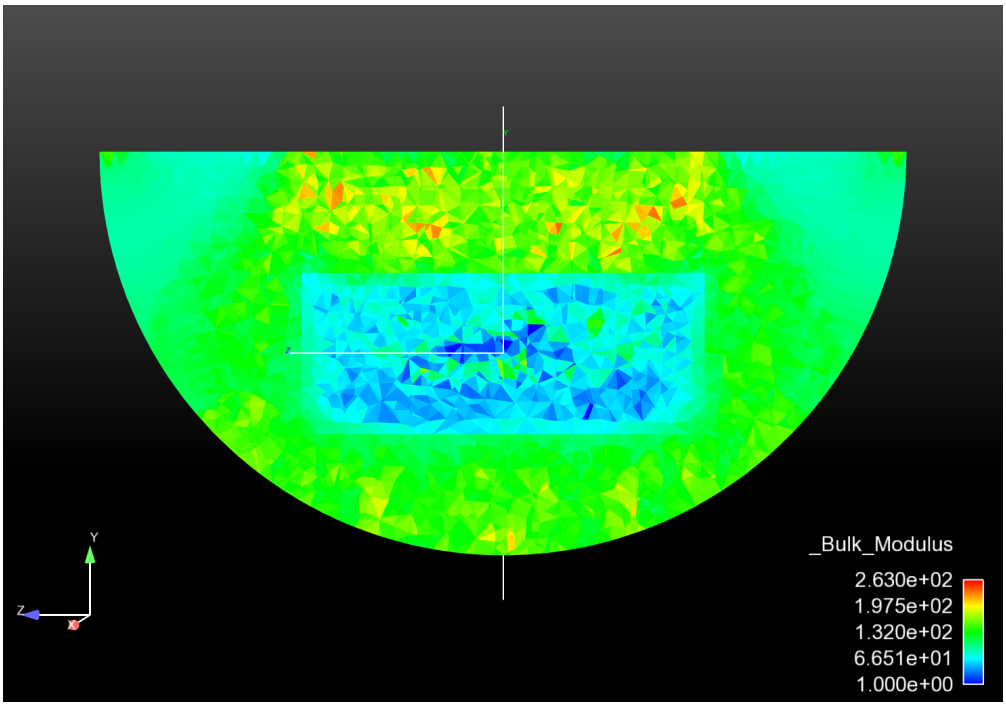

Figure 4-87. – Bulk modulus results for model elements, using least-squares objective.

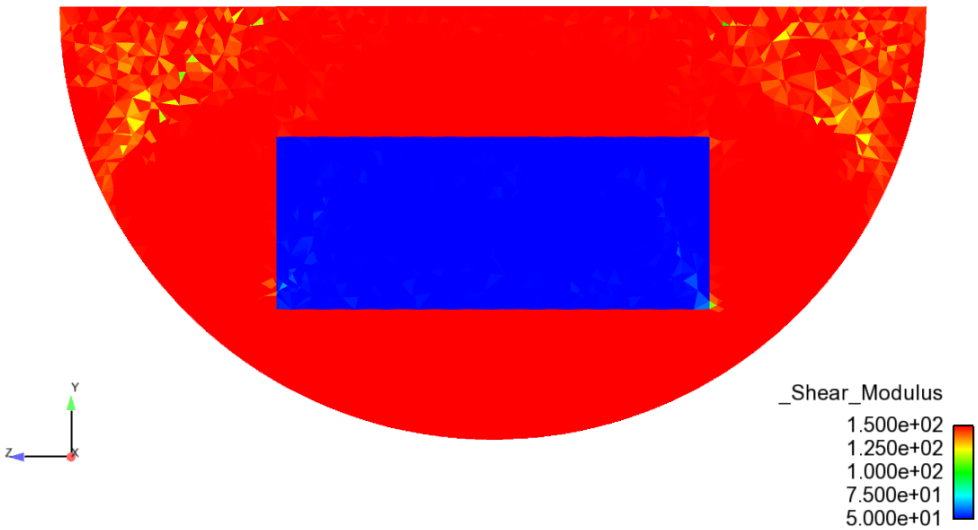

Figure 4-88. – Shear modulus results, using MECE objective.

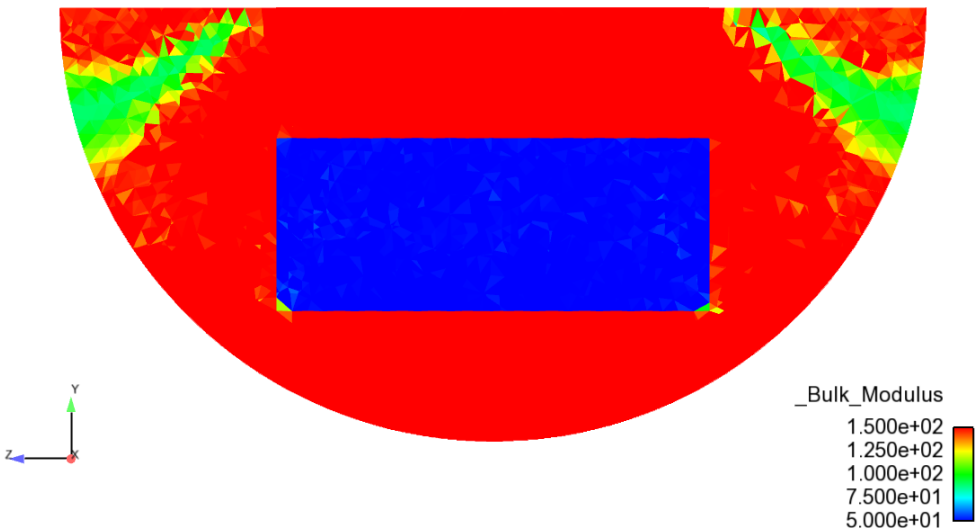

Figure 4-89. – Bulk modulus results, using MECE objective.

method, ran in parallel and underwent 30 iterations. Both the gradient and objective function were found to converge appreciably, though the objective function achieved much smaller error terms. Figure 4-90 shows the convergence behavior of the objective function and gradient for the least-squares optimization. The continuous optimization problem is solved using the Rapid Optimization Library (ROL) package in Trilinos.

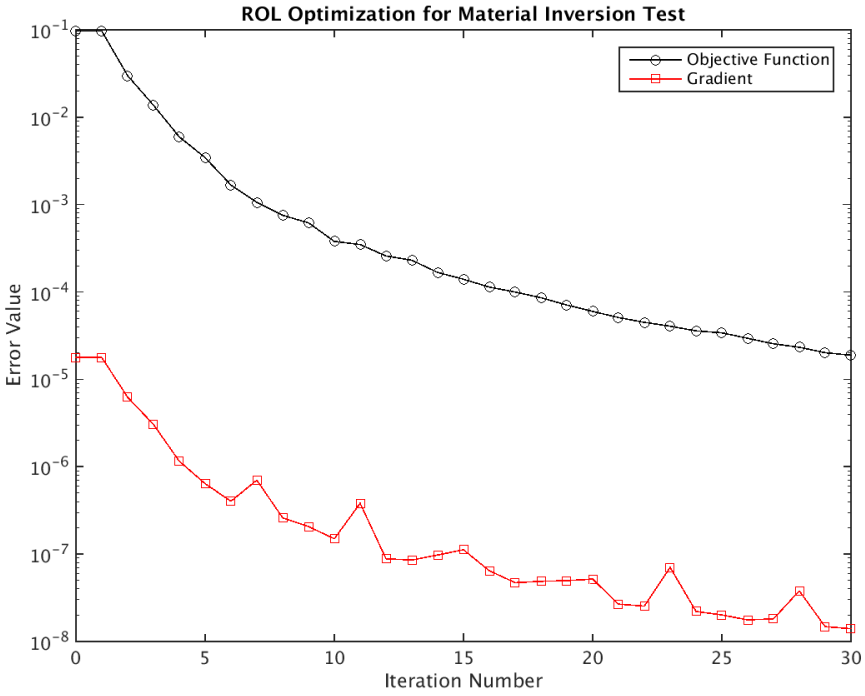

Figure 4-90. – ROL optimization of objective function and gradient, using least-squares objective.

10.4.2. Frequency Domain Viscoelastic Material Inversion

In this section, we describe a frequency-domain material inversion test performed on a solid assembly of two steel blocks joined by a region of viscoelastic foam material. Figure 4-91 shows the geometry of the test model.

As shown in Figure 4-91, the model assembly consists of two equally-sized steel blocks, depicted in yellow and green, joined by a region of viscoelastic foam material, shown in red. The model was discretized with a finite element mesh of Hex-8 elements. A periodic point load with a frequency of 500 Hz was applied to the yellow block, also as shown in the figure. It was desired to calculate the frequency-dependent viscoelastic material properties of the foam block, including complex values for the bulk (K) and shear (G) moduli.

Synthetic input data for the inverse problem was generated by performing a forward run in the frequency domain on the model. The data represented elastic displacements for element nodes caused by the point load acting on the model. Exact values for the foam

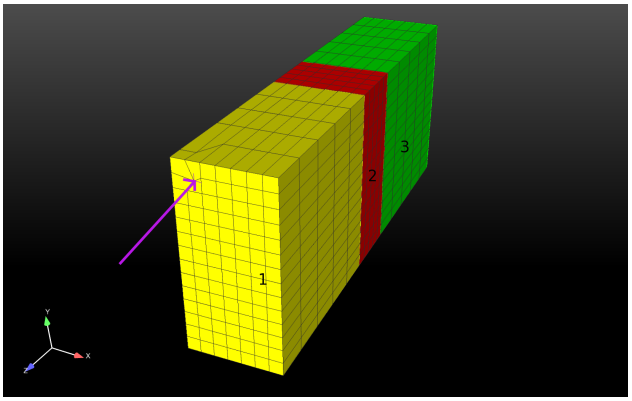

Figure 4-91. – Foam block model with finite element mesh and force location.

block material properties, shown in Table 4-38, were used to generate the displacement data. For the inverse run, initial guesses were chosen for the complex valued properties of the foam block region. The foam block region was designated as isotropic and viscoelastic, the entire block sharing the same complex-valued material properties. The initial guesses, along with the input data, were used to verify that the code could recover exact material properties of the foam block. Results for the computed material properties of the foam block are also shown in Table 4-38.

Table 4-38. – Exact and computed values for foam block's complex material properties.

Property	Exact	Initial Guess	Computed
G Real	4000	2000	40000.001556
G Imag.	0	0	-0.005484
K Real	16000	8000	15999.999388
K Imag.	5000	0	5000.000827

As shown in Table 4-38, despite halved initial guesses for the real moduli and poor assumptions of no damping behavior, the code was able to recover material property values well. The optimization, performed in parallel using a BFGS method, ran in parallel and underwent 95 iterations. Both the gradient and objective function were found to converge appreciably, the error decreasing especially rapidly following 80 iterations. Figure 4-92 illustrates the convergence behavior for the objective function and gradient. The continuous optimization problem is solved using the Rapid Optimization Library (ROL) package in Trilinos.

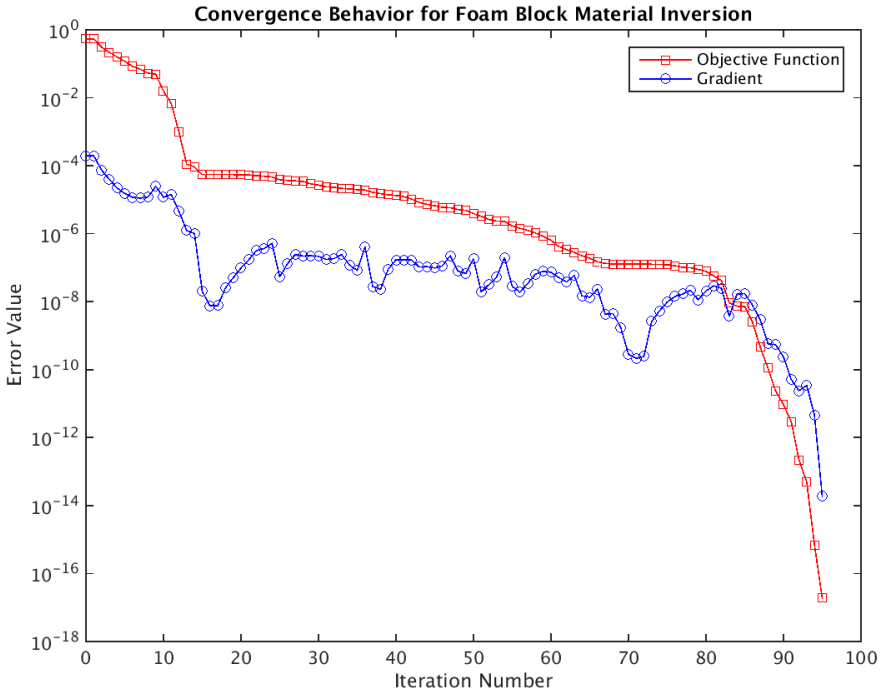

Figure 4-92. – Convergence Behavior of Foam Block Material Inversion.

10.5. Solution Procedures

10.5.1. Verification of Time Integration

10.5.1.1. Verification of generalized alpha damping

Though it is not always done in finite element code verification, it was deemed appropriate to verify that the generalized alpha time integrator[13] was implemented correctly. To isolate that feature, a single degree of freedom simple harmonic oscillator problem was solved. In this problem, the mass and stiffness were each set to unity. The period of free vibration would be 2. A unit load was imposed for a half a period and the resulting free vibration was calculated. The exact solution to this problem is

$$u(t) = 2\cos t$$

The **Sierra/SD** results for time steps $2\pi/200$, $2\pi/400$, $2\pi/800$, and $2\pi/1600$ were computed. The resulting displacements for all four cases are almost identical and are shown in Figure 5-93.

Values at time 8π were compared and the resulting convergence plot is shown in Figure 5-94. We see that the convergence rate is almost exactly two – the theoretical value.

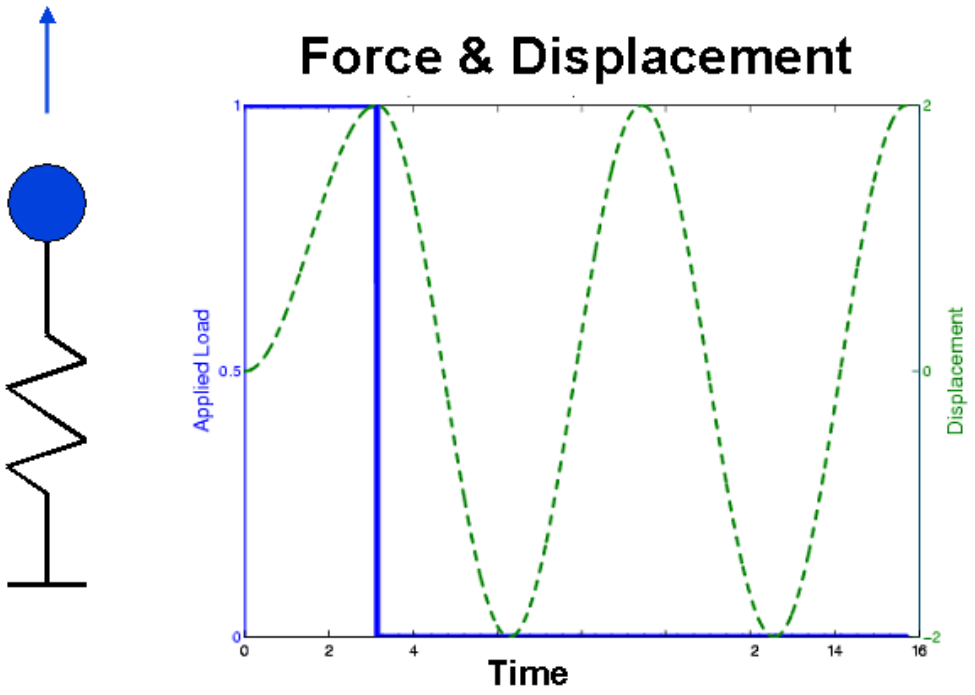

Figure 5-93. – The time integrator is tested against a simple harmonic oscillator. Values of displacement at time 8π are compared and tested for convergence.

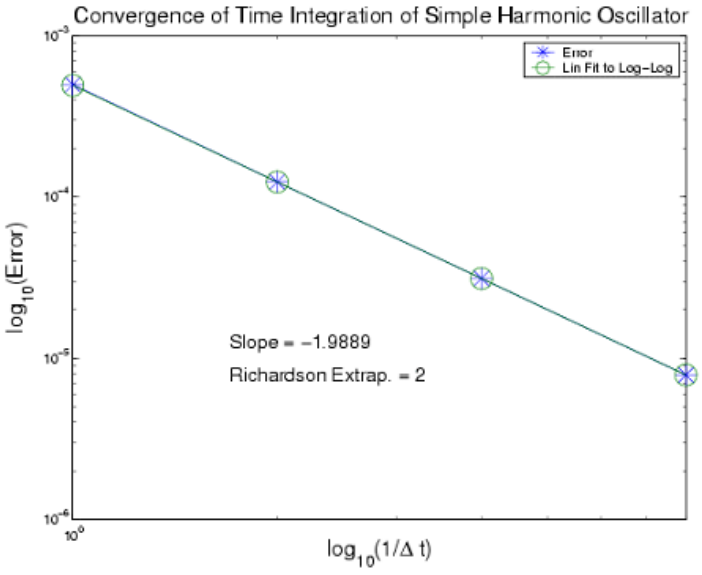

Figure 5-94. – Convergence of Simple Harmonic Oscillator.

10.5.1.2. Verification of prescribed acceleration capability

In this section we present an example of verification for the prescribed acceleration capability. The example consists of a cantilever beam model 10 meters in length, with a square cross section of 1 meter dimension. The beam is subjected to an end-loaded acceleration in the axial direction given by

$$a(t) = cos(\omega t) \tag{10.5.1}$$

where $\omega = 2\pi f$, and $f = 16$Hz. The initial conditions, including initial displacement and initial velocity of the beam are set to zero. Given these conditions, we can integrate the acceleration equation twice to obtain the following expression for the displacement at the loaded end

$$D(t) = \frac{1}{(32\pi)^2}(1 - cos(32\pi t)) \tag{10.5.2}$$

Figure 5-95 shows a comparison of the analytical solution for displacement against the **Sierra/SD** result. Excellent agreement is observed. We note that this example can be found in the test suite at the following location.

`Salinas_rtest/verification/transient/bar_prescribed.xml`

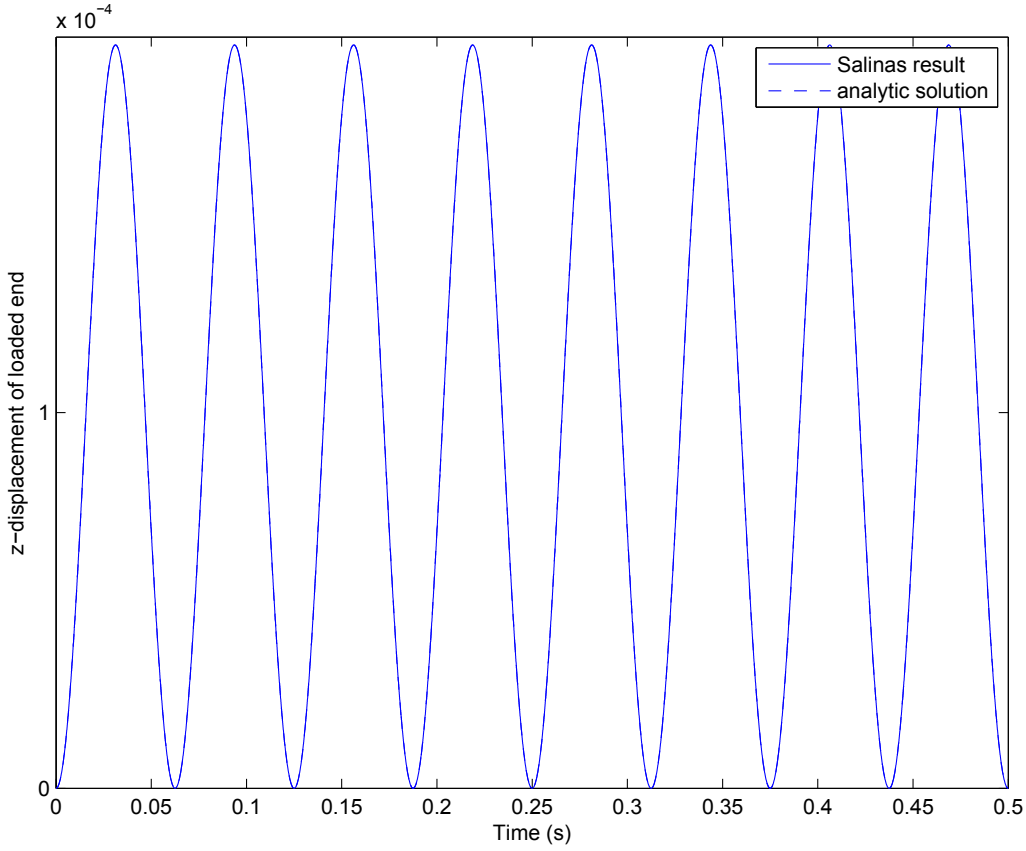

Figure 5-95. – Comparison of **Sierra/SD** result with analytical solution of a beam with end-loaded prescribed acceleration.

10.5.2. Direct Frequency Response

In this section we give two examples of verification of the direct frequency response driver in **Sierra/SD**. Both examples involve mass spring systems. The first is a mass spring system with stiffness proportional damping, and the second is a mass spring system with mass proportional damping.

The exact solution to this problem is given by equation 4.21a in Craig's book,.[15]

$$D_s = \frac{U}{U_0} = \frac{1}{\sqrt{((1-r^2)+(2\zeta r)^2)}} \tag{10.5.3}$$

where U is the displacement of the mass, U_0 is the magnitude of the forcing function, $r = \frac{\omega}{\omega_0}$ is the ratio of the circular frequency to the fundamental resonant frequency, and $\zeta = \frac{c}{2\sqrt{km}}$ is the level of damping, normalized with respect to the stiffness and mass of the spring mass system. See Figure 3.1 in Craig[15] for a diagram of the problem.

For proportional damping, we have $c = \alpha m + \beta k$. The exact solutions corresponding to equation 10.5.3 were computed and compared with simulations in **Sierra/SD** for two cases. In case 1, $\alpha = 0.0$ and $\beta = 1.0$. In case 2, $\alpha = 1.0$ and $\beta = 0.0$. Also, for convenience we set $k = m = U_0 = 1$ for this problem. In this way, the exact solutions for both mass and stiffness proportional damping were exactly the same.

Figure 5-96 shows the comparison of the computed and exact solutions for the case of stiffness proportional damping. The mass proportional damping case was exactly the same, and thus is not shown. We see that proportional damping decreases the peak of the resonant frequency, and shifts the frequency to the left. Excellent agreement is seen between **Sierra/SD** and the exact solutions.

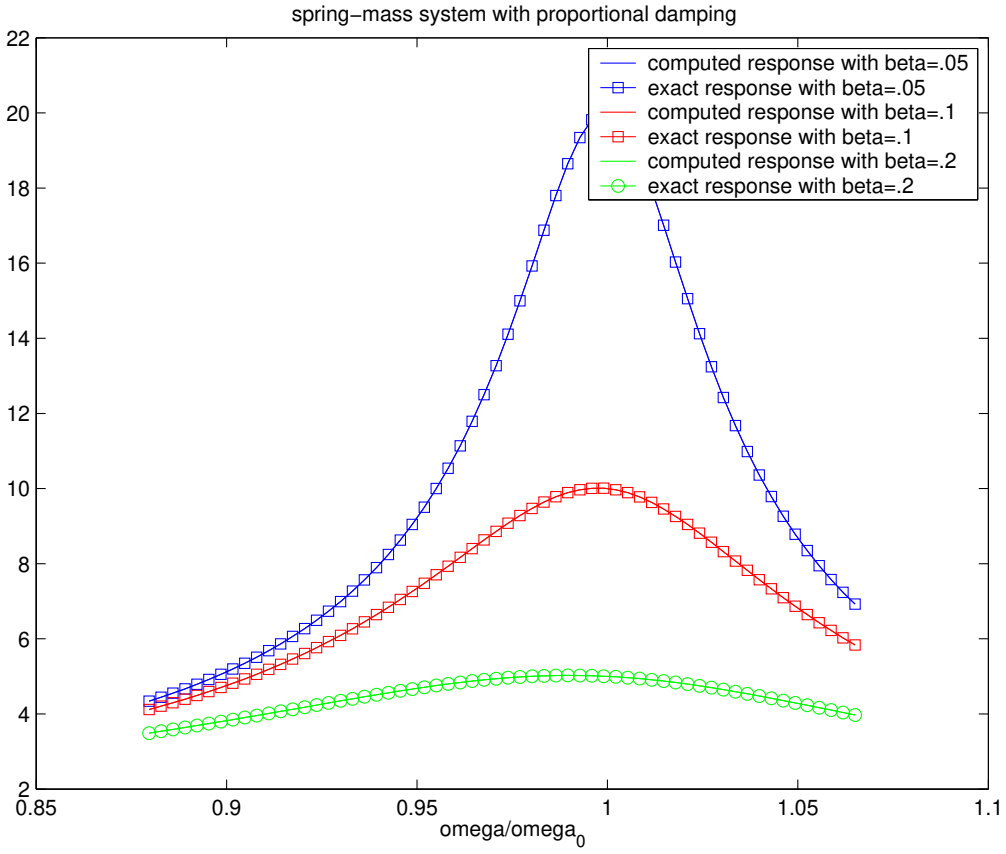

Figure 5-96. – Comparison of exact and computed responses from direct frequency response of a damped spring mass system.

10.5.3. Modal Frequency Response

This section presents verification examples for modal frequency response. The truth model used in these tests is the result from the corresponding direct frequency response analysis. The convergence of the modal expansion is verified.

The first test involves a free-free beam composed of $2x2x20$ hex8 elements. The beam is subjected to a uniform pressure load on both ends and a modal frequency response solution is computed. The comparison of the results at a point in the center of the beam, versus the results from direct frequency response is given in Table 5-39. The modal frequency response results converge to the direct frequency response results as the number of modes in the modal expansion increases.

The second test involves the same geometry as the previous test, and instead has one end fixed and the other subjected to a traction load of 111. Also, in this test, the modal acceleration method is used instead of modal frequency response. The results, compared with a direct solution, are given in Table 5-40. The modal frequency response results converge to the direct frequency response results as the number of modes in the modal expansion increases. We note that both of these tests are located in the **Sierra/SD** test suite under

`Salinas_test/verification/frf`

Table 5-39. – Convergence of Modal Frequency Response Method.

quantity	direct frf	modal			
		14 modes	30 modes	50 modes	100 modes
accx	12.7659	14.28	13.5	13.9	12.79
accy	-12.7659	-14.28	-13.5	-13.9	-12.79
accz	117.309	139.0	111.0	118.0	117.353

Table 5-40. – Convergence of Modal Acceleration Method.

quantity	direct frf	modal accel, 14 modes	modal accel, 30 modes
accx	-2350.82	-2349.75	-2350.81
accy	-2415.098	-2414.12	-2415.097
accz	-718.587	-718.321	-711.578

10.5.4. Eigen Analysis

Eigen analysis is performed as part of the verification of the element quantities. Practically speaking, it is difficult to verify the analysis independent of the element. For example, the hex20 and tet10 element convergence studies utilize eigen analysis for the convergence study. See Figures 1-3 and 1-4 for example.

Similarly, the elastodynamics tests examined in section 10.7.1 are built on the structure of modal analysis procedures. As these tests correspond to semi-analytic solutions (such as those from Blevins [10]) they constitute true verification.

10.5.5. Quadratic Eigen Analysis

There are several different solution approaches within the package that computes the solution to the quadratic eigenvalue problem. Each requires its own verification.

10.5.5.1. QEP – Proportionally Damped

The proportionally damped system is straightforward because the eigenvectors of the real system diagonalize the complex (or damped) solution. Consider

$$(K-\omega^2 M)\phi = 0 \tag{10.5.4}$$

For this system $\phi^T K \phi = \Lambda$ is diagonal, and $\phi^T M \phi = I$. The proportional damping matrix is given by $C = \alpha M + \beta K$. Also $\phi^T C \phi = \alpha I + \beta \Lambda$.

The solution to the j^{th} mode of the damped system is given by,

$$\Lambda_{jj} + \omega(\alpha + \beta\Lambda_{jj}) + \omega^2 = 0 \tag{10.5.5}$$

All quantities are known from the real eigenvalue analysis, and we can solve in terms of ω.

$$\omega_j = \frac{-(\alpha+\beta\Lambda_{jj}) \pm \sqrt{(\alpha+\beta\Lambda_{jj})^2 - 4\Lambda_{jj}}}{2} \tag{10.5.6}$$

Table 5-41 lists the eigenvalues and errors for a proportionally damped system with $\alpha = 0$ and $\beta = 0.001$. This is a small *Hex8* model for which the eigenvalues are known from real eigen analysis.

These solutions are within the expected round off. Notice that as the natural frequency increases, the fractional damping is increasing to almost 25%.

Table 5-41. – Eigenvalues of Proportionally Damped Model.

#	Λ	$\sqrt{\Lambda}/2\pi$	$\omega/2\pi$	error
1	5375.07	11.6684	(-0.427735,11.6606)	1.6e-6
2	108926	52.5275	(-8.66809,51.8074)	2.7e-6
3	219052	74.4893	(-17.4316,72.4209)	4.1e-7

10.5.5.2. QEP – Viscoelastically Damped

There are no verification tests yet for this solution.

10.5.5.3. QEP – Discrete Dampers

There are no verification tests yet for this solution.

10.5.6. SA_eigen

Verification of the SA_eigen solution is complicated by the model reduction inherent in the process. Kinsler[32] has a closed form expression for a coupled one dimensional structural acoustic system. The finite element solution will approach this solution as,

a the finite element mesh converges, and

b the modal truncation is eliminated.

Without both of these considerations, there will be no convergence of the solution. Unfortunately, while we can show a $1/h$ type convergence for the FE mesh, no such convergence can be expected for modal truncation. For some forms of basis functions the convergence will be rapid. In other cases, convergence may not be acceptable until the entire space has been spanned.

Because of model size issues, such convergence is demonstrated independently. Thus, we first show convergence of the mesh to the analytic solution. Then, with a coarse mesh, we demonstrate convergence as the number of modes in the basis is increased. Figure 5-97 shows the mesh convergence study. We note that for $1/H > 100$ the solution no longer appears to be converging. The *polyeig()* routine in MATLAB does a full factorization. Computing accurate modes with polyeig involves techniques that are beyond the scope of this document.

Figure 5-98 shows the convergence of the reduced model to the first coupled modal frequency when using 2 structural and 10 acoustic modes. Note that this mode converges from below to a value 1% higher than the mode of the solution without truncation.

Figure 5-99 shows the convergence of the modal frequency as the number of basis modes is increased. There is no damping for this system. Introducing radiation damping to the right

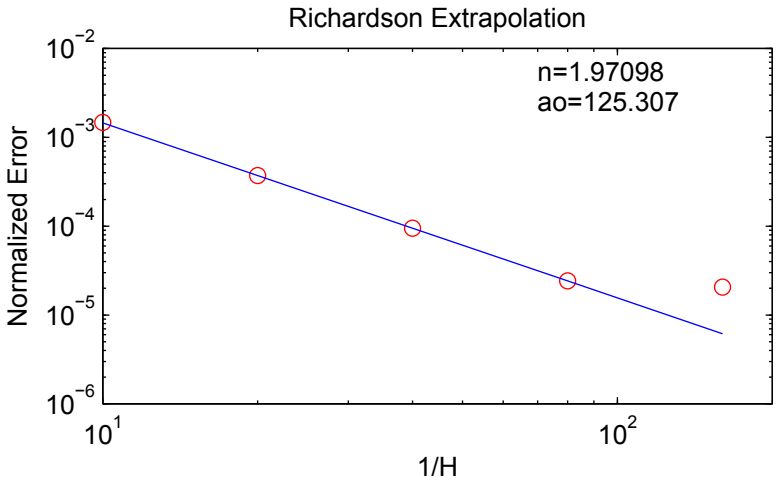

Figure 5-97. – Mesh convergence to 1D Structural Acoustics Example. The example, taken from Kinsler[32] uses $a = 1/25$ and $b = 8/3$, where a and b are defined in the reference. The eigen solution is found using MATLAB's `polyeig()` function. The analytical solution from equation 9.42a of Kinsler[32] is 125.2783.

side of the acoustic system impacts the modal convergence rate. As shown in Figure 5-100, radiation damping (or non-reflecting boundary conditions), delays convergence and degrades accuracy.

To examine the dependence of this error on the coupling, we sweep through various structural mass quantities while holding all other parameters fixed. Sweeping the mass results in a change of structural resonant frequency. In addition, the type of coupling experienced by the acoustic cavity changes from approximately unbounded to fixed boundary conditions. Results shown in Figure 5-101, show variation as the parameter a of Kinsler is varied. The error is highest, and the coupling is greatest, when the structural and acoustic domains have similar resonant frequencies.

To examine the effects of impedance matching while maintaining the resonance frequencies, the structural mass and stiffness are varied together such that the resonance frequency is maintained at 160 Hz, below the acoustic resonance (166 Hz). Figure 5-102 provides the results. The error is largest when the impedance approximates an open acoustic termination.

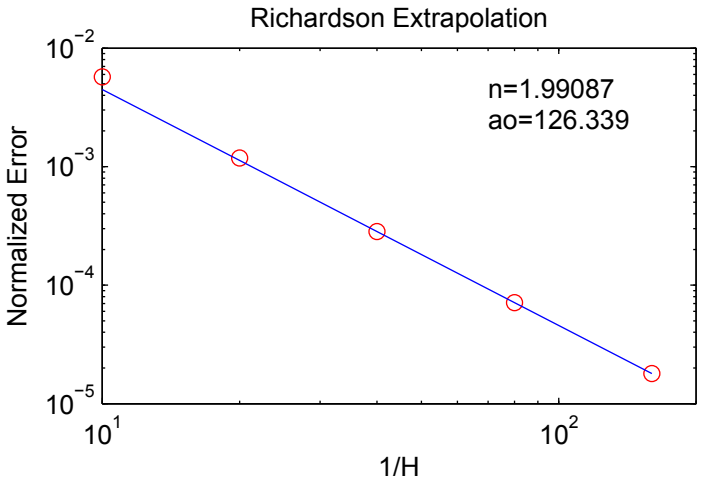

Figure 5-98. – Mesh convergence to 1D Structural Acoustics Example using a modal basis. The example is that of Figure 5-97. The quadratic eigen solution is computed using 2 structural and 10 acoustic modes in **Sierra/SD**.

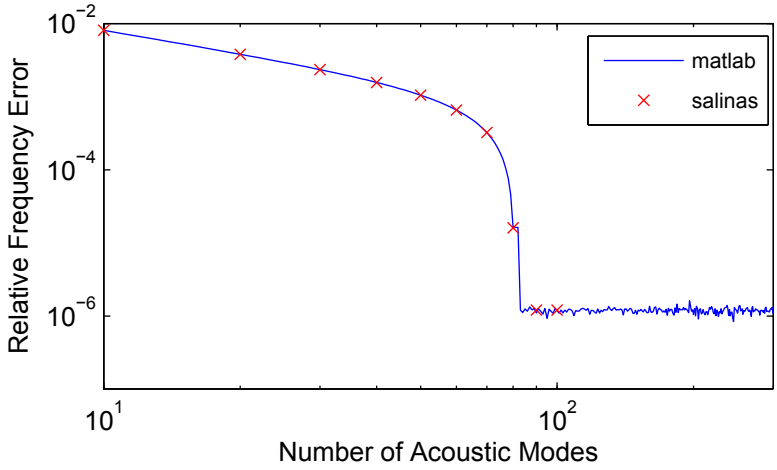

Figure 5-99. – Modal convergence to 1D Structural Acoustics Example using a modal basis. The example is that of Figure 5-97, with $1/h = 80$. The quadratic eigen solution is computed using 2 structural modes, while the number of acoustic modes varied. Computation is in MATLAB, with selective comparison to **Sierra/SD**. Convergence is not rapid as a solution requires components of all axial modes. After about 80 modes, no further improvement is obtained.

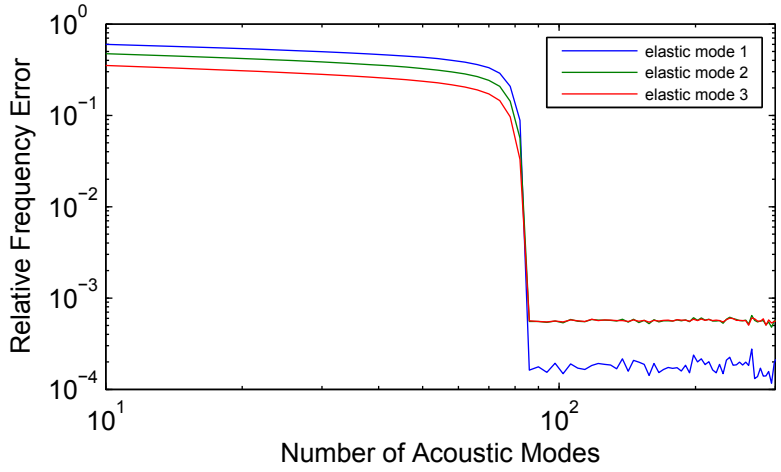

Figure 5-100. – Mesh convergence to *Damped* 1D Structural Acoustics Example using a modal basis. The model is unchanged from Figure 5-99 except that there is a non-reflecting boundary condition applied on the end opposite to the structure. MATLAB comparisons with `polyeig` truth model, with direct verification to **Sierra/SD** solution.

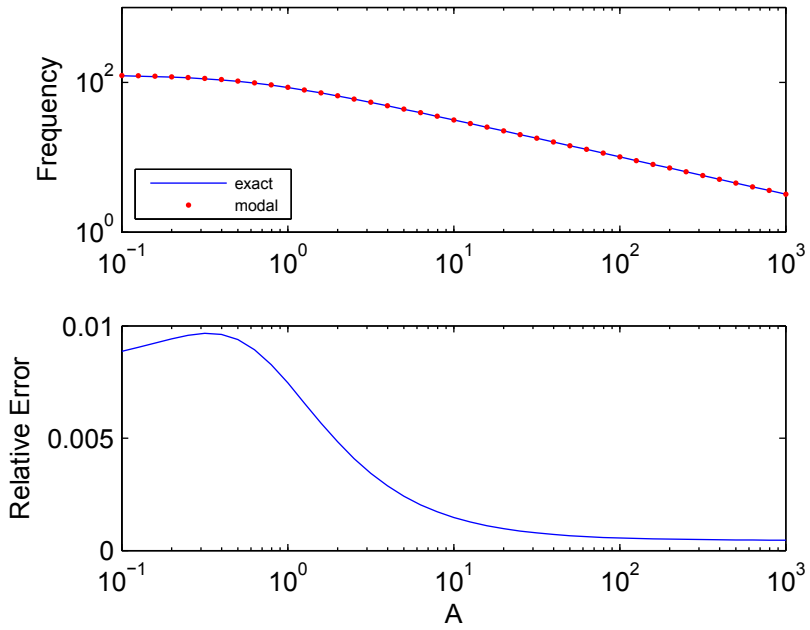

Figure 5-101. – Modal convergence of 1D Structural Acoustics Example using a modal basis. The example is that of Figure 5-97, with $h = 1/80$. The quadratic eigen solution is computed using 2 structural modes and 10 acoustic modes in **Sierra/SD**, while the mass parameter, a is varied.

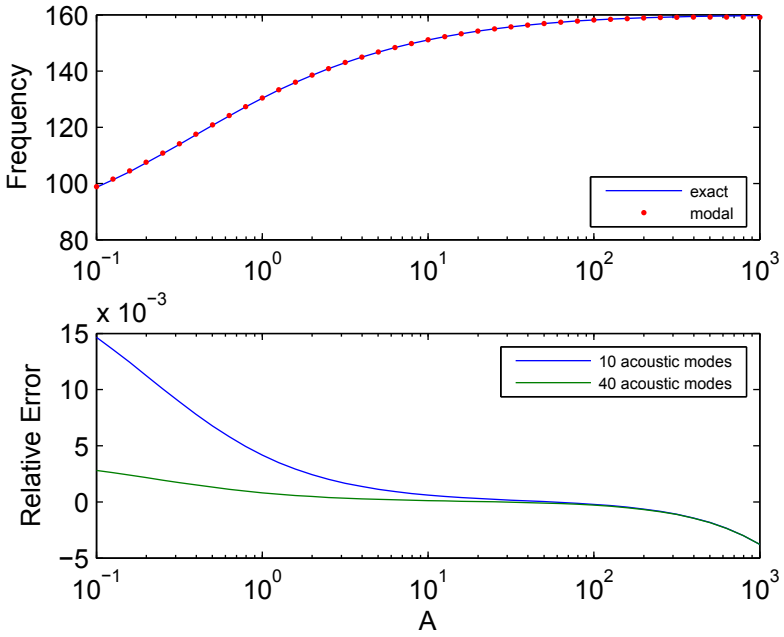

Figure 5-102. – Modal convergence of 1D Structural Acoustics Example using a modal basis as the impedance is swept. The example is that of Figure 5-97, with $h = 1/80$. The quadratic eigen solution is computed while both the mass parameter, a and the stiffness parameter, b, are varied. We maintain a structural resonance of 160 Hz.

10.5.7. Buckling of a Cantilever Beam

The buckling of a cantilever beam modeled using solid elements is verified. The geometry for this example consists of a cantilever beam with one end clamped, and with the other subjected to a compressive load P. Euler-Bernoulli beam theory predicts the critical buckling load to be

$$P_{cr} = \frac{2.4674EI}{L^2} \tag{10.5.7}$$

A simple mesh of this example was created, consisting of a $2 \times 2 \times 10$ hex elements. The critical buckling load is predicted to be

$$P_{cr} = \frac{2.4676 \times 30 \times 10^6 \times \frac{1}{12}}{10^2} = 61675 \tag{10.5.8}$$

The computed buckling load was 61370.1.

10.5.8. Thermal Expansion

In this section we give verification examples for thermal expansion.

10.5.8.1. Free beam

This example consists of a free floating beam that is subjected to a uniform temperature increase of 178^o. The built-in end is such that expansion can occur without generating any stresses. In the end, the beam is stress free but undergoes a uniform expansion. The exact solution for the tip displacement is

$$\Delta L = \alpha L \Delta T = 0.0001 \times 50 \times 178 = 0.89 \tag{10.5.9}$$

where α is the coefficient of thermal expansion, and L is the length of the beam. **Sierra/SD** gives the exact answer of 0.89. This test is included in the verification test suite in the following directory

`tests/Salinas_rtest/verification/thermal/thermal_beam.xml.`

10.5.8.2. Free beam with linear temperature distribution

This is also a free floating beam example, except that the temperature variation is linear along the length of the beam, instead of the uniform temperature of the previous example. The exact axial displacement of the end of the beam is given by (thanks to Jason Hales for the derivation of this equation)

$$u(x) = \alpha(T_0 - T_i)x + \alpha(T_L - T_0)\frac{x^2}{2L} \tag{10.5.10}$$

where T_0 is the temperature of the beam at the fixed end, T_L is the temperature of the beam at the free end, and T_i is the initial (uniform) temperature of the beam. Plugging in the parameters for this example gives

$$u(L) = 0.0001 * 1 * 50 + 0.0001 * 1 * 25 = 0.0075 \tag{10.5.11}$$

This example is also included in the verification test suite in the following directory,

`tests/Salinas_rtest/verification/thermal/thermal_beam2.xml.`

A note about the boundary conditions for these tests may be useful. These examples simulate free expansion. The boundary conditions are applied at one end to eliminate rigid body modes which generate solution difficulty. The example with linear temperature distribution results in a free expansion solution that is concave at the constraint end. Original boundary conditions constrained that surface to be planar, and resulted in a solution that was about 1% in error. Relaxing the boundary conditions to the minimal set results in a much better solution.

10.5.8.2.1. User Evaluation: A code to code comparison for a single thermal load is described in section 10.8.6.1.

10.5.9. Thermal/Structural Responses (TSR)

Sierra/SD is not used to compute a thermal solution. However, input temperature or energy density may be applied to the materials or to determining the thermal stress and strain We support this interaction as follows.

TSR_preload reads an initial stress and stores it on the body. An internal force response is computed. No deformation is determined, and the element matrices are not modified. It is typically followed by a static or transient dynamic response.

Thermal load may be applied to a body. The load may be specified on all nodes, on element centroids, or on element integration (or Gauss) locations.

Material Properties Temperature dependent material properties are supported. A user provided function determines the property as a function of temperature.

Energy Density may be used as a thermal input for elements. The energy density is specified on element centroids or element integration points and converted to temperature using the specific heat capacity. Energy density may not be specified as a nodal quantity.

More detailed information is available in the corresponding sections of the SierraSD Users' Guide. **Test Matrix**

We would like to generate effective tests that verify that these capabilities are working properly, and especially that they work together. The test matrix shown in Table 5-42 summarizes the tests. Particular emphasis is paid to combined capabilities.

Section	TSR_preload	statics	NLstatics	trans	load	Material
10.5.9	X					
10.5.9	X					X
10.5.9	X	X				X
10.5.9	X		X			X
10.5.9	X			X		X
10.5.9	X	X			X	X
10.5.9	X	X		X	X	X
10.5.9	X	X		X	X	X

Table 5-42. – Thermal/Structural Test Matrix. All tests apply temperature inputs except 10.5.9, which is a repeat of 10.5.9 applying energy inputs.

Thermal Model Definition The model is a perfect unit cube with a uniform thermal load on a single block. No other boundary conditions are applied. In the following NLStatics refers to the nonlinear statics solution method.

TSR The model, defined in section 10.5.9, results in a uniform stress throughout the single hex element. For this solution case, no deformation results. Applying a Young's modulus of 30×10^6, and a thermal expansion coefficient, $\alpha = 10^{-6}$ together with the

temperature change of $\Delta T = 5$, results in a thermal strain of 5×10^{-6} and a stress of 150. Note that the total structural strain is zero, as the body cannot deform in this solution.

TSR with Thermal Material Results are identical to section 10.5.9, but the material properties are determined using a Young's modulus which depends on temperature.

TSR, with Thermal Material followed with Statics Following the solution of section 10.5.9 with linear statics equilibrium results in a solution with zero stress and a net strain of 5×10^{-6}. Deformations match the strain. The statics solution is only well posed when the rigid by motion is constrained.

TSR, with Thermal Material followed with NLStatics Following the solution of section 10.5.9 with nonlinear static equilibrium results in a solution with zero stress and a net strain of 5×10^{-6}. Deformations match the strain. The statics solution is only well posed when the rigid by motion is constrained.

TSR, with Thermal Material followed with Transient Following the solution of section 10.5.9 with damped transient equilibrium results in a solution that oscillates about the solution of section 10.5.9, with a net strain of 5×10^{-6}. Deformations match the strain.

TSR, with Thermal Material followed with Loaded Statics Section 10.5.9 determines an unloaded equilibrium. The same thermal load may be applied with a negative scale factor, resulting in zero strain – the initial (TSR) stress is exactly balanced by an opposing stress. To better verify the code, we apply a negative thermal stress that is three times the original stress, resulting in a solution with zero stress and a net strain of -10×10^{-6}. Deformations match the strain. The statics solution is only well posed when the rigid by motion is constrained.

TSR, Thermal Material followed with Loaded Statics & Dynamics We follow the solution of section 10.5.9 with a transient load scaled with the original force. This TSR pushes the solution out. The statics solution pushes it back in, to a total of twice the strain of TSR. Dynamics results in a solution that oscillates about 5×10^{-6}.

TSR, Thermal Material, Loaded Statics & Dynamics with Energy Specific energy may be supplied as the input to the TSR and static and dynamic loading. The specific energy is converted to temperature using the specific heat. Material properties are determined from the *temperature*, not the energy in the body.

10.5.10. Direct Energy Deposition at Gauss Points

Energy deposited in the body (as by an X-ray event) can result in an instantaneous change in temperature. For consistency with other applications, the energy is applied as a specific energy, i.e. the energy per unit mass, $\tilde{E} = Q/(\rho V)$. Because such energy typically decays exponentially, it is important that energy be provided at the Gauss points especially for larger, higher order elements.

10.5.10.1. Two Element Linear Variation Hex20

The example consists of two unit Hex20 elements forming a beam of dimension 2x1x1. The specific energy varies as the long dimension of the beam, X. The geometry is shown in Figure 5-103. We have verified the following.

1. The specific energy is properly read into **Sierra/SD**, as verified with line sample output.
2. The specific energy is properly converted to temperature using the specific heat of the material.
3. The total energy input is determined properly.
4. Resulting displacements meet the analytic solutions (see Figure 5-104). The numerical results are obtained by using *Ensight* to post process the displacements through the center of the body. The analytic displacement may be obtained by using the one dimensional ODE generated by the thermal stress.

$$\epsilon_{thermal} = \frac{du}{dX} = \alpha_t T(X) \tag{10.5.12}$$

$$= \alpha_t X / C_v \tag{10.5.13}$$

$$u(x) = \frac{\alpha_t}{2C_v} X^2 \tag{10.5.14}$$

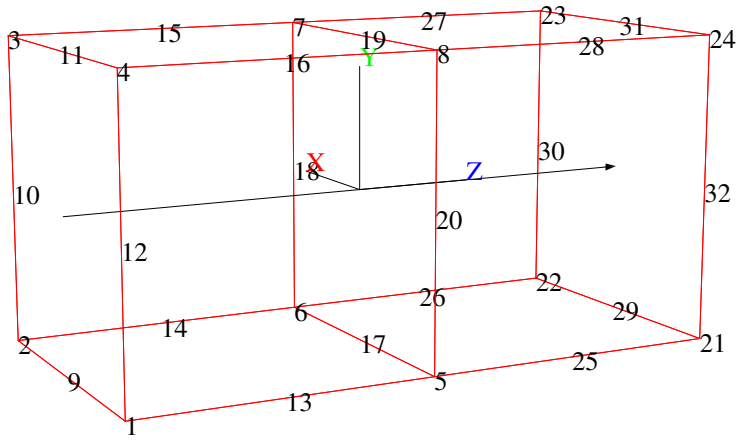

Figure 5-103. – Simple Energy Deposition Test Geometry.

The example is found in,

`tests/Salinas_rtest/verification/thermal/edep_lin.xml`.

Resulting displacements are quadratic as from equation 10.5.10, with $\alpha = 0.001$, and $T_L = 1$.

A comparison to Abaqus thermal strains is reviewed in Section 10.8.6.1.

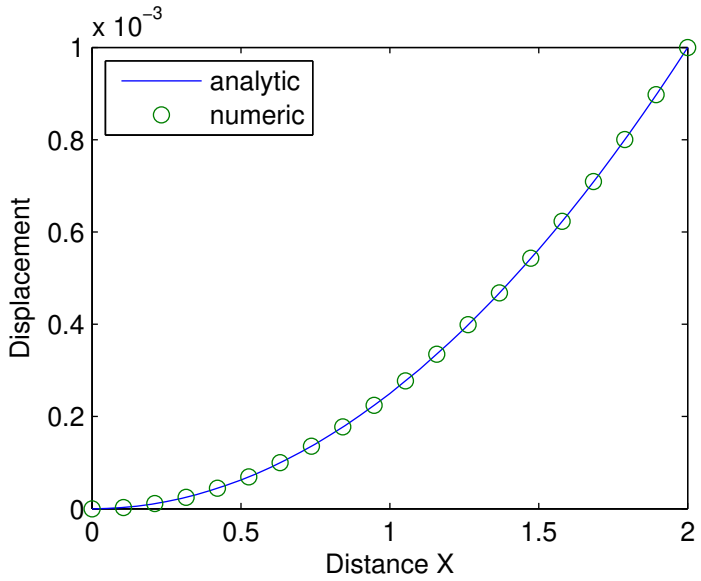

Figure 5-104. – Displacements Resulting from Linear Temperature Profile.

10.5.10.2. Two Element Quadratic Variation Hex20

This test uses the same geometry described in section 10.5.10.1 and Figure 5-103, but with specific energy variation, $\tilde{E}(x,y,z) = x^2 + y^2 + z^2$. The example ensures the following:

1. Exact representation of the energy and temperature as shown in linedata.
2. The total energy is $\rho \int_{elem}(x^2+y^2+z^2)dx\,dy\,dz$, which is 3ρ, where ρ is the density.
3. Ensures numbering of the Gauss points.
4. The displacement is inexact, as the analytic solution is cubic.

10.5.10.3. Two Element Exponential Decay Variation Hex20

This test uses the same geometry described in section 10.5.10.1, but with specific energy variation, $\tilde{E}(x,y,z) = e^{-x}$. The example ensures the following:

1. Approximate representation of the energy and its error can be extracted using line sample (`linesample`) data and is represented in Figure 5-105.
2. The total energy is $E_t = \rho(1-e^{-2})$. The solution is approximate, because the energy is represented by a quadratic in each element, but the error is less than 10^{-5}.
3. The displacement is inexact. The one dimensional thermal strain equation provides the ODE for the solution. We use $T(x) = \tilde{E}/C_v$. Then,

$$\epsilon_{thermal} = \frac{du}{dX} = \frac{\alpha_t}{C_v} e^{-\gamma X} \tag{10.5.15}$$

The solution for this equation is,

$$u = \frac{\alpha_t}{C_v \gamma} \left(1 - e^{-\gamma X}\right) \tag{10.5.16}$$

Numeric and analytic solutions for this solution are shown in Figure 5-106.

The test is `edep_expx`.

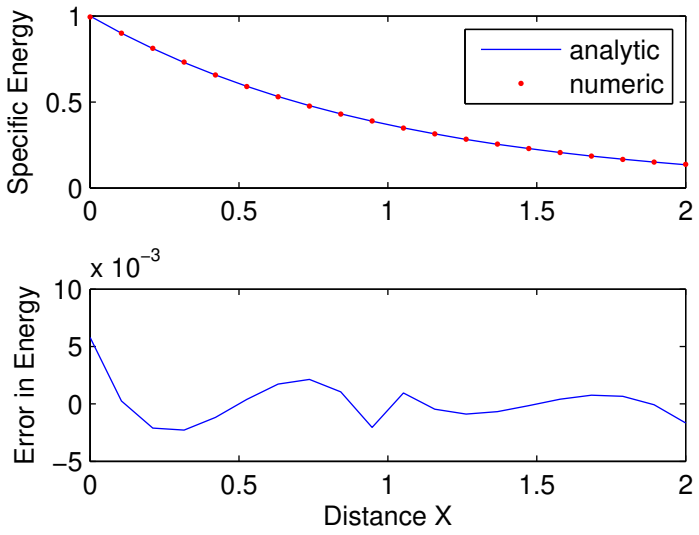

Figure 5-105. – Exponential Energy Deposition. Comparison of exact and interpolated solutions from the Gauss Points.

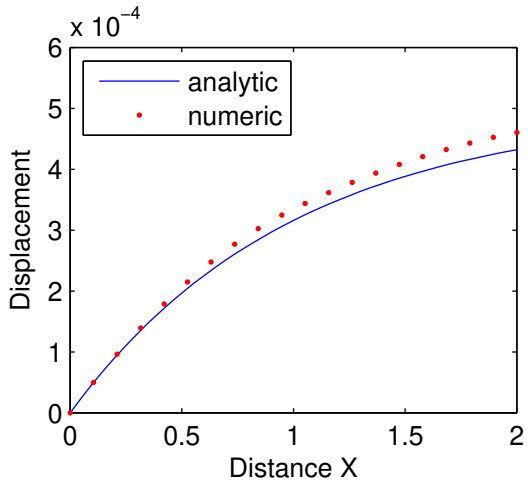

Figure 5-106. – Exponential Energy Deposition, computed Displacements. The numerical results are measured at Gauss points and interpolated within the elements. Displacements are interpolated from nodal values.

.

10.5.10.4. Two Element, Two Material Hex20

Again, the same geometry is used, but with two different materials for the Hex20 elements. We require that temperature be a linear function of X, and compute specific energy, $\tilde{E} = C_v T$ to meet that requirement. This provides a simple solution for the quadratic displacement. The specific energy is shown in Figure 5-107, as extracted from line sample (`linesample` . The resulting quadratic displacement (and corresponding analytic solutions) is shown in Figure 5-108. For these solutions, the heat capacity is 1 in the first element, and 2 in the second.

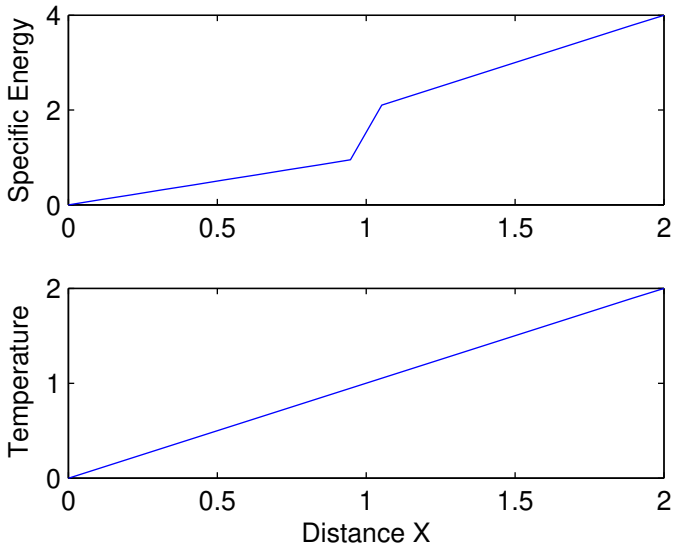

Figure 5-107. – Linear Deposition on 2 Blocks. The sampled specific energy and temperature across the two blocks is shown.

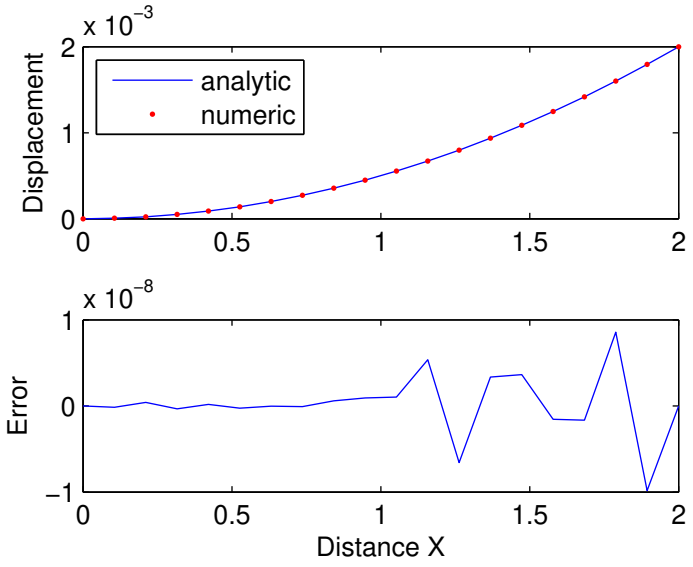

Figure 5-108. – Linear Energy Deposition. The displacement response and associated error is shown.

10.5.11. Craig-Bampton Model Reduction

10.5.11.1. OTM Verification

CBR in general and the Output Transfer Matrix (OTM) are discussed in[48] and.[46] The following steps are to be used for verification. The model used is the multi-element/olio_cbr_test.

1. ensure eigenvalues are consistent between models (reduced versus full)

   This portion of the test that is evaluated as part of the automated test.

2. check OTM for displacement in serial.

   a) Is data consistent with ϕ and ψ?

   This is checked in the debugger.

   b) does the product make sense (i.e.)

$$x_k = [OTM][x_1]$$

$$\bar{x}_k = K^{-1}x_1$$

   and,

$$x_k \approx \bar{x}_k$$

   This is done as follows.

   a) The model is clamped away from the interface to eliminate the confusion caused by redundant modes and zero energy modes. The system response is computed for mode 1 (a flexible mode). This is done by pulling in Kssr and Mssr and computing the eigenvalues, **E**, and eigenvectors, **V**.

   b) The reduced model is also computed for mode 1. We do this by computing the eigenvalues and eigenvectors of **Kr** and **Mr**.

   ```
   [vr, er]=eig(Kr,Mr);
   ```

   We ensure that the eigenvalues are approximately the same. See figure 5-109.

   c) The first eigenvectors is expanded to the system from both systems. The reduced eigenvectors contain both a physical coordinate and a modal coordinate component. MATLAB code to do this expansion is shown in Figure 5-111. A comparison of the two vectors is shown in Figure 5-110. Note that there is a scale factor difference of -1 in the two vectors. This is acceptable as eigenvector scaling is arbitrary to that factor.

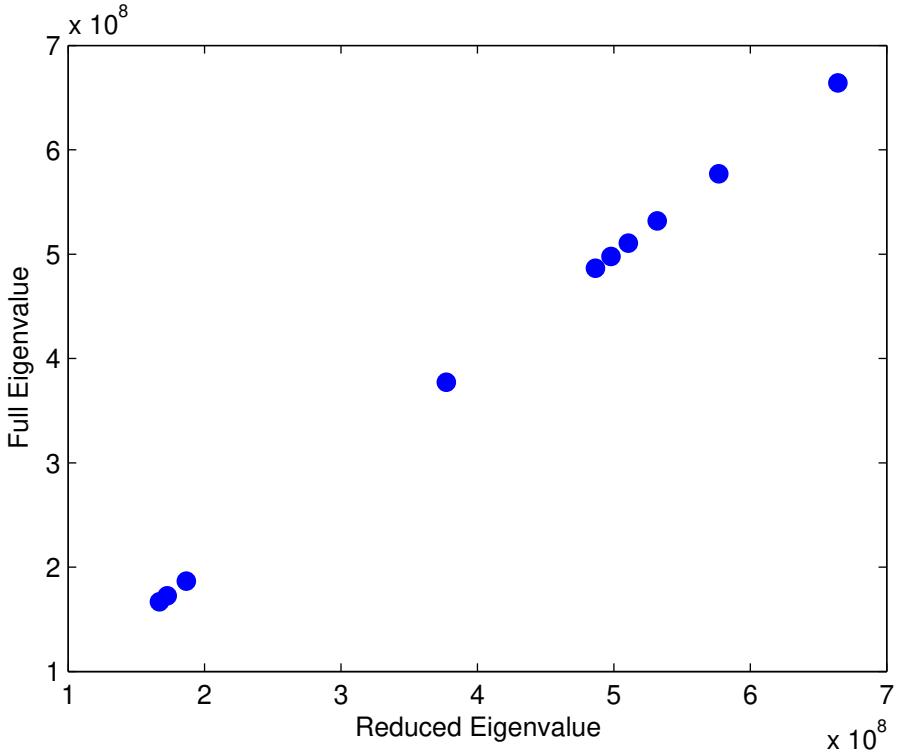

Figure 5-109. – Comparison of reduced and full eigenvalues.

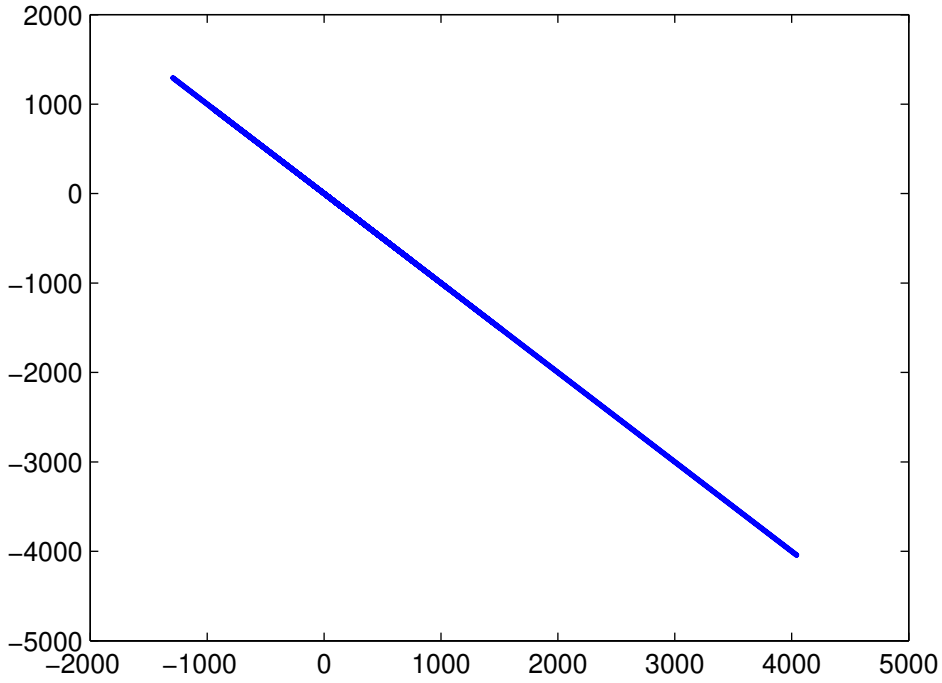

Figure 5-110. – Comparison of reduced and full eigenvectors.

```
function [dispgr,nodes]=expandRmodel( cbmap, OTM, OutMap, vr )
% expands a vector in the reduced, Craig Bampton space into the
% full physical space.
% cbmap - map to interface dofs. Output into cbr.m
% OTM - Output transfer matrix. also in cbr.m
% OutMap - map to interior (and interface) nodes in output.
% vr - the reduced space vector.
%         vr(1:numeig) is the amplitude of the fixed interface modes
%         vr(numeig:end) is the amplitude of the constraint modes (physical
%                         degrees of freedom).
% results are output sorted by node number. 6 dofs per node are output.

nodes=[cbmap(:,1)' OutMap];
nodes=unique(nodes);
nout=size(nodes,2);
nr=max(size(vr));
nc=size(cbmap,1);
nmodes=nr-nc;

dispgr=zeros(nout*6,1);
ur=OTM*vr;   % compute vector on OTM space, ur

% store components from OTM space.
for i=1:size(OutMap,2)
  n=OutMap(i);
  k=find(nodes==n);
  for cid=1:6
    k2=(k-1)*6+cid;
    k1=(i-1)*6+cid;
    dispgr(k2)=ur(k1);
  end
end

% transfer interface dofs directly
for i=1:nc
  n=cbmap(i,1);
  cid=cbmap(i,2);
  k=find(nodes==n);
  k2=(k-1)*6+cid;
  dispgr(k2)=vr(i+nmodes);
end
```

Figure 5-111. – MATLAB code to convert from reduced space.

10.5.12. Residual Vectors

As a small problem to test the residual vector computations in **Sierra/SD**, two beams are connected to each other to simulate a longer beam. To keep the overall number of DOFs as small as possible, the finite element mesh of the beam cross-section is limited to two elements in each direction. This is the bare minimum required to model bending vibrations. The physical parameters for the beams are listed in Table 5-43.

Table 5-43. – Physical parameters for the beams.

Parameter	Beam 1	Beam 2
Density	7860 Kg/m3	7860 Kg/m3
Poisson Rs Ratio	0.29	0.29
Modulus of Elasticity	200 Gpa	200 Gpa
Width (Y-direction)	0.01 m	0.01 m
Height (Z-direction)	0.005 m	0.005 m
Length	0.25 m	0.225 m

When the two beams are combined the overall length is 0.475 m. Analytical solutions for the resonance frequencies are available in the book by Weaver, Timoshenko and Young[56] for a variety of boundary conditions.

The analysis strategy is standard. Component modes synthesis (CMS) has been in use for a long time and many variations on the general analysis procedure are available. The basic idea of all CMS computations is to divide the structure into Scomponents T whose displacements are represented as a summation of Snormal modes T with the mode sets truncated above an upper limiting frequency. This representation is adequate to accurately compute displacements, but not nodal forces or stresses (which represent spatial derivatives of the displacement field). Thus, some method must be used in a CMS analysis to account for truncated modes, especially at locations where the forces must be computed accurately. One simple method is to add Sresidual T or Smodal truncation augmentation T vectors to the analysis for specified nodal locations and DOFs. An excellent derivation of modal truncation augmentation vectors is given in.[16] The vectors are orthogonal to the normal modes, have same normalization, and may be added to the basis.

In the most general form of CMS analysis, interfaces are defined between each of the components and Sinterface modes T are used to represent the connections themselves. Here, a simplified form of CMS is used where the connections between components is at discrete nodal locations instead of interfaces. This eliminates the need to compute Sinterface modes T. It applies to problems (and frequency ranges) where the interfaces can be considered to vibrate as rigid bodies. For the current example of two connected beams, rigid elements are used to make all the nodes at the ends of the beams dependent on nodes

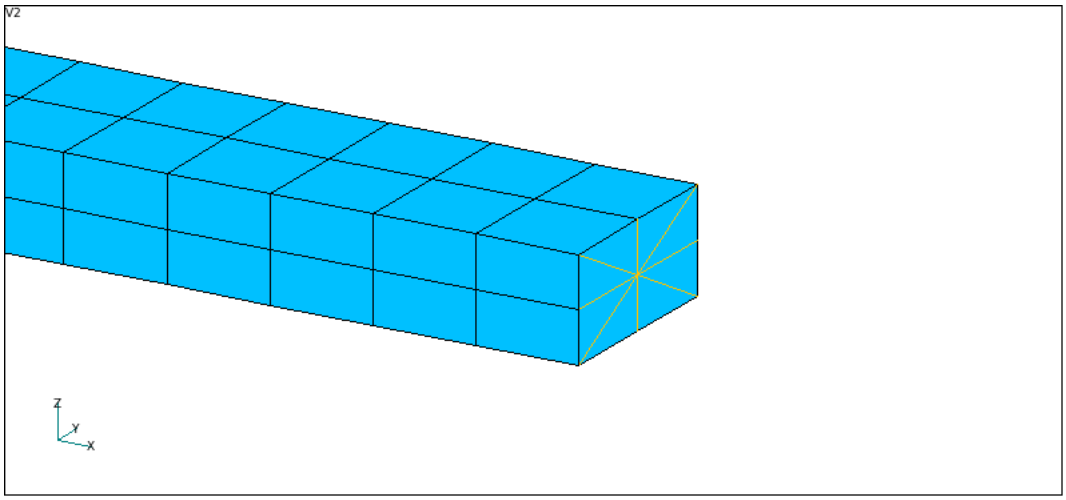

Figure 5-112. – Illustration of a rigid element making all the nodes at the end of the beam dependent on a single node.

at the beam center line. Figure 104 illustrates the implementation of one of the rigid elements in NASTRAN.

This is a reasonable assumption for the beams under consideration because modes with significant variations across the cross-section occur above the frequency range of interest.

As mentioned previously, the user must specify the nodes for the residual vectors calculations. The connection forces between the components must be computed accurately in a CMS solution, and thus residual vectors are included in the basis set for all 6 DOFs at any location where two components are connected to each other. It is often useful to also include residual vectors for nodal locations where boundary conditions are to be applied instead of explicitly including the boundary conditions as nodal constraints in the finite element analysis. The the normal modes and residual vectors are extracted only once, and a variety of boundary conditions can be applied subsequently. Since forces also have to be computed accurately at the locations where boundary conditions are to be applied, residual vectors are also included for all the DOFs at these nodes. For the present case, one end of each beam connects to the other beam and the other end may possibly be used to apply boundary conditions. Residual vectors are not extracted for all the nodes at the ends of the beams. Instead rigid elements are used to make all the nodes dependent on a single node at the beam centerline. Ultimately, this means that residual vectors are extracted for nodes at both ends of each beam, thus adding 12 residual vectors to the basis set for each beam.

The computations for the single beam were performed in a variety of ways and validated in NASTRAN first before proceeding with the component modes synthesis (CMS) analysis. The goal is to allow 6 DOF for each beam at the connection location and at the ends, RBar elements are used at the ends of the beams to force all the nodes to move together as

rigid entities. This representation does not allow the cross-section at the beam ends to deform. It is first compared to a contiguous model without RBars to verify that it does not significantly change the resonance frequencies for the bending modes. Table 5-44 lists the analytical solution for the resonance frequencies assuming free boundary conditions along with the two NASTRAN computations.

Table 5-44. – Analytical solution for the resonance frequencies of a free-free beam along with solutions from NASTRAN.

N	Primary Direction	Analytical	Contiguous	RBar at Connection
2	Y	114.9 Hz	114.8 Hz	115.0 Hz
2	Z	229.8 Hz	229.3 Hz	229.6 Hz
3	Y	316.7 Hz	316.2 Hz	316.3 Hz
4	Y	621.0 Hz	619.3 Hz	620.0 Hz
3	Z	633.5 Hz	630.0 Hz	630.0 Hz
5	Y	1026.4 Hz	1022.4 HZ	1022.6 Hz
4	Z	1242.0 Hz	1229.5 Hz	1230.7 Hz
6	Y	1533.4 Hz	1525.0 Hz	1526.5 Hz

The integer N in the table lists the number of nodal lines along the beam's length. The table does not include N = 0 and N = 1 modes because they represent rigid body vibrations (and are at 0 Hz). The beam's width was chosen to be twice its height, and thus the resonance frequencies in the Z-direction are double those for the Y-direction. The results show that the mesh is refined enough to give accurate results, although it is not clear why the resonance frequencies from NASTRAN are lower than those for the analytical solution.

The next step is to perform the calculations as a CMS analysis with the resonance frequencies, mode shapes and residual vectors computed separately for each beam. For both beams in both CMS analyses, 10 normal modes are retained and residual vectors are included for all 6 DOFs for a single node at both ends of the beams. For reference purposes, Table 5-45 lists the resonance frequencies for both the normal modes (excluding rigid body modes) and residual vectors for the two shorter beams.

For the CMS analyses, a separate computer program is used to combine the mode sets and apply the connections between the components and the boundary conditions. The calculations are performed in "modal space" similar to that discussed in the NASTRAN Basic Dynamics User's Guide.[8] The connections and boundary conditions are applied with user-specified stiffnesses between two nodes or between a single node and ground. Specifying large stiffnesses (1x1012 N/m for the current analysis) has the effect of rigidly constraining two nodes to each other or constraining specific DOFs to zero displacement at a single node.

Once the CMS analysis is set-up, it is possible to rapidly perform the computations for the beam with a variety of specified boundary conditions. The NASTRAN solution with the

Table 5-45. – Resonance frequencies for the normal modes and residual vectors in NASTRAN and **Sierra/SD**.

Type	Beam 1 NASTRAN	Beam 1 **Sierra/SD**	Beam 2 NASTRAN	Beam 2 **Sierra/SD**
Normal Mode	414.5 Hz	414.5 Hz	511.7 Hz	511.7 Hz
	825.7 Hz	825.7 Hz	1018.3 Hz	1018.3 Hz
	1142.1 Hz	1142.1 Hz	1409.6 Hz	1409.6 Hz
	2237.7 Hz	2237.9 Hz	2761.4 Hz	2761.7 Hz
Residual Vector	2335.3 Hz	2335.2 Hz	2877.5 Hz	2877.4 Hz
	4030.5 Hz	4030.8 Hz	4976.4 Hz	4976.9 Hz
	4684.9 Hz	4684.7 Hz	5767.6 Hz	5767.3 Hz
	5521.6 Hz	5520.6 Hz	6133.1 Hz	6131.8 Hz
	6181.5 Hz	6182.3 Hz	7634.8 Hz	7636.1 Hz
	11174.2 Hz	11164.8 Hz	12422.1 Hz	12410.5 Hz
	12270.5 Hz	12265.1 Hz	13622.0 Hz	13615.9 Hz
	16403.7 Hz	16399.7 Hz	20131.7 Hz	20126.7 Hz
	22639.3 Hz	22627.8 Hz	27801.1 Hz	27789.8 Hz
	25214.8 Hz	25151.2 Hz	28060.7 Hz	27981.9 Hz
	28419.4 Hz	28412.3 Hz	34774.4 Hz	34766.1 Hz
	32990.6 Hz	32980.5 Hz	40458.6 Hz	40453.8 Hz

two beams connected to each other with a rigid RBar element is used as the reference since the CMS analysis should produce identical results. Table 5-46 Table 5-47 Table 5-48 Table 5-49 list the beam resonance frequencies for various boundary conditions using the NASTRAN solution with an RBar connection and for the two CMS analyses.

The results in the tables show good agreement between the NASTRAN model and the CMS analyses that include residual vectors. Without residual vectors, the resonance frequencies are considerably too high. While the CMS analyses require some extra effort to set-up, it is possible to perform all the computations with a single model by changing the stiffnesses applied at the ends of the beams. The NASTRAN computations for the model required a separate mode extraction analysis for each boundary condition.

Table 5-46. – Comparison of the NASTRAN solution with an RBar connecting the beams to the CMS solutions using NASTRAN and **Sierra/SD** for free-free boundary conditions.

N	Primary Direction	RBar at Connection	CMS, NASTRAN	CMS, **Sierra/SD**	CMS, NASTRAN w/o Residual Vectors
2	Z	115.0 Hz	115.1 Hz	115.1 Hz	132.4 Hz
2	Y	229.6 Hz	229.8 Hz	229.8 Hz	319.3 Hz
3	Z	316.3 Hz	316.7 Hz	316.7 Hz	319.2 Hz
4	Z	620.0 Hz	621.3 Hz	621.4 Hz	706.1 Hz
3	Y	630.0 Hz	631.3 Hz	631.3 Hz	654.6 Hz
5	Z	1022.6 Hz	1025.9 Hz	1026.0 Hz	1053.9 Hz
4	Y	1230.7 Hz	1235.5 Hz	1235.6 Hz	$>$ 2000 Hz
6	Z	1526.5 Hz	1533.7 Hz	1533.9 Hz	1769.0 Hz

Table 5-47. – Comparison of the NASTRAN solution with an RBar connecting the beams to the CMS solutions using NASTRAN and **Sierra/SD** for clamped-clamped boundary conditions.

N	Primary Direction	RBar at Connection	CMS, NASTRAN	CMS, **Sierra/SD**	CMS, NASTRAN w/o Residual Vectors
2	Z	115.2 Hz	115.3 Hz	115.3 Hz	167.3 Hz
2	Y	229.9 Hz	230.0 Hz	230.0 Hz	$>$ 2000 Hz
3	Z	317.2 Hz	317.4 Hz	317.4 Hz	411.3 Hz
4	Z	622.0 Hz	622.7 Hz	622.9 Hz	877.8 Hz
3	Y	631.2 Hz	631.8 Hz	631.8 Hz	$>$ 2000 Hz
5	Z	1026.1 Hz	1028.2 Hz	1028.4 Hz	1346.5 Hz
4	Y	1232.8 Hz	1235.4 Hz	1235.6 Hz	$>$ 2000 Hz
6	Z	1532.0 Hz	1537.0 Hz	1537.4 Hz	$>$ 2000 Hz

Table 5-48. – Comparison of the NASTRAN solution with an RBar connecting the beams to the CMS solutions using NASTRAN and **Sierra/SD** for simply supported boundary conditions.

N	Primary Direction	RBar at Connection	CMS, NASTRAN	CMS, **Sierra/SD**	CMS, NASTRAN w/o Residual Vectors
2	Z	50.7 Hz	50.7 Hz	50.8 Hz	56.5 Hz
2	Y	101.4 Hz	101.4 Hz	101.4 Hz	126.8 Hz
3	Z	202.6 Hz	202.7 Hz	202.8 Hz	203.9 Hz
3	Y	404.4 Hz	404.7 Hz	404.7 Hz	412.8 Hz
4	Z	456.2 Hz	456.7 Hz	456.7 Hz	527 6 Hz
5	Z	809.5 Hz	811.0 Hz	811.1 Hz	839.5 Hz
4	Y	907.7 Hz	909.4 Hz	909.5 Hz	$>$ 2000 Hz
6	Z	1264.6 Hz	1268.3 Hz	1268.4 Hz	1444.3 Hz

Table 5-49. – Comparison of the NASTRAN solution with an RBar connecting the beams to the CMS solutions using NASTRAN and **Sierra/SD** for clamped-free boundary conditions.

N	Primary Direction	RBar at Connection	CMS, NASTRAN	CMS, **Sierra/SD**	CMS, NASTRAN w/o Residual Vectors
1	Z	18.1 Hz	18.1 Hz	18.1 Hz	20.4 Hz
1	Y	36.1 Hz	36.2 Hz	36.2 Hz	46.1 Hz
2	Z	113.4 Hz	113.4 Hz	113.4 Hz	148.1 Hz
2	Y	226.3 Hz	226.4 Hz	226.4 Hz	458.6 Hz
3	Z	316.9 Hz	317.2 Hz	317.2 Hz	362.1 Hz
4	Z	621.0 Hz	622.0 Hz	622.1 Hz	798.1 Hz
3	Y	630.9 Hz	631.8 Hz	631.8 Hz	$>$ 2000 Hz
5	Z	1024.3 Hz	1027.0 Hz	1027.2 Hz	1172.5 Hz

10.6. Mass Properties Verification Tests

The following problems were used to verify the mass properties calculations in **Sierra/SD**. These problems cover most element types, however superelements are not addressed here. The tests and results described here were generated with release 2.9.

10.6.1. 0D Verification Test

The following test was used to verify mass properties for conmass elements. The test consists of an assembly of three conmass elements as shown in Figure 6-113. In the finite element model, the masses were connected with RBar elements which do not add mass to the system.

The total mass of the assembly is $m_{total} = 3m$. The center-of-gravity is

$$x_{cg} = (mb + 0 - mb)/m_{total} = 0 \tag{10.6.1}$$
$$y_{cg} = (0 + mb + 0)/m_{total} = b/3 \tag{10.6.2}$$
$$z_{cg} = (0 + mb + 2mb)/m_{total} = 1 \tag{10.6.3}$$

The components of the inertia tensor are

$$I_{xx} = \bar{I}_{xx} + mr_x^2 \tag{10.6.4}$$
$$= \bar{I}_{xx} + m\left[(2b)^2 + (b^2 + b^2) + 0\right] = \bar{I}_{xx} + 6mb^2 \tag{10.6.5}$$
$$I_{yy} = \bar{I}_{yy} + mr_y^2 \tag{10.6.6}$$
$$= \bar{I}_{yy} + m\left[\left(b^2 + (2b)^2\right) + b^2 + b^2\right] = \bar{I}_{yy} + 7mb^2 \tag{10.6.7}$$
$$I_{zz} = \bar{I}_{zz} + mr_z^2 \tag{10.6.8}$$
$$= \bar{I}_{zz} + m\left[b^2 + b^2 + b^2\right] = \bar{I}_{zz} + 3mb^2 \tag{10.6.9}$$
$$I_{xy} = \bar{I}_{xy} + md_x d_y \tag{10.6.10}$$
$$= \bar{I}_{xy} + m\left[0 + 0 + 0\right] = \bar{I}_{xy} \tag{10.6.11}$$
$$I_{xz} = \bar{I}_{xz} + md_x d_z \tag{10.6.12}$$
$$= \bar{I}_{xz} + m\left[0 + 0 - 2b^2\right] = \bar{I}_{xz} - 2b^2 \tag{10.6.13}$$
$$I_{yz} = \bar{I}_{yz} + md_y d_z \tag{10.6.14}$$
$$= \bar{I}_{yz} + m\left[0 + b^2 + 0\right] = \bar{I}_{yz} + b^2 \tag{10.6.15}$$

A comparison between these answers and the **Sierra/SD** predictions is shown in Table 6-50. Parameters used for this problem were $m = 1$, $b = 1$, and $\bar{I}_{xx} = \bar{I}_{yy} = \bar{I}_{zz} = \bar{I}_{xy} = \bar{I}_{xz} = \bar{I}_{yz} = 0$.

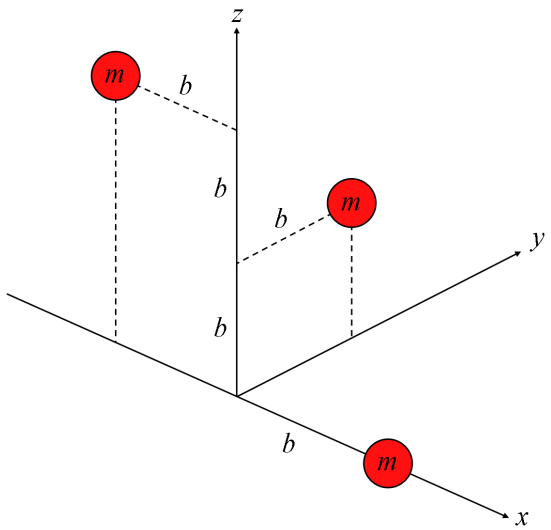

Figure 6-113. – Verification problem for conmass elements.

Table 6-50. – Comparison of **Sierra/SD** with exact solutions for the 0D verification problem.

Property	Exact	**Sierra/SD**
m_{total}	3.0	3.0
x_{cg}	0.0	0.0
y_{cg}	0.3333	0.3333
z_{cg}	1.0	1.0
I_{xx}	6.0	6.0
I_{yy}	7.0	7.0
I_{zz}	3.0	3.0
I_{xy}	0.0	0.0
I_{xz}	-2.0	-2.0
I_{yz}	1.0	1.0

10.6.2. 1D Verification Test

The following test was used to verify mass properties for the 1D elements which include the Beam2, TiBeam, Nbeam, and truss. This test case consists of a beam offset in all three dimensions from the coordinate frame as shown in Figure 6-114.

The total mass of the beam is

$$m_{total} = \rho V = \rho \pi r^2 l = 0.60kg \tag{10.6.16}$$

where V is the volume of the beam, r is the radius of the beam taken to be $5mm$, l is the length of the beam, and ρ is the beam material density taken as $2.8294 \times 10^{-5} kg/mm^3$ to give a total mass of $0.6kg$. The center-of-gravity is

$$x_{cg} = 180mm - \left(\frac{180mm + 90mm}{2}\right) = 45mm \tag{10.6.17}$$

$$y_{cg} = 150mm \tag{10.6.18}$$

$$z_{cg} = 90mm \tag{10.6.19}$$

The components of the inertia tensor are

$$I_{xx} = \bar{I}_{xx} + mr_x^2 \tag{10.6.20}$$

$$= \frac{1}{2}mr^2 + m(d_y^2 + d_z^2) = 18367.5kg \cdot mm^2 \tag{10.6.21}$$

$$I_{yy} = \bar{I}_{yy} + mr_y^2 \tag{10.6.22}$$

$$= \left[\frac{1}{4}mr^2 + \frac{1}{12}ml^2\right] + m(d_x^2 + d_z^2) = 9723.75kg \cdot mm^2 \tag{10.6.23}$$

$$I_{zz} = \bar{I}_{zz} + mr_z^2 \tag{10.6.24}$$

$$= \left[\frac{1}{4}mr^2 + \frac{1}{12}ml^2\right] + m(d_x^2 + d_y^2) = 18363.75kg \cdot mm^2 \tag{10.6.25}$$

$$I_{xy} = \bar{I}_{xy} + md_x d_y \tag{10.6.26}$$

$$= 0 + md_x d_y = 4050.0kg \cdot mm^2 \tag{10.6.27}$$

$$I_{xz} = \bar{I}_{xz} + md_x d_z \tag{10.6.28}$$

$$= 0 + md_x d_z = 2430.0kg \cdot mm^2 \tag{10.6.29}$$

$$I_{yz} = \bar{I}_{yz} + md_y d_z \tag{10.6.30}$$

$$= 0 + md_y d_z = 8100.0kg \cdot mm^2 \tag{10.6.31}$$

A comparison between these answers and the **Sierra/SD** predictions for the 1D elements is shown in Table 6-51. The finite element model used to generate these results contained 27 elements.

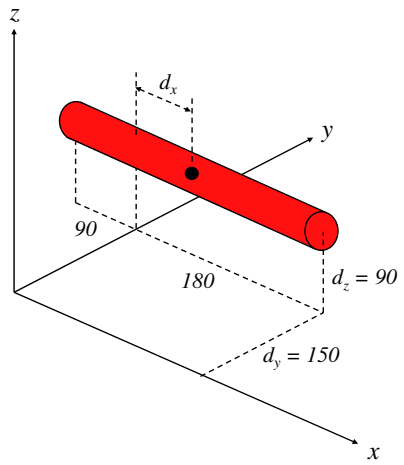

Figure 6-114. – Verification problem for 1D elements.

Table 6-51. – Comparison of **Sierra/SD** with exact solutions for the 1D verification problem.

Property	Exact	Beam2	Nbeam	TiBeam	Truss
m_{total}	0.60	0.60	0.06	0.60	0.60
x_{cg}	45	45	45	44.875	45
y_{cg}	150	150	150	150	150
z_{cg}	90	90	90	90	90
I_{xx}	18367.5	18367.0	18367.0	18368.0	18360.0
I_{yy}	9723.75	9732.2	9733.7	9723.8	9720.0
I_{zz}	18363.75	18372.0	18374.0	18358	18360.0
I_{xy}	4050.0	4050.0	4050.0	4050.0	4050.0
I_{xz}	2430.0	2430.0	2430.0	2423.3	2430.0
I_{yz}	8100.0	8100.0	8100.0	8100.0	8100.0

10.6.3. 2D Verification Test

The following test was used to verify mass properties for the 2D elements which include all the triangular and quadrilateral elements. This test case consists of an L-shaped plate as shown in Figure 6-115.

The total mass of the plate is

$$m_{total} = m_1 + m_2 = \rho\left(abt + \frac{1}{2}bct\right) \tag{10.6.32}$$

where m_1 and m_2 are the masses of the rectangular section and triangular section respectively. Both sections have the same material density, ρ, and the same thickness, t. The center-of-gravity is

$$x_{cg} = -\frac{1}{m_{total}}\left[m_1 a + m_2\left(a + \frac{t}{2}\right)\right] \tag{10.6.33}$$

$$y_{cg} = \frac{1}{m_{total}}\left[m_1\left(\frac{b}{2}\right) + m_2\left(\frac{2}{3}b\right)\right] \tag{10.6.34}$$

$$z_{cg} = \frac{1}{m_{total}}\left[0 + m_2\left(\frac{c}{3}\right)\right] \tag{10.6.35}$$

The components of the inertia tensor are

$$I_{xx} = \left(\bar{I}_{xx} + m_1 r_x^2\right) + \left(\bar{I}_{xx} + m_2 r_x^2\right) \tag{10.6.36}$$

$$= \left(\rho_1 t_1 \bar{I}_x + m_1 d_y^2\right) + \left[\left(\bar{I}_{yy} + \bar{I}_{zz}\right) + m_2\left(d_x^2 + d_y^2\right)\right] \tag{10.6.37}$$

$$= \left(\frac{m_1 b^2}{12} + \frac{m_1 b^2}{4}\right) + \left(\frac{m_2 c^2}{6} + \frac{m_2 b^2}{2}\right) \tag{10.6.38}$$

$$= \frac{m_1 b^2}{3} + \frac{m_2 c^2}{6} + \frac{m_2 b^2}{2} \tag{10.6.39}$$

$$I_{yy} = \left(\bar{I}_{yy} + m_1 r_y^2\right) + \left(\bar{I}_{yy} + m_2 r_y^2\right) \tag{10.6.40}$$

$$= \left(\rho_1 t_1 \bar{I}_x + m_1 d_x^2\right) + \left[\rho_2 t_2 \bar{I}_x + m_2\left(d_x^2 + d_z^2\right)\right] \tag{10.6.41}$$

$$= \left(\frac{m_1 a^2}{12} + \frac{m_1 a^2}{4}\right) + \left(\frac{m_2 c^2}{18} + \frac{m_2 c^2}{9} + m_2 a^2\right) \tag{10.6.42}$$

$$= \frac{m_1 a^2}{3} + \frac{m_2 c^2}{6} + m_2 a^2 \tag{10.6.43}$$

$$I_{zz} = \left(\bar{I}_{zz} + m_1 r_z^2\right) + \left(\bar{I}_{zz} + m_2 r_z^2\right) \tag{10.6.44}$$

$$= \left(\rho_1 t_1 \bar{I}_z + m_1 d_x^2\right) + \left[\left(\bar{I}_{xx} + \bar{I}_{yy}\right) + m_2\left(d_x^2 + d_y^2\right)\right] \tag{10.6.45}$$

$$= \left(\frac{m_1 a^2}{3} + \frac{m_1 b^2}{3}\right) + \left(\frac{m_2 b^2}{18} + \frac{8 m_2 b^2}{18} + m_2 a^2\right) \tag{10.6.46}$$

$$= \frac{m_1 a^2}{3} + \frac{m_1 b^2}{3} + \frac{m_2 b^2}{2} + m_2 a^2 \tag{10.6.47}$$

$$I_{xy} = \left(\bar{I}_{xy} + m_1 d_x d_y\right) + \left(\bar{I}_{xy} + m_2 d_x d_y\right) \tag{10.6.48}$$

$$= \left[0 + m_1\left(-\frac{a}{2}\right)\left(\frac{b}{2}\right)\right] + \left[0 + m_2(-a)\left(\frac{2b}{3}\right)\right] \tag{10.6.49}$$

$$= -\frac{m_1 ab}{4} - \frac{2 m_2 ab}{3} \tag{10.6.50}$$

$$I_{xz} = \left(\bar{I}_{xz} + m_1 d_x d_z\right) + \left(\bar{I}_{xz} + m_2 d_x d_z\right) \tag{10.6.51}$$

$$= (0+0) + \left[0 + m_2(-a)\left(\frac{c}{3}\right)\right] \tag{10.6.52}$$

$$= -\frac{m_2 ac}{3} \tag{10.6.53}$$

$$I_{yz} = \left(\bar{I}_{yz} + m_1 d_y d_z\right) + \rho_2 t_2 \int_0^b \int_0^{\frac{c}{b}y} yz\,dz\,dy \tag{10.6.54}$$

$$= (0+0) + \frac{\rho_2 t_2 c^2}{2b^2} \int_0^b y^3\,dy \tag{10.6.55}$$

$$= \frac{m_2 bc}{4} \tag{10.6.56}$$

A comparison between these answers and the **Sierra/SD** predictions is listed in Table 6-52. The finite element model of the plate contained 1679 elements. Parameters used for this problem were $a = 40in$, $b = 50in$, $c = 30in$, $t = 0.1in$, and $\rho = 0.1lb/in^3$.

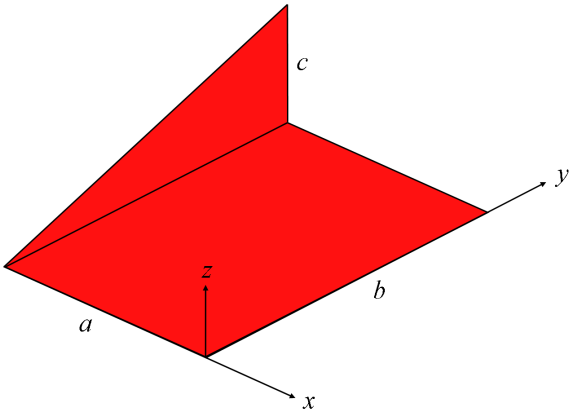

Figure 6-115. – Verification problem for shell elements.

Table 6-52. – Verification of 2D Mass Properties.

Property	Exact	Tri	Triashell	QuadTM
m_{total}	27.5	27.5	27.5	27.5
x_{cg}	-25.4682	-25.455	-25.455	-25.455
y_{cg}	27.2727	27.273	27.273	27.273
z_{cg}	2.7273	2.7273	2.7273	2.7273
I_{xx}	27167	27178	27167	27167
I_{yy}	23792	23801	23792	23792
I_{zz}	48708	48726	48708	48708
I_{xy}	-20000	-20000	-20000	-20000
I_{xz}	-3000	-3000	-3000	-3000
I_{yz}	2813	2812.4	2812.5	2812.5

10.6.4. 3D Verification Tests

The following tests were used to verify mass properties for the 3D elements which include the hexahedron, tetrahedron, and wedge elements. Solutions for these problems were mostly taken from the dynamics text by Meriam and Kraige.[37]

10.6.4.1. Offset Block

The first 3D test consists of an offset cube as shown in Figure 6-116. The total mass of the block is given by

$$m_{total} = \rho l^3 = 3.375. \tag{10.6.57}$$

where ρ is the density of the block and l is the length of each side of the block. The center-of-gravity is

$$x_{cg} = y_{cg} = z_{cg} = 0.8 + \frac{1}{2}(1.5) = 1.55. \tag{10.6.58}$$

The components of the inertia tensor are

$$I_{xx} = \bar{I}_{xx} + mr_x^2 \tag{10.6.59}$$

$$= \frac{1}{12} m \left(2l^2\right) + m\left(d_y^2 + d_z^2\right) = 17.4825 \tag{10.6.60}$$

$$= I_{yy} = I_{zz} \tag{10.6.61}$$

$$I_{xy} = \bar{I}_{xy} + md_x d_y = 8.1084375 \tag{10.6.62}$$

$$= I_{xz} = I_{yz} \tag{10.6.63}$$

A comparison between these answers and the **Sierra/SD** predictions is listed in Table 6-53. The tet model contained 26,430 elements, and the hex model contained 343 elements. Parameters used for this problem were $\rho = 1.0$ and $l = 1.5$

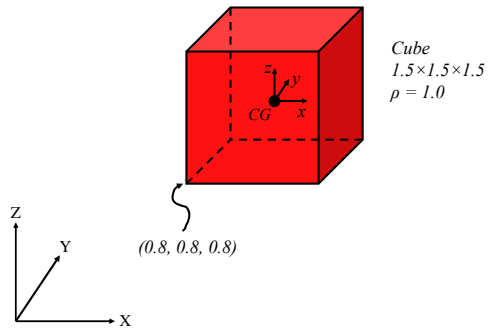

Figure 6-116. – Verification problem for solid elements.

Table 6-53. – Comparison of **Sierra/SD** with exact solutions for the 3D block.

Property	Exact	Tet4	Hex8
m_{total}	3.375	3.375	3.375
x_{cg}	1.55	1.55	1.55
y_{cg}	1.55	1.55	1.55
z_{cg}	1.55	1.55	1.55
I_{xx}	17.4825	17.48	17.482
I_{yy}	17.4825	17.48	17.482
I_{zz}	17.4825	17.48	17.482
I_{xy}	8.1084	8.1084	8.1084
I_{xz}	8.1084	8.1084	8.1084
I_{yz}	8.1084	8.1084	8.1084

10.6.4.2. Half-torus

This test consists of a half-torus as shown in Figure 6-117. The total mass is

$$m_{total} = \rho V = \rho \pi r^2 (\pi R) = 0.61685. \tag{10.6.64}$$

where V is the volume of the body, and r and R are the radii as shown in the problem figure. The density, ρ, was taken as 1.0 in this non-dimensional problem. The center-of-gravity is

$$x_{cg} = y_{cg} = 0 \tag{10.6.65}$$

$$z_{cg} = \frac{r^2 + 4R^2}{2\pi R} = -0.64657. \tag{10.6.66}$$

The components of the inertia tensor are

$$I_{xx} = I_{zz} = \frac{1}{2} mR^2 + \frac{5}{8} mr^2 = 0.3474875 \tag{10.6.67}$$

$$I_{yy} = mR^2 + \frac{3}{4} mr^2 = 0.645765 \tag{10.6.68}$$

$$I_{xy} = I_{xz} = I_{yz} = 0. \tag{10.6.69}$$

A comparison between these answers and the **Sierra/SD** predictions is listed in Table 6-54. The tet model contained 175,592 elements. The hex model contained 62,300 elements.

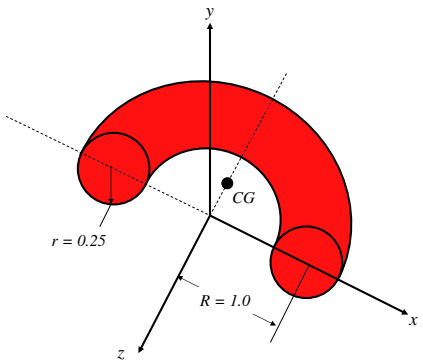

Figure 6-117. – Verification problem for solid elements.

Table 6-54. – Comparison of **Sierra/SD** with exact solutions for the 3D half-torus.

Property	Exact	Tet4	Hex8
m_{total}	0.61685	0.6153	0.61634
x_{cg}	0.0	0.0	0.0
y_{cg}	0.0	0.0	0.0
z_{cg}	-0.6466	-0.6465	-0.6465
I_{xx}	0.3475	0.3315	0.3321
I_{yy}	0.6458	0.6440	0.6451
I_{zz}	0.3475	0.3315	0.3321
I_{xy}	0.0	0.0	0.0
I_{xz}	0.0	0.0	0.0
I_{yz}	0.0	0.0	0.0

10.6.4.3. Hemispherical Shell

This test consists of a hemispherical shell as shown in Figure 6-118. The total mass is

$$m_{total} = \rho V = \frac{1}{2}\left[\frac{4}{3}\pi\left(r_o^2 - r_i^2\right)\right] = 0.318348. \tag{10.6.70}$$

where V is the volume of the body, and r_o and r_i are the outer and inner radii as shown in the problem figure. The density, ρ, was taken as 1.0 in this non-dimensional problem. The center-of-gravity is

$$x_{cg} = \frac{r}{2} = 0.25 \tag{10.6.71}$$

$$y_{cg} = z_{cg} = 0. \tag{10.6.72}$$

The components of the inertia tensor are

$$I_{xx} = I_{yy} = I_{zz} = \frac{2}{3}mr^2 = 0.053058 \tag{10.6.73}$$

$$I_{xy} = I_{xz} = I_{yz} = 0. \tag{10.6.74}$$

A comparison between these answers and the **Sierra/SD** predictions is listed in Table 6-55. The finite element model used to generate these results contained 108,000 hex elements.

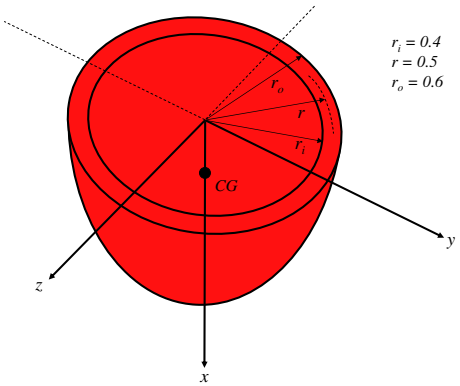

Figure 6-118. – Verification problem for solid elements.

Table 6-55. – Comparison of **Sierra/SD** with exact solutions for the 3D hemispherical shell.

Property	Exact	Hex8
m_{total}	0.3183	0.3182
x_{cg}	0.25	0.2566
y_{cg}	0.0	0.0
z_{cg}	0.0	0.0
I_{xx}	0.05306	0.05653
I_{yy}	0.05306	0.05653
I_{zz}	0.05306	0.05653
I_{xy}	0.0	0.0
I_{xz}	0.0	0.0
I_{yz}	0.0	0.0

10.6.4.4. Tetrahedron

This test consists of a tetrahedron with side lengths of a, b, and c as shown in Figure 6-119. The total mass is

$$m_{total} = \rho V = \rho \frac{1}{6} abc \tag{10.6.75}$$

where V is the volume of the tetrahedron. The density, ρ, was taken as 1.0 for this non-dimensional problem. The center-of-gravity is

$$x_{cg} = \frac{a}{4} \tag{10.6.76}$$

$$y_{cg} = \frac{b}{4} \tag{10.6.77}$$

$$z_{cg} = \frac{c}{4} \tag{10.6.78}$$

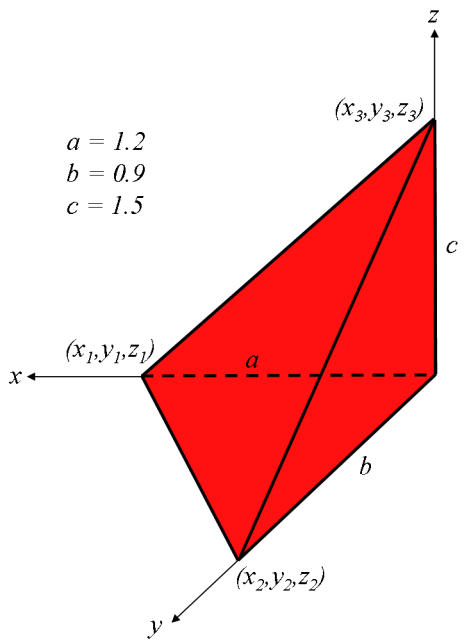

Figure 6-119. – Verification problem for solid elements.

The components of the inertia tensor are

$$I_{xx} = \frac{1}{10}\left(b^2 + c^2\right) \tag{10.6.79}$$

$$I_{yy} = \frac{1}{10}\left(a^2 + c^2\right) \tag{10.6.80}$$

$$I_{zz} = \frac{1}{10}\left(a^2 + b^2\right) \tag{10.6.81}$$

$$I_{xy} = \int_m xydm = \rho \int_V xydV \tag{10.6.82}$$

$$= \int_0^a \int_0^{1-\frac{x}{a}} \int_0^{1-\frac{x}{a}-\frac{z}{c}} xydydzdx = \frac{1}{20}mab \tag{10.6.83}$$

$$I_{xz} = \int_m xzdm = \rho \int_V xzdV \tag{10.6.84}$$

$$= \int_0^a \int_0^{1-\frac{x}{a}} \int_0^{1-\frac{x}{a}-\frac{y}{b}} xzdzdydx = \frac{1}{20}mac \tag{10.6.85}$$

$$I_{yz} = \int_m yzdm = \rho \int_V yzdV \tag{10.6.86}$$

$$= \int_0^b \int_0^{1-\frac{y}{b}} \int_0^{1-\frac{x}{a}-\frac{y}{b}} yzdzdxdy = \frac{1}{20}mbc \tag{10.6.87}$$

A comparison between these answers and the **Sierra/SD** predictions is listed in Table 6-56. The finite element model used for this problem used tet elements. Two different mesh

Table 6-56. – Comparison of **Sierra/SD** with exact solutions for the 3D tetrahedron.

Property	Exact	Tet4 Coarse	Tet4 Fine
m_{total}	0.27	0.27	0.27
x_{cg}	0.3	0.3	0.3
y_{cg}	0.225	0.225	0.225
z_{cg}	0.375	0.375	0.375
I_{xx}	0.08262	0.08249	0.08262
I_{yy}	0.09963	0.09950	0.09963
I_{zz}	0.06075	0.06062	0.06075
I_{xy}	0.01458	0.01458	0.01458
I_{xz}	0.0243	0.02430	0.02430
I_{yz}	0.01823	0.01823	0.01823

densities were used and results for both are presented. The models contained 3933 elements and 26,650 elements respectively.

10.7. Phenomenon Based Testing

Each of the phenomena identified in the Phenomenology Identification and Ranking Table (PIRT) from the V&V plan has specific tests for evaluation of the predictability of the software. Details are described in the sections below.

10.7.1. Elastodynamics

The requirements for elastodynamics are detailed in the requirements document and the computational plan. They may be summarized in Table 7-57. Verification aspects for each requirement will be detailed in sections of this chapter.

Table 7-57. – Elastodynamics Requirements.

#	**Requirement**
1	Compute static responses
2	Compute modes for large models (10M DOFS or greater). Include: - Frequency Response Functions - Random Vibration inputs and Response - Shock Spectra
3	Compute Time domain analysis of these models, using direct time integration. An interface to facilitate time domain analysis using modal superposition will also be provided.
4	Output Stresses, Strains, Displacements, Velocities and Accelerations
5	Provide a platform for development of additional structural dynamics capabilities. These will include system identification, design optimization, nondeterministic methods, coupled/multi-physics solutions and others.
6	Provide portability and scalability to allow effective use on ASC platforms, and data file compatibility with other ASC codes.
7	Loads: - point loads (applied though node sets) - gravity loads on elements - pressure loads
8	Support standard elements from FE analysis - solid elements (Hex,Wedge,Tet) - shells (Triangle, Quad) - Beams - point masses, springs - MultiPoint Constraints
9	Support linear, elastodynamic material models with anisotropy.
10	Documentation: - a users manual -programmers manual - software engineering practices

10.7.2. Verification With Respect to Semi-Analytical Static Tests

Analytic and semi-analytic solutions for static deformation problems have been determined for many geometries and reported in *Roark*.[57] Note that these solutions are for idealized models. Thus, the beam models are appropriate to Euler Beams, but are exact for beams made of solid elements only in the limits where shear terms can be neglected.

Tables 7-58 and 7-59 will be used for Beam Elements: For Shell elements Tables 7-60 through 7-62 are used. The reference table is from *Roark*.[57]

Table 7-58. – Straight Beam Element Analytic Solutions.

Roark Table	Description	Case	Max Disp	Max Rot.
3 1a	cantilever free. Applied point force	*Roark*	-13.33	20.0
		Beam2	-13.33	20.0
		Tria3	-12.13	18.2
		Tria3⊥	-13.33	20.0
		Hex8	-13.44	N/A
3 1e	simply supported simply supported. Applied point force	*Roark*	.6356	2.311
		Beam2	.6356	2.312
		Tria3	.5783	2.104
		Tria3⊥	.5785	2.104
3 3b	cantilever guided. Applied point moment	*Roark*	4.032	-8.064
		Beam2	4.032	-8.064

The "Tria6⊥" model is rotated so a pure membrane deformation occurs. A finer mesh is required.

Table 7-59. – Curved Beam Element Analytic Solutions.

Roark Table	Description	Case	Dv
17 1	opposed radial loading on circular ring	*Roark*	-5.9513
		Beam2	-5.950
17 2	opposed in-line loading on circular ring (measured at $\theta = 30^o$)	*Roark*	.8263
		Beam2	.8259
17 3	opposed moments on circular ring (measured at $\theta = 30^o$)	*Roark*	7.9743
		Beam2	7.967

For solids, we employ Table 1-7. In addition, examples from the beams and shells may be computed using solid elements and a suitable discretization.

Table 7-60. – Annular Plate with Uniform Annular Line Load.
The test of having the outer edge simply supported and the inner edge free cannot be done at this time because the loading would require a non-cartesian coordinate system.

Roark Table	Description	Case	Max Disp
24 1a	Outer edge simply supported. Inner edge free	*Roark*	0.01701
		Tria3	0.01696
24 1b	Outer edge simply supported. Inner edge guided	*Roark*	.0068853
		Tria3	.006885
24 1e	Outer edge fixed. Inner edge free	*Roark*	.0034952
		Tria3	.0034946
24 5a	Outer edge simply supported. Inner free		

Table 7-61. – Square Plate.

Roark Table	Description	Case	Max Disp	Center Stress
26 1a	Simply supported.	*Roark*	5.3280	1.0346e7
	Uniform load over plate	Tria3	5.3225	1.03327e7
		QuadT	5.3225	1.03327e7
26 8a	Fixed edges.	*Roark*	1.6560	4.9896e6
	Uniform load over entire plate	Tria3	1.6590	4.9407e6
		QuadT	1.6590	4.9406e6

Table 7-62. – Thin Walled Pressure Vessels.
The second half of this table cannot be computed at this time because the pressure load would require using a non-cartesian coordinate system.

Roark Table	Description	Case	Max Disp	Max Stress	Comment
28 1a	uniform axial load on cylinder	*Roark*	-4.074e-6	407.4	ΔZ =2.037E-5
		Tria3	-4.626e-6	408.4	ΔZ =2.039E-5
		Hex8	-3.67e-6	408.0	ΔZ =2.057E-5
28 1b	uniform radial pressure on cylinder	*Roark*	3.333e-7	10.0	R=1, h=1.5, t=.1
		Tria3	3.333e-7	10.035	
		Hex8	3.445e-7	10.231	
28 3a	uniform pressure on sphere	*Roark*			
		Tria3			
28 5	uniform pressure on toroid	*Roark*			
		Tria3			
30 1a	uniform radial force on edge of partial sphere	*Roark*			
		Tria3			
30 1b	uniform edge moment on partial sphere	*Roark*			
		Tria3			

Table 7-63. – Solid Spheres.

Roark Table	Description	Exact Disp	FE Disp	Exact Stress	FE Stress
33 1A	Sphere on a flat plate				
33 1B	Sphere on a sphere				

10.7.3. Verification With Respect to Semi-Analytical Eigen Analysis

Analytic and semi-analytic eigenvalue decompositions are known for most simple geometries. Summaries are available.[10] Note however, that these solutions are for idealized models. For exeThus, the Euler beam models are appropriate to Euler Beams, but are exact for beams made of solid elements only in the limits where shear terms can be neglected.

An eigenvector provides information about the global solution. A correct solution requires both a correct stiffness and mass matrix. Further, accuracy of the solution is easily determined by examination of the eigenvalues alone. On the other hand, the load vector is irrelevant, which simplifies the test matrix.

The "truth" model for these analyses are the eigenvalues obtained from analytic and semi-analytic solutions tabulated in *Blevins*. Note that the accuracy of the textbook solutions is limited to about 0.5% in most cases. Spring and Mass analysis matrix is detailed in Table 7-64. For beam elements, eigenvalues Tablulated in 7-65 through 7-67. Shell elements use Tables 7-68 through 7-70. Note that beams and shells have simplifying assumptions which may cause the solid based solutions to differ from the textbook solutions. For example, the "beams" built of solid elements will contain shear effects that are not present in a standard beam element. The geometry for these tests is illustrated in Figure 7-120.

The computational results represent the converged solution. In most cases a Richardson extrapolation has been performed to arrive at the minimum error due to discretization.

For all the following examples in this section (i.e. Tables 7-64 through 7-70, unless otherwise noted we use material properties for steel, i.e. $E = 30\text{x}10^6$ psi, $\nu = 0.30$ and $\rho = 0.288$ lbs/in^3 ($7.4592\text{x}10^{-4}$ slugs/in^3).

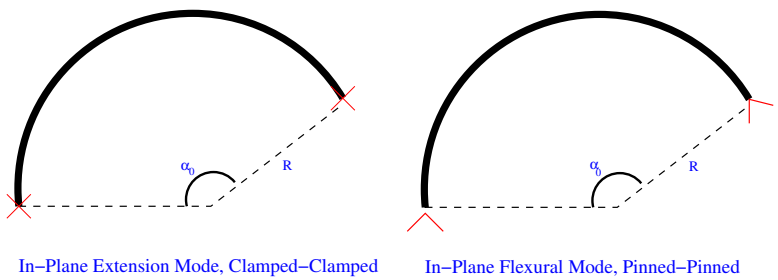

Figure 7-120. – Blevins Table 9-2.1 and 9-2.2 Geometries.

Table 7-64. – Spring Mass Vibration.

Blevins Table	Description	Sol'n Type	Mode Number		
			1	2	3
6-2 2	two equal masses,	Exact	.0983632	.2575181	N/A
	two equal springs	FE	.0983632	.2575181	N/A
6-2 18	Three equal masses,	Exact	.159155	.3183100	.3183100
	six equal springs	FE	.159155	.3183100	.3183100

Note: The Lanczos solver (in ARPACK) cannot find all the modes of the system. Some modes were found by exporting the matrices and solving in MATLAB

Table 7-65. – Beam Mass Vibration.
Massless beam has square cross section with I1=1, L=20, 100 elements.

Table	Description	Sol'n	Mode 1
6-2 19	End mass on cantilever beam	Exact	16.88
		FE	16.88
6-2 20	Center mass, pinned-pinned beam	Exact	67.52
		FE	67.52
6-2 22	Center mass, clamped-clamped beam	Exact	135.05
		FE	135.05

Table 7-66. – Beam Vibration - Using Beam2.
The sample beam has a square cross section with area=1, length=20. 100 elements. No torsion spring is yet available.

Blevins Table	Description	Sol'n Type	Mode Number			
			1	2	3	4
8-1 1	Free-free bending	Exact	515.36	1420.6	2785.0	4603.7
		FE	515.15	1419.6	2781.9	4596.9
8-1 2	Free-sliding bending	Exact	128.84	696.24	1719.3	3197.0
		FE	128.83	696.05	1718.5	3194.7
8-1 3	Clamped-free	Exact	80.99	507.56	1421.2	2784.9
		FE	80.98	507.44	1420.6	2783.2
8-1 5	Pinned-pinned	Exact	227.34	909.37	2046.1	3637.5
		FE	227.34	909.29	2045.7	3636.4

Table 7-67. – Uniform Shaft Torsional.

Note. The discrepancy in this table stems from a mismatch of geometry (which we intend to clear up soon). The analytic results are for circular cross sections. We have a square cross section in the FE results. It is clear that the frequencies should be ratios of 1,3,5,7, etc. This holds for the FE results.

Blevins Table	Description	Sol'n Type	Mode Number			
			1	2	3	4
8-19 2	Fixed-Free	analytic	1427.93	4283.78	7139.64	9995.5
		FE-Beam2	1554.68	4663.66	7771.49	10877.4
		FE-Hex8	1545.97	4642.1	7750.76	10880

Table 7-68. – Circular Arcs.

Blevins Table	Description	Sol'n Type	Mode Number			
			1	2	3	4
9-2 1	Extension Mode	analytic	52632	N/A	N/A	N/A
	Clamped-Clamped	FE Beam2	52693	N/A	N/A	N/A
9-2 2	In-Plane flexural mode	analytic	2579.35	13137.2	30989.4	56026.3
	Pinned-Pinned	FE Beam2	2587.73	13189.5	30671.7	54445.7
9-2 5	Out-of-Plane Flexural	analytic	1763.56	N/A	N/A	N/A
	Clamped-Clamped	FE Beam2	1741.11	N/A	N/A	N/A

Table 7-69. – Circular Plates - Bending.

Circular disk made of QuadT elements.

Blevins Table	Description	Sol'n Type	Mode Number			
			1	2	3	4
11-1.1	Free edge	Exact	126.84	219.35	295.32	495.50
		FE	129.31	217.25	300.16	493.72
11-1.2	Simply supported edge	Exact	120.18	336.61	619.37	718.61
		FE	119.20	335.69	618.69	718.64
11-1.3	Clamped edge	Exact	246.78	513.36	842.25	960.32
		FE	246.62	513.00	841.97	961.03
11-1.12	Clamped edge with point mass at center (M large)	Est.	25.98	N/A	N/A	N/A
		FE	25.83	N/A	N/A	N/A

Table 7-70. – Rectangular Plates - Bending.
Using *Tria3* elements, aspect ratio $a/b = 1.5$ in all cases.

Blevins Table	**Description**	**Sol'n Type**	**Mode Number**			
			1	**2**	**3**	**4**
11-4.1	Free-free-free-free	Exact	864.14	927.25	2002.59	2158.85
		FE	862.61	919.15	1989.43	2142.13
11-4.21	Clamped-clamped-clamped-clamped.	Exact	2608.74	4029.22	6387.69	6428.04
		FE	2608.29	4027.90	6387.04	6425.11
11-4.16	Simply supported (all 4 edges)	Exact	1377.13	2648.23	4237.00	4765.01
		FE	1376.97	2648.01	4237.05	4766.57
11-4.6	Clamped-free-simply supported-free	Exact	652.94	1103.68	2127.08	2747.82
		FE	648.82	1100.31	2113.90	2733.90

10.7.4. Linear MultiPoint Constraints

MultiPoint Constraints (MPCs) are applied in structural dynamics for a number of reasons. Typical uses include spreading a load over many input nodes, attaching dissimilar meshes, connecting lumped structures, applying boundary conditions and approximating rigid structures. The variety of uses for MPCs makes verification of their application difficult. Only small problems may typically be solved analytically.

Analytic problems for which some degrees of freedom may be eliminated using constraints will be compared with solutions from **Sierra/SD**. The problems for which these comparisons may be made are still to be determined at this time.

In addition to analytic problems, code comparisons for practical problems will be made. While code comparisons suffer from a number of problems, they have the advantages of comparing solutions to the type of problems expected in practice, and they provide some level of verification for components of the software which could otherwise not be tested.

10.7.5. Linear Viscoelasticity

Linear viscoelasticity is a physics whose implementation in structural dynamics code is not uncommon. The most conventional implementation is that which employs Prony series (see Theory and User's manuals.) Again, the purpose of verification is to assure that the conventional implementation is done correctly.

For this test, we consider a beam of isochoric, isotropic viscoelastic material subject to normal displacements in one direction consistent with a uniform compression. The imposed displacement is ramped up and held at a fixed value. After the material is deformed at a rate $\dot{\gamma}$ for a period Δt and then held, the resulting stress will be,

$$\sigma(t) = \dot{\gamma} E_\infty \Delta t - \dot{\gamma} \sum_n (E_G - E_\infty)\tau_n (1 - e^{\Delta t/\tau_n}) e^{-(t+\Delta t)/\tau_n} \tag{10.7.1}$$

A plot of the above exact solution and the predictions of **Sierra/SD** are presented in Figure 7-121.

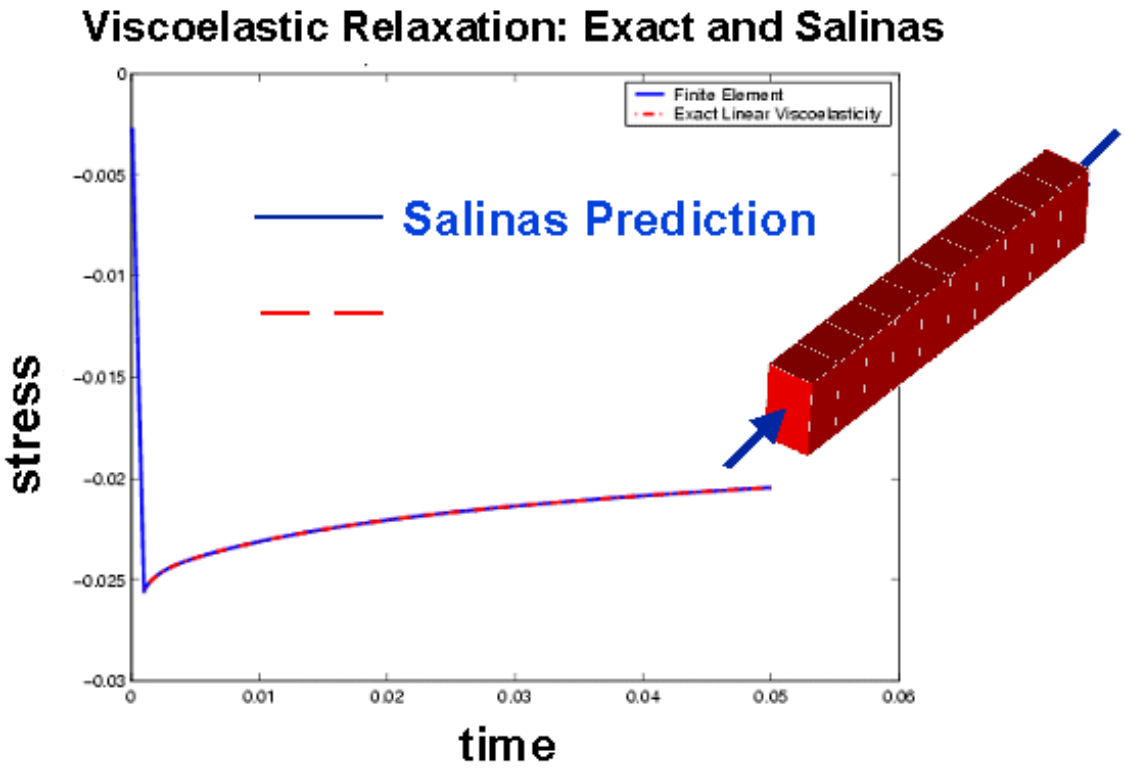

Figure 7-121. – Viscoelastic Relaxation. The **Sierra/SD** results reproduce the exact solution viscoelastic relaxation after ramp and hold deformation.

10.7.6. Code to Code Comparisons

Extreme care must be used when using code to code comparisons. They are no replacement for more rigorous verification techniques (see *Trucano*[55]). However, they may be useful when the following conditions are met.

- The "truth" model code has been adequately verified.
- The two codes can be determined to solve *exactly* the same differential equations.
- Comparisons are made to asymptotic quantities, i.e. quantities for which the accuracy of the truth model code must ultimately converge.
- The value gained by the comparison provides important insight not readily obtained by solution of analytic problems.

Any method that provides additional examination of the application is valuable.

A number of benchmark problems exist in the literature (see for example *MacNeal*[34]). Some of these benchmark problems will be solved using **Sierra/SD** and using MSC/Nastran, an industry standard for elastodynamics. Comparisons of the mesh-refined solutions will be made. Other codes may be used for other phenomena.

The list of such code to code comparisons will necessarily grow over time. An example includes a mock-AF&F which was analyzed for eigen response. This is a 500,000 degree of freedom model designed for optimization studies. It is a real design with the level of detail anticipated in practical models of this structure. It contains mostly Tet10 elements with shells constructed of Tria6. Much of the model was constructed using automatic mesh generation methods. Comparisons of the first 4 modes of this model are shown in Table 7-71.

Table 7-71. – AF&F code to code comparison.

#	Description	Nastran	Sierra/SD	Difference
1	Aft plate drum mode	434.3 Hz	437.0 Hz	.6%
2	First bending, X	627.4 Hz	629.1 Hz	.3%
3	First bending, Y	657.2 Hz	659.2 Hz	.3%
4	torsion	793.6 Hz	793.2 Hz	.05%

10.7.6.1. Membranes and Transfer from SierraSM

In this case, analyses of a preloaded (inflated) tire from Sierra are compared to Abaqus^{TM}. The tire model (Figure 7-122) consists of a rim, and multiple layers of rubber and membranes. The tire is preloaded using **Sierra/SM**. The **Sierra/SD** analysis in this test case involves reading the results from that SM analysis, transferring material parameters, and computation of the eigenvalues of the system.

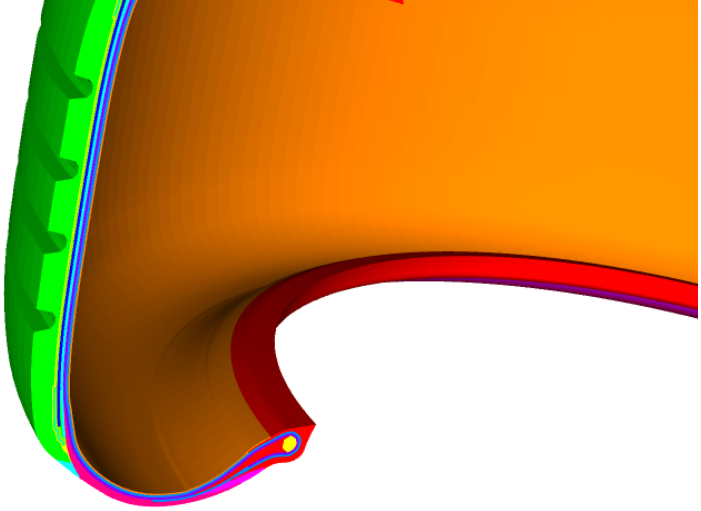

Figure 7-122. – Tire Analysis Model.

Eigenvalue results are shown in Table 7-72. As seen in the table, there is excellent agreement between Abaqus and **Sierra/SD** for this problem.

#	**Abaqus**	**Sierra**	**% difference**
1	39.912	40.3718	1.1
2	53.586	51.3133	4.3
3	55.650	53.5655	3.8
5	75.071	73.3562	2.3
7	97.202	96.6323	0.6
9	98.984	98.6028	0.4
11	119.35	119.045	0.3
13	142.54	142.219	0.2
15	142.56	142.287	0.2
17	167.07	166.891	0.1
19	171.37	171.045	0.2
21	193.59	193.372	0.1
23	193.75	193.540	0.1
25	214.47	214.001	0.2
27	221.77	221.814	0.0
29	235.20	234.640	0.2

Table 7-72. – Comparison of Eigen Frequencies of the Mooney-Rivlin Inflated Tire. For double modes one frequency is listed.

10.8. User Evaluations

While not rigorous in the same sense as closed form solutions, most analysts would agree that evaluation by independent outside analysts is a valuable criteria in determining the suitability of an analysis package. Such evaluation measures the answers to well-defined problems, and it provides confidence in the product. For example, if the tools are lacking to provide a reasonable model, this becomes readily apparent.

Where outside evaluations have been performed, we provide a summary and contact information.

10.8.1. Newport News Shipyard

Contact: Travis Kerr `kerr_te@nns.com` and Jay Warren `warren_je@nns.com`

On two separate occasions, Newport News shipyard has worked with *Sandia National Labs* to model their aircraft carriers. In October of 2000, and then again in October of 2002, they sent analysts to *Sandia National Labs* to perform a whole ship model eigen and transient dynamics analysis. Part of the first visit involved evaluation of a suite of tests. Unfortunately, *Sandia National Labs* was not provided with any report on this evaluation. Newport News shipyard has continued interest in using **Sierra/SD**.

10.8.2. British Atomic Weapons Establishment (AWE)

Contact: Trevor Hensley. `Trevor.Hensley@awe.co.uk`

From June to December of 2002, Trevor Hensley of the AWE evaluated *Sandia National Labs*'s ASC applications in Albuquerque. **Sierra/SD** was among the first evaluated. One problem was identified in statics. The displacements converged. Stress is reported in the element coordinate system.

The AWE is currently negotiating to obtain a copy of **Sierra/SD** for their analysis at their site.

10.8.3. NASA

Contact: Lloyd Purves, `lpurves@hist.nasa.gov`

This evaluation did not go well for several reasons.

1. There was a shortage of manpower. Lloyd had a summer student who was doing most of the work, but the student did not have sufficient expertise to finish.
2. There were hardware and software installation problems. NASA personnel were not able to visit us here, nor were **Sierra/SD** personnel given access to NASA machines. Thus installation of the software became a real road block.

3. Probably most importantly, the goals did not match. **Sierra/SD** is not a plug-in replacement for NASTRAN. It has a wide variety of elements, but it also lacks capability that may be unique to NASTRAN. For example, **Sierra/SD** has no axially symmetric elements. Other translation issues (such as differences in spring formulations) caused a good deal of difficulty.

10.8.4. Lockheed Martin – Denver

Contact: Dan Morganthaler, `daniel.r.morganthaler@lmco.com`

This interaction was funded under the Lockheed Martin shared vision program. It met limited success. The main impediments were with the difficulty in getting **Sierra/SD** to run properly on the parallel platforms. Dan visited *Sandia National Labs* for a few days. The runs had not completed by the end of Dan's visit. Eventually, Dan was able to get the analysis done using superelement capabilities in Nastran. The report is available in draft form.[50]

10.8.5. Advatech Pacific

Contact: Peter Rohl, `peter.rohl@advatechpacific.com`

Advatech comparing the results of **Sierra/SD** to NE/Nastran on a variety of structures. This is available as conference proceedings.[45]

10.8.6. Sandia National Labs

10.8.6.1. Comparison to Abaqus thermal strains

In December 2005, an analyst compared the Abaqus and **Sierra/SD** thermal expansions. This provides a real world comparison. However many would not consider this to be verification.

Figures 8-123 and 8-124 relate to the analysis of a thin walled frustum for thermal loads. Two model versions were created, one in Abaqus and the other in **Sierra/SD**. The energy deposition data was provided by mapping the data from the element centroids to the nodes using Paraview. A scaling term was applied to convert energy deposition to equivalent thermal loads. The figures compare plots of e33 volumetric strains. The two approaches compare well.

The model is about 135000 degrees of freedom, which is too large for our standard test suite. However, it is available for comparison purposes.

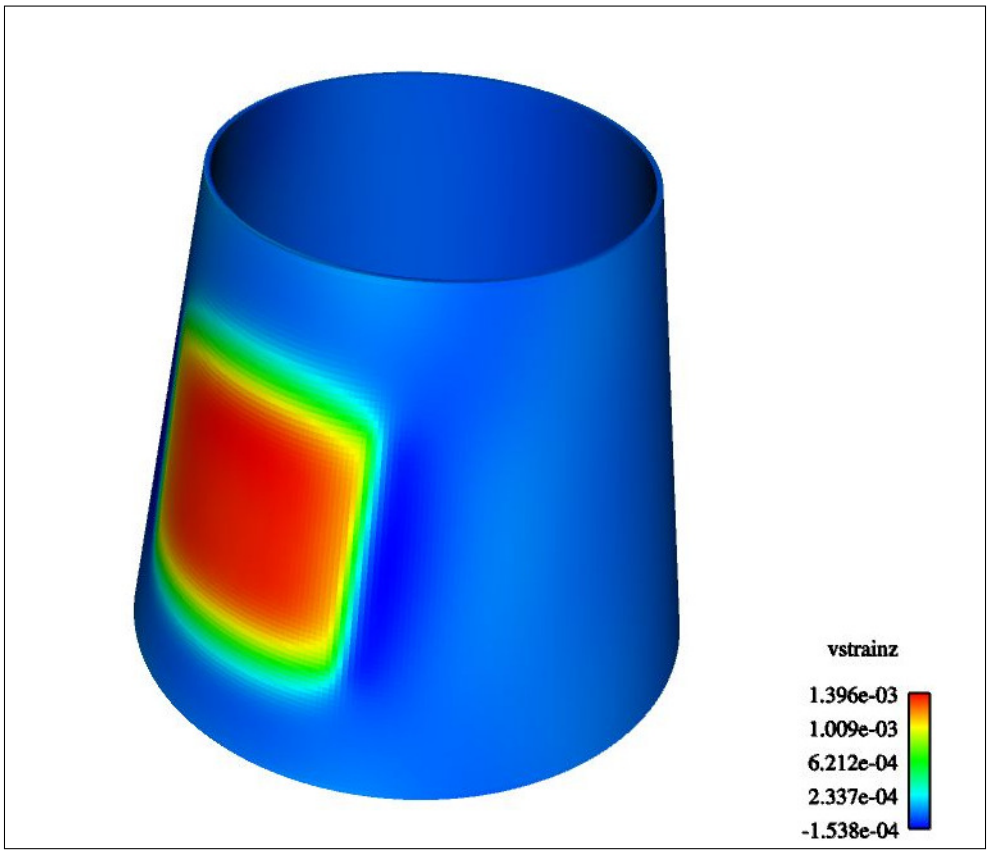

Figure 8-123. – **Sierra/SD** Thermal Strains.

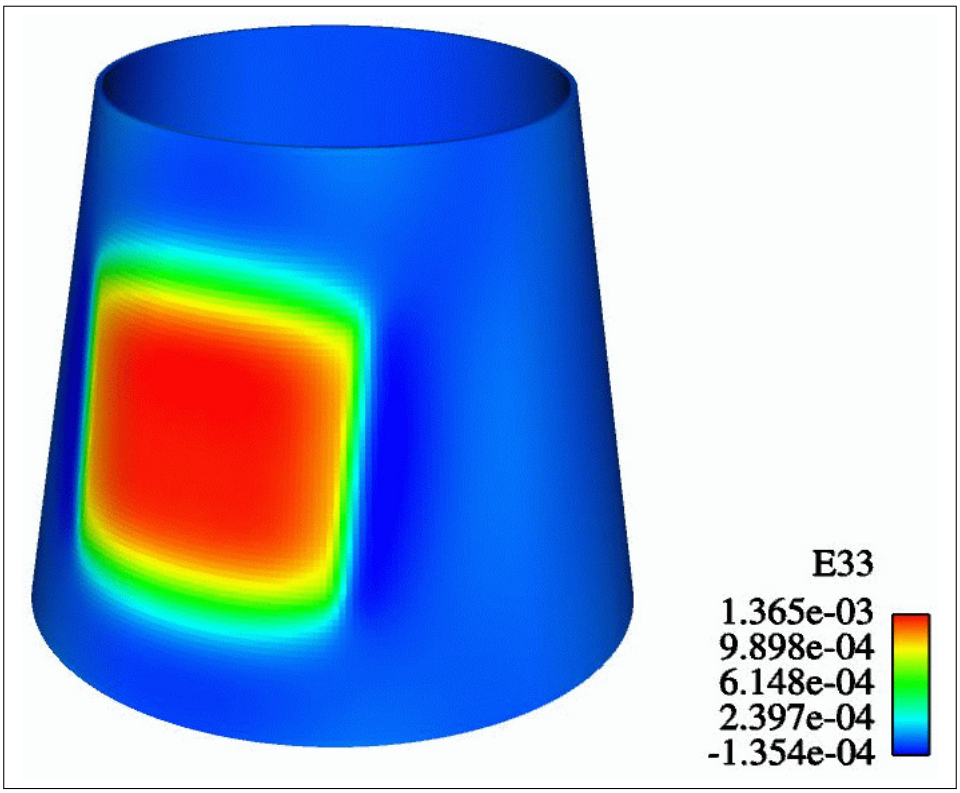

Figure 8-124. – Abaqus Thermal Strains.

10.8.6.2. Superelement User Verification

Superelement insertion was examined by Fernando Bitsie, the product manager for **Sierra/SD**, and a lead analyst in a sister organization. A nonlinear time domain analysis was used to compare results between a full model and a reduced superelement model (using two superelements). Of particular concern is the generation of high frequency response. The coupling element between the two superelements is an *Iwan* element, which generates shot noise as the spring/sliders alternatively open and close. This can be amplified as it is fed into a superelement. This is a challenging test. The low frequency response of the reduced order model may be correct. Also loading may generate significant contributions in the high frequency spectrum.

The full and reduced order models are illustrated in Figure 8-125. In the reduced model, the top and bottom solid sections are replaced by superelements. There are 8 nodes in the reduced model, while the full model is composed of about 33,000 nodes.

images currently not available. under review and approval.

Figure 8-125. – Exploded view of 3 Leg structure with the full model on the left and the reduced model on the right. Iwan elements connect the top and bottom structures of both models. These Iwan elements are not shown because they connect co-located nodes.

Figure 8-126 shows the acceleration of the top and bottom as a function of time. There is a much greater response for the superelement than for the full model. This is also illustrated in Figure 8-127, where the force across the joints is examined in the time domain for both the full and reduced models. Again, there is a significant difference.

However, examination of the response of the model in the frequency domain reveals that the differences are primarily in the high frequency. Figure 8-128 shows the frequency response of the accelerations in Figure 8-126. As seen in the figure, there is good agreement between the models at lower frequencies. The discrepancies occur at the Nyquist frequency (50 kHz), and twice that (the sampling frequency). The response at 100 kHz is strong for the CMS model, and it is this response which is dominating the time response.

Figure 8-129 illustrates the same issue for the loading across the *Iwan* element. Compare this with the time domain in Figure 8-127. Again, the low frequency response is accurate, while there are significant issues at the sampling frequency.

As expected the response of the reduced order model agrees with the full order model at lower frequencies, and not at higher frequencies.

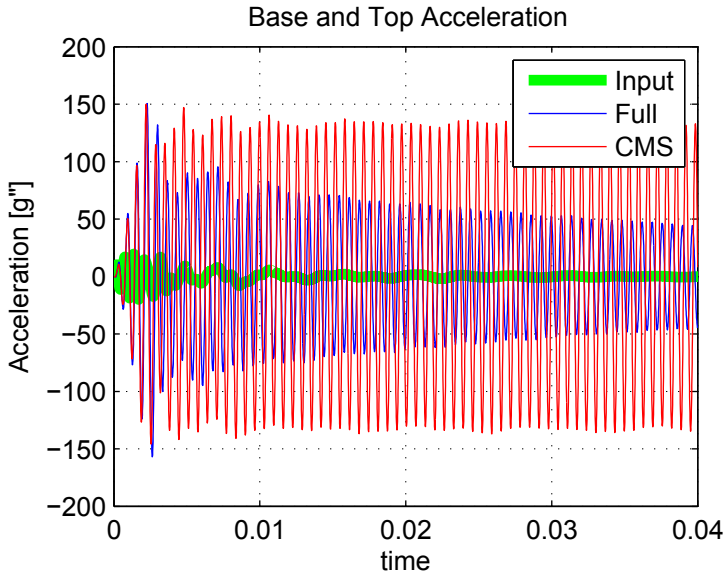

Figure 8-126. – Time Domain Acceleration Response of Comparative Model.

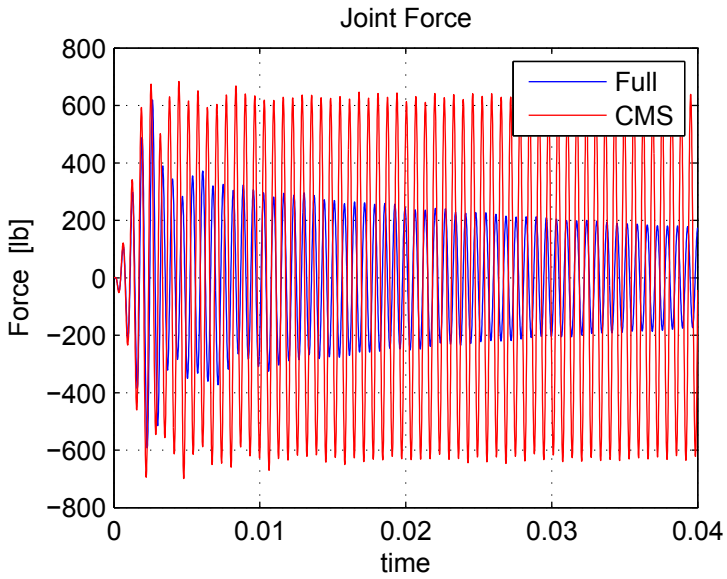

Figure 8-127. – Time Domain Element Force of Comparative Model.

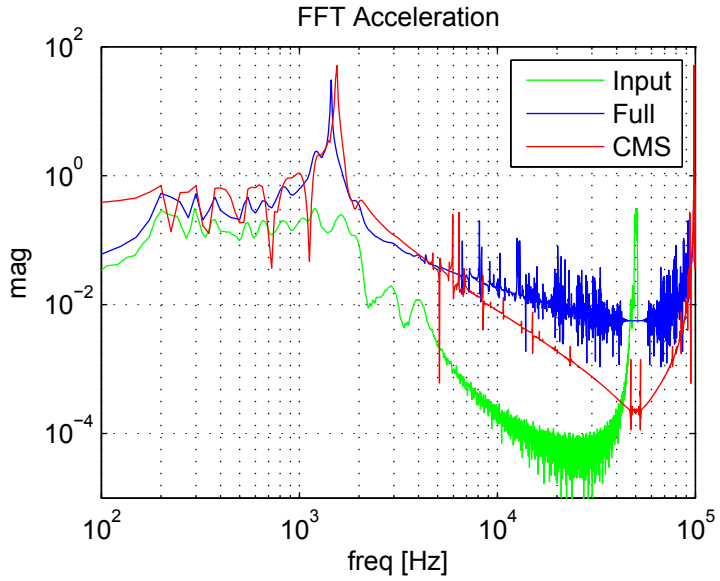

Figure 8-128. – Frequency Domain Acceleration Response of Comparative Model

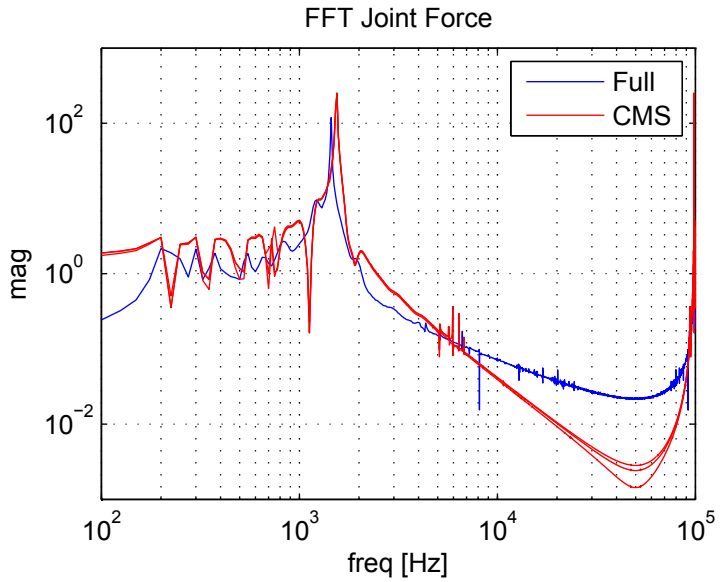

Figure 8-129. – Frequency Domain Element Force of Comparative Model.

10.9. Other Tests

The goal of any software verification effort is to ensure that the equations are being solved properly. This includes input and output, and to an extent documentation as well. The crucial question is whether analysts can trust the results of the calculations. *Any* test or evaluation which improves confidence in this process is of value. As stated by Myers,[40] "A good test is one that has a high probability of detecting an as-yet undetected error." Interestingly enough, the tests that catch most of our errors are emphatically *not* those that have been presented in previous sections!

10.9.1. Regression Tests

Part of the process development for **Sierra/SD** is a nightly regression test. These are typically small tests that have been assembled to examine parts of the code. These examples are results of either artifacts of development, or of bugs that have been identified and fixed in the code. They are in no way rigorous verification tests; instead they detect if results change. The changes may be introduced by additions or changes in the software, or they may be introduced by operating system variations (including new libraries and new platforms). These regression tests are evaluated and reported on our web site nightly, and they have been responsible for identifying the vast majority of the issues in the software.

At the time of this writing (October 2003), we evaluate approximately 800 regression results. Approximately half of these tests are repeated in parallel. Detailing these tests is beyond the scope of this document. Indeed, the nature of the regression test is different from the nature of standard verification tests, and it is not simple to sort the tests into categories that verify element formulations.

10.9.2. Static Tests

Static tests provide a mechanism for evaluating the software outside of the operational environment. They include source code evaluations and software to test our software. Source code compliance with standards and dangerous practices may be evaluated.

Our group found that source code evaluations have limited to no value. They are also resource demanding. As a consequence we have discontinued source code evaluations. We review source code rarely and only as an aid in our understanding of the development.

However, there has been some evidence of improved software though other static tests. As specified in our *Procedures* document, some sections of the code are subjected to this type of evaluation at each release. To date, we have evaluated the finite element portion of the code at each release excluding the third party libraries.

10.9.3. Dynamic Testing

Another important aspect of software testing includes memory errors in the code. As part of our release process, we run the regression tests through memory checking software before release. Typically all the regression tests are run through the software, and if the tools are available, we run through both serial and parallel tests. These tests are also run periodically through the development process. They are effective in finding bugs that are not readily apparent through other tests.

11. INPUT DECKS FOR VERIFICATION TESTS

11.1. Parallel Distribution of Load through Rbars

Refer to section 3.1

```
solution
 case eig
   eigen nmodes=4
   shift -1e8
   enforce_modeshape_residual = false
 case out
   modalranvib
   keepmodes=3   // force modal truncation
   lfcutoff=-10
  title 'hex and spiders'
end
ranloads
   matrix=1
   load=1
     nodeset 1
force=0 1 0
        scale=1000
end
frequency
   freq_step=100
   freq_min=300
   freq_max=1e4
   BLOCK=all
   accel
end
matrix-function 1
   Name=input_psd
   symmetry=symmetric
   dimension=1x1
   data 1,1
     real function 1
end
function 1
   Name='psd'
   type=loglog
   data 1.0 1e-8
   data 299 1e-8
   data 300 0.01
   data 2000 1
   data 8000 1.
   data 10000 0.01
   data 10001 1e-8
end
damping
  gamma=0.01
end
parameters
 wtmass=0.00259
end
file
     geometry_file 'hex_spider.exo'
```

```
end
boundary
  nodeset 1
  roty=0 rotz=0 rotx=0 x=0 z=0
end
loads
end
outputs
        disp
vrms
end
echo
      mass=block
        mass
end

gdsw
  solver_tol 1e-9
end

block 1
   material 1
end
block 2
  ConMass
    Mass=0.7075
    Ixx =0
    Ixy =0
    Iyy =0
    Ixz =0
    Iyz =0
    Izz =0
    Offset= 0 0 0 // patran/exo type 'BEAM'/BEAM. Number nodes 2
end
block 10
    RBAR  // RBE type element
end
material 1
   density=0.283
   E=29e2
   nu=0.3
end
```

11.2. RigidSet Compared to Rbar

Refer to section 3.2

```
//input deck for a rigidset verification test

SOLUTION
    solver=gdsw
  title 'rigidset verficiation test'
  eigen
    nmodes 50
  shift -1e6
END

PARAMETERS
 wtmass=0.00259
END

FILE
   geometry_file 'rigidset.exo'
END

OUTPUTS
  displacement
END

ECHO
  mass block
END

RIGIDSET set1
  sideset 1
END

RIGIDSET set2
  sideset 2
END

GDSW
  max_numterm_C1 500
  overlap 2
  krylov_method 1
//   orthog_option 3
END

BLOCK 1
   material 1
   hex8b
END

BLOCK 2
  dead
END

BLOCK 3
  dead
END

MATERIAL 1
   density 0.3
   E = 3.0e7
   nu = 0.3
END
```

11.3. Multiple Tied-Surfaces and Curved Surfaces

Refer to section 3.3

```
SOLUTION
    solver=gdsw
  title 'tied surface example with holes'
  eigen
  nmodes 15
  shift = -1e8
END
Parameters
  RemoveRedundancy=yes
  wtmass=0.00259
end

File
  geometry_file 'tied_surface.exo'
end
Outputs
  displacement
  vonmises
  Constraint_Info
end

Block 1
   material 1
end

Block 2
  material 1
end

Block 10
  material 1
end

Material 1
   E=1.0e7
   nu=0.33
   density=0.098
end

TIED DATA
   surface 2,1
   transverse tied
   search tolerance 1.e-3
   edge tolerance   1.e-5
end
TIED DATA
   surface 102,2
   gap removal = on
   search tolerance 1.e-3
   edge tolerance   1.e-6
end
TIED DATA
   surface 3,101
   search tolerance 1.e-1
   edge tolerance   1.e-6
end
GDSW
  con_tolerance 1e-2
  max_numterm_C1=6
end
```

11.4. Craig Bampton Reduction

Refer to section 2.1

```
SOLUTION
    solver=gdsw
    eigen nmodes=all
    shift = -1e6
END

FILE
    geometry_file  'system_plus_se.exo'
END

BOUNDARY
   sideset 1
       fixed
END

LOADS
END

ECHO
END

OUTPUTS
    disp
END

MATERIAL 'steel'
    E 30e6
    nu 0.3
    density 0.288
END
BLOCK 1
    material 'steel'
END

BLOCK 2
    dead  // unused
END

BLOCK 3
    superelement
    sensitivity_param 1 0.28800
    // this will use taylor series expansion to get the matrices
    file = 'onehex_super.ncf'
    map locations
END
```

11.5. Superelement Damping

Refer to section 2.2

```
SOLUTION
    solver=gdsw
  transient
    time_step 2.0e-5
    nsteps 250
END

FILE
  geometry_file 'full_system.exo'
END

BOUNDARY
    sideset 3
  fixed
END

LOADS
  sideset 4
  pressure = 10.0
  function = 1
END

FUNCTION 1
  type linear
  data 0 0
  data 1e-4 1
  data 3e-4 -1
  data 4e-4 0
  data 10 0
END

HISTORY
  nodeset 3
    disp
    stress
END

OUTPUTS
  deform
    elemeigchecks
END

// the following element block is hex.
// exodus tells us it is an 8-node hex.
// The default integration mode is "UNDER"
// The only required arguement is the material card
BLOCK 1
  material "steel"
        hex8u
END

MATERIAL "steel"
  E 30e6
  nu .3
  density 0.288
END

BLOCK 3 // Formerly block 2
   superelement
   file=SE_DampTwoBlock.ncf
   map locations
END
```

11.6. Euler Beam Bending

Refer to section 5.1

```
SOLUTION
    solver=gdsw
statics
title 'single beam model. 100 elements. xy only'
lumped
END

FILE
geometry_file 100.exo
END

BOUNDARY
    nodeset 1
    fixed
    nodeset 3
      x = 0
      z = 0
      rotx = 0
      roty = 0
END

LOADS
nodeset 2
force = 0. .25 0.
END

OUTPUTS
     deform
END

ECHO
END



BLOCK 1
material 'Aluminum'
Beam2
Area 0.1
orientation 0 .1 0
I1 .2
I2 .3
J .5
END

Material 'Aluminum'
E 10.0E6
nu 0.33
density 253.82e-6
END
```

11.7. Euler Beam Properties

Refer to section 5.2

```
//salinas input for 100 element beam
SOLUTION
    solver=gdsw
  title='multi-element beam modal'
  eigen
  nmodes=10
  shift=-1
END

FILE
   geometry_file 'beam2.exo'
END

PARAMETERS
END

BOUNDARY
  nodeset 1
  fixed
END

LOADS
END

OUTPUTS
        disp
END

HISTORY
    disp
    block '1'
END

ECHO
      mass
END

BLOCK 1
   Beam2
   material=1
   Area=0.03
   I1=0.09
   I2=0.01
   J=0.1
   orientation = 1 1 0
END

MATERIAL  1
   Isotropic
   E = 1e+07
   NU = 0.3
   density = 1
END
```

11.8. A Navy Beam

Refer to section 5.3

```
//salinas input for 100 element beam
SOLUTION
    solver=gdsw
  title='multi-element beam modal'
  eigen
  nmodes=10
  shift=-1
END

FILE
   geometry_file 'nbeam.exo'
END

PARAMETERS
END

BOUNDARY
  nodeset 1
  fixed
END

LOADS
END

OUTPUTS
        disp
END

HISTORY
    disp
    block '1'
END

ECHO
      mass
END

BLOCK 1
   Nbeam
   material=1
   Area=0.03
   I1=0.09
   I2=0.01
   J=0.1
   orientation = 1 1 0
END

MATERIAL  1
   Isotropic
   E = 1e+07
   NU = 0.3
   density = 1
END
```

11.9. Two Layered Hexshell

Refer to section 5.4

```
SOLUTION
    solver=gdsw
  title 'Two-ply_rectangular_plate_pressure_A'
  statics
END
FILE
  geometry_file 'Two-ply_rectangular_plate.g'
end
PARAMETERS
  wtmass = 0.00259
end
BOUNDARY
  nodeset 1
    y = 0.0
  node_list_file=node1.txt
    x = 0.0
    z = 0.0
  node_list_file=node2.txt
    x = 0.0
end
LOADS
  sideset 1
  pressure 2.0
end
OUTPUTS
  disp
  eorient
  force
end
ECHO
  mass block
  disp
end
BLOCK 1
  HexShell
   tcoord 0 2
   layer 1
   material 1
   thickness .5
   layer 2
   material 2
   thickness .5
end
MATERIAL 1
  density 0.1
  E 1.0e5
  nu 0.25
end
MATERIAL 2
  density 0.05
  E 1.0e3
  nu 0.2
end
```

11.10. Perfectly Matched Layers: Offset Sphere

Refer to section 5.18 for details of the test.

```
SOLUTION
  directfrf
end
FILE
   geometry_file 'OffsetSphere3.exo'
end
FREQUENCY
  freq_min = 100.0
  freq_step = 1
  freq_max = 101.0
  disp
  block 1
end
LOADS
    sideset 1
    acoustic_vel = 1.0
    function = 2
end
BOUNDARY
  sideset 2
   pml_element
   use block 57
end
FUNCTION 2
    type LINEAR
    data 0 1
    data 1e6 1
end
OUTPUTS
  apressure
end
BLOCK 1
    material "air"
end
BLOCK 57
   pml_element
   stack_depth 5
   ellipsoid_dimensions 5 5 5
   pml_thickness 1
   loss_function = polynomial
   loss_params = 0 960 960 0
end
MATERIAL "air"
  density 1.293
  acoustic
  c0 332.0
end
GDSW
   precondUpdateFreq 3
end
```

11.11. Thermally Induced Elastic Waves: Hollow Sphere

Refer to section 5.19 for details of the test.

11.11.1. Sierra SD Input Deck

```
SOLUTION
    solver=gdsw
case t2
  transient
  nsteps 200
  time_step 1e-3
  nUpdateTemperature 1
END

FILE
  geometry_file 'hollow_sphere.e'
END

OUTPUTS
force
disp
elmat
temperature
thermal_strain
END

ECHO
END

BOUNDARY
  sideset 1
    x=0
  sideset 2
    y=0
  sideset 3
    z=0
END

PARAMETERS
  thermal_exo_var = "TND"
END

DAMPING
  alpha 1.0e-3
  beta  1.0e-3
END


LOADS
  body
    thermal
    function 8245
END

function 8245
    type linear
    data 0 1
    data 1 1
end

BLOCK 1
        material "foo"
END
```

```
// Based on "Thermal Stress-Wave Propagation in Hollow Elastic Spheres" - Tsui and Kraus (1965)
// Parameters are chosen such that their gamma = 1/5 to match figure 1.
// Note that this choice of gamma implies an unphysically small G and/or an unphysically large kappa
// The scaled time tau is the same as physical time, but the displacements are scaled by
// a factor of (1-nu)/(a*alpha*Ta*(1+nu)) = 50, i.e., scale result by 50 to match figure in paper.

// shear modulus: G = 25/4
// Poisson ratio: nu = 1/3
// density = 1
// pressure wave speed: c = sqrt( 2*(1-nu)*G/(density*(1-2*nu)) ) = 5
// inner sphere radius: a = 1 (inner sphere radius)
// thermal diffusivity: kappa = 1
// dimensionless inertia parameter: gamma = kappa/(c*a) = 1/5

MATERIAL "foo"
        G = {25/4.0}
        density = 1
        nu = {1/3.0}
        alphat = 1e-2
        tref 0.0
END
```

11.11.2. Aria Input Deck

```
begin sierra Calore

  title heat conduction through concentric sphere, test of dash contact


  Begin Aria Material mat1
    # kappa = k/(cp*rho)
    density  = constant rho = 1
    specific heat = constant    cp = 1
    thermal conductivity = constant k = 1
    heat conduction = basic
  End

  BEGIN FINITE ELEMENT MODEL test
    Database Name = hollow_sphere.exo
    use material  mat1 for block_1
  END FINITE ELEMENT MODEL test

  BEGIN TPETRA EQUATION SOLVER solve_temperature
    BEGIN BICGSTAB SOLVER
      BEGIN JACOBI PRECONDITIONER
      END
      CONVERGENCE TOLERANCE = 1.0e-8
      MAXIMUM ITERATIONS = 1000
      RESIDUAL SCALING = NONE
    END
  END

  begin procedure myProcedure

      Begin Solution Control Description
         Use System Main
         Begin System Main
            Simulation Start Time = 0.0
            simulation Termination Time = 0.2
            begin transient timeblock
               advance myRegion1
            end
         End
```

```
      Begin Parameters For Transient TimeBlock
         Start Time = 0.0
         Begin Parameters For Aria Region myRegion1
            Time Step Variation     = Adaptive
            Time Integration Method = First_Order
            Initial time step size  = 1e-3
            Maximum Time Step Size Ratio  = 1.5
            minimum resolved time step size = 1.e-4
            minimum time step size = 1.e-4
            maximum time step size = 1e-2
            Predictor Order = 1
            Predictor-corrector tolerance = 1e-3
            Predictor-Corrector Begin After Step = 4
         End
      End

    End

  begin Aria region myRegion1

    Begin Results Output Label diffusion output1
      database Name = hollow_sphere.e
      At Step 0, Increment = 1
      Title Aria Dash Tied Contact Test
      Nodal Variables = solution->temperature as TND
    End

    ############################
    ### boundary conditions ###
    ############################

    Begin Temperature Boundary Condition  t1
      temperature = 1.0
      add surface surface_1000
    End
    Begin Temperature Boundary Condition  t2
      temperature = 0.0
      add surface surface_2000
    End

    IC for Temperature on all_blocks = constant value = 0

    use finite element model test
    $ model coordinates are model_coordinates
    use linear solver solve_temperature

    nonlinear solution strategy = newton

    maximum nonlinear iterations = 10
    nonlinear residual tolerance = 1.0e-8
    nonlinear relaxation factor  = 1.0
    use dof averaged nonlinear residual
    accept solution after maximum nonlinear iterations = true

     EQ Energy for Temperature On all_blocks Using Q1 With Lumped_Mass Diff

  end

 end procedure myProcedure

end sierra Calore
```

11.12. Preloaded Beam

Refer to section 5.5

```
SOLUTION
 case statics
   statics
   load = 1
 case update
    tangent
 case modal
    eigen
    nmodes = 10
end
FILE
    geometry_file  'kgperm3.exo'
end
LOAD 1
    nodeset 2
    force 44482 0 0
end
OUTPUTS
    disp
    force
end
ECHO
    mass
    mass=block
end
BOUNDARY
   nodeset 1
       fixed




end
BLOCK 1
    beam2
    material="steel"
    area=0.0000202683
    i1 = 3.2690739721e-11
    i2 = 3.2690739721e-11
    j = 6.5381479442e-11

end
MATERIAL "steel"
    E 187e9
    nu .3
    density 8015.19
end
```

11.12.1. Prescribed displacement

Refer to subsection 5.5.3

```
SOLUTION
    solver=gdsw
 case statics
   statics
   load = 1
 case update
    tangent
 case modal
    eigen
    nmodes = 30
END
FILE
    geometry_file  'Beam.exo'
end
LOAD 1
    nodeset 2
        force 1e10 0 0
end
OUTPUTS
    disp
    force
end
ECHO
    mass
    mass=block
end
BOUNDARY
   nodeset 1
      x=0 y=0
   nodeset 3
      x=1.3368983957E-01 y=0
   nodeset 4
    z=0 rotx=0 roty=0
end
BLOCK 1
    beam2
    material="steel"
    area=4
    i1=1.33333
    i2=1.33333
    j=2.6666
    orientation 0 0 1
end
MATERIAL "steel"
    E 187e9
    nu .3
    density 8015.19
end
```

11.13. Partial Cylinder Patch

Refer to section 5.6

```
$ Algebraic Preprocessor (Aprepro) version 6.04 (2021/10/26)
SOLUTION
       statics
END

FILE
  geometry_file 'cyl_q4.g'
END

BOUNDARY
  nodeset 100
     x=0
  nodeset 200
     y=0
  nodeset 300
     z=0
  nodeset 301
     z=0.01
  nodeset 1000
     rotx=0
     roty=0
     rotz=0
END

LOADS
END

OUTPUTS
  eorient
  strain
  stress
  disp
  energy
  genergies
END

ECHO
  genergies
END

BLOCK 1000
  MATERIAL "STEEL"
$ loop
  THICKNESS 0.01
$
$
END

MATERIAL "STEEL"
  E 1.0E+6
  NU 0.3
  DENSITY 1.0E-6
END
```

11.14. Membrane Geometrical Stiffness

Refer to section 5.7

```
SOLUTION
    solver=gdsw
   case transfer
     receive_sierra_data
   case eig
     eigen nmodes=all
     lumped
END

file
   geometry_file membrane_geometric.exo
//   geometry_file plate101.exo
end

$$
boundary
  nodeset 1
    y=0
  nodeset 4
    x=0
  nodeset 2
    y=0
  nodeset 5
    z=0
end

boundary
end

loads
end

block 100
   QuadM
//   thickness=0.1
//   thickness = 0.095435875007294
   thickness = from_transfer
   material=1
end

material 1
  e=10.
  nu=0.49
//  density=1e-9
  density = 1.047823996923137e-9
end

outputs
   disp
   mfile
end
parameters
    mfile_format 3column
end
echo
  mass
end
```

11.15. Membrane Quad

Refer to section 5.8

```
SOLUTION
    solver=gdsw
  case two
  eigen
  lumped
  nmodes 14
  shift = -1.e8
END
File
  geometry_file 'temp1/Membrane_quad.par'
end
Boundary
  nodeset 1 x=0 y=0
  nodeset 2 x=0 y=0
end

Loads
end
Outputs
  deform
end
Block 100
  QuadTM
  material "steel"
  thickness 0.1
end
Material "steel"
  E 10.0
  nu 0.49
  density 1.0e-9
end
```

11.16. QuadM membrane Patch

Refer to section 5.9

```
SOLUTION
    solver=gdsw
   statics
END
FILE
geometry_file 'model.exo'
end
BOUNDARY
  nodeset 2 fixed
  nodeset 3 x=0
  nodeset 1 x=0.1
  nodeset 4 z=0
  nodeset 5 y=0
end
LOADS
end
OUTPUTS
deform
stress
end
BLOCK 1
  QuadM
material "steel"
thickness 1.0
end
BLOCK 2
  QuadM
  material "steel"
  thickness 1.0
end
BLOCK 3
  QuadM
  material "steel"
  thickness 1.0
end
BLOCK 4
  QuadM
  material "steel"
  thickness 1.0
end
BLOCK 5
  QuadM
  material "steel"
  thickness 1.0
end
BLOCK 6
  QuadM
  material "steel"
  thickness 1.0
end
BLOCK 7
  QuadM
material "steel"
  thickness 1.0
end
MATERIAL "steel"
E 30e6
nu 0.3
density 0.288
end
```

11.17. QuadS_GY Shear Membrane Shell

Refer to section 5.10

```
SOLUTION
    solver=gdsw
   eigen
   nmodes = 20
   shift = -1.e5
   lumped
END

GDSW
  solver_tol = 1e-10
end

Parameters
   wtmass 0.00259
end

FILE
    geometry_file   'mesh_quadt.g'
end

BOUNDARY
  nodeset 1 rotx=0 roty=0 rotz=0 x=0 y=0 z=0
  nodeset 2 rotx=0 roty=0 rotz=0 x=0 y=0 z=0
  nodeset 3 rotx=0 roty=0 rotz=0 x=0 y=0 z=0
  nodeset 4 rotx=0 roty=0 rotz=0 x=0 y=0 z=0
end

OUTPUTS
   globals
end

ECHO
end

BLOCK 1
  QuadS_GY
  material "steel"
  thickness 0.001
  fiber orientation = 0
end

MATERIAL "steel"
  orthotropic_layer
  E1 = 30e6
  E2 = 0.5e6
  nu12 = 0.3
  G12 = 0.5e6
  density 0.288
end
```

11.18. QuadS_GY Shear Membrane Shell - Geometric Stiffness and Preload

Refer to section 5.11

```
SOLUTION
    solver=gdsw
 case one
     receive_sierra_data
     lumped
 case out
    eigen
    nmodes = 10
END


FILE
//     geometry_file  'shell_beam.exo'
    geometry_file 'shell_adagio_salinas.e'
END

LOAD 1
    sideset 1
    pressure -2245852908.28
    // pressure 0
END

OUTPUTS

    disp
    force
END

ECHO
    mass=block
END

BOUNDARY
   nodeset 1
       fixed
   nodeset 3
    z=0
//    y=0
END

BLOCK 1
    material "steel"
    QuadS_GY
    thickness = 0.004450425122033
END

MATERIAL "steel"
        E 187e9
        nu 0.3
        density 8015.19
END
```

11.19. Hex Membrane Sandwich

Refer to section 5.12

```
SOLUTION
    solver=gdsw
   statics
END
File
geometry_file 'Model_hex.exo'
end
Boundary
  nodeset 2 fixed
  nodeset 3 x=0
  nodeset 1 x=0.1
  nodeset 4 z=0
  nodeset 5 y=0
end
Loads
end
Outputs
deform
stress
end

Block 1
  Hex8u
material "steel"
end
Block 2
  Hex8u
  material "steel"
end
Block 3
  Hex8u
  material "steel"
end
Block 4
  Hex8u
  material "steel"
end
Block 5
  Hex8u
  material "steel"
end
Block 6
  Hex8u
  material "steel"
end
Block 7
  Hex8u
material "steel"
end
MATERIAL "steel"
E 30e6
nu 0.3
density 0.288
end
```

11.20. Sierra/SM to Sierra/SD Coupling

Refer to section 2.3

11.20.1. Files for Preloaded Static Beam

Sierra/SM input file

```
begin sierra chatter_contact

  begin function ramp1
    type is piecewise linear
    begin values
      0.0     0.0
      0.5     1.0
      1.0     1.0
    end
  end

  begin function ramp2
    type is piecewise linear
    begin values
      0.0     0.0
      0.5     0.0
      1.0     1.0
    end
  end

  define direction x with vector 1.0 0.0 0.0
  define direction y with vector 0.0 1.0 0.0
  define direction z with vector 0.0 0.0 1.0

  begin material aluminum
    density         = 2.59e-2
    begin parameters for model neo_hookean
      youngs modulus = 7.8e+7
      poissons ratio = 0.0
    end
  end

  begin material stiff
    density         = 2.59e-2
    begin parameters for model neo_hookean
      youngs modulus = 7.8e+11
      poissons ratio = 0.0
    end
  end

  begin finite element model mesh1
    Database Name = bar.g
    Database Type = exodusII

    begin parameters for block block_1
      material = aluminum
      model = neo_hookean
    end
    begin parameters for block block_2
      material = stiff
      model = neo_hookean
    end
  end finite element model mesh1

  begin adagio procedure Apst_Procedure

    begin time control
```

```
  begin time stepping block p1
    start time = 0.0
    begin parameters for adagio region adagio
      time increment = 0.05
    end
  end
  termination time = 1.0
end time control

begin adagio region adagio
  use finite element model mesh1


  begin user output
    nodeset = nodelist_2
    compute global extension as average of nodal displacement
  end

  begin user output
    surface = surface_1000
    compute global deflection as average of nodal displacement
  end


  ### output description ###
  begin Results Output output_adagio
    Database Name = bar_preload_{extensionPressure}_{deflectionPressure}.e
    Database Type = exodusII
    At Step 0, Increment = 1
    nodal Variables = displacement as displ
    nodal variables = coordinates
     nodal variables = reaction
    element variables = stress
    element variables = log_strain
    component separator character = none
  end results output output_adagio

  begin history output
database name = bar_preload_{extensionPressure}_{deflectionPressure}.h
     at time 1.0 interval = 1.0
     global extension
     global deflection
  end


  ### definition of BCs ###
  begin fixed displacement
    node set = nodelist_1
    component = xy
  end
  begin fixed displacement
    node set = nodelist_2
    components = Y
  end
  begin fixed displacement
    block = block_1 block_2
    components = z
  end

  begin traction
    surface = surface_2
    direction = x
    function = ramp2
    scale factor = {extensionPressure}
  end


  begin traction
```

```
         surface = surface_1000
         direction = y
         function = ramp1
         scale factor = {deflectionPressure}
      end

      begin solver
        begin cg
          target relative residual = 1.0e-6
          begin full tangent preconditioner
          end
        end
      end

    end
  end
end
```

Sierra/SD input file for

```
solution
{ifdef(preload)}
case preload
  receive_sierra_data
  load = 0
  {ifdef(no_geom_stiff)}
  no_geom_stiff
  {endif}
  {ifdef(equilibrium)}
  include_internal_force = off
  {endif}
{endif}
case static
  statics
  solver = gdsw
  load = 10
end

GDSW
END

file
  geometry_file '{geomFile}'
end

history
  database name = '{historyFile}'
  sideset = surface_1000
  displacement
end

outputs
  disp
  stress
end

boundary
  nodeset 1 x=0 y=0
  nodeset 2 y=0
  block 1 2 z=0
end

BLOCK 1
  material aluminum
END
```

```
BLOCK 2
  material stiff
END

MATERIAL aluminum
  E 7.8e7
  nu = 0.0
  density 2.59e-2
END

MATERIAL stiff
  E 7.8e11
  nu = 0.0
  density 2.59e-2
END


LOAD 0
END

function ramp
  type = linear
  data 0 1
  data 1 1
end


load 10
{ifdef(extensionPressure)}
  sideset surface_2    traction 1 0 0 scale {extensionPressure}
{endif}
{ifdef(deflectionPressure)}
  sideset surface_1000 traction 0 1 0 scale {deflectionPressure}
{endif}
end

ECHO
  input
END
```

11.20.2. Files for Preloaded Eigen Comparison to Abaqus

Sierra/SM input file

```
Begin sierra  cylinder only
  title  Membrane

  define direction y with vector 0.0 1.0 0.0
  define direction x with vector 1.0 0.0 0.0
  define direction z with vector 0.0 0.0 1.0
  define point origin with coordinates 0.0 0.0 0.0

  Begin definition for function zero
    type is constant
    Begin values
      0.0
    end values
  end
  Begin definition for function one
    type is constant
    Begin values
      1.0
```

```
  end values
end
Begin definition for function function_100
  type is piecewise linear
  Begin values
    0.0  0.0
    0.8  1.0
    1.0  1.0
  end values
end definition for function function_100

Begin property specification for material mat_100
   density = 0.1E-08                    # 10+3 kgm/mm3
   Begin parameters for model elastic
      youngs modulus = 6
      poissons ratio =0.3
   end parameters for model elastic
end property specification for material mat_100

Begin solid section solid_100
   strain incrementation = strongly_objective
   hourglass formulation = total
end solid section solid_100

Begin finite element model plate
  Database name = bar.exo
  Database type = exodusII
  component separator character = ""
  Begin parameters for block block_100
    material mat_100
    solid mechanics use model elastic
    section = solid_100
  end parameters for block block_100
end

Begin adagio procedure procedure_1
  Begin time control
    Begin time stepping block p0
      start time = 0.0
      Begin parameters for adagio region region_1
        number of time steps = 100
      end parameters for adagio region region_1
    end time stepping block p0
    termination time = 1.0
  end time control

  Begin adagio region region_1
    jas mode solver
    jas mode output
    jas mode reactions
    failure debug output
    logfile detail = -1

    use finite element model plate

    Begin fixed displacement
      node set = nodelist_1
      components = x,y,z
    end fixed displacement
    Begin fixed displacement
      node set = nodelist_2
      components = y,z
    end fixed displacement
    Begin prescribed displacement
      node set = nodelist_2
      component = x
      function = function_100
      scale factor = 1.0
```

```
      end prescribed displacement

      Begin results output output_1
        database name = c_adagio_preload.e
        database type = exodusII
        component separator character = ""
        at step 0 increment = 1
        nodal variables = displacement as displ
      end results output output_1
    Begin results output output_2
        database name = salinas_preload.e
        database type = exodusII
        component separator character = ""
        additional times = 1.0
        nodal variables = displacement as displ
        nodal variables = node_filter as filter
        element variables = stress as stress
        element variables = density as fiberdensity
        element Variables = element_thickness as fiberthickness
        element variables = ends_per_length as epl
        element variables = cord_modulus as fibmod
        element variables = memb_stress as memstr
        element variables = cord_ax as ax
        element variables = cord_ay as ay
      end results output output_2
      Begin solver
        Begin loadstep predictor
          type = scale_factor
          scale factor = 1.0 0.0
        end loadstep predictor
        Begin control contact
          level = 1
          target relative residual = 0.01
          acceptable relative residual = 0.1
          target relative contact residual = 0.001
          acceptable relative contact residual = 0.01
          maximum iterations = 500
          minimum iterations = 10
          lagrange initialize = none
          lagrange adaptive penalty = off
        end control contact
        Begin cg
          target relative residual = 0.005
          acceptable relative residual = 0.05
          minimum residual improvement = 0.5
          maximum iterations = 500
          minimum iterations = 10
          reset limits 70 30 10.0 0.5
          iteration print = 1
          line search actual
          preconditioner = block
        end cg
      end solver
    end adagio region region_1
  end adagio procedure procedure_1
end sierra  cylinder only
```

Sierra/SD input file

```
SOLUTION
    solver=gdsw
  case one
    receive_sierra_data
    lumped
  case two
    eigen
```

```
    nmodes all
    shift = -1000
END

FILE
geometry_file 'salinas_preload.e'
end

BOUNDARY
  nodeset 1 x=0 y=0 z=0
  nodeset 2 y=0 z=0
end

OUTPUTS
deform
end

ECHO
  mass=block
end

BLOCK 100
  material "steel"
  hex8u
  sd_factor 1.0
end
//E=6C10 @ 0.001 strain
//bulk modulus = E/[3(1-2*nu0]=16.66E=100
MATERIAL "steel"
E  6.0
nu 0.3
density 0.1E-08
end
```

11.21. Waterline of a ship

Refer to section 4.1

```
SOLUTION
    solver=gdsw
  title=' uhwm_20150113'
  waterline
  max_iterations 100
  vizoption = ensight
  tolerance_force   1e-10
  delta 1e-8
  point_a 2479.9 0. 100
  point_b 3479.9 0. 100
  point_c 2479.9 1000. 100
  load 1
END

FILE
   geometry_file 'uhwm_20150113.exo'
end

PARAMETERS
   eigen_norm=visualization
end

BOUNDARY
end

LOAD 1
  sideset 50000001
    pressure = 1
    function = 1
  body
    gravity = 0 0 -980.0
end
LOADS
end
FUNCTION 1
  name 'pressure versus depth'
  type LINEAR
  data 0.0 0.0
  data 1000.0 980e3
end
OUTPUTS
      force // applied forces
      npressure
end
HISTORY
    nodeset '500000011,'
    disp
    velocity
    acceleration
    nskip 1
end
include uhwmBlocks
include uhwmMaterials
```

11.22. Transient Convergence

Refer to section 4.2

```
SOLUTION
    solver=gdsw
  transient
  nsteps  4500
  time_step  1.0e-3
END

FILE
  geometry_file 'beam.exo'
END

OUTPUTS
END

BOUNDARY
  nodeset 1
  fixed
END

BLOCK 1
  Beam2
  material=1
  Area=0.03
  I1=0.09
  I2=0.01
  J=0.1
  orientation = 1 1 0
END

MATERIAL 1
  Isotropic
  E = 1e+07
  NU = 0.3
  density = 1
END

LOADS
  nodeset 2
  force 0 1 0
  function 1
END

ECHO
END

HISTORY
  nodeset '2'
  disp
END

FUNCTION 1
  type LINEAR
  name "test_func1"
  data 0 0
  data 1 1
  data 2 0
END
```

11.23. Modal Transient Temporal Convergence

Refer to section 4.3

```
SOLUTION
    solver=gdsw
  case dummyEigen
    eigen
      shift=-1
      nmodes 3
  case out
    modaltransient
      nsteps  4500
      time_step  1.0e-3
      nmodes 3
END

FILE
  geometry_file 'beam.exo'
end

OUTPUTS
  disp
end

BOUNDARY
  nodeset 1
  fixed
end

BLOCK 1
  Beam2
  material=1
  Area=0.03
  I1=0.09
  I2=0.01
  J=0.1
  orientation = 1 1 0
end

MATERIAL 1
  Isotropic
  E = 1e+07
  NU = 0.3
  density = 1
end

LOADS
  nodeset 2
  force 0 1 0
  function 1
end

HISTORY
  nodeset '2'
  disp
end

FUNCTION 1
  type LINEAR
  name "test_func1"
  data 0 0
  data 1 1
  data 2 0
end
```

11.24. Transient Restart Examples

11.24.1. Linear Transient in Step 1

Refer to section 4.4 for results of the tests.

```
SOLUTION
    solver=gdsw
  case eig
    eigen
    nmodes 40
    shift = -1e6
    restart=auto
  case out
    transient
    time_step 1.0e-4
    nsteps    30
    nskip=1
    restart=WRITE
    load=1
END
FILE
  geometry_file  ninjabot.exo
end
BOUNDARY
end
LOAD 1
  sideset 28 pressure 100 function 1
  sideset 30 pressure 100 function 1
end
Function 1
  type Linear
  name "test_func1"
    data 0 0
    data 1 1
end

History
  nskip 1
  sideset 28
  disp
end
Outputs
  disp
  velocity
end

Tied Joint
  Normal Definition = slip
  surface 13 14
  search tolerance = 1e-6
  connect to block 50
end
  Tied Joint
  Normal Definition = slip
  surface 16 17
  search tolerance = 1e-6
  connect to Block 51
end
RigidSet set1
  sideset 30
  sideset 31
  sideset 32
end
Tied Data
  surface 20, 21
```

```
  search tolerance =1e-3
end
Tied Data
  surface 22, 23
  search tolerance =1e-3
end
Tied Data
  surface 24, 26
  search tolerance =1e-3
end
Tied Data
  surface 25, 27
  search tolerance =1e-3
end
Tied Data
  surface 28, 29
  search tolerance =1e-3
end
Tied Data
  surface 40, 41
  search tolerance =1e-3
end
Tied Data
  surface 42, 43
  search tolerance =1e-3
end
Tied Data
  surface 42, 44
  search tolerance =1e-3
end
MATERIAL "steel"
  E 30e6
  nu 0.3
  density 0.288
end
MATERIAL 'dead'
  isotropic
  E = 1
  nu = 0.29
  density = 0
end

MATERIAL 'aluminum'
  isotropic
  E = 10e6
  nu = 0.45
  density = 0.27
end

Block 1 2 3 4 5 6 7 8 9 10
  material 'aluminum'
end

Block 11 12 15
  material "steel"
end

Block 16
  RBAR
end

Block 17
  RBAR
end

Block 18
  conmass
  MASS = 100
```

```
end

Block 19
  conmass
  MASS = 100
end

Block 20
  superelement
  file = 'super_sword.ncf'
  map locations
end

Block 21
  superelement
  file = 'super_shield.ncf'
  map locations
end

Block 50
  Joint2g
  kx = iwan 1
  ky = iwan 1
  krz = elastic 1.0e9
end

Block 51
  Joint2g
  kx = iwan 1
  ky = iwan 1
  krz = elastic 1.0e9
end

Property 1
    chi -.82
    phi_max = 1.75e-4
    R = 5.5050e+6
    S = 2.1097e+6
end
```

11.24.2. Restarted Modal Transient in Step 2

```
SOLUTION
    solver=gdsw
  case eig
    eigen
    nmodes 40
    shift = -1e6
    restart=auto
  case out
    modaltransient
    time_step 1.0e-4
    nsteps    40
    nskip=1
    restart=READ
    load=1
END
FILE
  geometry_file  ninjabot.exo
end
BOUNDARY
end
LOAD 1
  sideset 28 pressure 100 function 1
  sideset 30 pressure 100 function 1
end
```

```
Function 1
  type Linear
  name "test_func1"
    data 0 0
    data 1 1
end

History
  nskip 1
  sideset 28
  disp
end
Outputs
  disp
  velocity
end

Tied Joint
  Normal Definition = slip
  surface 13 14
  search tolerance = 1e-6
  connect to block 50
end
  Tied Joint
  Normal Definition = slip
  surface 16 17
  search tolerance = 1e-6
  connect to Block 51
end
RigidSet set1
  sideset 30
  sideset 31
  sideset 32
end
Tied Data
  surface 20, 21
  search tolerance =1e-3
end
Tied Data
  surface 22, 23
  search tolerance =1e-3
end
Tied Data
  surface 24, 26
  search tolerance =1e-3
end
Tied Data
  surface 25, 27
  search tolerance =1e-3
end
Tied Data
  surface 28, 29
  search tolerance =1e-3
end
Tied Data
  surface 40, 41
  search tolerance =1e-3
end
Tied Data
  surface 42, 43
  search tolerance =1e-3
end
Tied Data
  surface 42, 44
  search tolerance =1e-3
end
MATERIAL "steel"
  E 30e6
```

```
  nu 0.3
  density 0.288
end
MATERIAL 'dead'
  isotropic
  E = 1
  nu = 0.29
  density = 0
end

MATERIAL 'aluminum'
  isotropic
  E = 10e6
  nu = 0.45
  density = 0.27
end

Block 1 2 3 4 5 6 7 8 9 10
  material 'aluminum'
end

Block 11 12 15
  material "steel"
end

Block 16
  RBAR
end

Block 17
  RBAR
end

Block 18
  conmass
  MASS = 100
end

Block 19
  conmass
  MASS = 100
end

Block 20
  superelement
  file = 'super_sword.ncf'
  map locations
end

Block 21
  superelement
  file = 'super_shield.ncf'
  map locations
end

Block 50
  Joint2g
  kx = iwan 1
  ky = iwan 1
  krz = elastic 1.0e9
end

Block 51
  Joint2g
  kx = iwan 1
  ky = iwan 1
  krz = elastic 1.0e9
end
```

```
Property 1
    chi -.82
    phi_max = 1.75e-4
    R = 5.5050e+6
    S = 2.1097e+6
end
```

11.25. Eigenvalue Restart with Virtual Nodes and Elements

Refer to section 2.4

```
SOLUTION
    solver=gdsw
  case grbm
    geometric_rigid_body_modes
  case eig
    eigen
  shift = -1e5
  restart=write
END
FILE
geometry_file 'ninja_SE_IE_TJ.exo'
end

BOUNDARY
end

LOADS
  sideset 101
    pressure 1.0
    function 1
end

Parameters
  num_rigid_mode 6
  eig_tol = 1.0e-16
end

FUNCTION 1
  type LINEAR
  name "test_func1"
    data 0 0
    data 1 1
end

OUTPUTS
disp
end

TIED JOINT
Normal Definition = slip
surface 13 14
search tolerance = 1e-6
connect to block 50
end

TIED JOINT
  Normal Definition = slip
  surface 16 17
  search tolerance = 1e-6
connect to Block 49
end

RIGIDSET set1
sideset 30
sideset 31
sideset 32
end

TIED DATA
  surface 20, 21
  search tolerance =1e-3
end
```

```
TIED DATA
  surface 22, 23
  search tolerance =1e-3
end

TIED DATA
  surface 24, 26
  search tolerance =1e-3
end

TIED DATA
  surface 25, 27
  search tolerance =1e-3
end

TIED DATA
  surface 28, 29
  search tolerance =1e-3
end

TIED DATA
  surface 40, 41
  search tolerance =1e-3
end

TIED DATA
  surface 42, 43
  search tolerance =1e-3
end

TIED DATA
  surface 42, 44
  search tolerance =1e-3
end

///////  tying new sword together   /////

MATERIAL "steel"
E 30e6
nu 0.3
density 0.288
end

MATERIAL 'dead'
 isotropic
  E = 1
  nu = 0.29
  density = 0
end

MATERIAL 'aluminum'
isotropic
E = 10e6
nu = 0.45
density = 0.27
end

MATERIAL 'kevlar'
isotropic
E = 83e6
density = .143
nu = 0.36
end

MATERIAL "steel_5"
  E 30e6
  nu .3
  density 0.288
```

```
end

MATERIAL 6
  E 20e3
  nu 0.3
  density 0.288
end

MATERIAL 7
  E 40e8
  nu 0.3
  density 0.288
end

MATERIAL 8
  E 20e4
  nu 0.3
  density 0.288
end

MATERIAL 9
  E 30e6
  nu 0.3
  density 0.15
end

MATERIAL 10
   acoustic
   density = 997
   c0 = 1497
end


BLOCK 1
material 'aluminum'
end

BLOCK 2
material 'aluminum'
end

BLOCK 3
  material 'aluminum'
end

BLOCK 4
material 'aluminum'
end

BLOCK 5
  material 'aluminum'
end

BLOCK 6
  material 'aluminum'
end

BLOCK 7
  material 'aluminum'
end

BLOCK 8
  material 'aluminum'
end

BLOCK 9
  material 'aluminum'
end
```

```
BLOCK 10
  material 'aluminum'
end

BLOCK 15
  material "steel"
end

BLOCK 16      ///beams
RBAR
// material "steel"
end

BLOCK 17     ///beams
RBAR
// material "steel"
end

BLOCK 18
  conmass
MASS = 100
end

BLOCK 19
  conmass
MASS = 100
end


BLOCK 11
  material "steel"
end

BLOCK 12
  material "steel"
end

BLOCK 51
  dead
  material "steel_5"
  thickness 0.75
end

BLOCK 52
  dead
  material 6
  thickness 0.5
end

BLOCK 53
  dead
  material 7
  thickness 0.5
end

BLOCK 54
  dead
  material "steel"
  I1 = 100
  I2 = 200
j = 100
  orientation = 0 0 1
end

BLOCK 60
  dead
  material 9
```

```
end

BLOCK 61
  dead
  material 8
end

BLOCK 62
  dead
  material 9
end

BLOCK 50
joint2g
kx = iwan 1
ky = iwan 1
krz = elastic 1.0e9
end

BLOCK 49
  joint2g
  kx = iwan 1
  ky = iwan 1
  krz = elastic 1.0e9
end

BLOCK 100
dead
  material 10
end

PROPERTY 1
    chi -.82
    phi_max = 1.75e-4
    R = 5.5050e+6
    S = 2.1097e+6
end

GDSW
  solver_tol 1.0e-12
end
```

11.26. Filter Rigid Modes from Loads

Refer to section 2.5

```
SOLUTION
    solver=gdsw
  statics
END


FILE
geometry_file 'temp1/beam_hex8.par'
// geometry_file 'beam_hex8.exo'
END

BOUNDARY
END

PARAMETERS
  FilterRbmLoad=allStructural
  rbmtolerance=1e-6
  num_rigid_mode 6
END

GDSW
  prt_summary = 3
END

LOADS
        sideset 1
              traction = 0 1000.0 0
END

OUTPUTS
disp
  force
  rhs
END

ECHO
 none
END


BLOCK 1
material "steel"
         hex8u
END

MATERIAL "steel"
E 30.0e6
nu 0.0
density 0.288
END
```

11.27. Modal Transient

Refer to section 4.5

```
//salinas input created using pat2exo from patran file 'vtube.out'
SOLUTION
    solver=gdsw
  case rig
    geometric_rigid_body_modes
  case eig1
   restart=none
   eigen nmodes=10
   shift=-1.e8
  case filter1
   modalfiltercase
   modalfilter norot
  case one
   modaltransient
   time_step=0.001
   nsteps=400
   load=1
  case four
   modaltransient
   time_step=0.001
   nsteps=2000
   load=4
  title 'verification of modal solution'
END

modalfilter norot
   add all
   remove 4,5,6,9
end

modalfilter norbm
   add 7:10
end

HISTORY
    block 101
    disp
    acceleration
END

DAMPING
//  gamma=0.01
END

PARAMETERS
 wtmass=0.00259
 num_rigid_mode 6
END

FILE
   geometry_file 'temp1/modaltransver.exo'
END

BOUNDARY
//  nodeset 124
//  fixed
//  rotx=0 roty=0 rotz=0 x=0 z=0
//    fixed
//  nodeset 25
//    fixed
//  nodeset 26
//    fixed
```

```
END

LOAD=1
   nodeset 12
      force = 0 0 1
      scale 1e5
      function 10
END

LOAD=4
   nodeset 12
      force = 0 0 1
      scale 1e5
      function 2
END

function 10
   type linear
   name constant
   data 0.0 1.
   data 1.0 1.
end

function 1
  type linear
  name 'triangle 1'
  data 0.0 0.0
  data 1.5e-2 1
  data 3e-2 0
  data 1 0
end

function 2
  type linear
  name 'triangle'
  data 0.0 0.0
  data 1e-2 1
  data 2e-2 0
  data 1 0
end
OUTPUTS
        disp
END

ECHO
      mass
    modalvars
END

BLOCK 101
   material 101
  quadt
   thickness= 0.200000003E+00
   // patran/exo type 'QUAD'/QUAD. Number nodes 4
END

BLOCK 102
//   material 0
  ConMass
    Mass=1000
    Ixx =0
    Ixy =0
    Iyy =0
    Ixz =0
    Iyz =0
    Izz =0
    Offset= 0 0 0
   // patran/exo type 'BEAM'/BEAM. Number nodes 2
```

```
END

Block 1000
    RBE3  // RBE type elements
    // # links 16
END
Block 1001  // not used
   material=1000
   beam2
   area=1
   i1=.1
   i2=.1
   j=.2
   orientation=1 0 .10
end

MATERIAL 101
   // material type 'Iso'
   density=0.1
   Isotropic
   E=1e+07
   nu=0.35
END

MATERIAL 1000
   // material type 'Iso'
   density=0.1e-5
   Isotropic
   E=1e+09
   nu=0.35
END
```

11.28. Sensitivity to Parameters

Refer to section 2.6

```
//salinas input created using nasgen from nastran file 'springrbar.bdf'
SOLUTION
    solver=gdsw
  case sens
  title 'two hexes, connected by tied joint'
   eigen nmodes=1

END

FILE
//   geometry_file 'twoHex.exo'
   geometry_file 'twoHex.exo'
END

sensitivity
   values = all
end

gdsw
  solver_tol=1e-12
  prt_debug=2
  orthog_option 0
end


PARAMETERS
// wtmass=0.00259
//   eigen_norm=visualization
END

BOUNDARY
    sideset 2  // nastran SID=2
        fixed
    sideset 4  // nastran SID=2
        fixed
    sideset 1
        y=0 x=0
END

LOADS
END

OUTPUTS
        disp
END

ECHO
END

BLOCK 1
   material 1
END

BLOCK 2
   material 2
END

material 1
   E=10e6
   nu=0.0
   density = 0.000256
end
```

```
material 2
   E=20e6
   nu=0.0
   density = 0.000256
end

tied joint
  normal definition = none
    surface 1,3
    search tolerance = 0.02
    connect to block 13
    side = average
end

block 13
   joint2g
   Kx = elastic 1e8
   Ky = elastic 1e8
   Kz = elastic 1e7  +/- 10 %
   Krx = elastic 1e8
   Kry = elastic 1e8
   Krz = elastic 1e8
End
```

11.29. Sensitivity Analysis with a Superelement

Refer to section 2.7

```
SOLUTION
    solver=gdsw
  title 'sensitivity of system with CBR model'
  eigen nmodes=20
END
FILE
   geometry_file blade1_residual_se.exo
end
PARAMETERS
   eigen_norm=visualization
end
BOUNDARY
    nodeset 11
        fixed
end


OUTPUTS
        disp
end
ECHO
      mass
      input
end
BLOCK 13
   // 1 element of type SHELL. 4 nodes/element
   // property card 'PSHELL   1       '
   dead
   material=3001
   thickness=0.111
end
BLOCK 17
   // 2 elements of type SPHERE-MASS. 1 node/element
   // no property card
   ConMassA
   // 'CONM2    4800719'
   mass=11268.5
   Ixx=0
   Iyy=0
   Izz=0
   Ixy=0
   Ixz=0
   Iyz=0
   offset=0 0 0
end
BLOCK 480000
   // 6 elements of type BEAM. 2 nodes/element
   // property card 'PBAR     48000   '
   material=48001
   Area=0.05693
   I1=0.00374
   I2=0.00374
   J=0.00749
end
BLOCK 480020
   // 14 elements of type TRIANGLE. 3 nodes/element
   // property card 'PSHELL   48002   '
   material=48000
   thickness=0.0254
end
BLOCK 480023
   // 209 elements of type SHELL. 4 nodes/element
   // property card 'PSHELL   48002   '
```

```
   material=48000
   thickness=0.0254
end
BLOCK 480024
    superelement
    file='blade1_se.ncf'
    diagnostic=0
    sensitivity_param 1 = 2.04e11  // E
    sensitivity_param 2 = 8017.2
    map locations
end
MATERIAL  3001
   // from 'MAT1     3001   '
   Isotropic
   E=2e+11
   NU=0.3
   density=7861.06
end
MATERIAL  48000
   // from 'MAT1     48000  '
   Isotropic
   E=2e+11
   NU=0.29
   density=7860
end
MATERIAL  48001
   // from 'MAT1     48001  '
   Isotropic
   E=2e+11
   NU=0.29
   density=7860
end
```

11.30. Shock Tube SI

Refer to section 2.8

```
SOLUTION
    solver=gdsw
    nltransient
    tolerance 1.0e-8
    time_step 4e-05
    nsteps 400
END

FILE
    geometry_file 'temp1/shocktube_SI.par'
END

LOADS
    sideset 4
    acoustic_vel = -5
    function = 1
END

BOUNDARY
    sideset 6
    absorbing
END

HISTORY
    node_list_file 'nodeshock'
    apressure
END

FUNCTION 1
   type analytic
   name "sine 1000"
   evaluate expression = "omega = 2 * pi * 1000; sin(omega*t)"
END

OUTPUTS
END

ECHO
NLresiduals
END

BLOCK 1
material "air"
END

MATERIAL "air"
density 1.1934
        acoustic
        nonlinear
        c0 343.2048
        B_over_A 0.4
END

GDSW
   solver_tol 1.0e-8
   prt_summary 0
END
```

11.31. Fluid Structure Interaction Added Mass

Refer to section 4.6

```
SOLUTION
    solver=gdsw
  case 'qevp'
    qevp
       method=sa_eigen
       nmodes = 400
       nmodes_acoustic=100
       nmodes_structure=100
       shift = -1.e+5
       sort method= magnitude
       reorthogonalize=yes
      check_diag=yes
END

FILE
 //  geometry_file addedmass_shell_0.01_sphere.exo
   geometry_file temp1/addedmass_shell_0_01_sphere.par
END

BOUNDARY
   sideset 1
   fixed
nodeset 1
fixed
   nodeset 10
      y=0 x=0 rotx=0 roty=0 rotz=0
END

OUTPUTS
        disp
END

ECHO
disp
mass = block
END

BLOCK 1
material "steel"
quadT
thickness = 0.1
        membrane_factor 0.0005
END

BLOCK 3
        material "water"
END

BLOCK 4
material "water"
END

BLOCK 5
material "water"
END

BLOCK 2
// name "spring"
// Coordinate 1
         spring
 kx=10000
         ky=10000
         kz=10000
```

```
END

//TIED DATA
//  surface 3,2
//  search tolerance = 1e-1
//END

MATERIAL "steel"
E 19.5e9
nu .3
density 7700.0
END

MATERIAL "water"
density 1000
        acoustic
        c0 1500
END

GDSW
  solver_tol 1e-11
  overlap = 3
  prt_memory yes
  prt_timing yes
END
```

11.32. Fluid Structure Cavitation

Refer to section 4.7

```
SOLUTION
    solver=gdsw
     transient
     time_step = 1.313e-5
     nsteps 1200
     rho = 0.8
     scattering
END

FILE
  geometry_file 'Plate_fluid_shell.exo'
END

damping
  beta = 1.5e-5
end

Frequency
  freq_min = 1.0
  freq_step = 2.0
  freq_max = 80.0
  apressure
  block 1
End

OUTPUTS
apressure
velocity
END


HISTORY
    block all
    apressure
    velocity
    nskip  10
END


ECHO
END

BOUNDARY
  sideset 10
    infinite_element
    use block 111
sideset 5
        x=0 z=0 rotx=0 rotz=0
sideset 4
        x=0 z=0 rotx=0 rotz=0
sideset 2
        x=0 z=0 rotx=0 rotz=0
sideset 3
        x=0 z=0 rotx=0 rotz=0
END

TIED DATA
   Surface 1, 6
    search tolerance =1e-3
END

FUNCTION 3
  type planar_step_wave
```

```
  direction 0 1 0
  material "water"
  origin 0 149 0
  beta = 1.0042e3
END

LOADS
    sideset 1
       acoustic_vel = 103
       function = 3
    sideset 6
       pressure = 103
       function = 3
END

BLOCK 1
     quadT
        material "Steel"
        thickness = 1.0
END

BLOCK 2
        material "water"
END

Block 111
       infinite_element
       radial_poly legendre
       order 3
       ellipsoid_dimensions 20000 20000  20000
       source_origin = 0 19850 0
END

MATERIAL "Steel"
        E 30e6
        nu 0.3
density 5.32986e-4
//        density 0.288
END

MATERIAL "water"
        density 9.3455e-5
        c0 57120
        acoustic
END

GDSW
        solver_tol = 1e-8
END
```

11.33. Higher Order Hex Acoustic Element Convergence

Refer to section 5.13

```
SOLUTION
    solver=gdsw
   eigen
   nmodes 10
   shift = -1.e4
END

FILE
geometry_file 'temp1/wg_hex2.par'
// geometry_file '1/wg_hex5.par'
END

BOUNDARY
END

LOADS
END

OUTPUTS
  globals
END

ECHO
END


BLOCK 1
pelement
order=3
material "steel"
END

MATERIAL "steel"
acoustic
c0 332.0
density 1.3
END

PARAMETERS
  usepelements
END

GDSW
  solver_tol 1.0e-12
  orthog 0
  sc_option no
END
```

11.34. Higher Order Tet Acoustic Element Convergence

Refer to section 5.14

```
SOLUTION
    solver=gdsw
   eigen
   nmodes 10
   shift = -1.e3
END

FILE
geometry_file 'temp1/wg_tet2.par'
END

BOUNDARY
END

LOADS
END

OUTPUTS
   globals
END

ECHO
END


BLOCK 1
pelement
order=3
material "steel"
END

MATERIAL "steel"
acoustic
c0 332.0
density 1.3
END

PARAMETERS
  usepelements
END

GDSW
  solver_tol 1.0e-12
  orthog 0
  sc_option no
END
```

11.35. Tied-Joint with Joint2G and Spring

Inputs for comparison of manually generated constraints with TiedJoint.

11.35.1. Manual Constraints

```
SOLUTION
    solver=gdsw
 eigen
 nmodes=20
 shift=-1e7
END

FILE
geometry_file lap_simple.exo
END

OUTPUTS
disp
END

ECHO
mpc
END

BLOCK 1
material "mat"
END
BLOCK 2
material "mat"
END
BLOCK 3
dead
END

Block 33
   spring
    kx=20776000
        ky=20776000
        kz=26080000
END

HISTORY
 sideset 1,2
 displacement
END

Rigidset 1
    sideset 1
end
Rigidset 2
    sideset 2
end

MPC
 254 x 1
 207 x -1
END

MPC
 254 y 1
 207 y -1
END

MPC
```

```
 254 z 1
 207 z -1
END

MPC
 253 x 1
 58 x -1
END

MPC
 253 y 1
 58 y -1
END

MPC
 253 z 1
 58 z -1
END

MATERIAL "mat"
E 200e9
nu 0.3
    density 7800
END

BOUNDARY
    sideset 3
       fixed
END

LOADS
    sideset 4
        pressure = -1e3
        function = 1
END

FUNCTION 1
       type LINEAR
       name "const_one"
       data 0.0 1.0
       data 2.0e4 1.0
END
```

11.35.2. Tied Joint Constraints

Refer to section 5.15 for details of the test.

```
SOLUTION
    solver=gdsw
 eigen
 nmodes=20
 shift=-1e7
restart=write
END

FILE
    geometry_file lap_tied_spring_slip.exo
END

OUTPUTS
disp
END

ECHO
```

```
mpc
input
END

Tied Joint
    Normal Definition = slip
        surface 1,2
        side = rrod
        connect to Block 33
end

BLOCK 1
material "mat"
END

BLOCK 2
material "mat"
End

BLOCK 3
  dead
END

BLOCK 33
   spring
        kx=20776000
        ky=20776000
        kz=26080000
END



HISTORY
 sideset 1,2
 displacement
END


MATERIAL "mat"
E 200e9
nu 0.3
    density 7800
END


BOUNDARY
    sideset 3
       fixed
END

LOADS
    sideset 4
        pressure = -1e3
        function = 1
END

FUNCTION 1
       type LINEAR
       name "const_one"
       data 0.0 1.0
       data 2.0e4 1.0
END
```

11.36. Beam CBR

Refer to section 2.9 for details of the test.

```
SOLUTION
cbr
        nmodes=90
title 'single beam model. 100 elements. xy only'
END

FILE
geometry_file 'beam100b.exo'
END

cbmodel
   file=beamcbr.ncf
   format=netcdf
   nodeset 1
end

BOUNDARY
    nodeset 3
      y = 0
      z = 0
      rotx = 0
      roty = 0
      rotz = 0
END

LOADS
END

OUTPUTS
     deform
END

ECHO
END



BLOCK 1
material 'Aluminum'
Beam2
Area 0.1
orientation 0 .1 0
I1 .2
I2 .3
J .5
END

Material 'Aluminum'
E 10.0E6
nu 0.33
density 253.82e-6
END
```

11.37. Slide RBE2. Selected DOFS

Refer to section 5.16 for details of the test.

```
//created with Nasgen from Nastran file 'sliderbe.nas'
SOLUTION
  title=' NEi Nastran Static Analysis Set'
  statics
END

FILE
  geometry_file 'sliderbe.exo'
END

PARAMETERS
  eigen_norm=visualization
END

BOUNDARY
  nodeset 11  x=0
  nodeset 12  y=0
  nodeset 13  z=0
  nodeset 14  Rotx=0
  nodeset 15  Roty=0
  nodeset 16  Rotz=0
END

LOADS
  nodeset 112
    force = 0 1 0
END

OUTPUTS
  disp
END

ECHO
  mass
END

BLOCK 13
  material=1
  thickness=0.5
END

BLOCK 23
  material=1
  thickness=0.375
END

BLOCK 24
  // 25 links
  RBAR
END

MATERIAL 1
  Isotropic
  E = 3e+07
  NU = 0.3
  density = 0.0007324
END
```

11.38. Thin Plate Bending

Refer to section 5.17 for details of the test.

```
//salinas input created using nasgen from nastran file 'bending.nas'
SOLUTION
    solver=gdsw
  title=' NEi Nastran Static Analysis Set'
   statics
END

GDSW
    solver_tol=1.0e-10
END

FILE
   geometry_file 'bending.exo'
END


PARAMETERS
// wtmass=0.00259
   eigen_norm=visualization
END

BOUNDARY
    nodeset 11  // nastran SID=1
        fixed
END

LOADS
  sideset 1
      pressure 1.0
END

OUTPUTS
        disp
        stress
        genergies
END

ECHO
      input
      mass
END

BLOCK 13
   material=1
   thickness=0.5
   { QUAD }
END

MATERIAL        1
   Isotropic
   E = 3e+07
   NU = 0.3
   density = 0.0007324
END
```

11.39. Modal Force on a Biplane Model

Refer to section 2.10 for details of the test.

```
SOLUTION
    solver=gdsw
   case eig2
      eigen
      shift=-1e5
      nmodes=30
   case two
     modaltransient
     nsteps 260
     time_step 1e-3
     load=10
END

FILE
//   geometry_file 'biplane.exo'
   geometry_file 'biplane.exo'
END

LOAD 10
  body
    modalforce
    function 60
END

FUNCTION 60
  type table
    tablename 35
END

TABLE 35
   dimension 2
   size 260 30
   delta 1e-3 1
   origin 1e-3 0
   datafile=ModalForces.txt
END



BOUNDARY
END

OUTPUTS
        disp
END

ECHO
  mass
  modalvars
END

GDSW
        krylov_method=1
        max_iter=2000
        solver_tol=1e-10
        orthog=2000
        prt_summary=1
        prt_debug=1
        prt_timing 1
        coarse_option 0
END
```

```
BLOCK 1 //tail stalk (hex8)
        material "aluminum"
        hex8b
END

BLOCK 2 //main body (hex20)
        material "beam-titanium"
        hex20
END

BLOCK 3 //tail side fins (tetra10)
        material "aluminum"
        tet10
END

BLOCK 4 //tail top fin (tetra4)
        material "aluminum"
        tet4
END

BLOCK 5 //top wing (shell8)
        material "miraculum-steel"
        quad8T
        thickness=0.3
END

BLOCK 6 //bottom wing (tria6)
        material "miraculum-steel"
        tria6
        thickness=0.3
END

BLOCK 7 //upper main beams (beam2)
        material "beam-titanium"
        beam2
END

BLOCK 8 //lower main beams (beam2)
        material "beam-titanium"
        beam2
END

BLOCK 9 //side trusses (truss)
        material "beam-titanium"
        truss
END

BLOCK 10 //Upper main beam rbe3s
        rbe3
END

BLOCK 11 //Upper main beam rbe3s
        rbe3
END

BLOCK 12 //Upper main beam rbe3s
        rbe3
END

BLOCK 13 //Upper main beam rbe3s
        rbe3
END

BLOCK 14 //Upper main beam rbe3s
        rbe3
END

BLOCK 15 //Upper main beam rbe3s
```

```
        rbe3
END

BLOCK 16 //Upper main beam rbe3s
        rbe3
END

BLOCK 17 //Upper main beam rbe3s
        rbe3
END

BLOCK 18 //Lower main beam rbe3s
        rbe3
END

BLOCK 19 //Lower main beam rbe3s
        rbe3
END

BLOCK 20 //Lower main beam rbe3s
        rbe3
END

BLOCK 21 //Lower main beam rbe3s
        rbe3
END

BLOCK 22 //Lower main beam rbe3s
        rbe3
END

BLOCK 23 //Lower main beam rbe3s
        rbe3
END

BLOCK 24 //Lower main beam rbe3s
        rbe3
END

BLOCK 25 //Lower main beam rbe3s
        rbe3
END

BLOCK 26 //Side truss rbe3s
        rbe3
END

BLOCK 27 //Side truss rbe3s
        rbe3
END

BLOCK 28 //Side truss rbe3s
        rbe3
END

BLOCK 29 //Side truss rbe3s
        rbe3
END

BLOCK 30 //Side truss rbe3s
        rbe3
END

BLOCK 31 //Side truss rbe3s
        rbe3
END

BLOCK 32 //Side truss rbe3s
```

```
        rbe3
END

BLOCK 33 //Side truss rbe3s
        rbe3
END

BLOCK 34 //Blades (quad8)
        material "miraculum-steel"
        quad8T
        thickness=0.15
END

BLOCK 35 //Beams on Propellar Blades (rbars)
        rbar
END

BLOCK 36 //Propellar Body (tri6)
        material "titanium"
        tria6
        thickness=0.1
END

BLOCK 37 //Beam in center of Propellar Body (rbar)
        material "miraculum-steel"
        beam2
END

BLOCK 38 //rbars connecting blades to center beam
        rbar
END

BLOCK 39 //surface on fin
        material "aluminum"
        tria3
        thickness=0.05
END

BLOCK 40 //rear surface of tailstalk (quadT)
        material "aluminum"
        quadT
        thickness=0.05
END

BLOCK 41 //cone connecting beams
        material "miraculum-steel"
        beam2
END

BLOCK 42 //cone connecting beams
        material "miraculum-steel"
        beam2
END


TIED DATA
  surface 1,6 //tail stalk to main body
END
TIED DATA
  surface 2,7 //top fin to top of tailstalk
END
TIED DATA
  surface 3,9 //right fin to tailstalk
END
TIED DATA
  surface 4,8 //left fin to tailstalk
END
```

```
MATERIAL "aluminum"
E 72e9 //(N/m^2)
        nu .33
        density 2700 //(kg/m^3)
END

MATERIAL "titanium"
E 105e9 //(N/m^2)
nu 0.33
density 4510 //(kg/m^3)
END

MATERIAL "miraculum-steel"
        E 200e10 //(N/m^2)
        nu 0.3
        density 7.850 //(kg/m^3)
END

MATERIAL "beam-titanium"
E 105e9 //(N/m^2)
nu 0.33
density 4.510 //(kg/m^3)
END
```

11.40. Lighthill Analogy - Helmholtz Resonator

Refer to section 2.11 for details of the test.

```
SOLUTION
    solver=gdsw
  transient
    time_step 0.5e-3
    nsteps 500
END
File
   geometry_file temp1/lighthill_helmholtz_resonator_ns.par
end
Loads
  nodeset 1
  lighthill = 1.0
  function = 1
end
Damping
alpha 50
end
Function 1
  type readnodalset
  nodeset 1
  name "divT"
  exo_var vector divT
  interp = linear
end
Boundary
sideset 13 absorbing radius = 100
end
History
   node_list_file nodelist1873
   aforce
   apressure
end

Outputs
end

Block 1
material 1
end

Block 2
material 1
end

MATERIAL 1
acoustic
density 1.2256e-3
c0 34300 // cm/s
end

Tied Data
surface 1, 10
End

Tied Data
surface 2, 11
End

Tied Data
surface 3, 12
End
```

11.41. Lighthill Tensor Verification Input

Refer to section 2.12 for details of the test.

```
SOLUTION
    solver=gdsw
    solver=gdsw
  transient
    time_step 0.5
    lumped_consistent
    nsteps 600
END

LINESAMPLE
  samples per line 1000
  endpoint -500. 0. 0. 500. 0. 0.
  format exodus
END

FILE
  geometry_file temp1/lighthill_waveguide_1000x1x1_pulse.par
END

LOADS
  nodeset 1
  lighthill = 1
  function = 1
END

FUNCTION 1
  type readnodalset
  nodeset 1
  name "divT"
  exo_var vector divT
  interp = linear
END

BOUNDARY
  sideset 1
    absorbing
END

OUTPUTS
  apressure
  aforce
END

ECHO
END

BLOCK 1
  material 1
END

MATERIAL 1
  acoustic
  density 1
  c0 1
END
```

11.42. Acoustic Point Source in Frequency Domain

Refer to section 2.13 for details of the test.

```
SOLUTION
    directfrf
END

FILE
   geometry_file 'point_source.exo'
END

Frequency
  freq_min = 1.0
  freq_step = 10.0
  freq_max = 150.0
  sideset 1
  pressure
End

LOADS
    nodeset 1
    point_volume_vel = 1.0
    function = 2
END

DAMPING
  beta 1.0e-5
END

BOUNDARY
  sideset 1
    absorbing
    radius 2.0
END

FUNCTION 2
       type LINEAR
       name "test_func1"
       data 0.0 1.0
       data 5.0e9  1.0
END

OUTPUTS
 apressure
END

ECHO
END

BLOCK 1
    material "air"
END

MATERIAL "air"
        density 1.293
        acoustic
        c0 343.0
END

GDSW
  solver_tol 1.0e-8
  prt_summary 3
  max_previous_sols 10
  cull_method eigen
  orthog 40
  num_GS_steps 2
```

```
END
```

11.43. Acoustic Point Source in Time Domain

Refer to section 2.14 for details of the test.

```
SOLUTION
     transient
     time_step 1.0e-4
     nsteps 1000
     rho 0.7
END

FILE
   geometry_file 'point_source.exo'
END

LOADS
    nodeset 1
    point_volume_vel = 1.0
    // point_volume_accel = 1.0
    function = 1
END

DAMPING
    beta 1.0e-5
END

BOUNDARY
  sideset 1
    absorbing
    radius 2.0
END

FUNCTION 1
   type analytic
   evaluate expression = "omega = pi * 50; sin(omega*time)"
END

OUTPUTS
 apressure
END

ECHO
END

BLOCK 1
material "air"
END

MATERIAL "air"
        density 1.293
        acoustic
        c0 343.0
END


GDSW
  solver_tol 1.0e-10
END
```

11.44. Acoustic Plane Wave Scattering in Frequency Domain

Refer to section 2.15 for details of the test.

```
# rho0 = {rho0 = 1.21}
# c0 = {c0 = 343.0}
# vscale = {vscale = 1/(rho0*c0)}

SOLUTION
    directfrf
    scattering
    solver=gdsw
END

FILE
    geometry_file mie/cylinderScatterer.exo
END

Frequency
    freq_min = 1000.0
    freq_step =100.0
    freq_max = 1000.0
    block 1,2
    apressure
    disp
End

LOADS
    sideset 2
        acoustic_vel = 1.0
        scale = {vscale}
        function = 1
    sideset 2
        iacoustic_vel = 1.0
        scale = {vscale}
        function = 2
    sideset 3
        pressure = 1
        scale = {vscale}
        function = 1
    sideset 3
        ipressure = 1
        scale = {vscale}
        function = 2
END

BOUNDARY
    nodeset 1
        z = 0
    sideset 1
        pml_element
        use block 326
        hex
END

BLOCK 326
    pml_element
    stack_depth 20
    source_origin 0 0 0
    ellipsoid_dimensions 0.8 0.8 1000
    pml_thickness 0.00025
    loss_function = polynomial
    loss_params = 0 6000 6000 6000
END

Function 1
    type plane_wave_freq
```

```
    Material "air"
    Direction 1.0 0.0 0.0
    Origin 0 0 0
END
Function 2
    type iplane_wave_freq
    Material "air"
    Direction 1.0 0.0 0.0
    Origin 0 0 0
END

TIED DATA
    Surface 2,3
END

OUTPUTS
    deform
    apressure
END

ECHO
END

BLOCK 1
    material "air"
END

BLOCK 2
    material "steel"
END

MATERIAL "air"
    acoustic
    density {rho0}
    c0 {c0}
END

MATERIAL "steel"
    E 19.5e10
    nu 0.3
    density 7700.0
END

GDSW
    solver_tol 1.0e-11
    overlap 1
    SC_optionH yes
    max_iter 100
END
```

11.45. Superelement Superposition

Refer to section 2.16 for details of the test.

11.45.1. Full Model

```
//salinas input created using nasgen from nastran file 'trusses-4.bdf'
SOLUTION
  title=' MSC.Nastran job created on 02-Apr-12 at 16:56:43'
  case full
  transient
     time_step=1e-5
     nsteps=1000
     load=1
END

FILE
   geometry_file 'truss_full.exo'
END


BOUNDARY
    nodeset 11  // nastran SID=1
        x=0
    nodeset 32  // nastran SID=3
        y=0
    nodeset 33  // nastran SID=3
        z=0
END

LOAD 1
   node_list_file 'endtruss_node_list'
      force 1 0 0
      function=1
END

function 1
    type=linear
    data 0 0
    data 1e-3 1
    data 4e-3 -1
    data 5e-3 0
end

OUTPUTS
        disp
END

ECHO
      mass
END


BLOCK 12
   material=1
   Area=0.01
   Truss
END

MATERIAL  1
   // from 'MAT1     1      '
   Isotropic
   E=1e+07
   NU=0
   density=0.1
```

```
END
```

11.45.2. CB Reduction

```
//salinas input created using nasgen from nastran file 'trusses-4.bdf'
SOLUTION
  title=' MSC.Nastran job created on 02-Apr-12 at 16:56:43'
  case basis
   cbr nmodes=1
   lumped
END

FILE
   geometry_file 'endtruss.exo'
END

CBMODEL
  nodeset 11
  format=netcdf
  file=endtruss.ncf
  inertia_matrix=yes
END

BOUNDARY
    nodeset 32  // nastran SID=3
        y=0
    nodeset 33  // nastran SID=3
        z=0
END

LOADS
END

OUTPUTS
        disp
        genergies
END

ECHO
      mass
END


BLOCK 12
   // 4 elements of type TRUSS. 2 nodes/element
   // property card 'PROD     1       '
   material=1
   Area=0.01
   Truss
END

MATERIAL  1
   // from 'MAT1     1       '
   Isotropic
   E=1e+07
   NU=0
   density=0.1
END
```

11.45.3. System Analysis with Superelement

```
//salinas input created using nasgen from nastran file 'trusses-4.bdf'
SOLUTION
  title='2 residual trusses, and a superelement'
```

```
  transient
     time_step=1e-5
     nsteps=1000
END

FILE
   geometry_file 'truss_se.exo'
END


BOUNDARY
    nodeset 11  // nastran SID=1
        x=0
    nodeset 32  // nastran SID=3
        y=0
    nodeset 33  // nastran SID=3
        z=0
END

LOADS
   node_list_file 'endtruss_node_list'
      force 1 0 0
      function=1
END

function 1
    type=linear
    data 0 0
    data 1e-3 1
    data 4e-3 -1
    data 5e-3 0
end

OUTPUTS
        disp
END

ECHO
      mass
END


BLOCK 12
   // 2 elements of type TRUSS. 2 nodes/element
   // property card 'PROD     1       '
   material=1
   Area=0.01
   Truss
END

block 13
    superelement
    map = locations
    file = endtruss.ncf
END

MATERIAL  1
   // from 'MAT1     1       '
   Isotropic
   E=1e+07
   NU=0
   density=0.1
END
```

11.46. Superelement Inertia Tensor Input

Refer to section 2.17 for details of the test.

```
include beam_model.inp

outputs
 genergies
 eorient
   disp
end


cbmodel
  nodeset 1
  format=dmig
  file=cbr.dmig
  inertia_matrix=yes
end
```

11.46.1. beam_model

```
//#############################################################################
//#
//# This salinas input file was generated by lsdyna2sierra
//#
//#############################################################################

SOLUTION
    solver=gdsw
 title 'beam_med'
 cbr
 nmodes = 10
 correction=vectors
 rbmdof=123456
END

file
 geometry_file 'temp1/beam_med.exo'
end

echo
 mass
end

block 1
 material 'boxsolid'
end

material 'boxsolid'
 isotropic
 e = 207
 nu = 0.300000
 density = 0.0000071
end
```

11.47. Nastran/Sierra/SD Interoperability with Superelements

Refer to section 2.18 for details of the test.

11.47.1. Sierra/SD *full model*

```
//salinas input created using nasgen from nastran file 'tuningforkz.bdf'
SOLUTION
  title=' MSC.Nastran job created on 28-Nov-17 at 08:50:40'
  case eig
    eigen
        nmodes=10
        shift=-1e6
   case frf
      modalfrf
      load=1
   case trn
      modaltransient
      time_step=2e-5
      nsteps=200
      load=30
END

FILE
   geometry_file 'tuningforkz.exo'
END


PARAMETERS
// wtmass=0.00259
   eigen_norm=visualization
END

BOUNDARY
    nodeset 11  // nastran SID=1
        x=0 y=0 z=0
    nodeset 53  // nastran SID=4
        z=0
END

LOAD 1
   sideset 1
      pressure 1
      function 1
END

function 1
   type linear
   data 0 1
   data 1e4 1
end

LOAD 30
   sideset 1
      pressure 1
      function 30
END

function 30
   type linear
   data 0 0
   data 0.5e-3 1
   data 1e-3 0
end
```

```
damping
   gamma=0.03
end

frequency
   freq_min   1
   freq_step  1
   freq_max   1000
   nodeset 43
   displacement
end

OUTPUTS
        disp
END

ECHO
      mass
END

BLOCK 11
   // 5 elements of type HEX. 20 nodes/element
   // property card 'PSOLID   1      '
   material=1
END

BLOCK 21
   // 5 elements of type HEX. 20 nodes/element
   // property card 'PSOLID   2      '
   material=1
END

BLOCK 31
   // 4 elements of type HEX. 20 nodes/element
   // property card 'PSOLID   3      '
   material=1
END

MATERIAL  1
   // from 'MAT1     1      '
   Isotropic
   E = 1e+07
   NU = 0.3
   density = 0.000259
END
```

11.47.2. Nastran full model

```
$ NASTRAN input file created by the Patran 2010.2.3 64-Bit input file
$ translator on November  28, 2017 at 08:52:49.
$ Direct Text Input for Nastran System Cell Section
$ Direct Text Input for File Management Section
$ Direct Text Input for Executive Control
$ Linear Static Analysis, Database
SOL 101
CEND
$ Direct Text Input for Global Case Control Data
TITLE = MSC.Nastran job created on 28-Nov-17 at 08:50:40
ECHO = NONE
SUBCASE 1
   SUBTITLE=no-bc-on-interface
   SPC = 2
   LOAD = 2
   DISPLACEMENT(SORT1,REAL)=ALL
   SPCFORCES(SORT1,REAL)=ALL
   STRESS(SORT1,REAL,VONMISES,BILIN)=ALL
```

```
$ Direct Text Input for this Subcase
BEGIN BULK
$ Direct Text Input for Bulk Data
PARAM    POST    0
PARAM   PRTMAXIM YES
$ Elements and Element Properties for region : load-tine
PSOLID   1       1       0
$ Pset: "load-tine" will be imported as: "psolid.1"
CHEXA    10      1       36      12      8       30      72      52
         48      71      157     103     158     159     160     104
         96      161     162     108     163     164
CHEXA    11      1       37      36      30      31      74      72
         71      73      165     159     166     167     168     160
         161     169     170     164     171     172
CHEXA    12      1       38      37      31      32      76      74
         73      75      173     167     174     175     176     168
         169     177     178     172     179     180
CHEXA    13      1       39      38      32      33      78      76
         75      77      181     175     182     183     184     176
         177     185     186     180     187     188
CHEXA    14      1       40      39      33      34      80      78
         77      79      189     183     190     191     192     184
         185     193     194     188     195     196
$ Elements and Element Properties for region : rom-tine
PSOLID   2       1       0
$ Pset: "rom-tine" will be imported as: "psolid.2"
CHEXA    5       2       24      6       14      18      60      47
         55      59      117     111     118     119     120     97
         113     121     122     116     123     124
CHEXA    6       2       25      24      18      19      62      60
         59      61      125     119     126     127     128     120
         121     129     130     124     131     132
CHEXA    7       2       26      25      19      20      64      62
         61      63      133     127     134     135     136     128
         129     137     138     132     139     140
CHEXA    8       2       27      26      20      21      66      64
         63      65      141     135     142     143     144     136
         137     145     146     140     147     148
CHEXA    9       2       28      27      21      22      68      66
         65      67      149     143     150     151     152     144
         145     153     154     148     155     156
$ Elements and Element Properties for region : fork
PSOLID   3       1       0
$ Pset: "fork" will be imported as: "psolid.3"
CHEXA    1       3       4       3       1       2       44      41
         42      43      81      82      83      84      85      86
         87      88      89      90      91      92
CHEXA    2       3       8       4       2       6       48      44
         43      47      93      84      94      95      96      85
         88      97      98      92      99      100
CHEXA    3       3       12      11      4       8       52      49
         44      48      101     102     93      103     104     105
         85      96      106     107     98      108
CHEXA    4       3       6       2       13      14      47      43
         54      55      94      109     110     111     97      88
         112     113     99      114     115     116
$ Referenced Material Records
$ Material Record : aluminum
$ Description of Material : Date: 27-Nov-17          Time: 08:57:23
MAT1     1      1.+7            .3      2.59-4
$ Nodes of the Entire Model
GRID     1               0.      0.      0.
GRID     2              1.       0.      0.
GRID     3               0.     1.       0.
GRID     4              1.      1.       0.
GRID     6              2.       0.      0.
GRID     8              2.      1.       0.
GRID     11             1.      2.       0.
```

```
GRID     12             2.      2.       0.
GRID     13             1.      -1.      0.
GRID     14             2.      -1.      0.
GRID     18             3.      -1.      0.
GRID     19             4.      -1.      0.
GRID     20             5.      -1.      0.
GRID     21             6.      -1.      0.
GRID     22             7.      -1.      0.
GRID     24             3.       0.      0.
GRID     25             4.       0.      0.
GRID     26             5.       0.      0.
GRID     27             6.       0.      0.
GRID     28             7.       0.      0.
GRID     30             3.      1.       0.
GRID     31             4.      1.       0.
GRID     32             5.      1.       0.
GRID     33             6.      1.       0.
GRID     34             7.      1.       0.
GRID     36             3.      2.       0.
GRID     37             4.      2.       0.
GRID     38             5.      2.       0.
GRID     39             6.      2.       0.
GRID     40             7.      2.       0.
GRID     41              0.     1.      .5
GRID     42              0.      0.     .5
GRID     43             1.       0.     .5
GRID     44             1.      1.      .5
GRID     47             2.       0.     .5
GRID     48             2.      1.      .5
GRID     49             1.      2.      .5
GRID     52             2.      2.      .5
GRID     54             1.      -1.     .5
GRID     55             2.      -1.     .5
GRID     59             3.      -1.     .5
GRID     60             3.       0.     .5
GRID     61             4.      -1.     .5
GRID     62             4.       0.     .5
GRID     63             5.      -1.     .5
GRID     64             5.       0.     .5
GRID     65             6.      -1.     .5
GRID     66             6.       0.     .5
GRID     67             7.      -1.     .5
GRID     68             7.       0.     .5
GRID     71             3.      1.      .5
GRID     72             3.      2.      .5
GRID     73             4.      1.      .5
GRID     74             4.      2.      .5
GRID     75             5.      1.      .5
GRID     76             5.      2.      .5
GRID     77             6.      1.      .5
GRID     78             6.      2.      .5
GRID     79             7.      1.      .5
GRID     80             7.      2.      .5
GRID*    81                             .5              1.
*       -1.46144-8
GRID*    82                            -5.9644-10      .5
*       -6.88986-9
GRID*    83                             .5              -2.08654-9
*       -4.99122-9
GRID*    84                             1.              .5
*       -5.11059-9
GRID     85             1.      1.      .25
GRID*    86                             4.25148-10      1.
*       .25
GRID*    87                             2.65251-9       7.2653-9
*       .25
GRID*    88                             1.              3.57292-9
*       .25
```

```
GRID     89             .5      1.      .5
GRID*    90                             4.44603-9       .5
*       .5
GRID*    91                             .5              6.6322-9
*       .5
GRID     92             1.      .5      .5
GRID*    93                             1.5             1.
*       -1.46144-8
GRID*    94                             1.5             -2.08654-9
*       -4.99122-9
GRID*    95                             2.              .5
*       -5.11059-9
GRID     96             2.      1.      .25
GRID*    97                             2.              3.57292-9
*       .25
GRID     98             1.5     1.      .5
GRID*    99                             1.5             6.6322-9
*       .5
GRID     100            2.      .5      .5
GRID*    101                            1.5             2.
*       -1.46144-8
GRID*    102                            1.              1.5
*       -6.88986-9
GRID*    103                            2.              1.5
*       -5.11059-9
GRID     104            2.      2.      .25
GRID     105            1.      2.      .25
GRID     106            1.5     2.      .5
GRID     107            1.      1.5     .5
GRID     108            2.      1.5     .5
GRID*    109                            1.              -.5
*       -6.88986-9
GRID*    110                            1.5             -1.
*       -4.99122-9
GRID*    111                            2.              -.5
*       -5.11059-9
GRID     112            1.      -1.     .25
GRID     113            2.      -1.     .25
GRID     114            1.      -.5     .5
GRID     115            1.5     -1.     .5
GRID     116            2.      -.5     .5
GRID*    117                            2.5             1.5939-8
*       -1.46144-8
GRID*    118                            2.5             -1.
*       -4.99122-9
GRID*    119                            3.              -.5
*       -5.11059-9
GRID*    120                            3.              1.94968-8
*       .25
GRID     121            3.      -1.     .25
GRID*    122                            2.5             1.6149-9
*       .5
GRID     123            2.5     -1.     .5
GRID     124            3.      -.5     .5
GRID*    125                            3.5             1.5939-8
*       -1.46144-8
GRID*    126                            3.5             -1.
*       -4.99122-9
GRID*    127                            4.              -.5
*       -5.11059-9
GRID*    128                            4.              1.94968-8
*       .25
GRID     129            4.      -1.     .25
GRID*    130                            3.5             1.6149-9
*       .5
GRID     131            3.5     -1.     .5
GRID     132            4.      -.5     .5
GRID*    133                            4.5             1.5939-8
```

```
*       -1.46144-8
GRID*    134                        4.5             -1.
*       -4.99122-9
GRID*    135                        5.              -.5
*       -5.11059-9
GRID*    136                        5.              1.94968-8
*       .25
GRID     137            5.      -1.     .25
GRID*    138                        4.5             1.6149-9
*       .5
GRID     139            4.5     -1.     .5
GRID     140            5.      -.5     .5
GRID*    141                        5.5             1.5939-8
*       -1.46144-8
GRID*    142                        5.5             -1.
*       -4.99122-9
GRID*    143                        6.              -.5
*       -5.11059-9
GRID*    144                        6.              1.94968-8
*       .25
GRID     145            6.      -1.     .25
GRID*    146                        5.5             1.6149-9
*       .5
GRID     147            5.5     -1.     .5
GRID     148            6.      -.5     .5
GRID*    149                        6.5             1.5939-8
*       -1.46144-8
GRID*    150                        6.5             -1.
*       -4.99122-9
GRID*    151                        7.              -.5
*       -5.11059-9
GRID*    152                        7.              1.94968-8
*       .25
GRID     153            7.      -1.     .25
GRID*    154                        6.5             1.6149-9
*       .5
GRID     155            6.5     -1.     .5
GRID     156            7.      -.5     .5
GRID*    157                        2.5             2.
*       -1.46144-8
GRID*    158                        2.5             1.
*       -4.99122-9
GRID*    159                        3.              1.5
*       -5.11059-9
GRID     160            3.      2.      .25
GRID     161            3.      1.      .25
GRID     162            2.5     2.      .5
GRID     163            2.5     1.      .5
GRID     164            3.      1.5     .5
GRID*    165                        3.5             2.
*       -1.46144-8
GRID*    166                        3.5             1.
*       -4.99122-9
GRID*    167                        4.              1.5
*       -5.11059-9
GRID     168            4.      2.      .25
GRID     169            4.      1.      .25
GRID     170            3.5     2.      .5
GRID     171            3.5     1.      .5
GRID     172            4.      1.5     .5
GRID*    173                        4.5             2.
*       -1.46144-8
GRID*    174                        4.5             1.
*       -4.99122-9
GRID*    175                        5.              1.5
*       -5.11059-9
GRID     176            5.      2.      .25
GRID     177            5.      1.      .25
```

```
GRID     178            4.5     2.      .5
GRID     179            4.5     1.      .5
GRID     180            5.      1.5     .5
GRID*    181                            5.5             2.
*       -1.46144-8
GRID*    182                            5.5             1.
*       -4.99122-9
GRID*    183                            6.              1.5
*       -5.11059-9
GRID     184            6.      2.      .25
GRID     185            6.      1.      .25
GRID     186            5.5     2.      .5
GRID     187            5.5     1.      .5
GRID     188            6.      1.5     .5
GRID*    189                            6.5             2.
*       -1.46144-8
GRID*    190                            6.5             1.
*       -4.99122-9
GRID*    191                            7.              1.5
*       -5.11059-9
GRID     192            7.      2.      .25
GRID     193            7.      1.      .25
GRID     194            6.5     2.      .5
GRID     195            6.5     1.      .5
GRID     196            7.      1.5     .5
$ Loads for Load Case : no-bc-on-interface
SPCADD   2       1       3       4       5
LOAD     2      1.      1.       1
$ Displacement Constraints of Load Set : base
SPC1     1       123     1       3       41      42      82      86
         87      90
$ Displacement Constraints of Load Set : interface
SPC1     3       1       6       14      47      55      97      111
         113     116
$ Displacement Constraints of Load Set : otm
SPC1     4       3       67
$ Displacement Constraints of Load Set : z0
SPC1     5       3       1       2       3       4       6       8
         11      12      13      14      18      19      20      21
         22      24      25      26      27      28      30      31
         32      33      34      36      37      38      39      40
         81      82      83      84      93      94      95      101
         102     103     109     110     111     117     118     119
         125     126     127     133     134     135     141     142
         143     149     150     151     157     158     159     165
         166     167     173     174     175     181     182     183
         189     190     191
$ Pressure Loads of Load Set : pressure
PLOAD4   1       14      1.                              40      78
$ Referenced Coordinate Frames
ENDDATA
```

11.48. Sierra/SD Superelement File Formats

Refer to section 2.19 for details of the test.

11.48.1. Sierra/SD *full model*

```
//salinas input created using nasgen from nastran file 'tuningfork.bdf'
SOLUTION
  title=' MSC.Nastran job created on 27-Nov-17 at 09:29:23'
   eigen
       nmodes=10
       shift=-1e6   // needed only for floating
END

FILE
   geometry_file 'tuningfork.exo'
END


PARAMETERS
// wtmass=0.00259
   eigen_norm=visualization
END

BOUNDARY
    nodeset 11  // nastran SID=1
        x=0
    nodeset 12  // nastran SID=1
        y=0
    nodeset 13  // nastran SID=1
        z=0
    nodeset 33  // nastran SID=3
        z=0
END

history
  nodeset 100
  disp
end

OUTPUTS
  disp
END

ECHO
      mass
END


BLOCK 11
   // 5 elements of type HEX. 20 nodes/element
   // property card 'PSOLID   1       '
   material=1
END

BLOCK 21
   // 5 elements of type HEX. 20 nodes/element
   // property card 'PSOLID   2       '
   material=1
END

BLOCK 31
   // 4 elements of type HEX. 20 nodes/element
   // property card 'PSOLID   3       '
   material=1
```

```
END

MATERIAL  1
   // from 'MAT1     1      '
   Isotropic
   E = 1e+07
   NU = 0.3
   density = 0.000259
END
```

11.48.2. Netcdf output

```
SOLUTION
  title='ROM tine of tuning fork'
  cbr
    nmodes=10
END

cbmodel
   nodeset 41
   format=netcdf
   file=rom4.ncf
end

FILE
   geometry_file 'rom4.exo'
END


PARAMETERS
   eigen_norm=visualization
END

BOUNDARY
    nodeset 33  // nastran SID=3
        z=0
END

LOADS
END

OUTPUTS
        disp
END

ECHO
      mass
END


BLOCK 21
   // 5 elements of type HEX. 20 nodes/element
   // property card 'PSOLID   2      '
   material=1
   blkbeta=1e-6
END

MATERIAL  1
   // from 'MAT1     1      '
   Isotropic
   E = 1e+07
   NU = 0.3
   density = 0.000259
END
```

11.48.3. DMIG output

```
SOLUTION
  title='ROM tine of tuning fork'
  cbr
    nmodes=10
END

cbmodel
   nodeset 41
   format=dmig*
   file=rom4.dmig
   inertia_matrix=no
end

FILE
   geometry_file 'rom4.exo'
END


PARAMETERS
   eigen_norm=visualization
END

BOUNDARY
    nodeset 33  // nastran SID=3
        z=0
END

LOADS
END

OUTPUTS
        disp
END

ECHO
      mass
END


BLOCK 21
   // 5 elements of type HEX. 20 nodes/element
   // property card 'PSOLID   2      '
   material=1
   blkbeta=1e-6
END

MATERIAL  1
   // from 'MAT1     1      '
   Isotropic
   E = 1e+07
   NU = 0.3
   density = 0.000259
END
```

11.48.4. Netcdf input

```
SOLUTION
  title='Residual calculations using a CBR/ROM of right tine'
  case eigNCF
    eigen
        nmodes=10
        shift=-1e6
END
```

```
FILE
   geometry_file 'residual.exo'
END

gdsw
    solver_tol=1e-12
end

PARAMETERS
   eigen_norm=visualization
END

BOUNDARY
    nodeset 11  // nastran SID=1
        x=0 y=0 z=0
    nodeset 33  // nastran SID=3
        z=0
END

LOAD 30
   sideset 1
      pressure 1
      function 30
END

function 30
   type linear
   data 0 0
   data 0.5e-3 1
   data 1e-3 0
end

damping
   gamma=0.03
end

frequency
   freq_min   1
   freq_step  1
   freq_max   1000
   nodeset 33
   displacement
end

history
  nodeset 100
  disp
end

OUTPUTS
        disp
END

ECHO
      mass
END


BLOCK 11
   // 5 elements of type HEX. 20 nodes/element
   // property card 'PSOLID   1      '
   material=1
END

$$ BLOCK 21
   // 5 elements of type HEX. 20 nodes/element
   // property card 'PSOLID   2      '
   material=1
```

```
END

BLOCK 31
   // 4 elements of type HEX. 20 nodes/element
   // property card 'PSOLID   3      '
   material=1
END

BLOCK 32
   superelement
   map=locations
   file=rom4.ncf
END

MATERIAL  1
   // from 'MAT1     1      '
   Isotropic
   E = 1e+07
   NU = 0.3
   density = 0.000259
END
```

11.48.5. DMIG input

```
SOLUTION
  title='Residual calculations using a CBR/ROM of right tine'
  case eigDMIG
    eigen
        nmodes=10
        shift=-1e6
END

FILE
   geometry_file 'residual.exo'
END

gdsw
    solver_tol=1e-12
end

PARAMETERS
   eigen_norm=visualization
END

BOUNDARY
    nodeset 11  // nastran SID=1
        x=0 y=0 z=0
    nodeset 33  // nastran SID=3
        z=0
END

LOAD 30
   sideset 1
      pressure 1
      function 30
END

function 30
   type linear
   data 0 0
   data 0.5e-3 1
   data 1e-3 0
end

damping
   gamma=0.03
```

```
end

frequency
   freq_min   1
   freq_step  1
   freq_max   1000
   nodeset 33
   displacement
end

OUTPUTS
        disp
END

history
  nodeset 100
  disp
end

ECHO
      mass
END


BLOCK 11
   // 5 elements of type HEX. 20 nodes/element
   // property card 'PSOLID   1      '
   material=1
END

$$ BLOCK 21
   // 5 elements of type HEX. 20 nodes/element
   // property card 'PSOLID   2      '
   material=1
END

BLOCK 31
   // 4 elements of type HEX. 20 nodes/element
   // property card 'PSOLID   3      '
   material=1
END

BLOCK 32
   superelement
   format = dmig
   file=rom4.dmig
END

MATERIAL  1
   // from 'MAT1     1      '
   Isotropic
   E = 1e+07
   NU = 0.3
   density = 0.000259
END
```

11.49. Transient Reaction Forces

Refer to section 2.20 for details of the test.

11.49.1. Vibration from Initial Conditions

```
FILE
    geometry_file = bars.g
END
SOLUTION
    case 'transient'
      transient
      time_step 1e-2
      nsteps 1000
      load 1
      solver=gdsw
      lumped
END
GDSW
END
BOUNDARY
    nodeset 2 3 4 5
        fixed
END
LOAD 1
END

INITIAL-CONDITIONS
  velocity = by_block
END

OUTPUTS
    database name = initCond.e
    disp
    velocity
    accel
    force
    reaction_force
END

ECHO
  mass
END

HISTORY
END

BLOCK 1
    dashpot
    cid=1
    k=1.1
    c = 0.7
END
BLOCK 2
    dashpot
    cid=1
    k=1.2
    c = 0.8
END
BLOCK 3
    dashpot
    cid=2
    k=1.3
    c = 0.9
END
```

```
BLOCK 4
    dashpot
    cid=2
    k=1.4
    c = 1.0
END

BLOCK 100
    conmass
    mass = 2.5
    velocity = 10 20 0
end
```

11.49.2. Prescribed Acceleration

```
FILE
    geometry_file = bars.g
END
SOLUTION
    case 'transient'
      transient
      time_step 1e-2
      nsteps 1000
      load 1
      solver=gdsw
      lumped
END
GDSW
END
BOUNDARY
    nodeset 2 3 4 5
        fixed
    nodeset 1
        accelx 1
        function xfun
        disp0 = 0
        vel0 = 0
    nodeset 1
        accely 1
        function yfun
        disp0 = 0
        vel0 = 0
END

FUNCTION xfun
    type = linear
    data 0 4
    data 1 4
END

FUNCTION yfun
    type = linear
    data 0 8
    data 1 8
END

LOAD 1
    nodeset 1
       force 0 0 1.5
END

OUTPUTS
```

```
    database name = accel.e
    disp
    velocity
    accel
    force
    reaction_force
END

ECHO
  mass
END

HISTORY
END

DAMPING
  alpha = 0.1
  beta = 0.2
END

BLOCK 1
    dashpot
    cid=1
    k=1.1
    c = 0.7
END
BLOCK 2
    dashpot
    cid=1
    k=1.2
    c = 0.8
END
BLOCK 3
    dashpot
    cid=2
    k=1.3
    c = 0.9
END
BLOCK 4
    dashpot
    cid=2
    k=1.4
    c = 1.0
END

BLOCK 100
    conmass
    mass = 2.5
    velocity = 10 20 0
end
```

11.50. Relative Displacement PSD

Refer to section 2.21 for details of the test.

11.50.1. In Phase Response

```
Solution
  solver=gdsw
  case eig
    eigen nmodes=all
  case random
    modalranvib
    lfcutoff -1
end
Parameters
  wtmass 0.00259
end
File
  geometry_file oneD.exo
end
Boundary
  nodeset 1,2 y = 0 z = 0 rotx = 0 roty = 0 rotz = 0
end
Outputs
  disp
  relative_disp
  vrms
end
Ranloads
  matrix matFun
  load=1
    nodeset 2
    force 1 0 0
    scale 1e6
  load=2
    nodeset 1
    force 1 0 0
    scale 1e6
end

Matrix-function matFun
  symmetry hermitian
  dimension 2x2
  data 1,1
    real function squareBand scale 1
  data 1,2
    real function squareBand scale 1
  data 2,2
    real function squareBand scale 1
end
Function squareBand
  type linear
  data 1       1e-6
  data 9.9999  1e-6
  data 10      1e-1
  data 25      1e-1
  data 25.0001 1e-6
  data 30      1e-6
end
Damping
  gamma = 0.05
end
Frequency
  freq_min 10
  freq_max 25
```

```
  freq_step 0.1
  nodeset 1 2 disp
  block 12 relative_disp
end
Block 1 2
  conmass
  mass 1e2
end
Block 12
  joint2g
  kx elastic 1e5
  ky elastic 1e5
  kz elastic 1e5
end
```

11.50.2. Opposite Phase Response

```
Solution
  solver=gdsw
  case eig
    eigen nmodes=all
  case random
    modalranvib
    lfcutoff -1
end
Parameters
  wtmass 0.00259
end
File
  geometry_file oneD.exo
end
Boundary
  nodeset 1,2 y = 0 z = 0 rotx = 0 roty = 0 rotz = 0
end
Outputs
  disp
  relative_disp
  vrms
end
Ranloads
  matrix matFun
  load=1
    nodeset 2
    force 1 0 0
    scale 1e6
  load=2
    nodeset 1
    force 1 0 0
    scale 1e6
end

Matrix-function matFun
  symmetry hermitian
  dimension 2x2
  data 1,1
    real function squareBand scale 1
  data 1,2
    real function squareBand scale -1
  data 2,2
    real function squareBand scale 1
end
Function squareBand
  type linear
  data 1       1e-6
  data 9.9999  1e-6
  data 10      1e-1
```

```
  data 25      1e-1
  data 25.0001 1e-6
  data 30      1e-6
end
Damping
  gamma = 0.05
end
Frequency
  freq_min 10
  freq_max 25
  freq_step 0.1
  nodeset 1 2 disp
  block 12 relative_disp
end
Block 1 2
  conmass
  mass 1e2
end
Block 12
  joint2g
  kx elastic 1e5
  ky elastic 1e5
  kz elastic 1e5
end
```

11.50.3. One Node Fixed Response

```
Solution
  solver=gdsw
  case eig
    eigen nmodes=all
  case random
    modalranvib
    lfcutoff -1
end
Parameters
  wtmass 0.00259
end
File
  geometry_file oneD.exo
end
Boundary
  nodeset 1 fixed
  nodeset 2 y = 0 z = 0 rotx = 0 roty = 0 rotz = 0
end
Outputs
  disp
  relative_disp
  vrms
end
Ranloads
  matrix matFun
  load=1
    nodeset 2
    force 1 0 0
    scale 1e6
end
Matrix-function matFun
  symmetry hermitian
  dimension 1x1
  data 1,1
    real function squareBand scale 1
end
Function squareBand
  type linear
  data 1       1e-6
```

```
  data 9.9999  1e-6
  data 10      1e-1
  data 25      1e-1
  data 25.0001 1e-6
  data 30      1e-6
end
Damping
  gamma = 0.05
end
frequency
  freq_min 10
  freq_max 25
  freq_step 0.1
  nodeset 2 disp
  block 12 relative_disp
end
Block 1 2
  conmass
  mass 1e2
end
Block 12
  joint2g
  kx elastic 1e5
  ky elastic 1e5
  kz elastic 1e5
end
```

11.50.4. Tuning fork response

```
Solution
  solver gdsw
  case eig
    eigen
    nmodes 12
    shift -100
  case mRand
   modalranvib
   truncationMethod none
   lfcutoff -10
end
GDSW
  max_numterm_c1 1000
end
Parameters
  wtmass 0.00259
end
File
  geometry_file tuningFork.exo
end
Damping
  gamma 0.08
end
Boundary
  block 1
    z=0
  nodeset 1
    x=0 y=0
end
Matrix-function 1x1
  symmetry hermitian
  dimension=1x1
  data 1,1
    real function 2 scale 1
end
Function 2
  type linear
```

```
  data 1.000000e-16 1.000000e-16
  data 1.99999999 1.000000e-16
  data 2.0 1.000000e-01
  data 100.0 1.000000e-01
  data 100.00000001 1.000000e-16
  data 125.0 1.000000e-16
end
Ranloads
  matrix 1x1
  load = 1
  nodeset 2
  force 0 1 0
  scale 1
end
Outputs
  disp
  relative_disp
end
Frequency
  freq_min 1
  freq_max 150
  freq_step 0.1
  block '100 10 11 12 13 14 15 16 17 18 19'
  nodeset all
  relative_disp
  disp
end
Block 1
  material 1
end
Material 1
  e 1e7
  nu 0.3
  density 0.1
end
Block 100
  Joint2g
  kx elastic 0
  ky elastic 0
  kz elastic 0
  nsm 1e-4
end
Tied Joint
 normal definition none
 surface 100, 200
 connect to block 100
 side average
end

//{ind=0}
{loop(10)}

Block {10+ind}
  joint2g
  kx elastic 0
  ky elastic 0
  kz elastic 0
  nsm 1e-4
end
tied joint
 normal definition none
 surface {10+ind}, {20+ind}
 connect to block {10+ind}
 side average // do not stiffen the surface
end

//{ind++}
{endloop}
```

11.51. Contact Verification

Refer to section 3.4 for details of the test.

```
Solution
case static_gap
  statics
end

File
  geometry_file bar_curve_r1000.g
end

Boundary
  nodeset 1
    z=0
  sideset 1
    x=0 y=0
End

Block 1
  material "steelish"
end
Block 2
  material "steelish"
end
Block 3
  material "steelish"
end

Material "steelish"
  isotropic
  density = 0.0343
  nu = 0.0
  E = 29.e6
end
Loads
  body
  gravity = 0 -1 0
  function = 1
end
Function 1
  name "impulse"
  type LINEAR
  data 0 1
  data 1 1
end
Outputs
  disp
  stress
  energy
end
Tied Data
  Surface 101, 100
  search tolerance 0.125
  gap removal = off
end
Tied Data
  Surface 200, 201
  search tolerance 0.125
  gap removal = off
end
```

11.52. Buckling of Constant Pressure Ring Input

Refer to section 4.8 for details of the test.

```
SOLUTION
    solver=gdsw
  buckling
  nmodes 1
  shift=-100
END

FILE
  geometry_file 'temp1/ring20.par'
END

BOUNDARY
nodeset 1
  y=0
nodeset 2
  x=0
nodeset 3
  z=0
END

LOADS
  sideset 1
    pressure = 1.0
END

OUTPUTS
  deform
END

ECHO
END

BLOCK 1
  material 1
END

Material 1
  E 10e6
  nu 0.0
  density 0.098 // not used in statics
END
```

11.53. Buckling of Cantilever Beam Input

Refer to section 4.9 for details of the test.

```
SOLUTION
    solver=gdsw
    buckling
    nmodes 4
    shift=-1.e5
END

FILE
  geometry_file 'bar.exo'
// geometry_file 'bar.exo'
END

OUTPUTS
    deform
END

ECHO
END

BOUNDARY
  sideset 1
   fixed
END


BLOCK 1
        material "steel"
END

MATERIAL "steel"
density 1.293
        E 3.0e7
        nu 0.0
END

LOADS
  sideset 2
  pressure=1.0
END
```

11.54. Rotating Dumbbell Statics

Refer to section 6.1

```
SOLUTION
    solver=gdsw
     statics
END
loads
     body
       angular_velocity 0 0 1.1
end
file
    geometry_file 'dumbbell.exo'
end
boundary
    nodeset 1 fixed
end
outputs
  force
end
echo
    mass
end
block 2
    conmass
    mass=2
end
block 1
    beam2
    material=light
    area=1e-2
    i1=1e-2
    i2=1e-2
    j=2e-2
    orientation 0 0 1
end
material light
    isotropic
    density = 0
    nu = .3
    E = 1E7
end
```

11.55. Rotating Beam Statics

Refer to section 6.2

```
SOLUTION
    solver=gdsw
 case one
   statics
   load = 1
 case two
    tangent
 case out
     qevp
     method=anasazi
     nmodes=10
     subspace_size 100
END
file
geometry_file 'beam_hex8.exo'
end

parameters
  eig_tol=1.0e-12
end

load 1
    body
      angular_velocity 0 0 50.0
    function = 1
end
FUNCTION 1
       type LINEAR
       name "test_func1"
       data 0.0 1.0
       data 1.0 1.0
       data 2.0e4 1.0
end
OUTPUTS
disp
force
end
echo
mass
mass=block
end
boundary
   nodeset 1
       fixed
end
block 1 //        hex8u
        material "steel"
        rotational_type lagrangian
end
material "steel"
        E 19.5e10
        nu 0
        density 7700.0
end
```

11.56. Rotating Shell Statics

Refer to section 6.3

```
SOLUTION
    solver=gdsw
 case one
   statics
   load = 1
 case two
    tangent
 case out
     qevp
     method=anasazi
     nmodes=10
     subspace_size 100
END
FILE
geometry_file 'beam_shell.exo'
end

parameters
  eig_tol=1.0e-12
end

LOAD 1
    body
      angular_velocity 0 0 50.0
      function = 1
end
FUNCTION 1
       type LINEAR
       name "test_func1"
       data 0.0 1.0
       data 1.0 1.0
       data 2.0e4 1.0
end
OUTPUTS
disp
force
end
ECHO
mass
mass=block
end
BOUNDARY
   nodeset 1
       fixed
end
BLOCK 1 //        hex8u
        material "steel"
        quadt
        thickness 1.0
        rotational_type lagrangian
end
MATERIAL "steel"
        E 19.5e10
        nu 0
        density 7700.0
end
```

11.57. Rotating Ring Statics

Refer to section 6.4

```
SOLUTION
    solver=gdsw
    statics
END
loads
     body
       angular_velocity 0 0 1.1
       coordinate 10
end
coordinate 10
    3 1 4
    3 1 5
    4 1 4
end
file
    geometry_file 'ring.exo'
end
boundary
    nodeset 1 fixed
end
outputs
  force
end
echo
    mass
end
block 1
    quadt
    material "Al6061-2"
end
block 2
    beam2
    material=light
    area=1e-2
    i1=1e-2
    i2=1e-2
    j=2e-2
    orientation 0 0 1
end
material "Al6061-2"
    isotropic
    density = 4
    nu = .3
    E = 1E7
end
material light
    isotropic
    density = 0
    nu = .3
    E = 1E7
end
```

11.58. Rotating Ring Acceleration

Refer to section 6.5

```
SOLUTION
    solver=gdsw
    statics
END
loads
     body
       angular_acceleration 0 0 1.1
       coordinate myCoord
end
coordinate myCoord
    3 1 4
    3 1 5
    4 1 4
end
file
    geometry_file 'ring.exo'
end
boundary
    nodeset 1 fixed
end
outputs
  force
end
echo
    mass
end
block 1
    quadt
    material "Al6061-2"
end
block 2
    beam2
    material=light
    area=1e-2
    i1=1e-2
    i2=1e-2
    j=2e-2
    orientation 0 0 1
end
material "Al6061-2"
    isotropic
    density = 4
    nu = .3
    E = 1E7
end
material light
    isotropic
    density = 0
    nu = .3
    E = 1E7
end
```

11.59. Rotating Superelement Statics

Refer to section 6.6

```
// solution should be identical to the single hex solution, but
// this model uses a superelement.
SOLUTION
    solver=gdsw
     statics
END

loads
     body
       angular_velocity 3 0 0
end

file
    geometry_file 'rotating_hex_se.exo'
end

boundary
    nodeset 1 fixed
    nodeset 2 fixed
end

outputs
  force
end

echo
    mass
    force
end

block 1
    superelement
    file=rotating_hex_gold.ncf
    map locations
end
```

11.60. Rotating Superelement Beam Statics

Refer to section 6.7

```
SOLUTION
    solver=gdsw
 case out
 statics
     load=1
END

HISTORY
   nodeset 2
   disp
end
FILE
geometry_file 'beam_se.exo'
end
LOAD 1
    body
      angular_velocity 0 0 5.0
    function = 1
end
FUNCTION 1
       type LINEAR
       name "test_func1"
       data 0.0 1.0
       data 1.0 1.0
       data 2.0e4 1.0
end
outputs
disp
force
end
echo
mass
mass=block
        input
end
block 1
        dead
end
block 2
    superelement
    file=cbr_hex.netcdf
    map = location
end
```

11.61. Point Mass in a Rotating Frame

Refer to section 6.8

```
SOLUTION
    solver=gdsw
     title 'pt hex starting at rest in rotating frame'
     transient
        time_step = 0.001
        nsteps = 1000
END

loads
     body
       angular_velocity 0 0 1.1
       function 1
end

file
    geometry_file 'phex.exo'
end

function 1
   type=linear
   data 0 1
   data 1 1
end

boundary
end


outputs
  disp
  force
end

echo
    mass
end

block 1
    material heavy
    rotational_type lagrangian
end

material heavy
    isotropic
    E = 30.0e6
    nu = 0.3
    density = 10
end
```

11.62. Force Identification from Structural Acoustic Frequency Responses

7.1

11.63. Force Identification from Frequency Responses

7.2

11.64. Force Identification from Temporal Pressures

7.3

11.65. Force Identification from Temporal Tractions

7.4

11.66. Force Identification from Temporal Acoustic Pressures

7.5

11.67. Force Identification with Modal Transient

7.6

11.68. PSD Identification with Modal FRF

7.7

11.69. Orthotropic Material Identification with Transient

7.8

```
SOLUTION
    solver=gdsw
    solver=gdsw
    transient-inverse
      title 'Inverse Solution'
      nsteps = 10
      time_step 0.1
END


INVERSE-PROBLEM
  design_variable = material
  data_truth_table = ttable.txt
  data_file =  data.txt
END

BLOCK 1
    material 'orthotropic'
    inverse_material_type = HOMOGENEOUS
    hex8f
END

MATERIAL 'orthotropic'
   density = 1.0
   orthotropic
   AlphaParametrization = yes
   InequalityConstraints = no
   Cij = 3.0 1.0 1.0
             3.0 1.0
                 3.0
                    1.0
                       1.0
                          1.0
    Eii_bounds = 0.01 20.0 0.01 20.0 0.01 20.0
    Gij_bounds = 0.01 10.0 0.01 10.0 0.01 10.0
    Aij_bounds = -1.0 1.0 -1.0 1.0 -1.0 1.0
END

FILE
    geometry_file 'DeepBeam.exo'
END

BOUNDARY
    sideset 1
      x=0 y=0 z=0
END

LOADS
    sideset 2
      traction 1.0 1.0 1.0
      function = 1
    sideset 3
      traction 1.0 1.0 1.0
      function = 1
END

HISTORY
    displacement nodeset 1
END

OUTPUTS
END
```

```
ECHO
END

FUNCTION 1
  type LINEAR
  data  0.0  0.0
  data 10.0 10.0
END

GDSW
  solver_tol 1.0e-13
  prt_summary 0
END

OPTIMIZATION
//  ROLmethod = linesearch
//  LSstep = secant
//  check_grad = no
//  LS_curvature_condition = null
//  Max_iter_Krylov = 30
//  Use_FD_hessvec = false
//  Use_inexact_hessvec = false
//  opt_tolerance = 1e-10
//  opt_iterations = 500
  boundconstraints = yes
  scaleDesignVars = no
  xml_file = DeepBeamRol.xml
END
```

11.70. Fatigue Output of Single DOF in Random Vibration

Refer to section 8.1

11.70.1. Modal Random Vibration

```
Solution
   title 'test of a single dof example for fatigue'
   case eig
        eigen nmodes=all
   case frf
        modalfrf
        load=1
   case ran
        modalranvib
        noSVD
end

FILE
   geometry_file 'onehexran.exo'
end

Ranloads
   matrix 97
   load=1
      sideset 2
      pressure 7
end

Matrix-function 97
   dimension 1x1
   symmetry=symmetric
   data 1,1
   real function 99
end

Function 99
   type linear
   data 0 9
   data 5000 9
end

Frequency
  freq_min 10
  freq_max  100
  freq_step  10
  sideset 2
  disp
  acceleration
end
BOUNDARY
  sideset 1
   fixed
  sideset 2
    y=0 z=0
end
OUTPUTS
   maa
   disp
   vrms
end
Echo
 input
 disp
 force
```

```
 rhs
 mass
end
LOAD 1
   sideset 2
       pressure 3
       function 1
end
Function 1
   type linear
   data 0 3.0
   data 1e5 3.0
end
Block 1
    material 3
end
Material 3
        E = 1e7
        nu = .3
        density 0.000259
end
```

11.70.2. Fatigue Solution

```
SOLUTION
   title 'test of a single dof example for fatigue'
   case eig
        eigen nmodes=all
   case frf
        modalfrf
        load=1
   case ran
        modalranvib
        noSVD
   case out
        fatigue
           method=wirsching
           duration=0.001
end

FILE
   geometry_file 'onehexran.exo'
end

Ranloads
   matrix 97
   load=1
      sideset 2
      pressure 7
end

Matrix-function 97
   dimension 1x1
   symmetry=symmetric
   data 1,1
   real function 99
end

Function 99
   type linear
   data 0 9
   data 5000 9
end

Frequency
  freq_min 10
```

```
  freq_max  100
  freq_step  10
  sideset 2
  disp
  acceleration
end

BOUNDARY
  sideset 1
   fixed
  sideset 2
    y=0 z=0
end

OUTPUTS
   disp
   vrms
end

ECHO
 input
 disp
 force
   rhs
 mass
 fatigue
end

LOAD 1
   sideset 2
       pressure 3
       function 1
end

Function 1
   type linear
   data 0 3.0
   data 1e5 3.0
end

BLOCK 1
    material 3
end

MATERIAL 3
        E = 1e7
        nu = .3
        density 0.000259
        Fatigue_A1 12.1689
        Fatigue_A2 -3
        Stress_Ratio -1.0
        Fatigue_Stress_Scale 1.0 // 0.001
        std_err 0.01
        t_dist 123.4
end
```

11.71. Fatigue Output of Dogbone

Refer to section 8.2

```
SOLUTION
case eig
eigen nmodes=150 // a 5 Hz wave is effectively static loading for this thing. We need a TON of modes for this to work.
shift=-1e9
        restart = auto
    case rand
      modalranvib
      lfcutoff = 10 // DON"T USE -1 FOR STRESS.
      nosvd
    case fatigue
        fatigue
           method=wirsching
end

FILE
   geometry_file 'dogbone_eng.exo'
end


PARAMETERS
   wtmass=0.002589
end

BOUNDARY
nodeset 1
 rotx=0
 roty=0
 rotz=0
end

RANLOADS
   matrix=11
   load=1
      nodeset 1
      force=1 0 0
      scale = 1.0
      nodeset 2
      force=1 0 0
      scale = -1.0
end

Matrix-Function 11
   symmetry = symmetric
   dimension = 1x1
   data 1,1
   real FUNCTION 1
end


FUNCTION 1
   Name="psd"
   type  loglog
   data 4.0 1e-13
   data 4.49 1e-13
   data 4.5 4931280.0 // 2219.96  // for sine wave of 3.141165e3, want rms of sqrt(4933460)=2221.139.
   data 5.5 4931280.0 // 2219.96
   data 5.51 1e-13
   data 6.0 1e-13
end

// PSD magnitude based on integral function from wolfram alpha. Execute the following line:
// 4931280.000000*1.000000+integral 10^-13307.372658 * x^20382.441146 dx from x=4.490000 to x=4.500000 + integral 10^18487.81812
```

```
Frequency
   nodeset 1
   freq_min=4.0
   freq_max=6.0
   freq_step=0.01
end

LOADS
end

HISTORY
end

OUTPUTS
    vrms
end

ECHO
  mass
end

BLOCK 77
   rbar
end

BLOCK 99
  material AISI4140
end

BLOCK 100
   material AISI4140
end

block  1
dead
end

MATERIAL AISI4140
   E=29.0e6 // psi
   nu=0.32
   density=0.283 // lb/in^3
   // these values are not appropriate for this material
        Fatigue_A1 31.6
        Fatigue_A2 -14.0845
   fatigue_stress_scale 1.0e-3
end
```

11.72. Fatigue Output of Pinned Shell

Refer to section 8.3

```
SOLUTION
   title 'test of a simple pinned plate for fatigue'
   case statics
       statics
       load=11
   case eig
        eigen
        nmodes=1
   case ran
        modalranvib
        noSVD
   case nb
        fatigue
           method=wirsching
END

FILE
   geometry_file 'pinned_plate_fatigue.exo'
END

Ranloads
   matrix 97
   load=1
      sideset 1
      pressure 1
END

matrix-function 97
   dimension 1x1
   symmetry=symmetric
   data 1,1
   real function 99
end

function 99
   type linear
   data 1 1e-20
   data 4 1e-20
   data 4.01 1
   data 4.99 1
   data 5.00 1e-20
   data 500 1e-20
end


frequency
  freq_min 4
  freq_max  5
  freq_step  0.001
  block 1 displacement
end


damping
end

BOUNDARY
  nodeset 1
   x=0 y=0 z=0
  nodeset 2
   x=0 y=0 z=0
END
```

```
OUTPUTS
   disp
   vrms
   stress
END

ECHO
 input
 mass
END

LOAD 11
   sideset 1
       pressure 1
END

LOAD 14
   sideset 1
       pressure 1
       function=14
END

function 14
   // white noise
   type linear
   data 0 1.0
   data 1e5 1.0
end

BLOCK 1
    material 3
END

MATERIAL 3
        E = 1e7
        nu = .3
        density 0.000259
        Fatigue_A1 12.1689
        Fatigue_A2 -3
        Stress_Ratio -1.0
        Fatigue_Stress_Scale=1e-4
END
```

11.73. Periodic Boundary Conditions

Refer to section 3.5 for details of the test.

```
SOLUTION
    solver=gdsw
    statics
END

FILE
    geometry_file 'SingleVoidCenterPbc.exo'
END

BOUNDARY
    nodeset 1
       x=0 y=0 z=0
    nodeset 2
       x=0 z=0
    nodeset 2
       x=0
END

BEGIN-PERIODIC
    side a = 1
    side b = 2
    name = X_directional_PBC
    search tolerance = 1e-2
    geometric offset = -1.0 0.0 0.0
    Ux = -1.5
END

LOADS
END

HISTORY
    element stress nearest location  0.0 0.4 0.0 as ExpectedMaxStress1
    element stress nearest location  0.0 0.0 0.4 as ExpectedMaxStress2
    element stress nearest location -0.4 0.0 0.0 as ExpectedMinStress
END

OUTPUTS
    displacement
    stress
END

ECHO
  MPC
END

BLOCK 1
    material "simple_solid"
END

MATERIAL "simple_solid"
    E 100.0
    nu 0.3
    density 1.0
END
```

11.74. Moving Mesh MPCs

Refer to section 3.7 for details of the test.

```
SOLUTION
    solver=gdsw
  case trans
  transient
    time_step {time_step}   //1.0e-4
    nsteps {nsteps}  //150
    nskip {nskip}  //10
    nUpdateConstraints = 1
    predictorcorrector = 0
END

FILE
  geometry_file = {geometry_file}   //brick_gap.g
END

LINESAMPLE
  samples per line 1000
  endpoint -4  0.  0.   4 0. 0.
  format mfile
END


LOADS
  sideset 1
  acoustic_accel = 0.0
  function 1
END

INITIAL-CONDITIONS
  acoustics = by_block
END

FUNCTION 1
  type linear
  data 0 0
  data 1 0
END

BOUNDARY
  sideset 2
    absorbing
END


OUTPUTS
    apressure
END

ECHO
    none
END

BLOCK 1
  acoustics 4
  material "air"
END

BLOCK 2
  acoustics 2
  material "air"
END

MATERIAL "air"
```

```
    density 1.293
        acoustic
        c0 332.0
END

begin contact definition
  gap removal = off
  skin all blocks = on
  begin interaction defaults
     general contact = on
  end
end

GDSW
    solver_tol = 1e-8
END
```

11.75. Nodal Loading vs Sideset Loading for Modal Random Vibration

Refer to section 8.4

```
// Flat Plate Problem Solution in Roark

solution
case 'eig'
eigen
       nmodes=50
case 'randomvib'
modalranvib
end

RANLOADS
matrix = 1
load = 1
nodeset 10
force = 0 0 1
scale = 9.3234e-4
END

MATRIX-FUNCTION 1
name 'pressure spectral density'
symmetry = hermitian
dimension = 1x1
data 1,1
real function 1
END

FUNCTION 1
name = 'psd'
type = 'loglog'
data 10.0   690.0
data 20.0   690.0
  data 30.0   6900.0
data 100.0  6900.0
data 500.0  690.0
data 1000.0 690.0
END

parameters
end

damping
gamma 0.02
end

FREQUENCY
method=log
freq_min 1.0
freq_max 1000
NF 1000
nodeset 5
disp
accel
END

file
    geometry_file 'flat_input.exo'
end

boundary
    nodeset 1
z = 0.0
nodeset 2
z = 0.0
```

```
nodeset 3
fixed
nodeset 4
fixed
end

history
nodeset '5'
disp
end

outputs
  disp
end

echo
end

block 1
    HEXSHELL
    sideset 1
    material "Example-2"
end

material "Example-2"
    isotropic
    density = 8.56e3
    nu = 0.34
    E = 9.02e10
end
```

11.76. Multidirectional Periodic BC: Periodic Volume Elements

Refer to section 3.6 for details of the test.

```
SOLUTION
    solver=gdsw
    statics
END

FILE
    geometry_file 'SingleVoidCenterPve.exo'
END

BOUNDARY
    nodeset 1
       x=0 y=0 z=0
END

BEGIN-PERIODIC
    side a = 1
    side b = 2
    name = X_directional_PBC
    search tolerance = 1e-4
//    geometric offset = 1.0 0.0 0.0
    Ux = 1.5
    Uy = 1.0
    Uz = 0.5
END

BEGIN-PERIODIC
    side a = 3
    side b = 4
    name = Y_directional_PBC
    search tolerance = 1e-4
//    geometric offset = 0.0 1.0 0.0
    Ux = 1.0
    Uy = -1.0
    Uz = 0.25
END

BEGIN-PERIODIC
    side a = 5
    side b = 6
    name = Z_directional_PBC
    search tolerance = 1e-4
//    geometric offset = 0.0 0.0 1.0
    Ux = 0.5
    Uy = 0.25
    Uz = -0.5
END

LOADS
END

HISTORY
    element stress nearest location  -0.1 -0.5 -0.5 as Stress1
    element stress nearest location  -0.5 -0.1 -0.5 as Stress2
    element stress nearest location  -0.5 -0.5 -0.1 as Stress3
END

OUTPUTS
    displacement
    stress
END

ECHO
  MPC
```

```
END

BLOCK 1
    material "simple_solid"
END

MATERIAL "simple_solid"
    E 100.0
    nu 0.3
    density 1.0
END
```

12. MAKING THE VERIFICATION DOCUMENT

This appendix provides instructions to developers to assist in building this reference. It is not of general use to analysts. Note that this procedure depends on the code, docs, and test repositories: make sure they are *all* up to date.

There are two steps. If an issue arises, and it's necessary to repeat this process, it is necessary to restart from step 1 if one or more tests have changed significantly.

NOTE: all of the following steps are also contained in a single script, "RunMe.sh".

Step 1 is to run the tests. Remove a pre-existing `results` directory. Be aware that even if `makeLocalDocuments.py` claims success, one or more of the individual LaTeX files may be broken.

```
cd /scratch/$USER/code
assign -p Salinas_rtest -k self-documenting
assign -p InverseOpt_rtest/InverseSD_rtest -k self-documenting --union
assign -p arpeggio_rtest/aria_sd -k self-documenting --union
assign -p arpeggio_rtest/salinas_verification -k self-documenting --union
assign -p sd_sm_coupled_rtest/verification_manual -k self-documenting --union
bake4tests.sh -e release
rm -rf results
testrun -e release --save-all-results -D
```

If it is necessary to repeat the second step, and no tests have changed, then (fortunately) skip the first step and start here. The last step is generating a single, concatenated verification document. As many supporting files are in the docs/Salinas/doc directory, we go to that directory to run the scripts.

```
cd /scratch/$USER/docs/Salinas/doc
ln -sf /scratch/$USER/code/results
make verificationAutodoc.pdf
xdg-open Verification/verificationAutodoc.pdf
```

If step 2 fails, the tail of an `.aux` will point to the cause.

Finally, you may clean up that directory.

```
make clean
unlink results
```

Note however, the SrcVerification and InpVerification files may need to be manually updated. There is a tool to help! Use "gatherLocalTests.sh" to generate a list of all tests in the results directory. These are in the right format to be added to verificationAutodocSrc, but must be copied over by hand. I've also recently found that the graphicspath should be terminated with "/", and not with a space. LaTeX is picky about that.

13. RICHARDSON EXTRAPOLATION

Richardson extrapolation[44] is a numerical technique. The convergence of a solution is identified and used to provide an improved accuracy solution. We here discuss this technique as applied to a finite element model.*

Assume that an exact solution, a_o is sought and that the mesh with a characteristic element length h is within the region of geometric convergence.† The solution, a_o, may be an eigenvalue for example. In that region, the error may be written,

$$err_h = a(h) - a_o = C h^n \tag{13.0.1}$$

where C and n are unknown.

Take another mesh of characteristic element size, αh.‡

$$a(\alpha h) - a_o = C\alpha^n h^n \tag{13.0.2}$$

We further refine the mesh.

$$a(\alpha^2 h) - a_o = C\alpha^{2n} h^n \tag{13.0.3}$$

There are thus three equations to solve for the three unknowns, C, n and a_o.

$$a(h) - a(\alpha h) = Ch^n - \alpha^n Ch^n = Ch^n(1-\alpha^n) \tag{13.0.4}$$

$$a(\alpha h) - a(\alpha^2 h) = \alpha^n Ch^n - \alpha^{2n} Ch^n = Ch^n\alpha^n(1-\alpha^n) \tag{13.0.5}$$

Thus,

$$\alpha^n = \frac{a(\alpha h) - a(\alpha^2 h)}{a(h) - a(\alpha h)} \tag{13.0.6}$$

And,

$$n = \frac{\log\left(a(\alpha h) - a(\alpha^2 h)\right) - \log\left(a(h) - a(\alpha h)\right)}{\log(\alpha)} \tag{13.0.7}$$

Knowing n, we solve for a_o.

$$a_o = \frac{a(\alpha h) - \alpha^n a(h)}{1-\alpha^n} \tag{13.0.8}$$

Having a_o, one may plot $a(h) - a_o$ versus mesh size on a log-log plot and achieve a line. A fourth mesh is necessary to confirm that we are in the region of geometric convergence.

The extrapolation must be performed using the FEM predictions at a node or element center which does not change spatial location during mesh refinement. If a nodal variable is chosen, $1/\alpha$ will be even (2). For element centroids, odd values of $1/\alpha$ are needed so the element centroid does not move during refinement.

Richardson extrapolation is valuable because it provides both an improved estimate for a_o, and a convergence rate, n. Typically *a priori* estimates for this rate exist. While it is not practical to accomplish 4 levels of mesh refinement on most real models, the technique can be valuable for determining the convergence rates of simpler examples.

---

*Richardson extrapolation was first developed in 1910. It is a well established technique. This description is based on notes from Dan Segalman.

†The region of geometric convergence is that part of the solution where the error is decreasing monotonically, and may be well represented by a decaying exponential. Richardson's extrapolation allows an approach either from above or below (i.e. the error may have either sign). This write up describes convergence from above.

‡Usually we take $\alpha = 1/2$, but other values are sometimes useful. Also, the mesh need not be uniform, but the mesh does need to be scaled uniformly. For example, slicing each element in half in each dimension does result in a uniform refinement with $\alpha = 0.5$.

14. LEGACY TEST MATRIX

The following tables identifies the verification tests for **Sierra/SD**, and provides a cross reference between the descriptions in this document and the tests run. Tests are found in two major test systems. The `Salinas_rtest/test_tool` tests contain the regression tests, and some of the verification tests. The `Salinas_rtest` directory contains the remainder of the tests.

Table 0-1. – Test Matrix.

Dir/Name of Test	Doc. Table	Row	Ref Table	Element Type
beam_analytic/cantilever_free_beam2_test	7-58	2	*3 1a*	Beam2
./cantilever_free_tria3_test	7-58	3	*3 1a*	Tria3
./cantilever_free_tria3r_test	7-58	4	*3 1a*	Tria3⊥
./simply_simply_beam2_test	7-58	7	*3 1e*	Beam2
./simply_simply_tria3_test	7-58	8	*3 1a*	Tria3
./simply_simply_tria3r_test	7-58	9	*3 1a*	Tria3⊥
./cantilever_guided_beam2_test	7-58	11	*3.3b*	Beam2
beam-curved/roark_table17_1_test	7-59	2	*17.1*	Beam2
./roark_table17_2_test	7-59	4	*17.1*	Beam2
./roark_table17_3_test	7-59	6	*17.1*	Beam2
beam_eigen/free_free_test	7-66	2	*8-1.1*	Beam2
beam_eigen/free_sliding_test	7-66	4	*8-1.2*	Beam2
beam_eigen/clamped_free_test	7-66	6	*8-1.3*	Beam2
beam_eigen/pinned_pinned_test	7-66	8	*8-1.5*	Beam2
beam-mass/blevins_table6-2_19_test	7-65	2	*6-2.19*	Beam2
beam-mass/blevins_table6-2_20_test	7-65	4	*6-2.20*	Beam2
beam-mass/blevins_table6-2_22_test	7-65	6	*6-2.22*	Beam2
plate_annular/roark_table24_1a_test	7-60	2	*24.1a*	Tria3
plate_annular/roark_table24_1b_test	7-60	4	*24.1b*	Tria3
plate_annular/roark_table24_1e_test	7-60	6	*24.1e*	Tria3
plate_rectangular/roark_table26_1a_test	7-61	3	*26.1a*	QuadT
plate_rectangular/roark_table26_1a_t_test	7-61	2	*26.1a*	Tria3
plate_rectangular/roark_table26_8a_test	7-61	6	*26.8a*	QuadT
plate_rectangular/roark_table26_8a_t_test	7-61	5	*26.8a*	Tria3
spring-mass/blevins_table6-2_2_test	7-64	2	*6-2.2*	spring
spring-mass/blevins_table6-2_18_test	7-64	4	*6-2.18*	spring

Table 0-2. – Test Matrix (cont).

Dir/Name of Test	Doc. Table	Row	Ref Table	Element Type
thinShellsOfRevolution/.				
./roark_table28_1a_hex8_test	7-62	3	*28.1a*	Hex8
./roark_table28_1a_tria3_test	7-62	2	*28.1a*	Tria3
./roark_table28_1b_hex8_test	7-62	6	*28.1b*	Hex8
./roark_table28_1b_tria3_test	7-62	5	*28.1b*	Tria3
shaft/fixed_free_beam2_test	7-67	2	*8-19.2*	Beam2
shaft/fixed_free_hex8_test	7-67	3	*8-19.2*	Hex8
plate_eigen_circ/free_test	7-69	2	*11-1.1*	QuadT
plate_eigen_circ/simple_test	7-69	4	*11-1.2*	QuadT
plate_eigen_circ/clamped_test	7-69	6	*11-1.3*	QuadT
plate_eigen_circ/clamped_mass_test	7-69	8	*11-1.12*	QuadT
plate_eigen_rect/all_edges_free_test	7-70	2	*11-4.1*	Tria3
plate_eigen_rect/all_edges_fixed_test	7-70	4	*11.4.21*	Tria3
plate_eigen_rect/all_edges_simple_test	7-70	6	*11-4.16*	Tria3
plate_eigen_rect/sFixed_lFree_sSS_lFree_test	7-70	8	*11-4.6*	Tria3

This page intentionally left blank.

BIBLIOGRAPHY

[1] Ertas. A., J. T. Krafcik, and S. Ekwaro-Osire. "Performance Of An Anisotropic Allman/DKT 3-Node Thing Triangular Flat Shell Element". In: *Composite Engineering* 2.4 (1992), pp. 269–280 (cit. on p. 275).

[2] D. J. Allman. "A Compatible Triangular Element Including Vertex Rotations for Plane Elasticity Problems". In: *Comput. and Struct.* 19.1-2 (1996), pp. 1–8 (cit. on p. 275).

[3] Kenneth F. Alvin. "A method for Treating Discretization Error in Nondeterministic Analysis". In: *AIAA Journal* 99.1611 (1999) (cit. on p. 268).

[4] V. Anes et al. "New approach for analysis of complex multiaxial loading paths". In: *International Journal of Fatigue* 62 (2014), pp. 21–33 (cit. on p. 234).

[5] Jean-Louis Batoz, Klaus-Jurgen Bathe, and Lee-Wing Ho. "A Study of Three-Node Triangular Plate Bending Elements". In: *Int. J. Numer. Meth. Engng.* 15 (1980), pp. 1771–1812 (cit. on p. 275).

[6] Boris Beizer. *Software Testing Techniques*. Intnl Thompson Computer Press, 1990 (cit. on p. 260).

[7] D. Blackstock. "Connection between the Fay and Fubini Solutions for Plane Sound Waves of Finite Amplitude". In: *JASA* 39 (1966), pp. 1019–1026 (cit. on p. 382).

[8] K. Blakely. *MSC/NASTRAN Users Guide: Basic Dynamic Analysis*. Vol. 68. The MacNeal-Schwendler Corporation, 1993 (cit. on p. 420).

[9] Hans Heinrich Bleich and Ivan Seth Sandler. "Interaction between structures and bilinear fluids". In: *International Journal Solids and Structures* 6.5 (1970), pp. 617–639 (cit. on p. 122).

[10] Robert D. Blevins. *Formulas for Natural Frequency and Mode Shape*. Malabar, FL, USA: Krieger, 1984 (cit. on pp. 118, 133, 157, 162, 401, 443).

[11] Edward A. Bourcheron et al. *Sandia National Laboratories Advanced Simulation and Computing (ASC) Software Quality Plan Part 1: ASC Software Quality Engineering Practices Version 1.0*. Tech. rep. SAND2004-6602. PO Box 5800, Albuquerque, NM 87185-5800: Sandia National Laboratories, 2005 (cit. on p. 3).

[12] Gregory Bunting et al. "Parallel Ellipsoidal Perfectly Matched Layers for Acoustic Helmholtz Problems on Exterior Domains". In: *Journal of Computational Acoustics* (2018) (cit. on p. 184).

[13] J. Chung and G. M. Hulbert. "A Time Integration Algorithm for Structural Dynamics with Improved Numerical Dissipation - The Generalized Alpha Method". In: *JAM* 60.2 (1993), pp. 371–375 (cit. on p. 394).

[14] *COMSOL MEMS Module User Guide, version 5.4*. COMSOL Inc, 2020 (cit. on pp. 253, 255).

[15] R. R. Craig. *Structural Dynamics: An Introduction to Computer Methods*. John Wiley & Sons, 1981 (cit. on p. 398).

[16] J. M. Dickens, J. M. Nagawa, and M. J. Wittbrodt. "A critique of mode acceleration and modal truncation augmentation methods for modal response analysis". In: *Comput. and Struct.* 62.6 (1997), pp. 985–998 (cit. on p. 418).

[17] C. Dohrmann, S. Key, and M. Heinstein. "A Method for Connecting Dissimilar Finite Element Meshes in Two Dimensions". In: *Int. J. Numer. Meth. Engng.* 48 (2000), pp. 655–678 (cit. on p. 326).

[18] C. Dohrmann, S. Key, and M. Heinstein. "Methods for Connecting Dissimilar Three-Dimensional Finite Element Meshes". In: *Int. J. Numer. Meth. Engng.* 47 (2000), pp. 1057–1080 (cit. on p. 326).

[19] A. Ertas, J. T. Krafcik, and S. Ekwaro-Osire. "Explicit Formulation of an Anisotropic Allman/DKT 3-Node Thin Triangular Flat Shell Elements". In: *Composite Material Technololgy* 37 (1991), pp. 249–255 (cit. on p. 275).

[20] G. C. Everstine and F. M. Henderson. "Coupled finite element/boundary element approach for fluid/structure interaction". In: *JASA* 87.5 (1990), pp. 1938–1947 (cit. on p. 333).

[21] C. Felippa and J. DeRuntz. "Finite Element Analysis of Shock-Induced Hull Cavitation". In: *Computer Meth. in Appl. Mech. Eng.* 44 (1984), pp. 297–337 (cit. on p. 123).

[22] C. A. Felippa. *The SS8 Solid-Shell Element: A Fortran Implementation*. Tech. rep. CU-CAS-02-04. Univ. Colo. at Boulder, 2002 (cit. on p. 136).

[23] C. A. Felippa. *The SS8 Solid-Shell Element: Formulation and a Mathematica Implementation*. Tech. rep. CU-CAS-02-03. Univ. Colo. at Boulder, 2002 (cit. on pp. 136, 273, 274).

[24] F. Fuentes et al. "Orientation embedded high order shape functions for the exact sequence elements of all shapes". In: *Computers and Mathematics with Applications* 70.1 (2015), pp. 353–458 (cit. on p. 2).

[25] N. Guo, P. Cawley, and D. Hitchings. "The finite element analysis of the vibration characteristics of piezoelectric discs". In: *Journal of Sound and Vibration* 159.1 (1992), pp. 115–138 (cit. on pp. 257, 258).

[26] M. F. Hamilton and D. T. Blackstock. *Nonlinear Acoustics*. Academic Press, 1998 (cit. on pp. 381, 382).

[27] Daniel C. Hammerand. *Laminated Composites Modeling In Adagio/Presto*. Tech. rep. SAND2004-2143. Sandia National Laboratories, May 2004 (cit. on pp. 285, 287).

[28] J. Hoffelner, H. Landes, and R. Lerch. "Calculation of Acoustic Streaming Velocity and Radiation Force Based on Finite Element Simulations of Nonlinear Wave Propagation". In: *Proceedings of IEEE Ultrasonics Symposium* 1 (2000), pp. 585–588 (cit. on p. 381).

[29] J. Hoffelner et al. “Finite Element Simulation of Nonlinear Wave Propagation in Thermoviscous Fluids Including Dissipation”. In: *IEEE Transactions on Ultrasonics, Ferroelectrics, and Frequency Control* 48.3 (2001), pp. 779–786 (cit. on p. 381).

[30] H. Huang. “Transient Interaction of Plane Acoustic Waves with a Spherical Elastic Shell”. In: *Journal of the Acoustical Society of America* 45.3 (1969), pp. 661–670 (cit. on p. 346).

[31] Thomas J. R. Hughes. *The Finite Element Method–Linear Static and Dynamic Finite Element Analysis*. Prentice-Hall, Inc, 1987 (cit. on p. 156).

[32] Kinsler et al. *Fundamentals of Acoustics*. John Wiley & Sons, 1982 (cit. on pp. 294, 319, 364, 402, 403).

[33] V. P. Kuznetsov. “Equations of Nonlinear Acoustics”. In: *Sov. Phys. Acoust.* 16 (1971), pp. 467–470 (cit. on p. 381).

[34] Richard H. MacNeal and Robert L. Harder. “A Proposed Standard Set of Problems to Test Finite Element Accuracy”. In: *Finite Elements in Analysis and Design* 1 (June 1985), pp. 3–20 (cit. on pp. 260, 261, 450).

[35] R. Martin. *Clean Code: A Handbook of Agile Software Craftsmanship*. Prentice Hall, 2008 (cit. on pp. 4, 6).

[36] David R. Martinez and Garth M. Reese. *Structural Dynamics Computational Plan*. Tech. rep. Unpublished. PO Box 5800, Albuquerque, NM 87185-5800: Sandia National Laboratories, 1996 (cit. on p. 260).

[37] J. L. Meriam and L. G. Kraige. *Engineering Mechanics Volume 2 - Dynamics*. John Wiley & Sons, 1986 (cit. on p. 431).

[38] Morse and Ingard. *Theoretical Acoustics*. Mcgraw-Hill Book Company, 1968 (cit. on p. 366).

[39] Thomas Moyer et al. “Navy Enhanced Sierra Mechanics (NESM): Toolbox for Predicting Navy Shock and Damage”. In: *Computing in Science and Engineering* 18.6 (2016), pp. 10–18 (cit. on p. 305).

[40] Glenford J. Myers. *The Art of Software Testing*. John Wiley & Sons, 1979 (cit. on pp. 260, 460).

[41] A. D. Pierce. *Acoustics: An Introduction to Its Physical Principles and Applications*. ASA, 1989 (cit. on pp. 44, 309, 319, 323, 336, 369, 371, 381, 382).

[42] Douglass Post et al. “The Computational Research and Engineering Acquisition Tools and Environments (CREATE) Program”. In: *Computing in Science and Engineering* 18.6 (2016), pp. 7–9 (cit. on p. 305).

[43] Garth M. Reese. *Salinas - RV Modeling*. Tech. rep. Unpublished Presentation. PO Box 5800, Albuquerque, NM 87185-5800: Sandia National Laboratories, 1998 (cit. on p. 260).

[44] L. F. Richardson. “The Approximate Arithmetic Solution by Finite Differences of Physical Problems Involving Differential Equations, With Applications to the Stresses in a Masonry Dam”. In: *Philosophical Transactions of the Royal Society of London. A* 210 (1910), pp. 307–357 (cit. on pp. 268, 593).

[45] Peter J. Rohl and Garth Reese. “A Practical Look at the Massively Parallel Code Salinas”. In: *Presented at the 47nd AIAA/ASME/ASCE/AHS/ASC SDM* (Apr. 2006) (cit. on p. 454).

[46] S D Team. *SD – User's Manual*. Tech. rep. SAND2021-12052. PO Box 5800, Albuquerque, NM 87185-5800: Sandia National Laboratories, 2021 (cit. on pp. 4, 415).

[47] S D Team. *Sierra Structural Dynamics - Theory Manual*. Tech. rep. SAND2021-11328. PO Box 5800, Albuquerque, NM 87185-5800: Sandia National Laboratory, 2021 (cit. on pp. 4, 325).

[48] S D Team. *Sierra Structural Dynamics How To*. Tech. rep. SAND2021-11328. PO Box 5800, Albuquerque, NM 87185-5800: Sandia National Laboratories, 2020 (cit. on p. 415).

[49] Daniel J. Segalman. *A Four-Parameter Iwan Model for Lap-Type Joints*. Tech. rep. SAND 2002-3828. Sandia National Laboratories, Nov. 2002 (cit. on p. 288).

[50] Todd Simmermacher and Dan Morganthaler. *Lockheed Martin Shared Vision Virtual Testing Final Report*. Tech. rep. Internal Report. PO Box 5800, Albuquerque, NM 87185-5800: Sandia National Laboratories, 2003 (cit. on p. 454).

[51] MSC Software. *MSC/NASTRAN 2017 Superelements User's Guide*. The MacNeal-Schwendler Corporation, 2016 (cit. on p. 60).

[52] M. A. Sprague and T. L. Geers. “Response of Empty and Fluid-Filled, Submerged Spherical Shells to Plane and Spherical, Step-Exponential Acoustic Waves”. In: *Shock and Vibration* 6 (1999), pp. 147–157 (cit. on p. 347).

[53] S. Timoshenko. *Strength of Materials*. 3rd ed. D. Van Nostrand Company, Inc., 1955 (cit. on p. 273).

[54] S. Timoshenko. *Theory of Elastic Stability*. McGraw Hill Book Company, 1936 (cit. on p. 125).

[55] Timothy G. Trucano, Martin Pilch, and William L. Oberkampf. *On the role of Code Comparisons in Verification and Validation*. Tech. rep. SAND 2003-2752. PO Box 5800, Albuquerque, NM 87185-5800: Sandia National Laboratories, 2003 (cit. on p. 450).

[56] W. Weaver, Jr. and S. P. Timoshenko. *Vibration Problems in Engineering*. 5th ed. John Wiley and Sons, 1990 (cit. on p. 418).

[57] Warren C. Young. *Roark's Formulas for Stress & Strain*. 6th ed. McGraw-Hill Book Company, 1989 (cit. on pp. 273, 440).

[58] John D. Zepper et al. *ASCI Applications Software Quality Engineering Practices*. Tech. rep. SAND2002-0121. PO Box 5800, Albuquerque, NM 87185-5800: Sandia National Laboratories, 2002 (cit. on p. 3).

[59] X D Zhang and C T Sun. “Formulation of an Adaptive Sandwich Beam”. In: *Smart Materials and Structures* 5.6 (1996), pp. 814–823 (cit. on p. 250).

This page intentionally left blank.

DISTRIBUTION

Hardcopy—Internal

Number of Copies	Name	Org.	Mailstop
1	K. H. Pierson	1542	0845

Email—Internal [redacted]

Name	Org.	Sandia Email Address
Technical Library	1911	sanddocs@sandia.gov

This page intentionally left blank.

Sandia National Laboratories

Sandia National Laboratories is a multimission laboratory managed and operated by National Technology & Engineering Solutions of Sandia LLC, a wholly owned subsidiary of Honeywell International Inc., for the U.S. Department of Energy's National Nuclear Security Administration under contract DE-NA0003525.